



Stephen P. Radzevich
Editor

Recent Advances in Gearing

Scientific Theory and Applications

 Springer

Recent Advances in Gearing

Stephen P. Radzevich
Editor

Recent Advances in Gearing

Scientific Theory and Applications

 Springer

Editor

Stephen P. Radzevich
Mechanical Engineering
Sterling Heights, MI, USA

ISBN 978-3-030-64637-0 ISBN 978-3-030-64638-7 (eBook)
<https://doi.org/10.1007/978-3-030-64638-7>

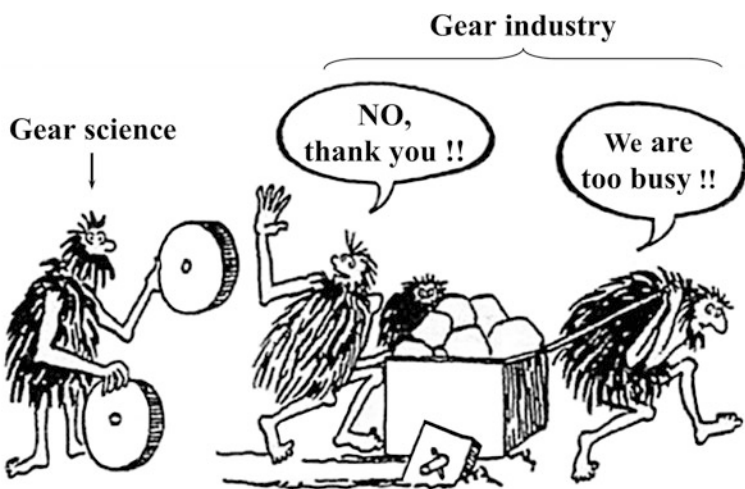
© Springer Nature Switzerland AG 2022

This work is subject to copyright. All rights are solely and exclusively licensed by the Publisher, whether the whole or part of the material is concerned, specifically the rights of translation, reprinting, reuse of illustrations, recitation, broadcasting, reproduction on microfilms or in any other physical way, and transmission or information storage and retrieval, electronic adaptation, computer software, or by similar or dissimilar methodology now known or hereafter developed.

The use of general descriptive names, registered names, trademarks, service marks, etc. in this publication does not imply, even in the absence of a specific statement, that such names are exempt from the relevant protective laws and regulations and therefore free for general use.

The publisher, the authors, and the editors are safe to assume that the advice and information in this book are believed to be true and accurate at the date of publication. Neither the publisher nor the authors or the editors give a warranty, expressed or implied, with respect to the material contained herein or for any errors or omissions that may have been made. The publisher remains neutral with regard to jurisdictional claims in published maps and institutional affiliations.

This Springer imprint is published by the registered company Springer Nature Switzerland AG
The registered company address is: Gewerbestrasse 11, 6330 Cham, Switzerland



Introduction

Knowledge is power
(*Scientia potestas est*) – Francis Bacon (1561–1626)

Historical Background

Gears and gear transmissions are extensively used in the nowadays industry. Practically, gears can be found out in the design of almost all mechanisms. Despite enormous amount of the research in the field has been carried out in the past, the gear science is still extensively evolving nowadays. The accumulated experience in the field of gearing, both, from the theory side, and from the experimental side, is summarized in several fundamental monographs, novel attempts had been undertaken in the recent years, and important novel results of the research are obtained in the field of gearing. Latest accomplishments in the gear science are outlined in this volume.

Uniqueness of this Publication

Newest accomplishments in the gear theory, gear design, gear production, and gear application are covered in this book. A team of the world lead experts in gear science have contributed their achievements in the field of gearing. The most important subjects are the gear science are covered in the book. Numerous gaps between the current needs of the advanced gear designers and the gear manufacturers are bridged by the gear science. This book is a unique one as the latest accomplishments in the scientific theory of gearing and in production and application of gears are considered to the best possible extent.

Intended Audience

This book is written by world-known experts in the field of gear design, gear production, and gear application. This volume is dedicated to gear experts, concerned with gears and gear transmissions of advanced design: first of all, of gear drives with a highest possible power density (or, in other words, “*power-to-mass ratio*”) and low-noise (or almost “*noiseless*”) gear transmissions. Most gear engineers and gear researchers from the industry, as well as graduate students will be benefitted by the book.

Organization of this Book

The book contains nine chapters. The scientific theory of gearing, gear design, and gear production are covered in these chapters.

Chapter 1 of the book deals with vector diagrams of gear pairs, and with a potential possibility of their application to classify gears and gear pairs. The concept of vector diagram of gearing is briefly outlined at the very beginning of the chapter. It is shown that all commonly used in the today’s industry gearing feature one degree of freedom. Transmission of a rotary motion from an input shaft to an output shaft is the only purpose this degree of freedom serves to. This discussion is followed by a detailed analysis of gearing with one-, two-, and three complementary degrees of freedom. Non-circular gearing is an example of gearing with one (or two) complementary degree of freedom. This section of the chapter is ended by a scientific classification of all possible kinds of gearing. All the kinds of gearing, that is gearing with no complementary *DoF*, as well as gearing having up to three complementary *DoF*, are covered in the proposed classification. Then, a transition from the vector diagrams to gear tooth flanks is discussed. For this purpose, a plurality of potentially possible and desirable lines of contact that feature reasonable geometry are involved into the consideration. Taken as a whole, the reported results of the analysis form a potentially complete and self-consistent classification of gearing of all kinds.

Chapter 2. The proposed chapter starts with the theory defining *S*– gears and their properties and compares *S*– and involute gears. Most of the text deals with cylindrical spur gears. The basic idea behind the *S*– gear theory is to define a rack profile which would define a curved path of contact. So, the *S*– rack profile is defined as a half-symmetric parabolic type function. Mathematical formulation thus enables a calculation from the rack, via the path of contact to gear flanks with any number of teeth and reversely.

Chapter 3. The research deals with kinematic pairs in gearing, as well as in mechanisms of other design. The introduced by *Franz Reuleaux* concepts of lower and higher kinematic pairs are briefly discussed, and insufficiency of distinguishing only of these two groups of kinematic pairs (that is, of “*lower*” and “*higher*” kinematic pairs) is stated. It is stressed on that gearing of all designs feature either

line or point contact of the interacting tooth flanks of a gear and a mating pinion. Both of them (namely, line and point contacts of the interacting tooth flanks) are commonly referred to as “*higher kinematic pairs*.” Only gear couplings feature the so-called *lower kinematic pairs*, when the interacting tooth flanks make “*surface-to-surface contact*.” The performance of gearing of all kinds significantly depends on the design parameters of the kinematic pairs in a gear pair. Insufficiency of the nowadays interpretation of kinematic pairs is revealed by the undertaken research. It is shown that instead of kinematic pairs of only two kinds (that is, of lower, and of higher kinematic pairs), 126 different kinds of kinematic pairs have to be taken into account. All the newly discovered kinematic pairs are classified.

Chapter 4. Plastic gears have been used for decades in a wide variety of applications such as consumer articles or electromechanical actuators in the automotive sector. Plastic-specific material properties such as low density and high damping characteristics as well as the possibility of mass production through injection molding are advantageous and contribute to the increasing application of plastic gears. However, the comparatively large differences in material properties compared to steel result in plastic gears mostly being used in low-power drives. In particular, the high temperature dependence of the material properties and lower strength present a challenge for the application of plastic gears.

In most cases, the gears are running dry or under starved lubrication. In the context of these operational conditions, the transmission of motion is often of principal importance as the potential to transmit power is limited due to the high level of frictional heat in combination with limited capability for heat removal.

The use of a lubricant is required for the transmission of increased power. Grease lubrication offers the possibility of heat dissipation and the reduction of wear. If even higher power is to be transmitted, oil lubrication is required. Operation under oil lubrication separates the tooth flanks from each other and ensures effective dissipation of the heat generated in tooth contact. Today, VDI 2736 is mainly used for the design and calculation of plastic gears. In addition to information on the design of the wheel body and production, this guideline contains approaches for temperature calculation and load carrying capacity calculation. Due to the high temperature dependency of the material properties of thermoplastic materials, knowledge of the gear temperature is of essential importance in the design of plastic gears and one of the main steps of the load carrying capacity calculation.

VDI 2736 uses the basic principles of the standard DIN 3990 developed for steel gears to calculate the tooth root and tooth flank load capacity. Especially the high deflections under load compared to steel gears are currently not sufficiently considered in VDI 2736. Current research provides new knowledge on the consideration of deflection effects and their influence on the gear carrying capacity of modern thermoplastic materials and contributes to the optimized design of plastic gears.

On the material side, new high-performance plastics are constantly being developed, which further increase the temperature resistance and strength properties required. In addition to widely used materials such as polyacetal and polyamides,

polyetheretherketones, and other high-performance materials are increasingly being applied.

Today, the low availability of standardized strength values represents a challenge for the design of ideally dimensioned components. For this reason, in addition to the investigation of the thermal and tribological operating behavior of plastic gears, the generation of standardized determined strength values is of particular interest.

Chapter 5. Many objectives of gear design and manufacturing can be considered and resolved by task-based multifunctional conceptual design method developed on the base of career long experience of design and manufacturing of numerous custom-made machine tools, innovative hand tools, and other mechanical devices. Requirements of geometrical accuracy and manufacturing efficiency are major objectives for gear manufacturing technologies and for gear chamfering technologies in particular. To satisfy those requirements, the proposed task-based conceptual design methodology is modified and applied in a way to take into account specific needs and features of gear chamfering procedure. The proposed method of conceptual design method can be advantageously pointed out from existing design methodologies by direct consideration of challenged functions at any step of mechanism synthesis, thus avoiding the exhausting combinational search of large variety of options, by simultaneous consideration of several tasks, by similarity and repeatability of analyses and synthesis tools and design cycles, by development and usage of mechanical–functional models, and by quantitative evaluation of different design scenarios. The methodology of creation of gear chamfering mechanisms is serving as an example for extending the scope of application of conceptual, parametric, and analytical resources of the task-based method to the case of surface reproduction technological machines. A concept of multi-degree freedom duplication of different geometrical shapes is the base of methodology for creation of surface reproduction mechanisms, when two parallel chains are simulating first the geometrical concept of surface reproduction and the second a mechanical set of links and chains necessary for such reproduction. First, an analyzing methodology is applied for consideration and evaluation of various known conceptual diagrams and solutions for reproduction of chamfer surface. Then based on analyses of existing solutions proper point, linear and surface models are developed as basic and start structures for future mechanism development, and finally those models are upgraded by additional degrees of freedom and parallel chains for satisfying of remained challenges and functions of conceptual design. Thus, a number of design scenarios are created and filtered for evaluation and rejection of not valid solutions. In the end, a series of novel structures are created and proper manufacturing technology is worked out satisfying different needs of gear chamfering process. Conceptual design phase is commonly preceded by phase of analyses of existing solutions and proceeded by phase of parametrical design. Worthy to note that all three procedures are based on the same methodical base which conceptual phase has and hence have the same methodical values and same efficiency in application. An objective of parametric optimization for a type of gear chamfering mechanism is formulated as requirement of providing a stable surface quality along the involute pattern of a gear teeth. Scope of application of developed methodology of conceptual design is generalized and extended for

analyses and synthesis for a class of surface reproduction technological machines. Necessary and clarifying examples are presented for verification of validity and efficiency of task-based conceptual design methodology for surface reproduction mechanisms.

Chapter 6 of the book deals with the principal accomplishments in the scientific theory of gearing. The names of the scientists, who are credited with these accomplishments, are mentioned in a chronological order. Two periods of time are proposed to be considered. They are the *pre-Eulerian*, and the *post-Eulerian*, period of the evolution of the gear art. No principal accomplishments in the theory of gearing were attained in the *pre-Eulerian* period of evolution of the gear art. It is stated that scientific theory of gearing is originated from publication by *Leonhard Euler* of two of his famous papers (the eighteenth century). All the accomplishments in the scientific theory of gearing are achieved in the *post-Eulerian* period of evolution of the theory of gearing.

The “*main theorem of parallel-axes gearing*,” or, in other words, the “*conjugate action law*” in parallel-axes gearing, is loosely attributed to *R. Willis* (1841), which is not correct. *Charles Camus* has carried out a research on this subject, and he was the first (1733), who obtained a result that deserves to be remembered by the gear community. Unfortunately, *Ch. Camus* committed a principal mistake in his research, and he failed to formulate the “*conjugate action law*” of gearing correctly. In the final form, the “*main theorem of parallel-axes gearing*” was known to *L. Euler* and to *F. Savary*. Therefore, it is proposed to refer to the main theorem of parallel-axes gearing as to the “*Camus-Euler-Savary theorem of gearing*” (or just as to the “*CES– theorem of gearing*,” for simplicity).

A huge mistake in the theory of gearing was committed by *Th. Olivier* (1842). The negative effect of this mistake onto the evolution of the theory of gearing is discussed in detail. The contribution by *G. Grant* (1887) to the kinematics and geometry of intersected-axes gearing is discussed. The contribution by *V. Shishkov* (1948), that is, his well-known equation of contact, $\mathbf{n} \cdot \mathbf{V}_{\Sigma} = 0$, is outlined. Equation of conjugacy, $\mathbf{p}_{ln} \times \mathbf{V}_m \cdot \mathbf{n}_g = 0$ (*S.P. Radzevich*, 2018), of the interacting tooth flanks of a gear and a mating pinion is discussed. The introduced (in around 2008) concept of operating base pitch in gearing considered in detail. Latest accomplishments in the theory of gearing are summarized and briefly discussed in this section of the book. These accomplishments form the foundation of the self-consistent scientific theory of gearing (*S.P. Radzevich*, 2012, 2018). The scientific theory of gearing is not threatened with destruction, but only superstructure and development are expected (every scientific theory features this property).

Chapter 7 Hobs are extensively used in the nowadays industry to cut gears. This entails the necessity to improve the accuracy of hobs. Use of hyperboloidal-type hobs sounds promising for the improvement of the gear machining operation, along with the increasing accuracy of the hobbled gears. Hyperboloidal-type hobs may feature up to 7–11 starts. The number of cutting edges can reach up to 60–120 teeth.

Use of hyperboloidal-type hobs of the modern designs enables a significant increase in productivity on the gear hobbing operation and to improve the accuracy of the cut gears.

Chapter 8. The Torque Method is an easy way for kinematic and power analysis of planetary gear trains, both simple and compound ones. Moreover, it gives possibility of optimal choice of a structural scheme (and its parameters) of compound planetary gear trains.

In this chapter, most common ways of optimization of planetary gear trains are overviewed. Appropriate optimization criteria of the most common simple planetary gear train (with one external and one internal meshing) are discussed. Multi-objective choice of structural scheme and its parameters of two-carrier planetary gear trains is proposed. Two-carrier planetary gear trains with three and four external shafts are considered. The choice is made between all possible structural schemes of planetary gear trains in question through the torque method.

Chapter 9. Power transmission has been a challenge during human history. Men used gears to accomplish this task already at the emergence of our civilization. Gears were simple wooden aids at first, but the evidences of complex mechanical devices of antiquity exist. Water and animal powered devices were used during the middle ages, whereas the renaissance and subsequent development of science discovered steam engines. The combustion engine, the turbines, and electricity imposed new impact to the mechanical transmissions which developed up to contemporary highly efficient devices embedded into aircrafts, vehicles, machine tools, etc. The question is if there is still a possibility to improve gears, which are substantial part of these transmissions, in any way.

Contributed by Prof. *Stephen P. Radzevich*, appendices are titled as follows:

Appendix A: *Elements of Differential Geometry of Surfaces*

Appendix B: *Applied Coordinate Systems and Linear Transformations*

Appendix C: *Contact Geometry of a Gear and a Mating Pinion Tooth Flanks*

Appendix D: *Closest Distance of Approach between a Gear, and a Mating Pinion Tooth Flanks*

Appendix E: *On Inadequacy of the Terms “Wildhaber-Novikov Gearing,” and “W-N Gearing”*

It is likely this book is not free from omissions or mistakes; or that it is as clear and ambiguous as it should be. If you have any constructive suggestions, please communicate them to me via e-mail: radzevich@usa.com.

Stephen P. Radzevich

Scientific editor of:

Recent Advances in Gearing—Scientific Theory and Applications

Sterling Heights, MI, USA

July 31, 2020

Contents

1 Kinematic Foundations of Scientific Classification of Gearing	1
Stephen P. Radzevich	
2 Theory and Applications Based on S-Gear Geometry	51
Gorazd Hlebanja, Miha Erjavec, Matija Hriberšek, Luka Knez, and Simon Kulovec	
3 Kinematic Pairs: Novel Kinds and Classification	89
Stephen P. Radzevich	
4 High-Performance Plastic Gears	143
C. M. Illenberger, T. Tobie, and K. Stahl	
5 Application of Task-Based Conceptual Design Method for Gear Chamfering Mechanisms	183
Hrayr V. Darbinyan	
6 A Brief Overview of the Evolution of the Scientific Theory of Gearing	233
Stephen P. Radzevich	
7 Hyperboloid-Type Hobs: Design, Manufacture, and Application . . .	293
Valentyn Nastasenko	
8 Optimal Selection of the Structural Scheme of Compound Two-Carrier Planetary Gear Trains and Their Parameters	339
Dimitar P. Karaivanov and Sanjin Troha	
9 Development of Gears from the Antiquity to the Present Time	405
Jože Hlebanja and Gorazd Hlebanja	
Appendix A: Elements of Differential Geometry of Surfaces	435

Appendix B: Applied Coordinate Systems and Linear Transformations 455

Appendix C: Contact Geometry of a Gear and a Mating Pinion’ Tooth Flanks 493

Appendix D: Closest Distance of Approach between a Gear and a Mating Pinion’s Tooth Flanks 523

Appendix E: On Inadequacy of the Terms “Wildhaber-Novikov Gearing” and “W-N Gearing” 529

Index 541

Editors and Contributors

About the Editor



Stephen P. Radzevich is a Professor of Mechanical Engineering and a Professor of Manufacturing Engineering (Institution). He received the M.Sc. (1976), the Ph.D. (1982), and the Dr. (Eng)Sc. (1991)—all in mechanical engineering. Dr. Radzevich has extensive industrial experience in gear design and manufacture. He has developed numerous software packages dealing with CAD and CAM of precise gear finishing for a variety of industrial sponsors. His main research interest is Kinematic Geometry of Surface Generation, particularly with the focus on (a) precision gear design, (b) high power density gear trains, (c) torque share in multi-flow gear trains, (d) design of special purpose gear cutting/finishing tools, (e) design and machining (finishing) of precision gears for low-noise/noiseless transmissions of cars, light trucks, etc. Dr. Radzevich has spent about 40 years developing software, hardware, and other processes for gear design and optimization. Besides his work for industry, he trains engineering students at universities and gear engineers in companies. He authored and co-authored over 30 monographs, handbooks, and textbooks. The monographs entitled *Generation of Surfaces* (2001), *Kinematic Geometry of Surface Machining* (CRC Press, 2008), *CAD/CAM of Sculptured Surfaces on Multi-Axis NC Machine: The DG/K-Based Approach* (M&C Publishers, 2008), *Gear Cutting Tools: Fundamentals of Design and Computation* (CRC Press, 2010, 2nd edition 2017), *Precision Gear Shaving* (Nova Science Publishers, 2010), *Dudley's Handbook of Practical*

Gear Design and Manufacture (CRC Press, 2012, 2nd edition 2016), *Theory of Gearing: Kinematics, Geometry, and Synthesis* (CRC Press, 2012, 2nd edition 2018), *Geometry of Surfaces: A Practical Guide for Mechanical Engineers* (Wiley, 2013, 2nd edition Springer, 2019), and *Advances in Gear Design and Manufacture* (CRC Press, 2019) are among the recently published volumes. He also authored and co-authored about 350 scientific papers and holds over 260 patents on invention in the field, both US patents and International patents.

Contributors



Hrayr V. Darbinyan is a mechanical engineer with over 40 years of experience in the field. His extensive engineering experience has been grown into a task-based conceptual design methodology providing an approach for this less studied and understood phase of the mechanical design. Along the way of its development and application, the method has revealed its resources and regularities which helped the formation of two adjacent design phases—namely, the analysis of the prior art and parametric optimization of the already synthesized structure. Widely being tested on many custom-made machines and a large variety of hand tools and homeowner products, in this book, the method is presented in action for analysis, structural development, and parametric optimization for a specific case of gear processing technology—for gear chamfering techniques.



Miha Erjavec is currently a project manager at Podkrižnik d.o.o. Before that he was a development engineer at AMSC Windtec GmbH and at SET GmbH, where he led the department of numerical simulation and analysis. At Podkrižnik, he took the role of a lead designer and project manager for gearboxes in robotic applications. He leads and participates in many research activities as well as development projects associated with gearing technology or robotics. Furthermore, due to his expertise he supports the gear manufacturing group at Podkrižnik and a Podkrižnik-owned company, ORA-Drive. Mr. Erjavec graduated from the Faculty of Mechanical Engineering of the University of Ljubljana.



Gorazd Hlebanja is retired professor at the University of Novo mesto, Faculty of Mechanical Engineering.

He is still involved in teaching Mechatronics and Contemporary manufacturing systems. His research interest and engineering projects involved parametric drafting systems, algorithms for coloring arbitrary contours, group technology-based drafting system, concept of the online engineering office, and other. He is also active in S-gear development and research. The corresponding expertise includes various programming techniques, CAD/CAM, gear design and technology, system development, group technology, etc. Currently, he is consultant in Podkrižnik Company, where he is involved in the development of intelligent planetary gear trains based on S-gearing. He authored numerous journal and conference papers, invited lectures, and patents.



Jože Hlebanja graduated from the Technical Faculty of the University of Ljubljana in 1952. He was employed at Metalna Factory, where he was the chief designer for transport devices and cable cars. In 1960, the Faculty of Mechanical Engineering invited him to participate in the field of machine elements as an assistant professor. He wrote several textbooks to facilitate study and collaborated with industry. He received his doctorate in 1967 and later became a full professor. He led an extensive research group that undertook demanding industrial projects. The research results enabled the justification and inclusion of several new subjects in the pedagogical process: Design Methodology, Tribology,

Fundamentals of Design, Transport Devices, Planetary Gears, etc.. Under his mentorship, numerous doctorates were created. When he retired in 1991, he left an orderly field of expertise, well-equipped laboratories, and effective international cooperation. For his special contribution to higher education and science, the University awarded him the title of Professor Emeritus. He still professionally works and develops gears with a special profile, S-gears. In 2006, the Republic of Austria awarded him a Grand Honor Medal of Merit for his work in the Slovenian and International Mauthausen Committee.



Matija Hriberšek is a researcher and project manager at Podkrižnik d.o.o. When he finished his studies at Faculty of Mechanical Engineering at the University of Ljubljana, he got employed at Gorenje d.o.o in technology and development department, but soon returned to the faculty to work as a young researcher. He obtained Ph.D. in Mechanical Sciences at Faculty of Mechanical Engineering at the University of Ljubljana in the field of thermal conditions during cryogenic machining. At Podkrižnik d.o.o., he works as a researcher who studies different polymer gears used in power train applications. He is an expert in the field of thermal heat state mechanism, tribological, wear and durability characteristics of polymer materials. He is the lead project manager for research projects in the company. He is the author of eight different publications published in different International SCI journals and conferences.



Christopher Martin Illenberger has studied mechanical engineering and management at the Technical University of Munich. Since 2016, he has been working as a research associate at the Gear Research Centre (FZG) at the Technical University of Munich. His field of activity is the load carrying capacity of spur gears and gear materials. Since 2019, he is responsible as team leader for the area of plastic gears at FZG. In this position, Christopher Martin Illenberger is involved in basic research on the operating behavior of plastic gears, the development of test and calculation methods as well as in the development of polymer powertrains in electric vehicles.



Dimitar P. Karaivanov is an Associate Professor undergraduate at the Sofia University of Chemical Technology and Metallurgy, and an Associate Professor at Faculty of Fire Safety and Civil Protection at the Academy of Ministry of Interior Affairs, Bulgaria. He has been a guest lecturer in several Kazakhstan universities and co-mentor of 7 graduated Ph.D. students (from Croatia and from Kazakhstan). Dr. Karaivanov is the author of over 100 publications, including three monographs, 2 BG and 1 KZ patents. Over 80 citations are noticed.

Dr. Karaivanov also serves as an Expert in Bulgarian Institute of Standardization (BIS); National expert of Bulgarian Scientific-Technical Union of Mechanical Engineering in Gear Trains and Power Transmissions; President of the Balkan

Association of Power Transmissions; and Reviewer of several International Scientific Journals and Member of the Editorial Board of five of them.



Luka Knez received his M.Sc. and Ph.D. in Mechanical Engineering from the University of Ljubljana. Until 2019, he was employed at the Faculty of Mechanical Engineering (UL), working in the areas of Dynamics, Vibration testing, Numerical Simulations, and Human Vibration Research. During that time, he has authored 7 publications and scientific papers, 6 monographs, and 52 specific industrial studies and research reports. He is currently working in the R&D department of the company Podkrižnik, where he is responsible for Gear Design, Numerical Simulations, and Prototype Testing. Recently, he has extended his

interest into the field of Robotics, focusing on precision hardware development and testing.



Simon Kulovec is the Director of the R&D department at the company Podkrižnik and is an expert in the field of free form construction, gear systems and design, FEM and CFD analysis, modeling, computer-aided design, CAD programming, and programming languages (C, C++, Python, Fortran Algorithms). He is a leading person and responsible for several industrial projects: GOSTOP (Factories of the Future, Industry 4.0), SGU (S-Gearbox, Horizon 2020, SME Instrument), EDYN (Development of advanced electric outboard and inboard motors for e-boats), MAP gears (Advanced materials, methodologies, and technologies for development of lightweight power transmission components for drives technology), and SACHS RS (Electric drive system for MTB bikes). Dr. Kulovec is a member of Research group LECAD, Faculty of Mechanical Engineering, the University of Ljubljana, and author and co-author of 59 publications, papers, and patents.



Valentyn Nastasenko (of Ukraine) is a Professor of Mechanical Engineering at Kherson State Maritime Academy (city of Kherson, Ukraine). He received the M.Sc., the Ph.D., and the Dr.Sc.—all in mechanical engineering. Dr. Nastasenko has extensive industrial experience in gear design and manufacture. For about a decade, he used to manage a privately owned manufacturing company. His main research interest is *theory of gearing and gear production*. He is a highly

experienced expert in other areas of mechanical engineering as well. He authored two monographs, authored and co-authored numerous manuals, and textbooks. He also authored and co-authored about 500 scientific papers and holds over 100 patents on invention in the field.



Stephen P. Radzevich is a Professor of Mechanical Engineering and a Professor of Manufacturing Engineering. He received the M.Sc., the Ph.D., and the Dr. Sc.—all in mechanical engineering. Dr. Radzevich has extensive industrial experience in gear design and manufacture. His main research interest is Theory of Gearing, and Sculptured Part Surface Generation, particularly with the focus on (a) precision gear design, (b) high power density gear trains, (c) design of special purpose gear cutting/finishing tools, etc. Besides his work for industry, he trains engineering students at universities and gear engineers in companies. He authored and co-authored over 30 monographs, handbooks, and textbooks. He also authored and co-authored about 350 scientific papers and holds over 260 patents on invention in the field, both US patents and International patents.



Karsten Stahl is director of the Gear Research Centre (FZG) and full professor at the Technical University Munich. His research is focused on experimental, simulative, and analytical investigations of endurance, tribology, NVH, materials, and fatigue life analysis of gears and transmission elements with the target to develop methods and tools for reliable determination of fatigue life, efficiency, and vibration characteristics.

Prof. Stahl is the author of over 200 scientific publications. He is a board member of several scientific associations, convener of DIN and ISO working groups, editor of several scientific journals, and president of the VDI International Conference on Gears.



Thomas Tobie is head of the department “Load Carrying Capacity of Cylindrical Gears” at the Gear Research Centre (FZG), Technical University of Munich. He is specialized in the fields of gear materials, heat treatment, gear lubricants, gear strength, and gear testing with focus on all relevant gear failure modes like tooth root fracture, pitting, micro-pitting, scuffing, and wear as well as subsurface initiated fatigue failures. Dr. Tobie is an active member of several national and international working groups of DIN, ISO, IEC, and CEC and author of numerous papers at scientific journals and conferences.



Sanjin Troha is an Associate Professor with the Faculty of Engineering at the University of Rijeka. He teaches several courses for undergraduate students: with mechanical engineering, shipbuilding, and electrical engineering background. He is also the lecturer of the course multi-speed mechanical converters at the doctoral studies of mechanical engineering at the Faculty of Engineering at the University of Rijeka. He has authored and co-authored over 50 scientific papers, published in domestic and international journals and proceedings. His scientific interest is primarily in the fields of complex gearboxes. He has been a collaborator on several scientific research projects in Croatia and abroad.

Chapter 1

Kinematic Foundations of Scientific Classification of Gearing



Stephen P. Radzevich

1.1 Introduction

The discussion in this chapter of the book pertains to the scientific theory of gearing. In a certain sense, scientific theory of gearing can be viewed as a kind of “road map” that helps one traveling “from one location” (i.e., from a problem that one is current encountered with) to “another location” (i.e., to a desirable solution to this problem).

Classification of gearing is one of the main outputs of the proposed [1] *scientific theory of gearing*. The core of the *Classification* is already developed. It will take certain time to elaborate all the details of the *Classification*. This is a boring and time-consuming portion of job to be done in order to finalize the *Classification*. Of course, all the details are of importance; however, all of them are not fundamental in nature.

The author began to work in the field of gears and in the manufacture of gears at around 1975. Since then I have been asked many times: “Who needs the theory of gears, and especially your scientific theory of gears? The industry needs high-quality gears, not gear theory!” This question is incorrect by nature, as the scientific theory of gearing can be viewed as a kind of “road map” that helps one traveling “from one location” (i.e., from a problem that one is current encountered with) to “another location” (i.e., to a desirable solution to this problem).

The *gear theory* [1] is vital for the development and in in-depth analysis of gearing, the best suitable for a particular application. All kinds of gearing proposed in the recent couple centuries [George Grant bevel gearing (1887), Samuel Cone worm gear drive (1925), Mikhail Novikov conformal gearing (1956), as well as the rest of the others] can be easily derived from the *scientific theory of gearing*. Moreover, novel kinds of gearing (not known yet) are predicted by the *gear theory*, as all kinds of gearing are covered by the *scientific theory of gearing*.

S. P. Radzevich (✉)
Mechanical Engineering, Sterling Heights, MI, USA

The *gear theory* [1] is a powerful mean that helps the user to save funds and time in cases when subject of a gear project is poorly understood (or even not understood at all) and when the project has no chance for success from the very beginning.

The origination of gear theory can be traced back to the mid-eighteenth century when two famous papers on involute gear tooth profile were published by *Leonhard Euler* [2, 3]. Lots of research have been carried out since the time of *L. Euler*. Almost all of the gear scientists and engineers focused their attention on practical application of gears, and a very limited number of researchers have investigated gear tooth flank geometry and gear meshing process—the core of the theory of gearing.

The first ever monograph on gears and gearing, titled *Théorie Géométrique des Engrenages destines (Geometrical Theory of Gearing)*, was authored by *Théodore Olivier* and published in 1842 [4]. An attempt to generalize the theory of gearing has been undertaken by the author. The research carried out by *Th. Olivier* significantly affected the evolution of gear science, as *Th. Olivier* committed a huge mistake in the research. Unfortunately, the condition of conjugacy of tooth flanks of a gear and a mating pinion was ignored by *Th. Olivier*. The mistake, committed by *Th. Olivier* in 1842, misleads gear experts all around the world for about two centuries. Tons of research in the gear science and gear application had no chance for success due to this mistake even before the research [1] has started.

1.1.1 Vector Diagram of Gear Pair

At the beginning, a few terms, which less experienced readers might be not familiar with, need to be introduced. Three kinds of gearing are used in the nowadays industry. These kinds of gearing are as follows:

- Gear pairs having crossing axes of rotation of a gear and a mating pinion. Gearing of this kind is referred to as “crossed-axes gearing” (or just “ C_a -gearing,” for simplicity). Hypoid gearing, spiroid gearing, worm gearing, and a few others are good examples of C_a -gearing.
- Gear pairs having intersecting axes of rotation of a gear and a mating pinion. Gearing of this kind are referred to as “intersected-axes gearing” (or just “ I_a -gearing,” for simplicity). Bevel gearing having different geometries of the tooth flank in the lengthwise direction, i.e., straight bevel gears, skew bevel gears, spiral bevel gears, as well as a few of others, are good examples of I_a -gearing.
- Gear pairs having parallel axes of rotation of a gear and a mating pinion. Gearing of this kind are referred to as “parallel-axes gearing” (or just “ P_a -gearing,” for simplicity). Spur gearing, helical gearing, as well as a few of others are good examples of P_a -gearing.

Crossed-axes gearing is the most general kind of gearing that is extensively used in the nowadays industry. Gearing of two other kinds (i.e., I_a -gearing and P_a -gearing) can be viewed as a corresponding reduced cases of C_a -gearing. In the first case (I_a -gearing), the center-distance in the gear pair is zero. In the second

case (P_a -gearing), the axes of gears in a gear pair are parallel: the axes are at zero shaft angle in design of internal gearing, and the axes are at 180° angle in design of external gearing.

With that said, let's proceed to consideration of gear vector diagrams (for gear pairs that features zero complementary degrees-of-freedom).

1.1.1.1 Vector Diagram of Gear Pair Having Zero Complementary Degrees-of-Freedom

Despite application of gear vector diagrams is known from the earlier times (approximately since the mid of the XX century), in scientific theory of gearing, vector diagrams are extensively used since the early two-thousands. Gear vector diagram is a powerful mean for the gear theoreticians.

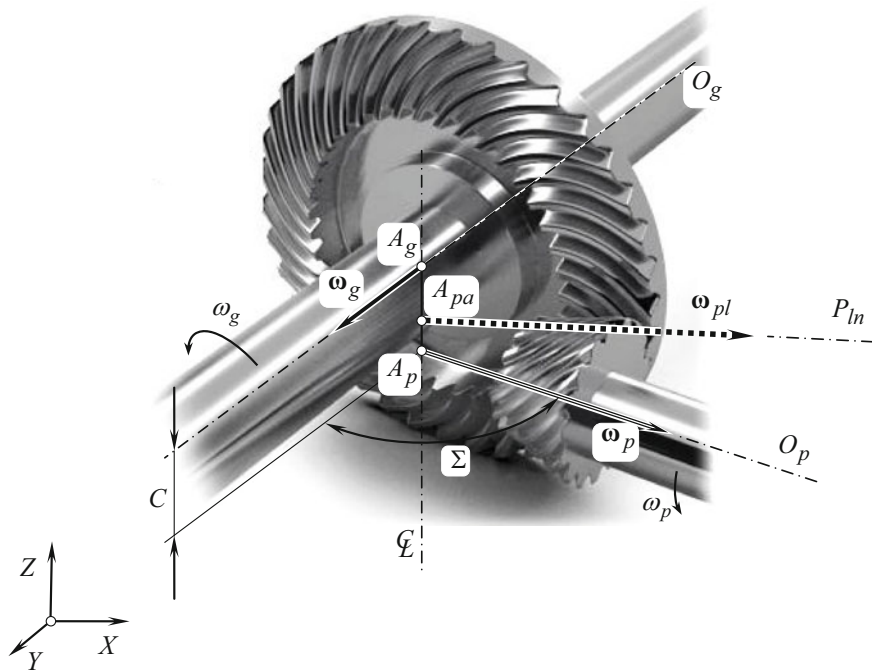
Taking into account that crossed-axes gearing is the most general kind of gearing, gear vector diagrams for I_a -gearing and P_a -gearing are considered as corresponding reduced cases of gear vector diagram constructed for C_a -gearing.

1.1.1.2 Concept of Vector Representation of Gear Pair Kinematics

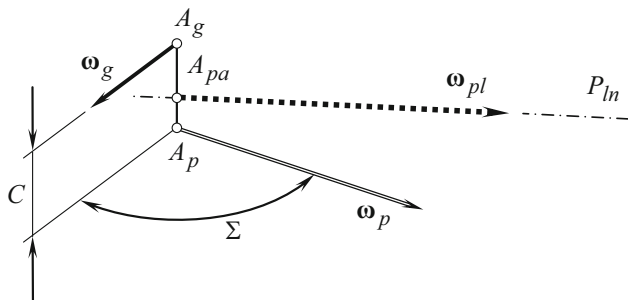
Vector diagram for crossed-axes gearing can be specified by four principal design parameters. The rotation vectors, ω_g and ω_p , of a gear and of a mating pinion, the center-distance, C , and the crossed-axes angle, Σ , are these four design parameters. It should be stressed here on the following. As rotations are not vectors in nature, that special care is required to be undertaken when treating rotations as vectors.

Referring to Fig. 1.1a, [1], consider a crossed-axes gear pair together with the associated rotation vectors ω_g and ω_p . A "Cartesian" coordinate system, XYZ , is associated with the crossed-axes gear pair. The rotation vectors, ω_g and ω_p , of a gear and its mating pinion are at a center-distance, C . The center-distance, C , is a straight-line segment that is measured along the centerline, \mathcal{C} , and equals to the closest distance of approach between the axes of rotation, O_g and O_p , of the gear and its mating pinion. In the particular case under consideration, the crossed-axes angle, Σ , is equal to 90° . However, crossed-axes angle, Σ , can also be either acute ($\Sigma < 90^\circ$) or obtuse ($\Sigma > 90^\circ$).

The rotation vectors of a gear, ω_g , and its mating pinion, ω_p , are in fact sliding vectors (see Fig. 1.1b). They can be applied at any point within the gear axis, O_g , and the pinion axis, O_p , correspondingly. It is convenient to apply the rotation vectors, ω_g and ω_p , at points of intersection, A_g and A_p , of the corresponding axes of rotation, O_g and O_p , by the centerline, \mathcal{C} (i.e., by a line along which the center-distance, C , is measured). As it will be shown later on in this chapter of the book, points A_g and A_p are by nature the apexes of the base cones of a gear and its mating pinion, correspondingly. In a case when the axes of rotation, O_g and O_p , intersect one another (i.e., when $C = 0$), it is convenient to apply the rotation vectors, ω_g and ω_p , at point of intersection of the axes [1].



(a)



(b)

Fig. 1.1 Kinematics of crossed-axes gearing with a constant tooth ratio, u , (a) a schematic of the gear pair, and (b) an equivalent vector diagram: The rotation vectors, ω_g and ω_p , of a C_a -gearing are at a center-distance, C , from each other, and form a crossed-axes angle, Σ . (Adapted from: Radzevich, S.P., *Theory of Gearing: Kinematics, Geometry, and Synthesis*, 2nd Edition, revised and expanded, CRC Press, Boca Raton, FL, 2018, 934 pages.)

The magnitude of rotation vector of the gear, ω_g , equals $\omega_g = |\boldsymbol{\omega}_g|$, whereas the magnitude of rotation vector of the pinion, ω_p , equals $\omega_p = |\boldsymbol{\omega}_p|$. The magnitudes, ω_g and ω_p , of the rotation vectors, $\boldsymbol{\omega}_g$ and $\boldsymbol{\omega}_p$, are synchronized with each other.

The rotation vectors, $\boldsymbol{\omega}_g$ and $\boldsymbol{\omega}_p$, form a crossed-axes angle, Σ , that is, an equality:

$$\Sigma = \angle(\boldsymbol{\omega}_g, \boldsymbol{\omega}_p) \quad (1.1)$$

is valid for a gear pair.

Equation (1.1) immediately yields a formula:

$$\Sigma = \tan^{-1} \frac{|\boldsymbol{\omega}_g \times \boldsymbol{\omega}_p|}{\boldsymbol{\omega}_g \cdot \boldsymbol{\omega}_p} \quad (1.2)$$

for the calculation of the actual value of the crossed-axes angle, Σ .

An analytical criterion of an actual kind of crossed-axes gearing can be composed based on the actual configuration of the rotation vectors, $\boldsymbol{\omega}_g$ and $\boldsymbol{\omega}_p$. The just mentioned different kinds of gearing are as follows:

- (a) Rotary-negative gearing.
- (b) Rotary-positive gearing.
- (c) Rotary-zero gearing.

In the nowadays practice, these three kinds of gearing are commonly referred to as:

- 1. External gearing.
 - 2. Rack-type (or crown) gearing.
 - 3. Internal gearing.
- correspondingly.

The nowadays terminology [namely, the items (i) through (iii)] is inconsistent because of the following.

A direction of an input rotation in external gearing of conventional design is changed to an opposite direction. However, in external gearing [5, 6] (see also Fig. 6.10 on page 125 in [1]), a direction of an input rotation is remained the same.

Similarly, a direction of an input rotation in internal gearing of conventional design is remained the same. However, in internal gearing [5, 6] (see also Fig. 6.10 on page 125 in [1]), a direction of an input rotation is changed to an opposite direction.

A discussed example reveals that in scientific analysis, the proposed differentiation of gearing [see items (a) through (c)] should be adopted, instead of the conventional differentiation of gearing [see items (i) through (iii)].

The angle that is formed by the rotation vector of a gear, $\boldsymbol{\omega}_g$, and the vector, $\boldsymbol{\omega}_p$, of instant rotation of the mating pinion in relation to the gear is the principal feature for the difference between crossed-axes gear pairs of different kinds. This angle is either of the following:

Table 1.1 Analytical criteria of type of crossed-axes gear pairs

Type of crossed-axes gear pair	Analytical criterion
Rotary-negative gearing: (“external”, and “internal”) crossed-axes gear pairs	$\omega_g \cdot (\omega_p - \omega_g) < 0$
Rotary-zero gearing: Generalized rack-type crossed-axes gear pairs	$\omega_g \cdot (\omega_p - \omega_g) = 0$
Rotary-positive gearing: (“internal”, and (“external”) crossed-axes gear pairs	$\omega_g \cdot (\omega_p - \omega_g) > 0$

(x) Negative value (for rotary-negative gearing)

(y) Zero value (for rotary-zero gearing)

(z) Positive value (for rotary-positive gearing)

These differences can be described analytically.

An equality:

$$\omega_{pl} = \omega_p - \omega_g \quad (1.3)$$

is valid for crossed-axes gearing of all kinds.

The actual sign of the angle [see items (x) through (z)] is the same as the sign of the dot product $\omega_g \cdot \omega_{pl}$, that is, the angle (I) is negative when $\omega_g \cdot \omega_{pl} < 0$, (II) is zero when $\omega_g \cdot \omega_{pl} = 0$, and (III) is positive when $\omega_g \cdot \omega_{pl} > 0$.

Ultimately, analytical criteria of a kind of crossed-axes gearing of different design are summarized in Table 1.1.

Analytical expressions that specify the criteria for the crossed-axes gear pair are composed on the premise of well-known properties of the dot product of two vectors.

The interested reader is referred to [1] for more in detail discussion of gear vector diagrams.

1.1.1.3 Vector Diagram of Gear Pair Having a Plurality of Complementary Degrees-of-Freedom

Noncircular gearing is a good example of gearing that features a plurality of complementary degrees-of-freedom. The idea of noncircular gears originates from the precursors of the engineering thought. Gears of this kind were sketched by *Leonardo da Vinci*. In the nowadays industry, they found their application in many mechanical devices.

The nowadays literature pertaining to the design and manufacture of noncircular gears is less developed than that on gearing of other design.

In addition to gear pairs with a constant fundamental design parameters (gear pairs of this type may be referred to as “gearing with no complementary degrees-of-freedom” or as “ $C\Sigma u$ —constant gear pairs”), gearing of other types are also known. Well-known from many sources, noncircular gearing is an example of gearing with variable design parameters. Generally speaking, each of the fundamental design parameters (C , Σ , and u) can be time-dependent. “Gears featuring a plurality of complementary degrees-of-freedom” (or, in other words, “ $C\Sigma u$ —variable gear pairs”) possess lots of undiscovered yet important properties to be used in the industry.

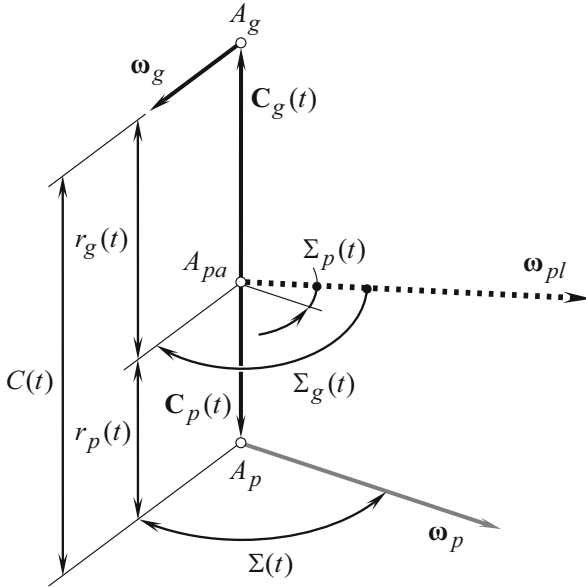


Fig. 1.2 Gear vector diagram with three variable fundamental design parameters: of a $C\Sigma u$ -variable gear pair

In the analysis below, each of the fundamental design parameters of a gear pair is considered as a time-dependent design parameter, that is, as $C = C(t)$, $\Sigma = \Sigma(t)$, and $u = u(t)$. It is reasonable to refer to gear pairs of this kind [that feature variable the $C = C(t)$, $\Sigma = \Sigma(t)$, and $u = u(t)$ parameters] as to “ $C\Sigma u$ -variable gear pairs.” For convenience, the numberings of the vector diagrams that are used in the proposed classification of the vector diagrams (see Fig. 1.10 below) are also used for the analysis of the $C\Sigma u$ -variable gear pairs.

An example of vector diagram of $C\Sigma u$ -variable gearing is illustrated in Fig. 1.2. All the principal design parameter in the gear pair [namely, C , Σ , ω_g , and ω_p (or the design parameters C , Σ , and $u = |\omega_p| / |\omega_g|$)] may be time-dependent—all of them can vary in time while a gear pair operates.

“ $C\Sigma u$ -variable” gear pairs of all possible kinds are a challenging subject to be investigated in the future.

1.1.2 Classification of Gear Vector Diagrams

Gearing of every kind feature at least one degree-of-freedom (DoF). Transmission of a rotary motion from a driving shaft to a driven shaft is the main purpose of this degree-of-freedom. In addition to just mentioned degree-of-freedom, one or more

complementary degrees-of-freedom can be added to a particular design of gearing in order to keep control over one or more design parameters:

- (a) The gear ratio, $u - var$.
- (b) The center-distance, $C - var$.
- (c) The shaft angle, $\Sigma - var$.

From this standpoint, the following kinds of gearing are distinguished:

1. Three-degree-of-freedom gearing: $C\Sigma u - var$ gearing (kinematically, this kind of gearing is the most general one).
2. Two-degree-of-freedom gearing: either $C\Sigma - var$ (or $u - const$) gearing or $Cu - var$ (or $\Sigma - const$) gearing or $\Sigma u - var$ (or $C - const$) gearing.
3. One-degree-of-freedom gearing: either $u - var$ (or $C\Sigma - const$) gearing or $C - var$ (or $\Sigma u - const$) gearing or $\Sigma - var$ (or $Cu - const$) gearing.
4. Zero-degree-of-freedom gearing: $C\Sigma u - const$ gearing (kinematically, this kind of gearing is the simplest one).

Zero-degree-of-freedom gearing (namely, $C\Sigma u - const$ gearing) is the most extensively used in the nowadays industry kind of gearing. Numerous applications of one-degree-of-freedom gearing [i.e., $u - var$ (or $C\Sigma - const$) gearing] are known since the nineteenth century. Gearing of the rest of the kinds (i.e., $C\Sigma u - var$, $C\Sigma - var$, $Cu - var$, $\Sigma u - var$, $C - var$, and $\Sigma - var$ gearing) got no extensive application in the industry yet.

The total number of the principal design parameters of gearing is limited to four design parameters (C , Σ , ω_g , and ω_p). Taking into account that the rotations, ω_g and ω_p , somehow correlate to one another, the total number of the principal design parameters of three-degree-of-freedom gearing can be reduced to three design parameters (C , Σ , and u). With that said, a self-consistent classification of various types of gear vector diagrams can be developed as discussed immediately below.

A proposed generalized classification of gear vector diagrams is shown in Fig. 1.3.

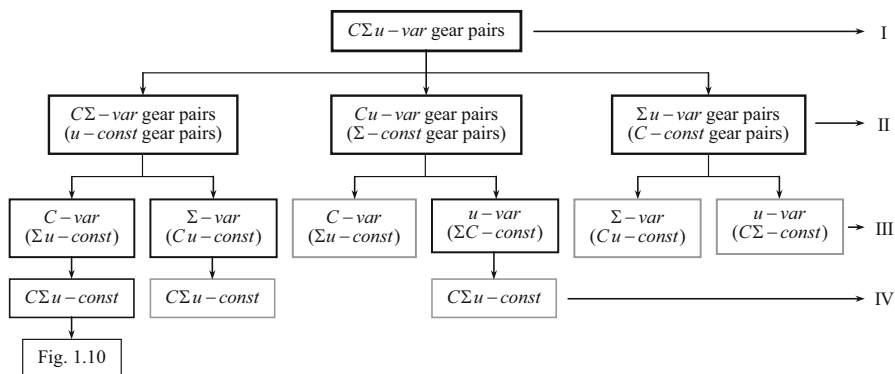


Fig. 1.3 Generalized classification of gear vector diagrams

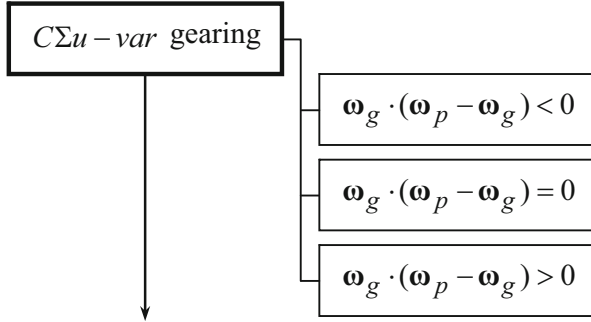


Fig. 1.4 Possible kinds of $C\Sigma u$ - variable gear pairs (the first stratum of the generalized classification in Fig. 1.3)

1.1.2.1 Gear Vector Diagrams for Three-Degree-of-Freedom Gearing

Shown in Fig. 1.2 is an example of gear vector diagram for three-degree-of-freedom gearing (for $C\Sigma u$ -variable gear pairs). Actually, a gear vector diagram of a single kind can be constructed for three-DoF gearing. Three particular kinds of gear vector diagram for three-DoF gearing can be distinguished. They are as follows (see Fig. 1.4):

- Rotary-negative $C\Sigma u$ -variable gear pairs [$\omega_g \cdot (\omega_p - \omega_g) < 0$].
- Rotary-zero $C\Sigma u$ -variable gear pairs [$\omega_g \cdot (\omega_p - \omega_g) = 0$].
- Rotary-positive $C\Sigma u$ -variable gear pairs [$\omega_g \cdot (\omega_p - \omega_g) > 0$].

Potential kinds of $C\Sigma u$ -variable gear pairs are not limited just to three abovementioned kinds of gearing, as different portions of a gear periphery may feature gear sectors of various geometry. In particular, different portions of a gear periphery may feature all three kinds of the listed above $C\Sigma u$ -variable gearing.

$C\Sigma u$ -variable gearing can be construed as the most general kind of gearing. Varying each of the parameters C , Σ , and u (individually, or in any and all possible combinations), reduced gearing of all kinds can be derived. It is right point to stress here that when the gears rotate, only crossed-axes angle, Σ , can be varied independently [i.e., $\Sigma = \Sigma(t)$]. A variation of the center-distance, C , and the angular velocity ratio, u , is prespecified by the design parameters of the gear pair [$C = C[\varphi_{input}(t)]$ and $u = u[\varphi_{input}(t)]$].

Gear vector diagrams for three-degree-of-freedom gearing form the first stratum (I stratum) of the generalized classification (see Fig. 1.3). The first stratum (I) of the classification consists of just one gear vector diagram ($C\Sigma u$ - var gearing), as there is no need for more detail in their classification now, as well as in the nearest future. It is right point to stress here that plurality of reduced cases of $C\Sigma u$ - var gearing with specific features of gear pairs is possible.

1.1.2.2 Gear Vector Diagrams for Two-Degree-of-Freedom Gearing

The second stratum (II stratum) in the generalized classification of gear vector diagrams (see Fig. 1.3) is formed by the gear vector diagrams for two-degree-of-freedom gearing of three different kinds:

- $C\Sigma - var$ (or $u - const$) gear vector diagrams
- $Cu - var$ (or $\Sigma - const$) gear vector diagrams
- $\Sigma u - var$ (or $C - const$) gear vector diagrams

Illustrative examples of gear vector diagrams for two-degree-of-freedom gearing of each of three possible kinds are shown in Fig. 1.5, namely, in Fig. 1.5a for $C\Sigma - var$ (or $u - const$) gearing; in Fig. 1.5b for $Cu - var$ (or $\Sigma - const$) gearing; and in Fig. 1.5c for $\Sigma u - var$ (or $C - const$) gearing.

It is necessary to point out here that each of the two-degree-of-freedom gear vector diagrams constructed for $C\Sigma - var$ gearing, $Cu - var$ gearing, and $\Sigma u - var$ gearing can be either rotary-negative [$\omega_g \cdot (\omega_p - \omega_g) < 0$] or rotary-zero [$\omega_g \cdot (\omega_p - \omega_g) = 0$] or, finally, rotary-positive [$\omega_g \cdot (\omega_p - \omega_g) > 0$]. More in detail, the second stratum of the generalized classification of vector diagrams of gearing is schematically shown in Fig. 1.6.

Gear vector diagrams for numerous reduced kinds of two-degree-of-freedom gearing are distinguished. As an example, gear vector diagrams for (a) crossed-axes gearing, (b) intersected-axes gearing, and (c) parallel-axes gearing are listed below:

Reduced cases of crossed-axes gearing:

- Rotary-negative Σu -variable gear pairs: $C = const \neq 0$.
- Rotary-negative Cu -variable gear pairs: $\Sigma = const \neq 0$.
- Rotary-negative $C\Sigma$ -variable gear pairs: $u = const$.
- Rotary-zero Σu -variable gear pairs: $C = const \neq 0$.

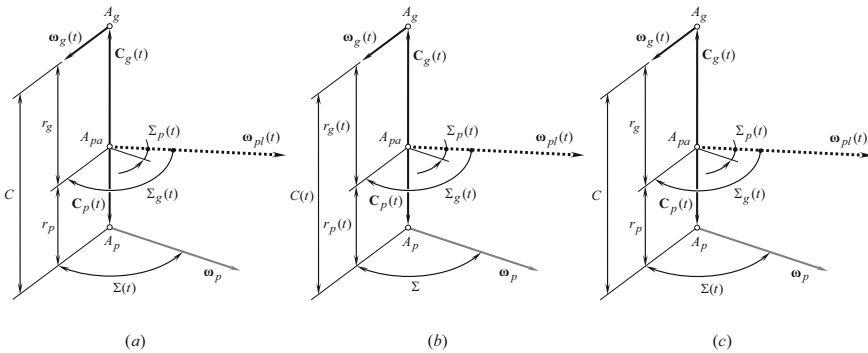


Fig. 1.5 Gear vector diagrams with two variable fundamental design parameters: of (a) $\Sigma - u$ variable gear pair (or $C - constant$ gear pair); (b) $Cu - u$ variable gear pair (or $\Sigma - constant$ gear pair); and (c) $\Sigma - C$ variable gear pair (or $u - constant$ gear pair)

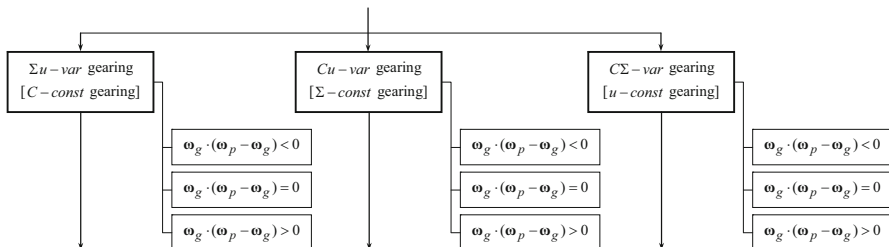


Fig. 1.6 Possible kinds of the gear vector diagrams for two-degree-of-freedom gearing (the second stratum of the generalized classification in Fig. 1.3)

- Rotary-zero Cu -variable gear pairs: $\Sigma = \text{const} \neq 0$.
- Rotary-zero $C\Sigma$ -variable gear pairs: $u = \text{const}$.
- Rotary-positive Σu -variable gear pairs: $C = \text{const} \neq 0$.
- Rotary-positive Cu -variable gear pairs: $\Sigma = \text{const} \neq 0$.
- Rotary-positive $C\Sigma$ -variable gear pairs: $u = \text{const}$.

Reduced cases of intersected-axes gearing:

- Rotary-negative Σu -variable gear pairs: $C = 0$.
- Rotary-zero Σu -variable gear pairs: $C = 0$.
- Rotary-positive Σu -variable gear pairs: $C = 0$.

Reduced cases of parallel-axes gearing:

- Rotary-negative Cu -variable gear pairs: $\Sigma = 0^\circ$.
- Rotary-zero Cu -variable gear pairs: $\Sigma = \text{const} \neq 0^\circ$.
- Rotary-positive Cu -variable gear pairs: $\Sigma = 180^\circ$.

1.1.2.3 Gear Vector Diagrams for One-Degree-of-Freedom Gearing

The third stratum (III stratum) in the generalized classification of gear vector diagrams (see Fig. 1.3) is formed by the gear vector diagrams for one-degree-of-freedom gearing of three different kinds. These are the following gear vector diagrams for one-degree-of-freedom gearing (see Fig. 1.7):

- u - var (or $C\Sigma$ - const) gear vector diagrams
- C - var (or Σu - const) gear vector diagrams
- Σ - var (or Cu - const) gear vector diagrams.

Illustrative examples of gear vector diagrams for one-degree-of-freedom gearing of each of three possible kinds are shown in Fig. 1.7, namely, in Fig. 1.7a for Σ - var (or Cu - const) gearing; in Fig. 1.7b for C - var (or Σu - const) gearing; and in Fig. 1.7c for u - var (or $C\Sigma$ - const) gearing.

It is necessary to stress here that each of the one-degree-of-freedom gear vector diagrams constructed for u - var gearing (or $C\Sigma$ - const gearing), C - var gearing (or Σu - const gearing), as well as Σ - var gearing (or Cu - const gearing) can be

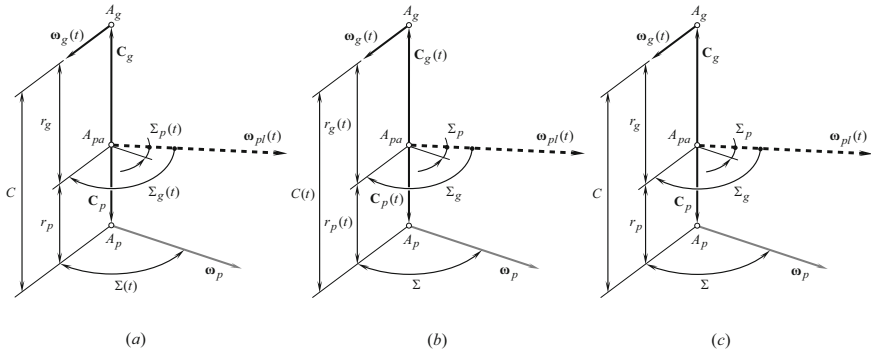


Fig. 1.7 Gear vector diagram with a single variable fundamental design parameter: of (a) Σ -variable gear pair (or Cu – constant gear pair); (b) C - variable gear pair (or $\Sigma - u$ constant gear pair); and (c) u – variable gear pair (or $\Sigma - C$ constant gear pair)—not feasible

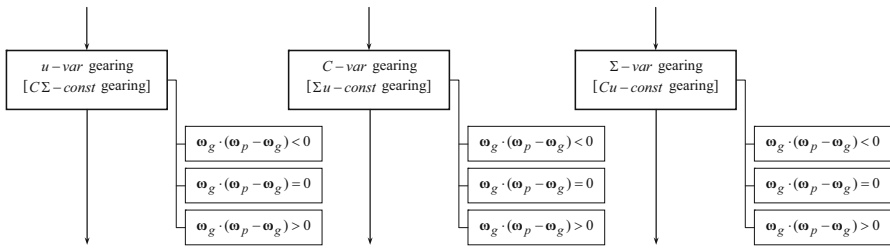


Fig. 1.8 Possible kinds of gear vector diagrams for one-degree-of-freedom gearing (the third stratum of the generalized classification in Fig. 1.3)

either rotary-negative $[\omega_g \cdot (\omega_p - \omega_g) < 0]$ or rotary-zero $[\omega_g \cdot (\omega_p - \omega_g) = 0]$ or, finally, rotary-positive $[\omega_g \cdot (\omega_p - \omega_g) > 0]$. More in detail, the third stratum of the generalized classification of vector diagrams of gearing is schematically shown in Fig. 1.8.

Gear vector diagrams for numerous reduced kinds of one-degree-of-freedom gearing are recognized. As an example, gear vector diagrams for (a) crossed-axes gearing, (b) intersected-axes gearing, and (c) parallel-axes gearing are listed below:

Possible reduced cases of one-degree-of-freedom gearing:

- Rotary-negative C -variable gear pairs: $\Sigma = \text{const}, u = \text{const}$.
- Rotary-negative Σ -variable gear pairs: $C = \text{const}, u = \text{const}$.
- Rotary-negative u -variable gear pairs: $C = \text{const}, \Sigma = \text{const}$.
- Rotary-zero C -variable gear pairs: $\Sigma = \text{const}, u = \text{const}$.
- Rotary-zero Σ -variable gear pairs: $C = \text{const}, u = \text{const}$.
- Rotary-zero u -variable gear pairs: $C = \text{const}, \Sigma = \text{const}$.
- Rotary-positive C -variable gear pairs: $\Sigma = \text{const}, u = \text{const}$.
- Rotary-positive Σ -variable gear pairs: $C = \text{const}, u = \text{const}$.
- Rotary-positive u -variable gear pairs: $C = \text{const}, \Sigma = \text{const}$.

The C -variable gear pairs (or Σu -constant gear pairs), Σ -variable gear pairs (or Cu -constant gear pairs), and u -variable gear pairs (or $C\Sigma$ -constant gear pairs) are not feasible because the fundamental design parameters, namely, (a) $C = \text{var}, \Sigma = \text{const}, u = \text{const}$, (b) $C = \text{const}, \Sigma = \text{var}, u = \text{const}$, and (c) $C = \text{const}, \Sigma = \text{const}, u = \text{var}$, are not compatible with one another.

It is critical for the further analysis that the total number of the gear vector diagrams listed above is not an infinite, but, instead, it is limited to a reasonably small number of the gear vector diagrams. No gear vector diagrams except of the above considered are possible at all. This means that each one of the gear vector diagrams can be investigated to the best possible extent aiming application of them in design gearing.

In “ $C\Sigma u$ -variable” gear pairs of all possible kinds, at every instant of time, that is, for any and all possible configurations of a gear and its mating pinion, instant base pitch of a gear, and instant base pitch of a mating pinion, both have to be equal to instant operating base pitch of the gear pair—this is a must.

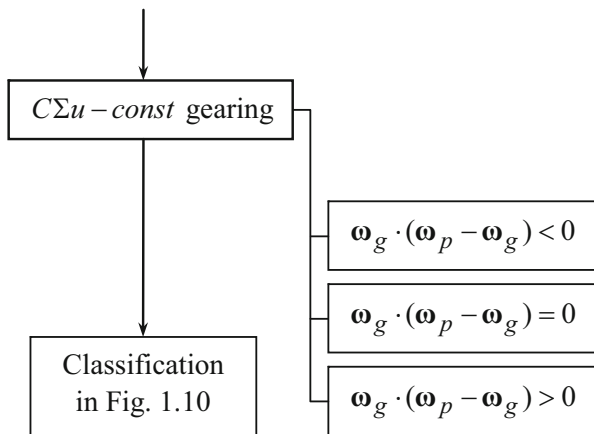
1.1.2.4 Gear Vector Diagrams for Zero-Degree-of-Freedom Gearing (with no Complementary DoF)

Finally, the fourth stratum (IV stratum) in the generalized classification of gear vector diagrams (see Fig. 1.3) is formed by the gear vector diagrams for zero-degree-of-freedom gearing. These is the only zero-degree-of-freedom gear vector diagram $C\Sigma u - \text{const}$ gearing (see Fig. 1.9).

Crossed-axes zero-degree-of-freedom gear pairs are considered in this section of the book as the most general type of gear pairs. The remaining possible kinds of gear pairs can be construed as a reduction (simplification) of the corresponding type of the crossed-axes gear pairs.

There are only three different types of zero-degree-of-freedom gearing having crossing axes of rotation of a gear and a mating pinion:

Fig. 1.9 Possible kinds of $Cu \Sigma - \text{const}$ gear pairs (the fourth stratum of the generalized classification in Fig. 1.3)



- “Rotary-negative crossed-axes gear pairs,” in which the input rotation is altered (i.e., $\omega_g/\omega_g = -\omega_p/\omega_p$); the gear ratio is negative ($u < 0$).
- “Rotary-positive crossed-axes gear pairs,” in which the gear rotation is remained the same (i.e., $\omega_g/\omega_g = \omega_p/\omega_p$); the gear ratio is positive ($u > 0$).
- “Rotary-zero crossed-axes gear pairs,” in which the gear cone angle, Σ_g , is a right angle (i.e., $\Sigma_g = 90^\circ$); rotation of the gear is not zero¹ ($\omega_g \neq 0$).

No other kind of crossed-axes gearing is possible.

The first stratum of the classification of possible kinds of vector diagrams for zero-degree-of-freedom gearing (Fig. 1.10) is comprised by three different kinds of crossed-axes gearing:

- Rotary-negative crossed-axes gear pairs.
- Rotary-zero crossed-axes gear pairs.
- Rotary-positive crossed-axes gear pairs.

Numbers 1.1, 1.2, and 1.3 are assigned to crossed-axes gear pairs that comprise the first stratum of the classification (see Fig. 1.10).

Crossed-axes gear pairs can be reduced to gear pairs of a simpler design. There are two possible ways for the reduction: first, the center-distance, C , can be set to a zero value, and, second, the gear and the pinion axes of rotation, O_g and O_p , can be set parallel to each other. In the second case, the crossed-axes angle, Σ , is equal to either $\Sigma = 180^\circ$ or $\Sigma = 0^\circ$.

Let us begin the consideration from the first case when the center-distance, C , of a rotary-negative intersected-axes gear pair is reduced to zero.

When the equality $C = 0$ is observed, the gear and the pinion axes of rotation, O_g and O_p , intersect each other at point, A_{pa} . This point is commonly referred to as the “plane-of-action apex, A_{pa} .” The rotation vectors, ω_g and ω_p , are the two vectors through the point A_{pa} . They are pointed along the axes of rotation, O_g and O_p , correspondingly.

For gear pairs of this kind, a sphere that is centered at the point “plane-of-action apex, A_{pa} ” is convenient to be used for the investigation of engagement of the gear teeth. Because of this, intersected-axes gear pairs are loosely referred to as “spherical gear pairs.” The term “spherical” is because the tooth profiles of the gear, and the pinion in this case are generated on spheres.² For rotary-negative intersected-axes

¹The term “rotary-zero crossed-axes gear pair” is due to that in parallel-axes gearing of this kind the rotation of the gear is zero (i.e., $\omega_g = 0$). “Gear-to-rack gear pair” of a conventional design features a zero rotation of the gear: for a certain rotation of the pinion, ω_p , the rotation of the gear, ω_g , is always zero, $\omega_g = 0$. In a more general case of zero crossed-axes gearing, the gear rotation is not zero (i.e., $\omega_g \neq 0$). By convention, the term “rotary-zero crossed-axes gear pair” is applied to gearing of all types, that is, to parallel-axes, intersected-axes, and crossed-axes gearing as well.

²The term “spherical gear pair” is incorrect as gears of other types, for example, crossed-axes gear pairs, are also engaged in mesh on a sphere. Therefore, replacement of the obsolete and extensively used term “conical gear pair” with the term “spherical gear pair” is not valid. In order to avoid ambiguities in further discussions, gearing of this type is referred to as “intersected-axes gearing,” or just as “ I_a -gearing,” for simplicity.

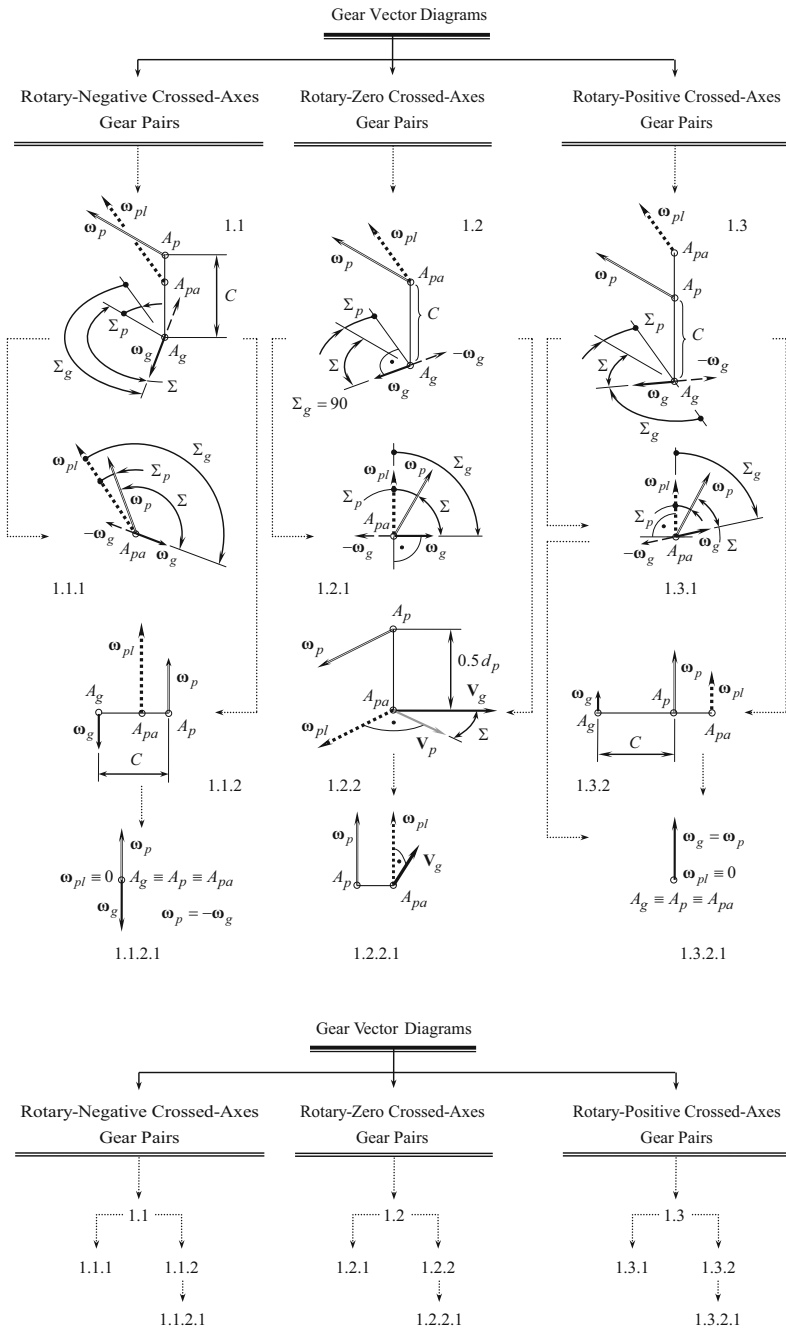


Fig. 1.10 Classification of possible kinds of gear vector diagrams for one-degree-of-freedom gear pairs

gear pairs of all kinds, the inequality $\boldsymbol{\omega}_g \cdot (\boldsymbol{\omega}_p - \boldsymbol{\omega}_g) < 0$ is valid. The component Σ_g of the crossed-axes angle, Σ , exceeds a right angle, 90° (i.e., $\Sigma_g > 90^\circ$). Rotary-negative intersected-axes gear pairs can feature crossed-axes angles of various values. In particular, the crossed-axes angle, Σ , can be chosen so as to fulfil the equality $\Sigma_g = 90^\circ$.

The first row of the second stratum of the classification of all possible kinds of vector diagrams of gear pairs (see Fig. 1.10) is comprised by three different kinds of intersected-axes gear pairs, namely, by:

- Rotary-negative intersected-axes gear pairs.
- Rotary-zero intersected-axes gear pairs.
- Rotary-positive intersected-axes gear pairs.

The numbers 1.1.1, 1.2.1, and 1.3.1 are assigned to intersected-axes gear pairs comprising the first row of the second stratum of the classification.

This is followed by the second case in which the gear and the pinion axes of rotation are parallel to each other. The shaft angle in these cases is either $\Sigma = 0^\circ$ or $\Sigma = 180^\circ$.

When the equality $\Sigma = 180^\circ$ is observed, the rotation vectors, $\boldsymbol{\omega}_g$ and $\boldsymbol{\omega}_p$, are pointed oppositely to one another. Gear pairs of this type are referred to as “parallel-axes gear pairs” (or just “ P_a -gear pairs,” for simplicity). Sometimes the term “planar gear pair” is used with respect to gearing of this type. The term “planar” is used as the tooth profiles of the gear, and the pinion in this case are generated within a plane. The term “parallel-axes gear pair” is preferred and is recommended for use in scientific publications on theory of gearing. For all rotary-negative parallel-axes gear pairs, the inequality $\boldsymbol{\omega}_g \cdot (\boldsymbol{\omega}_p - \boldsymbol{\omega}_g) < 0$ is observed.

On the other hand, when for a parallel-axes gear pair the equality $\Sigma = 0^\circ$ is valid, the rotation vectors, $\boldsymbol{\omega}_g$ and $\boldsymbol{\omega}_p$, are pointed in the same direction, which corresponds to a rotary-positive parallel-axes gear pair. For all rotary-positive parallel-axes gear pairs, the inequality, $\boldsymbol{\omega}_g \cdot (\boldsymbol{\omega}_p - \boldsymbol{\omega}_g) > 0$, is observed.

Parallel-axes gear pairs of two kinds, namely, rotary-negative gear pairs and rotary-positive parallel-axes gear pairs, comprise the second row of the second stratum of the classification of possible types of vector diagrams of zero-degree-of-freedom gearing (see Fig. 1.10). The numbers 1.1.2 and 1.3.2 are assigned to the vector diagrams of parallel-axes gear pairs comprising the second row of the second stratum of the classification.

Ultimately, consider a simplified case of rotary-zero crossed-axes gear pair. In the extreme cases, the tooth number of the gear can approach infinity. An infinite radius of the gear is the only case to reduce the rotary-zero crossed-axes gear pair when the center-distance is not equal to zero (i.e., $C \neq 0$). The vectors of linear velocities, \mathbf{V}_g and \mathbf{V}_p , are at a crossed-axes angle, Σ , in relation to each other.

The third row of the second stratum of the classification of all possible kinds of gear vector diagrams (see Fig. 1.10) is comprised by rotary-zero crossed-axes gear pairs of this kind. The number 1.2.2 is assigned to the gear pair that comprises the third row of the second stratum of the classification.

In a particular case, say, when the crossed-axes angle is equal to zero ($\Sigma = 0^\circ$), a rotary-zero crossed-axes gear pair reduces to a conventional rotary-zero parallel-axes gear-to-rack gear pair.

The number 1.2.2.1 is assigned to the parallel-axes gear-to-rack gear pair.

The gear-to-rack gear pair is a perfect example of a rotary-zero parallel-axes gear pairs of this type.

It is instructive to note here that a rotary-zero parallel-axes rack-type gear pair can be obtained as an extreme case of either a rotary-negative parallel-axes gear pair (i.e., of the gear pair 1.1.2) or a rotary-positive parallel-axes gear pair (i.e., of the gear pair 1.3.2) under the condition that the radius of the gear approaches infinity.³ In this case, the corresponding vector diagrams 1.1.2.1 or 1.3.2.1 are formally possible. Gear pairs that correspond to the vector diagrams 1.1.2.1 and 1.3.2.1 are not profoundly investigated yet.⁴

Finally, another extreme case is required to be mentioned. In a particular case when the rotation vectors, ω_g and ω_p , are equal to each other (i.e., $\omega_g \equiv \omega_p$), the rotary-positive parallel-axes gear pair 1.3.2 reduces to a gear coupling. For a gear coupling, the rotation vector, ω_{pt} , is equal to zero ($\omega_{pt} \equiv 0$). The base cones apexes, A_g and A_p , are coincident with one another. Because the equality $\omega_g \equiv \omega_p$ is valid, the diameters, \tilde{d}_g and \tilde{d}_p , are both equal to zero (i.e., $\tilde{d}_g \equiv \tilde{d}_p \equiv 0$). Therefore, the plane-of-action apex, A_{pa} , is coincident with the base cone apexes, A_g and A_p ($A_g \equiv A_p \equiv A_{pa}$).

This particular case can also be construed as a reduced case of internal intersected-axes gear pair featuring a zero intersected-axes angle ($\Sigma = 0^\circ$).

The coupling can be composed of an internal and external spur gears with equal tooth numbers, of a pair of similar bevel gears, or of two face gears. The number 1.3.2.1 is assigned to a degenerate gear pair of this kind.

³More accurately, the radius of the gear “sector,” and not of the gear, approaches infinity.

⁴The vector diagrams 1.1.2.1 and 1.3.2.1 correspond to the deeply degenerate designs of gear pairs. Because of these, significant features could be observed when developing tooth flanks for gearing that correspond to the gear vector diagrams 1.1.2.1 and 1.3.2.1. When friction between the interacting tooth flanks of the gear, G , and the pinion, P , is ignored, the tangential force by means of which the torque is transmitted from the driving shaft to the driven shaft acts along the common perpendicular, \mathbf{n}_g , to the interacting tooth flanks, G and P . The common perpendicular, \mathbf{n}_g , intersect the pitch line, P_{ln} , that is, it intersects the line of action of the vector of instant rotation, ω_{pt} . In cases of gear pairs that correspond to the vector diagrams 1.1.2.1 and 1.3.2.1, all three rotation vectors, that is, ω_g , ω_p , and ω_{pt} , are along a common straight line, P_{ln} . Once the line of action of the vector \mathbf{n}_g intersects the line of action of the velocity vector, ω_{pt} , the arm of tangential force in the gear pair becomes zero. This means that no torque can be transmitted by a gear pair of these particular kinds of gearing. Gear coupling is not a kind of gearing (no contact ratio can be defined). This discrepancy needs to be thoroughly investigated.

In reality, a gear axis and its mating pinion axis always are slightly misaligned. Under such a scenario no discrepancy is observed, and gear pairs can be designed in accordance to the vector diagrams 1.1.2.1 and 1.3.2.1.

The third stratum of the classification of all possible kinds of the gear vector diagrams (see Fig. 1.10) is represented by two types of parallel-axes gear pairs: (1) the rotary-zero gear pair 1.2.2.1 and (2) the gear coupling 1.3.2.1.

The total number of the gear vector diagrams of zero-degree-of-freedom gearing is limited to 11 different kinds of vector diagrams. Gear vector diagrams of all possible kinds are covered by the classification (see Fig. 1.10). No gear vector diagrams are missed, as well as no gear vector diagrams not covered by the classification are feasible. This makes it possible to conclude that the proposed classification (shown in Fig. 1.10) is complete and self-consistent.

The classification can be used for the investigation of the kinematics and the geometry of gearing of all kinds, that is, of all known kinds of gearing, as well as of all kinds of gearing not known yet and to be developed in the future.

1.1.3 Line of Contact of Favorable Geometry in a Gear Pair

When a geometrically-accurate gear pair operates, tooth flanks of a gear, \mathcal{G} , and that of a mating pinion, \mathcal{P} , make line contact with one another. The line of contact, LC , is viewed as a planar curve that is entirely located within the plane of action, PA , and that travels with the plane of action when the gears rotate.

Lines of contact of various geometries can be used to generate the teeth flanks of a gear and that of a mating pinion in gearing of all kinds. A few examples are illustrated in Fig. 1.11.

Consider a crossed-axes geometrically accurate gear pair.

Three apexes are recognized in perfect (or, in other words, in geometrically accurate) crossed-axes gear pair [1]. They are:

- (a) The plane-of-action apex, A_{pa} .
- (b) The gear-base-cone apex, A_g .
- (c) The pinion-base-cone apex, A_p .

Note: in a geometrically accurate intersected-axes gear pair, all three apexes, A_{pa} , A_g , and A_p , are coincident with one another. Therefore, in a geometrically accurate straight bevel gear pair, the line of contact, LC , is a straight line through the apex, $A_{pa} \equiv A_g \equiv A_p$.

In a case of geometrically accurate crossed-axes gears, the problem of design a gear pair with “straight” teeth is a bit tricky.

In a particular case, a tooth flank of a gear and that of a mating pinion in a crossed-axes gear pair can be designed so as to keep a straight line of contact, LC_{straight} , between the teeth flanks, \mathcal{G} and \mathcal{P} , aligned with a straight line through the plane-of-action apex, A_{pa} . This is schematically illustrated in Fig. 1.11a. The gears, the teeth flanks, \mathcal{G} and \mathcal{P} , of which are generated by means of the line of contact, LC_{straight} , are referred to as the “pseudo-straight crossed-axes gears,” regardless of the tooth flanks, \mathcal{G} and \mathcal{P} , of this particular kind of gearing are curved in their lengthwise direction. The term “pseudo-straight crossed-axes gears” reflects that the tooth flanks, \mathcal{G} and \mathcal{P} ,

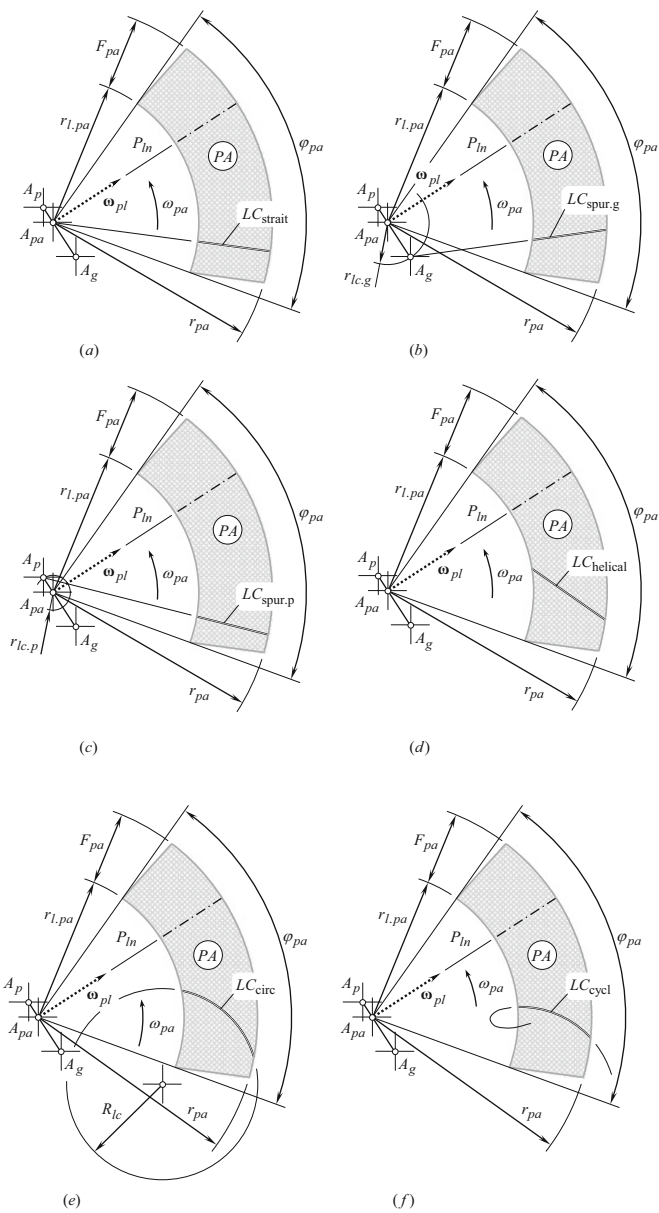


Fig. 1.11 Examples of possible geometries of the lines of contact, LC , between a gear tooth flank, G , and a mating pinion tooth flank, P , in perfect crossed-axes gear pair: (a) “pseudo-straight crossed-axes gears”, (b) “straight-gear crossed-axes gears”, (c) “straight-pinion crossed-axes gears”, (d) helical crossed-axes gears, (e) spiral crossed-axes gears, and (f) cycloidal crossed-axes gears. (Adapted from: Radzevich, S.P., Theory of Gearing: Kinematics, Geometry, and Synthesis, 2nd Edition, revised and expanded, CRC Press, Boca Raton, FL, 2018, 934 pages.)

are generated by a straight line through the plane-of-action apex, A_{pa} . When the gears rotate, at a certain instant of time, the line of contact, in addition, is aligned with the axis of instant rotation, P_{ln} .

Pseudo-straight crossed-axes gearing features face contact ratio of a zero value ($m_F = 0$).

Straight-line segments that have other configurations within the plane of action, PA , are of particular interest from the perspective of the tooth flank generation when machining gears. In a particular case, the tooth flanks of a gear and a mating pinion in a geometrically accurate crossed-axes gear pair can be designed so as to keep the line of contact, $LC_{spur. g}$, between the tooth flanks, \mathcal{G} and \mathcal{P} , aligned with a straight line through the gear apex, A_g . This design is schematically depicted in Fig. 1.11b. Both the gear tooth flank, \mathcal{G} , and the tooth flank, \mathcal{P} , of the mating pinion that are generated by means of the line of contact, $LC_{spur. g}$, of such a configuration are not straight; they are curved in their lengthwise direction instead.

Similarly, the tooth flanks of a gear and a mating pinion in a crossed-axes gear pair can be designed so as to keep the line of contact, $LC_{spur. p}$, between the tooth flanks, \mathcal{G} and \mathcal{P} , aligned with a straight line through the pinion apex, A_p . This case is schematically shown in Fig. 1.11c. Both the gear tooth flank, \mathcal{G} , and the tooth flank, \mathcal{P} , of the mating pinion, that are generated by means of the line of contact, $LC_{spur. p}$, of such a configuration are not straight; they are curved in their lengthwise direction instead.

Ultimately, the tooth flanks of a gear and a mating pinion in a crossed-axes gear pair can be generated by an arbitrary straight line, $LC_{helical}$, that is entirely located within the plane of action, PA . The straight line of contact, $LC_{helical}$, passes neither through the plane-of-action apex, A_{pa} , nor through the gear apex, A_g , nor through the pinion apex, A_p . The configuration of the line of contact for this particular kind of crossed-axes is illustrated in Fig. 1.11d. Under such a scenario, the tooth flanks, \mathcal{G} and \mathcal{P} , of the gear and the pinion are a kind of screw surfaces.

Finally, one can conclude from that that no geometrically accurate crossed-axes straight bevel gearing is feasible at all.

Not only straight lines can be used for the purpose of the generation of the tooth flanks of the gear and the pinion in crossed-axes gearing.

Figure 1.11e illustrates a case when the circular arc of a certain radius, R_{lc} , is used to generate the tooth flanks of a gear and a mating pinion in crossed-axes gearing. The arc is centered at a point within the plane of action, PA , and it is entirely located within the plane, PA . The tooth flanks, \mathcal{G} and \mathcal{P} , of complex geometry are generated by the circular arc. Geometrically accurate spiral bevel gears are generated in this way.

One more example of a planar line of contact, LC_{cycl} , between the gear tooth flank, \mathcal{G} , and the pinion tooth flank, \mathcal{P} , is depicted in Fig. 1.11f. The line of contact, LC_{cycl} , is entirely located within the plane of action, PA . Geometrically accurate cycloidal bevel gears are generated in this way.

The main advantage of a straight line (see Fig. 1.11a through Fig. 1.11d), of a circular arc (see Fig. 1.11e), and of an arc of a cycloidal curve (see Fig. 1.11f) is that these lines are easy to be reproduced kinematically on a machine tool. Planar curves of other geometries (namely, involute of a circle arc, sine-curve arc, a few more to be

mentioned) that could be kinematically generated on a machine tool can also be implemented to generate the tooth flanks of a gear and a mating pinion in a crossed-axes gear pair. The convenience of generation of the line of contact, LC , is of critical importance in this concern.

The approach used above for the derivation of an expression for the position vector of a point of the tooth flank generated by means of an arbitrary planar curve [1] can be used for the derivation of an equation for the position vector of a point of tooth flanks, G and P , generated by means of planar curves those shown in Fig. 1.11.

It is right point to stress here on the importance of the geometry of the line of contact, LC , for solving the problem of synthesizing a desirable crossed-axes gear pair. The geometry of the line of contact, LC , is a powerful mean to take control over the contact geometry of tooth flanks of a gear, G , and its mating pinion, P . This means that the contact geometry of the tooth flanks, G and P (see **Appendix C**), is the key for the determination of the best possible geometry of the line of contact, LC , for any particular case of crossed-axes gearing.

The total number of planar curves that can be used to design gears with a line of contact, LC , with a favorable geometry is large and is almost infinite. In the developed classification of gearing, the discussion of the planar curves LC is limited only to those curves that are easy to be generated on machine tools. They are:

- A straight-line segment (through the plane-of-action apex, A_{pa}).
- An arbitrary-straight-line segment (not through the plane-of-action apex, A_{pa}).
- Two straight-line segments (herring-bone gears).
- Two straight-line segments (separated from one another).
- Arc of a circle.
- Arc of a cycloidal curve.
- Arc of an involute of a circle.
- Arc of a sine-curve.

In a case of necessity, more planar curves LC can be involved into the consideration.

Taken in a whole, the kinematics of gearing forms a robust foundation for scientific classification of geometrically accurate gearing. Later on use of this concept enables development of scientific classification of gearing of all kinds, including, but not limited to, approximate gears.

1.1.4 On Classification of Approximate Gearing

Approximate gearing is extensively used in the nowadays industry as they are cheaper. Tooth flanks of a gear and that of a mating pinion do not obey the conjugate action law of gearing—this is the first principal feature of approximate gearing of all design. The second feature is due to neither base pitch of a gear nor base pitch of a mating pinion; both can be identified in approximate gearing. An example of approximate gearing is shown in Fig. 1.12. Low to moderate rotations and low to moderate loading are the two main areas of application of approximate gearing.



Fig. 1.12 Example of approximate gearing

Similar to the classification of geometrically accurate gearing, the kinematic approach can be implemented for the development of a scientific classification of approximate gearing as well.

When two rotation vectors associated with an input and with an output shafts are specified, gears of various geometries can be used to transmit and to transform a rotation from the driving shaft to the driven shaft. Skew axes helical gears, worm gearing, and others are used to transmit and to transform a rotation from an input shaft to an output shaft, the axes of which cross each other at crossed-axes angle of a certain value.

Gears that feature various gear generic surfaces can be used to transmit and to transform a given rotation. This makes it possible to conclude that the gear vector diagram is necessary but not sufficient to identify the actual type of a gear pair. In this regard, the gear generic surface, of which a gear pair is composed, is of importance. If the gear generic surface is incorporated into consideration, this makes possible a further development of the classification of possible kinds of gear pairs. The orderly classification of gear pairs along with the classification of gears themselves is a desirable prerequisite for the study of gears in general. It is a challenging problem to develop a scientific classification of gear pairs.

In general engineering practice, names have been given to most of the numerous kinds of gear members and gear combinations. However, these names, although generally accepted and used, are sometimes indefinite and ambiguous. In some cases, it is hard to find a sufficient number of names to distinguish between variants, which deserve some recognition of their individuality; in others, the same gear operating in different ways may have different names. The problem of classification, moreover, yields different results according to the direction from which it is approached. By treating gears according to the character of their teeth, one system of grouping emerges; by considering the relative position of the shafts they connect, another system is possible; and from the point of view of the real nature of tooth action, a third grouping is possible.

Below, in this section of the book, an attempt to classify approximate gear pairs based on their associated vector diagrams is undertaken.

1.1.4.1 Origination of the Term “Gear Generic Surface”

Gears, those used in the design of various machines and mechanisms, are somehow machined on machine tools. Nowadays, machine tools, especially numerical control machines (*NC*), are capable of performing any desirable motion of the cutting tool in relation to the workpiece. This makes possible machining a gear that has any desirable tooth flank geometry. It is necessary to stress here that use of any desirable motion of the cutting tool with respect to the work-gear is not a common practice in machining gears, especially machining gears in high-volume production industries.

The motions the gear cutting tool performs in relation to a work-gear are either a kind of translation, or a kind of rotation, or a combination of translations and rotations [7]. This is because a translation and a rotation are the two elementary motions that can be easily performed on a machine tool. If a relative motion of a gear-cutting tool is limited either to a translation, or a rotation, or a combination of a few translations and rotations, then all possible types of gears and gear pairs can be identified and investigated.

Let us proceed with a discussion of possible gear generic surfaces of gears machined on conventional machine tools for gear production.

1.1.4.2 Evaluation of the Total Number of Possible Geometries of Gear Generic Surfaces

Once all possible kinds of gear design are limited to those gears, for which gear generic surfaces are generated either by a straight-line segment, or by a circular arc, the following two actions are possible:

1. Identification of all possible types of gears.
2. Development of a classification of possible kinds of gear generic surfaces.

This classification is important for the purpose of designing gear pairs that feature the most favorable (nearly optimal) design parameters.

1.1.4.3 Possible Geometries of Axial Profile of Gear Generic Surfaces

Referring to Fig. 1.13, consider gear generic surfaces designed for an intersected-axes gear pair.

If no constraints are imposed, the ideal gear generic surface can be construed as a locus of consecutive positions of the axis of instant rotation, P_{ln} , when the axis is rotated about the gear axis, O_g . In this way, the gear generic surface is shaped in the form of a one-sheet hyperboloid of revolution. Two hyperbolas appear in the section of this surface by a plane through the gear axis of rotation, O_g .

An expression for the analytical description of a gear generic surface can be derived in the following way: consider a gear generic surface that is referred to a

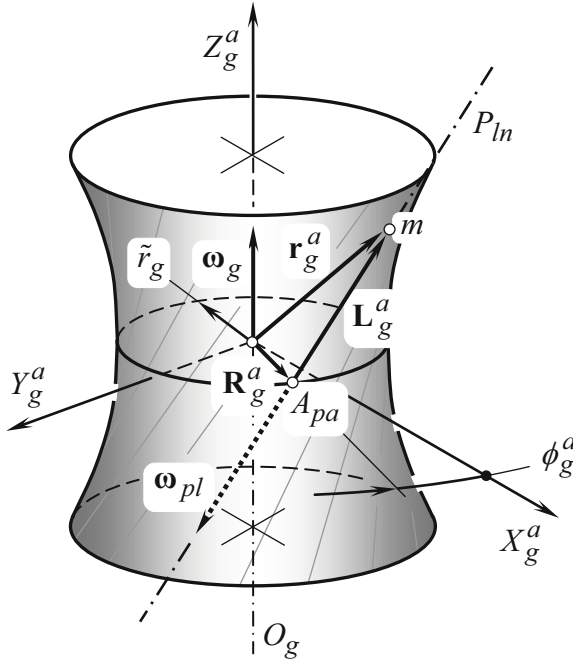


Fig. 1.13 On analytical description of a gear generic surface

Cartesian coordinate system, $X_g^a Y_g^a Z_g^a$, as shown in Fig. 1.13. The position vector, \mathbf{r}_g^a , of an arbitrary point, m , of the gear generic surface can be considered as summa of two components, that is:

$$\mathbf{r}_g^a = \mathbf{R}_g^a + \mathbf{L}_g^a \quad (1.4)$$

In the reference system, $X_g^a Y_g^a Z_g^a$, one of the components, \mathbf{R}_g^a (see Fig. 1.13), yields analytical representation in vector form:

$$\mathbf{R}_g^a = \mathbf{i} \cdot \tilde{r}_g \cos \phi_g^a + \mathbf{j} \cdot \tilde{r}_g \sin \phi_g^a \quad (1.5)$$

where:

\tilde{r}_g is the radius of throat of the gear generic surface (the radius, \tilde{r}_g , is measured in the coordinate plane, $X_g^a Y_g^a$)

ϕ_g^a is the angular parameter of the gear generic surface.

For analytical description of another component, \mathbf{L}_g^a , of the position vector, \mathbf{r}_g^a , the following expression can be used:

$$\mathbf{L}_g^a = -\mathbf{i} \cdot z_g^a \tan \Sigma_g \sin \phi_g^a + \mathbf{j} \cdot z_g^a \tan \Sigma_g \cos \phi_g^a + \mathbf{k} \cdot z_g^a \quad (1.6)$$

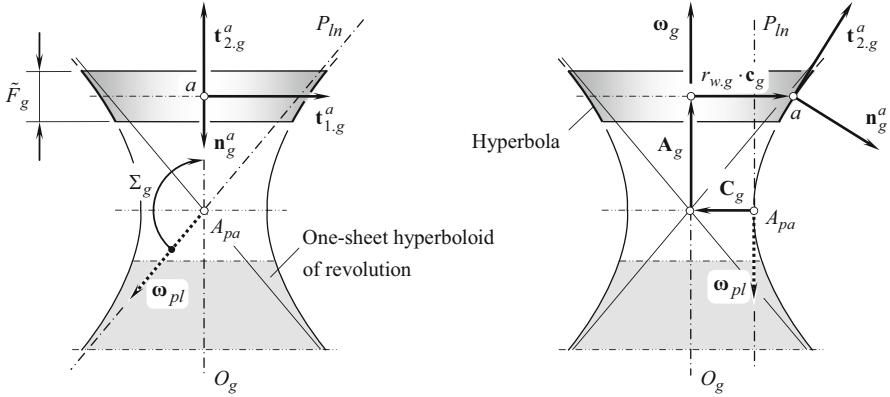


Fig. 1.14 “Darboux frame”, $\mathbf{n}_g^a, \mathbf{t}_{1,g}^a, \mathbf{t}_{2,g}^a$, associated with the desirable gear generic surface

The angular parameter, ϕ_g^a , of the gear generic surface is the first *Gauss* parameter of the gear generic surface.

Equations (1.5) and (1.6) allow for the derivation of an expression:

$$\mathbf{r}_g^a(\phi_g^a, z_g^a) = \begin{bmatrix} \tilde{r}_g \cos \phi_g^a - z_g^a \tan \Sigma_g \sin \phi_g^a \\ \tilde{r}_g \sin \phi_g^a + z_g^a \tan \Sigma_g \cos \phi_g^a \\ z_g^a \\ 1 \end{bmatrix} \quad (1.7)$$

for the position vector, \mathbf{r}_g^a , of an arbitrary point, m , of the gear generic surface.

In Eq. (1.7), other *Gauss* parameter of the gear generic surface is denoted by z_g^a , and Σ_g designates the angle that the rotation vector of the gear, ω_g , makes with the vector, ω_{pl} of instant rotation [$\Sigma_g = \angle(\omega_g, \omega_{pl})$].

The rotation vector of the gear, ω_g , is pointed along the gear axis of rotation, O_g . The vector, ω_g , is applied at the throat of the gear generic surface. The vector of instant rotation, ω_{pl} , is pointed along the axis of instant rotation, P_{ln} . This vector is applied at the plane-of-action apex, A_{pa} .

The face width of the gear is denoted by \tilde{F}_g . The location of the middle section of the generic gear surface is specified by the vectors $\mathbf{C}_g, \mathbf{A}_g$, and $r_{w.g} \cdot \mathbf{c}_g$, as shown in Fig. 1.14.

A local reference system is associated with the gear generic surface. The origin of the reference system is at a point, a , within the axial profile of the gear generic surface. The origin, a , is at the middle of the width, \tilde{F}_g . In the particular case under consideration, a “Darboux⁵ frame” is used as the reference system. The “Darboux frame” is comprised by three unit vectors, $\mathbf{n}_g^a, \mathbf{t}_{1,g}^a$, and $\mathbf{t}_{2,g}^a$.

⁵Jean-Gaston Darboux (August 14, 1842–February 23, 1917), a French mathematician.

The vector, \mathbf{n}_g^a , is a unit normal vector to the gear generic surface at the point, a . An equation:

$$\mathbf{n}_g^a = \mathbf{u}_g \cdot \mathbf{v}_g \quad (1.8)$$

can be used for the calculation of the unit normal vector, \mathbf{n}_g^a .

In Eq. (1.8), two unit tangent vectors at a point at a of the gear generic surface are designated as \mathbf{u}_g and \mathbf{v}_g . The unit vectors, \mathbf{u}_g and \mathbf{v}_g , are unitless. They are given as follows:

$$\mathbf{u}_g = \frac{\mathbf{U}_g}{|\mathbf{U}_g|} \quad (1.9)$$

$$\mathbf{v}_g = \frac{\mathbf{V}_g}{|\mathbf{V}_g|} \quad (1.10)$$

correspondingly.

In Eqs. (1.9) and (1.10), the tangent vectors, \mathbf{U}_g and \mathbf{V}_g , are given by $\mathbf{U}_g = \partial \mathbf{r}_g^s / \partial U_g$ and $\mathbf{V}_g = \partial \mathbf{r}_g^s / \partial V_g$, correspondingly, and $\mathbf{r}_g^s \delta$ is the position vector of a point of the gear generic surface. The *Gauss* parameters of the gear generic surface are denoted by U_g and V_g .

The unit normal vector, \mathbf{n}_g^a , is a unitless parameter as it is expressed in terms of the unitless unit tangent vectors, \mathbf{u}_g and \mathbf{v}_g [see Eq. (1.8)].

Labeling of the principal directions depends upon the curvature of the gear generic surface. The principal direction that features a greater curvature, $k_{1,g}^a$ (and, thus, a smaller radius of curvature, $R_{1,g}^a$), is labeled as $\mathbf{t}_{1,g}^a$. The principal direction that features a smaller curvature, $k_{2,g}^a$ (and, thus, a greater radius of curvature, $R_{2,g}^a$) is labeled as $\mathbf{t}_{2,g}^a$ [1, 7] (Here, the curvatures, $k_{1,g}^a$ and $k_{2,g}^a$, and the corresponding radii of curvature, $R_{1,g}^a$ and $R_{2,g}^a$, are signed values. They are positive in a case of convex section of the gear generic surface by a normal plane, and they are negative when the section is concave). As the equality $R_1 = k_1^{-1}$ is valid by definition, the inequalities, $k_{1,g}^a > k_{2,g}^a$ and $R_{1,g}^a < R_{2,g}^a$, are always valid.⁶ In umbilical points on a surface, when all the radii of normal curvature are of a constant value ($R_g^a = \text{const}$), the ‘‘Darboux frame’’ does not exist. In this reduced case, a limit case of the ‘‘Darboux frame’’ when $R_{1,g}^a$ approaches infinity (i.e., $R_{1,g}^a \rightarrow \infty$) is used instead of the trihedron, $\mathbf{n}_g^a \mathbf{t}_{1,g}^a \mathbf{t}_{2,g}^a$.

The unit tangent vectors, $\mathbf{t}_{1,g}^a$ and $\mathbf{t}_{2,g}^a$, are the principal vectors at point within the gear generic surface. The first and the second principal directions on the gear generic

⁶Remember that the algebraic values of the radii of principal curvatures, $R_{1,g}^a$ and $R_{2,g}^a$, relate to each other as $R_{2,g}^a > R_{1,g}^a$. In the case of umbilical points, all radii of normal curvature are equal. Therefore, the principal directions, $\mathbf{t}_{1,g}^a$ and $\mathbf{t}_{2,g}^a$ (and, consequently, the principal radii of curvature, $R_{1,g}^a$ and $R_{2,g}^a$), are not identified for umbilical points on gear generic surface.

surface are specified by the tangent vectors, $\mathbf{t}_{1.g}^a$ and $\mathbf{t}_{2.g}^a$. The vector, $\mathbf{t}_{1.g}^a$, is tangential to the section of the gear generic surface by a transverse plane through the point, a , as this section is convex. The first principal direction is specified by the unit tangent vector, $\mathbf{t}_{1.g}^a$. The vector, $\mathbf{t}_{2.g}^a$, is tangential to the cross section of the gear generic surface by an axial plane through the point, a , as this section is concave. The second principal direction is specified by the unit tangent vector, $\mathbf{t}_{2.g}^a$.

The unit tangent vectors, $\mathbf{t}_{1.g}^a$ and $\mathbf{t}_{2.g}^a$, are specified by the expressions:

$$\mathbf{t}_{1.g}^a = \frac{\mathbf{T}_{1.g}^a}{|\mathbf{T}_{1.g}^a|} \quad (1.11)$$

$$\mathbf{t}_{2.g}^a = \frac{\mathbf{T}_{2.g}^a}{|\mathbf{T}_{2.g}^a|} \quad (1.12)$$

where $\mathbf{T}_{1.g}^a$ and $\mathbf{T}_{2.g}^a$ are the vectors of the first and the second principal directions of the gear generic surface. Known methods [1, 7] are used for the calculation of the unit tangent vectors, $\mathbf{t}_{1.g}^a$ and $\mathbf{t}_{2.g}^a$.

Once the unit vectors, \mathbf{n}_g^a , $\mathbf{t}_{1.g}^a$, and $\mathbf{t}_{2.g}^a$, are mutually orthogonal, and two of them (namely, $\mathbf{t}_{1.g}^a$ and $\mathbf{t}_{2.g}^a$) are pointed along the principal directions on the gear generic surface, they comprise a trihedron that is commonly referred to as ‘‘Darboux frame.’’

As shown in Fig. 1.14, the gear generic surface has a favorable geometry as it is generated by the axis, P_m , when the axis is given a rotation about the gear axis of rotation, O_g . Unfortunately, a gear generic surface of this geometry is impractical, mostly because it is inconvenient from manufacturing perspective. Gear generic surfaces of simplified geometries are commonly used instead of the one depicted in Fig. 1.14.

As it is adopted in this text, all possible elementary motions of the gear cutting tool in relation to a work-gear are limited to just translations, rotations, and feasible combinations of translations and rotations. Bearing this concept in mind, all possible shapes of gear generic surface can be identified. The ‘‘Darboux frame,’’ $\mathbf{n}_g^a \mathbf{t}_{1.g}^a \mathbf{t}_{2.g}^a$, is helpful to this end.

Consider the gear generic surface of a gear machined by the gear cutting tool that performs a straight motion relative to the work-gear. No physical constraints are imposed on machining of the gear this way. The parameters of the straight motion are assigned so as to make a trajectory of the straight motion of the gear cutting tool tangential to the hyperbola at the point, a , as schematically illustrated in Fig. 1.15. In the case under consideration, the desirable hyperbolic profile of the gear generic surface is substituted by the straight-line segment, which is tangential to the hyperbola at a . The straight-line segment is at an angle, φ_g^a , relative to the gear axis of rotation, O_g . The angle, φ_g^a , can be expressed in terms of the first derivative of an equation of the hyperbola calculated at the point, a . The actual form of an equation for the calculating the angle φ_g^a depends on the kind of parameterization of the equation of the hyperbolic axial profile of the desirable gear generic surface.

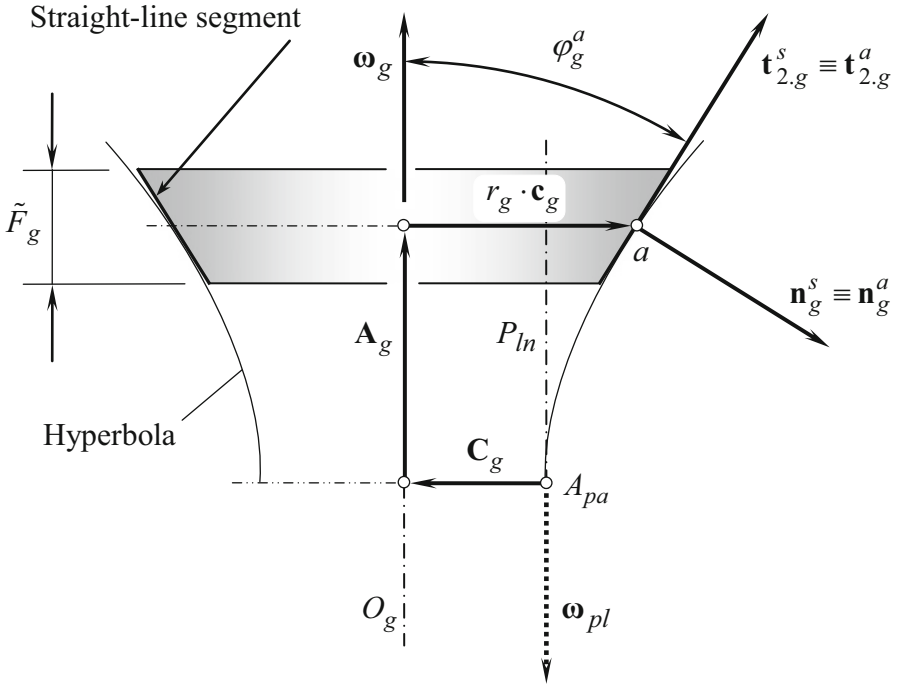


Fig. 1.15 Axial profile of a gear generic surface approximated by a straight-line segment tangential to the hyperbola at point, a

The approximation of the hyperbolic arc segment by the straight-line segment results in zero curvature of the gear generic surface in the second principal direction ($k_{2,g}^a = 0$). The first principal curvature, $k_{1,g}^a$, can be determined using for this purpose the “Meusnier’s⁷ theorem”:

$$k_{1,g}^a = \frac{\cos \left[\angle \left(\mathbf{c}_g, \mathbf{n}_g^a \right) \right]}{r_{w.g}} \tag{1.13}$$

As of the straight-line axial profile is tangential at a to the hyperbola, no changes to the orientation of the axial profile are observed. As a result, the “Darboux frame,” $\mathbf{n}_g^s \mathbf{t}_{1,g}^s \mathbf{t}_{2,g}^s$, associated with the approximated gear generic surface is identical to the trihedron $\mathbf{n}_g^a \mathbf{t}_{1,g}^a \mathbf{t}_{2,g}^a$ associated with the desirable gear generic surface.

Crossed-axes gears of conventional design, “Hypoid gearing” in particular, feature the gear generic surface that feature the geometry illustrated in Fig. 1.15.

⁷Jean Baptiste Marie Charles de la Place **Meusnier** (June 19, 1754–June 17, 1793), a French mathematician.

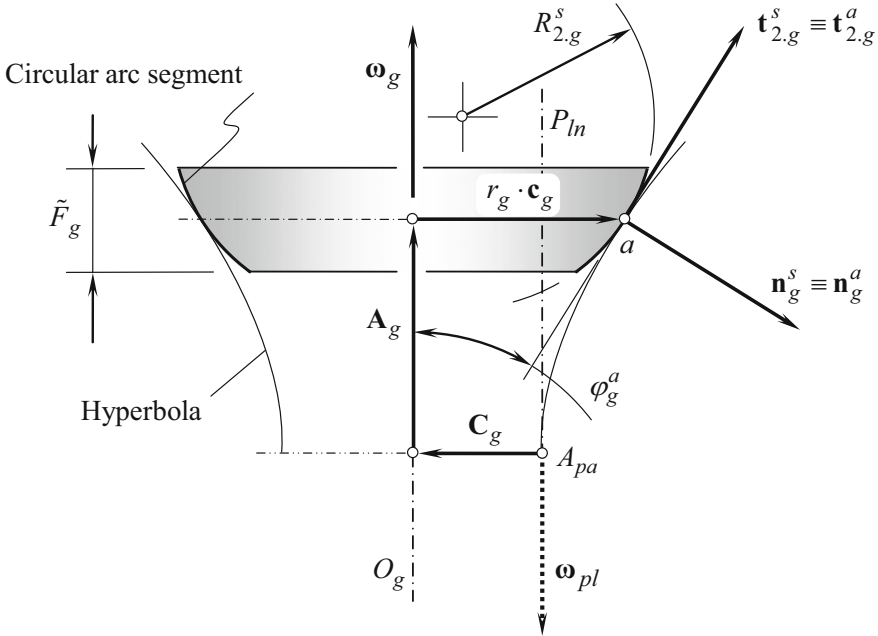


Fig. 1.16 Axial profile of the gear generic surface approximated by a convex circular arc tangential at point, a , to the hyperbola

Consider gear generic surface of a gear that is machined by the gear cutting tool, that performs a rotary motion relative to the work-gear. Again, no physical constraints are imposed on machining the gear this way.

Two different methods of cutting the gear can be distinguished in this case.

First, the parameters of the rotary motion are set up so as to make the trajectory of the rotary motion of the gear cutting tool tangential to the hyperbola at point a , as illustrated in Fig. 1.16. In the case under consideration, the desirable hyperbolic profile of the gear generic surface is replaced with a circular-arc segment that is tangential to the hyperbola at a . The approximation of the hyperbolic arc segment by the circular-arc segment results in a positive curvature of the section of the gear generic surface by an axial plane. The direction at which the normal curvature is the greatest possible is labeled as $\mathbf{t}_{1.g}^s$. The normal curvature in this direction is labeled as $k_{1.g}^s$. The direction at which the normal curvature is of the smallest possible value is labeled as $\mathbf{t}_{2.g}^s$. The normal curvature in this direction is labeled as $k_{2.g}^s$. Ultimately, either the two identities $\mathbf{t}_{1.g}^s \equiv \mathbf{t}_{1.g}^a$ and $\mathbf{t}_{2.g}^s \equiv \mathbf{t}_{2.g}^a$ (as depicted in Fig. 1.16) or the inverse identities, $\mathbf{t}_{1.g}^s \equiv \mathbf{t}_{2.g}^a$ and $\mathbf{t}_{2.g}^s \equiv \mathbf{t}_{1.g}^a$, are valid. In this way, the gear generic surface is affected by the kinematics of the gear-machining process. Consequently, the kinematics affects the labeling of the unit vectors of which the “Darboux frame” is composed.

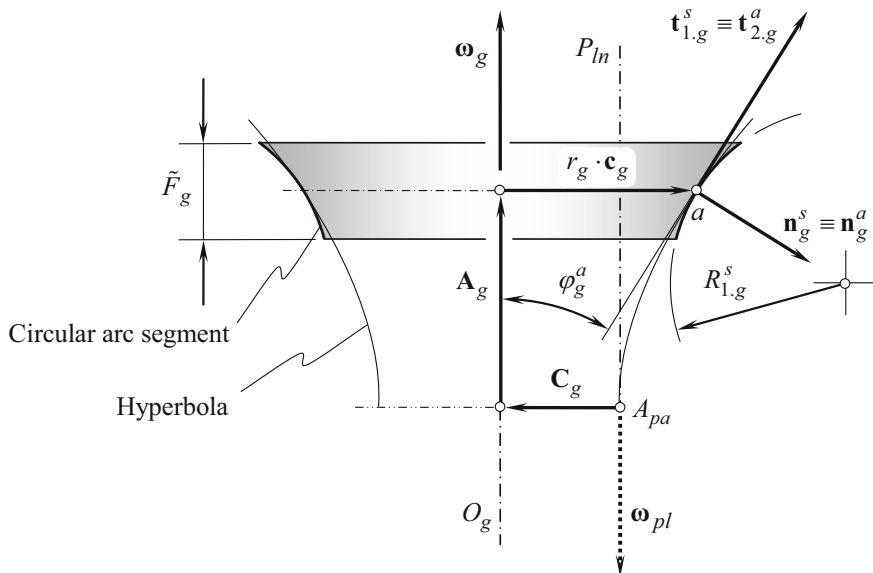


Fig. 1.17 Axial profile of the gear generic surface approximated by a concave circular arc tangential to the hyperbola at point, a

Because the circular-arc axial profile is tangential at point *a* to the hyperbola, no changes to the orientation of the axial profile are observed. As a result, the “Darboux frame,” $\mathbf{n}_g^s \mathbf{t}_{1.g}^s \mathbf{t}_{2.g}^s$, associated with the approximated gear generic surface is identical to that, $\mathbf{n}_g^a \mathbf{t}_{1.g}^a \mathbf{t}_{2.g}^a$, associated with the desired gear generic surface.

Second, the parameters of the rotary motion are set up so as to make the trajectory of the rotary motion of the gear cutting tool tangential to the hyperbola at point *a*, as schematically illustrated in Fig. 1.17. In this scenario, the desirable hyperbolic profile of the gear generic surface is replaced with a circular-arc segment that is tangential to the hyperbola at point, *a*. The approximation of the hyperbolic arc segment by the circular-arc segment results in a negative curvature of the section of the gear generic surface by an axial plane. The identities $\mathbf{t}_{1.g}^s \equiv \mathbf{t}_{2.g}^a$ and $\mathbf{t}_{2.g}^s \equiv \mathbf{t}_{1.g}^a$ are valid in the case under consideration, as illustrated in Fig. 1.17.

Because the circular-arc axial profile is tangential at *a* to the hyperbola, no changes to the orientation of the axial profile are observed. As a result, the “Darboux frame,” $\mathbf{n}_g^s \mathbf{t}_{1.g}^s \mathbf{t}_{2.g}^s$, associated with the approximated gear generic surface is similar to the $\mathbf{n}_g^a \mathbf{t}_{1.g}^a \mathbf{t}_{2.g}^a$ associated with the desirable gear generic surface.

Gears that have circular-arc axial profiles of the gear generic surface (see Fig. 1.16 and Fig. 1.17) do not have an extensive application in the industry yet.

Methods to cut gears on both, on machine tools, and on gear generators are not limited to those in which the actual and desired axial profiles of generic gear surface

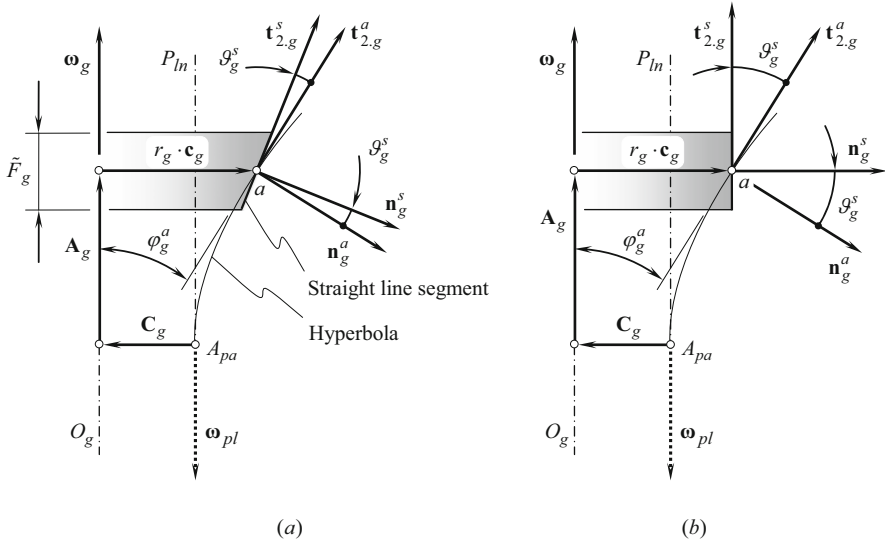


Fig. 1.18 Axial profile of the gear generic surface approximated at point, a , by a straight-line segment that makes a certain positive angle, ϑ_g^s , in relation to the unit normal vector, \mathbf{n}_g^s : (a) conical gear, and (b) cylindrical gear

are in tangency to each other at a certain point. The profiles can intersect each other at a certain angle.

The straight-line segment of an actual axial profile of the gear generic surface can be tilted at an angle, ϑ_g^s , as schematically shown in Fig. 1.18. The angle, ϑ_g^s , measured in the counterclockwise direction is considered to be of a positive value. The orientation of the “Darboux frame,” $\mathbf{n}_g^s \mathbf{t}_{1,g}^s \mathbf{t}_{2,g}^s$, of the actual gear generic surface in relation to the “Darboux frame,” $\mathbf{n}_g^a \mathbf{t}_{1,g}^a \mathbf{t}_{2,g}^a$, of the desirable gear generic surface is specified by the angle, ϑ_b^s . The trihedron, $\mathbf{n}_g^s \mathbf{t}_{1,g}^s \mathbf{t}_{2,g}^s$, is turned about the unit vector, $\mathbf{t}_{1,g}^s$, in a counterclockwise direction through the angle, ϑ_g^s (see Fig. 1.18a).

The actual value of the angle, ϑ_g^s , is in the range of $0^\circ < \vartheta_g^s < \varphi_g^a + 90^\circ$. In a particular case, the value of angle, ϑ_g^s , can be chosen as equal to angle, φ_g^a , at which the tangent to the hyperbola is tilted relative to the gear axis of rotation, O_g , as shown in Fig. 1.18b. A cylindrical gear for a crossed-axes gear pair is machined under such conditions.

Similarly, the straight-line segment of an actual axial profile of the gear generic surface can be tilted at an angle, ϑ_g^s , in the opposite direction as shown in Fig. 1.19. The angle, ϑ_g^s , in this case is of a negative value. The trihedron, $\mathbf{n}_g^s \mathbf{t}_{1,g}^s \mathbf{t}_{2,g}^s$, is turned about the unit vector, $\mathbf{t}_{1,g}^s$, in a clockwise direction through the angle, ϑ_g^s (see Fig. 1.19a).

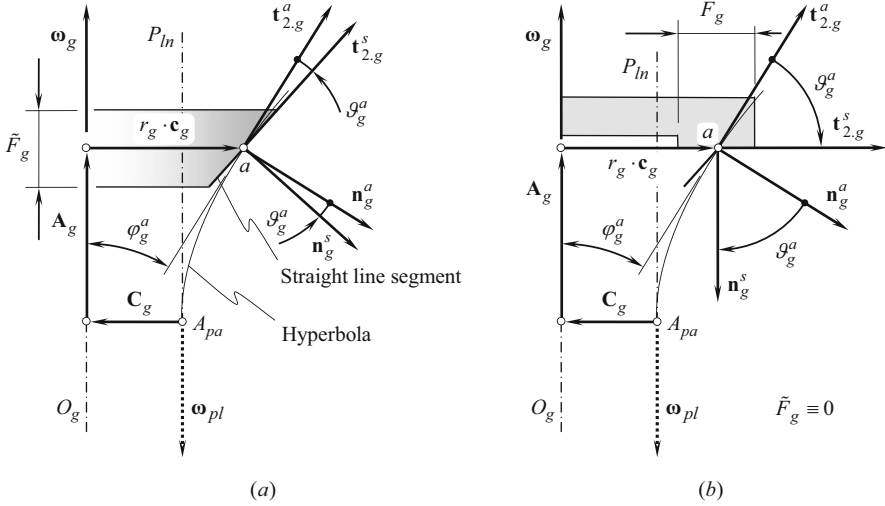


Fig. 1.19 Axial profile of a gear generic surface approximated at the point, a , of the hyperbola by a straight line segment at a certain negative angle, ϑ_g^s , in relation to the unit normal vector, \mathbf{n}_g^a : (a) conical gear, and (b) face gear

The actual value of the angle, ϑ_g^s , is in the range of $-(\varphi_g^a + 90^\circ) < \vartheta_g^s < 0^\circ$. In a particular case, an actual value of the angle ϑ_g^s can be set up equal to $\vartheta_g^s = 90^\circ - \varphi_g^a$. In this scenario, the straight-line segment is perpendicular to the gear axis of rotation, O_g , as shown in Fig. 1.19b. A face gear for a crossed-axes gear pair is machined in this case.

Gears that feature axial profile of the gear generic surface in the form of straight-line segments tilted at a certain angle, ϑ_g^s (see Fig. 1.18 and Fig. 1.19) are used in the design of special-purpose gear trains.

Similar to the gears that have an inclined straight-line profile (see Fig. 1.18 and Fig. 1.19), circular-arc axial profile of gear generic surface can also be tilted at either positive or negative angle, ϑ_g^s , relative to the unit normal vector, \mathbf{n}_g^a , to the desirable gear generic surface.

The results of the analysis performed for convex circular-arc axial profiles inclined at a certain angle, ϑ_g^s , in relation to the unit normal vector, \mathbf{n}_g^a , at the point, a , to the hyperbola are illustrated in Fig. 1.20.

When the angle, ϑ_g^s , is of a positive value (see Fig. 1.20a), the “Darboux frame,” $\mathbf{n}_g^s \mathbf{t}_{1,g}^s \mathbf{t}_{2,g}^s$, of the actual gear generic surface in relation to the “Darboux frame,” $\mathbf{n}_g^a \mathbf{t}_{1,g}^a \mathbf{t}_{2,g}^a$, of the desirable gear generic surface is turned about the unit vector, $\mathbf{t}_{1,g}^a$, in a counterclockwise direction through the angle, ϑ_g^s . The actual value of the angle, ϑ_g^s , is in the range of $0^\circ < \vartheta_g^s < \varphi_g^a + 90^\circ$. In a particular case, the value of angle, ϑ_g^s , can be set up equal to the angle, φ_g^a , at which the tangent to the hyperbola is tilted relative to the gear axis of rotation, O_g , as shown in Fig. 1.20b. A torus-like gear for a

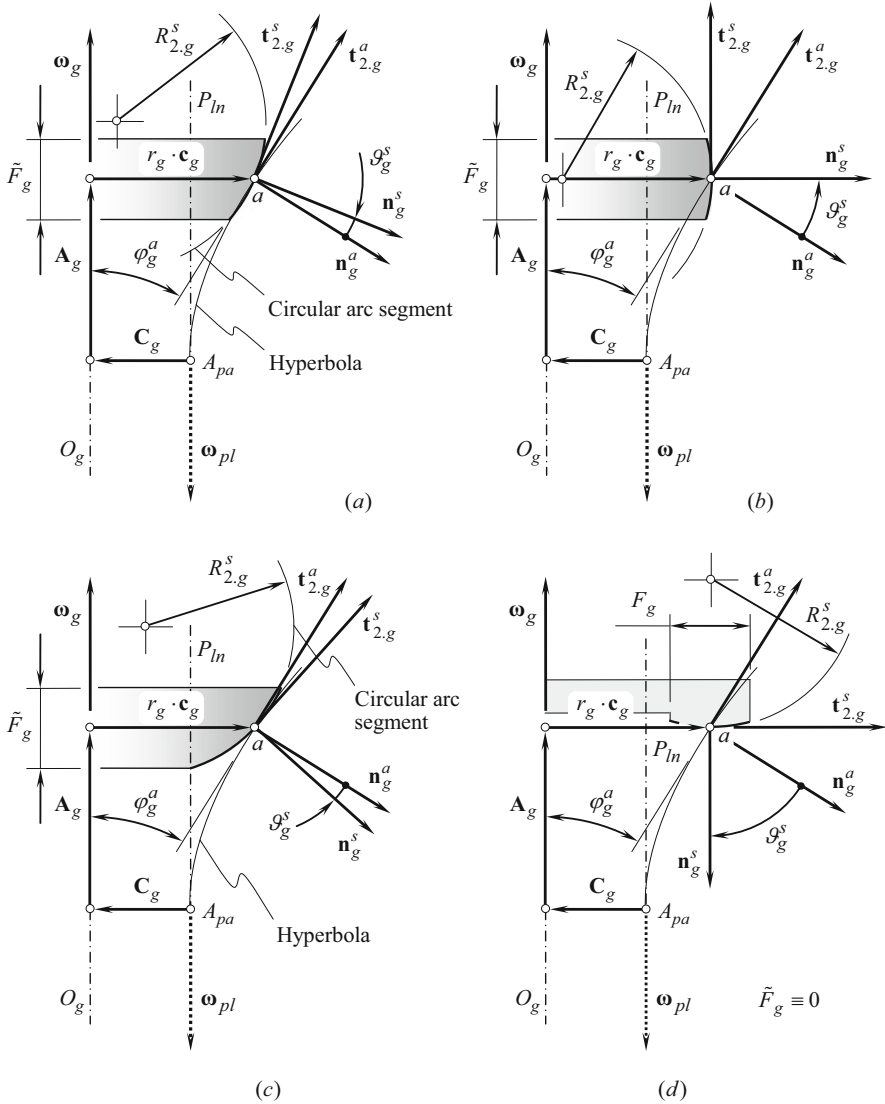


Fig. 1.20 Axial profile of a gear generic surface approximated by a convex circular arc at a certain angle, ϑ_g^s , in relation to the unit normal vector, \mathbf{n}_g^a , at the point, a , to the hyperbola

crossed-axes gear pair is machined in this scenario. The outer portion of the torus is employed in this case as the gear generic surface.

When the actual value of the angle, ϑ_g^s , is of a negative value (see Fig. 1.20c), the “Darboux frame,” $\mathbf{n}_g^s \mathbf{t}_{1.g}^s \mathbf{t}_{2.g}^s$, of the actual gear generic surface in relation to the “Darboux frame,” $\mathbf{n}_g^a \mathbf{t}_{1.g}^a \mathbf{t}_{2.g}^a$, of the desirable gear generic surface is turned about the unit vector, $\mathbf{t}_{1.g}^a$, in a clockwise direction through the angle, ϑ_g^s . The value of the

angle, ϑ_g^s , is in the range of $-(\varphi_g^a + 90^\circ) < \vartheta_g^s < 0^\circ$. In a particular case, the value of angle, ϑ_g^s , can be set up equal to $\vartheta_g^s = 90^\circ - \varphi_g^a$, at which the tangent to the hyperbola is tilted relative to the gear axis of rotation, O_g , as shown in Fig. 1.20d. A torus-like face gear for a crossed-axes gear pair is machined under such conditions.

The results of the analysis performed for a concave circular-arc axial profile that is inclined at a certain angle, ϑ_g^s , in relation to the unit normal vector, \mathbf{n}_g^a , at the point, a , to the hyperbola are illustrated in Fig. 1.21.

When the angle, ϑ_g^s , is of a positive value (see Fig. 1.21a), the ‘‘Darboux frame,’’ $\mathbf{n}_g^s \mathbf{t}_{1,g}^s \mathbf{t}_{2,g}^s$, of the actual gear generic surface in relation to the ‘‘Darboux frame,’’ $\mathbf{n}_g^a \mathbf{t}_{1,g}^a \mathbf{t}_{2,g}^a$, of the desirable gear generic surface is turned about the unit vector, $\mathbf{t}_{1,g}^a$, in a counterclockwise direction through the angle, ϑ_g^s . The actual value of the angle, ϑ_g^s , is in the range of $0^\circ < \vartheta_g^s < \varphi_g^a + 90^\circ$. In a particular case, the actual value of the angle, ϑ_g^s , can be set up equal to the angle, φ_g^a . In this scenario, the equality $\vartheta_g^s = \varphi_g^a$ is valid. The angle, φ_g^a , is the angle at which the tangent to the hyperbola is tilted relative to the gear axis of rotation, O_g , as shown in Fig. 1.21b. A torus-like gear for a crossed-axes gear pair is machined under such conditions. The inner portion of the torus serves in this case as the gear generic surface.

When the angle ϑ_g^s is of a negative value (see Fig. 1.21c), the ‘‘Darboux frame,’’ $\mathbf{n}_g^s \mathbf{t}_{1,g}^s \mathbf{t}_{2,g}^s$, of the actual gear generic surface in relation to the ‘‘Darboux frame,’’ $\mathbf{n}_g^a \mathbf{t}_{1,g}^a \mathbf{t}_{2,g}^a$, of the desirable gear generic surface is turned about the unit vector, $\mathbf{t}_{1,g}^a$, in the clockwise direction through the angle, ϑ_g^s . The actual value of the angle, ϑ_g^s , is in the range of $-(\varphi_g^a + 90^\circ) < \vartheta_g^s < 0^\circ$. In a particular case, the actual value of the angle, ϑ_g^s , can be set up equal to $\vartheta_g^s = 90^\circ - \varphi_g^a$, at which the tangent to the hyperbola is tilted relative to the gear axis of rotation, O_g , as shown in Fig. 1.21d. A torus-like face gear for a crossed-axes gear pair is machined under such conditions.

In addition to the possible gear generic surfaces shown in Fig. 1.14 through Fig. 1.21, a few more gear generic surfaces can be derived under an assumption that the axial vector, \mathbf{A}_g , is equal to zero (i.e., $\mathbf{A}_g = 0$). Examples of such gear generic surfaces are schematically illustrated in Fig. 1.22.

The total number of generic gear surfaces in this case is limited to six different kinds from three surfaces.

First, the straight-line segment can be either tangential to the hyperbola at point, a (see Fig. 1.22a), or inclined to the hyperbola at a certain angle, ϑ_g^s (see Fig. 1.22b). From the perspective of a gear design, it makes no difference whether the angle, ϑ_g^s , is of a positive or of a negative value.

Second, the convex circular-arc profile also can be either tangential to the hyperbola at point, a (see Fig. 1.22c), or it can be inclined to the hyperbola at a certain angle, ϑ_g^s (see Fig. 1.22d). From the perspective of a gear design, it makes no difference whether the angle, ϑ_g^s , is of a positive or of a negative value.

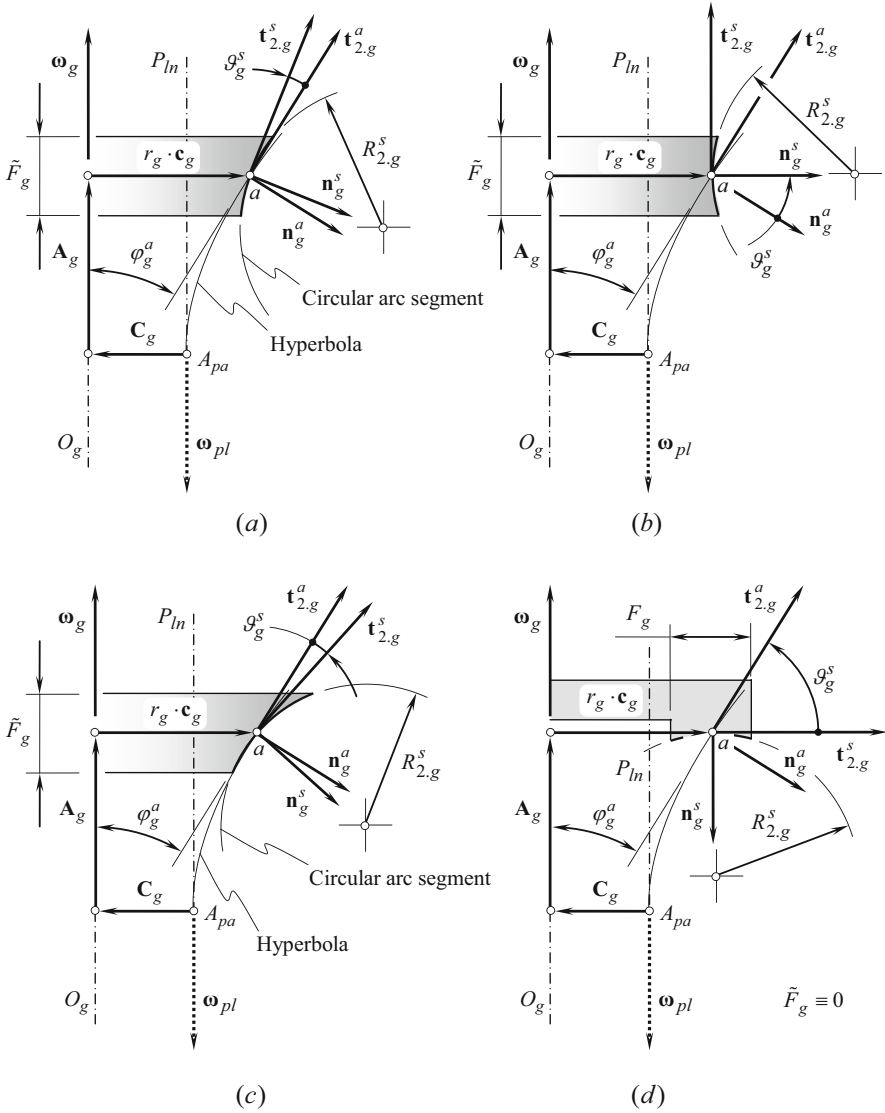


Fig. 1.21 Axial profile of the gear generic surface approximated by a concave circular arc at a certain angle, θ_g^s , in relation to the unit normal vector, \mathbf{n}_g^a , at the point, a , to the hyperbola. Parts (a) through (d) are discussed in the text

Third, this statement is also true with respect to a concave circular-arc profile, which also can be either tangential to the hyperbola at point, a (see Fig. 1.22e), or it can be inclined to the hyperbola at a certain angle, θ_g^s (see Fig. 1.22f).

An intermediate conclusion can be drawn up from this discussion: the total number of possible gear generic surfaces of the considered geometry is a finite

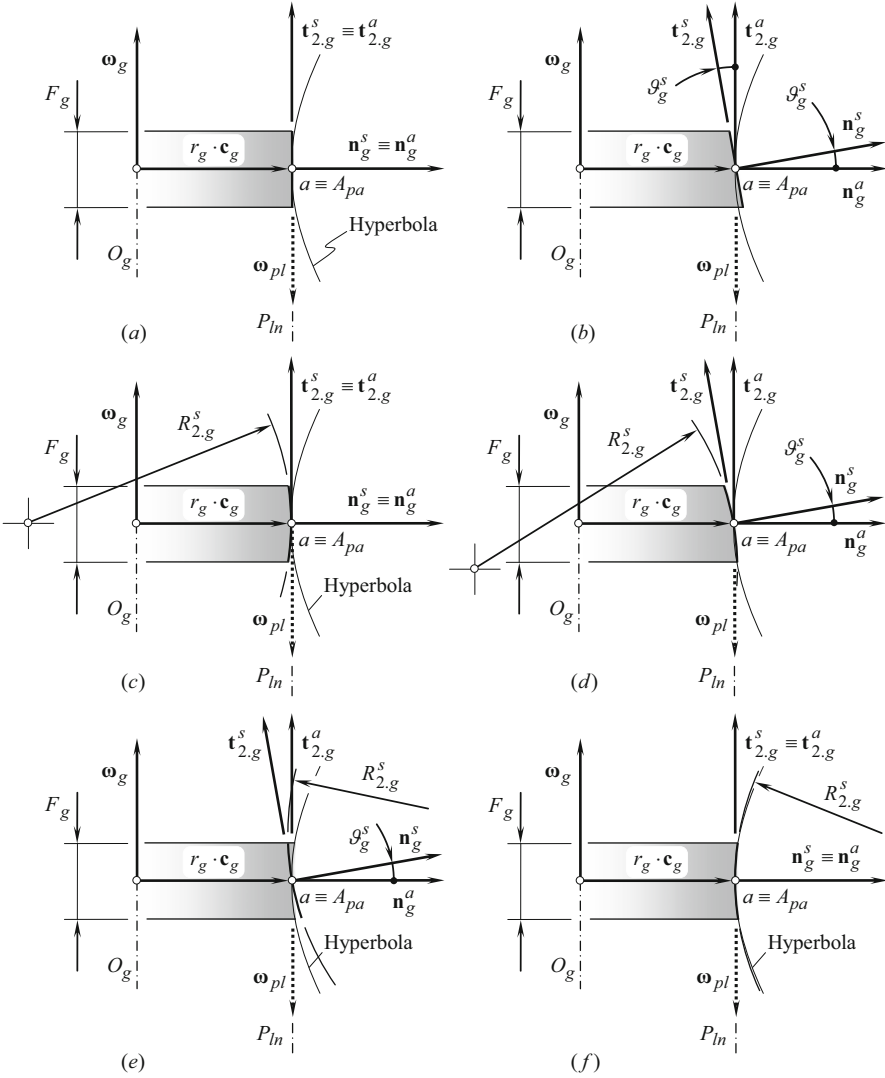


Fig. 1.22 Gear generic shapes of gears that feature the axial vector, \mathbf{A}_g , of a zero length ($\mathbf{A}_g = 0$). Parts (a) through (f) are discussed in the text

value and is limited just to 27 gear generic surface profiles. They are constructed in a section of a gear by an axial plane.

In addition to ideal gear generic surfaces (see Fig. 1.14), gear generic surfaces of three more kinds can be drawn up from each of Fig. 1.15 through Fig. 1.17. Then, analysis of Fig. 1.18 and Fig. 1.19 returns four gear generic surfaces: two of them feature the angle, ϑ_g^s , of an arbitrary value, and two more of them feature the angle, ϑ_g^s , of a specific value, that is, either $\vartheta_g^s = \varphi_g^a$ in the first case or $\vartheta_g^s = 90^\circ - \varphi_g^a$ in the

second case. Similarly, gear generic surfaces of four more geometries can be drawn up from the analysis of Fig. 1.20 and Fig. 1.21. Gear generic surfaces of three more geometries for face gears can be obtained similar to that illustrated in Figs. 1.19b, Fig. 1.20d, and Fig. 1.21d. The geometry of gear generic surfaces of these kinds is evident; therefore, it is not illustrated in the figures. Ultimately, nine more gear generic surfaces are drawn up from Fig. 1.22.

Ultimately, it is possible to investigate all the designs of gears those machined on conventional machine tools, as well as on gear generators of conventional design.

1.1.4.4 Profile of Gear Generic Surface Constructed in Section by Plane at an Angle to Gear Axis

Discussed earlier in this section of the book, possible gear generic surfaces are constructed in a section of a gear by a plane through the gear axis of rotation. More opportunities in this regard are available if sections by a plane at an angle to the gear axis of rotation are considered. A plane at an angle to the gear axis of rotation is referred to as the “inclined cross section” of the gear.

Section of a gear by an axial plane is a convenient reference for the specification of the configuration of an inclined section of the gear.

The axial section of a gear is specified as a section by a plane through the gear axis of rotation, O_g . An equivalent specification of an axial cross section of the approximate gear can be given in terms of the unit tangent vectors, $\mathbf{t}_{1,g}^a$ and $\mathbf{t}_{2,g}^a$, of the principal directions on the desirable gear generic surface, as illustrated in Fig. 1.23.

It is convenient to specify an inclined plane section of a gear in terms of the unit tangent vectors, $\mathbf{t}_{1,g}^s$ and $\mathbf{t}_{2,g}^s$, of the principal directions on the actual generic gear surface. The inclined cross section is a plane through the unit tangent vectors, $\mathbf{t}_{1,g}^s$ and $\mathbf{t}_{2,g}^s$.

At point, a , configuration of the “Darboux frame,” $\mathbf{n}_g^s \mathbf{t}_{1,g}^s \mathbf{t}_{2,g}^s$, of the actual gear generic surface in relation to the “Darboux frame,” $\mathbf{n}_g^a \mathbf{t}_{1,g}^a \mathbf{t}_{2,g}^a$, of the perfect gear generic surface can be specified by an angle, ν_g^s . The trihedron $\mathbf{n}_g^s \mathbf{t}_{1,g}^s \mathbf{t}_{2,g}^s$ is turned about the common unit normal vector, $\mathbf{n}_g^a \equiv \mathbf{n}_g^s$, through the angle, ν_g^s , in the clockwise direction looking from the end of the vector, \mathbf{n}_g^a (see Fig. 1.23a). In a particular case, when the equality $\nu_g^s = 0^\circ$ is valid, an inclined plane section reduces to the aforementioned axial plane section. When the angle, ν_g^s , is not of a zero value ($\nu_g^s \neq 0^\circ$), three different cases can be distinguished. Before proceeding with this issue, it is necessary to point out here the following observation: as the unit normal vector, \mathbf{n}_g^a , in the general case is not perpendicular to the gear axis of rotation, O_g [the angle between the vector, \mathbf{n}_g^a , and the gear axis, O_g , is given by $\angle(\mathbf{n}_g^a, O_g) = 90^\circ - \varphi_g^a$], the projection, θ_g^s , of the angle, ν_g^s , onto the plane through the gear axis of rotation, O_g , perpendicular to the axial plane section is not equal to the angle, ν_g^s , itself ($\theta_g^s \neq \nu_g^s$). However, the angles, ν_g^s and θ_g^s , correlate to each other. The

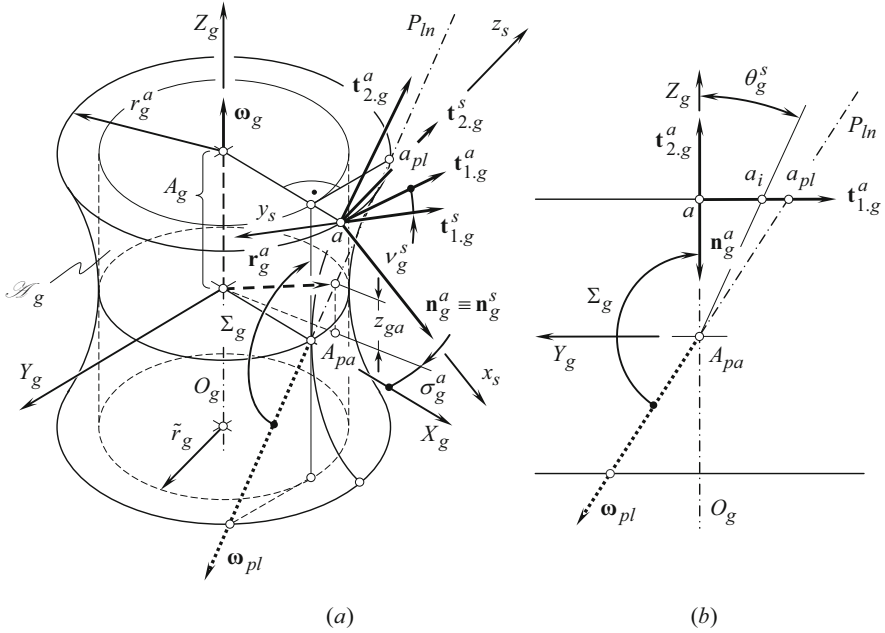


Fig. 1.23 Possible configurations of the characteristic cross section of a gear generic surface. Parts (a) and (b) are discussed in the text

correlation is of importance for further discussion and can be established in the following way.

The angle, θ_g^s , can be defined as the angle that is formed by the unit tangent vector, $\mathbf{t}_{2,g}^s$, and the gear axis of rotation, O_g . In a local reference system, $x_s y_s z_s$, that has the axes along the unit vectors, \mathbf{n}_g^s , $-\mathbf{t}_{1,g}^s$, and $\mathbf{t}_{2,g}^s$, the unit tangent vector, $\mathbf{t}_{2,g}^s$, can be expressed as $\mathbf{t}_{2,g}^s = \mathbf{k}_s$. The directions of the axes of this reference system are specified by the “Darboux trihedron,” $\mathbf{n}_g^s \mathbf{t}_{1,g}^s \mathbf{t}_{2,g}^s$, as shown in Fig. 1.23. In the Cartesian coordinate system, $X_g Y_g Z_g$, associated with the gear, the direction of the gear axis, O_g , can be specified by the unit vector, \mathbf{k}_g . In order to calculate the value of the angle, θ_g^s , both the vectors, $\mathbf{t}_{2,g}^s$ and \mathbf{k}_g , have to be represented in a common reference system. Let us represent the vector, $\mathbf{t}_{2,g}^s$, in the coordinate system, $X_g Y_g Z_g$. For this purpose, a local coordinate system, $x_s y_s z_s$, that has its origin at point a is used. The unit tangent vector together with the coordinate system, $x_s y_s z_s$, have to be turned about the axis, x_s [about the unit normal vector $\mathbf{n}_g^s (\equiv \mathbf{n}_g^a)$] through the angle, ν_g^s . The operator of rotation, $\mathbf{Rt}(\nu_g^s, \mathbf{n}_g^a)$, is used for the analytical description of this coordinate system transformation:

$$\mathbf{Rt}(\nu_g^s, \mathbf{n}_g^a) = \begin{bmatrix} 1 & 0 & 0 & 0 \\ 0 & \cos \nu_g^s & \sin \nu_g^s & 0 \\ 0 & -\sin \nu_g^s & \cos \nu_g^s & 0 \\ 0 & 0 & 0 & 1 \end{bmatrix} \quad (1.14)$$

In this new position of the local reference system, $x_s y_s z_s$, the unit vectors, \mathbf{n}_g^s , $\mathbf{t}_{1.g}^s$, and $\mathbf{t}_{2.g}^s$, align with corresponding unit vectors of the ‘‘Darboux frame,’’ $\mathbf{n}_g^a \mathbf{t}_{1.g}^a \mathbf{t}_{2.g}^a$.

Then, it is necessary to turn the ‘‘Darboux frame,’’ $\mathbf{n}_g^a \mathbf{t}_{1.g}^a \mathbf{t}_{2.g}^a$, about the y_s -axis [about the unit tangent vector, $\mathbf{t}_{1.g}^a$] through the angle, φ_g^a (see Fig. 1.15). The operator of the rotation, $\mathbf{Rt}(\varphi_g^a, \mathbf{t}_{1.g}^a)$, is used for the analytical description of this coordinate system transformation:

$$\mathbf{Rt}(\varphi_g^a, \mathbf{t}_{1.g}^a) = \begin{bmatrix} \cos \varphi_g^a & 0 & -\sin \varphi_g^a & 0 \\ 0 & 1 & 0 & 0 \\ \sin \varphi_g^a & 0 & \cos \varphi_g^a & 0 \\ 0 & 0 & 0 & 1 \end{bmatrix} \quad (1.15)$$

The operator, $\mathbf{Rs}(s \mapsto g)$, of the resultant coordinate system transformation is calculated as the product of the operators of rotation, $\mathbf{Rt}(\nu_g^s, \mathbf{n}_g^a)$ and $\mathbf{Rt}(\varphi_g^a, \mathbf{t}_{1.g}^a)$:

$$\mathbf{Rs}(s \mapsto g) = \mathbf{Rt}(\varphi_g^a, \mathbf{t}_{1.g}^a) \cdot \mathbf{Rt}(\nu_g^s, \mathbf{n}_g^a) \quad (1.16)$$

It should be noted here that the order of multipliers in Eq. (1.16) is of importance and this order cannot be altered.

Once the operator $\mathbf{Rs}(s \mapsto g)$ of the resultant coordinate system transformation is calculated, the expression:

$$\mathbf{t}_{2.g}^{s(g)} = \mathbf{Rs}(s \mapsto g) \cdot \mathbf{t}_{2.g}^s \quad (1.17)$$

can be used for the analytical description of the unit tangent vector, $\mathbf{t}_{2.g}^s$, in the reference system, $X_g Y_g Z_g$.

Use of the expression for the unit tangent vector, $\mathbf{t}_{2.g}^{s(g)}$ [see Eq. (1.17)], makes the calculation of the angle θ_g^s possible:

$$\theta_g^s = \tan^{-1} \left(\frac{|\mathbf{t}_{2.g}^{s(g)} \times \mathbf{k}_g|}{\mathbf{t}_{2.g}^{s(g)} \cdot \mathbf{k}_g} \right) \quad (1.18)$$

Equations (1.15) through (1.18) yield derivation of an expression:

$$\theta_g^s = \cos^{-1} \left[\cos \varphi_g^a \cdot \cos \nu_g^s \right] \quad (1.19)$$

for the calculation of the angle, θ_g^s .

When the angle, ν_g^s , is equal:

$$\nu_g^s = \cos^{-1} \left[\frac{\cos \Sigma_g}{\cos \varphi_g^a} \right] \quad (1.20)$$

the unit tangent vector, $\mathbf{t}_{2.g}^s$, is aligned with the axis of instant rotation, P_{In} . The actual value of the angle, θ_g^s (see Fig. 1.23b) in this particular case is equal to Σ_g .

Four different configurations of the inclined plane section of a gear are distinguished depending on the actual value of the angle, θ_g^s .

First, the angle, θ_g^s , can be equal to zero. When the equality $\theta_g^s = 0^\circ$ is valid, the inclined plane section reduces to the axial plane section of the gear.

Second, an actual value of the angle θ_g^s can be in the range of $0^\circ < \theta_g^s < 180^\circ - \Sigma_g$. For convenience, the difference $(180^\circ - \Sigma_g)$ is denoted by $\left[\theta_g^s \right]$. It can be shown that the rotation of the inclined plane section about the x_s -axis through an angle, ν_g^s , is equivalent to its rotation about the centerline through a corresponding angle, θ_g^s . This is due to the perfect gear generic surface which is a surface of revolution. Surfaces of revolution allow for sliding over themselves. Therefore, the parameters of rotation of an inclined plane section about the centerline can be expressed in terms of the parameters of rotation of the same inclined plane section about the unit normal vector, $\mathbf{n}_g^a \equiv \mathbf{n}_g^s$, and vice versa. Under such an interpretation, point a is not considered; instead, point, a_i , is considered (see Fig. 1.23b).

Third, the actual value of the angle, θ_g^s , can be equal to its critical value, $\left[\theta_g^s \right]$. When an equality $\theta_g^s = \left[\theta_g^s \right]$ is valid, the unit tangent vector, $\mathbf{t}_{2.g}^{s(g)}$, is aligned with the vector of instant rotation, $\boldsymbol{\omega}_{pl}$. In this particular case, point a is not considered; instead, point a_{pl} is considered (see Fig. 1.23b).

Fourth, the actual value of the angle, θ_g^s , can exceed its critical value, $\left[\theta_g^s \right]$, and, thus, the inequality $\theta_g^s > \left[\theta_g^s \right]$ is valid. Corresponding point, a_j (not shown in Fig. 1.23b), in this particular case is located beyond point, a_{pl} .

Taking into account that the first case ($\theta_g^s = 0^\circ$) returns 26 possible gear generic surfaces, one of which is the perfect gear generic surface, the total number of possible gear generic surfaces is limited to just 105. Some of the gear generic surfaces resemble each other. However, even for gear generic surfaces with a similar appearance, the conditions of generation of tooth flanks can be different. Therefore, all of the gear generic surfaces are required to be carefully investigated individually.

The following three important conclusions can be drawn up from this discussion:

1. The total number of feasible gear generic surfaces is not infinite, but it is a finite number. This means that it is possible to count and investigate all possible designs of gears machined on conventional gear generators.
2. Gears with any of the gear generic surfaces are convenient for machining as only rotations and translations are required to reproduce the required motion of the gear cutting tool in relation to the work-gear.
3. An appropriate area of application can be specified for all the gears briefly discussed in this section of the book.

The above discussion is helpful to systemize possible geometries of the gear generic surfaces.

1.1.5 Possibility of Classification of Approximate Gearing

As the total number of possible gear generic surfaces is limited just to 105, it is possible to combine the surfaces by two and in this way to obtain all possible gear pairs. It can be proved that the total number of such combinations does not exceed 105^2 . Not all of them are possible physically. For example, no parallel-axes gear pair can be designed using two gear generic surfaces with concave axial profiles. Because interference of gear generic surfaces in this case is inevitable, gear pair of this particular kind cannot be designed. A few examples of feasible and infeasible combinations of gears by two are schematically shown in Fig. 1.24. A gear with a convex axial profile and a pinion with a straight axial profile comprise a possible combination of gears. A gear pair of this kind can exist physically (see Fig. 1.24a). In contrast, a gear with a concave axial profile and a pinion with a straight axial profile do not comprise a possible combination of gears. A gear pair of this kind cannot exist physically (see Fig. 1.24b). A similar behavior is observed with a gear and a pinion that have convex and concave axial profiles, correspondingly, as illustrated in Fig. 1.24c, d. In order to come up with a feasible combination of gears comprising a gear pair, the magnitude of the radius of curvature of the concave profile, R_p , has to be greater than the radius of curvature, R_g , as shown in Fig. 1.24c. Otherwise, when the inequality $R_p < R_g$ is observed, a gear pair of this geometry becomes infeasible (see Fig. 1.24d). More examples in this regard can be provided.

It can be assumed from these simple examples that the total number of possible gear pairs is significantly less than 105^2 .

In order to evaluate the maximum number of possible kinds of gear pairs, it is useful to recall that 105 possible kinds of the gear generic surfaces are composed of one perfect gear generic surface, 26 gear generic surfaces with a convex axial profile, 26 gear generic surfaces with a straight axial profile, and 26 gear generic surfaces with a concave axial profile.

Gear generic surfaces that feature a convex axial profile can be properly combined with all 105 kinds of gear generic surfaces of the pinion. Therefore, the total

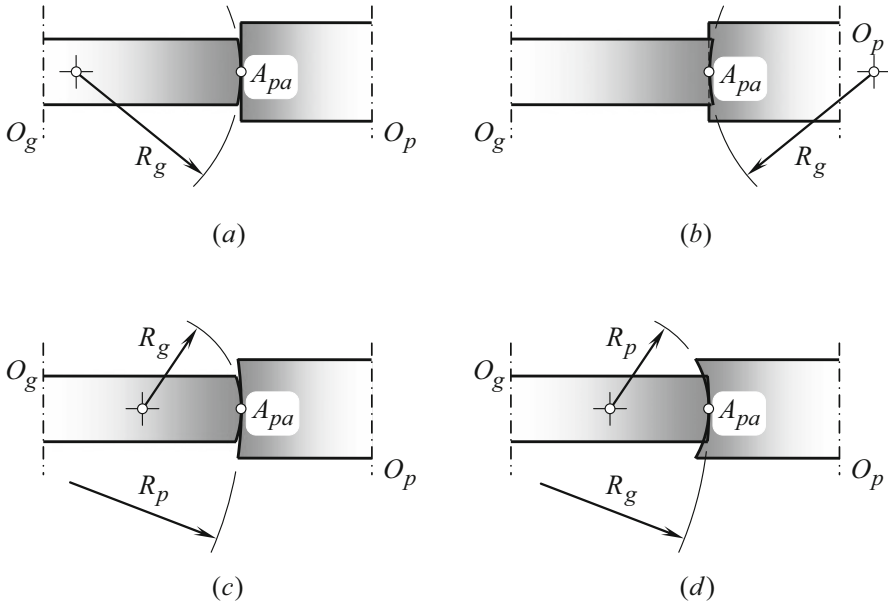


Fig. 1.24 Combinations of two gear generic surfaces: (a) and (c) feasible, and (b) and (d) infeasible combinations

number of combinations of this particular kind is limited to $26 \cdot 105 = 2730$ combinations.

Gear generic surfaces that feature straight axial profile can be properly combined with all 70 pinion generic surfaces. Therefore, the total number of combinations of this particular kind is limited just to $26 \cdot 70 = 1820$ combinations.

Finally, gear generic surfaces that feature straight axial profile can be properly combined with all 70 pinion generic surfaces. Therefore, the total number of combinations of this particular kind is limited to $26 \cdot 35 = 910$ combinations.

Because the numbers, 2730, 1820, and 910, are finite numbers, the total number of possible combinations of gear generic surfaces is also a finite number. This number does not exceed 5460 combinations. Evidently, not all of these combinations exist physically. After a detailed investigation of all the possible combinations is carried out, it is possible to realize that the total number of practical types of gear pairs is significantly less than the precalculated number of 5460 combinations.

The total number of approximate gearing (namely, non-conjugate gearing) is huge. However, all of them are covered by the proposed classification that is based on inherent features of gear machining/generating process.

Possible kinds of gear pairs to be determined should be considered together with the possible kinds of vector diagrams for geometrically accurate gear pairs (see Fig. 1.10). All the possible kinds of gear pairs can be investigated. This is due to the total number of possible kinds of gear pairs which is equal to a finite number, and not to an infinite number.

Use of the aforementioned technique makes it possible to investigate all possible kinds of gear pairs. No gear pair is missed under such an investigation. Novel designs of gear pairs can be discovered as the output of such an investigation.

1.1.6 Examples of Implementation of Classification of Approximate Gearing

Once the number of possible combinations of generic gear surfaces by two is found to be finite, it is possible to consider individually every possible combination of the gear generic surfaces by two and identify a possibility and an appropriate area of application for each particular combination. A few illustrative examples in this regard are considered immediately below.

The desired gear generic surfaces of a gear pair that features intersecting axes of the gear and its mating pinion are represented with two cones having a common apex. The perfect gear generic surfaces for the case of an external gear pair are schematically shown in Fig. 1.25a. The gear generic surfaces contact each other along a straight line that is aligned with the axis of instant rotation, P_{ln} . The axis of rotation of the gear, O_g , the axis of rotation of the pinion, O_p , and the axis of instant rotation, P_{ln} , intersect one another at a common point, which is coincident with the plane-of-action apex, A_{pa} .

In Fig. 1.25, a trivial case of interacting of the gear generic surfaces in gear pairs is shown. Many kinds of external conical gear pairs can be designed on the premise of this particular combination of the gear generic surfaces. One of the many possible examples is illustrated in Fig. 1.25b.

Internal gear pairs as well as rack-type gear pairs that have intersecting axes of a gear and a mating pinion also feature the desirable gear generic surfaces, shaped in

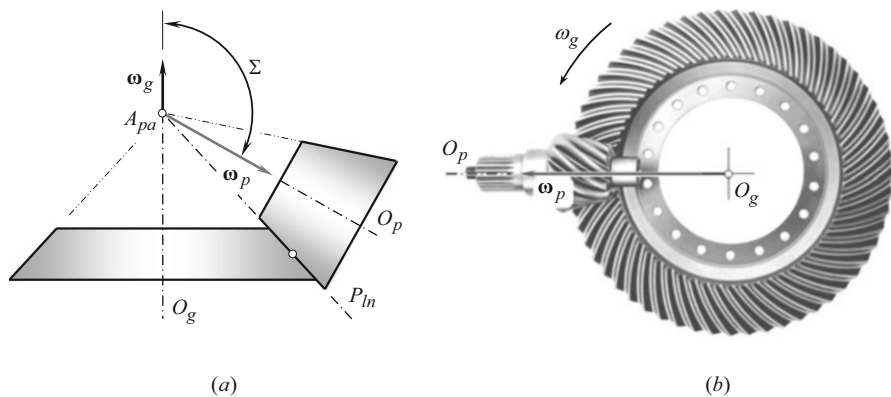


Fig. 1.25 Desirable gear generic surface for an external gear pair that features intersecting axes of rotation of a gear and a mating pinion

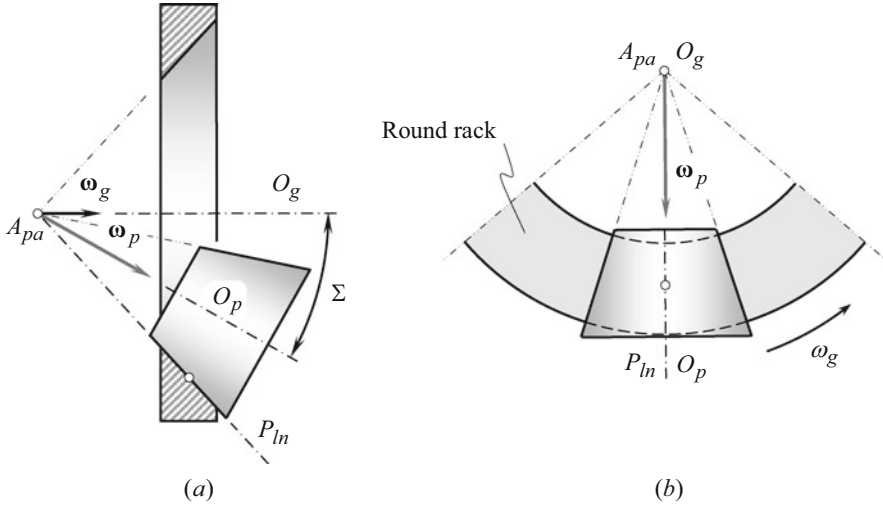


Fig. 1.26 Desirable gear generic surfaces for intersected-axes gearing: (a) an internal gear pair and (b) a rack-type gear pair

the form of cones. The apexes of the cones are snapped together. For internal gear pairs, a gear generic surface is represented by a surface of an internal cone of revolution as depicted in Fig. 1.26a. The generic surface of the pinion is represented by a surface of an external cone of revolution.

In a particular case, the pitch cone angle of a gear can be set up equal to 90° . In this scenario, the gear degenerates into a flat gear, as schematically shown in Fig. 1.26b. A gear of this kind is commonly referred to as the “round rack” (or as a “crown gear,” in other terminology). The apex of the round rack is always snapped together with the apex of the pinion.

Gear pairs designed on the basis of perfect gear generic surfaces, as schematically shown in Fig. 1.26, have limited application in practice. The lack of comprehensive investigation of generic gear surfaces of these kinds is one of the main reasons for this.

A gear and a pinion can be designed and machined in such a way that the actual gear generic surfaces of each of them differ from their perfect geometry. In cases like these, either the apex of the gear or of the pinion or both is off the axis of instant rotation, P_{ln} .

Two examples of gear generic surfaces of external gear pairs that feature intersecting axes of rotation of the gear and the pinion are shown in Fig. 1.27.

A gear pair may feature generic surfaces shaped in the form of external cones of revolution. When the cone angles of the cones of revolution differ from the cone angle for the perfect gear generic surfaces, as illustrated in Fig. 1.27a, the apex of the gear is off the axis of instant rotation, P_{ln} . Ultimately, a conical gear pair can be designed on the basis of the actual gear generic surfaces of this kind. Gear pairs of this kind do not have an extensive application in the nowadays practice.

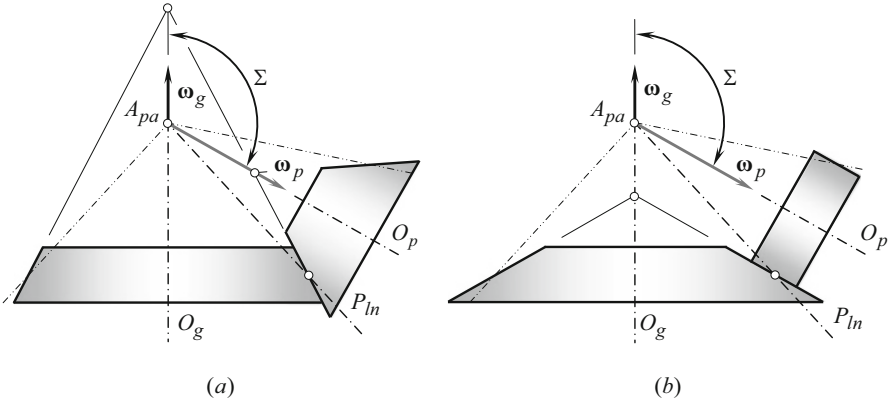


Fig. 1.27 Two examples of gear generic surfaces for external intersected-axes gearing, that feature straight-line axial profiles

In a particular case, a gear pair can be designed so that the generating straight-line segment of the actual pinion generic surface is parallel to the pinion axis of rotation, O_p (see Fig. 1.27b). Under such a scenario, the actual pinion generic surface is not a cone of revolution; it is shaped in the form of a cylinder of revolution instead. Gear pairs composed of an external conical gear and a mating cylindrical pinion are used, for example, in the design of helicopter transmissions; they also have numerous other applications.

In both cases, shown in Fig. 1.27, gears are often referred to as “external crown gears.”

A gear pair can be designed and machined in such a way that the actual gear generic surface is shaped in the form of an internal cone of revolution (Fig. 1.28). Many similarities can be found between external (see Fig. 1.27) and internal gear pairs of these two kinds. Again, in a particular case, the actual pinion generic surface is not a cone of revolution, but is shaped in the form of a cylinder of revolution instead. Gear pairs composed of internal conical gear and a mating cylindrical pinion have limited application in the industry. Gear pairs of this kind are not thoroughly investigated yet, and their area of potential application has not been properly identified so far.

In both cases shown in Fig. 1.28, gears are often referred to as “internal crown gear.”

Ultimately, the gear generic cone of a gear pair that has intersecting axes of rotation of the gear and the pinion is degenerated into a plane that is rotated about the gear axis of rotation, O_g . Two examples of the gear generic surfaces of this type are schematically shown in Fig. 1.29a, b. In a particular case, when the pitch radius of the gear approaches infinity, the gear is transformed into a straight rack (see Fig. 1.29c). Gear pairs of this kind have not been thoroughly investigated yet, and their area of potential application is not properly identified so far.

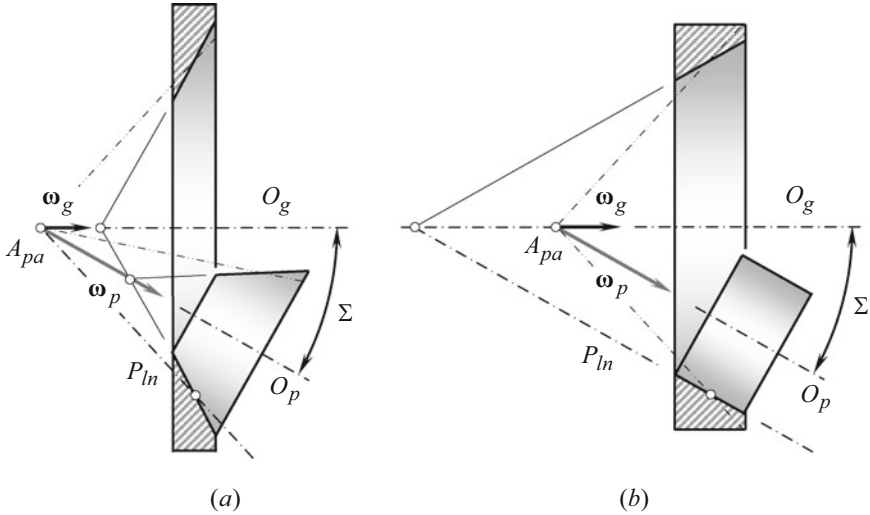


Fig. 1.28 Two examples of gear generic surfaces for internal intersected-axes gearing, that feature straight-line axial profiles

In all cases illustrated in Fig. 1.29, the gear is referred to as “rack-type crown gear.” Rack-type gear pairs have the following two features: (1) the pitch plane of the gear is the plane through the centerline, and (2) the apex of the pitch cone of the pinion is located within the centerline.

Based on the developed classification of vector diagrams of gear pairs, and on the concept of gear generic surfaces, all known gear drives can be developed. For example, advanced gear drives such as *Spiroid* gearing [8], *Helicon* gearing [9], as well as others can be developed using the proposed approach. Moreover, many novel designs of gearing can be developed using the proposed approach.

Use of the discussed approach makes possible to cover all known designs of gear pairs, as well as all novel, potentially possible designs of gear pairs, many of which have potential areas of implementation still to be identified. As the approach is based on the extensive application of vector representation of gear pairs, use of axodes and operating pitch surfaces in many cases becomes useless. However, pitch surfaces relevant to the corresponding gear-machining process are still useful.

The discussion on classification can be ended with a generalized classification of possible kinds of gear pairs that is schematically depicted in Fig. 1.30.

Based on the classification of possible kinds of gear vector diagrams (see Fig. 1.10), a certain number of gear pairs can be developed for each gear vector diagram. The gear pairs differ from one another by the geometry of tooth flanks in the lengthwise direction. All these gear pairs are referred to as “geometrically accurate gear pairs,” (or “perfect gear pairs,” in other terminology).

Taking into account possible displacements of the tooth flanks of a gear and a mating pinion, a certain number of S_{pr} -gear pairs can be developed. The number of possible designs of S_{pr} -gear pairs is equal to the number of ideal gear pairs. Gear

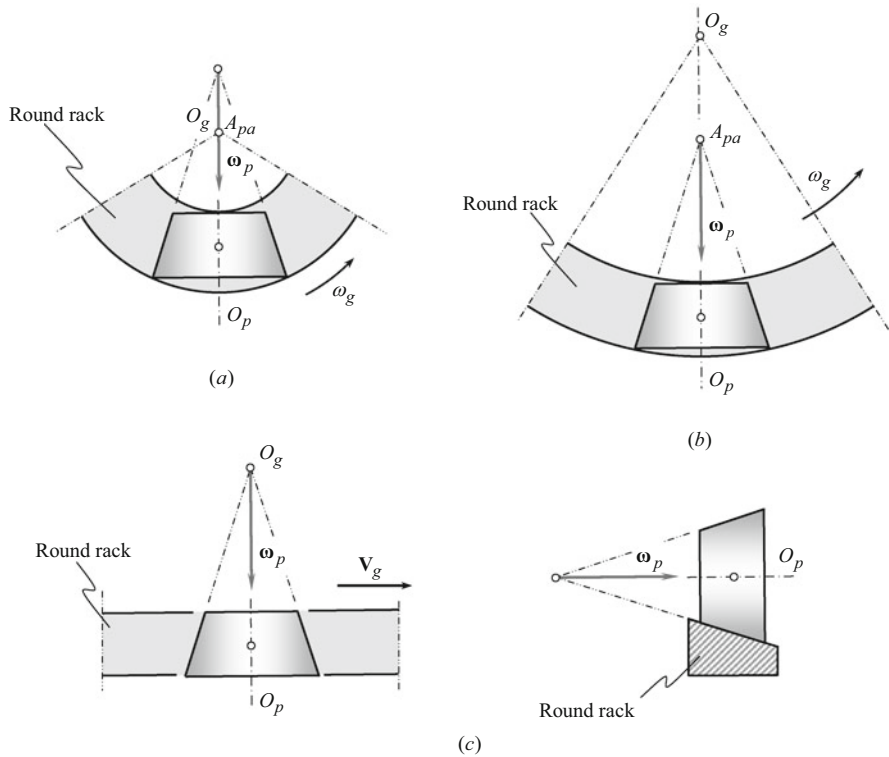


Fig. 1.29 Examples of gear generic surfaces of rack-type crown gear pairs that feature intersecting axes of rotation of the gear and the pinion and with straight-line axial profiles

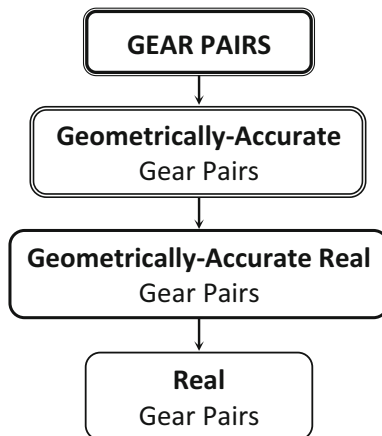


Fig. 1.30 A generalized classification of possible kinds of gear pairs

pairs of this kind can also be referred to as “desirable (geometrically accurate) real gear pairs.”

Ultimately, a certain number of “real gear pairs” can be developed based on a corresponding desirable gear pair. The total number of real gear pairs significantly exceeds the total number of desirable real gear pairs.

The discussion in this chapter of the book illustrates the possibility of the development of a scientific classification of all possible designs of gearing. It is clear now that the classification (see Fig. 1.30) can be represented in detail based on the results of the analysis discussed in this monograph.

1.2 Concluding Remarks

This section of the book deals with kinematic foundations of scientific classification of gearing. For this purpose, gear vector diagrams with zero, as well as with plural complementary degrees-of-freedom are implemented. It is demonstrated that all possible kinds of gearing can be classified based on the vector representation of gear pair kinematics. Such a classification is necessary and beneficial for many purposes. The development of all possible kinds of gears, and later on of all possible kinds of gearing, is one of the reasons for the development of the classification.

A scientific classification of gear vector diagrams for gearing having from three to zero complementary degree-of-freedom is proposed. In the most general case, gearing of this kind is referred to as “ $C\Sigma u$ –variable gearing.” “ $C\Sigma u$ –variable gearing” features a huge potential for the researchers. This chapter is just an illustration of capabilities of “ $C\Sigma u$ –variable gearing.” Each particular kind of “ $C\Sigma u$ –variable gear pairs” deserves to be considered in a separate chapter.

Desired lines of contact of a gear and that of a mating pinion are discussed. A possibility of classification of approximate gearing is analyzed. Gear generic surfaces are recommended to implement for this purpose. A few examples of implementation of the classification of approximate gearing are provided.

References

1. Radzevich, S. P. (2018). *Theory of Gearing: Kinematics, Geometry, and Synthesis, 2nd edition, revised and expanded* (p. 934). Boca Raton, FL: CRC Press.
2. Euler, L. (1765). *De Optissima Figura Rotatum Dentibus Tribuenda*. Novi Commentarii Academiæ Petropolitanae, 1754/55.
3. Euler, L. (1767). Supplementum de Figura Dentium Rotatum. *Novi Comm. Acad. Sc. Petropol*, 11, 207–231.
4. Olivier, T. (1842). *Théorie Géométrique des Engrenages destinés* (p. 132). Paris: Bachelier.
5. Bayazitov, N. (1964). *Helical Gears with a New Type of Gearing, Ph.D. thesis*. Kazan: Kazan’ Technological & Chemical Institute.

6. Pat. USSR No. 163857, *A Helical Gearing*. /B.V. Shitikov, N.A. Bayazitov, Int. Cl. F06h, Filed: February 25, 1963, 1964.
7. Radzevich, S. P. (2017). *Gear cutting tools: Science and engineering* (2nd ed., p. 606). Boca Raton, FL: CRC Press.
8. Pat. U.S.A. No. 2,696,125, *Speed-Reduction Gearing*. /O.E. Saari, Cl. 74-459.5, Filed: July 12, 1954.
9. Pat. U.S.A. No. 2,954,704, *Skew Axis Gearing*. /O.E. Saari, Cl. 74-466, Filed: April 10, 1957.

Chapter 2

Theory and Applications Based on S-Gear Geometry



Gorazd Hlebanja, Miha Erjavec, Matija Hriberšek, Luka Knez,
and Simon Kulovec

2.1 Introduction

Involute gears, which transmit power through convex-convex contact, are used in contemporary machines almost without a competition. This is due to gradual development of *Euler's* [1] invention over centuries and important improvements in both manufacturing technologies and materials. This reflects in higher quality and loading capacity. However, the intrinsic property of the involute gear is its curvature radii function that is approaching to exceedingly small values in the dedendum part when approaching the base circle, where the said radius becomes zero. Therefore, high contact loads arise in this area. Additionally, for gears with a low number of teeth, the dedendum flank is comparatively short, thus invoking excessive sliding and friction losses and the possibility of premature damage in this area. Yet another problem is undercutting of the dedendum area. Therefore, there exists a permanent need for improved gears, with such features as a convex-concave contact, a stronger root, improved curvature radii, better lubrication conditions, etc. And S-gear geometry is an attempt in this context.

Many papers discussed various aspects of S-gears, e.g., their definition [2], possibilities of various gear types (e.g., helical, crossed, worm gears, planetary gears, etc.) [3], their radii of curvature, contact pressure, relative and sliding velocities, oil thickness, initial pressure angles, etc. [4–6], thermal properties [7], and various gearing aspects as well toward miniaturization or heavy industry. This

G. Hlebanja (✉)
University of Novo Mesto, Novo Mesto, Slovenia
e-mail: gorazd.hlebanja@siol.net

M. Erjavec · M. Hriberšek · L. Knez · S. Kulovec
Podkrižnik d.o.o., Nazarje, Slovenia
e-mail: miha.erjavec@podkrižnik.si; matija.hribersek@podkrižnik.si;
luka.knez@podkrižnik.si; simon.kulovec@podkrižnik.si

chapter discusses some shaping possibilities of external and internal gear pairs. Besides, an important issue—thermal properties and comparison to the involute gears – is presented in the chapter. This becomes of the utmost importance in plastic gears. Experiments with plastic gears confirm theoretically discussed properties.

2.1.1 Plastic Gears: Lifetime Testing

In the past decades, polymer materials for gears have been increasingly used. Polymer gears provide in many applications alternatives to traditional metal gears. The worldwide market for plastic gears in 2017 was estimated to be 2.67 billion € (3.06 billion US\$); it will grow with a compound average growth rate (CAGR) of approximately 1.3% to 2.88 billion € (3.31 billion US\$) in 2023. When polymer gears were entering the market in the second half of the twentieth century, they were predominantly used as cheap replacement for metal gears in simple applications. As designers and engineers have been constantly pushing the limits, polymer gears can in the meantime be found in a variety of power transmissions applications, including demanding high-performance uses in product with high added values.

Modern polymer gears have many benefits of their unique properties (e.g., lower specific weight, reduced moment of inertia, improved NVH performance—noise, vibration, harshness). Thermoplastic gears are mostly manufactured by injection molding process. Additionally, to achieve narrow tolerance requirements, in some cases they may also be made by hobbing.

Technical resins used for engineering purposes possess improved mechanical, electrical, and thermal characteristics compared to commodity plastics and are capable of withstanding complex loads in structurally demanding applications. The most common materials for gears are polyamide (PA), polyoxymethylene (POM), polyether ether ketone (PEEK), and polybutylene terephthalate (PBT). Additives are used sometimes to improve mechanical properties of polymer, e.g., glass, carbon, and aramid fibers. To decrease the temperature and consequently prolong lifetime, PTFE, silicon, graphite, and boron nitride can be used. Mechanical properties of plastics depend on material; however, production and test conditions also have influence. To predict mechanical stresses and consequently lifetime of gear pair, temperature-dependent material polymer materials must be modeled due to meshing process which is mechanically and thermally exposed phenomenon.

To determine the optimum material combination in terms of lifetime, temperatures, type of damage for appropriate gear application, the choice of materials for the driving, and the driven gear is crucial. Due to this fact, it is desirable to perform tests of polymer gears to determine behavior of chosen gear pair. The test can be accelerated with the aim to rapidly obtain suitability of meshed materials in terms of temperatures and wear. In order to optimize proper selection of a material, it is necessary to conduct lifetime tests under different loads with several repetitions for the same testing conditions. So, data cycles for thermoplastic gears are produced, which can be used for modeling a real gear pair for application in KISSsoft. Many

researchers in the past used different material combinations, which have been proven as appropriate in the context of optimal operating lifetime, temperature distribution development (flank/tooth), and thermoplastic gear wear. According to the literature, the most used material combinations are Steel/POM, POM/PA, PA/PBT, and Steel/PA, sometimes in combination with various additives. S- and E-gears in a combination of driving alloy steel and driven POM gear lifetime tests are discussed in the chapter.

2.1.2 Planocentric Gearboxes with S-Gear Geometry

Planocentric gear boxes are in technical use for many decades due to their main characteristic, which is reduction of rotational speed and accordingly increased torque in the smallest available volume. The expected efficiency may be as high as 90% or more, and gear ratios can achieve up to 160:1 in a single step configuration. Basic arrangements of this type are described in renowned references, e.g., [8], and [9]. Gearboxes of this type are used in robotics, machine tools, aeronautics, aircraft, marine, and many other industries. The efficiency can be above 90%, and gear ratios can achieve up to 160:1 (160 rotations of the input shaft for a single turn of the output shaft). The available industrial solutions include *Sumitomo* cyclo gearboxes [10], *Spinea* drives [11], *Nabtesco* [12], *Onvio* [13], and many others. The device with the same function and different principle is Harmonic Drive. Gearings are usually cycloidal or lantern.

Pure mechanical drives can conform to high-tech industry requirements regarding backlash, lost motion, stiffness, hysteresis, etc. However, supplementary features based on sensorics can add additional functionalities to such gearbox. So, an accurate output shaft positioning and an output torque sensorics can be installed in the device as an option. Such new functionalities can enable incorporation of such devices in collaborative robot's arm joints and adaptive control. An upgrade to a self-aware condition monitoring system could increase the overall reliability of the drive and the effective predictive maintenance. And a corresponding condition monitoring could enable safe human interactions which is of special importance, e.g., in the field of robotics. Many analytical tools were used to analyze tolerances, to discover impact of some influencing factors like backlash, shaft deformation, and single or cumulative pitch deviation, and some of these methods are presented in the chapter.

2.2 S-Gears Geometrical and Thermal Properties

Some important properties of S-gears are the following:

1. Possibility of shaping by two parameters defining the rack flank curve, which can be used to modify teeth, e.g., a pressure angle, tooth thickness, etc.
2. Cylindrical spur S-gears can operate with a low number of teeth down to 6 or even 4.

3. Convex-concave contact in the vicinity of meshing start and end.
4. Comparatively lower radii of curvature, which implies lower contact pressure.
5. Higher contact oil film thickness, which is due to higher relative velocities in the contact.
6. S-gears exhibit relatively longer dedendum part of a pinion tooth flank (comparing to the involute gear) which is meshing with a gear addendum. Difference between the pinion dedendum length and the gear addendum length indicates amount of sliding. And less sliding means less frictional work and less developed heat, which is of special importance for plastic gears.

These properties are elaborated and compared to the involute gears. First, let us examine S-gear definition as illustrated in Fig. 2.1. To define a gear tooth flank, one needs to define a rack profile.

The rack profile with the coordinate origin in the kinematic pole is defined by the following function:

$$f(x) = \begin{cases} a_p m \left(1 - \left(1 - \frac{x}{m}\right)^n\right), & x \geq 0 \\ -a_p m \left(1 - \left(1 + \frac{x}{m}\right)^n\right), & x < 0 \end{cases} \quad (2.1)$$

where $\lim_{x \rightarrow 0^+} f'(x) = \lim_{x \rightarrow 0^-} f'(x)$.

Factors a_p and n , namely, the height factor and the exponent in Eq. (2.1), act as form factors, which affect the tooth shape properties. The initial pressure angle amounts to $\alpha_{w0} = 90^\circ - \alpha_p(0)$ and $\alpha_p(0) = f'(0) = n a_p m$. So, the initial pressure angle is a dependent variable, $\alpha_{w0} = f(n, a_p)$, whereas the module m acts as a scaling factor. The rack tooth can be regarded as a cutting tool.

As illustrated in Fig. 2.1, the arbitrary point P_i on the rack tooth flank defines the unique point U_i on the path of contact. And this point U_i defines the point G_i on the tooth flank of a pinion and the point H_i on the tooth flank of a wheel, both with any number of teeth. This trigonometrical procedure, described in detail in [2], is valid for internal gear pairs as well. The transformations from the rack profile flank through the path of contact to gears are bijective, that is, they always give the same rack flank in the reverse direction. These transformations could also have been represented by object translations and rotations in appropriate coordinate systems, of course by employing the basic law of gearing.

As already stated, the gear flank and tooth shape influencing factors are a_p and n ; however, one of them can be replaced by the initial pressure angle α_{w0} . Two gear pairs are shown here to illustrate the tooth shape variability, namely, the external (Fig. 2.2) and the internal gear pair (Fig. 2.3) with $z_p = 10$ and z_w or $z_r = 30$. Two gear pairs were designed: the first with $\alpha_w = 22^\circ$ and $a_p = 1.3$ and the second one with $\alpha_w = 18^\circ$ and $a_p = 1.5$ in both cases. All gears were designed with the module $m = 50$ mm, and since the module acts only as a scaling factor, its size is of no importance in this context. Rack profiles and paths of contact are the same for internal and external gears. Both rack profiles do not differ much, apart from the inclination and corresponding pressure angle. But the derived paths of contact

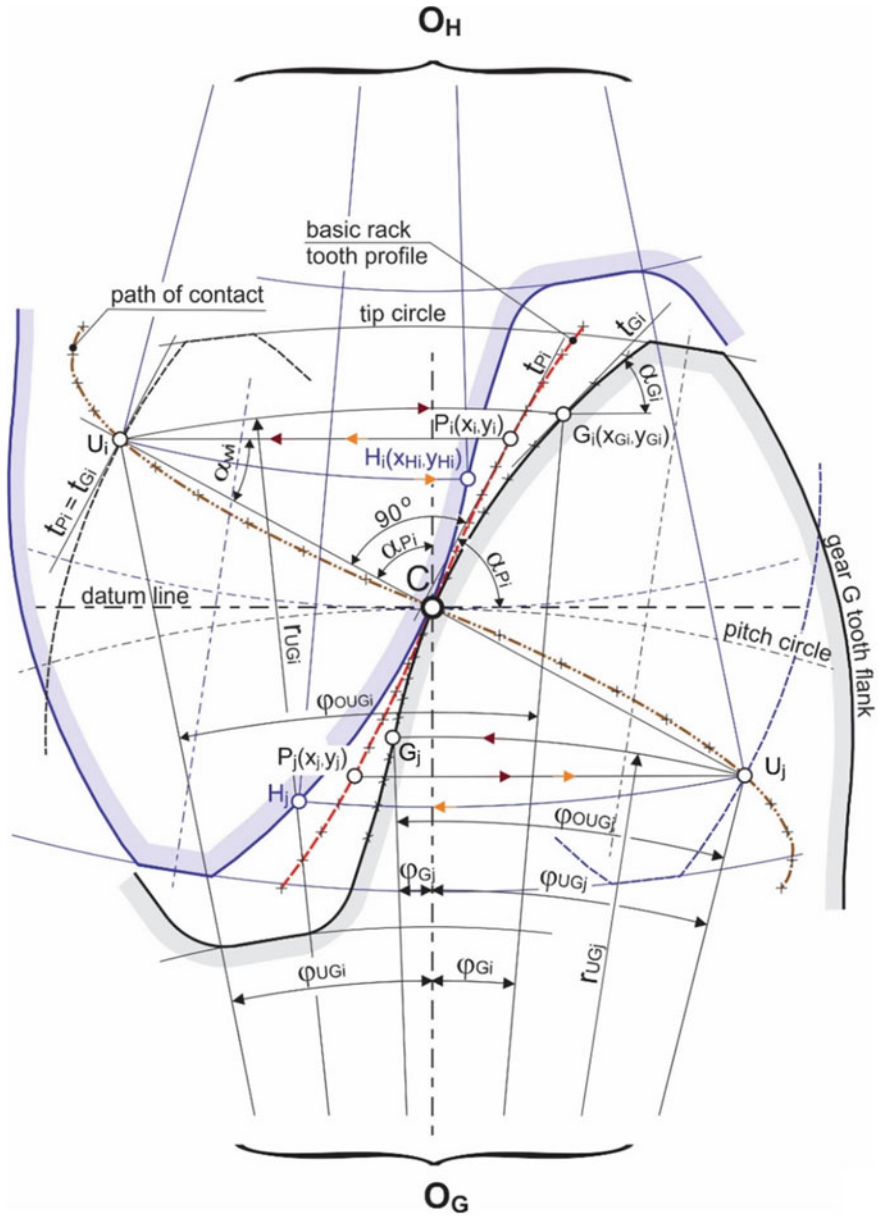


Fig. 2.1 Design of the path of contact, teeth flanks of both gears based on the rack profile [2]

apparently differ in their length and curvature in the meshing starting and end zones, as one can observe in Figs. 2.2 and 2.3. The active parts of both paths of contact delimited by gear tip circles are designated as $\widetilde{A_1E_1}$ and $\widetilde{A_2E_2}$. So, for the higher

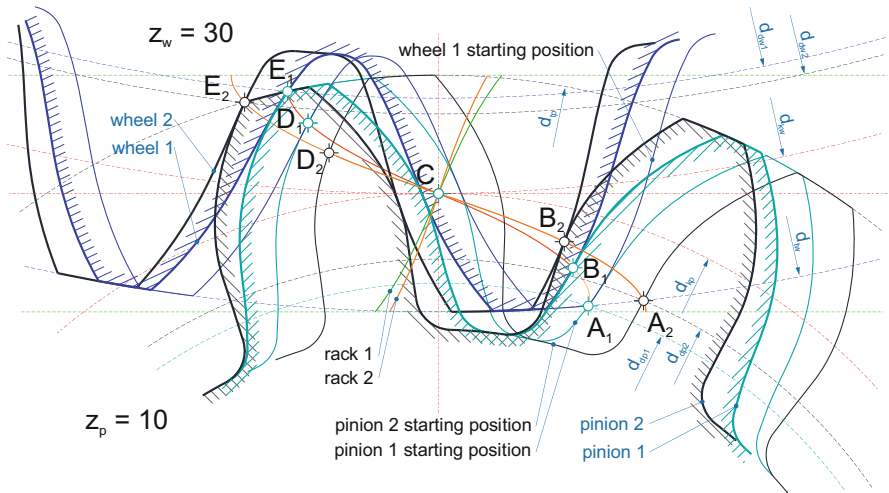


Fig. 2.2 External gear pairs with pinion $z_p = 10$ and wheel $z_w = 30$. The generating rack 1 with (initial) pressure angle $\alpha_w = 22^\circ$ and rack 2 with $\alpha_w = 18^\circ$

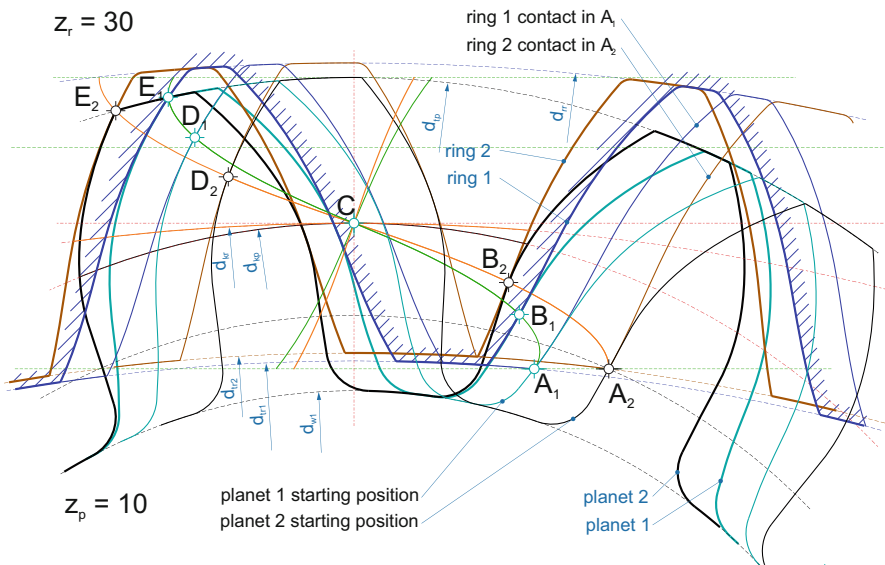


Fig. 2.3 Internal gear pairs with pinion $z_p = 10$ and wheel $z_w = 30$. The generating rack 1 with (initial) pressure angle $\alpha_w = 22^\circ$ and rack 2 with $\alpha_w = 18^\circ$

pressure angle, the path of contact shortens and becomes more curved and inversely (longer and less curved path of contact) for lower pressure angles. The external tooth root becomes stronger and tooth tip thinner for the larger pressure angle and inversely for smaller pressure angles, whereas the internal gear tooth tip and tooth

Table 2.1 Path of contact characteristics for internal and external S-gear pairs ($z_p = 10$, $z_w = 30$, $m = 50$ mm)

Initial pressure angle α_{w0}	18	22
<i>Internal gear pair</i>		
Active length, $l_{\widetilde{AE}}$ [mm]	190.6	165.76
Base pitch, $l_{\widetilde{AD}}$ [mm]	150.4	145.6
Contact ratio, ε [I]	1.27	1.14
<i>External gear pair</i>		
Active length, $l_{\widetilde{AE}}$ [mm]	190.7	162.920
Base pitch, $l_{\widetilde{AD}}$ [mm]	148.2	144.5
Contact ratio, ε [I]	1.29	1.13

space at its root become thinner to some extent for higher pressure angles. And the internal gear addendum height shortens for lower pressure angles, as the meshing start points A_1 and A_2 show (Figs. 2.2 and 2.3). The active length of the path of contact \widetilde{AE} , the length \widetilde{AD} which corresponds to the base pitch, and the contact ratio for all combinations from Figs. 2.2 and 2.3 are collected in Table 2.1.

A combination of internal and external S-gears can be used to design a planetary gear train, as the one illustrated in Fig. 2.4 [14]. It is true that the involute ring gear assures the concave contact in the entire contact zone, whereas the S-gears have a change to the convex-concave type of contact in the vicinity of the ring gear tip. So, the concave contact prevails. And more important, the planet and sun gear contacts are convex-concave, and gears with a small number of teeth can be designed.

2.2.1 Thermal Properties

Thermal load has a disadvantageous effect on the power transmission of a mating gear pair for all types of gears, regardless of size, material, or any other parameters. However, it is of a high importance in plastic gears due to their thermal sensitivity. Heat is generated by friction at the contacting surfaces of the mating teeth flanks where the load transmitting surfaces slide with the relative velocities. Work of friction depends on the flank load, the friction coefficient and on the sliding path length of a contact, whereas thermal power additionally depends on the sliding speed. The generated heat is treated as energy loss, where surface heating is unfavorable, and the temperature rise depends on heat flow into the gear material. Thermal properties of the employed gear material(s) are of the utmost importance in this context.

The mating gear teeth flanks combine the pinion dedendum and the gear addendum flanks from the meshing start to the kinematic pole C and the pinion addendum and the gear dedendum from C toward the meshing end point. The contact is propagating on the path of contact by rolling and sliding. The active size of the pinion dedendum is smaller than that of the gear addendum. This implies amount of sliding of the addendum on the shorter pinion dedendum, which is illustrated in

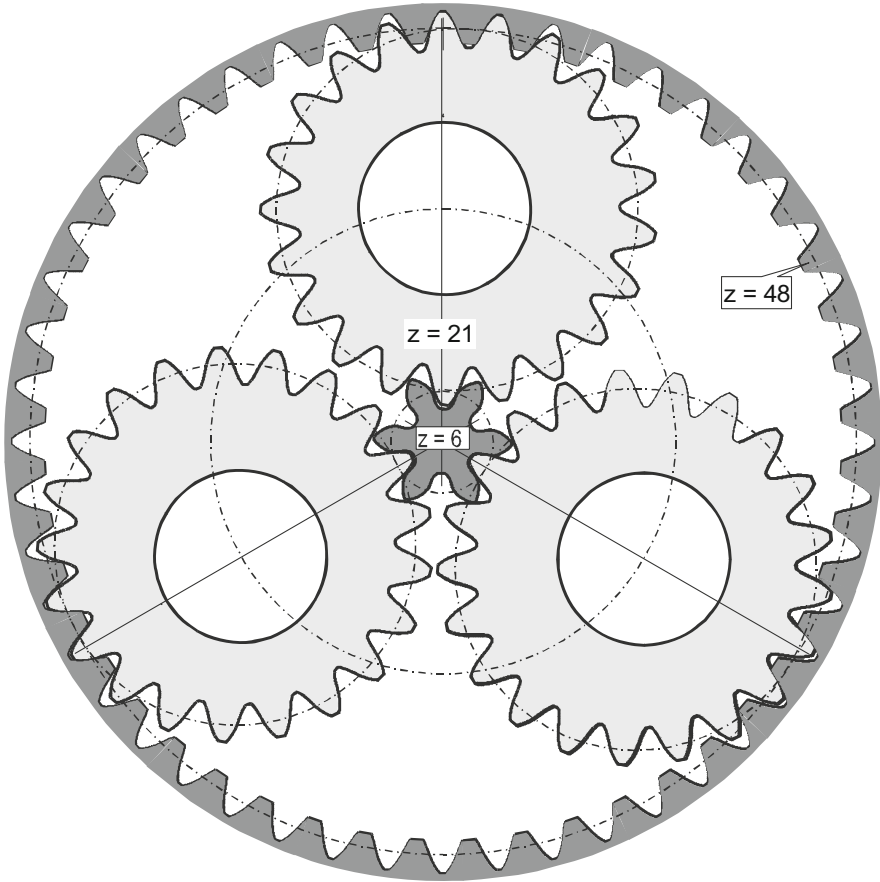


Fig. 2.4 A planetary (spur) gear train (sun gear $z = 6$, planet gear $z = 21$, ring gear $z = 48$)

Fig. 2.5 for both S- and E-gear pair. Amount of sliding also implies thermal impact. In general, the dedendum-addendum length difference depends on module, number of teeth, and pressure angle. For S-gears the said difference also depends on forming factors—the height factor a_p and the exponent n . The length difference in the case of S-gears is comparatively more convenient, so less sliding is produced along the contact propagation compared to the involute case. As Fig. 2.5. suggests:

$$\Delta l_E = l(\mathbf{A}_{ew}\widetilde{\mathbf{B}}_{ew}) - l(\mathbf{A}_{ep}\widetilde{\mathbf{B}}_{ep}) > \Delta l_S = l(\mathbf{A}_{sw}\widetilde{\mathbf{B}}_{sw}) - l(\mathbf{A}_{sp}\widetilde{\mathbf{B}}_{sp}) \quad (2.2)$$

Typical circumstances of the involute gears in the vicinity of the meshing start point disclose small driving pinion radii of curvature and rather high radii of curvature of the driven gear, which imply high sliding velocities in this area. The normal force F_N is transmitted through the contact, which causes the force of friction

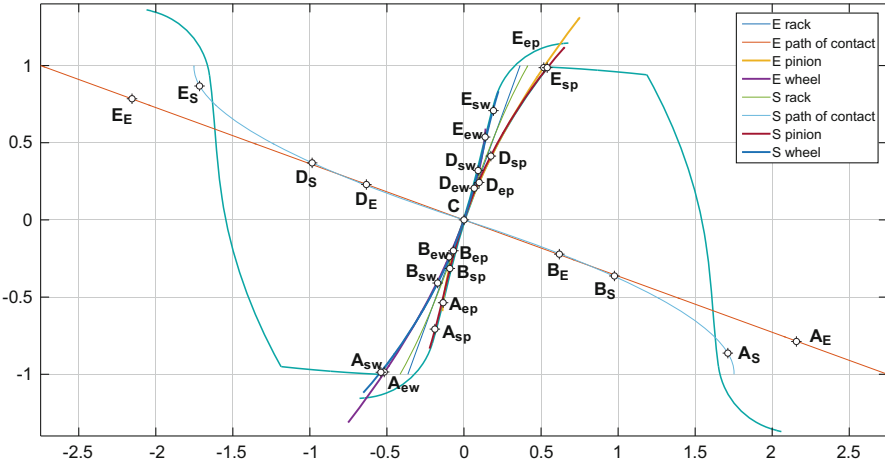


Fig. 2.5 Comparison of the E- and S-spur gear pair with $m = 1 \text{ mm}$, $z_p = z_w = 20$, $\alpha_{wE} = 20^\circ$, and $\alpha_{wS} = 18^\circ$

F_{fr} oriented tangentially to the contact and the corresponding power of friction, $P_{fr} = F_{fr} v_g$. The power of friction being generated in the contact representing losses transforms to the heat flow, distributed to both involved flanks. A greater part of the heat is therefore distributed to the slower driving gear and the rest to the longer contacting area of the driven gear. The friction force grows to high levels already at the meshing start, which negatively influences (braking) the contact point velocity along the path of contact and induces negative sliding on the driving gear flank.

2.2.2 Analytical Approach

A program for calculation of the S-gear rack profile, the path of contact, the pinion, and the inner or outer gear was supplemented by necessary computations of power, work, flank pressure, contact width, velocities, and flash temperatures. All the parameters can be represented along the path of contact or the active flank profile. Power of friction is therefore given by:

$$P_{fr} = F_{fr} \cdot v_g = (\mu \cdot F_t / \cos \alpha_w) \cdot v_g \tag{2.3}$$

The work of friction along the active contact from $t_A = 0$ to t_E is given by the sum:

$$A_{fr} = \sum_{iA}^{iE} P_{fri} \cdot \Delta t_i \tag{2.4}$$

So, the frictional work in a single pinion rotation is $z_p \cdot A_{fr}$ and multiplied by the rotational frequency frictional work accomplished in a minute $\nu \cdot z_G \cdot A_{fr}$. The

Table 2.2 Frictional work and average frictional power [7]

	S-gears	E-gears
$T_t = 0.6 \text{ nm}$, $P_t = 90.415 \text{ W}$, $\nu = 1439 \text{ min}^{-1}$, $l_U = 3.891 \text{ mm}$		
Work in a single contact	0.0052 J	0.0064 J
Work in a single rotation	0.1040 J	0.1278 J
Work in a minute	149.61 J	183,87 J
Average frictional power	2.4935 W	3.0644 W
$T_t = 0.7 \text{ nm}$, $P_t = 104.8 \text{ W}$, $\nu = 1428 \text{ min}^{-1}$, $l_U = 4.5976 \text{ mm}$		
Work in a single contact	0.0061 J	0.0075 J
Work in a single rotation	0.1213 J	0.1491 J
Work in a minute	173.21 J	212,87 J
Average frictional power	2.8868 W	3.5479 W

average frictional power is then $P_{fr\ av} = \nu \cdot z_G \cdot A_{fr}/60$. Table 2.2 collects data for the E- and S-spur gear pair with $m = 1 \text{ mm}$, $z_p = z_w = 20$, $\alpha_{wE} = 20^\circ$, $\alpha_{wS} = 18^\circ$, and $b = 6 \text{ mm}$.

A calculation of flash temperatures was also conducted in [7]. Whereas the S-gear pair develop similar maximum values in A, B, D, and E, that is, approximately 38 K, the maximum values for the E-gear pair are in A and E and range around 59 K for the nominal load $T = 0.6 \text{ Nm}$ and $\nu = 1439 \text{ min}^{-1}$.

2.3 Testing of Plastic Gears

Selection of material combinations for laboratory testing is based on the existing applications. Material alternatives were tested and characterized as well. Due to importance of proper material selection, the company decided to develop and produce own testbenches. Temperature measurements of a contact spot and temperature field of meshing gears were provided by a thermal camera. Optris Xi80 device was used for this purpose. Spot temperature was acquired during entire loading cycle of the lifetime tests, which was facilitated by Optris PIX Connect software. Based on test duration and rotational speed of the selected thermoplastic gears, lifetime cycles were calculated and imported together with flank/root temperature into Software KISSsoft (module Plastics Manager). Based on the processed input data in Plastics Manager, Wohler Curves (S-N) for selected material combinations were obtained. After each experimental lifetime test, the wear characterization has been performed according VDI 2736 [15, 16] with Alicona device and evaluation of the gear failure mode.

2.3.1 Gear Geometry and Manufacturing

Small gears of equal size are used, with the module of 1 mm and $z = 20$. Some crucial differences between E- and S-gears were revealed in previous paragraphs. Important characteristics of these gears are collected in Table 2.3, whereas Fig. 2.6 shows the distinction between S- and E-geometry and two plastic materials.

Many manufacturing technologies were used in initial experiments, whereas material pair was a popular combination POM PA66. First, molded gears were employed, where it was discovered that shrinkage and corresponding coefficients can be unreliable and results elusive [17]. So, it was decided, that gears should be hobbled to reflect correct gear geometry, first with a single cutting hob. And

Table 2.3 Tested gear characteristics

Gear geometry	E	S
Teeth number, z [/]	20	20
Width, b [mm]	6	6
Module, m [mm]	1	1
Pressure angle at normal section, α [°]	20	18
Tip diameter, d_a [mm]	22	22
Reference diameter, d [mm]	20	20
Root diameter, d_f [mm]	17.5	17.7
Base diameter, d_b [mm]	18.79	–
Dedendum limit, d_{lm} [mm]	18.95	18.59
Base tangent length, W_k	7.66	



Fig. 2.6 Involute (above) and S-gears (below) made of PA66 (left) and POM-C (right)

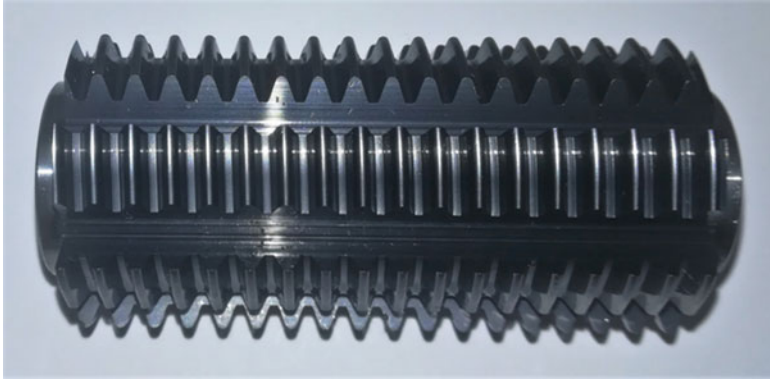


Fig. 2.7 S-gear hob for gears of module 1 mm

POM-PA66 raw material extruded rods. Since such operations are ineffective, regular hobs were produced for E- and S-gears (Fig. 2.7). Initially, raw parts are injection molded with the machine Krauss Maffei KM 50/100 CX. Raw parts were hobbled on Koepfer 200. Plastic parts are usually molded in general, whereas the expense for an injection tool could be too high for small lot sizes of a few thousand pieces. It was discovered [18] that the quality of molded gears compared to hobbled gears is at least two grades lower (measured with the 3D CMM Wenzel, with the gear inspection module). Inspection protocols according to DIN3961/62 revealed grade around Q8 for cut gears and above Q10 for molded gears. CMM is used regularly to ensure proper quality.

2.3.2 Testing Arrangement

Notable efforts in the promotion of a sustainable production lead toward more recycling and avoidance of harmful media. Therefore, lifetime tests are performed lubrication-free, i.e., dry on the own built testbenches in R&D laboratory of the Podkrižnik Company. The tests in discussion are conducted at ambient temperature. Figure 2.8 shows the testbench with a control and DAQ system.

The torque setting is based on a difference in the input values of frequency converters for a driving and a driven motor. The testbench calibration in terms of the selected torques was performed by measuring torsional deformations of a driving and a driven shaft at different setting frequencies.

During the entire duration of lifetime tests, spot temperatures and thermal state of meshing gears were measured with thermal camera Optris Xi80, where visualization was performed by PIX Connect software, as shown in Figs. 2.9a, 2.10a, and 2.11a. After each test, post-processing of time-temperature data was performed and aggregated. So, time-temperature diagrams were produced for the determined spot area of each meshing gear pair with S or E tooth flank profile. The prescribed conditions are

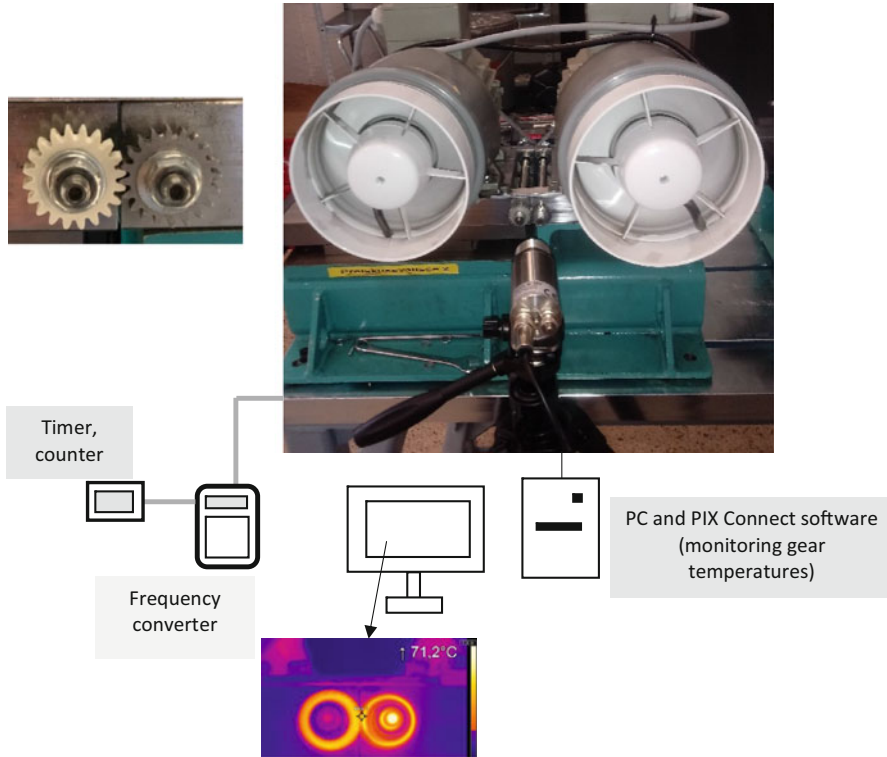


Fig. 2.8 Testing arrangement—testbench for lifetime testing of thermoplastic with thermal camera to monitor temperature data

presented in Table 2.4 and resulting temperature diagrams in Figs. 2.9b, 2.10b, and 2.11b.

Testbench is programmed to stop when a 5% decrease of input current of the motors and consequently torque decrease of the tested gear pair appear. A timer, which stops when the current drops due to gear failure, is connected to the frequency converters. The accurate test duration time is recorded in this way, and the duration time multiplied by RPM implies the number of cycles of the experiment.

In this series of experiments, a combination driving steel and driven POM gear was used. Torques leading to expediter lifetime characteristics were 1.5, 1.3, and 1.1 Nm. And a minimal statistical relevance was attained by three repetitions for each torque and both gear flank shapes. Lifetime tests were conducted at stable ambient laboratory temperature which was $22\text{ }^{\circ}\text{C} \pm 0.5\text{ }^{\circ}\text{C}$. The selection of torques was furthermore based on the preliminary lifetime testing of different types of polymer gears reported in [19].

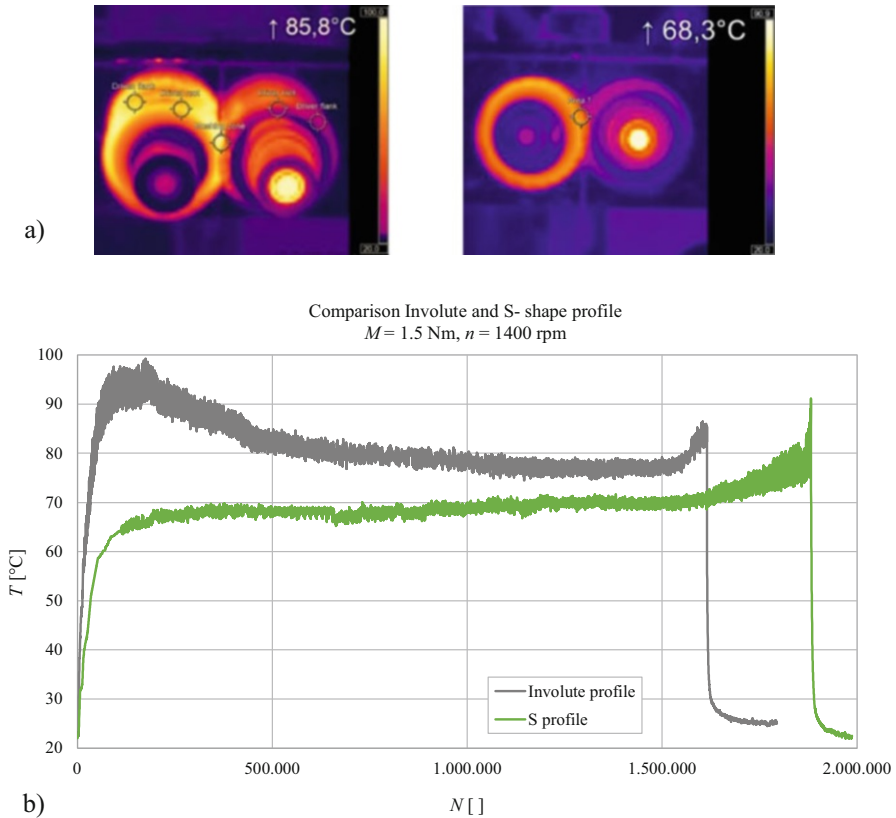


Fig. 2.9 Comparison of E- and S-tooth profile for a steel-POM gear pair at $M = 1.5 \text{ Nm}$ and $n = 1400 \text{ min}^{-1}$. (a) Temperature spot in the meshing area E (left) and S (right) profile of teeth. (b) Temperature-time profiles (S, green; E, grey)

2.3.3 Experimental Results

The temperature-time dependency consists of three main sections, which are (a) running-in area where thermoplastic driven gear fits to steel gear in terms of tooth flanks; (b) a phase of a quasi-stationary operating at stable temperature; and (c) a phase of increasing gear wear that, in combination with fatigue, causes failure of thermoplastic gears.

The running-in phase of the E-gear pair has a characteristic course in the form of a transient phenomenon where the increase in temperature on tooth flanks was detected, which is due to the unmodified involute tooth tip profile, a high load, and subsequent teeth deformation (see [9], p. 98). So, a driven gear suffers an additional impact at a meshing start point A and temperature rise. The consequence is rather high initial wear of a driven plastic gear. S-gears do not exhibit such effects, so the temperature rise proceeds until the second, stationary phase.

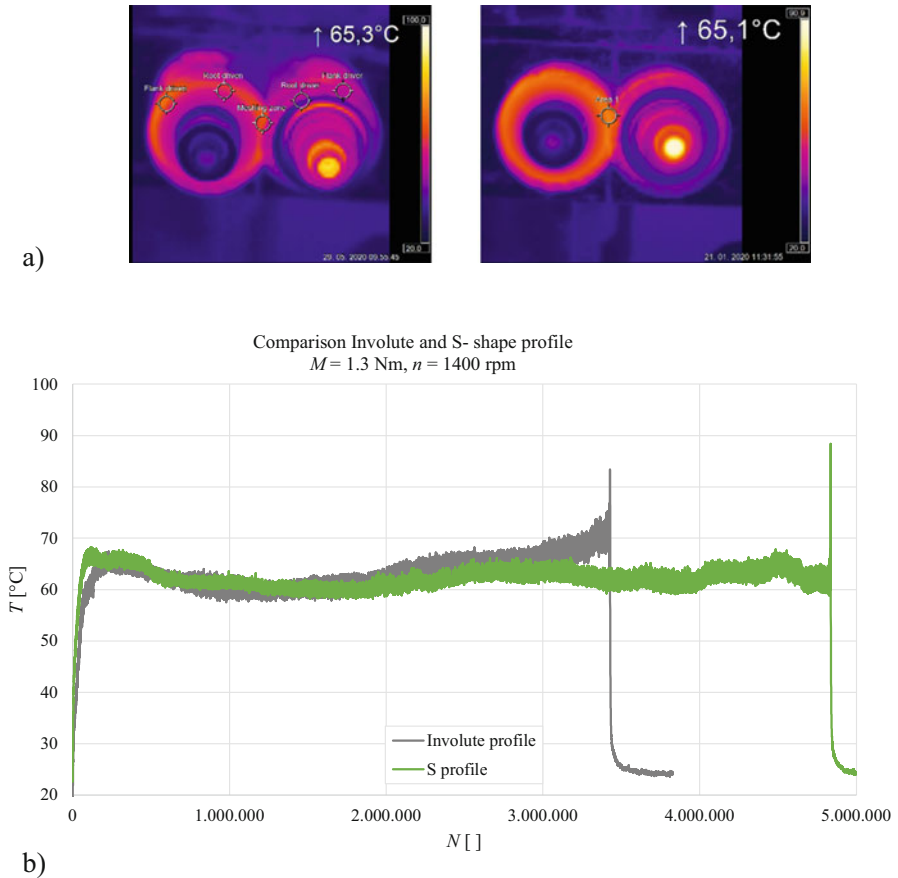


Fig. 2.10 Comparison of E- and S-tooth profile for a steel-POM gear pair at $M = 1.3 \text{ Nm}$ and $n = 1400 \text{ min}^{-1}$. (a) Temperature spot in the meshing area E (left) and S (right) profile of teeth. (b) Temperature-time profiles (S, green; E, grey)

In the next phase, relatively stationary conditions prevail. For E-gears the initially high temperature drops and prevails until the final phase. Uniform wear occurs in this phase for both gear types. The last phase of the lifetime test shows significant changes of the gears. This is due to the increased wear above the critical limit in connection with the fatigue of the material, which causes degradation of the bonds between the molecules in the material and the subsequent teeth failure.

The spot temperature for $M = 1.5 \text{ Nm}$ in the stationary zone is around $70 \text{ }^\circ\text{C}$ for S-gears and around $80 \text{ }^\circ\text{C}$ for E-gears. This temperature is in the zone above $60 \text{ }^\circ\text{C}$ for torque 1.3 Nm for both gear geometries. The E-gears do not show the abnormal temperature rise at start. However, S-gears have higher cycle numbers. The spot temperature for E-gears starts rising at about 2,000,000 cycles until final failure.

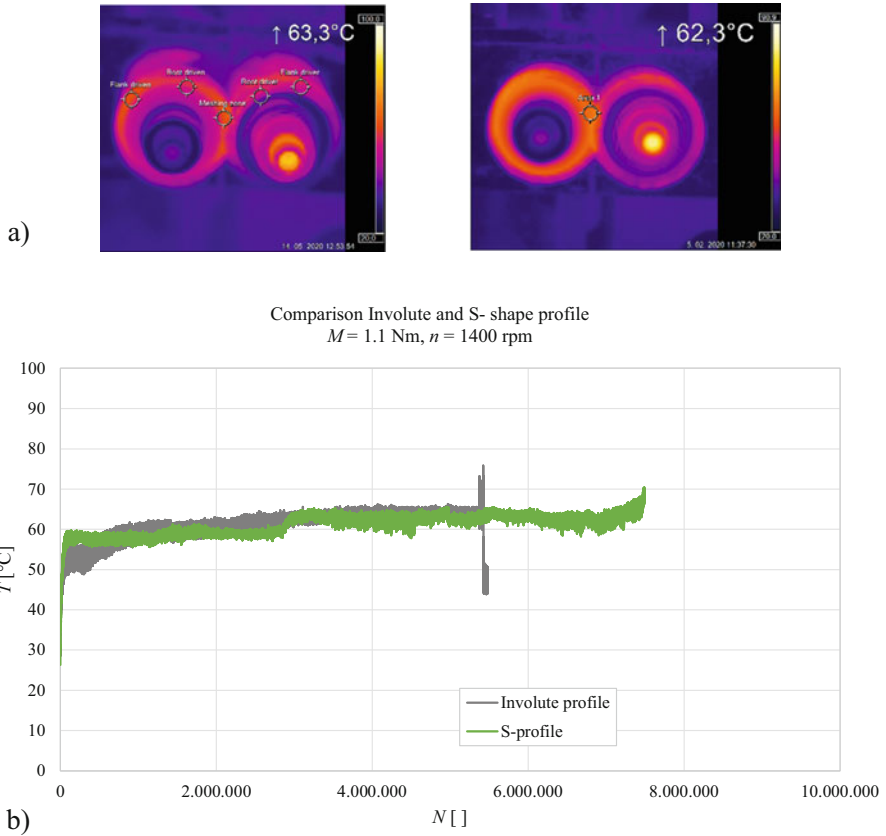


Fig. 2.11 Comparison of E- and S-tooth profile for a steel-POM gear pair at $M = 1.1 \text{ Nm}$ and $n = 1400 \text{ min}^{-1}$. (a) Temperature spot in the meshing area E (left) and S (right) profile of teeth. (b) Temperature-time profiles (S, green; E, grey)

Table 2.4 Testing parameters at ambient temperature

INPUT PARAMETERS				
Gear pairing (driving gear-driven gear)	Tooth profile	Torque, M [Nm]	Rotational frequency of gears, n [min^{-1}]	Repetitions
Steel—POM	E- and S-shape	1.5	1400	3
Steel—POM	E- and S-shape	1.3	1400	3
Steel—POM	E- and S-shape	1.1	1400	3

The temperature-time diagrams for 1.1 Nm show similar temperature for both gear geometries, initially below and later above 60 °C without abrupt deviations during entire lifetime test for both gear types. However, there is a distinct difference

Table 2.5 Lifetime cycles of E- and S-gear pairs, driving gear steel, and driven gear POM

Load M [Nm]	E [$\times 10^6$]	S [$\times 10^6$]
1.5	1.62	1.88
1.3	3.43	4.84
1.1	5.34	7.83

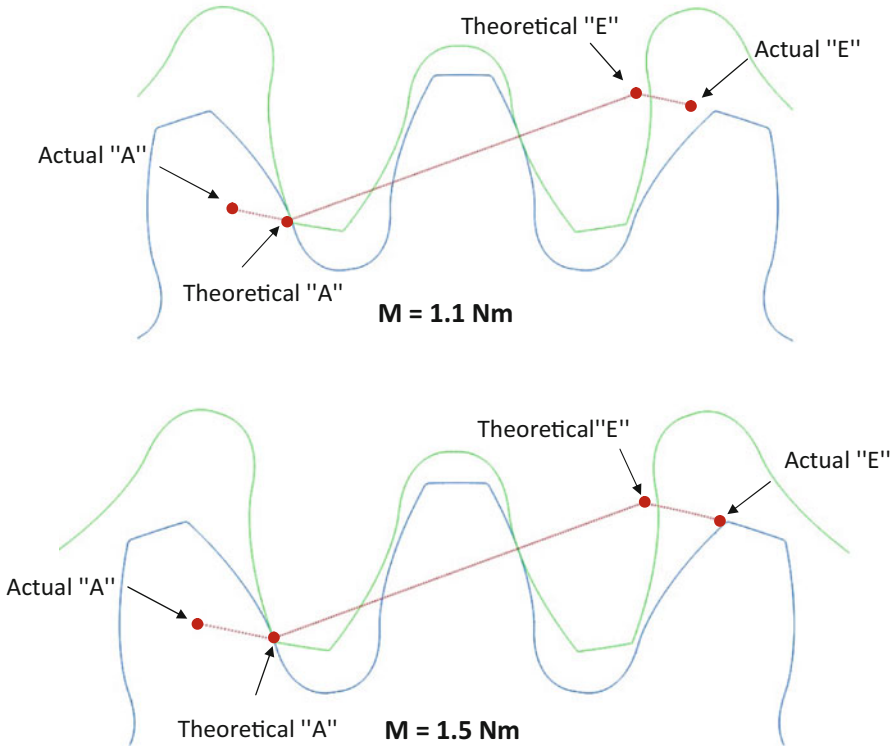


Fig. 2.12 Theoretical path of contact and actual meshing line (red) for 1.1 Nm (above) and 1.5 Nm (below) (driving steel gear, blue; driven POM gear, green)

in the number of loading cycles in favor of S-gears. The results are collected in Table 2.5.

The temperature behavior of E-gear pairs in the starting phase differs for higher and lower loads, which was numerically simulated for loads of 1.5 and 1.1 Nm. The contact analysis of meshing gears was provided by KISSsoft. Figure 2.12 shows results of the simulation for both loads for involute gear pair without tip relief.

The contact analysis for 1.1 Nm shows a transverse overlap ratio $\epsilon_\alpha = 1.905$, meanwhile the theoretical one is 1.534. The increase of 24% in the transverse overlap ratio is clearly visible through distinctively prolonged part at the start, before point “A,” and at the end, after point “E,” of a meshing gear pair.

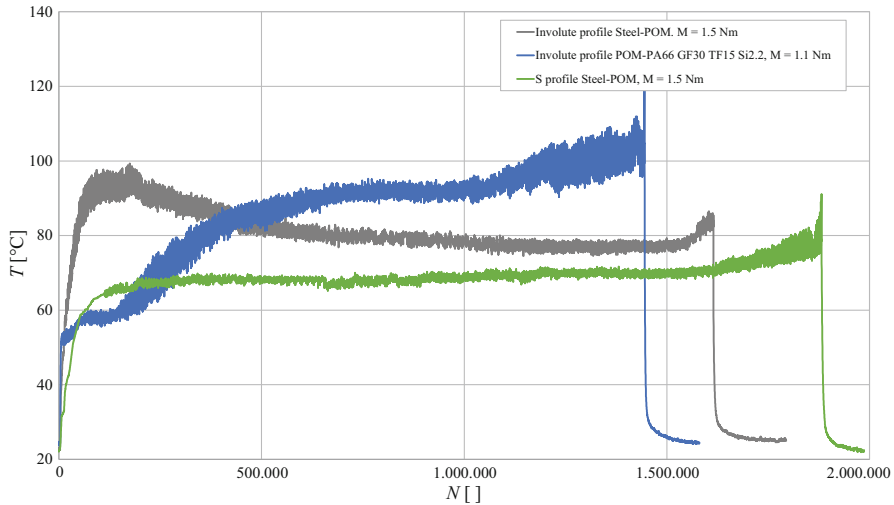


Fig. 2.13 Comparison of temperature-time diagrams for E- and S-gears for 1.5 Nm and E-gear pair with a POM-PA66 combination at 1.1 Nm—blue

For a higher load, 1.5 Nm, a transverse overlap ratio $\varepsilon_{\alpha} = 2.000$ is reported, which means the increase of 30% comparing to the theoretical one. The gears remain in mesh/contact for a longer time, hence producing more heat (out of roll—point “E”—location) due to higher teeth deformation which occurred at loading conditions $M = 1.5$ Nm compared to $M = 1.1$ Nm. It is assumed that the detected temperature distinction (Fig. 2.9b, E-gear shape) is due to unmodified tooth flank profile which induces increased wear of a POM gear driven by a steel gear.

The phenomenon of temperature increase for E-gear pairs with higher loads and material combination steel-POM (where POM is highly deformable) is typical for the said material combination, whereas two plastic materials tend to possess similar deformability. So, a combination of POM PA66 E-gear pairs when loaded with 1.5 Nm reveals continuous temperature rise to the short lifetime (around 200,000 cycles) with thermal failure. Figure 2.13 therefore shows POM-PA66 GF30 TF15 Si2–2 E-gears loaded by 1.1 Nm, compared to 1.5 Nm steel-POM combination (E- and S-gears). The temperature-time diagram for plastic gears shows different thermal behavior than steel-POM combination. Typically for the initial part of the lifetime test is that the temperature increases slowly due to uniform deformation of driver and driven gear for which thermo-mechanical properties are at the same level in terms of values. After the rise to around 60 °C, the temperature significantly increases again due to the drop in mechanical properties, especially Young Modulus E for both thermoplastics. This results in a higher deformation level and consequently higher temperatures generated in the meshing zone which imply higher wear of the gear tooth flanks. The increased wear rate in this case is also caused by fibers which can be on the surface of a hobbled gear. Temperature

stabilization is conditioned by the achieved wear of the tooth flanks. When fatigue of material in combination with wear becomes critical, the failure occurs.

2.3.4 Wear Detection

The basic idea is to detect a shape of worn plastic gear and compare it to the new one. Such an analysis is facilitated by an optical 3D measurement microscope, Alicona Infinite Focus SL. Some preliminary results for POM S-gear is presented below. So, the new S-gear is compared to a gear loaded by 1.1 Nm and failed after 7.851×10^6 cycles, which is illustrated for both gears in Fig. 2.14. Both profiles are compared in Fig. 2.15, where one can observe that the worn gear suffered severe wear and some plastic deformation before it failed. It seems reasonable to expect less wear with higher loads and lesser number of cycles.

2.4 Planocentric Gearbox with S-Gear Geometry

The planocentric gearbox has coaxial input and output shafts, and large transmission ratios can be achieved based on a gear ring with internal gearing in combination with usually two planet gears with external gearing, where the difference in the numbers of teeth between the gear ring z_v and the planet gears z_p rules the output gear ratio (Eq. 2.5). The difference in ring and planet numbers of teeth should be one, to achieve maximal reduction:

$$i_{out} = \frac{z_p - z_v}{z_p} \quad (2.5)$$

The planet gears are mounted on an eccentric shaft, where bearings separate the planet gears from the eccentric. The planet gears wobble around the gear ring, that is, they reverse for one tooth in each revolution of the eccentric. The wobbling movement is in accordance with a hypocycloidal movement where the generating circle with the radius of the eccentric is rolling on the kinematic circle of the ring gear. At the same time, the planet gear kinematic circle rolls in the inner side of the ring gear kinematic circle, which is simultaneous with the rotation of the eccentric. In this way the planetary gears develop rotation superimposed on the wobble. So, the input rotation of the eccentric is transformed into the reduced output rotation of the cage with the pins according to the gear ratio in the reverse direction of the input shaft in the same axis. And the gear ring is fixed to the housing.

SGU gearbox presented in this chapter is midsized device with $z_p = 80$ and $z_r = 81$ with reduction ratio 80 and nominal torque 120 Nm and backlash below 0.016° .

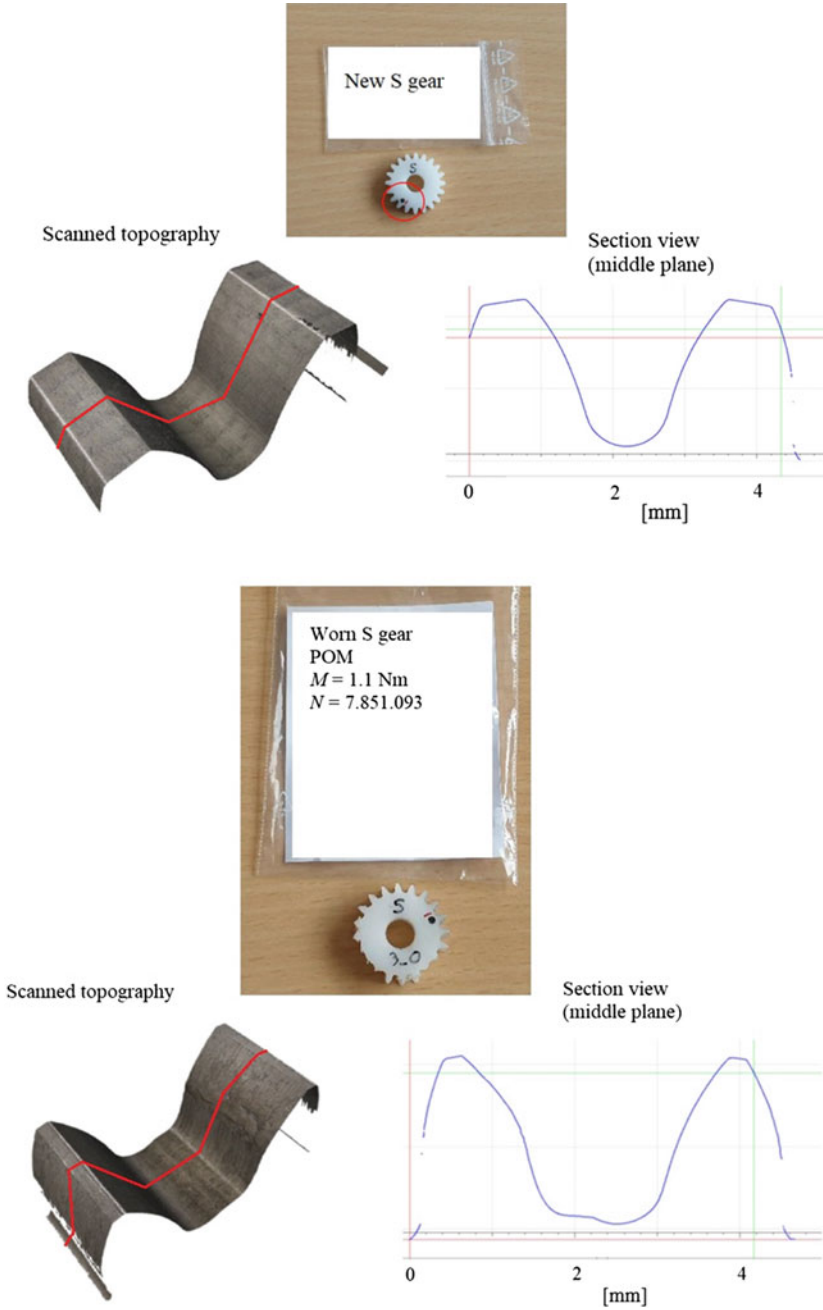


Fig. 2.14 3D scanned topography and 2D view of new (above) and worn (below) POM S-gear

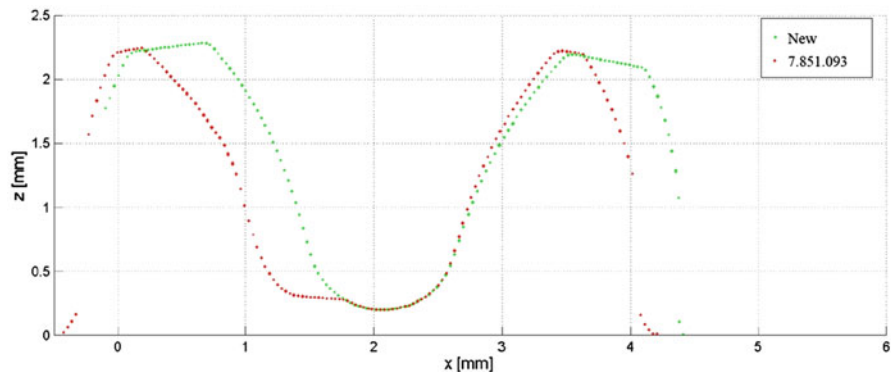


Fig. 2.15 2D wear presentation of S-gear at prescribed loading parameters: $M = 1.5 \text{ Nm}$, $n = 1400 \text{ min}^{-1}$ at ambient temperature (red) compared to a new S-gear (green)

2.4.1 Kinematic Circumstances

The eccentric driven planocentric gear train can be regarded as a simple mechanism with two links. The first link size is the radius of the eccentric, and its joint indicates its position. The second one connects the eccentric with a point on the planet gear (a rigid body), e.g., the contact point. The eccentric link rotates and induces movement of the chosen point on the planet gear, which is restricted by the following rule:

$$r_v = r_p \frac{\varphi_p}{\varphi_v} \quad (2.6)$$

r_v and r_p are the radii of the kinematic circles of the ring gear and the planet gear, respectively. If the ring gear rotates for φ_v , the planet rotates for φ_p . Figure 2.16 illustrates movement of the planet based on the rotation of the eccentric and rolling of the planet kinematic circle on the fixed ring circle.

A simple algorithm can be used to define movement of the planet based on the rotation of the eccentric and limited by Eq. (2.6):

- T_{p0} and T_{v0} coincide with C. P_0 is a point on the planet also coinciding with C.
- T_{p1} and T_{v1} are calculated according to Eq. (2.6). It is true: $p = \pi m = \widehat{CT}_{v1} = \widehat{CT}_{p1}$.
- Eccentric turns for φ_v to the new point O_{p1} . kkp rolls on kvv in such a way that T_{p1} coincides with T_{v1} . So, tangents and normals of kvv and kkp coincide in T_{v1} .
- The normal of the planet in this point runs through O_v and O_{p1} .
- Since the planet is a rigid body, the right leg of the angle φ_p rotates around O_{p1} in CW direction for the difference $\Delta\varphi = \varphi_v - \varphi_p$.
- The procedure is continuous, but it can be numerically calculated by any adequate number of steps.

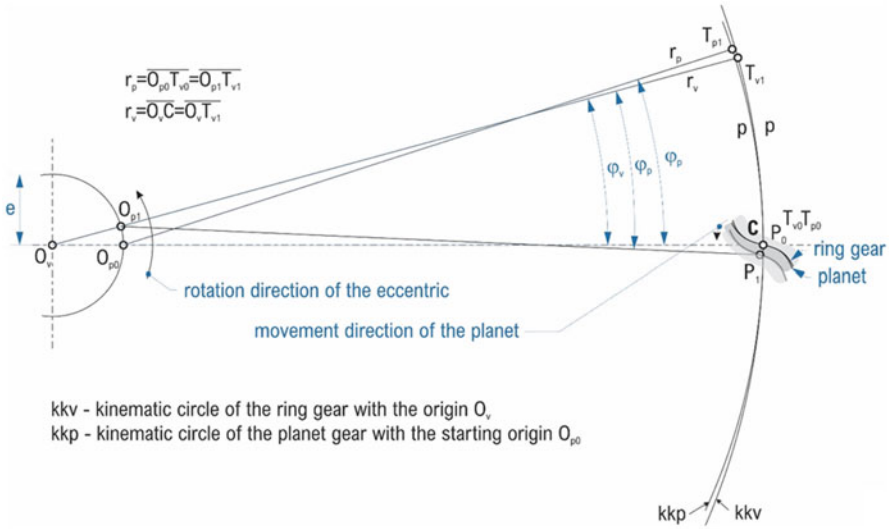


Fig. 2.16 Planetary gear movement as a simple mechanism with two links of the ring gear [14]

The above procedure can be formalized. Thus, successive points on the ring gear kinematic circle T_{vi} are defined as follows:

$$x_{Tvi} = r_v \cos \varphi_{vi} \quad \text{and} \quad y_{Tvi} = r_v \sin \varphi_{vi}. \tag{2.7}$$

Similarly, successive position points O_{pi} of the eccentric are:

$$x_{Opi} = e \cos \varphi_{vi} \quad \text{and} \quad y_{Opi} = e \sin \varphi_{vi}. \tag{2.8}$$

The coordinates of the moving point P_i on the planet gear are:

$$x_{Pi} = x_{Opi} + r_p \cos \Delta\varphi_i \quad \text{and} \quad y_{Pi} = y_{Opi} + r_p \sin \Delta\varphi_i. \tag{2.9}$$

The eccentricity e is defined by Eq. (2.10):

$$e = \frac{z_v - z_p}{2} \cdot m \tag{2.10}$$

The planet gear tooth movement into a new ring gear tooth space is illustrated in Fig. 2.17 by 20 iterations. So, each point and the planet gear position in Fig. 2.16 are based on successive rotations of the eccentric for 18° .

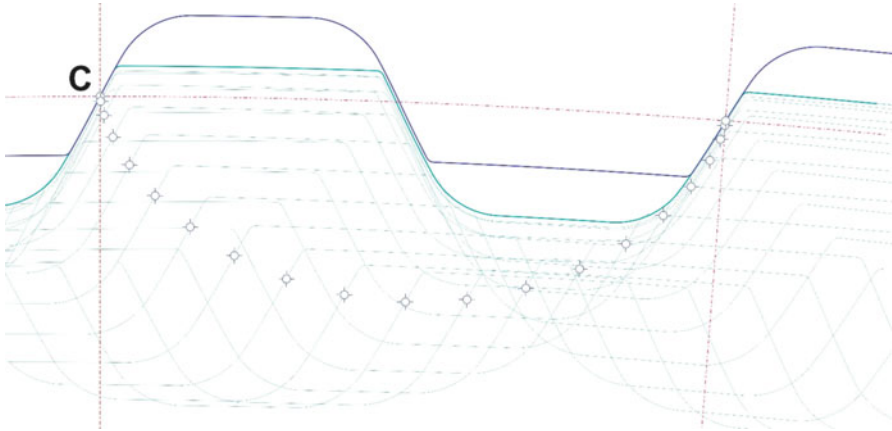


Fig. 2.17 Simulation of a planet gear tooth movement in accordance with hypocycloid generated on the kinematic circle of the ring gear [20]

2.4.2 Gradual Development

Several prototypes, named SGU, were produced, assembled, and tested during the development period. These prototypes were used for testing important characteristics and to acquire knowledge in design of succeeding gearbox. The gearbox contains an input shaft with eccentrics. As a motor rotates, the eccentric shaft rotates two planetary gears which wobble on the ring gear. Two planetary gears are positioned to enclose 180° . A cage consists of a supporting ring and output ring (serving also as the output shaft) that are connected by pins in an interference fit. The cage is rotated by planetary gears, having appropriate holes in which connecting pins with bearings comply. The cage is fixed to the input shaft by bearings at the extremities and in a similar manner to the housing with the ring gear. In this way a compact low-volume gearbox is designed. Initial prototypes are devices with a reduction ratio of 80 ($z_v = 81$ and $z_p = 80$), an outer diameter of around $\phi 100$, and having a module of 1 mm. The required maximal working torque is 120 Nm.

The device is presented in Fig. 2.18 with a 3D schematic and a photo. This gearbox incorporates an absolute output position encoder, which is also an innovative Slovenian product, namely, the *AksIM absolute rotary encoder* [21] made by RLS.

Crucial components, namely, the eccentric, the ring gear, and the planets are measured on a CMM before assembly. The tests include backlash, hysteresis and stiffness, kinematic error, vibrations, and noise, as well as durability tests. The devices were disassembled afterward, and critical components were inspected on the CMM and optically.

Figure 2.19 shows the ring gear and one of the planets of the specimen 01 after the conducted durability tests. The hole in the planet (which is adapted for the cage of pins with bearing bushings) is slightly worn in the circumferential direction

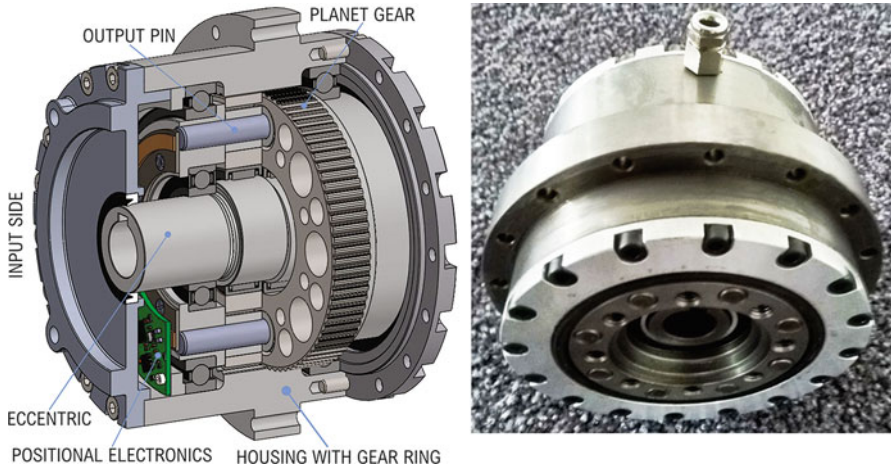
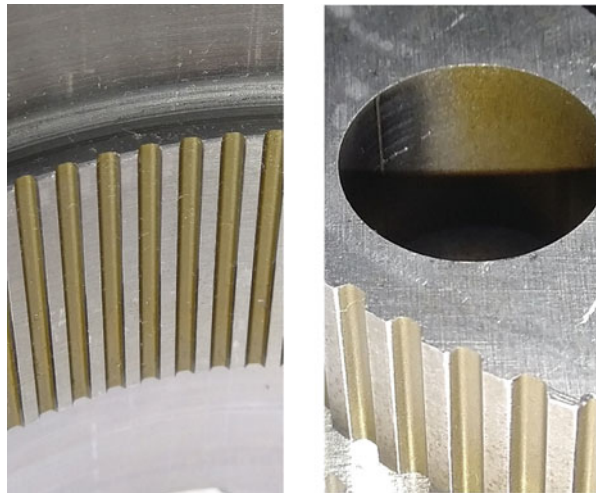


Fig. 2.18 3D schematics of the planocentric gearbox (left) and a prototype (right)

Fig. 2.19 Ring gear (left) and a planet (right) of a specimen 01 after durability tests



according to the acting force on the output bearing bushings of the pins. The specimen was submitted to high torques and speeds. The planet gears were made of 42CrMo4 and the ring of 25CrMo4, all gears plasma nitrided to HV700. The gears were also carefully examined by an optical microscope. The gear teeth did not show any wear or damages. Initial wear appeared in some planet teeth tips and at certain locations in teeth tips. The reason is in the meshing errors, which were discovered by measuring teeth of the planets and the ring gear with a CMM.

2.4.3 Backlash and Stiffness

The results presented in following paragraphs were done on a custom-built testbench, which was primarily used to conduct lifetime tests. The testbench is shown in Fig.2.20 and consists of two servo motors (SM), one on the input and one on the output side and a flange, which is used to attach the gearbox under test. SM1 drives the gearbox, and SM2 provides the torque load on the gearbox by breaking. The system is controlled by a PLC and uses the input and output torque sensors (both Kistler type 4520A200) and a hall sensor on the input side. Individual components of the system are connected by elastic couplings.

When needed the testbench was also upgraded with the Dewesoft, Dewe43A DAQ, system and the appropriate sensors for different tests. The obtained data was post-processed using a specific program written in Python. Two different types of tests are further presented in this manuscript:

- Measurement of the gearbox stiffness and backlash.
- Measurement of kinematic error.

The testbench described above in combination with the Dewesoft DAQ was adapted to measure the stiffness curves of the SGU gearbox as well as those of other robot gearboxes commercially available (labeled Drive 1 and Drive 2). For this purpose, the output shaft was fitted with the Renishaw incremental encoder (consisting of RESM20USA052 encoder ring and the reading head V2CKD20D20F). The torque was measured by the already mentioned Kistler torque sensor where the data acquisition (DAQ) rate was 20 kHz. The input shaft was held

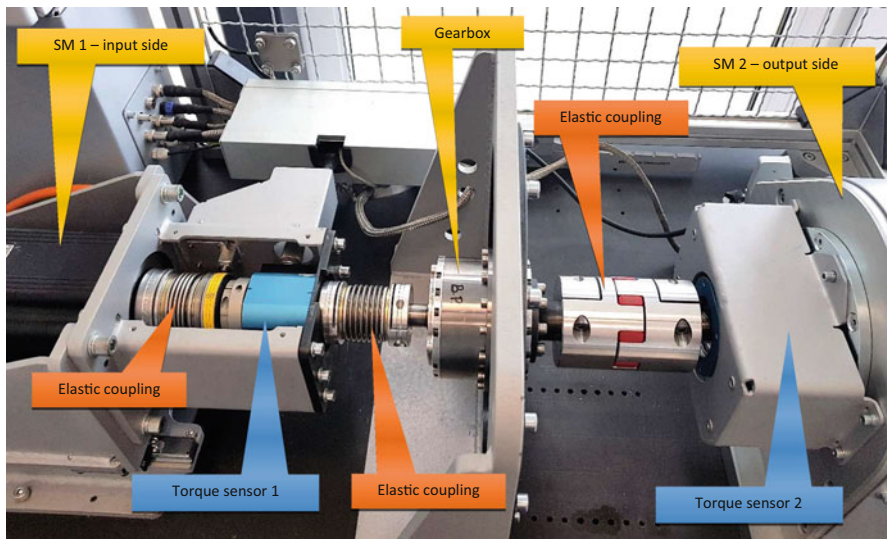


Fig. 2.20 Testbench used for lifetime tests (detailed view)

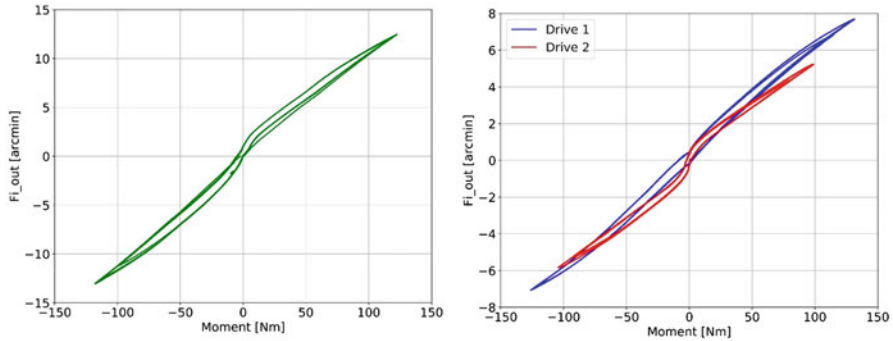


Fig. 2.21 Stiffness curve of the SGU gearbox (left) and commercially available gearboxes (right)

fixed by a clamp, and the output shaft was subjected to a torque load from approximately -130 Nm to 130 Nm by hand via a lever, which was purposely mounted at the output side of the testbench. The loading cycle was repeated three times as can be observed from Fig. 2.21 (left). The curve actually represents the characteristic of the discussed planocentric gearbox. The resulting stiffness curves practically overlap, showing high repeatability of the measurement cycles. The stiffness curve is sectionally linear, and the backlash for the data in Fig. 2.21 is 0.89 arcmin (measured at 0 Nm).

It is interesting to compare the developed gearbox to other available high-tech devices. So, Fig. 2.21 (right) shows the stiffness curves of Drive 1 and Drive 2. A comparison with the SGU drive reveals approximately equal backlash values: Drive 1 0.9 arcmin and Drive 2 0.8 arcmin. The stiffness of these gearboxes however is higher, also sectionally linear.

To determine the overall or averaged backlash of the SGU gearbox, 36 different points were measured in the following manner:

- The first four points were obtained by sequentially rotating the input shaft by 90° .
- The input shaft was then rotated for $9 \times 360^\circ$, and the next four points were then measured (90° apart).
- This pattern was repeated until the output shaft of the gearbox rotated for 360° , giving a total of 36 points (position of the first 4 points coincides with the last 4 points).

The result of each of the measuring points was a stiffness curve as shown in Fig. 2.21. From these curves, individual backlash values were determined, and the average value was calculated. The individual backlash values and the average value for the SGU gearbox are shown in Fig. 2.22. The average backlash was 0.52 arcmin, whereas individual values would rise to 1 arcmin. The standard deviation of the measured data is 0.49 arcmin, which we believe can be attributed to geometric tolerances of different gearbox parts, especially the runout and single pitch deviation.

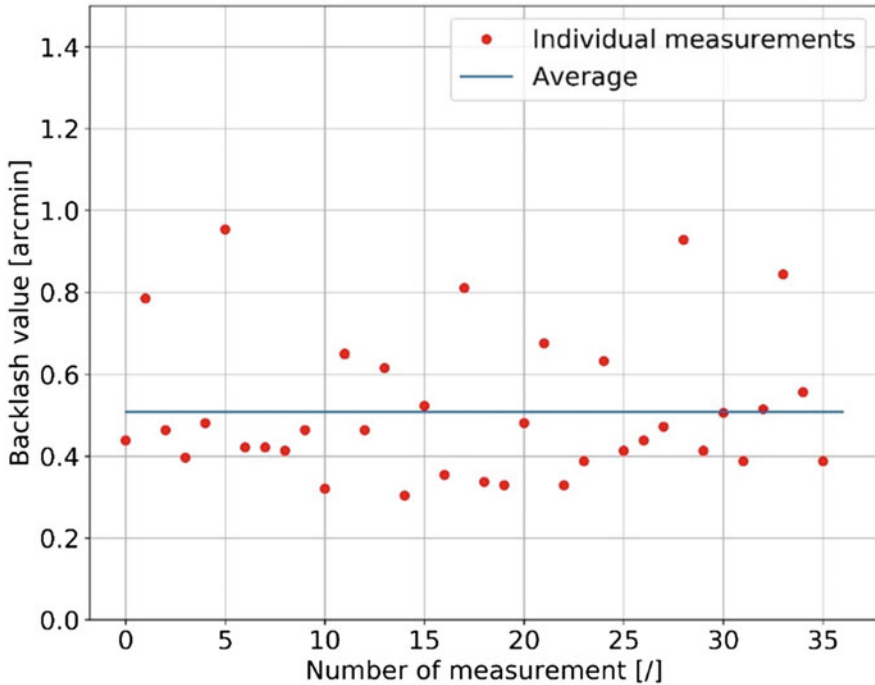


Fig. 2.22 Measured backlash values for 36 different points

2.4.4 Kinematic Error

The same testbench was also used to measure the kinematic error of the SGU gearbox. The measurements were done at a constant rotational speed. Two Renishaw incremental encoders were used on the input and output shaft to measure actual shaft positions. The ring RESM20USA075 and the reading head V2CLM20A20F was used on the input side, whereas the output side was equipped with the encoder ring RESM20USA052 and the reading head V2CKD20D20F. The acquisition speed of the DAQ was 200 kHz.

The kinematic error ($\Delta\varphi$) of a gearbox is the deviation of the angular position of the gearbox from its ideal, theoretical angular position. The kinematic error is measured as a difference between the input and output shaft rotation for full revolution (360°) of the output shaft, where the kinematic error is the difference between the maximal and minimal measured value. The kinematic error for SGU is:

$$\varphi_{out} + \Delta\varphi = i \cdot \varphi_{inp} \text{ or } \Delta\varphi = i \cdot \varphi_{inp} - \varphi_{out} \quad (2.11)$$

The output ratio i is defined by Eq. 2.5. The incremental encoder (its scale), which is used to measure the rotation of the output shaft is always mounted with a small

Fig. 2.23 Eccentrically aligned encoder

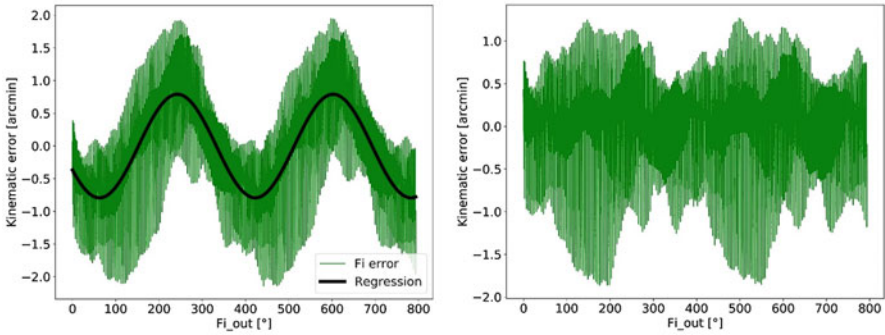
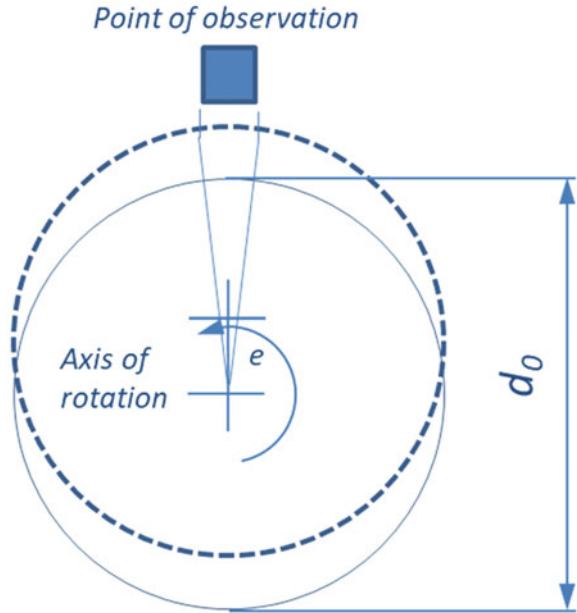


Fig. 2.24 Kinematic error of the SGU gearbox and the calculated regression line (left); the compensated kinematic error of the SGU gearbox (right); remark: vertical scale factors do not match

eccentric error as illustrated in Fig. 2.23. Consequently, the obtained measurements must be corrected with a regression curve [22]:

$$\frac{\Delta l}{\Delta \varphi} \approx r_0 + e \cdot \cos(\varphi_0 + \varphi) \tag{2.12}$$

r_0 is the scale radius, φ_0 the azimuth angle, e erroneous eccentricity, and φ phase angle.

The uncorrected (raw) results of the kinematic error measurements together with the fitted regression curve are presented in Fig. 2.24—left. And the corrected

kinematic error of the SGU prototype, using the calculated regression curve is presented in Fig. 2.24—right. The kinematic error after correction, measured from a minimal to maximal value, is around 2.8 arcmin.

2.4.5 Influence of Geometric Tolerances

KISSsys and KISSsoft software [23] were employed to simulate and calculate various aspects of the SGU gearbox performance. However, the simulation of attainable manufacturing tolerances proved difficult; therefore, the gearbox kinematics was calculated using analytical equations, and a special program was written in Python. The input of the developed program is the nominal geometry, the rotation of the input shaft, the time vector, and the geometric tolerances (errors) of each of the gearbox components. The errors are user input and can be either measured from an actual component or obtained from the technical documentation of a future component.

The result of this program is an envelope of planet gear teeth movement into the ring gear tooth spaces, which is integrated in the gearbox housing. This result can be used to predict the gearbox backlash and a possible interference. An example of the calculated envelope for a chosen SGU tooth with the nominal geometry for the first three ring gear positions is shown in Fig. 2.25. As expected for the nominal geometry, the tooth fits optimally into the internal gear, resulting in a low (but not zero) backlash.

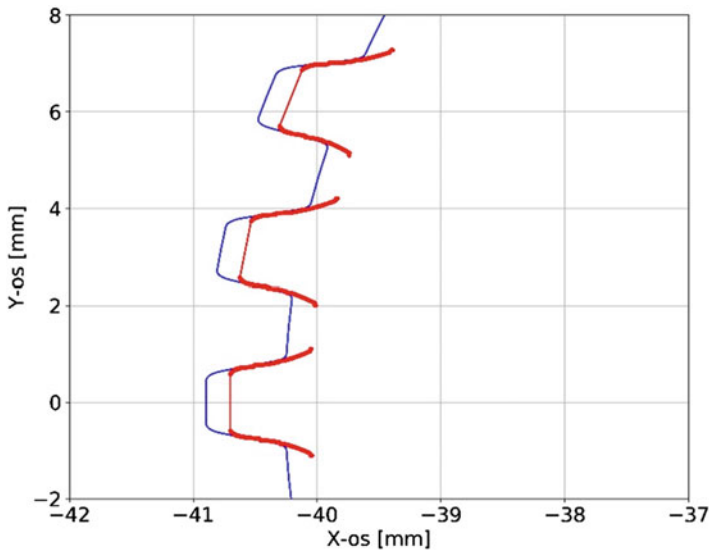


Fig. 2.25 Example of the kinematic envelope induced by a chosen planet gear tooth with nominal geometry into the first three spaces of the ring gear

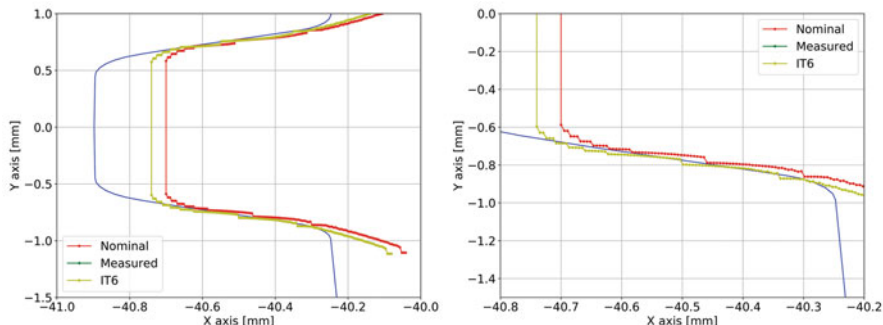


Fig. 2.26 Envelope of the SGU tooth in one of the internal gear slots; red, nominal geometry; green, measured tooth geometry; yellow, tolerances of IT6 and its detail (right)

Table 2.6 Input parameters used for the gearbox envelope calculation

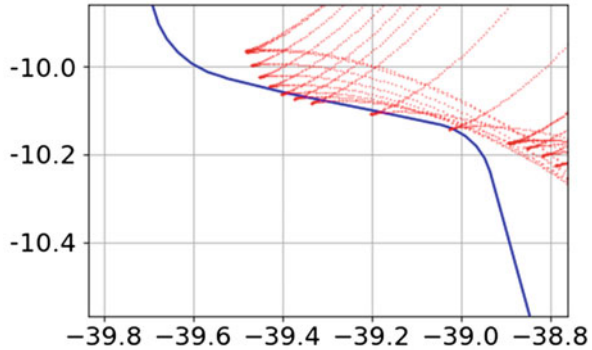
Input	f_p [μm]	F_r [μm]
Nominal	0	0
Measured	10	40
IT6	7.5	20

Besides the nominal geometry, the program was used with various input parameters. A comparison between the nominal geometry, the measured geometry of an erroneous component, and the tolerance class IT6 geometry is presented in Fig. 2.26 (left) and zoomed to disclose some details in Fig. 2.26 (right). The input parameters used for the gearbox envelope calculation are shown in Table 2.6.

The nominal geometry fits ideally into the internal gear tooth spaces. However, the IT6 geometry is required by the technical documentation of the SGU gearbox and defined to produce a minimal (near zero or zero) backlash as presented in the results; the measured results are added as an example of a non-fit geometry. The latter are taken from measurements of erroneous components that proved difficult to turn in the assembled gearbox and based on measured values they correspond to IT9 tolerance class. The ragged edge of the envelope results from the way it is calculated:

- The geometry of a tooth (or teeth) is generated at first as a cloud of points.
- These points are then moved according to the appropriate kinematics and traced as they move, as it can be observed from Fig. 2.27.
- A search algorithm then finds the points that are on the outer edge (border) of movement. As a result, the ragged edge is generated.

Fig. 2.27 Movement of individual tooth profile points



2.4.6 Single Pitch Deviation and Runout

Since the SGU gearbox should conform to requirements in high-tech industries, it is important to rule out also possible influences of the single pitch deviation f_p and runout F_r on the contact conditions of meshing gears. The definitions of the single pitch deviation and the runout are according to ISO1328-1 [24]. The simulation of the mesh conditions by the contact analysis considers influence of both parameters.

KISSsoft works with E-gears. However the current *KISSsoft* user manual [25] includes possibility of a progressive profile modification (p. 343 of the named manual), which can be used as a modification in the addendum and the dedendum of a gear tooth, and is defined as follows:

$$\Delta_{ad} = 2 \cdot C_{ad} \cdot \left(\frac{d - d_k}{d_t - d_k} \right)^{f_{ad}/5} \quad \text{and} \quad \Delta_{dd} = 2 \cdot C_{dd} \cdot \left(\frac{d - d_k}{d_v - d_k} \right)^{f_{dd}/5} \quad (2.13)$$

Δ_{ad} and Δ_{dd} stand for a profile modification function in addendum and dedendum. C_{ad} and C_{dd} are modifying tip relief (or corresponding active dedendum modification) and f_{ad} and f_{dd} power coefficients. If a coefficient amounts to 5, the relief becomes linear. d_t , d_v , d_k , and d , are diameters of the tip circle, dedendum circle, kinematic circle, and current circle. One can adapt the involute flank addendum and dedendum to S-gear flank in this way. Such a modification is justified since the addendum and dedendum heights are rather small, between 0.2 and 0.25 m.

The simulation takes the tolerance allowance requirement form gear drawings corresponding to the quality class Q6 in accordance with ISO1328-1, i.e., $f_p = 7.5 \mu\text{m}$ and $F_r = 21 \mu\text{m}$ for each gear, planet, and the ring gear.

Since eventually each tooth of a given gear will come in mesh with each tooth of its counterpart gear, a contribution of both pitch and runout deviations of both gears shall be considered. This is done by the quadratic tolerance sum, i.e., for the single pitch deviation f_p and for the runout F_r :

$$f_p = \sqrt{f_{p1}^2 + f_{p2}^2} \quad \text{and} \quad F_r = \sqrt{F_{r1}^2 + F_{r2}^2} \quad (2.14)$$

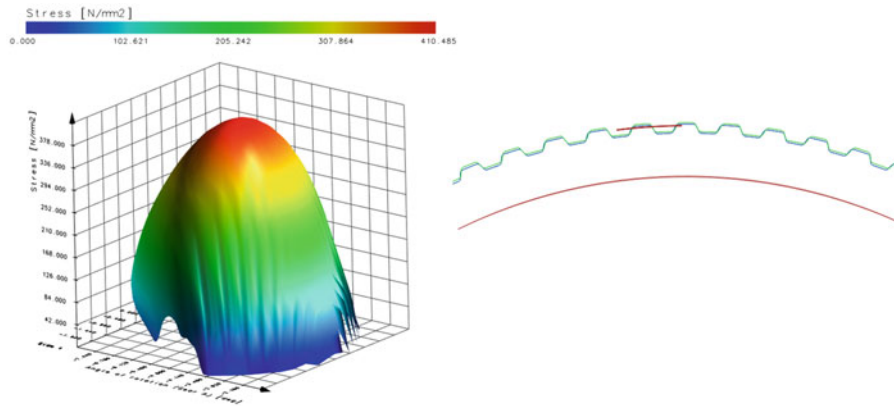


Fig. 2.28 Contact pressure (left) and mesh line at $f_p = +8.16 \mu\text{m}$ and $F_r/2 = +11,425 \mu\text{m}$ (right)

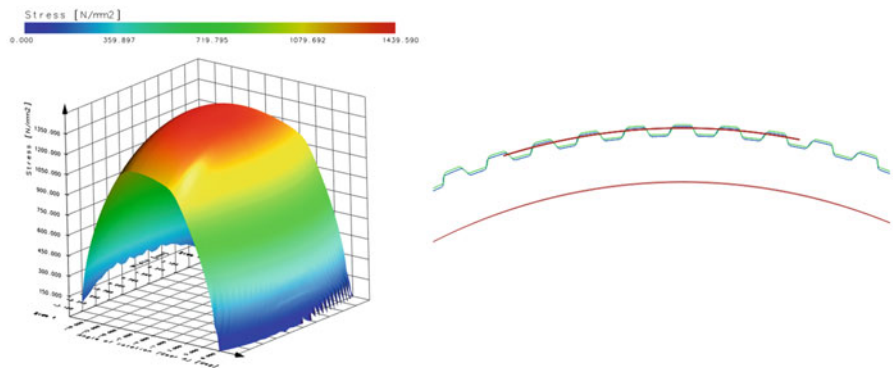


Fig. 2.29 Contact pressure (left) and mesh line at $f_p = -8.16 \mu\text{m}$ and $F_r/2 = +11,425 \mu\text{m}$ (right)

From the practical aspect, assuming the manufacturing process is stable, with $C_p \geq 1.33$ (C_p is the process capability index), and considering the equations above, the values to be considered are $f_p = 8.16 \mu\text{m}$ and $F_r = 22.85 \mu\text{m}$. Hence, the simulation parameters matrix consisting of four individual cases is defined:

1. $f_p = \pm 8.16 \mu\text{m}$,
2. $F_r/2 = \pm 11,425 \mu\text{m}$.

Figure 2.28 (right) depicts the mesh line at $f_p = +8.16 \mu\text{m}$ and $F_r/2 = +11,425 \mu\text{m}$, whereas Fig. 2.28 (left) illustrates the contact pressure of meshing gears. The transverse contact ratio is $\epsilon_\alpha = 1.45$ and the contact pressure 410 MPa, if both simulation parameters are positive.

Figure 2.29 collects results if the single pitch deviation becomes negative. So, the contact pressure of meshing gears and the mesh line at $f_p = -8.16 \mu\text{m}$ and $F_r/2 = +11,425 \mu\text{m}$

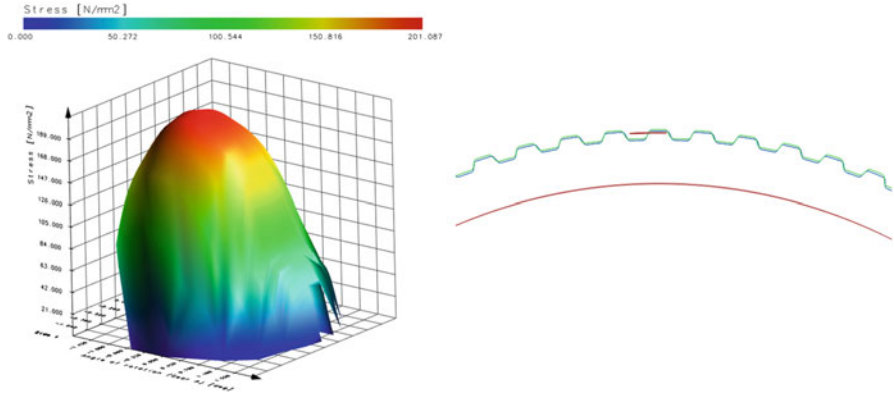


Fig. 2.30 Contact pressure (left) and mesh line at $f_p = +8.16 \mu\text{m}$ and $F_r/2 = -11,425 \mu\text{m}$ (right)

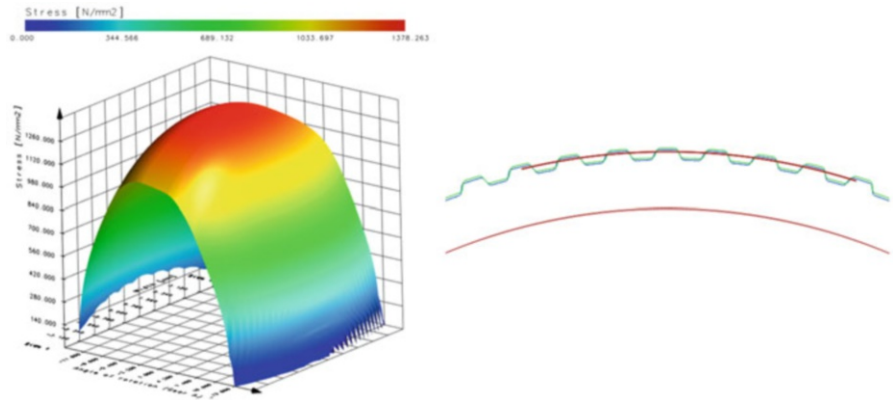


Fig. 2.31 Contact pressure (left) and mesh line at $f_p = -8.16 \mu\text{m}$ and $F_r/2 = -11,425 \mu\text{m}$ (right)

$2 = +11,425 \mu\text{m}$ are presented. The transverse contact ratio is $\epsilon_\alpha = 6.37$ and the contact pressure 1440 MPa.

The next combination is for the positive single pitch deviation $f_p = +8.16 \mu\text{m}$ and the negative runout $F_r/2 = -11,425 \mu\text{m}$ and presented in Fig. 2.30. The transverse contact ratio is $\epsilon_\alpha = 0.81$ and the contact pressure 201 MPa.

And finally, a simulation for both negative values is conducted, so the values for $f_p = -8.16 \mu\text{m}$ and $F_r/2 = -11,425 \mu\text{m}$ are considered in Fig. 2.31. The transverse contact ratio is $\epsilon_\alpha = 6.85$ and the contact pressure 1378 MPa.

Additional simulations for evaluation of the single pitch deviation influence should be performed with the values for a single pitch deviation $f_p = \pm 8.16 \mu\text{m}$ and without zero runout ($F_r = 0 \mu\text{m}$).

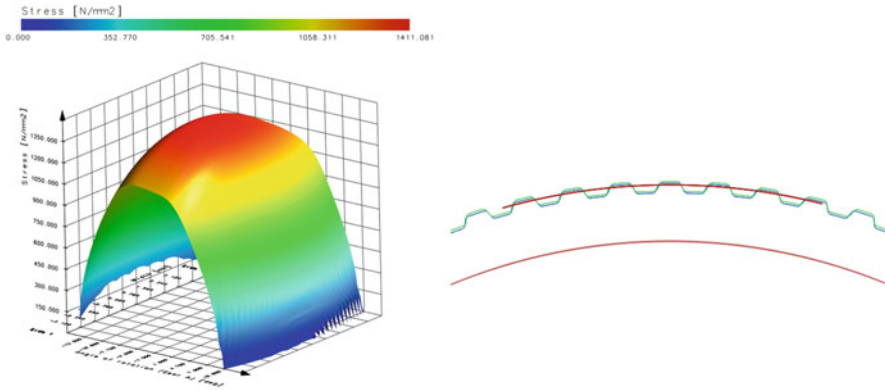


Fig. 2.32 Contact pressure (left) and mesh line at $f_p = -8.16 \mu\text{m}$ and $F_r/2 = 0 \mu\text{m}$ (right)

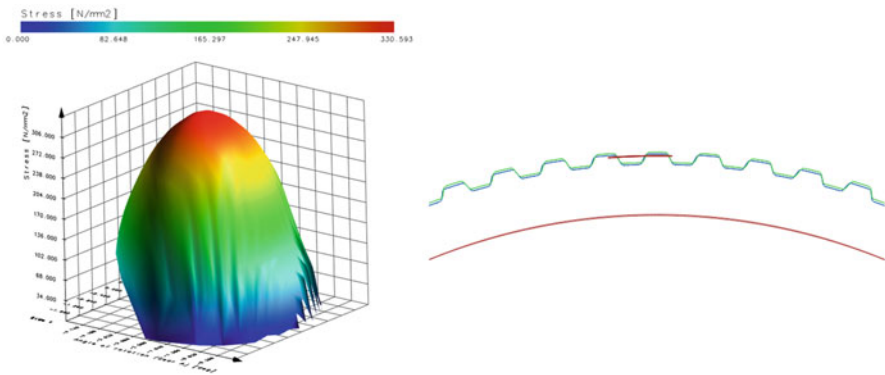


Fig. 2.33 Contact pressure (left) and mesh line at $f_p = +8.16 \mu\text{m}$ and $F_r/2 = 0 \mu\text{m}$ (right)

Two cases are possible, as shown in Fig. 2.32. with the negative $f_p = -8.16 \mu\text{m}$ and Fig. 2.33 with the positive $f_p = +8.16 \mu\text{m}$. In the first case, the transverse contact ratio amounts to $\epsilon_\alpha = 6.57$ and the contact pressure to 1411 MPa, and in the second case the transverse contact ratio amounts $\epsilon_\alpha = 1.22$ and the contact pressure to 331 MPa.

The analysis shows that a single pitch deviation influences the meshing gears with a high impact. The runout itself is neglectable compared to the single pitch deviation. Therefore, a special care for a single pitch deviation should be taken when manufacturing gears which means the optimization of the manufacturing technology should focus on achieving best possible single pitch deviation, hence a better quality than Q6.

2.5 Conclusion

The presented chapter deals with S-gears, which are defined with a half parabolic function of the rack flank, which then defines a single path of contact, and this implies an external or internal gear geometry. Furthermore, the definition parameters a_p and n and the derived parameter—the initial pressure angle α_w in C facilitate shaping of the gear, which was demonstrated in the chapter. Thermal properties of S-gears, i.e., their advantage over E-gears are due to the fact that the former mesh with less sliding and more rolling, so S-gears reveal less frictional force and frictional losses or heat.

The next subchapter deals with lifetime testing of S- and E-gears. The examined gear pairs were a combination of an alloy steel driving gear and a driven POM gear (POM contained some heat-resistant additives). The tests with loads of 1.5, 1.3, and 1.1 Nm were repeated at least three times. They were conducted on small testbenches with thermal camera coverage and data logging. The testbench automatics registered failure time. There was a clear distinction between the S- and E-gears in favor of the former.

SGU planocentric gearbox is designed with S-gear geometry. The prototype series has a reduction ratio of 80; it already contained an absolute position encoder. And as an option, it can incorporate a torque sensor as well. The development question was how to assemble a device with proper performance and how to implement fast and accurate certification tests, e.g., backlash and stiffness curves, kinematic error, noise and vibration, durability tests, etc. That is why the testbench was designed and built, which helped in the assessment of many important results. The second part of the subchapter 2.4 is about analytical approach which also disclosed many development guidelines. So, it was analytically ascertained that gears should be put in (sub)tolerance ranges, and ring gears and planets should be mated (one in the higher subclass and the other in the lower one) [20], to attain better accuracy of the device. Also, the influence of the bearing and carrier tolerances was analyzed and discovered that even the robust device can deform to such extent that gear teeth can be in interference and tooth tips should be adapted. It was also found out that the single pitch deviation has a high impact on the gearbox operation, so a special care for a manufacturing process is necessary.

Acknowledgments The investment is co-financed by the Republic of Slovenia and the European Union under the European Regional Development Fund, no. SME 2/17-3/2017 and C3330-18-952014.

References

1. Euler, L. (1760). *Novi Commentarii academiae scientiarum. Petropolitanae*, 5(1760), 299–316.
2. Hlebanja, J., & Hlebanja, G. (2010). Spur gears with a curved path of contact for small gearing dimensions. In *International Conference on Gears, Garching near Munich, Germany*, 4.-

- 6.10.2010: *Europe invites the world*, (VDI-Berichte, ISSN 0083–5560, 2108) (pp. 1281–1294). Düsseldorf: VDI-Verlag.
3. Hlebanja, J., & Hlebanja, G. (2005). Anwendbarkeit der S-Verzahnung im Getriebebau: Nichtevoventische Verzahnungen weiterentwickelt. *Antriebstechnik.*, ISSN 0722–8546, 44 (2), 34–38.
 4. Hlebanja, G. (2011). Specially shaped spur gears: A step towards use in miniature mechatronic applications. In V. Miltenović (Ed.), *Proceedings, The 7th International Scientific Conference Research and Development of Mechanical Elements and Systems - IRMES 2011*, 27.-28.4.2011 (pp. 475–480). Zlatibor: Mechanical Engineering Faculty.
 5. Hlebanja, G., & Hlebanja, J. (2012). Recent development of non-involute cylindrical gears. In G. Dobre & M. R. Vladu (Eds.), *Power Transmissions: Proceedings of the 4th Int. Conf., Sinaia, Romania, June 20–23, 2012, (Mechanisms and machine science, ISSN 2211–0984, ISSN 2211–0992, Vol. 13)* (pp. 83–98). Dordrecht: Springer. 2013.
 6. Hlebanja, G., & Hlebanja, J. (2013). Influence of axis distance variation on rotation transmission in S-gears: Example on heavy duty gears. In *International Conference on Gears, 7–9.10.2013, Garching (near Munich), Germany: Europe invites the world, (VDI-Berichte, ISSN 0083–5560, 2199)* (pp. 669–679). Düsseldorf: VDI-Verlag.
 7. Hlebanja G, Kulovec S, Zorko D, Hlebanja J, Duhovnik J (2017). Influence of the tooth flank shape on thermal load of the gear. Europe invites the world, International Conference on Gears, International Conference on Gear Production, International Conference on High Performance Plastic Gears, Technische Universität München, Garching, Sept. 13–15, (VDI-Berichte, ISSN 0083–5560, 2294.2). Düsseldorf: VDI., p.p 1583–1592.
 8. Radzevich, S. P. (2012). *Dudley's Handbook of Practical Gear Design and Manufacture, Second Edition*. Boca Raton: CRC Press, Taylor & Francis Group. ISBN 978–1–4398–6602–3 (eBook - PDF).
 9. Nieman, G., & Winter, H. (1989). *Maschinenelemente, Band II: Getriebe allgemein, Zahnradgetriebe Grundlagen, Stirnrad Getriebe. ISBN 3-540-11149-2*. Berlin, Heidelberg, New York: Springer Verlag.
 10. Sumitomo Drive Technologies (2018), *Fine Cyclo® - Zero Backlash Precision Gearboxes, Catalog #991333*. Accessed 01/07/2020, from www.sumitomodrive.com.
 11. Spinea TwinSpin (2017) *High Precision Reduction Gears, Ed. I/2017*. Accessed 01/07/2020, from <https://www.spinea.com/en/products/twinspin/index>.
 12. Nabtesco Precision Reduction Gear RV™ (2018). *E Series/C Series/Original Series CAT.180420*, Accessed 01/07/2020, from https://www.nabtesco.de/fileadmin/05_downloads/03_kataloge/produktkatalog_en.pdf
 13. Onvio Zero Backlash Speed Reducers (2005), Accessed 01/07/2020, from www.onviollc.com
 14. Hlebanja J, Hlebanja G (2009) Konkav-konvexe Sonderverzahnungen, Vorteile und Nachteile gegenüber Evoventenverzahnungen. Mihailidis A (Ed.). *Proceedings, The 3rd Int. Conf. – Power Transmission '09 Kallithea, Greece, 1–2.10.2009*. Thessaloniki: Sofia Publications. 2009, p. 21–26.
 15. VDI 2736 (2016a) VDI 2736 - part 4. Thermoplastic gear wheels: Determination of strength parameters on gears. VDI–Richtlinien (2016).
 16. VDI 2736 (2016b) VDI 2736 - part 1. Thermoplastic gear wheels: Materials, material selection, production methods, production tolerances, form design. VDI–Richtlinien (2016).
 17. Hlebanja, G., Kulovec, S., Hlebanja, J., & Duhovnik, J. (2014). S-gears made of polymers. *Ventil*, 20(5), 358–367.
 18. Hlebanja G, Hlebanja J (2018) S-gears: From Metal to Polymer Solution. Goldfarb V, Trubachev E, Barmina N (Edt.). *Advanced Gear Engineering, (Mechanisms and machine science, ISSN 2211–0984, ISSN 2211–0992, Vol. 51)*. Cham: Springer Nature. 2020, p. 255–269, doi: https://doi.org/10.1007/978-3-319-60399-5_12.
 19. Hlebanja, G., Hriberšek, M., Erjavec, M., & Kulovec, S. (2019). Durability investigation of plastic gears. In *Power transmissions 2019, 6th international BAPT conference power transmissions 2019, Varna, Bulgaria, June 19-22, 201, (MATEC web of conferences, ISSN 2261-236X, vol. 287)* (Vol. 287, pp. 1–9). Paris: EDP Sciences.

20. Hlebanja, G., Erjavec, M., Kulovec, S., & Hlebanja, J. (2020). Optimization of planocentric gear train characteristics with CA-tools: Chapter 14. In V. Goldfarb, E. Trubachev, & N. Barmina (Eds.), *New approaches to gear design and production, (Mechanisms and machine science, ISSN 2211-0984, ISSN 2211-0992, Vol. 81)* (pp. 323–347, https://link.springer.com/chapter/10.1007%2F978-3-030-34945-5_14). Cham: Springer Nature. https://doi.org/10.1007/978-3-030-34945-5_14.
21. AksIM 2 (2020) Absolute rotary encoder, datasheet, Accessed 15/06/2020, from <https://www.rls.si/en/aksim-2-off-axis-rotary-absolute-encoder>.
22. Renishaw (2020) The accuracy of rotary encoders (Whitepaper). Accessed 30/06/2020 from <https://resources.renishaw.com/en/details/white-paper-the-accuracy-of-angle-encoders-113122>.
23. KissSoft (2019a) *Design software for mechanical engineering applications*. Accessed 23/9/2019 from <https://www.kisssoft.ag/english/home/index.php>.
24. ISO1328-1 (2013). Cylindrical gears — ISO system of flank tolerance classification — Part 1: Definitions and allowable values of deviations relevant to flanks of gear teeth, International Organization for Standardization, 2013.
25. KissSoft. (2019). *KISSsoft release 2019 user manual*. Bubikon: KISSsoft AG - A Gleason Company.

Chapter 3

Kinematic Pairs: Novel Kinds and Classification



Stephen P. Radzevich

3.1 Introduction

The investigation of machines began in the ancient times. A simple machine uses a single applied force to do work against a single load force. The concept of “simple machine” was helpful at the beginning of the human activity in the area of machine design. The idea of a “simple machine” originated with the Greek philosopher *Archimedes* around the third century BC who investigated the so-called simple machines. Usually the term refers to the six classical simple machines that were defined by *Renaissance* scientists:

- *Wheel and axle*—makes work easier by moving objects across distances. The wheel (or round end) turns with the axle (or cylindrical post) causing movement.
- *Inclined plane*—a flat surface (or plane) that is slanted, or inclined, so it can help move objects across distances.
- *Wedge*—instead of using the smooth side of the inclined plane to make work easier, the pointed edges to do other kinds of work can be used.
- *Lever*—any tool that pries something loose is a lever. Levers can also lift objects. A lever is an arm that “pivots” (or turns) against a fulcrum (the point or support on which a lever pivots).
- *Pulley*—instead of an axle, a wheel could also rotate a rope, cord, or belt. This variation of the wheel and axle is the pulley. In a pulley, a cord wraps around a wheel. As the wheel rotates, the cord moves in either direction.
- *Screw*—when an inclined plane is wrapped around a cylinder, its sharp edge becomes a screw. A screw is actually just another kind of inclined plane.

S. P. Radzevich (✉)
Mechanical Engineering, Sterling Heights, MI, USA

The identification of simple machines arises from a desire for a systematic method to invent new machines. Therefore, an important concern is how simple machines are combined to make more complex machines. One approach is to attach simple machines in series to obtain compound machines.

A more successful strategy was identified by *Franz Reuleaux*. *Reuleaux* realized that a lever, pulley, and wheel and axle are in essence the same device: a body rotating about a hinge. Similarly, an inclined plane, wedge, and screw are a block sliding on a flat surface.

This realization shows that it is the joints, or the connections that provide movement, that are the primary elements of a machine. Starting with four types of joints, the “revolute joint,” “sliding joint,” “cam joint,” and “gear joint,” and related connections such as cables and belts, it is possible to understand a machine as an assembly of solid parts that connect these joints.

3.1.1 Kinematic Pairs: Basics

“Kinematic pair” is one of the fundamental concepts in the mechanisms and machine theory. Kinematic pairs can be found out in the design of every machine and of every mechanism. Examples of kinematic pairs of different kinds in gearing [(a) point-contact kinematic pair in the design of skew-axes gearing, (b) line-contact kinematic pair in the design of helical gearing, and (c) surface-to-surface-contact kinematic pair in the design of gear coupling] are illustrated in Fig. 3.1. Taking into account the importance of kinematic pairs to the science and practice of machines and

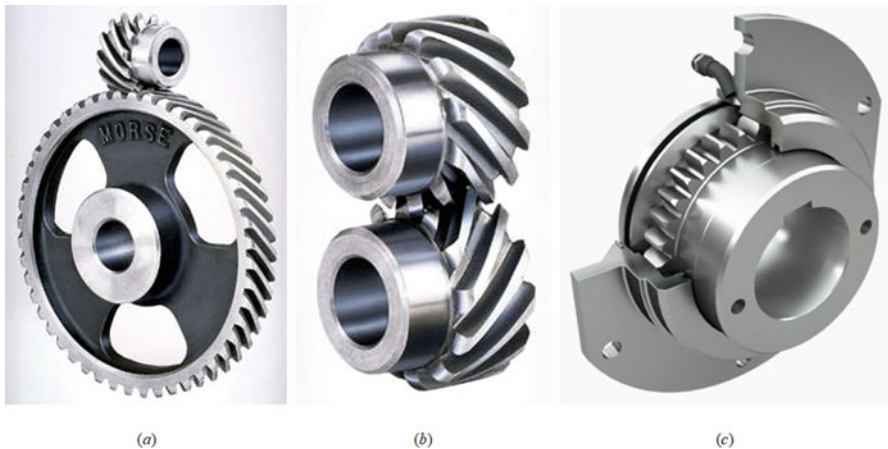
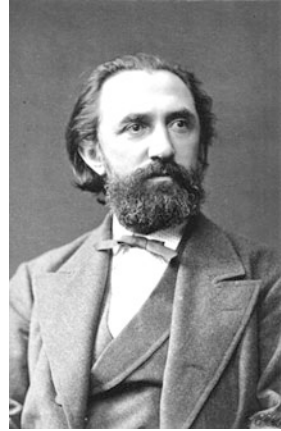


Fig. 3.1 Kinematic pairs of different kinds in gearing: (a) point-contact kinematic pair in the design of skew-axes gearing, (b) line-contact kinematic pair in the design of helical gearing, and (c) surface-to-surface-contact kinematic pair in the design of gear coupling

Fig. 3.2 *Franz Reuleaux*
(1829—1905)



mechanisms, properties of kinematic pairs of all kinds are required to be comprehensively investigated.

The beginning of investigation of kinematic pairs can be traced back to the 1875 research undertaken by *Franz Reuleaux* [1]. *Franz Reuleaux* introduced the kinematic pair as a new approach to the study of machines that provided an advance over the motion of elements consisting of simple machines [2]. *Reuleaux* (Fig. 3.2) was the first to introduce “kinematic pair” as a new approach to the study of machines that provided an advance over the motion of elements consisting of simple machines [2].

According to *Reuleaux*:

Definition 3.1 *Kinematic pair is a connection between two bodies that imposes constraints on their relative movement.*

In the nowadays terminology the definition to the term “kinematic pair” is formulated in a slightly different way:

Definition 3.2 *Kinematic pair is a combination of two contiguous links, allowing their relative movement.*

The following definitions are recommended by IFToMM:

Definition 3.3 *Kinematic pair is a connection between two links restricting their motion.*

Definition 3.4 *Lower kinematic pair is a kinematic pair that is formed by surface contact between its elements.*

Definition 3.5 *Higher kinematic pair is a kinematic pair that is formed by either line or point contact between the elements.*

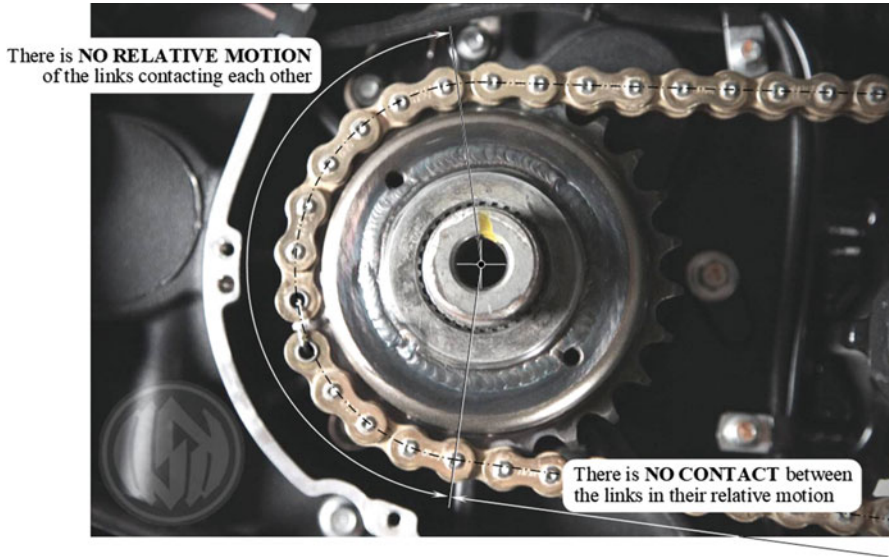


Fig. 3.3 The so-called “wrapping pair” (pulley-and-belt drive, chain drive, and so forth) is NOT a kind of “kinematic pair,” as it does not align to the *Reuleaux* definition for the term “kinematic pair”

In particular, *Reuleaux* stressed that kinematic pair consists exactly of *two* elements and that these *two* elements interact with one another (Fig. 3.3).¹ In the matter of connections between *rigid bodies*, *Reuleaux* recognized only two kinds of kinematic pairs. He called them “higher kinematic pairs” and “lower kinematic pairs” of elements. With higher kinematic pairs, the two elements are in contact at a point or along a line. Lower kinematic pairs are those featuring “surface-to-surface contact.” On the premise of this approach numerous classifications of kinematic pairs are developed by the researchers to this end. An example of such classifications of kinematic pairs is illustrated in Fig. 3.4 [4]. A plurality of variations of this classification can be easily found out in the public domain.

As it follows from the consideration below in this section of the book, in the meantime it is not sufficient to distinguish only the lower kinematic pairs with

¹According to the definition of the term “kinematic pair,” only *two rigid bodies* in contact are considered in this text. No flexible bodies [belts, chains, and so forth (*three* bodies!!)] are considered here as they are not covered by the definition to the term “kinematic pair” (mechanisms with flexible bodies are often loosely referred to as “wrapping pair/lower pair”. Such a term is incorrect as mechanisms with flexible bodies have to be considered separately of kinematic pairs: such mechanisms are not kinematic pairs by nature). In mechanisms with a flexible body there is no relative motion of a pulley and a mating flexible body at points of their contact, that is, they are motionless in relation to one another. No contact is observed at the rest of points, at which the pulley and the flexible body travel in relation to each other.

Two rigid bodies can make contact at a few points/lines (compound joints). Each of such a contact have to be considered as a separate point/line contact kinematic pair, as a conventional kinematic pair, and not in whole as a multiple-contact kinematic pair (see [3] and others).

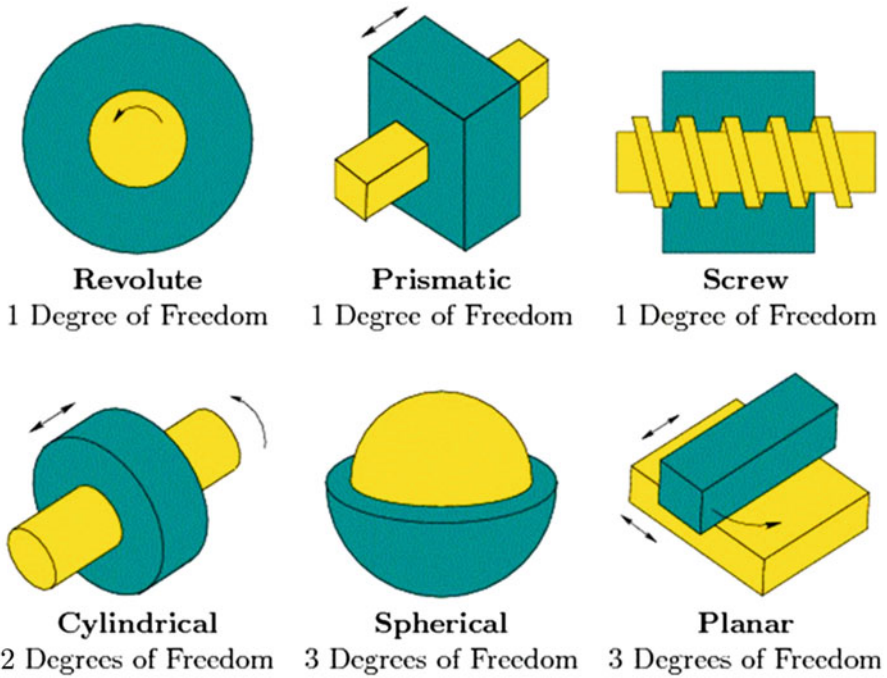


Fig. 3.4 An example of a conventional classification of kinematic pairs. (Adapted from [10])

“surface-to-surface contact” and the higher kinematic pairs that feature either line contact or point contact of the interacting functional surfaces, like it was permissible in the time of *Franz Reuleaux*. There are a few important reasons for that.

First, higher kinematic pairs with point contact, and those with line contact of the interacting functional surfaces, are not equivalent to one another. Therefore, they must be distinguished from one another and, thus, considered separately. Also, different terms are required to be introduced to refer to higher kinematic pairs with point contact and to those with line contact of the functional surfaces.

Second, even when the interacting functional surfaces of two kinematic pairs, both feature, either point or line contact, the performance of kinematic pairs with the same kind of contact can be significantly different depending on the parameters of contact geometry of the functional surfaces. In other words, the performance of two kinematic pairs with point contact (or of two kinematic pairs with line contact) is significantly affected by contact geometry of their functional surfaces and by the degree of their conformity in particular. The latter is vital (a) for gearing [5] in a general sense, (b) for high-conformal gearing in particular [6], (c) for contact and bending strength of kinematic pairs, (d) for functional surfaces wear, (e) for elastohydrodynamic lubrication (*EHD* lubrication) of heavily loaded kinematic pairs [7], and so forth.

The outlined features of kinematic pairs with point, and with line contact of functional surfaces, along with a few more features mentioned below in this chapter of the book, reveal the necessity in a more in-depth investigation into possible kinds of kinematic pairs for the needs of the nowadays industry.

3.1.2 Traditional Approach to Design and Analysis of Kinematic Pairs

When kinematic pairs are discussed, most sources available in the public domain provide mainly several kinematic pair schemes. “Plane-to-plane,” “ball in a pocket,” “round cylinder-to-plane,” “ball-to-plane,” and so forth are among them. The total number of designs of kinematic pairs, considered in the textbooks on theory of machines and mechanisms, does not exceed a dozen. No comprehensive and systematic analysis of all possible kinds of kinematic pairs has been done to this end.

Kinematic synthesis of linkages was carried out by *Denavit* and *Hartenberg* [8]. An extensive research on possible kinds of kinematic pairs was undertaken by Dr. *L.T. Dvornikov* [9], who also worked on the development of the theory of kinematic pairs [10]. Many efforts on the development of the theory and systematization of kinematic pairs of mechanical systems were undertaken by Dr. *E.Ya. Zhivago* [11], as well as numerous others.

Without going into details of the analysis of the results of the research achieved to this end, a following conclusion can be drawn up:

Conclusion 3.1

The theory of kinematic pairs is too far from to be completed.

Therefore, a more in-detail research into possible kinds of kinematic pairs and the development of their classification is required to be undertaken.

Following the terminology adopted since the time of *F. Reuleaux*, higher kinematic pairs are comprised of two functional surfaces that make contact at a point. Therefore, two functional surfaces in point contact are sufficient to specify a corresponding higher kinematic pair. However, a plurality of kinematic pairs that meet the specified requirements (two surfaces that make point contact) may feature significantly different performance properties. This means that the conventional definition of the term “higher kinematic pair” is insufficient as it doesn’t establish one-to-one correspondence between a particular kinematic pair and its anticipated performance. It is evident that, for example, “convex-to-convex contact” of two functional surfaces and their “convex-to-concave contact” are significantly different from one another from the perspective of bearing capacity, regardless of that in both cases the functional surfaces make point contact and in both cases they are referred to as “higher kinematic pair.” This practice is not good.

Another example of two higher kinematic pairs that, from the first glimpse, appear very similar (or almost identical) to one another pertains to “convex-to-

concave contact” of two functional surfaces with a small difference between radii of their normal curvature. When the difference between the radii of normal curvature in one of two kinematic pairs is significantly smaller than that in the other kinematic pair, the bearing capacity of the first one is drastically different from that of the second one (again, regardless of both the kinematic pairs are still referred to as “higher kinematic pair”).

Inconsistency of the adopted terminology in the realm of higher kinematic pairs is clearly illustrated by the two just considered examples. More in-detail analysis of contact geometry of two functional surfaces in a higher kinematic pair is necessary to be undertaken in order to better understand all the features and behavior of kinematic pairs of different design.

3.1.3 Instantaneous Kinematics (Mobility) in Kinematic Pairs

It is adopted below in this chapter of the book that a kinematic pair that features a highest possible degree of freedom is referred to as the most general one.

A kinematic pair of five degrees of freedom (five DoF kinematic pair) is schematically shown in Fig. 3.5. Here, two bodies, namely, a Body 1 and a Body 2, are bounded by smooth regular surfaces. The bodies B_1 and B_2 make contact at point K . The origin of a local reference system, $x_K y_K z_K$, coincides with the contact point, K . The coordinate axes, x_K , y_K , and z_K , are along the corresponding unit vectors \mathbf{t}_{1,B_1} , \mathbf{t}_{1,B_2} , and \mathbf{n}_{B_1} , of the *Darboux frame*, $\mathbf{t}_{1,B_1} \mathbf{t}_{1,B_2} \mathbf{n}_{B_1}$. Depending on timing of the elementary linear and rotary motions \mathbf{v}_x and $\boldsymbol{\omega}_x$, as well as of \mathbf{v}_y and $\boldsymbol{\omega}_y$, four motions of the Body 2 over the Body 1 are permissible:

- Sliding over the Body 1 (with the contact point trace within the plane $y_K z_K$).
- Rolling over the Body 1 (with the contact point trace within the plane $y_K z_K$).
- Sliding over the Body 1 (with the contact point trace within the plane $x_K z_K$).
- Rolling over the Body 1 (with the contact point trace within the plane $x_K z_K$).

The rotation, $\boldsymbol{\omega}_z$, of the body Body 2 about the common perpendicular, \mathbf{n}_{B_1} , is the fifth permissible motion of the Body 2 in relation to the Body 1.

Kinematic pairs that feature point contact between the functional surfaces may have up to five degrees of freedom. Kinematic pairs that feature “surface-to-surface contact” between the functional surfaces feature not more than three degrees of freedom. Therefore, from the standpoint of mobility, point contact kinematic pairs are more general compared to “surface-to-surface contact” kinematic pairs. Kinematic pairs that feature line contact between the functional surfaces occupy a position between the point contact kinematic pairs and between the “surface-to-surface contact” kinematic pairs.

The kinematic pairs with the lesser mobility than that shown in Fig. 3.5 can be viewed as a reduced case of the kinematic pair with point contact of the functional surfaces.

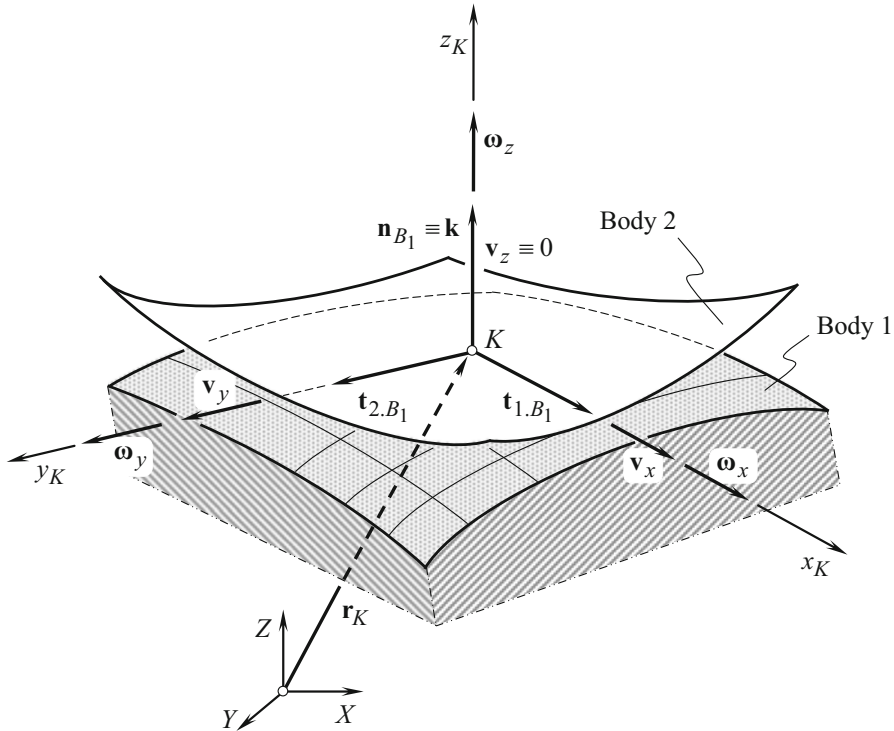


Fig. 3.5 Schematic of five degree-of-freedom kinematic pair

3.1.4 Contact Geometry in Kinematic Pairs

The problem of analytical description of contact geometry between two smooth regular surfaces in the first order of tangency is a challenging one. Contact geometry of curves and surfaces is under consideration by scientists for a long while. Investigation of contact geometry of curves and surfaces can be traced back to the eighteenth century. The study of the contact of curves and surfaces was undertaken in considerable detail by *J.L. Lagrange*² in his *Theorié des Fonctions Analytiques* (1797) [12] and *A.L. Cauchy*³ in his *Leçons sur les Applications du Calcul Infinitésimal à la Geometrie* (1826) [8]. Later on, in the twentieth century, an investigation in the realm of contact geometry of curves and surfaces was undertaken by *J. Favard*⁴ in his *Course de Géomètrie Différentielle Locale* (1957) [13]. A few more names of researchers in the field are to be mentioned.

²*Joseph-Louis Lagrange* (January 25, 1736–April 10, 1813) – an Italian born [born *Giuseppe Lodovico (Luigi) Lagrangia*] famous French mathematician and mechanician

³*Augustin-Louis Cauchy* (August 21, 1789–May 23, 1857) – a famous French mathematician

⁴*Jean Favard* (August 28, 1902–January 21, 1965) – a French mathematician

3.1.4.1 Dupin indicatrix at Point of Functional Surface

Various methods for analytical description of contact geometry between two smooth regular surfaces have been developed. An overview of the methods can be found out in the monograph by Prof. *Radzevich* [14]. Latest achievements in the field are discussed in the paper [15] and others and in the monographs [16, 17].

An earlier developed powerful method for analytical description of contact geometry of two functional surfaces in a kinematic pair is based on the geometry of *Dupin indicatrices*, $Dup(B_1)$ and $Dup(B_2)$, of the functional surfaces B_1 and B_2 , correspondingly.

In a common section of the functional surfaces, B_1 and B_2 , by a normal plane, consider a unit tangent vector, $\mathbf{t}_{cnf}(\varphi)$, through a contact point, K . The unit tangent vector, $\mathbf{t}_{cnf}(\varphi)$, is entirely located in a common tangent plane through K . In a common normal section, the radii of curvature of the functional surfaces, B_1 and B_2 , are designated as R_{B_1} and R_p , correspondingly. Let's designate $r_{B_1}(\varphi) = \sqrt{R_{B_1}(\varphi)}$ and $r_p(\varphi, \mu) = \sqrt{R_p(\varphi, \mu)}$.

By definition, position vector of point, \mathbf{r}_{B_1} , of the *Dupin indicatrix*, $Dup(B_1)$, is specified as:

$$Dup(B_1) \Rightarrow \mathbf{r}_{B_1}(\varphi) = \sqrt{R_{B_1}(\varphi)} \cdot \mathbf{t}_{B_1}(\varphi) \quad (3.1)$$

At point of a planar local patch of a functional surface, B , an inverse *Dupin indicatrix*, $Dup_k(B)$ [and a corresponding inverse *curvature indicatrix*, $Crv_k(B)$], can be used instead of conventional $Dup(B)$ [and instead of $Crv(B)$]. In this particular case, a following form of the *Dupin indicatrix*, $Dup(B_1)$, is preferred:

$$Dup_k(B_1) \Rightarrow \mathbf{r}_{B_{1,k}} = \mathbf{r}_{B_1}^{-1}(\varphi) = \left(\sqrt{R_{B_1}(\varphi)} \right)^{-1} \cdot \mathbf{t}_{B_1}(\varphi) \quad (3.2)$$

In a planar local patch of a functional surface, B , the inverse *Dupin indicatrix*, $Dup_k(B)$, shrinks to the contact point, K .

Here, in Eqs. (3.1) and (3.2), \mathbf{t}_{B_1} is the unit tangent vector through the contact point, K [in its current configuration, the vector \mathbf{t}_{B_1} forms an angle, φ , with the first principal direction, \mathbf{t}_{1,B_1} , on the functional surface B_1 , i.e., $\varphi = \angle(\mathbf{t}_{B_1}, \mathbf{t}_{1,B_1})$].

3.1.4.2 Indicatrix of Conformity at Point of Contact of Two Functional Surfaces

For the analytical description of contact geometry of two functional surfaces, the indicatrix of conformity, $Cnf_R(B_1/B_2)$, at point of contact of the bodies B_1 and B_2 can be used. The construction of this planar characteristic curve, $Cnf_R(B_1/B_2)$, of the fourth order is based on *Dupin indicatrices*, $Dup(B_1)$ and $Dup(B_2)$.

The functional surfaces are turned in relation to one another about the common perpendicular, \mathbf{n}_{B_1} , through an angle. This angle, μ , is referred to as the “angle of the surfaces local relative orientation, μ .” By definition, the angle, μ , is formed by the unit vectors of the first principal directions, $\mathbf{t}_{1.B_1}$ and $\mathbf{t}_{1.B_2}$ (or, the same, of the second principal directions, $\mathbf{t}_{2.B_1}$ and $\mathbf{t}_{2.B_2}$), that is, $\mu = \angle(\mathbf{t}_{1.B_1}, \mathbf{t}_{1.B_2})$ [or $\mu = \angle(\mathbf{t}_{2.B_1}, \mathbf{t}_{2.B_2})$]. In the common reference system, x_{KYK} , the position vector of point, \mathbf{r}_{B_2} , of the *Dupin indicatrix*, $Dup(B_2)$, is specified as:

$$Dup(B_2) \Rightarrow \mathbf{r}_{B_2}(\varphi, \mu) = \sqrt{R_{B_2}(\varphi, \mu)} \cdot \mathbf{t}_{B_1}(\varphi, \mu) \quad (3.3)$$

“Dupin indicatrices” for all possible kinds of smooth regular functional surfaces, B_1 and B_2 , are illustrated in Fig. 3.6. In total, there are ten different kinds of local patches of the functional surfaces, and, therefore, there are just ten different kinds of the corresponding “Dupin indicatrices.” Here, in Fig. 3.6, functional surfaces are designated as B .

Position vector, \mathbf{r}_{cnf} , of a point of the indicatrix of conformity,⁵ $Cnf_R(B_1/B_2)$ [18, 19], at point of contact of two functional surfaces, B_1 and B_2 , can be expressed in terms of the distances r_{B_1} and r_{B_2} as follows (see Fig. 3.7):

$$Cnf_R(B_1/B_2) \Rightarrow \mathbf{r}_{cnf}(\varphi, \mu) = [r_{B_1}(\varphi) - r_{B_2}(\varphi + \mu)] \cdot \mathbf{t}_{cnf}(\varphi) \quad (3.4)$$

A position vector of point, \mathbf{r}_{cnf} , of indicatrix of conformity, $Cnf_R(B_1/B_2)$, at point of contact, K , of the functional surfaces, B_1 and B_2 , is described by Eq. (3.4).

For kinematic pairs with a planar local patch of a functional surface, a following form of the “indicatrix of conformity, $Cnf_k(B_1/B_2)$,” is preferred:

$$\begin{aligned} Cnf_k(B_1/B_2) &\Rightarrow \mathbf{r}_{cnf.k}(\varphi, \mu) = \mathbf{r}_{cnf}^{-1}(\varphi, \mu) \\ &= [r_{B_1}(\varphi) - r_{B_2}(\varphi + \mu)]^{-1} \cdot \mathbf{t}_{cnf}(\varphi) \end{aligned} \quad (3.5)$$

The indicatrix of conformity, $Cnf_k(B_1/B_2)$, at point of contact of a gear tooth flank, \mathcal{G} , and a mating pinion tooth flank, \mathcal{P} , is shrunk to a point coincident with the contact point, K , in all cases of “surface-to-surface contact” and “locally-surface-to-surface contact” (and not only in cases of “plane-to-plane contact”) of the tooth flanks.

The unit vector, $\mathbf{t}_{cnf}(\varphi)$, can be expressed in terms of fundamental magnitudes of the first and the second order calculated at point of contact, K , of the functional surfaces, B_1 and B_2 .

⁵For the first time ever, an equation of the indicatrix of conformity, $Cnf_R(B_1/B_2)$, was published in: Pat. No. 1,185,749, USSR, *A Method of Sculptured Surface Machining on a Multi-Axis NC Machine*./S.P. Radzevich, Int. Cl. B23c 3/16, Filed: October 24, 1983

Pat. No. 1,249,787, USSR, *A Method of Sculptured Surface Machining on a Multi-Axis NC Machine*./S.P. Radzevich, Int. Cl. B23c 3/16, Filed: December 27, 1984

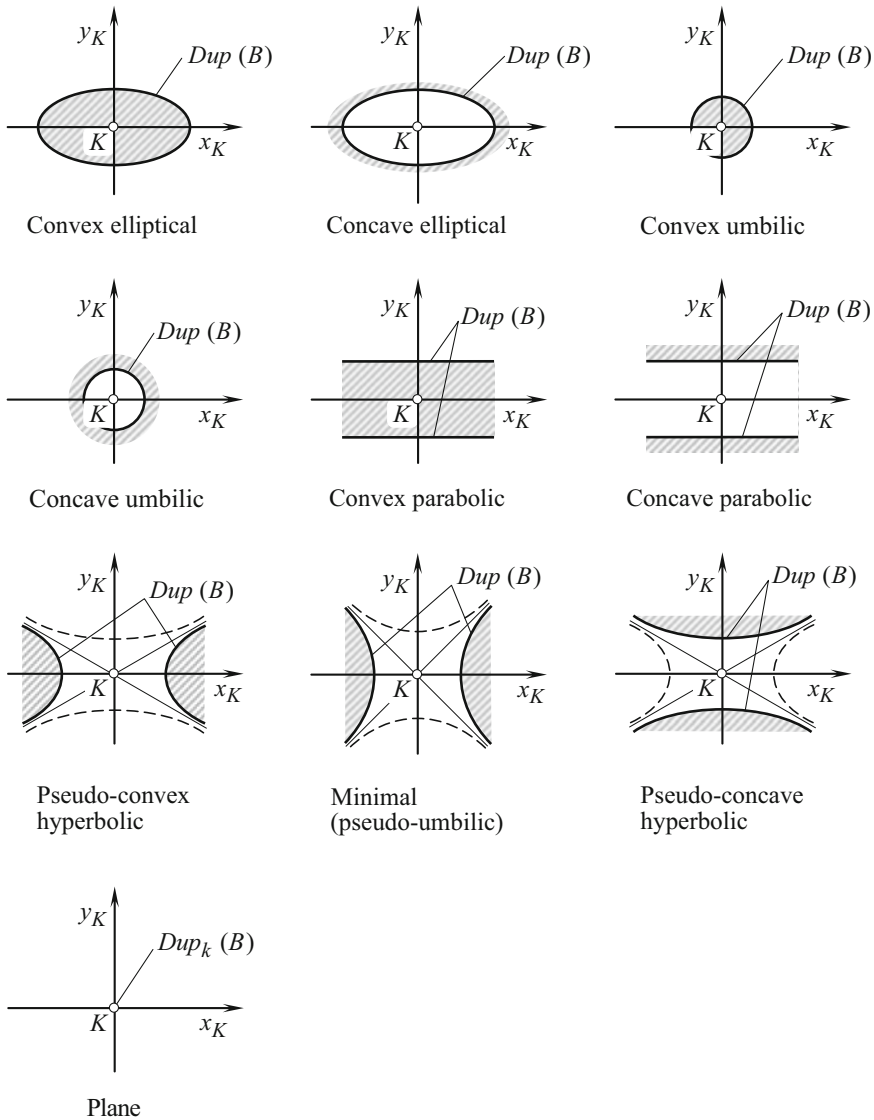


Fig. 3.6 Dupin indicatrices, $Dup(B)$, at point of all ten kinds of local patches of functional surfaces, B_1 and B_2 , in kinematic pairs [for planar local patch of functional surface B_1 (or of functional surface B_2) the Dupin indicatrix, $Dup(B)$, occupies the entire plane. Therefore, in such a case, it is recommended to construct the inverse Dupin indicatrix, $Dup_k(B)$, that is a point coincident with the point K , instead of the regular Dupin indicatrix, $Dup(B)$]

The interested reader is referred to [5, 6, 16, 17], as well as to other advanced sources, for more details on the indicatrix of conformity at point of contact between two smooth regular surfaces.

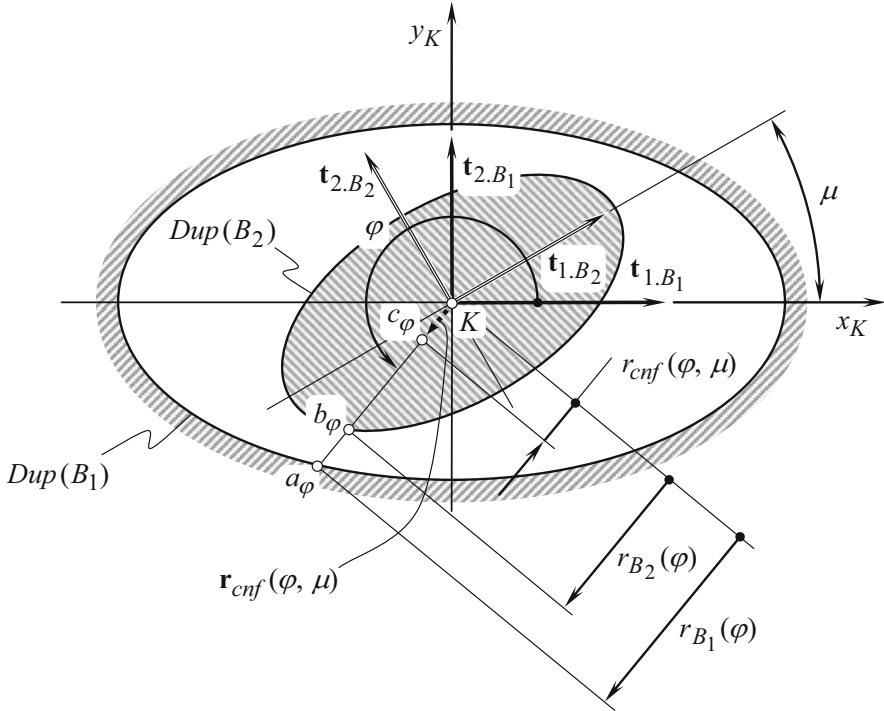


Fig. 3.7 On derivation of equation of the indicatrix of conformity, $Cnf_R(B_1/B_2)$, at point of contact, K , of two functional surfaces B_1 and B_2

“Dupin indicatrices,” $Dup(B_1)$ and $Dup(B_2)$, along with indicatrices of conformity, $Cnf_R(B_1/B_2)$, at point of contact, K , of two functional surfaces, B_1 and B_2 , are extensively used below for the analysis of contact geometry of the interacting surfaces, B_1 and B_2 .

3.1.5 Kinds of Functional Surfaces

The total number of different surfaces that bound real objects is infinitely large. A systematic consideration of surfaces for the purposes of investigation and analysis of kinematic pairs is of critical importance. Therefore, in order to proceed with the analysis of contact geometry in kinematic pairs, an in-detail analysis of possible kinds of functional surfaces is required to be performed.

The total number of possible kinds of functional surfaces in kinematic pairs actually is endless. An advantage can be taken from that in kinematic pairs of the most general kinds, only small portions of the entire functional surfaces interact with one another. It is common practice to refer to small portions of functional surfaces as

to the “local patches of functional surface.” At point of a local patch of every functional surface, two principal radii of curvature, R_1 and R_2 (here an equality, $R_2 > R_1$, is always valid), can be specified. The principal radii of curvature, R_1 and R_2 , are signed values: they are positive for convex, are negative for concave, and are equal to a zero for flatten section of a surface by principal planes, C_1 and C_2 . No inequality of the kind $R_2 \geq R_1$ is permissible; as in the case of $R_2 = R_1$, no principal directions at a surface point can be identified. An inequality, $k_1 > k_2$, that is equivalent to $R_2 > R_1$ is also extensively used in the analysis.

Mean curvature, \mathcal{M} , and *Gaussian curvature*, \mathcal{G} , can be attributed to every surface point:

$$\mathcal{M} = \frac{R_1 + R_2}{2} \quad (3.6)$$

$$\mathcal{G} = R_1 \cdot R_2 \quad (3.7)$$

Different kinds of local patches of functional surfaces are distinguished based on various permissible combinations of the actual values of the mean curvature, \mathcal{M} : ($\mathcal{M} > 0$, $\mathcal{M} < 0$, $\mathcal{M} = 0$), and the total curvature, \mathcal{G} : ($\mathcal{G} > 0$, $\mathcal{G} < 0$, $\mathcal{G} = 0$), at a surface point. At umbilic surface point, an equality, $\mathcal{M} = k$, is valid (here the normal curvature at the umbilic surface point is denoted by k).

The total number of local patches of functional surface is limited just to ten possible kinds [16, 17]. They are as follows:

1. Three kinds of convex, that is, with a positive *Gauss curvature* ($\mathcal{G} > 0$) and a positive *mean curvature* ($\mathcal{M} > 0$) local patches of functional surface.
2. Three kinds of concave, that is, with a positive *Gauss curvature* ($\mathcal{G} > 0$) and a negative mean curvature ($\mathcal{M} < 0$) local patches of functional surface.
3. Three kinds of hyperbolic, that is, with a negative *Gauss curvature* ($\mathcal{G} < 0$) and either with a positive ($\mathcal{M} > 0$) or with a negative ($\mathcal{M} < 0$) local patches of functional surface.
4. One kind of a flatten, that is, with a zero *Gauss curvature* ($\mathcal{G} = 0$) and either with a positive ($\mathcal{M} \rightarrow +\infty$) or with a negative ($\mathcal{M} \rightarrow -\infty$) local patches of functional surface. These two kinds of flatten local patches of functional surfaces (either with $\mathcal{M} \rightarrow +\infty$ or with $\mathcal{M} \rightarrow -\infty$) are equivalent to one another.

In a particular case, curvature indicatrix, $Crv(B)$, is convenient to visualize the features of shape of each of ten kinds of local patches of functional surfaces. Here, the curvature indicatrix, $Crv(B)$, is a portion of a plane bounded by a corresponding *Dupin indicatrix*, $Dup(B)$, constructed at that same point of the functional surface [17].

Dupin indicatrices, $Dup(B)$, along with curvature indicatrices, $Crv(B)$, for all possible kinds of local patches of functional surfaces in kinematic pairs are depicted in Fig. 3.6. Note that curvature indicatrices are not labeled here.

For a planar local patch of the functional surface B , points of the curvature indicatrices $Crv(B)$ either occupy all the plane surface or all of them are remote to

infinity. Therefore, no graphical interpretation is provided to the curvature indicatrices $Crv(B)$ of a planar local patch of the functional surface in kinematic pairs.

3.1.6 Kinds of Kinematic Pairs

On the premise of the definition to the term “kinematic pair” proposed by *F. Reuleaux* (i.e., that “kinematic pair” is a connection between two bodies that imposes constraints on their relative movement), a following approach is adopted in this text to develop a classification of kinematic pairs.

A kinematic pair that features a highest possible degree of freedom corresponds to the first stratus in the classification. The fewer the degree of freedom, the lower the stratus of a kinematic pair in the classification, and vice versa.

In the rest of the text below, the terms “higher kinematic pair” and “lower kinematic pair” are not used at all. Instead, the following kinds of kinematic pairs are distinguished:

1. “Point-contact kinematic pairs”
2. “Line-contact kinematic pairs”
3. “Surface-to-contact kinematic pairs”.

Kinematic pairs of all kinds fall into one of these categories.

Taking into account, that there are only ten different kinds of local patches of smooth, regular functional surfaces B_1 and B_2 (see Fig. 3.6), every kind of the surface contact can be represented more in detail. For the analysis, a square morphological matrix of size $10 \times 10 = 100$ is composed. An example of the morphological matrix is illustrated in Fig. 3.8. All possible combinations of the surfaces contact are covered by this morphological matrix. One axis of the morphological matrix is represented by ten kinds of local patches of the functional surfaces B_1 , while another axis is represented by ten kinds of local patches of the functional surfaces B_2 . The morphological matrix contains 100 different combinations of the local patches of a functional surfaces B_1 and of a functional surfaces B_2 . As not all contacts of local patches B_1 and B_2 are physically feasible, therefore, only:

$$C_{10}^2 + 10 = \frac{10!}{2!(10-2)!} + 10 = 55 \quad (3.8)$$

of them are necessary to be investigated in detail. For example, no contact is permissible between two concave surfaces B_1 and B_2 . Also, concave surfaces can't make contact with saddle-like surfaces and so forth. Ultimately, for kinematic pairs that feature true point contact between the functional surfaces, the total number of contacts between the bodies, B_1 and B_2 , is limited to 29 different kinds.

A morphological matrix 10×10 (see Fig. 3.8) is used with a goal to perform an in-detail analysis of kinematic pairs. In this matrix, the combinations of the

Local patch of functional surface B_1		Local patch of functional surface B_2									
		Elliptic, ${}^2\mathcal{B} > 0; {}^2\mathcal{M} \neq 0$				Parabolic, ${}^2\mathcal{B} = 0$			Hyperbolic, ${}^2\mathcal{B} < 0$		
		${}^2\mathcal{M} > 0$		${}^2\mathcal{M} < 0$		${}^2\mathcal{M} > 0$	${}^2\mathcal{M} = 0$	${}^2\mathcal{M} < 0$	${}^2\mathcal{M} > 0$	${}^2\mathcal{M} = 0$	${}^2\mathcal{M} < 0$
${}^1\mathcal{M} > 0$	${}^1\mathcal{M} > 0$	1.1	1.3	1.4	1.5	1.6	1.7	1.8	1.9	1.10	
	${}^1\mathcal{M} = 1_k$	2.1	2.3	2.4	2.5	2.6	2.7	2.8	2.9	2.10	
${}^1\mathcal{M} < 0$	${}^1\mathcal{M} < 0$	3.1	3.3	3.4	3.5	3.6	3.7	3.8	3.9	3.10	
	${}^1\mathcal{M} = 1_k$	4.1	4.3	4.4	4.5	4.6	4.7	4.8	4.9	4.10	
Parabolic, ${}^1\mathcal{B} = 0$	${}^1\mathcal{M} > 0$	5.1	5.3	5.4	5.5	5.6	5.7	5.8	5.9	5.10	
	${}^1\mathcal{M} = 0$	6.1	6.3	6.4	6.5	6.6	6.7	6.8	6.9	6.10	
	${}^1\mathcal{M} < 0$	7.1	7.3	7.4	7.5	7.6	7.7	7.8	7.9	7.10	
Hyperbolic, ${}^1\mathcal{B} < 0$	${}^1\mathcal{M} > 0$	8.1	8.3	8.4	8.5	8.6	8.7	8.8	8.9	8.10	
	${}^1\mathcal{M} = 0$	9.1	9.3	9.4	9.5	9.6	9.7	9.8	9.9	9.10	
	${}^1\mathcal{M} < 0$	10.1	10.3	10.4	10.5	10.6	10.7	10.8	10.9	10.10	

Fig. 3.8 Morphological matrix 10×10 with all permissible kinds of contact of the functional surfaces B_1 and B_2 in a kinematic pair

functional surfaces, B_1 and B_2 , along the “diagonal” formed by the pairs 1.1, 2.2, 3.3, . . . , 10.10 and below the diagonal are taken into account, while the rest of the combinations of the surfaces B_1 and B_2 located above the diagonal can be found out among those located below the diagonal.

Moreover, some of the combinations of the surfaces B_1 and B_2 cannot form a contact because of the physical constraints. For example, none of a concave functional surface B_1 can make contact with a concave functional surface B_2 (and vice versa) with no interference into one another. Similarly, none of the planar functional surface B_1 can make contact with a concave or a saddle-like functional surface B_2 (and vice versa) with no interference into one another. All of these and the similar combinations of the surfaces B_1 and B_2 are also eliminated from the further analysis (see Fig. 3.8).

3.1.6.1 Kinematic Pairs that Feature “Point-Contact” between Functional Surfaces

In “point-contact kinematic pairs” (or just “ P_c –kinematic pairs,” for simplicity), the functional surfaces, B_1 and B_2 , make contact at a single point. A more in-detail analysis reveals that the following kinds of contact between the functional surfaces, B_1 and B_2 , have to be recognized in “point-contact kinematic pairs.”

Kinematic Pairs with True-Point-Contact of Functional Surfaces

The “true-point-contact” kinematic pairs (or just “ TP_c –kinematic pairs,” for simplicity) of different kinds are distinguished.

First, there are several different kinds of “convex-to-convex” “true-point-contact” kinematic pairs that feature either elliptic or umbilic or parabolic functional surfaces in contact. The kinematic pairs of this kind are composed of two convex functional surfaces, B_1 and B_2 (Fig. 3.9):

- Elliptic-to-elliptic-contact kinematic pair.
- Elliptic-to-umbilic-contact kinematic pair.
- Elliptic-to-parabolic-contact kinematic pair.
- Umbilic-to-umbilic-contact kinematic pair.
- Umbilic-to-parabolic-contact kinematic pair.
- Parabolic-to-parabolic-contact kinematic pair.

The kinematic pairs of this kind feature a single contact point between the functional surfaces B_1 and B_2 . In Fig. 3.8, these kinematic pairs correspond to 1.1, 2.1, 2.2, 5.1, 5.2, and 5.5, contacts of the functional surfaces B_1 and B_2 . Relative orientation of the *Dupin indicatrices*, $Dup(B_1)$ and $Dup(B_2)$, at contact point of the kinematic pairs of this particular kind are shown in Fig. 3.9. There are no constraints onto the actual value of the angle of local relative orientation, μ , of the contacting functional surfaces, B_1 and B_2 , for the kinematic pairs labeled 1.1, 2.1, 2.2, 5.1, and

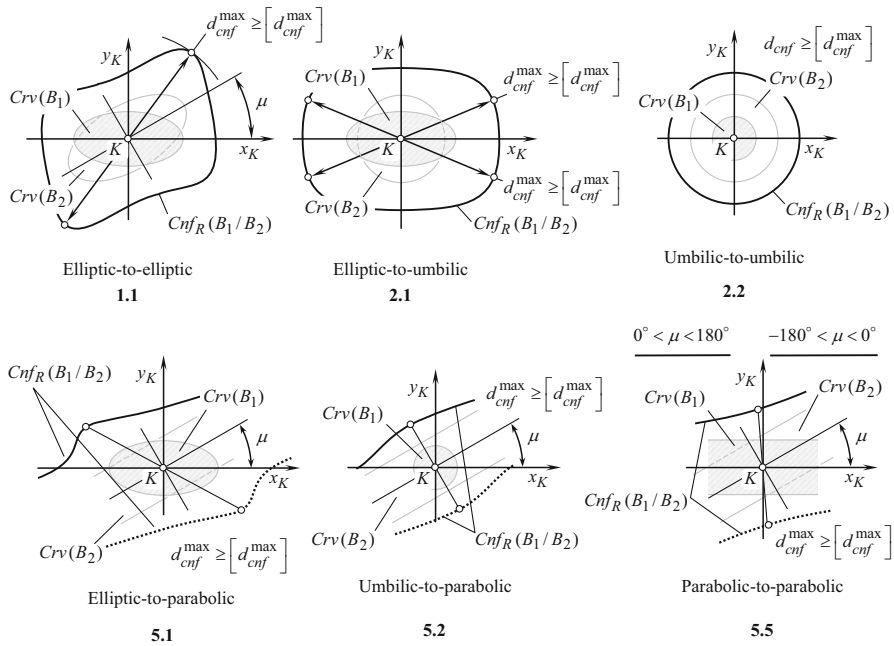


Fig. 3.9 Indicatrices of conformity, $Cnf_R(B_1/B_2)$, and the curvature indicatrices, $Crv_R(B_1)$ and $Crv_R(B_2)$, at contact point of kinematic pairs that feature convex-to-convex “true-point-contact” of the functional surfaces B_1 and B_2 (the values, $\mu = 0^\circ$ and $\mu = \pm 180^\circ$, of the angle, μ , of the functional surfaces, B_1 and B_2 , local relative orientation are not permissible in the design of the kinematic pair of the kind 5.5)

5.2. For the kinematic pair labeled 5.5, the values, $\mu = 0^\circ$ and $\mu = \pm 180^\circ$, of the angle, μ , are not permissible; as in this scenario, the kinematic pair 5.5 is no longer a kind of “convex-to-convex” “true-point-contact” kinematic pairs.

The diagrams, shown in Fig. 3.9, correspond to the so-called non-conformal kinematic pairs. The term “non-conformal kinematic pairs” is due to that in all sections of the functional surfaces by a plane through the common perpendicular, the lines of intersection of the surfaces make either *convex-to-convex* or *convex-to-straight line* contact (therefore, they are of nonnegative values).

Second, there are only two different kinds of “convex-to-planar” “point-contact” kinematic pairs that feature either elliptic or umbilic functional surface in contact with a planar local patch of a mating functional surface.

The kinematic pairs of this kind are composed of two functional surfaces, B_1 and B_2 (see Fig. 3.10):

- Planar-to-elliptic-contact kinematic pair.
- Planar-to-umbilic-contact kinematic pair.

Kinematic pairs of this kind feature a single contact point between the functional surfaces B_1 and B_2 . In Fig. 3.8, these kinematic pairs correspond to 6.1 and 6.2,

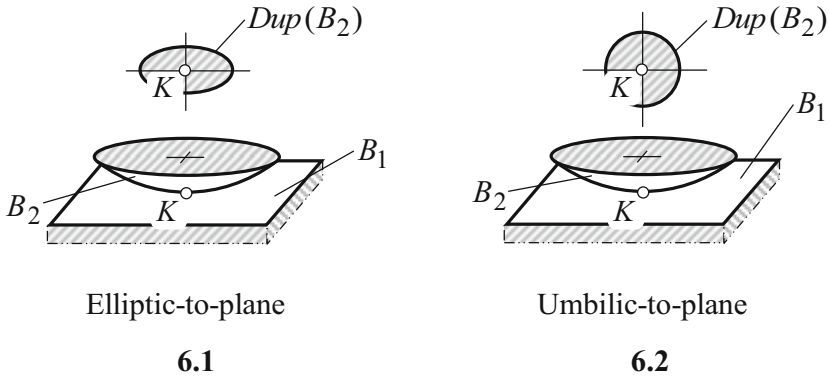


Fig. 3.10 Details of the “point-contact” kinematic pairs that feature a planar functional surface B_1 in contact with either elliptic, or umbilic functional surface B_2

contacts of the functional surfaces B_1 and B_2 . The cases 6.5 and 6.6 are not considered here, as the kinematic pairs of these kinds are not “true-point-contact” kinematic pairs. Details on the kinematic pairs of this particular kind are shown in Fig. 3.10. There are no constraints onto the actual value of the angle of local relative orientation, μ , of the contacting functional surfaces, B_1 and B_2 , for the kinematic pairs labeled 6.1 and 6.2.

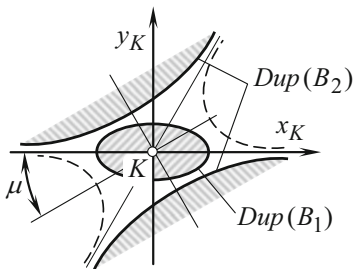
Third, there are several different kinds of “convex-to-hyperbolic” “point-contact” kinematic pairs that feature different kinds of hyperbolic functional surface in contact with convex local patches of a mating functional surface. Kinematic pairs of this kind feature a single contact point between the functional surfaces B_1 and B_2 . In Fig. 3.8, these kinematic pairs correspond to 8.1, 8.2, 9.1, 9.2, 10.1, and 10.2, contacts of the functional surfaces B_1 and B_2 . The kinematic pairs of this kind are composed of two convex functional surfaces, B_1 and B_2 (see Fig. 3.11):

- Elliptic-to-hyperbolic (pseudo-concave)-contact kinematic pair.
- Umbilic-to-hyperbolic (pseudo-concave)-contact kinematic pair.
- Elliptic-to-minimal (pseudo-umbilic)-contact kinematic pair.
- Umbilic-to-minimal (pseudo-umbilic)-contact kinematic pair.
- Elliptic-to-hyperbolic (pseudo-convex)-contact kinematic pair.
- Umbilic-to-hyperbolic (pseudo-convex)-contact kinematic pair.

For the kinematic pairs labeled 8.1, 9.1, and 10.1, the actual value of the angle, μ , of the functional surfaces local relative orientation is in the range of $\mu_{\min} < \mu < \mu_{\max}$, where μ_{\min} and μ_{\max} are the minimum and the maximum permissible values of the angle μ , correspondingly.

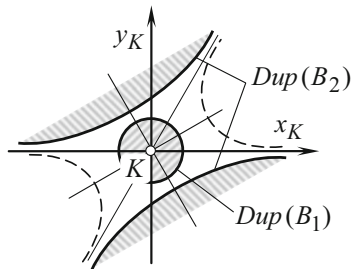
There are no constraints onto the actual value of the angle of local relative orientation, μ , of the contacting functional surfaces, B_1 and B_2 , for the kinematic pairs labeled 8.2, 9.2, and 10.2.

The diagrams, shown in Fig. 3.11, correspond to the so-called semi-conformal kinematic pairs. The term “semi-conformal kinematic pairs” is due to that in certain



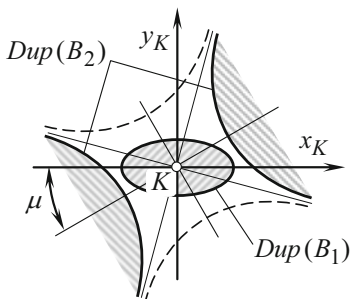
Elliptic-to-hyperbolic
(pseudo-concave)

8.1



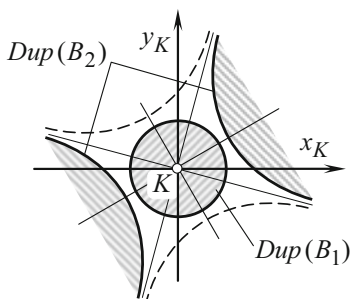
Umbilic-to-hyperbolic
(pseudo-concave)

8.2



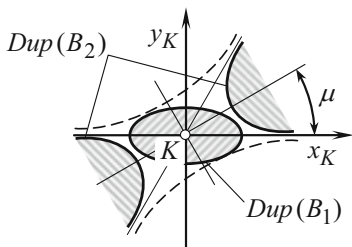
Elliptic-to-minimal
(pseudo-umbilic)

9.1



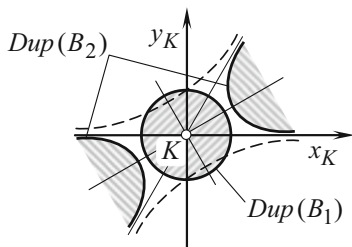
Umbilic-to-minimal
(pseudo-umbilic)

9.2



Elliptic-to-hyperbolic
(pseudo-convex)

10.1



Umbilic-to-hyperbolic
(pseudo-convex)

10.2

Fig. 3.11 Indicatrices of conformity, $Cnf_K(B_1/B_2)$, and the Dupin indicatrices, $Dup(B_1)$ and $Dup(B_2)$, at contact point of kinematic pairs that feature convex-to-saddle-like “point-contact” of the functional surfaces B_1 and B_2 [in contacts 8.1, 9.1, and 10.1, the actual value of the angle, μ , of the functional surfaces, B_1 and B_2 , local relative orientation, is in the range of: $-\lceil\mu\rceil < \mu < +\lceil\mu\rceil$]

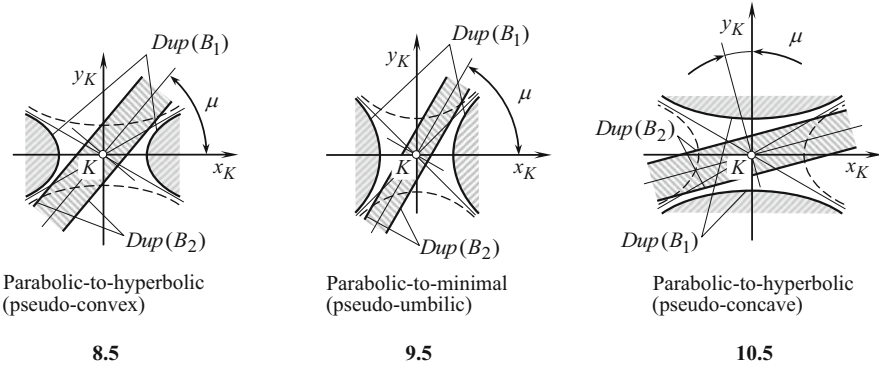


Fig. 3.12 Relative orientation of the Dupin indicatrices, $Dup(B_1)$ and $Dup(B_2)$, at contact point of kinematic pairs that feature convex-parabolic-to-hyperbolic “true-point-contact” of the functional surfaces B_1 and B_2 (the actual values of the angle, μ , of the functional surfaces, B_1 and B_2 , local relative orientation is in the range of: $\mu_{\min} \leq \mu \leq \mu_{\max}$)

sections of the functional surfaces by a plane through the common perpendicular, the lines of intersection of the surfaces make either *convex-to-convex* or *concave-to-convex* contact (i.e., curvature of the curves of intersection of the functional surfaces are of opposite sign).

Fourth, there are three different kinds of “convex-to-hyperbolic” “point-contact” kinematic pairs that feature different kinds of hyperbolic functional surfaces in contact with convex parabolic local patches of a mating functional surface. Kinematic pairs of this kind feature a single contact point between the functional surfaces B_1 and B_2 . In Fig. 3.8, these kinematic pairs correspond to 8.5, 9.5, and 10.5, contacts of the functional surfaces B_1 and B_2 . The kinematic pairs of this kind are composed of two convex functional surfaces, B_1 and B_2 (see Fig. 3.12):

- Parabolic-to-hyperbolic (pseudo-concave)-contact kinematic pair.
- Parabolic-to-minimal (pseudo-umbilic)-contact kinematic pair.
- Parabolic-to-hyperbolic (pseudo-convex)-contact kinematic pair.

For the kinematic pairs of these three kinds, the actual value of the angle, μ , of the functional surfaces local relative orientation is in the range of $\mu_{\min} < \mu < \mu_{\max}$, where μ_{\min} and μ_{\max} are the minimum and the maximum permissible values of the angle μ , correspondingly.

To a certain extent, the diagrams, shown in Fig. 3.12, can be considered as “semi-conformal kinematic pairs.” In certain sections of the functional surfaces by a plane through the common perpendicular, the lines of intersection of the surfaces make either *straight-to-convex* or *concave-to-convex* contact.

Fifth, there are three different kinds of “hyperbolic-to-hyperbolic” “point-contact” kinematic pairs that feature different kinds of hyperbolic functional surfaces in contact with hyperbolic local patches of a mating functional surface. Kinematic pairs of this kind feature a single contact point between the functional surfaces B_1 and B_2 . In Fig. 3.8, these kinematic pairs correspond to 10.8, 10.9, and 10.10, contacts of the

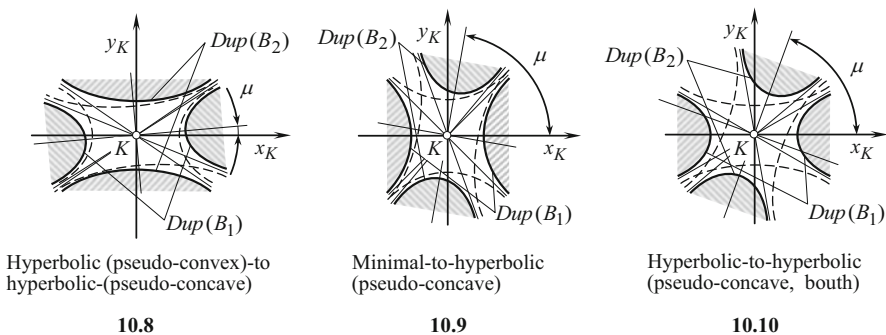


Fig. 3.13 Relative orientation of the Dupin indicatrices, $Dup(B_1)$ and $Dup(B_2)$, at contact point of kinematic pairs that feature hyperbolic-to-hyperbolic “true-point-contact” of the functional surfaces B_1 and B_2 (the actual values of the angle, μ , of the functional surfaces, B_1 and B_2 , local relative orientation is in the range of: $\mu_{min} \leq \mu \leq \mu_{max}$)

functional surfaces B_1 and B_2 . The kinematic pairs of this kind are composed of two convex functional surfaces, B_1 and B_2 (see Fig. 3.13):

- Hyperbolic (pseudo-convex)-to-hyperbolic (pseudo-concave)-contact kinematic pair.
- Hyperbolic (minimal)-to-hyperbolic (pseudo-concave)-contact kinematic pair.
- Hyperbolic (pseudo-concave)-to-hyperbolic (pseudo-concave)-contact kinematic pair.

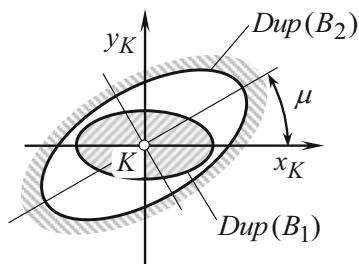
For the kinematic pairs of these three kinds, the actual value of the angle, μ , of the functional surfaces local relative orientation is in the range of $\mu_{min} < \mu < \mu_{max}$, where μ_{min} and μ_{max} are the minimum and the maximum permissible values of the angle μ , correspondingly.

The diagrams, shown in Fig. 3.13, correspond to the so-called semi-conformal kinematic pairs.

Sixth, there are a few different kinds of “point-contact” kinematic pairs composed of different kinds of elliptic, umbilic, and parabolic, functional surfaces in contact. Kinematic pairs of this kind feature a single contact point between the functional surfaces B_1 and B_2 . In Fig. 3.8, these kinematic pairs correspond to 3.1, 3.2, 4.1, 4.2, 7.1, and 7.2, contacts of the functional surfaces B_1 and B_2 . The kinematic pairs of this kind are composed of two convex functional surfaces, B_1 and B_2 (see Fig. 3.14):

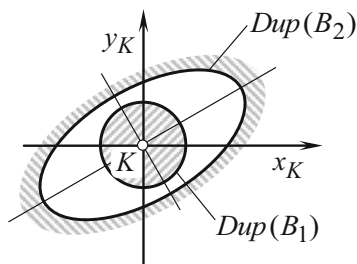
- Convex elliptic-to-elliptic (concave)-contact kinematic pair.
- Convex umbilic-to-elliptic (concave)-contact kinematic pair.
- Convex elliptic-to-umbilic (concave)-contact kinematic pair.
- Convex umbilic-to-umbilic (concave)-contact kinematic pair.
- Convex elliptic-to-parabolic (concave)-contact kinematic pair.
- Convex umbilic-to-parabolic (concave)-contact kinematic pair.

For the kinematic pairs of these six kinds, the actual value of the angle, μ , of the functional surfaces local relative orientation is in the range of $\mu_{min} < \mu < \mu_{max}$, where



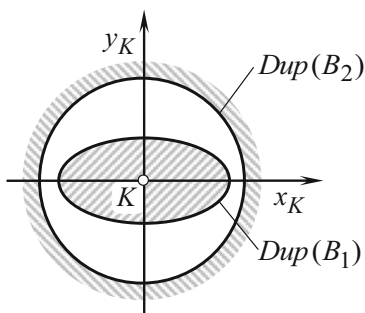
Elliptic-to-elliptic

3.1



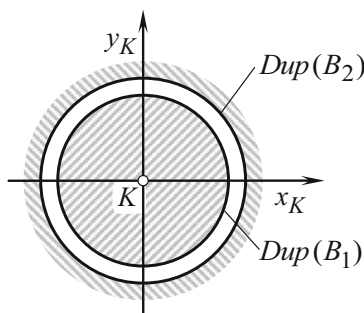
Umbilic-to-elliptic

3.2



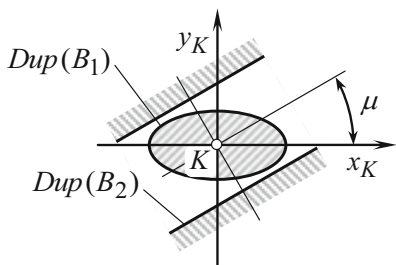
Elliptic-to-umbilic

4.1



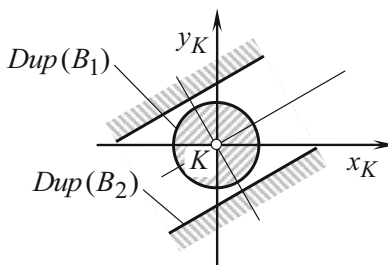
Umbilic-to-umbilic

4.2



Elliptic-to-parabolic

7.1



Umbilic-to-parabolic

7.2

Fig. 3.14 Relative orientation of the Dupin indicatrices, $Dup(B_1)$ and $Dup(B_2)$, at contact point of kinematic pairs that feature concave “true-point-contact” of the functional surfaces B_1 and B_2 of elliptic, umbilic, and parabolic type (in the kinematic pairs labeled 3.1 and 7.1 the actual value of the angle, μ , of the functional surfaces, B_1 and B_2 , local relative orientation is in the range of: $\mu_{\min} \leq \mu \leq \mu_{\max}$)

μ_{\min} and μ_{\max} are the minimum and the maximum permissible values of the angle μ , correspondingly.

As shown in Fig. 3.14, diagrams 3.1, 3.2, 4.1, and 4.2 correspond to the so-called conformal kinematic pairs. The term “conformal kinematic pairs” is due to that in all sections of the functional surfaces by a plane through the common perpendicular normal curvature, the lines of intersection of the surfaces is always of opposite sign. To a certain extent, the diagrams labeled 7.1 and 7.2 can also be considered as “conformal kinematic pairs.”

Kinematic Pairs with Locally-Line-Contact of Functional Surfaces

The “locally-line-contact” kinematic pairs (or just “ LL_c –kinematic pairs,” for simplicity) are those that feature zero difference between the magnitudes of radii of normal curvature, $R_{B,1}$ and $R_{B,2}$, in a section by a plane through a common perpendicular at contact point. A zero difference between the magnitudes of normal radii of curvature of two functional surfaces, B_1 and B_2 , is observed when the radii of normal curvature are of equal magnitudes, and of opposite sign, that is, when the equality $R_{B,1} = -R_{B,2}$ is valid. Due to this feature, the minimal diameter, d_{cnf}^{\min} , of the indicatrix of conformity, $Cnf_R(B_1/B_2)$, at point of contact of the functional surfaces, B_1 and B_2 , equals to zero, and, therefore, the equality $d_{cnf}^{\min} \equiv 0$ is always observed in all locally-extremal point-contact kinematic pairs. This is the reason kinematic pairs of the kind under consideration are referred to as “locally-extremal-contact” kinematic pairs as they feature an extremal value of minimal diameter of the indicatrix of conformity ($d_{cnf}^{\min} \equiv 0$).

Evidently, the “locally-extremal-contact” kinematic pairs can be composed either by a convex and a concave local patches of the functional surfaces, B_1 and B_2 , or by a convex and a saddle-like of the functional surfaces, B_1 and B_2 . No locally-extremal kinematic pairs can be composed if both of the functional surfaces are concave, or one of them is concave, while another one is a saddle-like local patch of the functional surface.

Different kinds of kinematic pairs with locally-line-contact of functional surfaces are distinguished.

First, several different kinds of “locally-line-contact” kinematic pairs that are composed by either convex elliptic or convex umbilic functional surfaces make contact with concave functional surfaces of various geometries. The kinematic pairs of this kind are composed of a convex and a concave functional surfaces, B_1 and B_2 (see Fig. 3.15):

- Elliptic (concave)-to-elliptic (convex)-contact kinematic pair.
- Elliptic (concave)-to-umbilic (convex)-contact kinematic pair.
- Umbilic (concave)-to-elliptic (convex)-contact kinematic pair.
- Parabolic (concave)-to-elliptic (convex)-contact kinematic pair.
- Parabolic (concave)-to-umbilic (convex)-contact kinematic pair.

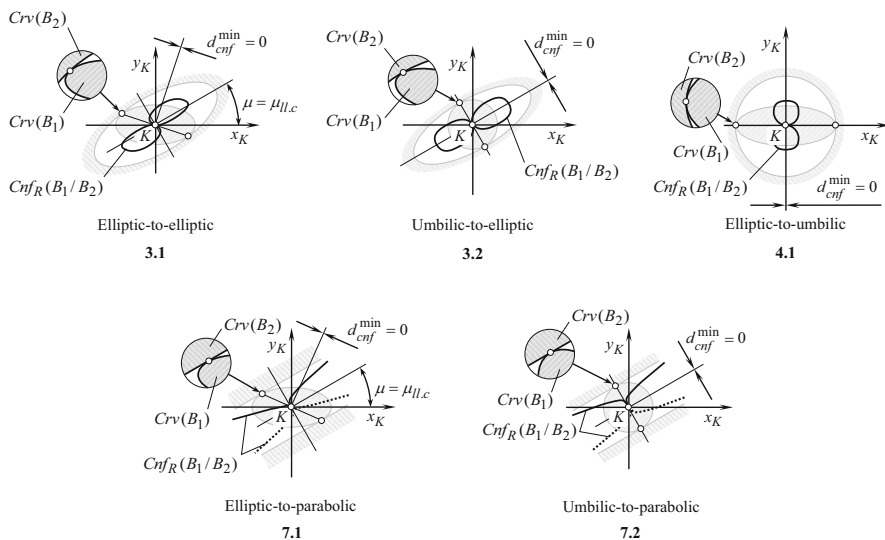


Fig. 3.15 Indicatrices of conformity, $Cnf_R(B_1/B_2)$, at contact point of kinematic pairs that feature convex-to-concave “true-point-contact” of the functional surfaces B_1 and B_2 (the actual value of the angle, μ , of the functional surfaces, B_1 and B_2 , local relative orientation equals to a value $\mu = \mu_{ll,c}$ at which the contacting surfaces form a locally-line contact)

Kinematic pairs of this kind feature a single contact point between the functional surfaces, B_1 and B_2 , along radii of normal curvature of equal magnitude and opposite sign. In Fig. 3.8, these kinematic pairs correspond to 3.1, 3.2, 4.1, 7.1, and 7.2, contacts of the functional surfaces B_1 and B_2 . Indicatrices of conformity, $Cnf_R(B_1/B_2)$, at contact point of the functional surfaces, B_1 and B_2 , of the kinematic pairs of this particular kind are shown in Fig. 3.15. There are no constraints onto the actual value of the angle of local relative orientation, μ , of the contacting functional surfaces, B_1 and B_2 , for the kinematic pairs labeled 3.2, 4.1, and 7.2. For the kinematic pairs labeled 3.1 and 7.1, the actual value of the angle, μ , of the functional surfaces, B_1 and B_2 , local relative orientation equals to a value $\mu = \mu_{ll,c}$ at which the contacting surfaces form a locally-line-contact.

Second, numerous different kinds of “locally-line” point-contact kinematic pairs composed either of elliptic or umbilic or parabolic, functional surfaces that make contact with functional surfaces of hyperbolic geometry. Kinematic pairs of this kind feature a single contact point between the functional surfaces. In Fig. 3.8, these kinematic pairs correspond to 8.1, 8.2, 8.5, 9.1, 9.2, 9.5, 10.1, 10.2, and 10.5, contacts of the surfaces, B_1 and B_2 (see Fig. 3.16):

- Hyperbolic (pseudo-concave)-to-elliptic (convex)-contact kinematic pair.
- Hyperbolic (minimal)-to-elliptic (convex)-contact kinematic pair.
- Hyperbolic(pseudo-convex)-to-elliptic (convex)-contact kinematic pair.
- Hyperbolic (pseudo-concave)-to-umbilic (convex)-contact kinematic pair.
- Hyperbolic (minimal)-to-umbilic (convex)-contact kinematic pair.

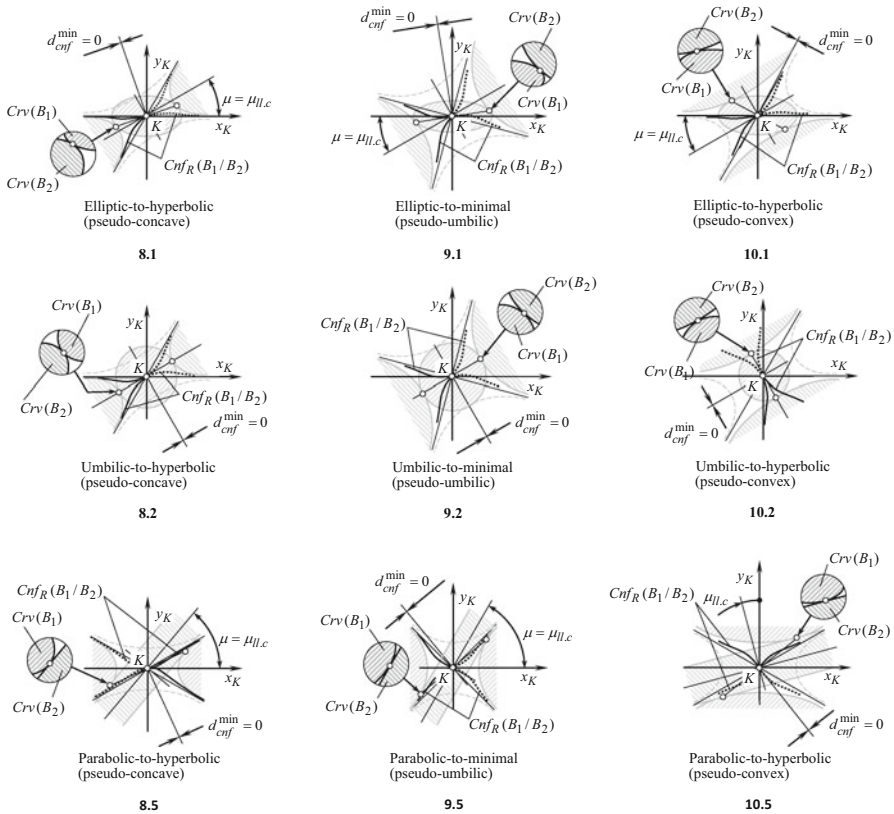


Fig. 3.16 Indicatrices of conformity, $Cnf_R(B_1/B_2)$, at contact point of locally-line kinematic pairs that feature hyperbolic-to-convex “point-contact” of the functional surfaces B_1 and B_2 (the actual value of the angle, μ , of the functional surfaces, B_1 and B_2 , local relative orientation equals to a value $\mu = \mu_{ll,c}$ at which the contacting surfaces form a locally-line contact)

- Hyperbolic(pseudo-convex)-to-umbilic (convex)-contact kinematic pair.
- Hyperbolic (pseudo-concave)-to-parabolic (convex)-contact kinematic pair.
- Hyperbolic (minimal)-to-parabolic (convex)-contact kinematic pair.
- Hyperbolic(pseudo-convex)-to-parabolic (convex)-contact kinematic pair.

Indicatrices of conformity, $Cnf_R(B_1/B_2)$, at contact point of the functional surfaces, B_1 and B_2 , of the kinematic pairs of this particular kind are shown in Fig. 3.16. For the kinematic pairs labeled as 8.1, 8.2, 8.5, 10.1, 10.2, and 10.5, the actual value of the angle, μ , of the functional surfaces local relative orientation equals to a value $\mu = \mu_{ll,c}$ at which the contacting surfaces form a locally-line-contact. No constraints on the actual value of the angle, μ , are imposed in the kinematic pairs 8.2, 9.2, 9.5, and 10.2.

Third, there are three different kinds of “locally-line” point-contact kinematic pairs composed of hyperbolic functional surfaces that make contact with functional

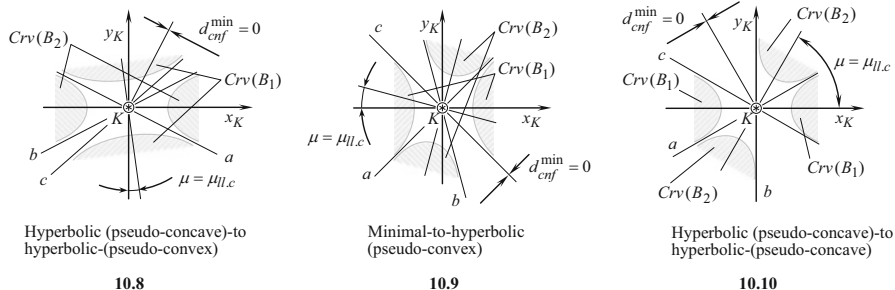


Fig. 3.17 Relative orientation of the *curvature indicatrices*, $Crv(B_1)$ and $Crv(B_2)$, at contact point of kinematic pairs that feature hyperbolic-to-hyperbolic “locally-line-contact” of the functional surfaces B_1 and B_2 (the actual value of the angle, μ , of the functional surfaces, B_1 and B_2 , local relative orientation equals to a value $\mu = \mu_{ll,c}$ at which the contacting surfaces form a locally-line contact)

surfaces of hyperbolic geometry. Kinematic pairs of this kind feature a single contact point between the functional surfaces. In Fig. 3.8, these kinematic pairs correspond to 10.8, 10.9, and 10.10, contacts of the surfaces, B_1 and B_2 (see Fig. 3.17):

- Hyperbolic (pseudo-concave)-to-hyperbolic (pseudo-convex)-contact kinematic pair.
- Hyperbolic (pseudo-concave)-to-hyperbolic (minimal)-contact kinematic pair.
- Hyperbolic (pseudo-concave)-to-hyperbolic (pseudo-concave)-contact kinematic pair.

Relative orientation of the *curvature indicatrices*, $Crv(B_1)$ and $Crv(B_2)$, at contact point of kinematic pairs that feature hyperbolic-to-hyperbolic “locally-line-contact” of the functional surfaces, B_1 and B_2 , is shown in Fig. 3.17. For the kinematic pairs of this design, the actual value of the angle, μ , of the functional surfaces local relative orientation equals to a value $\mu = \mu_{ll,c}$ at which the contacting surfaces form a locally-line-contact.

Locally Surface-to-Surface Contact Kinematic Pairs I

The “locally-surface-to-surface_I-contact” kinematic pairs (or just “LSS_{c.1}—kinematic pairs,” for simplicity) are those featuring zero difference between the magnitudes of the radii of normal curvature, $R_{B,1}$ and $R_{B,2}$, in all sections by a plane through a common perpendicular at contact point of the functional surfaces. A zero difference between the magnitudes of normal radii of curvature of two functional surfaces, B_1 and B_2 , is observed when the radii of normal curvature are of equal magnitude, and are of different sign, that is, when the equality $R_{B,1} = -R_{B,2}$ is valid. As this difference is extremely small (it is equal to zero), kinematic pairs of this kind are also referred to as “locally-extremal-contact” kinematic pairs.

“Locally-surface-to-surface_I-contact” kinematic pairs cannot be composed of two convex functional surfaces, B_1 and B_2 .

Different kinds of kinematic pairs with “locally-surface-to-surface_I-contact” of functional surfaces are distinguished.

Four different kinds of “locally-surface-to-surface_I-contact” kinematic pairs that are composed by hyperbolic functional surfaces make contact with hyperbolic functional surfaces of various geometries. The kinematic pairs of this kind are composed of two hyperbolic functional surfaces, B_1 and B_2 (see Fig. 3.18):

- Elliptic (concave)-to-elliptic (convex)-contact kinematic pair.
- Umbilic (concave)-to-umbilic (convex)-contact kinematic pair.
- Hyperbolic (concave)-to-hyperbolic (convex)-contact kinematic pair.
- Hyperbolic (minimal)-to-hyperbolic (minimal)-contact kinematic pair.

One more kinematic pair of the kind under consideration is represented with:

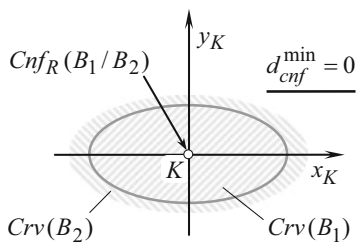
- Planar-to-planar-contact kinematic pair.

Kinematic pairs of this kind feature a single contact point between the functional surfaces, B_1 and B_2 , along with equal magnitude and opposite sign radii of normal curvature in sections by a plane through the common perpendicular. In Fig. 3.8, these kinematic pairs correspond to 3.1, 4.2, 9.9, and 10.8, contacts of the functional surfaces B_1 and B_2 . One can imagine that the principal radii of curvature, R_{1B_1} , R_{2B_1} , R_{1B_2} , and R_{2B_2} , in the kinematic pairs, 3.1, 4.2, 9.9, and 10.8, approach in infinity ($R_{1B_1} \rightarrow \infty$, $R_{2B_1} \rightarrow \infty$, $R_{1B_2} \rightarrow \infty$, and $R_{2B_2} \rightarrow \infty$). In such a scenario, the functional surfaces, B_1 and B_2 , are getting flatten. Actually, flattening of the functional surfaces is observed in any and all kind of kinematic pairs, and not only in the designs 3.1, 4.2, 9.9, and 10.8. Therefore, in Fig. 3.18, “locally-surface-to-surface_I-contact” kinematic pairs with flatten functional surfaces, B_1 and B_2 , are labeled as 1.1, 2.1, 2.2, 3.1, . . . , 10.9, and 10.10.

Relative orientation of the *Dupin indicatrices*, $Dup(B_1)$ and $Dup(B_2)$, at contact point of the kinematic pairs of this particular kind are shown in Fig. 3.18. For the kinematic pair labeled 3.1, 9.9, and 10.8, the actual value of the angle, μ , of the functional surfaces, B_1 and B_2 , local relative orientation equals to a value $\mu = \pm 90^\circ$ for all the “locally-surface-to-surface_I-contact” kinematic pairs. No constraints onto the actual value of the angle, μ , of the functional surfaces, B_1 and B_2 , local relative orientation are imposed in a case of hyperbolic (minimal)-to-hyperbolic (minimal)-contact kinematic pair (labeled as 4.2).

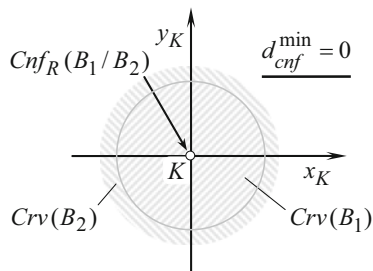
The indicatrices of conformity, $Cnf_R(B_1/B_2)$, for kinematic pairs featuring “locally-surface-to-surface_I-contact” of the functional surfaces, B_1 and B_2 , is always shrunk to a point. This point is coincident with the contact point, K , of the functional surfaces.

3.6.1.4. High-conformal point-contact kinematic pairs I. The performance of point-contact kinematic pairs is strongly correlated to the degree of conformity to each other of the functional surfaces, B_1 and B_2 , at every point of their contact. The more conformal the surfaces B_1 and B_2 at points of their contact, the better the performance of the kinematic pair, and vice versa.



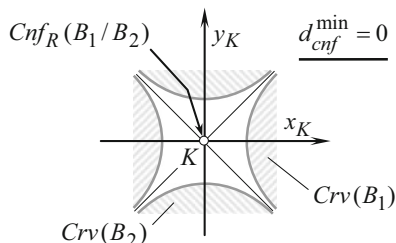
Elliptic (convex)-to-elliptic (concave)

3.1



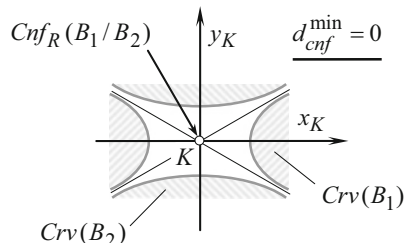
Umbilic (convex)-to-umbilic (concave)

4.2



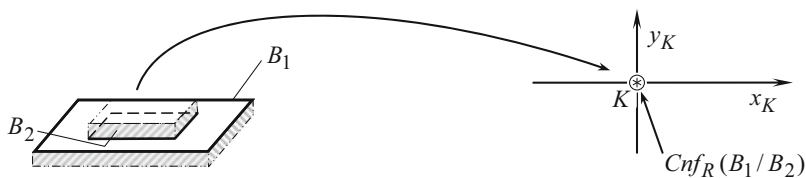
Hyperbolic (minimal)-to-hyperbolic (minimal)

9.9



Hyperbolic (pseudo-convex)-to-hyperbolic (pseudo-concave)

10.8



Planar-to-planar

1.1, 2.1, 2.2, 3.1, ..., 10.9, 10.10

Fig. 3.18 Indicatrices of conformity, $Cnf_R(B_1/B_2)$, and relative orientation of the curvature indicatrices, $Crv(B_1)$ and $Crv(B_2)$, at contact point of kinematic pairs featuring hyperbolic-to-hyperbolic “point-contact” of the functional surfaces B_1 and B_2 . In all the kinematic pairs indicatrix of conformity, $Cnf_R(B_1/B_2)$, is shrunk to a point coincident with contact point, K . (In the kinematic pairs 3.1, 9.9, and 10.10, the actual value of the angle, μ , of the functional surfaces, B_1 and B_2 , local relative orientation is restricted to $\mu = \pm 90^\circ$. No constraints onto the actual value of the angle, μ , is observed in the kinematic pair 4.2)

Qualitatively, the degree of conformity at a point of contact of two functional surfaces can be viewed as follows. Consider a section of two functional surfaces, B_1 and B_2 , by a plane through the common perpendicular. The radii of normal curvature of the surfaces, B_1 and B_2 , within the plane section are designated by R_{B_1} and R_{B_2} ,

correspondingly. A mismatch of the radii of normal curvature of the surfaces, R_{B_1} and R_{B_2} , is denoted by δR :

$$\delta R = | R_{B_1} - R_{B_2} | \tag{3.9}$$

The functional surfaces, B_1 and B_2 , are referred to as “high-conformal point-contact kinematic pairs Γ ” (or just “ $HC_{c.1}$ –kinematic pairs,” for simplicity), if the actual value of the normal radii mismatch, δR , is in the range of:

$$0 < \delta R \leq [\delta R] \tag{3.10}$$

where $[\delta R]$ is the maximum permissible mismatch of the radii of normal curvature of the surfaces, R_{B_1} and R_{B_2} , at which the contact is still referred to as “high conformal” (for details on conformity criterion in kinematic pairs, see section immediately below).

Conformity Criterion in Kinematic Pairs

In order to establish a criterion by means of which conformal contact in kinematic pairs is separated from their “high-conformal” contact, consider two functional surfaces, B_1 and B_2 , that are intersected by a normal plane through the contact point, K . The plane is constructed so as to be perpendicular to the common tangential straight line, t_{CL} . The constructed section of the tooth flanks is schematically shown in Fig. 3.19.

The plane section of the first functional surface is labeled B_1 . Within the differential vicinity of the contact point, radius of curvature of the curve B_1 is labeled R_{B_1} . The radius, R_{B_1} , is of a negative value ($R_{B_1} < 0$), as in this example the functional surface B_1 is considered concave.

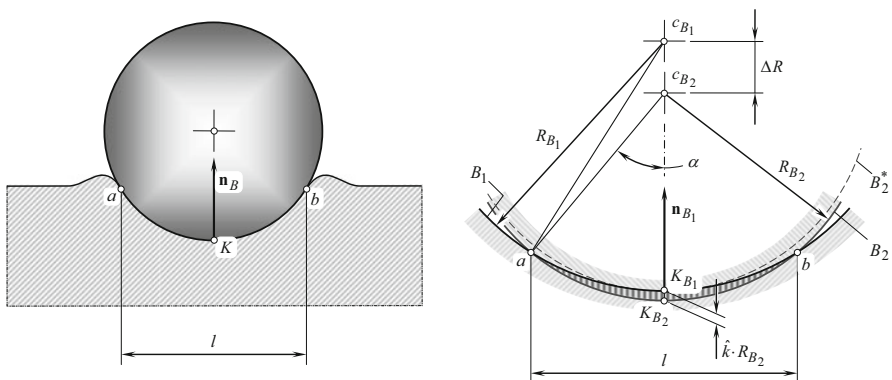


Fig. 3.19 Section of the functional surfaces, B_1 and B_2 , in a conformal kinematic pair by a plane through a current point of contact: The plane is perpendicular to the trace of the contact point across the surfaces, B_1 and B_2

Prior to the operating load is applied, the plane section of the second functional surface is labeled B_2^* . After the load is applied and the second functional surface is slightly penetrated into the first functional surface, the same section, B_2^* , is labeled B_2 . It is assumed here that within the differential vicinity of the point of contact, the radii of curvature of the curves of intersection of the surfaces, B_2^* and B_2 , are of the same value, R_{B_2} . The radius of curvature is of a positive value ($R_{B_2} > 0$), as in this example the second functional surface is considered convex.

In the initial configuration of the functional surfaces, B_1 and B_2 , contact point is labeled K_{B_1} . After the operating load is applied, and the functional surfaces interfere with each other, the contact point is labeled K_{B_2} (in the deformed stage of the functional surfaces).

The functional surfaces, B_1 and B_2 , intersect with each other at two points, a and b . The distance, l , between the points indicates the degree of conformity of the functional surfaces of radii R_{B_1} and R_{B_2} . The greater the distance, l , the higher the degree of conformity of the functional surfaces, and vice versa.

The distance, l , between points a and b can be expressed in terms of the radii of normal curvature, R_{B_1} and R_{B_2} , and the displacement, \hat{k} :

$$l = 2 R_{B_2} \sin \alpha \quad (3.11)$$

For the calculation of the actual value of the angle $\alpha(R_{B_1}, R_{B_2}, \hat{k})$, the following formula is derived:

$$\alpha(R_{B_1}, R_{B_2}, \hat{k}) = \cos^{-1} \left(\frac{R_{B_2}^2 - R_{B_1}^2 + (R_{B_2} + R_{B_1} - \hat{k} \cdot R_{B_2})^2}{2 R_{B_2} (R_{B_2} + R_{B_1} - \hat{k} \cdot R_{B_2})} \right) \quad (3.12)$$

Equation (3.12) is derived on the premise of the law of cosines.

As it follows from the analysis of Eq. (3.12), actual value of the angle α in Eq. (3.11) depends on actual values the radii of normal curvature, R_{B_1} and R_{B_2} , as well as on the displacement \hat{k} .

For convenience of the further analysis of the plane section (see Fig. 3.19), all the design parameters in Eq. (3.12) are normalized by the pinion radius R_{B_2} . The normalized design parameters are designated as follows: $R_{B_2}/R_{B_2} = 1$, $R_{B_1}/R_{B_2} = \hat{K}$, and $k R_{B_2}/R_{B_2} = \hat{k}$.

Actual value of the angle α can be expressed in terms of the normalized design parameters in the following form:

$$\alpha = \cos^{-1} \left(\frac{1 - \hat{K}^2 + (1 + \hat{K} - \hat{k})^2}{2 \cdot (1 + \hat{K} - \hat{k})} \right) \quad (3.13)$$

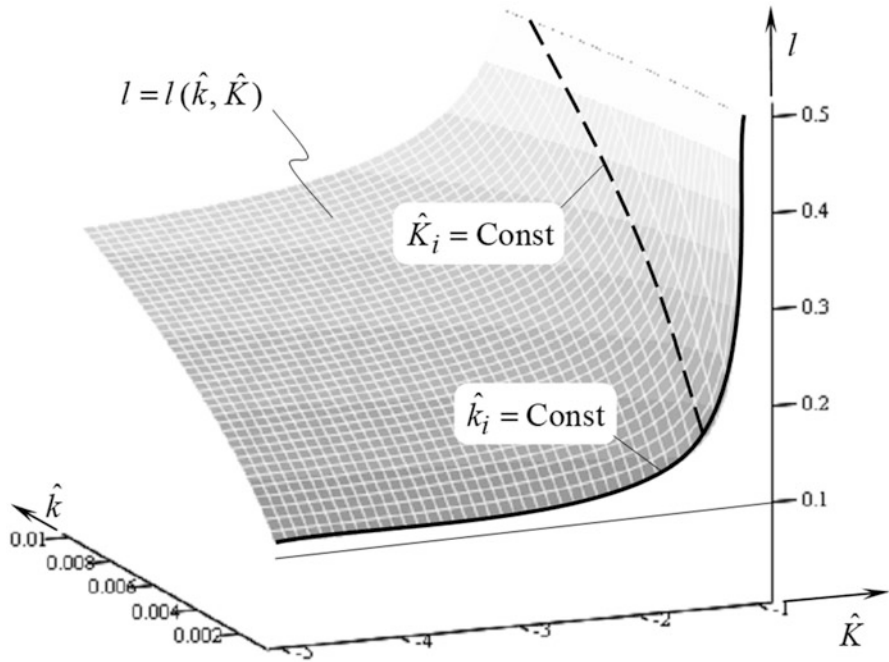


Fig. 3.20 Three-dimensional plot of the function $l = l(\hat{k}, \hat{K})$ constructed for *conformal* (“convex-to-concave” kind of contact between the functional surfaces, B_1 and B_2) kinematic pairs

The function $l = l(\hat{k}, \hat{K})$ is valid for both, for the “convex-to-convex” and for “convex-to-concave” contacts of the functional surfaces, B_1 and B_2 . For conformal kinematic pairs, only cases of “convex-to-concave” contacts of the functional surfaces are of interest.

In Fig. 3.20, a three-dimensional plot of the function $l = l(\hat{k}, \hat{K})$ is constructed for the cases of “convex-to-concave” contacts of the functional surfaces, B_1 and B_2 , in a kinematic pair.

A performed analysis of the 3D-plot allows the following conclusions.

The sections of the surface $l = l(\hat{k}, \hat{K})$ by the planes $\hat{k}_i = \text{Const}$ (see Fig. 3.20) are represented by the curves that have asymptotes. For a particular curve, $k_i = \text{Const}$, shown in Fig. 3.20 in the bold line, the axis l and the straight line $l = 1$ are the asymptotes.

The greatest possible degree of mismatch in the curvature of the functional surfaces, B_1 and B_2 , corresponds to an infinite value of the parameter $\hat{K} \rightarrow -\infty$. An interval of alteration of the parameter \hat{K} starting from $-\infty$ and going up to approximately $\hat{K} = -2$ can conveniently accommodate any desirable displacement of the functional surfaces, B_1 and B_2 , from their correct location. However, in the

range $-\infty < \widehat{K} < -2$ of alteration of the parameter \widehat{K} , an increase in the degree of conformity of the functional surfaces, B_1 and B_2 , is negligibly small. In the range of variation of the parameter \widehat{K} , the load-carrying capacity of a conformal kinematic pair remains approximately at the same value. Therefore, use of just the “convex-to-concave” contact of the functional surfaces gives almost no improvement to the load-carrying capacity of kinematic pairs. For the “convex-to-concave” contact, an additional requirement has to be fulfilled in order to significantly improve the load-carrying capacity of a conformal kinematic pair.

On the other hand, even a small alteration in the actual value of the parameter \widehat{K} within the interval $-2 < \widehat{K} < -1$ results in a significant increase in the degree of conformity of the functional surfaces, B_1 and B_2 . This immediately entails a corresponding increase in the load-carrying capacity of the kinematic pair.

High-conformal kinematic pairs feature “convex-to-concave” contacts of the functional surfaces. Moreover, the degree of conformity at point of contact of the functional surfaces in “high-conformal kinematic pairs” exceeds a certain critical value (the threshold, in other words).

In the aforementioned example (see Fig. 3.20), the value of parameter \widehat{K} (i.e., the value of $\widehat{K} \approx -2$) can be referred to as a critical value, that is, \widehat{K}_{cr} . This allows one to distinguish between “conformal kinematic pairs” (for which $-\infty < \widehat{K} < \widehat{K}_{cr}$) and “high-conformal kinematic pairs” (for which $\widehat{K}_{cr} \leq \widehat{K} < -1$). Because of the favorable conditions of contact of the functional surfaces, high-conformal kinematic pairs allow for a significantly greater power density.

Without going into the details of this analysis, it is clear that high-conformal kinematic pairs require tighter tolerances for any possible displacements of the functional surfaces, B_1 and B_2 , from their desirable locations and orientations. This relates not just for the tolerances on the manufacturing errors, but to any and all possible displacements caused by thermal extension, elastic deflection, and so forth. Otherwise, there could be no future for high-conformal transmission system.

The separate from one another area of existence of “conformal” and “high-conformal kinematic pairs” is schematically illustrated in Fig. 3.21.

The performed analysis of the 3D plot shown in Fig. 3.20 can be extended, although the extension is a bit aside of the main stream of the subject of this research.

Consider sections of the surface $l = l(\widehat{k}, \widehat{K})$ intersected by planes $\widehat{K}_i = \text{Const}$ (see Fig. 3.20). An example of such sections is shown by the bold dashed line. For high-conformal kinematic pairs, the parameter \widehat{K}_i for these lines is in the range of $\widehat{K}_{cr} \leq \widehat{K}_i < -1$. The degree of mismatch in the curvature of the functional surfaces in high-conformal kinematic pairs is smaller compared to that in conformal kinematic pairs.

The indicatrix of conformity $Cnf_R(B_1/B_2)$ [see Eq. (3.4)] [and inverse indicatrix of conformity, $Cnf_k(B_1/B_2)$] is developed aiming the analytical description of the contact geometry of two interacting functional surfaces, B_1 and B_2 , in a kinematic pair. The minimum diameter, d_{cnf} , of the indicatrix of conformity, $Cnf_R(B_1/B_2)$, at a current contact point, \widehat{K} , of the functional surfaces, B_1 and B_2 , can be used as a quantitative measure of the degree of conformity of the interacting bodies in a

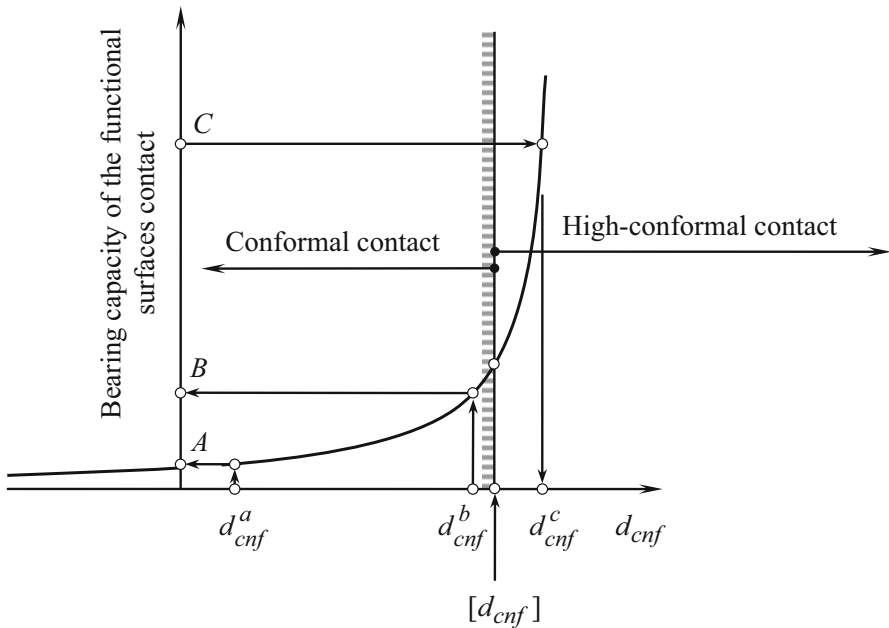


Fig. 3.21 Impact of the degree of conformity, δ_{cnf} , at contact point of two functional surfaces, B_1 and B_2 , onto the bearing capacity of the kinematic pair

kinematic pair. In “high-conformal kinematic pairs,” the degree of conformity of the functional surfaces, B_1 and B_2 , exceeds a threshold beyond which a significant increase in the bearing capacity of the interacting functional surfaces is observed. Schematically, this property of “high-conformal kinematic pairs” is illustrated in Fig. 3.22.

For a certain degree of conformity, d_{cnf}^a , at point of contact of the functional surfaces, B_1 and B_2 , the bearing capacity of the kinematic pair can be evaluated by a certain number, A . If the degree of conformity of the functional surfaces, B_1 and B_2 , is increased from d_{cnf}^a to a value of d_{cnf}^b , an insignificant increase in the bearing capacity of the kinematic pair from a number A to a number B occurs. An increase in the bearing capacity is insignificant in the case under consideration as both the degrees of conformity, d_{cnf}^a and d_{cnf}^b , are smaller than the threshold $[d_{cnf}]$, beyond which a significant increase in the bearing capacity of the functional surfaces, B_1 and B_2 , occurs.

Let us assume that the degree of conformity, d_{cnf}^c , is greater than the threshold, $[d_{cnf}]$. When the inequality $d_{cnf}^c > [d_{cnf}]$ is valid, the bearing capacity of the functional surfaces, B_1 B_2 , grows much faster.

In “high-conformal kinematic pairs,” the inequality $d_{cnf}^c \geq [d_{cnf}]$ is always observed.

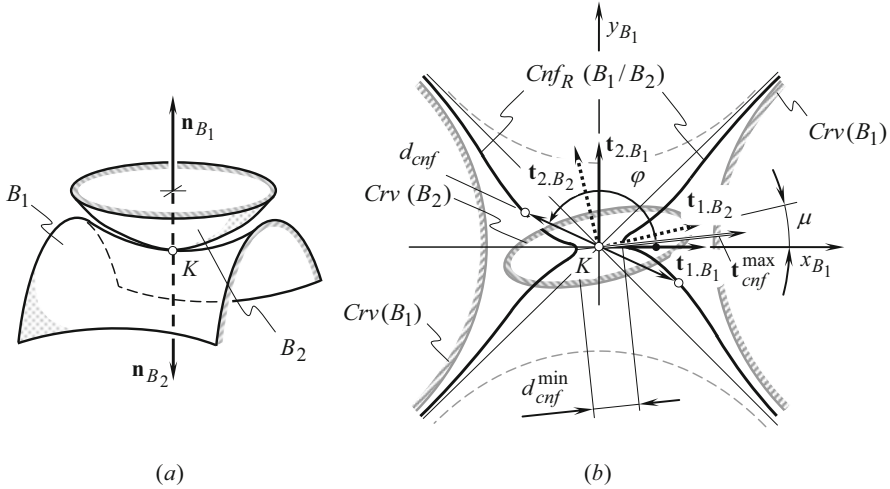


Fig. 3.22 An example of the indicatrix of conformity, $Cnf_R(B_1/B_2)$, constructed at point of contact of the functional surfaces, B_1 and B_2 , in a kinematic pair

Kinds of High-Conformal Point-Contact Kinematic Pairs I

At a single common point, K , high-conformal point-contact kinematic pairs feature convex-to-concave contact at least in a single plane through the common perpendicular (no “high-conformal point-contact kinematic pairs I” can be comprised by two convex functional surfaces, B_1 and B_2). Due to this feature, the minimal diameter, d_{cnf}^{min} , of the indicatrix of conformity, $Cnf_R(B_1/B_2)$, at point of contact of the functional surfaces, B_1 and B_2 , exceeds zero, that is, the inequality: $d_{cnf}^{min} > 0$ is always observed in all kinds of high-conformal point-contact kinematic pairs. On top of that, in high-conformal point-contact kinematic pairs, the minimum diameter of the indicatrix of conformity, $Cnf_R(B_1/B_2)$, is in the range of $0 < d_{cnf}^{min} \leq [d_{cnf}^{min}]$. Point-contact kinematic pairs of the kind under consideration are referred to as “high-conformal” as they feature a very small difference between radii of normal curvature in a common section by a plane through a common perpendicular. The “very small difference” can be quantified.⁶

⁶It is commonly adopted that “high-conformal point-contact kinematic pairs I” (as well as “high-conformal point-contact kinematic pairs II” below) cannot be composed of two convex functional surfaces, B_1 and B_2 , by a convex and a flatten surfaces and so forth. This is correct to a certain extent. For example, one can imagine a convex functional surface, B_1 , of elliptical kind with a flatten functional surface, B_2 . If the principal radii of curvature, $R_{1.B_1}$ and $R_{2.B_1}$, of the functional surface, B_1 , approach an infinity ($R_{1.B_1} \rightarrow \infty$ and $R_{2.B_1} \rightarrow \infty$), then any desirable degree of conformity of two convex functional surfaces, B_1 and B_2 , can be attained. Kinematic pairs of this particular kind (as well as of similar kinds) are not covered in this research. The same is valid with respect to “convex-to-convex” contacts of the functional surfaces.

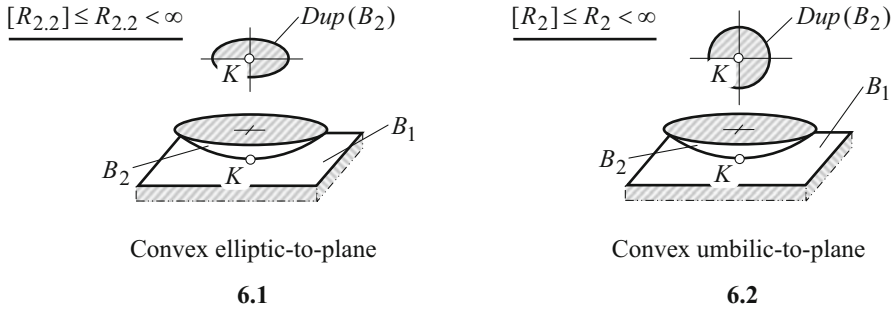


Fig. 3.23 Details on “high-conformal point-contact_I” kinematic pairs that feature a planar functional surface B_1 in contact with either elliptic, or umbilic functional surface B_2 . (In the diagram 6.1.: $R_{2,2}$ is the second principal radius of curvature of the B_2 (the following inequality is valid for $R_{2,2}$: $R_{2,2} > R_{1,2}$, where $R_{1,2}$ is the first principal radius of curvature of the B_2), $[R_{2,2}]$ is the minimal permissible value of the radii of normal curvature. In the diagram 6.2.: R_2 is the normal radius of curvature of the functional surface, B_2 (where $[R_2]$ is the minimal permissible value of the radii of normal curvature)

First, there are two different kinds of “high-conformal point-contact kinematic pairs I” kinematic pairs that feature either elliptic or umbilic functional surface, B_2 , in contact with a planar local patch of a mating functional pair, B_1 (see Fig. 3.23):

- Planar-to-elliptic-contact high-conformal kinematic pair.
- Planar-to-umbilic-contact high-conformal kinematic pair.

Kinematic pairs of this kind feature a single contact point between the functional surfaces B_1 and B_2 . In Fig. 3.8, these kinematic pairs correspond to 6.1 and 6.2, contacts of the functional surfaces B_1 and B_2 . Details on kinematic pairs of this particular kind are shown in Fig. 3.23. There are no constraints onto the actual value of the angle of local relative orientation, μ , of the contacting functional surfaces, B_1 and B_2 , for the kinematic pairs labeled 6.1 and 6.2.

Second, there are several different kinds of “convex-to-hyperbolic” “high-conformal point-contact kinematic pairs I” that feature different kinds of hyperbolic functional surface in contact with convex local patches of a mating functional surface. Kinematic pairs of this kind feature a single contact point between the functional surfaces B_1 and B_2 . In Fig. 3.8, these kinematic pairs correspond to 8.1, 8.2, 9.1, 9.2, 10.1, and 10.2, contacts of the functional surfaces B_1 and B_2 . The kinematic pairs of this kind are composed of two convex functional surfaces, B_1 and B_2 (see Fig. 3.24):

- Elliptic-to-hyperbolic (pseudo-concave) “high-conformal point-contact kinematic pairs I”.
- Umbilic-to-hyperbolic (pseudo-concave) “high-conformal point-contact kinematic pairs I”.
- Elliptic-to-minimal (pseudo-umbilic) “high-conformal point-contact kinematic pairs I”.

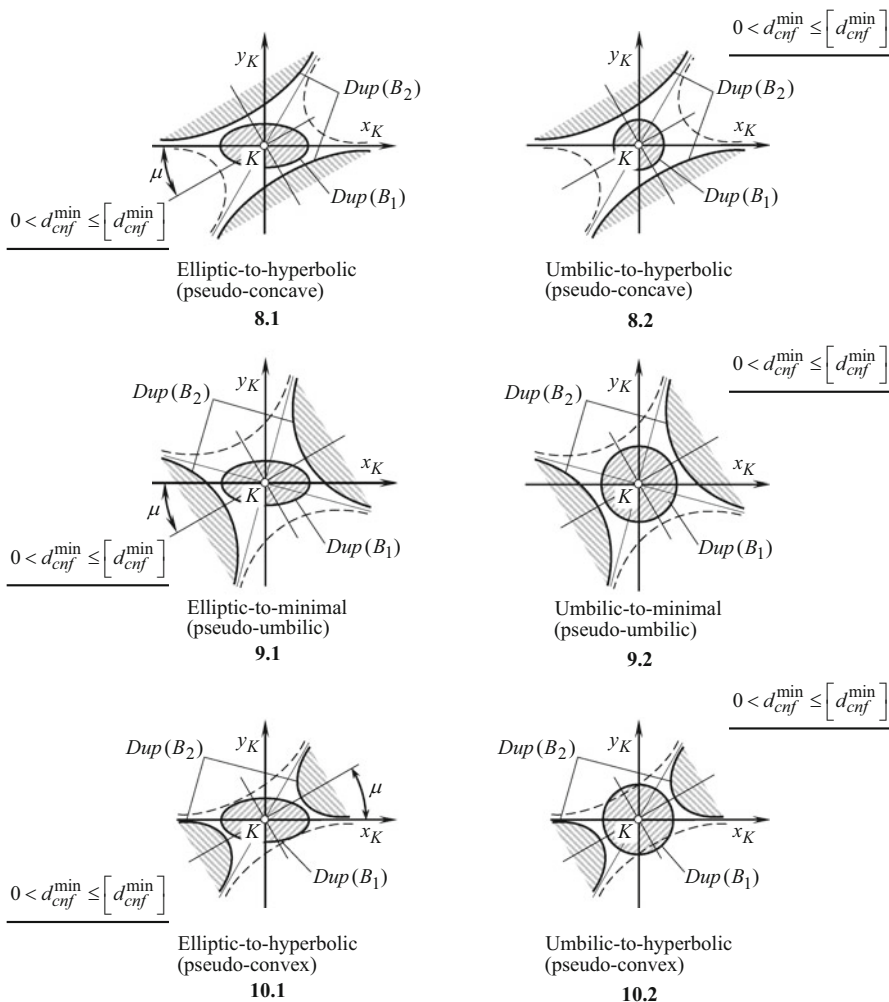


Fig. 3.24 The Dupin indicatrices, $Dup(B_1)$ and $Dup(B_2)$, at contact point of “high-conformal point-contact $_I$ ” kinematic pairs that feature convex-to-saddle-like “point-contact” of the functional surfaces B_1 and B_2 [in contacts 8.1, 9.1, and 10.1, the actual value of the angle, μ , of the functional surfaces, B_1 and B_2 , local relative orientation, is in the range of $-\mu < \mu < +\mu$]

- Umbilic-to-minimal (pseudo-umbilic) “high-conformal point-contact kinematic pairs Γ ”.
- Elliptic-to-hyperbolic (pseudo-convex) “high-conformal point-contact kinematic pairs Γ ”.
- Umbilic-to-hyperbolic (pseudo-convex) “high-conformal point-contact kinematic pairs Γ ”.

The following condition, $0 < d_{cnf}^{\min} \leq \left[d_{cnf}^{\min} \right]$, is valid for all six kinematic pairs listed above.

For the kinematic pairs labeled 8.1, 9.1, and 10.1, the actual value of the angle, μ , of the functional surfaces local relative orientation is in the range of $\mu_{\min} < \mu < \mu_{\max}$, where μ_{\min} and μ_{\max} are the minimum and the maximum permissible values of the angle μ , correspondingly.

There are no constraints onto the actual value of the angle of local relative orientation, μ , of the contacting functional surfaces, B_1 and B_2 , for the kinematic pairs labeled 8.2, 9.2, and 10.2.

Third, there are three different kinds of “convex-to-hyperbolic” “high-conformal point-contact kinematic pairs I” that feature different kinds of hyperbolic functional surfaces in contact with convex parabolic local patches of a mating functional surface. Kinematic pairs of this kind feature a single contact point between the functional surfaces B_1 and B_2 . In Fig. 3.8, these kinematic pairs correspond to 8.5, 9.5, and 10.5, contacts of the functional surfaces, B_1 and B_2 (see Fig. 3.25):

- Parabolic-to-hyperbolic (pseudo-concave)-contact kinematic pair.
- Parabolic-to-minimal (pseudo-umbilic)-contact kinematic pair.
- Parabolic-to-hyperbolic (pseudo-convex)-contact kinematic pair.

For the kinematic pairs of these three kinds, the actual value of the angle, μ , of the functional surfaces local relative orientation is in the range of $\mu_{\min} < \mu < \mu_{\max}$, where μ_{\min} and μ_{\max} are the minimum and the maximum permissible values of the angle μ , correspondingly.

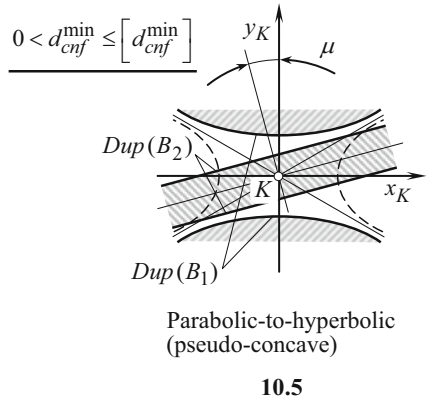
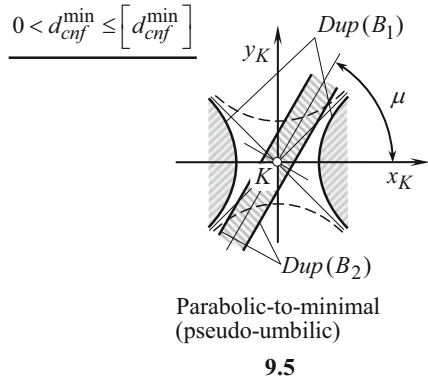
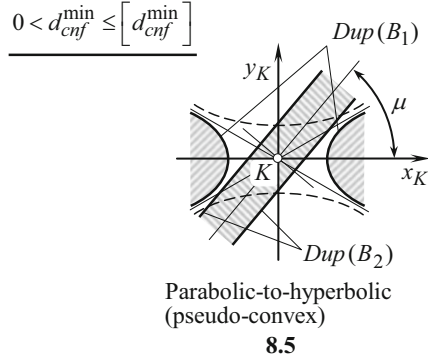
Fourth, there are three different kinds of “hyperbolic-to-hyperbolic” “high-conformal point-contact kinematic pairs I” that feature different kinds of hyperbolic functional surfaces in contact with hyperbolic local patches of a mating functional surface. Kinematic pairs of this kind feature a single contact point between the functional surfaces B_1 and B_2 . In Fig. 3.8, these kinematic pairs correspond to 10.8, 10.9, and 10.10, contacts of the functional surfaces B_1 and B_2 (see Fig. 3.26):

- Hyperbolic (pseudo-convex)-to-hyperbolic (pseudo-concave)-contact kinematic pair.
- Hyperbolic (minimal)-to-hyperbolic (pseudo-concave)-contact kinematic pair.
- Hyperbolic (pseudo-concave)-to-hyperbolic (pseudo-concave)-contact kinematic pair.

For the kinematic pairs of these three kinds, the actual value of the angle, μ , of the functional surfaces local relative orientation is in the range of $\mu_{\min} < \mu < \mu_{\max}$, where μ_{\min} and μ_{\max} are the minimum and the maximum permissible values of the angle μ , correspondingly.

Fifth, there are a few different kinds of “high-conformal point-contact kinematic pairs I” composed of different kinds of elliptic, umbilic, and parabolic, functional surfaces in contact. Kinematic pairs of this kind feature a single contact point between the functional surfaces B_1 and B_2 . In Fig. 3.8, these kinematic pairs

Fig. 3.25 Relative orientation of the Dupin indicatrices, $Dup(B_1)$ and $Dup(B_2)$, at contact point of “high-conformal point-contact_I” kinematic pairs that feature convex-parabolic-to-hyperbolic “true-point-contact” of the functional surfaces B_1 and B_2 (the actual values of the angle, μ , of the functional surfaces, B_1 and B_2 , local relative orientation is in the range of $\mu_{\min} \leq \mu \leq \mu_{\max}$)



correspond to 3.1, 3.2, 4.1, 4.2, 7.1, and 7.2, contacts of the functional surfaces B_1 and B_2 (see Fig. 3.27):

- Elliptic (convex)-to-elliptic (concave)-contact kinematic pair.
- Umbilic (convex)-to-elliptic (concave)-contact kinematic pair.

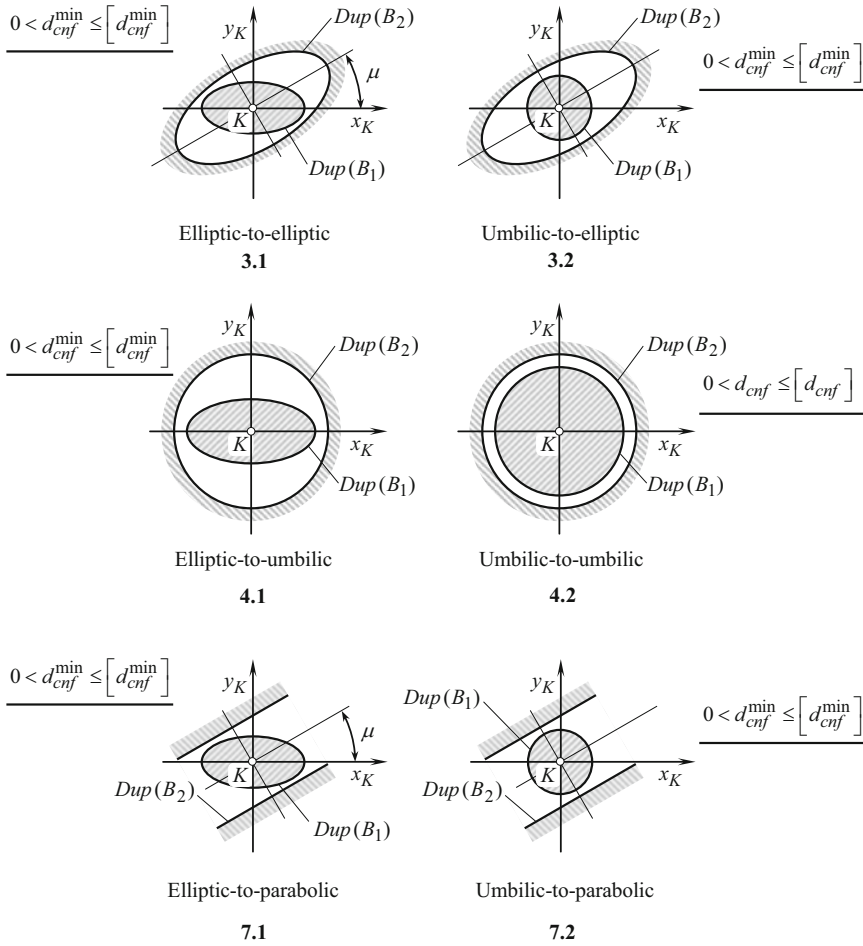


Fig. 3.26 Relative orientation of the Dupin indicatrices, $Dup(B_1)$ and $Dup(B_2)$, at contact point of kinematic pairs that feature concave “true-point-contact” of the functional surfaces B_1 and B_2 of elliptic, umbilic, and parabolic type (in the kinematic pairs labeled 3.1 and 7.1 the actual value of the angle, μ , of the functional surfaces, B_1 and B_2 , local relative orientation is in the range of $\mu_{min} \leq \mu \leq \mu_{max}$)

- Elliptic (convex)-to-umbilic (concave)-contact kinematic pair.
- Umbilic (convex)-to-umbilic (concave)-contact kinematic pair.
- Elliptic (convex)-to-parabolic (concave)-contact kinematic pair.
- Umbilic (convex)-to-parabolic (concave)-contact kinematic pair.

For the kinematic pairs of these three kinds, the actual value of the angle, μ , of the functional surfaces local relative orientation is in the range of $\mu_{min} < \mu < \mu_{max}$, where μ_{min} and μ_{max} are the minimum and the maximum permissible values of the angle μ , correspondingly.

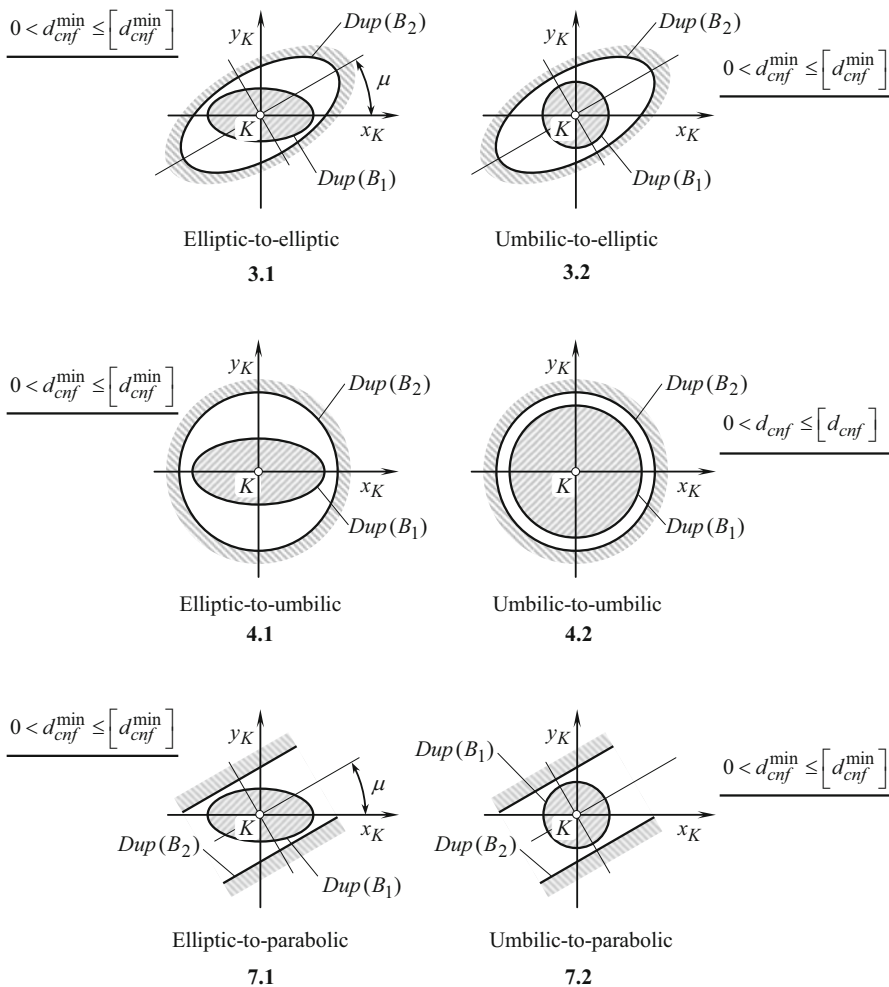


Fig. 3.27 Relative orientation of the Dupin indicatrices, $Dup(B_1)$ and $Dup(B_2)$, at contact point of kinematic pairs that feature concave “true-point-contact” of the functional surfaces B_1 and B_2 of either elliptic, or umbilic, or parabolic type (in the kinematic pairs labeled 3.1 and 7.1 the actual value of the angle, μ , of the functional surfaces, B_1 and B_2 , local relative orientation is in the range of $\mu_{\min} \leq \mu \leq \mu_{\max}$)

Summarizing, one can conclude that all possible kinds of point-contact kinematic pairs:

- Are composed of two functional surfaces B_1 and B_2 having one point in common.
- Feature five degrees of freedom.
- The minimal diameter, d_{cnf}^{\min} , of the indicatrix of conformity, $Cnf_R(B_1/B_2)$, at point of contact of the functional surfaces, B_1 and B_2 , is always of a positive value, that is, the inequality $d_{cnf}^{\min} > 0$ is always valid in point-contact kinematic pairs.

Point contact kinematic pairs of all kinds are covered in the discussion in Sect. 1.6.1.

3.1.6.2 Kinematic Pairs that Feature “Line-Contact” between the Functional Surfaces

In “line-contact kinematic pairs” (or just “ L_c -kinematic pairs,” for simplicity), the functional surfaces, B_1 and B_2 , make contact along an arc of a curve. A more in-detail analysis reveals that the following kinds of contact between the functional surfaces, B_1 and B_2 , have to be recognized in “line-contact kinematic pairs.”

Kinematic Pairs with True-Line-Contact of Functional Surfaces

The “true-line-contact” kinematic pairs (or just “ TL_c -kinematic pairs,” for simplicity) of different kinds are distinguished. In “true-line-contact” kinematic pairs, the functional surfaces, B_1 and B_2 , make contact along an arc of a curve. At every point of the line of contact, the arc of contact is entirely (locally) located in a section of the surfaces by a plane through the common perpendicular. In a particular case, this plane can be congruent to one of two principal planes of the surfaces. There is no correlation between radii of normal curvature in the rest of the normal planes. “True-line-contact” kinematic pairs of no design can be composed by two convex functional surfaces in contact.

First, there are numerous different kinds of “true-line-contact” kinematic pairs that are composed by either convex elliptic or convex umbilic or parabolic functional surfaces that make contact with concave functional surfaces of various geometries. The kinematic pairs of this kind are composed of two convex functional surfaces, B_1 and B_2 (see Fig. 3.28):

- Elliptic (concave)-to-elliptic (convex)-contact kinematic pair (3.1).
- Elliptic (concave)-to-umbilic (convex)-contact kinematic pair (3.2).
- Umbilic (concave)-to-elliptic (convex)-contact kinematic pair (4.1).
- Parabolic (convex)-to-parabolic (convex)-contact kinematic pair (5.5).
- Parabolic (convex)-to-parabolic (convex)-contact kinematic pair (6.5).
- Parabolic (concave)-to-flatten-contact kinematic pair (7.1).
- Parabolic (concave)-to-umbilic (convex)-contact kinematic pair (7.2).
- Parabolic (convex)-to-parabolic (convex)-contact kinematic pair (7.5).

In Fig. 3.8, these kinematic pairs correspond to 3.1, 3.2, 4.1, 5.5, 6.5, 7.1, 7.2, and 7.5, contacts of the functional surfaces B_1 and B_2 . Indicatrices of conformity, $Cnf_R(B_1/B_2)$, along with the Dupin indicatrices, $Dup(B_1)$ and $Dup(B_2)$, at contact point of the kinematic pairs of this particular kind are shown in Fig. 3.28. There are no constraints onto the actual value of the angle of local relative orientation, μ , of the contacting functional surfaces, B_1 and B_2 , for the kinematic pairs labeled 3.2, 4.1, 6.5, and 7.2. For the kinematic pairs labeled 3.1, 5.5, 6.5, and 7.1, the actual value of the angle, μ , of the functional surfaces, B_1 and B_2 , local relative orientation equals to $\mu = \pm 180^\circ$.

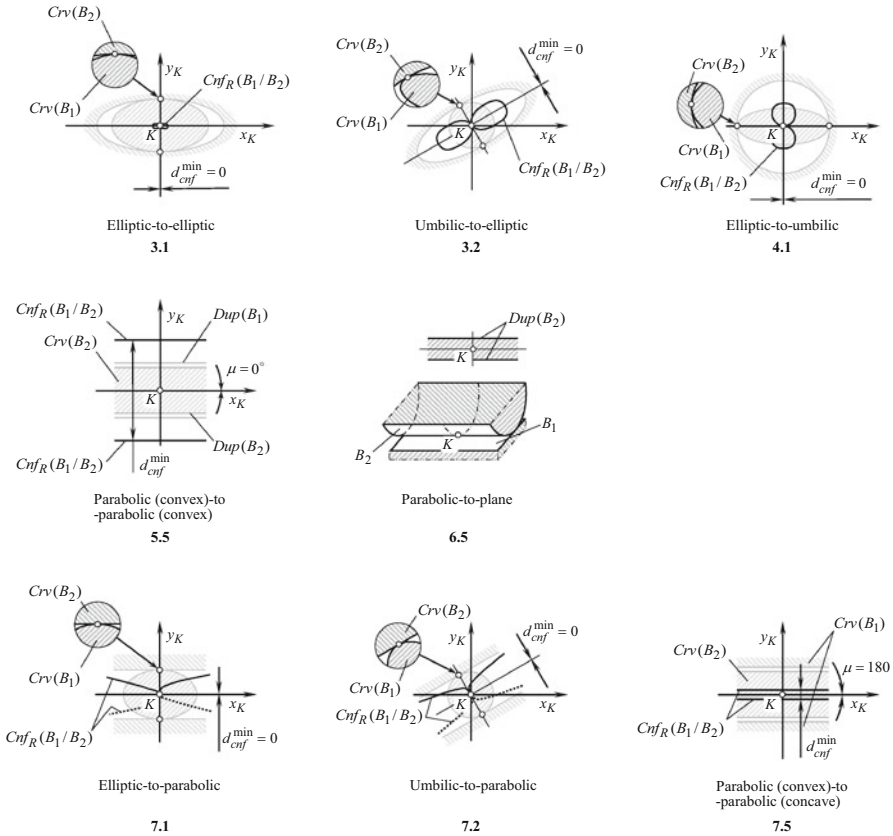


Fig. 3.28 Indicatrices of conformity, $Cnf_R(B_1/B_2)$, at contact point of kinematic pairs that feature convex-to-convex “true-line-contact” of the functional surfaces B_1 and B_2 (in the cases 3.1, 5.5, 7.1, and 7.5, the actual value of the angle, μ , of the functional surfaces, B_1 and B_2 , local relative orientation equals to $\mu = n \cdot 90^\circ$, n is an integer number; no constraints onto the angle, μ , is observed in the cases 3.2, 4.1, 6.5, and 7.2)

Second, there are several different kinds of “true-line-contact” kinematic pairs composed of elliptic, umbilic, and parabolic, functional surfaces that make contact with functional surfaces of hyperbolic geometry. Kinematic pairs of this kind feature a single contact point between the functional surfaces. In Fig. 3.8, these kinematic pairs correspond to 8.1, 8.2, 8.5, 9.1, 9.2, 9.5, 10.1, 10.2, and 10.5, contacts of the surfaces, B_1 and B_2 (see Fig. 3.29):

- Hyperbolic (pseudo-concave)-to-elliptic (convex)-contact kinematic pair (8.1).
- Hyperbolic (minimal)-to-elliptic (convex)-contact kinematic pair (8.2).
- Hyperbolic(pseudo-convex)-to-elliptic (convex)-contact kinematic pair (8.5).
- Hyperbolic (pseudo-concave)-to-umbilic (convex)-contact kinematic pair (9.1).
- Hyperbolic (minimal)-to-umbilic (convex)-contact kinematic pair (9.2).
- Hyperbolic(pseudo-convex)-to-umbilic (convex)-contact kinematic pair (9.5).

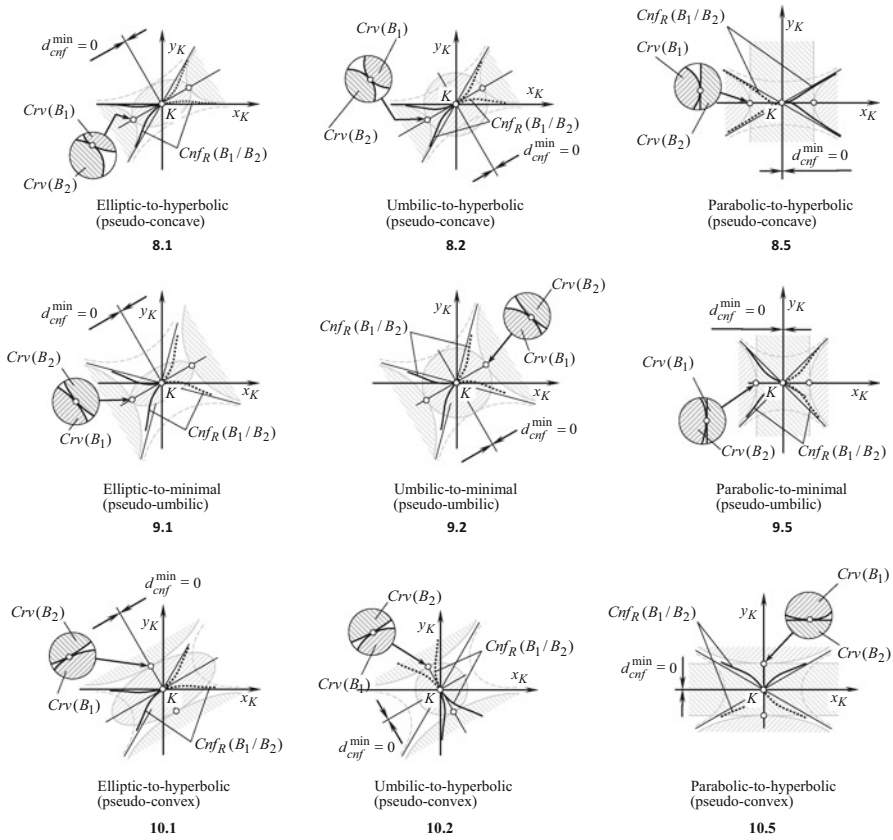


Fig. 3.29 Indicatrices of conformity, $Cnf_R(B_1/B_2)$, at contact point of true-line kinematic pairs that feature hyperbolic-to-convex “true-line-contact” of the functional surfaces B_1 and B_2 (in the cases 8.1, 9.5, 10.1, 8.5, 9.5, and 10.5, the actual value of the angle, μ , of the functional surfaces, B_1 and B_2 , local relative orientation equals to $\mu = n \cdot 90^\circ$, n is an integer number; no constraints onto the angle, μ , is observed in the cases 8.2, 9.9, and 10.2)

- Hyperbolic (pseudo-concave)-to-parabolic (convex)-contact kinematic pair (10.1).
- Hyperbolic (minimal)-to-parabolic (convex)-contact kinematic pair (10.2).
- Hyperbolic(pseudo-convex)-to-parabolic (convex)-contact kinematic pair (10.5).

For the kinematic pairs of the kinds labeled as 8.1, 8.2, 8.5, 10.1, 10.2, and 10.5, the actual value of the angle, μ , of the functional surfaces local relative orientation equals to $\mu = \pm 180^\circ$. No constraints on the actual value of the angle, μ , are imposed in the kinematic pairs 8.2, 9.2, 9.5, and 10.2.

Locally Surface-to-Surface Contact Kinematic Pairs II

The “locally-surface-to-surface_II-contact” kinematic pairs (or just “ $LSS_{c,2}$ —kinematic pairs,” for simplicity) are those that feature true line contact of the functional surfaces in a section by a normal plane and zero difference between magnitudes of radii of normal curvature, $R_{B,1}$ and $R_{B,2}$, in all the rest sections by a plane through a common perpendicular at contact point of the functional surfaces. Therefore, the *Dupin indicatrices*, $Dup(B_1)$ and $Dup(B_2)$, are congruent, and, thus, all the diameters of the indicatrix of conformity, $Cnf_R(B_1/B_2)$, are of a zero value, $d_{cnf}^{\min} = 0$.

“Locally-surface-to-surface_II-contact” kinematic pairs cannot be composed of two convex functional surfaces, B_1 and B_2 .

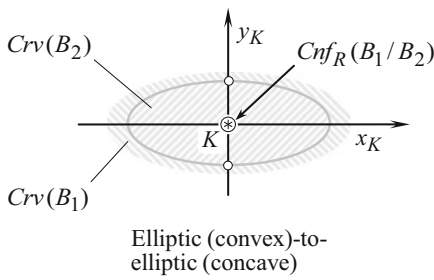
Different kinds of kinematic pairs with “locally-surface-to-surface_II-contact” of functional surfaces are distinguished.

There are four different kinds of “locally-surface-to-surface_II-contact” kinematic pairs that are composed by functional surfaces, B_1 and B_2 , of various geometries (see Fig. 3.30):

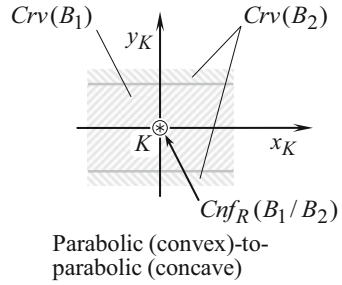
- Elliptic (convex)-to-elliptic (concave) “locally-surface-to-surface_II-contact” kinematic pair.
- Parabolic (convex)-to-parabolic (concave) “locally-surface-to-surface_II-contact” kinematic pair.
- Hyperbolic (minimal)-to-hyperbolic (minimal) “locally-surface-to-surface_II-contact” kinematic pair.
- Hyperbolic (pseudo-concave)-to-hyperbolic (pseudo-convex) “locally-surface-to-surface_II-contact” kinematic pair.

Kinematic pairs of this kind feature a common line of contact point between the functional surfaces, B_1 and B_2 , along with equal magnitude and opposite sign radii of normal curvature in sections by a plane through the common perpendicular. In Fig. 3.8, these kinematic pairs correspond to 3.1, 7.5, 9.9, and 10.8, contacts of the functional surfaces B_1 and B_2 . One can imagine the principal that the radii of curvature, R_{1B_1} , R_{2B_1} , R_{1B_2} , and R_{2B_2} , in the kinematic pairs 3.1, 4.2, 9.9, and 10.8, approach in infinity ($R_{1B_1} \rightarrow \infty$, $R_{2B_1} \rightarrow \infty$, $R_{1B_2} \rightarrow \infty$, and $R_{2B_2} \rightarrow \infty$). In such a scenario, the functional surfaces, B_1 and B_2 , are getting flatten. Actually, flattening of the functional surfaces is observed in any and all kind of kinematic pairs, and not only in the designs 3.1, 4.2, 9.9, and 10.8. Therefore, in Fig. 3.30, “locally-surface-to-surface_I-contact” kinematic pairs with flatten functional surfaces, B_1 and B_2 , are labeled as 1.1, 2.1, 2.2, 3.1, . . . , 10.9, and 10.10.

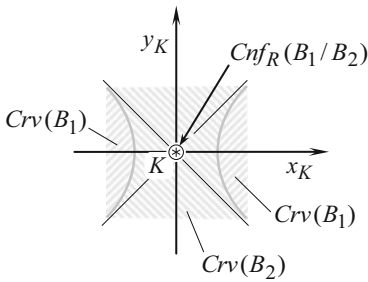
Relative orientation of the *curvature indicatrices*, $Crv(B_1)$ and $Crv(B_2)$, at contact point of the kinematic pairs of this particular kind is shown in Fig. 3.30. For the kinematic pairs under consideration, the actual value of the angle, μ , of the functional surfaces, B_1 and B_2 , local relative orientation equals to a value $\mu = \pm 180^\circ$.



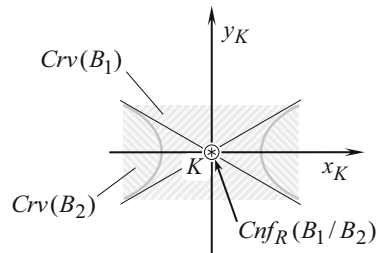
3.1



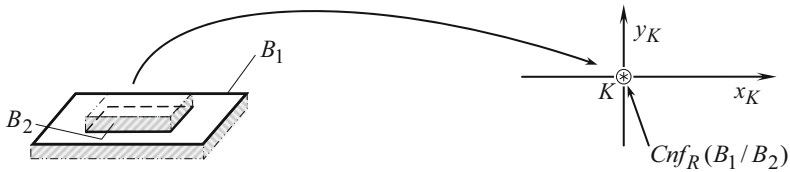
7.5



9.9



10.8



1.1, 2.1, 2.2, 3, ..., 10.9, 10.10

Fig. 3.30 Indicatrices of conformity, $Cnf_R(B_1/B_2)$, and the curvature indicatrices, $Crv(B_1)$ and $Crv(B_2)$, at contact point of “locally-surface-to-surface_II-contact” kinematic pairs [in all the contacts, the actual value of the angle, μ , of the functional surfaces, B_1 and B_2 , local relative orientation, equals $\mu = \pm 180^\circ$)]

The indicatrices of conformity, $Cnf_R(B_1/B_2)$, for kinematic pairs featuring “locally-surface-to-surface_II-contact” of the functional surfaces, B_1 and B_2 , are always shrunk to a point. This point is coincident with the contact point of the functional surfaces.

High-Conformal Point-Contact Kinematic Pairs II

The performance of kinematic pairs is strongly correlated to the degree of conformity of the functional surfaces, B_1 and B_2 , to each other at every point of their contact. The more conformal the surfaces B_1 and B_2 at points of their contact, the better the performance of the kinematic pair, and vice versa.

The “high-conformal point-contact kinematic pairs II” (or just “ $HC_{c,2}$ –kinematic pairs,” for simplicity) feature true line contact of the functional surfaces in one of two principal sections and a small difference between magnitudes of radii of normal curvature, $R_{B,1}$ and $R_{B,2}$, in all the rest sections by a plane through a common perpendicular at contact point of the functional surfaces. Therefore, the *curvature indicatrices*, $Crv(B_1)$ and $Crv(B_2)$, are congruent, and, thus, all the diameters of the indicatrix of conformity, $Cnf_R(B_1/B_2)$, are of a zero value, $d_{cnf}^{\min} = 0$.

Four different kinds of “high-conformal point-contact kinematic pairs II” composed of functional surfaces, B_1 and B_2 , of various geometries are distinguished (see Fig. 3.31):

- Elliptic (convex)-to-elliptic (concave) “locally-surface-to-surface_II-contact” kinematic pair.
- Parabolic (convex)-to-parabolic (concave) “locally-surface-to-surface_II-contact” kinematic pair.
- Hyperbolic (minimal)-to-hyperbolic (minimal) “locally-surface-to-surface_II-contact” kinematic pair.
- Hyperbolic (pseudo-concave)-to-hyperbolic (pseudo-convex) “locally-surface-to-surface_II-contact” kinematic pair.

At one of the principal sections, the functional surfaces make line contact, while in the other principal plane section, an inequality, $d_{cnf} \leq [d_{cnf}^{\min}]$, is observed [in all the contacts, the actual value of the angle, μ , of the functional surfaces, B_1 and B_2 , local relative orientation equals $\mu = \pm 180^\circ$]. In Fig. 3.8, these kinematic pairs correspond to 3.1, 7.5, 9.9, and 10.8, contacts of the functional surfaces B_1 and B_2 . Relative orientation of the *curvature indicatrices*, $Crv(B_1)$ and $Crv(B_2)$, at contact point of the kinematic pairs of this particular kind is shown in Fig. 3.31. For the kinematic pairs under consideration, the actual value of the angle, μ , of the functional surfaces, B_1 and B_2 , local relative orientation equals to a value $\mu = \pm 180^\circ$.

The indicatrices of conformity, $Cnf_R(B_1/B_2)$, for kinematic pairs featuring “locally-surface-to-surface_II-contact” of the functional surfaces, B_1 and B_2 , are always shrunk to a point. This point is coincident with the contact point of the functional surfaces.

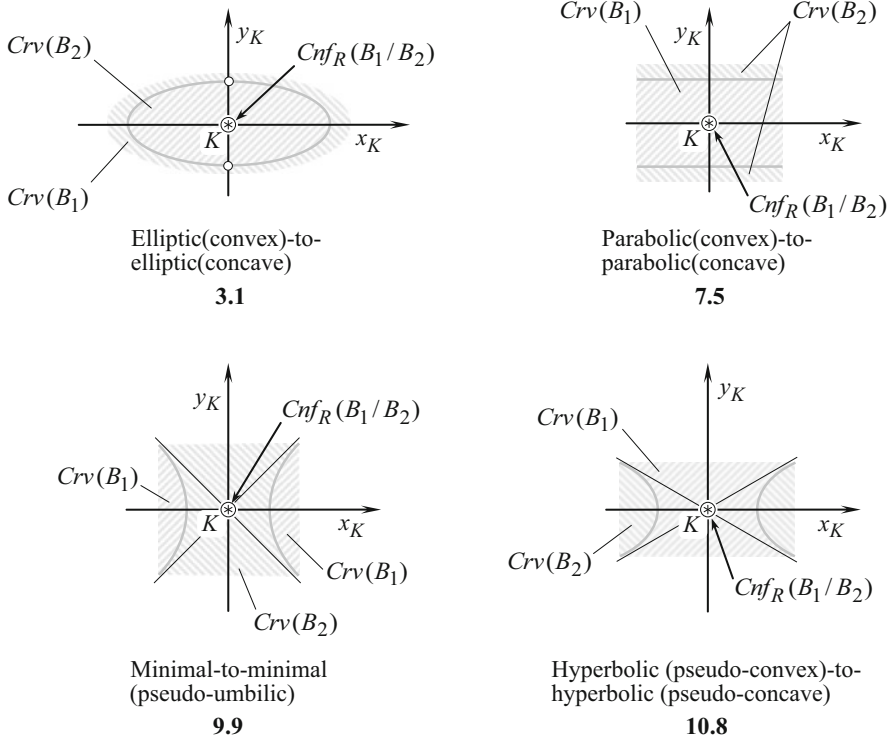


Fig. 3.31 Indicatrices of conformity, $Cnf_R(B_1/B_2)$, and the *curvature indicatrices*, $Crv(B_1)$ and $Crv(B_2)$, at “high-conformal point-contact kinematic pairs II” kinematic pairs. At one of the principal sections functional surfaces make line contact, while in the other principal plane section an inequality, $d_{cnf} \leq [d_{cnf}^{min}]$, is observed [in all the contacts, the actual value of the angle, μ , of the functional surfaces, B_1 and B_2 , local relative orientation, equals $\mu = \pm 180^\circ$]

3.1.6.3 Kinematic Pairs that Feature “Surface-to-Surface-Contact” between Functional Surfaces

In “surface-to-surface-contact kinematic pairs” (or just “ SS_c –kinematic pairs,” for simplicity), the functional surfaces, B_1 and B_2 , make contact within a common surface patch.⁷ A more in-detail analysis reveals that the following kinds of contact between the functional surfaces, B_1 and B_2 , have to be recognized in “surface-to-contact kinematic pairs.”

Considered locally, “surface-to-surface-contact kinematic pairs” cannot be distinguished from the shown in Fig. 3.18, “locally-surface-to-surface_I-contact”

⁷Kinematic pairs of the design under consideration can also be referred to as “true surface-to-surface contact kinematic pairs” (or just “ TSS_c –kinematic pairs,” for simplicity).

kinematic pairs and from the shown in Fig. 3.30 “locally-surface-to-surface_II-contact” kinematic pairs. Indicatrix of conformity at any point of contact of the functional surfaces in “surface-to-surface-contact kinematic pairs” is shrunk to a point. Moreover, “true-surface-to-surface-contact kinematic pairs” can be viewed as a reduced case of any of the shown in see Fig. 3.8. Kinematic pairs 1.1, 2.1, 2.2, 3.1, . . . , 10.9, and 10.10.

To avoid indefinites, the following is helpful to be taken into account.

In a kinematic pair, the functional surfaces, B_1 and B_2 , have to have at least one degree of freedom in relation to each other. Therefore, surfaces not of all geometries can be used in the design of kinematic pairs of the kind under consideration. In order to be suitable for application in the design of kinematic pairs that feature surface-to-surface-contact of the functional surfaces, a functional surface has to allow “sliding over itself.”

The property of surface B to allow for sliding over itself means that for the surface B there exists a corresponding motion: when performing this motion, the enveloping to the consecutive positions of the traveling surface B is congruent to the surface B itself.

According to that, the following functional surfaces that allow for sliding “over themselves” are recognized (see Fig. 3.32):

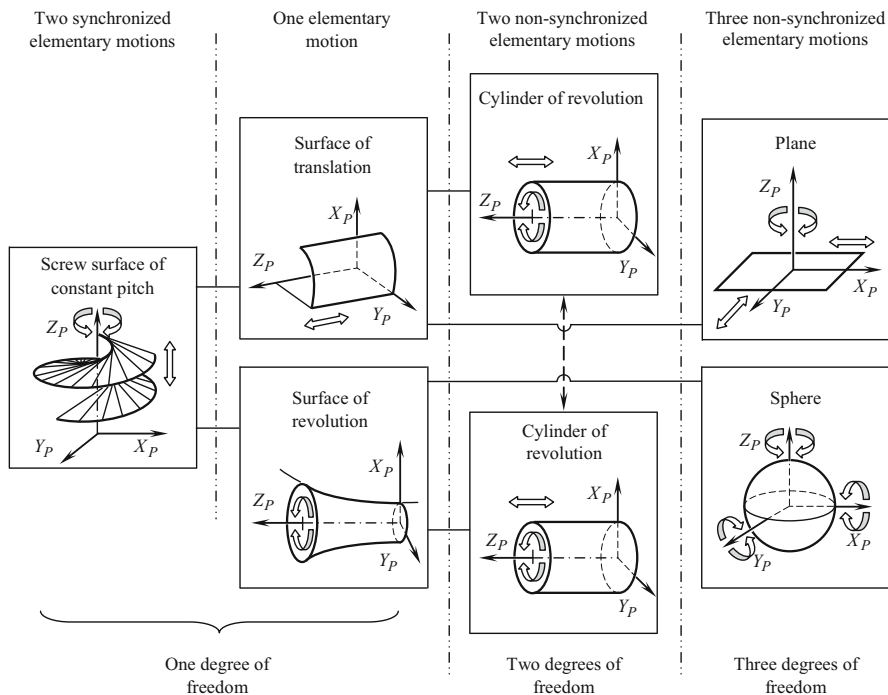


Fig. 3.32 Functional surfaces that allow for sliding over themselves

- A screw surface of a constant axial pitch ($p_x = Const$)—one degree of freedom.
- A surface of rotation about the centerline of the surface of revolution (the axial pitch of a screw surface is reduced to a zero $p_x = 0$)—one degree of freedom.
- A surface of translation along the directrix (the axial pitch of a screw surface approaches to an infinity $p_x \rightarrow \infty$)—one degree of freedom.

In addition, a few reduced cases of the surfaces that allow for sliding “over themselves” can also be distinguished:

- A cylinder of revolution (a cylinder of revolution allows a rotation about, as well as a straight motion along the centerline of the cylinder)—two degrees of freedom.
- A sphere (a sphere allows for three rotations about three axes independently)—three degrees of freedom.
- A plane (a plane surface allows straight motion in two different directions within the plane, as well as a rotation about an axis that is perpendicular to the plane)—three degrees of freedom.

It is proven [20–23] that there are no other kinds of functional surfaces that allow for sliding over themselves.

From the standpoint of surface geometry, kinematic pairs those composed of two screw surfaces are more complex (and are more general) compared to kinematic pairs composed either of the “sphere-to-sphere” surfaces (having a single degree of freedom) or of the “plane-to-plane” surfaces (both having three degrees of freedom).

A performed analysis of possible kinds of kinematic pairs composed of two surfaces congruent to one another reveals that there are only six possible kinds of kinematic pairs of this particular design. The kinematic pairs of all of these designs form a separate group of kinematic pairs.

There are six different kinds of kinematic pairs composed by two congruent local patches of functional surfaces, B_1 and B_2 :

- Screw-to-screw-contact kinematic pair (one DoF).
- Surface-of-rotation-to-surface-of-rotation-contact kinematic pair (one DoF).
- Surface-of-translation-to-surface-of-translation-contact kinematic pair (one DoF).
- Cylinder-of-rotation-to-cylinder-of-rotation-contact kinematic pair (two DoF).
- Sphere-to-sphere-contact kinematic pair (three DoF).
- Plane-to-plane-contact kinematic pair (three DoF).

“*True-surface-to-surface-contact kinematic pairs*” of no other design are feasible.

3.1.7 Classification of Kinematic Pairs

Depending on the kind of contact of two functional surfaces, the following groups of kinematic pairs are recognized:

P_c —kinematic pairs (i.e., point-contact kinematic pairs):

TP_c —kinematic pairs (i.e., true-point-contact kinematic pairs)—29 kinds in total.

LL_c —kinematic pairs (i.e., locally-line-contact kinematic pairs)—20 kinds in total.

$LS_{c,1}$ —kinematic pairs (i.e., locally-surface-to-surface_I-contact kinematic pairs)—7 kinds in total.

$HC_{c,1}$ —kinematic pairs (i.e., high-conformal-contact_I kinematic pairs)—20 kinds in total.

L_c —kinematic pairs (i.e., line-contact kinematic pairs):

TL_c —kinematic pairs (i.e., true-line-contact kinematic pairs)—23 kinds in total.

$LS_{c,2}$ —kinematic pairs (i.e., locally-surface-to-surface_II-contact kinematic pairs)—8 kinds in total.

$HC_{c,2}$ —kinematic pairs (i.e., high-conformal-contact_II kinematic pairs)—8 kinds in total.

SS_c —kinematic pairs (i.e., surface-to-surface-contact kinematic pairs):

TSS_c —kinematic pairs (i.e., true-surface-to-surface-contact kinematic pairs)—6 kinds in total.

The following classification of the discussed kinds of kinematic pairs, both, all earlier known, as well as all newly introduced kinematic pairs, are covered by the proposed classification.

Only $29 + 23 + 6 + 20 + 7 + 8 + 20 + 7 + 8 = 128$ kinds⁸ of contact of two smooth, regular surfaces P and T are possible in nature.⁹ For some kinds of the surfaces contact, no constraints are imposed on the actual value of the angle μ of local relative orientation of the functional surfaces, B_1 and B_2 . For the rest kinds of the functional surfaces contact, a corresponding range of the allowed value of the angle μ $[\mu_{\min}] \leq \mu \leq [\mu_{\max}]$ is specified. For particular cases of the functional surfaces contact, the only feasible value $\mu = [\mu]$ is allowed.

The proposed classification of possible kinds of kinematic pairs is illustrated by a chart shown in Fig. 3.33. As seen from Fig. 3.33, four stratum (I through IV) are distinguished in the classification. There are as many as 128 (in total) different kinds of kinematic pairs. The proposed classification (see Fig. 3.33) is self-consistent and complete (or, at least, potentially complete).

A more in-detail analysis of the kinematic pairs of all of the listed geometries is desirable.

In reality, the functional surfaces, B_1 and B_2 , in a kinematic pair are displaced in relation to one another (that is inevitable). The total displacement of the functional surfaces can be expressed in terms of three (a) elementary linear displacements (δ_x , δ_y , δ_z) along the axes of a local reference system, $x_K y_K z_K$, with the origin at contact point, K , and (b) three elementary angular displacements (φ_x , φ_y , φ_z) about the axes of the local reference system, $x_K y_K z_K$. If the linear, δ_x , δ_y , and δ_z , and the angular, φ_x , φ_y , and φ_z , displacements are taken into account, the so-called quasi-surface-to-

⁸It is desirable to have these numbers verified by an independent researcher(s).

⁹The results of a more in-detail investigation of all possible kinds of true point contact of two smooth, regular surfaces in the first order of tangency can be found in [5, 6, 16].

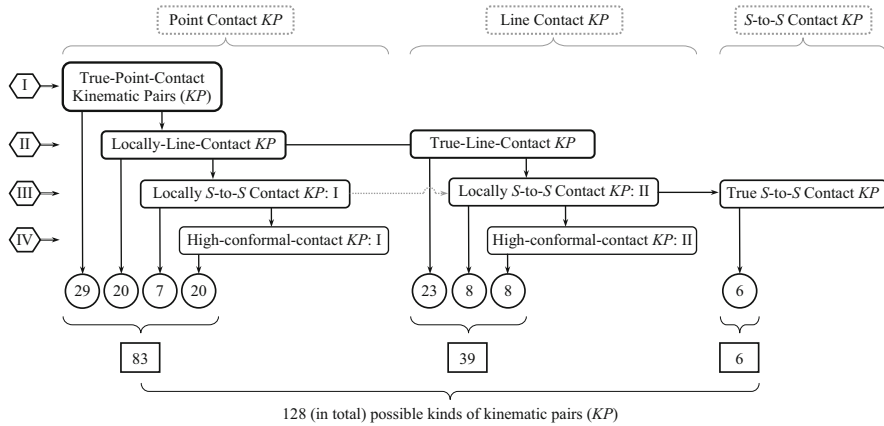


Fig. 3.33 Classification of possible kinds of kinematic pairs: There are as many as 128 (in total) different kinds of kinematic pairs (KP); S – to – S stands for “Surface-to-Surface” contact of the functional surfaces

surface-contact kinematic pairs of the first (I) and of the second (II) kind can be introduced into consideration. *Quasi-surface-to-surface-contact* kinematic pairs of the first (I) kind feature single contact point, *K*. *Quasi-surface-to-surface-contact* kinematic pairs of the second (II) kind feature a common contact line, *LC*. Incorporation of the *quasi-surface-to-surface-contact* kinematic pairs of the first (I) and of the second (II) kind into the analysis represents an additional way for further evolution of the proposed classification of the kinematic pairs (see Fig. 3.33). This potential concept is not covered in this text, and it may be a subject for future work.

3.2 Concluding Remarks

This chapter of the book deals with kinematic pairs. Possible kinds of kinematic pairs are investigated. Novel kinds of kinematic pairs are discovered. Correspondence between normal curvatures of functional surfaces in kinematic pairs is investigated. Instead of two groups of kinematic pairs commonly recognized in the nowadays practice (i.e., instead of the so-called *lower* kinematic pairs and *higher* kinematic pairs), it is proposed to distinguish three groups of kinematic pairs, namely:

- (a) “Point-contact kinematic pairs” (or just “ P_c –kinematic pairs,” for simplicity)
- (b) “Line-contact kinematic pairs” (or just “ L_c –kinematic pairs,” for simplicity)
- (c) “Surface-to-surface-contact kinematic pairs” (or just “ S_c –kinematic pairs,” for simplicity)

The concept of three groups of kinematic pairs is originated from two patents [18] (of 1983) and [19] (of 1984) and is based on the research undertaken by the author in the late 1970s.

A novel classification of all possible kinds of kinematic pairs is proposed. The proposed classification is potentially complete and is open for further improvements.

Proper labeling can be used for identification of kinematic pairs: instead of the indefinite terms “higher kinematic pair” and “lower kinematic pair,” appropriate labels (for instance, the kinematic pair #11.7) can be used instead.

A more in-detail analysis of the kinematic pairs of all of the listed geometries is desirable.

References

1. Reuleaux, F., *Lehrbuch der Kinematik*, Braunschweig, 1875, Bd. [Reuleaux, F., *The kinematics of machinery, 1876, (translated and annotated by A.B.W. Kennedy), reprinted by Dover, New York, 1963*].
2. Usher, A.P., *A History of Mechanical Inventions*, Harvard University press, 1929, (reprinted by Dover Publications, 1968).
3. Sacs, E., & Joskowicz, L. (1995). Computational kinematic analysis of higher pairs with multiple contacts. *Journal of Mechanism Design*, 117, 269–277.
4. https://www.google.com/search?biw=1600&bih=795&tbm=isch&sa=1&ei=wE-4XI71B4bGsQXx0LrIBQ&q=kinematic+pairs&oq=kinematic+pairs&gs_l=img.3..0j0i5i30j0i24i2j0i10i24j0i24.505617.511411..512063...0.0..0.151.1499.10j5.....0....1..gws-wiz-img.....0i67j0i8i30.h8wfvuv3iQL#imgcr=FcmEUK9k2CPn3M
5. Radzevich, S.P., *Theory of Gearing: Kinematics, Geometry, and Synthesis*, 2nd Edition, revised and expanded, CRC Press, Boca Raton, FL, 2018, 934 pages. (First edition: Radzevich, S.P., *Theory of Gearing: Kinematics, Geometry, and Synthesis*, CRC Press, Boca Raton, Florida, 2012, 743 pages).
6. Radzevich, S. P. (2020). *High-Conformal Gearing: Kinematics and Geometry* (2nd ed., p. 550). Amsterdam: Elsevier. [1st edition: CRC Press, Boca Raton, Florida, 2015, 332 pages].
7. Snidle, H. P., & Evans, H. P. (1995). Elastohydrodynamic lubrication of real surfaces. *Tribology Series*, 30, 219–227.
8. Cauchy, A. L. (1826). *Leçons sur les Applications du Calcul Infinitésimal à la Geometrie*. Paris: Imprimerie royale.
9. Dvornikov, L. T. (2014). Fundamentals of the theory of geometric connections (kinematic pairs) in mechanical systems. *Theory of Mechanisms and Machines*, 12(2), 25–49. <http://tmm.spbstu.ru/24/3Dvornikov.pdf>.
10. Dvornikov, L. T. (2001). *Theory of kinematic pairs*. Novokuznetsk: Siberia State Industrial University Publishers.
11. Zhivago, E.Ya., *Theory and Systematization of Kinematic Pairs of Mechanical Systems*, Dr.Sci Thesis, Siberia State Industrial University, Novokuznetsk, 2000, 261 pages.
12. Lagrange, J. L. (1797). *Theorie des Fonctions Analytiques*. Paris: Impr. De la République, prairial an V. 277 p.
13. Favard, J. (1957). *Course de Géométrie Différentielle Locale* (p. viii+553). Paris: Gauthier-Villars.
14. Radzevich, S.P., *Methods of Analysis of Contact Geometry of Free-Form-Part Surface and the Generating Surfaces of the Cutting Tool*, Dneprodzerzhinsk, DII (UkrNIINTI, 30.03.1988, No. 759-Uk88), 1987, 103 pages.

15. Radzevich, S. P. (May 2004). Mathematical modeling of contact of two surfaces in the first order of tangency. *Mathematical and Computer Modeling*, 39(9–10), 1083–1112.
16. Radzevich, S. P. (2014). *Generation of surfaces: Kinematic geometry of surface machining*. Boca Raton, Florida: CRC Press. 738 pages.
17. Radzevich, S. P. (2019). *Geometry of Surfaces: A Practical Guide for Mechanical Engineers* (2nd ed.). Springer International Publishing, Springer Nature Switzerland AG (2020), XXVI, 329 pages, (First edition: Wiley, 2013, 264 pages).
18. Pat. No. 1,185,749, USSR, *A Method of Sculptured Surface Machining on a Multi-Axis NC Machine*.S.P. Radzevich, Int. Cl. B23c 3/16, Filed: October 24, 1983.
19. Pat. No. 1,249,787, USSR, *A Method of Sculptured Surface Machining on a Multi-Axis NC Machine*.S.P. Radzevich, Int. Cl. B23c 3/16, Filed: December 27, 1984.
20. Darboux, G., *Sur le Déplacement d'une Figure Invariable*, Comptes rendus de l'Académie des science, XCII, 1981, pp.118–121. [Quoted after: Bottema, O. and Roth, B., *Theoretical Kinematics*, Dover Publications, Inc., New York, 1990, 558 pages (page 304)].
21. Denavit, J., & Hartenberg, R. S. (1955). A kinematics notation for lower-pair mechanisms based on matrices. *ASME Journal of Applied Mechanics*, 77, 215–221.
22. doCarmo, M.P., *Differential geometry of curves and surfaces*, Prentice-Hall, Englewood Cliffs, NJ, 1976, 503p.
23. Eisenhart, L. P. (1909; New York, reprint 1960). *A Treatise on the Differential Geometry of Curves and Surfaces* (p. 474). London: Dover Publications, Inc..
24. Hartenberg, R. S., & Denavit, J. (1964). *Kinematic synthesis of linkages* (pp. 17–18). New York: McGraw-Hill.

Further Readings

- Dvornikov, L.T., Zhivago, E.Ya., *Fundamentals of the Theory of Kinematic Pairs: The Monograph*, Novokuznetsk, SbGIU Publishers, 1999, 105 pages.
- Ertel, A.M, *Hydrodynamic Calculation of Lubrication of Spatial Surfaces Contact (Gear Meshes, Rolling Bearings, Extremely Heavily Loaded Journals, and so forth)*, Moscow, TsNIITMash, 1945, No. 1, 64 pages.
- Ertel, A. M. (1939). Hydrodynamic theory of lubrication in new applications. *Applied Mathematics and Mechanics*, 3(2), 41–49.
- Khrushchov, M. M. (1996). On the history of the development of the theory of Elastohydrodynamic lubrication. *Friction and Wear*, 17(5), 703–706.
- Krishna, R. K., & Sen, D. (2019). Second-order total freedom analysis of 3D objects in a single point contact. *Mechanism and Machine Theory*, 140, 10–30.
- Mohrenstein-Ertel, A., “Die Berechnung der hydrodynamischen Schmierung gekrümmter Oberflächen unter hoher Belastung und Relativbewegung”, *Fortschr.-Ber. VDI-Z, Reihe 1*, Nr. 115, Düsseldorf, 1984, s. 85–89.
- Radzevich, S. P. (November 2005). A possibility of application of Plücker’s Conoid for mathematical modeling of contact of two smooth regular surfaces in the first order of tangency. *Mathematical and Computer Modeling*, 42(9–10), 999–1022.

- Radzevich, S. P. (2001). *Fundamentals of surface generation* (p. 592). Kiev, Rastan: Monograph. (In Russian).
- Radzevich, S. P. (2007). *Kinematic geometry of surface machining*. Boca Raton, FL: CRC Press. 508p.
- Radzevich, S. P. (2005). On Analytical Description of the Geometry of Contact of Surfaces in Higher Kinematic Pairs. *Theory for Mechanisms and Machines*, 3(2), 3–14. <http://tmm.spbstu.ru>.
- Zhivago, E.Ya., *Fundamentals of the Theory of Kinematic Pairs*, Sci.Dr. Thesis, 05.02.18: Theory of Mechanisms and Machine, SibSIU, Novokuznetsk, 2000, 261 pages.

Chapter 4

High-Performance Plastic Gears



C. M. Illenberger , T. Tobie , and K. Stahl

Nomenclature

a (mm)	Center distance
a_{ACR} (–)	Auxiliary factor to calculate $Y_{\epsilon, ACR}$
A_G (m ²)	Heat dissipating surface of the mechanism housing
b (mm)	Face width
b_H (mm)	Hertzian semi-width
b_w (mm)	Common face width of the gear pair
C_α (μm)	Amount of tip relief
c' (N/(mm·μm))	Single stiffness
d_1 (mm)	Reference diameter
ED (–)	Relative tooth-engagement time
F_N (N)	Normal force
F_R (N)	Friction force
F_t (N)	Tangential force
f_{zi} (–)	Correction factor of $\Delta\epsilon_w$
$f_{\epsilon\beta}$ (–)	Correction factor of overlap ratio
i (–)	Transmission ratio
H_V (–)	Tooth loss factor
K_A (–)	Application factor
K_F (–)	Application factor for tooth root load
$K_{F\alpha}$ (–)	Face factor
$K_{F\beta}$ (–)	Width factor
K_H (–)	Factor for tooth flank loading
K_v (–)	Dynamic factor

C. M. Illenberger (✉) · T. Tobie · K. Stahl
Gear Research Centre (FZG), Technical University of Munich (TUM), Munich, Germany
e-mail: illenberger@fzg.mw.tum.de

k_W	$10^{-6} \cdot \text{mm}^3 / (\text{N} \cdot \text{m})$	Wear coefficient
$k_{\vartheta, Fla}$	$\text{K} \cdot (\text{m/s})^{0.75} \cdot \text{mm}^{1.75} / \text{W}$	Heat transfer coefficient of the plastic gear (flank)
$k_{\vartheta, Fu\beta}$	$\text{K} \cdot (\text{m/s})^{0.75} \cdot \text{mm}^{1.75} / \text{W}$	Heat transfer coefficient of the plastic gear (root)
l_{Fl}	(mm)	Profile line length of the active tooth flank
m_n	(mm)	Normal module
N_L	(-)	Number of load cycles
P	(W)	Power
p_{er}	(mm)	Transverse normal base pitch
p_H	(N/mm ²)	Hertzian pressure
$R_{\lambda, G}$	(K·mm ² /W)	Heat transfer resistance of the mechanism housing
S_{Fmin}	(-)	Required minimum safety factor (root)
S_{Hmin}	(-)	Required minimum safety factor (flank)
$T_{1, 2}$	(Nm)	Torque
T_d	(Nm)	Torque
u	(-)	Transmission ratio
$v_{1, 2}$	(m/s)	Circumferential speed
v_g	(m/s)	Sliding speed
v_t	(m/s)	Tangential speed
v_{Σ}	(m/s)	Sum speed
Vol	(m ³)	Volume
w	(N/mm)	Normal line load
W_m	(mm)	Averaged linear wear
W_{zul}	(mm)	Permissible linear wear
Y_{Fa}	(-)	Form factor
Y_{Sa}	(-)	Stress correction factor
Y_{St}	(-)	Stress correction factor
Y_{β}	(-)	Helix angle factor
Y_{ϵ}	(-)	Contact ratio factor
$Y_{\epsilon, ACR}$	(-)	Modified contact ratio factor
$z_{1, 2}$	(-)	Number of teeth (pinion/wheel)
Z_E	(-)	Elasticity factor
Z_H	(-)	Zone factor
Z_R	(-)	Surface roughness factor
Z_{β}	(-)	Spiral angle factor
Z_{ϵ}	(-)	Contact ratio factor
$\Delta \epsilon_w$	(-)	Load-induced increase in actual contact ratio
$\Delta \epsilon_{zi}$	(-)	Approximated increase in actual contact ratio due to the numbers of teeth
$\Delta \vartheta_{tooth}$	(K)	Increase of tooth temperature
ϵ_{α}	(-)	Transverse contact ratio
$\epsilon_{\alpha, w, mod}$	(-)	Modified actual contact ratio
ϑ_0	(°C)	Ambient temperature
$\vartheta_{Fu\beta}$	(°C)	Tooth root temperature
ϑ_{Fla}	(°C)	Tooth flank temperature

ϑ_M ($^{\circ}\text{C}$)	Bulk temperature
ϑ_{oil} ($^{\circ}\text{C}$)	Oil temperature
μ (-)	Coefficient of friction
σ_F (N/mm^2)	Tooth root stress
σ_{F0} (N/mm^2)	Nominal tooth root stress
σ_{FlimN} (N/mm^2)	Fatigue strength
σ_{FP} (N/mm^2)	Permissible root strength
σ_H (N/mm^2)	Flank pressure
σ_{HlimN} (N/mm^2)	Rolling contact fatigue strength
σ_{HP} (N/mm^2)	Permissible flank pressure

4.1 Introduction

Plastic gears are gaining more and more importance and are used in new applications. In the past, the focus was mostly on motion transmission in actuators, but current developments show a trend toward applications with higher drive power. In the automotive sector, in addition to a large number of electric actuators driven by plastic gears, safety-critical applications such as braking and steering systems are increasingly equipped with plastic gears. In the drive unit of e-bikes, plastic gears are the current state of the art, and the use of plastic gears is also conceivable in the drive train of small urban electric vehicles. In order to dimension plastic gears in line with requirements and to fully exploit the potential of thermoplastic materials, solid knowledge of material behavior is required both during production and in subsequent operation. This chapter explains the current state of the art for plastic gears and offers comprehensive insights into current research projects.

4.1.1 *State of the Art and Application of Plastic Gears*

4.1.1.1 Materials and Properties

The mechanical-thermal properties resulting from the molecular structure of different plastics allow a classification of the materials into different sub-categories: thermosetting plastics, elastomers and thermoplastics. In the environment of drive technology, semi-crystalline thermoplastics are mainly used as gear materials. Among others acc. to [1], the following semi-crystalline thermoplastics are particularly relevant for the production of plastic gears:

- High-molecular polyethylene of high density (PE-HD).
- Polyoxymethylene (POM).
- Polyamide (PA).

Table 4.1 Mechanical properties of typically applied thermoplastic gear materials [2]

Material	Density in kg/m ³	Young's modulus at 23 °C in N/mm ²	Tensile strength at 23 °C in N/mm ²	Max. continuous operating temperature in °C
PA 46	1.20	3300	100	140
PA 66	1.15	3000	85	90
POM	1.41	2900	65	90
PEEK	1.28	3600	100	250

- Polybutylene terephthalate (PBT).
- Polyetheretherketone (PEEK).

To further increase the mechanical properties or to specifically adjust them, fiber reinforcements are often added to the respective base material. Glass or carbon fibers are usually applied to the matrix materials to increase the mechanical parameters such as Young's modulus and tensile strength. Further, the addition of aramid fibers is possible to improve the mechanical properties. In order to positively influence the frictional properties, especially in dry running, friction-reducing additives such as graphite and polytetrafluoroethylene (PTFE) may be utilized. This enables on the one hand the reduction of the friction coefficient and the associated heat generation in the tooth contact; on the other hand, efficiency, wear, and service life can be optimized. When selecting friction-reducing fillers, however, it should be noted that the fillers are primarily recommended for improving the tribological properties on the tooth flank, where they have a positive effect, while other mechanical properties such as strength can be negatively influenced [2].

The mechanical properties of thermoplastics differ significantly from those of metallic construction materials. For instance, the Young's modulus and tensile strength are not only several times lower than those of steel but are also highly temperature-dependent. High-loading speeds increase tensile strength and Young's modulus, while elongation at break decreases. In static loading, plastics are deformed by creep [2]. Table 4.1 shows the mechanical properties as well as the maximum continuous operating temperature of exemplary thermoplastic gear materials that are chosen typically when designing plastic gears.

An increase in temperature reduces the fraction of semi-crystalline areas in the material, which results in a reduction of the Young's modulus and the strength properties. If the glass transition temperature is exceeded, a significant reduction of the mechanical properties is to be expected.

Humidity is another influencing parameter on the properties of plastic gears. Thermoplastic materials absorb moisture from the environment to varying degrees. An increasing moisture content reduces the yield stress and the modulus of elasticity. Furthermore, the absorption of moisture leads to volume changes due to expansion [2].

Thermoplastic materials exhibit viscoelastic material behavior. This behavior is responsible for the material damping of thermoplastic materials. The damping coefficients differ depending on the type of material and temperature. The high-

Table 4.2 Resistance of typically applied thermoplastics to chemicals acc. to [2] (+ resistant, ○ limited resistance, - not resistant)

Chemical		PA 46	PA 66	POM	PEEK
Alcohols	Methanol	+	○	+	+
	Ethanol	+	○	+	+
	Propanol	+	○	+	+
Water	Cold	+	+	+	+
	Hot	○	○	○	+
Fuels	Gasoline	+	+	+	+
	Diesel	+	+	+	+
Acids	Hydrochloric acid	-	-	-	○
	Sulfuric acid	-	-	-	-
	Acetic acid	-	-	-	+
Bases	Potassium hydroxide		+	+	+
	Sodium hydroxide		+	+	+
	Ammonium hydroxide		○	+	+

damping characteristics compared to steel materials have a positive effect on the noise emissions of plastic gears. Another important property of thermoplastics is their resistance to gaseous and liquid chemicals. Table 4.2 shows the resistance of exemplary thermoplastics to chemicals acc. to [2]. Resistance to chemicals allows plastic gears to operate in environments where steel gears cannot be used due to corrosion.

4.1.1.2 Manufacturing

The vast majority of plastic gears produced are injection molded. Depending on the material used, the desired gear quality as well as the quantities produced and the size of the individual components, other manufacturing processes such as casting or machining processes can also be considered. For the production of high volumes, the injection molding process is typically the most cost-effective manufacturing process in terms of individual unit costs. In this process, the thermoplastic granulate is melted and injected via a screw into a cavity, where the melt takes on the shape of the cavity after solidification. In addition to the low unit costs, another major advantage of the injection molding process is the largely free design of the mold. In addition to conventional involute gears, alternative geometries can also be manufactured which can only be machined to a limited extent by conventional hobbing. Highly integrated components can further be manufactured. In order to achieve a sufficiently precise gearing quality, however, it is necessary to consider the shrinkage of the material during the cooling process. Components with large wall thicknesses tend to form voids and to shrink during cooling, which is why the production of injection molded gears is subject to production limitations. The addition of fiber reinforcements can reduce shrinkage. Depending on the flow

direction, however, considerable differences in shrinkage behavior can occur, which can lead to distortion in the component [2].

A further manufacturing process is the unpressurized casting of larger components with part masses starting at approximately 1 kg. The raw component is machined after polymerization, since the materials used (PA6G, PA12G) lead to comparatively high shrinkage, which cannot be compensated by corrections in the mold [2].

For small and medium series, machining processes are applied to a large extent. For this purpose, the same tools are suitable as are used for the production of steel gears. However, the constraint on the hobbing movement for the production of involute gears represents a limitation in the design of machined plastic gears.

The manufacturing accuracy and the resulting gearing quality are strongly dependent on the manufacturing method and the respective process conditions.

4.1.1.3 Design

The design possibilities offered by injection molding are very diverse. In particular, it is possible to injection mold stepped gears and overmold shafts and hubs. Further, there is the possibility of direct manufacturing of highly integrated components. Different wall thicknesses cause an unequal shrinkage behavior during cooling of the component and can lead to distortion and internal stresses. For the purpose of economic production, the gears can be equipped with cutouts. On the one hand, this reduces the amount of resources required during production and, on the other hand, reduces the weight of the component. It is advisable to ensure that the cutouts are symmetrically arranged to minimize distortion of the plastic gear. In order to increase the stiffness of the gear body ribs can be applied.

If possible, the torque should be transmitted form-fittingly from the gear to the corresponding shaft. Overmolding of inserted shafts generally results in good centering of the gear teeth. When manufacturing large-size plastic gears, larger steel inserts can be overmolded to reduce dimensional changes due to shrinkage [2].

4.1.1.4 Fields of Application

Plastic gears are used within a wide range of power starting from less than 0.001 kW in small consumer goods to up to approximately 1 kW in high performance applications such as e-bike transmissions. A large share of the applications for plastic gears is in the household appliance sector. Here, plastic gears are used not only for drives in toys, but also, and in particular, in kitchen appliances and tools. In many cases, the plastic gears are operated dry or with starved lubrication. A lifetime lubrication with grease is often used. In applications in printing and food technology, the use of a lubricant is often completely avoided due to hygiene requirements. A growing market for plastic gear wheels can be found especially in the smart home sector, where new functions are realized by means of electric drives. Here,

automatically controlled roller blinds, venetian blinds as well as automatic garage doors, roof windows and other applications are suitable for the use of plastic gears.

Plastic gears are also increasingly used in the automotive sector. The reason for this is the constant introduction of new functions such as electrically adjustable mirrors, belt tensioners, seat adjustment, and many other applications, which above all increase comfort. But also, in the area of safety-relevant functions, plastic gears are increasingly used in the automotive sector. These include, for example, the parking brake and electric power steering, where plastic gears are used. In the powertrain segment, plastic gears are used primarily in the field of electric micromobility. Plastic gears are nowadays an essential part of the drive train of e-bikes. The power to be transmitted by the e-bike is in the range of the power that can be transferred with high-performance plastics. Although plastic gears are not yet used for the currently growing market of electrified urban light vehicles with drive powers of <15 kW, in view of new material developments and improved calculation and simulation possibilities, plastic gears appear at least conceivable, so that the achievable performance can be continually increased.

4.1.2 Design and Calculation Methods for Plastic Gear Applications

4.1.2.1 Tooth Temperature

The knowledge of the gear surface and bulk temperature is of essential meaning when designing plastic gears. Since material properties such as elasticity and strength are highly temperature dependent, the resulting temperature distribution during operation has to be known to avoid undesired failure such as melting or fatigue damage due to reduced gear strength at elevated temperatures. Particularly in dry or starve-lubricated systems the maximum drive power is limited due to the low thermal conductivity of the plastic gears and the rise of the gear temperatures during operation. Fig. 4.1. shows melting damages on a dry running PA12 gear. Grease lubrication is one possibility to reduce friction in the gear contact and thus minimize friction losses in order to increase the possible drive power. Operation under oil-lubricated conditions is another way to drastically increase the maximum drive power since the generated heat is not only reduced by means of lower friction losses due to lubrication but heat is also removed from the gear contact by the lubricant itself. Another possibility to reduce gear temperatures and to increase transferable power is to modify the tooth geometry in order to reduce friction losses by means of loss-optimized gear geometry [3].

Among the first investigations on the thermal behavior of plastic gears is the work of Hachmann and Strickle [4] in the 1960s. They conducted experimental investigations on the thermal operating behavior of polyamide gears and the resulting gear strength. As a result of their research they suggested a method to calculate the bulk and surface temperature of plastic gears under different lubrication modes. The basic

Fig. 4.1 Melting damage at PA12 gears [3]



calculation method consists of a thermal equilibrium between the heat generated in the tooth contact and the heat dissipated from the gearbox to the outside. Depending on the material pairing, geometry, lubrication conditions, and drive power, the tooth temperature will increase until a thermal equilibrium is achieved. Hachmann and Strickle derive equations for the determination of tooth temperatures from their experimental investigations. The influence of viscoelastic losses on the temperature rise is neglected. The basic method is used until present and forms also the core of the temperature calculation used in VDI 2736 [5].

Blok [6] introduces an approach to determine the flank surface temperature based on the model of a strip-shaped heat source moving over the tooth flank during tooth engagement. This model considers friction losses due to load, geometry, and the resulting sliding speeds. The calculation of the temperature rise in dependence of the sliding speeds results in the fact that there is no temperature rise calculated at the pitch point, which resembles a simplification since only friction losses are considered and other effects such as viscoelasticity are neglected when determining the tooth temperature with this approach.

A further method for tooth temperature determination is suggested by Takanashi and Shoji [7]. They consider not only the effect of frictional losses on the gear temperature but also viscoelastic losses. The viscoelastic effects are modelled using a spring-damper approach. The heat generated in the tooth contact is calculated from the sum of the two components, friction and viscoelasticity. The generated heat is also compared to the heat dissipated by the gearbox, and a state of equilibrium of

Table 4.3 Coefficient of friction [25]

Lubrication	Pairing	μ
Circulating oil	All	0.04
Oil mist	All	0.07
Grease	All	0.09
Dry	Plastic/steel	0.20
	PA/PA	0.40
	POM/POM	0.28
	POM/PA	0.18
	PA/PBT	0.35
	POM/PBT	0.18

Table 4.4 Heat transfer resistance of the metallic mechanism housing in $K \cdot m^2/W$ [25]

Mechanism	$R_{\lambda,G}$
Open with unimpeded entry of air	0
Partially open housing	0.015...0.045
Closed housing	0.060

Table 4.5 Heat transfer coefficients of the plastic gear in $K \cdot (m/s)^{0.75} \cdot mm^{1.75}/W$ [25]

Lubrication	Pairing	$k_{\theta, Fu\beta}$	$k_{\theta, Flanke}$
Circulating oil	All	0	0
Dry/grease/oil mist	Plastic/plastic	2.1×10^3	9.0×10^3
	Plastic/steel	0.9×10^3	6.3×10^3

constant steady-state temperature is determined. A particular challenge in the application of the calculation approach is often the availability of material characteristics. Due to the large number of parameters required, this method is used in comparatively few cases.

The currently most widely used method for determining tooth temperatures on plastic gears is published in VDI 2736 [5]. The calculation method is strongly derived from the approach of Hachmann and Strickle [4] and is based on the same basic assumptions. Eqs. (4.1) and (4.2) show the calculation approach for determining tooth root and tooth flank temperature according to VDI 2736 [5]. Tables 4.3, 4.4 and 4.5 show the required parameters for the temperature calculation according to VDI 2736 [5].

$$\vartheta_{Fu\beta} \approx \vartheta_0 + P \cdot \mu \cdot H_V \cdot \left(\frac{k_{\theta, Fu\beta}}{b \cdot z \cdot (v_t \cdot m_n)^{0.75}} + \frac{R_{\lambda, G}}{A_G} \right) \cdot ED^{0.64} \quad (4.1)$$

$$\vartheta_{Fla} \approx \vartheta_0 + P \cdot \mu \cdot H_V \cdot \left(\frac{k_{\theta, Fla}}{b \cdot z \cdot (v_t \cdot m_n)^{0.75}} + \frac{R_{\lambda, G}}{A_G} \right) \cdot ED^{0.64} \quad (4.2)$$

4.1.2.2 Tooth Load Carrying Capacity Acc. To VDI 2736

The considerable differences between the material properties of metallic gears and those of gears made of thermoplastics require a dedicated calculation method for determining load carrying capacity of plastic gears. In order to calculate the lifetime of involute metallic gears DIN 3990 [8] or ISO 6336 [9] are commonly used. These standards have been developed and improved for several decades and are also used as the basic framework for the tooth load carrying capacity of thermoplastic gears.

Tooth Root Load Carrying Capacity

To calculate the tooth root load carrying capacity, the single teeth of a plastic gear are represented by the model of a fixed cantilever beam. The area of maximum bending stress appears in the area of the tooth root at the contact point of 30°-tangent and the tooth root radius. The approach according to VDI 2736 [5] is based on DIN 3990 method C [8] and assumes that the tooth force attacks at the tooth tip of the plastic gear. Equations (4.3) to (4.5) show the calculation process for determining the tooth root load carrying capacity. The fatigue strength σ_{FlimN} thereby differs for each type of thermoplastic:

$$\sigma_F = \frac{F_t}{m_n \cdot b} \cdot Y_{Fa} \cdot Y_{Sa} \cdot Y_{\beta} \cdot Y_{\varepsilon} \cdot K_A \cdot K_v \cdot K_{F\beta} \cdot K_{Fa} \leq \sigma_{FP} \quad (4.3)$$

$$\sigma_{FP} = \sigma_{FlimN} \cdot Y_{St} / S_{Fmin} \quad (4.4)$$

$$\sigma_{FlimN} = f(\vartheta_{FuB}, N_L) \quad (4.5)$$

The occurring tooth root stress is determined by the external load and geometric parameters as well as other influencing factors such as dynamics of the overall system and load distribution. VDI 2736 [5] requires a safety factor of $S_{Fmin} = 1.6$ for intermittent operation at N_L load cycles and a safety factor of $S_{Fmin} = 2.0$ for continuous operation until $N_L = 10^8$ load cycles. VDI 2736 [5] contains temperature and load-cycle-dependent tooth root strength values for several thermoplastics such as POM and PA66. However, for a large number of relevant thermoplastic materials, no strength data is available.

Tooth Flank Load Carrying Capacity

The approaches used to determine the tooth flank load carrying capacity are based on those for the calculation of steel gears acc. to DIN 3990 [8]. Equations (4.6) to (4.8) show the calculation of the flank load carrying capacity of thermoplastic spur gears as a function of temperature and load cycles acc. to VDI 2736 [5]. The rolling contact fatigue strength σ_{HlimN} thereby differs for each type of thermoplastic:

$$\sigma_H = Z_E \cdot Z_H \cdot Z_\varepsilon \cdot Z_\beta \cdot \sqrt{\frac{F_t \cdot K_H}{b_w \cdot d_1} \cdot \frac{u+1}{u}} \leq \sigma_{HP} \quad (4.6)$$

$$\sigma_{HP} = \sigma_{HlimN} \cdot Z_R / S_{Hmin} \quad (4.7)$$

$$\sigma_{HlimN} = f(\vartheta_{Fla}, N_L) \quad (4.8)$$

The calculated flank pressure σ_H is compared to the permissible flank pressure σ_{HP} (Eq. (4.7)). VDI 2736 [5] requires a safety factor of $S_{Hmin} = 1.25$ for intermittent operation at N_L load cycles and a safety factor of $S_{Hmin} = 1.4$ for continuous operation until $N_L = 10^8$ load cycles. The respective strength values σ_{HlimN} are load cycle and temperature dependent. VDI 2736 [5] contains flank strength values for a limited number of thermoplastic materials such as PA66 and PBT.

Frictional Wear Load Carrying Capacity

Abrasive wear is particularly relevant for dry running, as the tooth surfaces are not separated by a lubricant film. VDI 2736 [5] contains a calculation approach to determine the averaged linear wear of dry running plastic gears. Equations (4.9) and (4.10) show the calculation approach for the determination of wear.

$$W_m = \frac{T_d \cdot 2 \cdot \pi \cdot N_L \cdot H_V \cdot k_W}{b_w \cdot z \cdot l_{Fl}} \leq W_{zul} \quad (4.9)$$

$$W_{zul} = (0.1 \dots 0.2) \cdot m_n \quad (4.10)$$

According to VDI 2736 [5], the averaged linear wear W_m is compared to a permissible linear wear W_{zul} in order to calculate the gear lifetime with regard to wear. Further details such as wear coefficients for various materials are contained in VDI 2736 [5].

4.1.3 Recent Research Results

4.1.3.1 Thermal Behavior

Since the resulting gear temperature during operation is one of the main influence factors on gear lifetime, investigations to determine the gear temperature, respectively the knowledge of the occurring gear temperature are necessary. Besides the drive power, the tooth temperature is mainly influenced by the lubrication conditions and the tooth geometry. Within the scope of extensive investigations, different geometries and materials are examined and evaluated with regard to their tooth temperature under varying test conditions. The following section shows essential

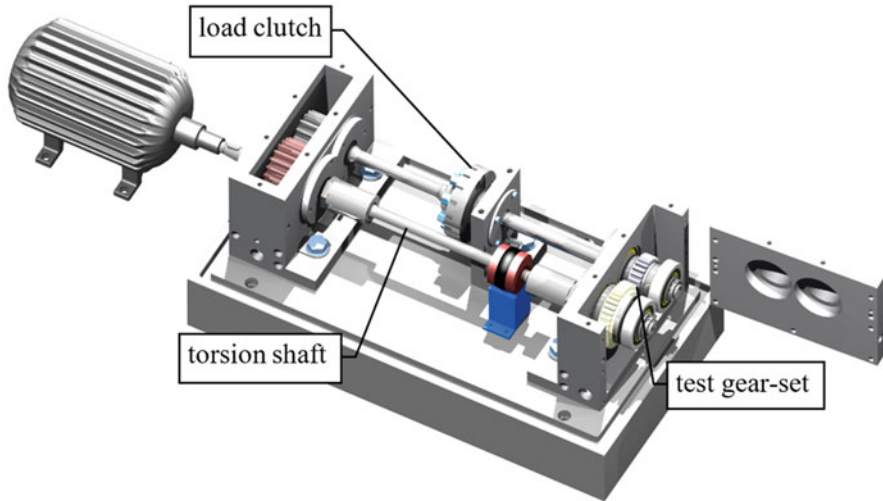


Fig. 4.2 FZG back-to-back test rig [10]

results from research projects investigating the operating behavior and load carrying capacity of plastic gears [3, 10, 11].

The tooth temperatures of plastic gears investigated in Klicken oder tippen Sie hier, um Text einzugeben. are determined on the FZG standard back-to-back test rig acc. to DIN ISO 14635 [12]. Fig. 4.2 shows the test rig with mounted test gears. It uses a closed power loop principle (four-square configuration) to provide a fixed torque to a pair of test gears. Two shafts connect the slave gear unit with the test gearbox. On the pinion shaft, there is a load clutch to apply a load torque (i.e., by using a load lever and weights). Therefore, one half of the load coupling is locked, while the other half can be loaded. During operation, the electric engine only provides the occurring losses of the system. The test rig can be run in different lubrication configurations. Apart from dry running, grease and oil lubrication can also be used. Using oil lubrication, either oil sump or oil injection lubrication can be applied. Heating cartridges and cooling pipes in the gear housing as well as an external tempering unit for the injected oil allow controlling of the lubricant temperature in the oil sump.

The gear temperature can be monitored during operation using thermal sensors that are applied in bores located at different positions in the plastic gear. The sensor signal is routed through a hollow shaft to a telemetry system which enables continuous sampling of the temperature measurements during back-to-back testing [11]. Fig. 4.3 shows a thermal sensor in the middle of the tooth chord of an exemplary plastic test gear. To characterize the thermal operating behavior of the plastic gears, stage tests are conducted where speed is raised in steps at constant torque until a thermal equilibrium is reached.

Fig. 4.3 Thermal sensor to measure tooth temperature [11]

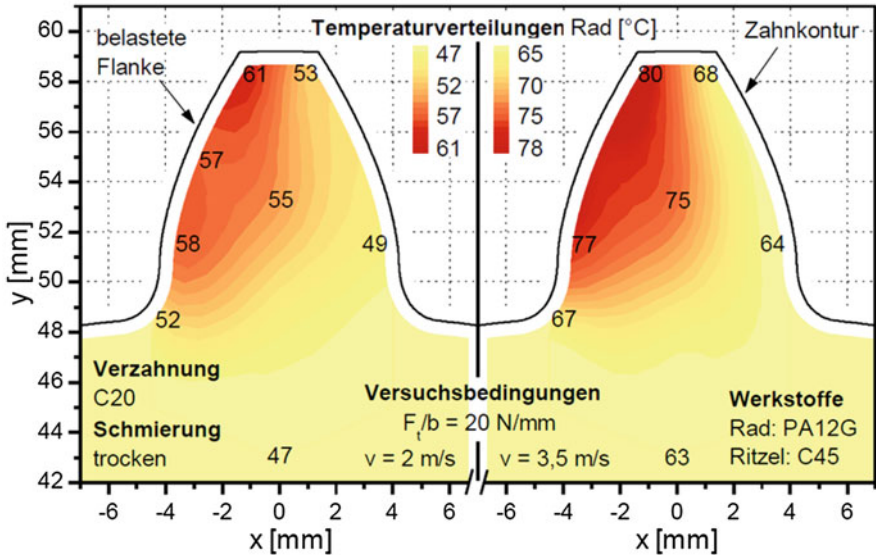
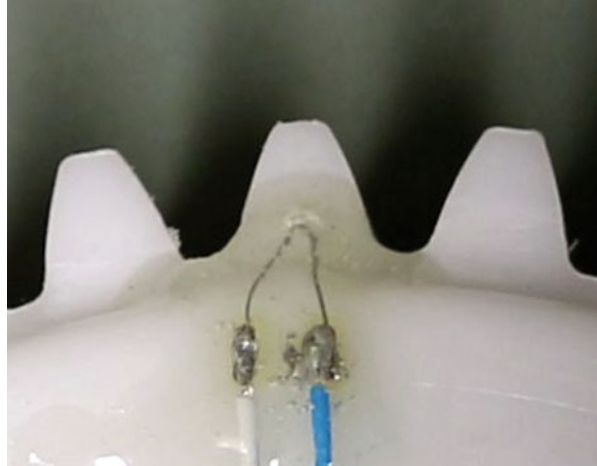


Fig. 4.4 Exemplary stationary temperature distribution of a PA12G test gear, operation at room temperature, geometry C20 (see Table 4.6) [3]

The comparatively low thermal conductivity of different plastic materials results in locally different tooth temperatures within the plastic tooth especially during dry running due to lower heat dissipation from the tooth contact without lubricant.

Figure 4.4 shows exemplary temperature distributions in a gear tooth of the test gear geometry C20 (see Table 4.6) at two different speeds. The temperature distributions are interpolated on the basis of the measured data. In addition to the loaded

Table 4.6 Low loss test gear geometry

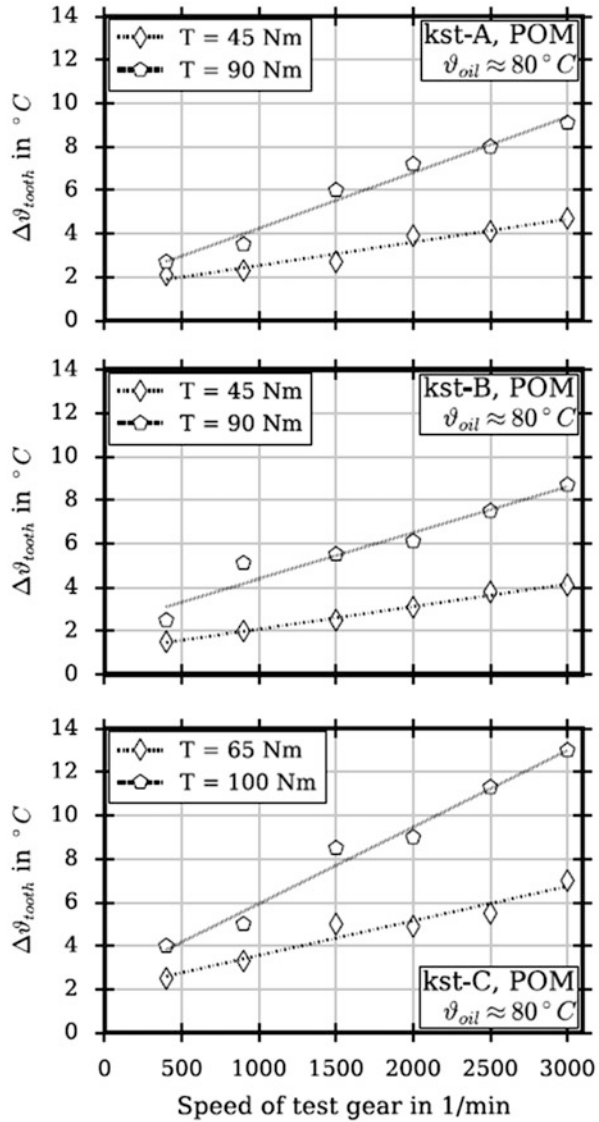
Geometry	C20		C20S		LL30		LL40	
	Pinion	Wheel	Pinion	Wheel	Pinion	Wheel	Pinion	Wheel
Centre distance (mm)	91.5							
Normal module (mm)	4.5		4.5		2.75		1.75	
Normal pressure angle (°)	20		20		30		40	
Helix angle (°)	0		31		26		15	
Face width (mm)	22	20	22	20	22	20	22	20
Number of teeth (-)	16	24	14	21	24	36	40	60
Tip diameter (mm)	82.5	118.5	84.4	119.7	78.2	114.1	74.8	110.8
Transverse contact ratio (-)	1.44		1.45		1.01		0.45	
Total contact ratio (-)	1.44		2.18		2.03		1.39	

tooth flanks, the temperature of the unloaded flank is determined as well. It is apparent that the loaded tooth flank has the highest temperatures. In the area of the pitch point there are slightly lower temperatures than in the dedendum and addendum flank area. This is attributed to the sliding speeds decreasing toward the pitch point. The temperature of the loaded tooth root area is below that of the loaded flank area. The tooth flank friction can therefore be identified as the decisive heat source. Damping losses in the tooth root area obviously play a subordinate role with PA12G in dry running [3].

The temperature increases, especially in dry running, due to the lack of cooling effect by the lubricant depending on the operating conditions, to some extent considerably. To enable the transmission of higher power, plastic gears are usually operated using a lubricant. Measurements of the tooth temperature under oil-lubricated conditions show a considerably lower temperature increase compared to dry-running plastic gears.

Following the equations for determining the tooth temperature according to VDI 2736 [5], the tooth temperature is influenced by the geometric parameters of the test gear, the heat transfer coefficient, and also the transferred power [10]. Investigations of the tooth bulk temperature with polyacetal (POM) gears are carried out at oil-lubricated conditions. The investigated geometries KST-A ($m_n = 1$ mm), KST-B ($m_n = 2$ mm), and KST-C ($m_n = 3$ mm) are of different design size. The geometries are described in detail in Table 4.8. The results of the temperature measurements are shown in Fig. 4.5. Speed is varied under constant load and oil-sump temperature. The difference between oil temperature and measured bulk temperature is evaluated and in the following referenced to as $\Delta\vartheta_{tooth}$. Speed is raised in stages from 400 rpm to 3000 rpm after the tooth bulk temperature has reached steady conditions. Under constant load, $\Delta\vartheta_{tooth}$ rises with increasing imparted energy. The amount of heat resulting from higher sliding velocities in tooth contact and viscoelastic losses, due to tooth deflection under load, leads to higher $\Delta\vartheta_{tooth}$. Higher loads affect higher Hertzian stress and tooth deflections,

Fig. 4.5 Measured temperature difference between tooth bulk temperature and oil temperature of KST-A,B,C (POM) [11]



resulting in increasing tooth temperatures. For all tooth geometries, $\Delta\vartheta_{tooth}$ is within the same dimension of approximately 4 to 12 K at 3000 rpm depending on the transferred torque. Additional tests at lower oil temperatures are conducted in which comparable values for $\Delta\vartheta_{tooth}$ are monitored [11].

Knowledge of the occurring tooth temperatures is essential in plastic gear design. Temperature is influenced by various parameters such as material, lubrication, geometry, and load. Extensive experimental research has been performed to investigate the thermal operation behavior of plastic gears. It was shown that oil

lubrication is a suitable measure to reduce frictional heat generation in comparison to dry running. Further research work has to be done in order to characterize more materials and to establish reliable thermal operating data required for the plastic gear design process.

4.1.3.2 Low Loss Plastic Gears

Temperature dependent material properties and limited operational temperatures limit the use of plastic gears. One possibility to enhance the operational scope of plastic gears is a change of the gear geometry. Low loss gears feature the following geometric properties: High pressure angles result in smaller tooth height and a shortened path of contact. The tooth contact is concentrated around the pitch point. This results in a reduction of frictional losses and thus less heat generation. Furthermore, a better coefficient of efficiency can be achieved and the transferable power can be raised significantly. Fig. 4.6 shows an exemplary steel-plastic pairing with low loss geometry.

In Fig. 4.7, a comparison between different test gear geometries is shown. The geometries are shown in true scale in axial cross section. The smaller normal module

Fig. 4.6 Low loss geometry
LL40, PA12G/16MnCr5 [3]

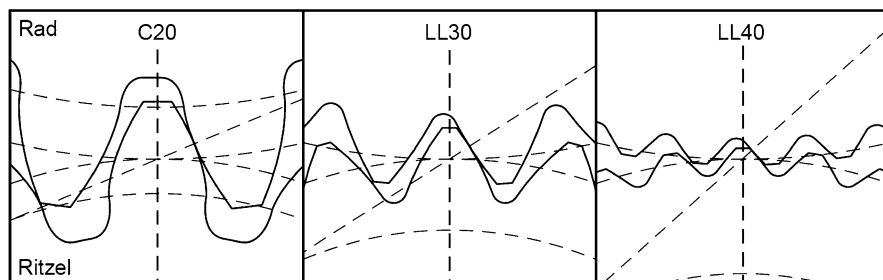
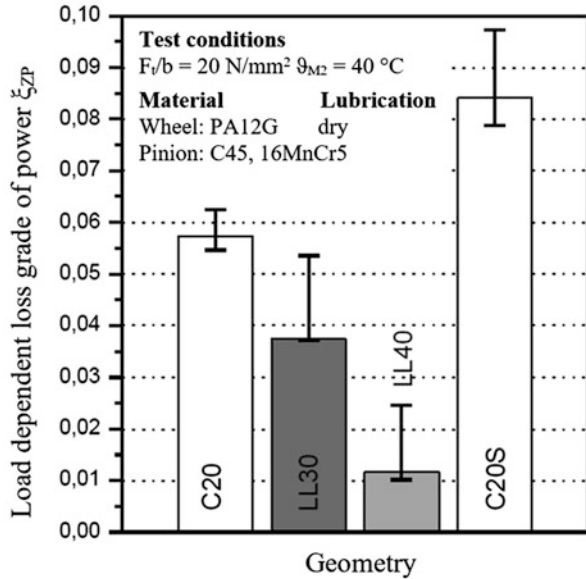


Fig. 4.7 Comparison of conventional tooth geometry (C20) with low loss geometries (LL30 & LL40) [3]

Fig. 4.8 Influence of gear geometry on efficiency [3]

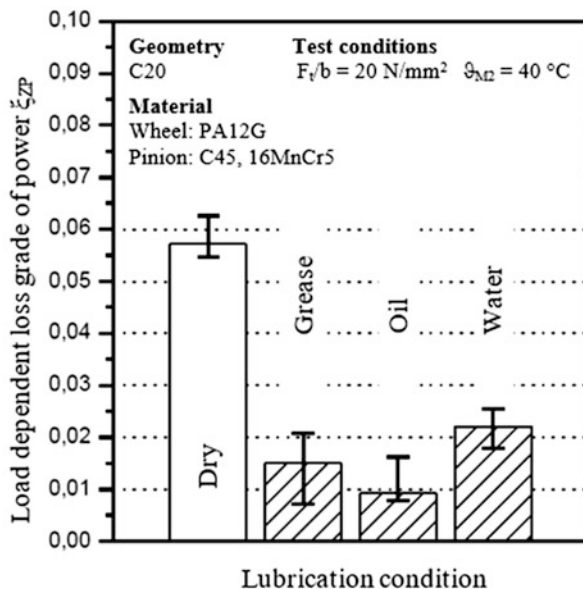


of the low loss gears is clearly visible. The larger pressure angles of the low loss gear geometries are indicated by the inclination of the tooth flanks and the pitch of the path of contact [3]. Table 4.6 shows the test gear geometries of the conventional C20 and C20S as well as the test gear geometries of the low loss geometries LL30 and LL40.

An FZG efficiency test rig is used to investigate the gear efficiency of the different geometries. The FZG efficiency test rig is based on the FZG standard back-to-back test rig acc. to DIN EN ISO 14635 [12]. Due to the parallel construction by mounting the test gear set both in the test gear and in the slave gearbox and the measurement of the occurring torque losses on the engine shaft, the gear efficiency of a single gear set can be measured and calculated. The detailed test rig setup is described in [3]. In Fig. 4.8, the load-dependent loss grades of power of the different investigated test gear geometries are shown. All tests are run in dry condition at constant mass temperature of the plastic test gears. As expected, the comparison shows that the loss-optimized design can be confirmed experimentally. The losses of the moderate variant LL30 are approximately 60% of the losses of the reference variant C20. The extreme low loss variant LL40 reaches approximately 20% of the losses of the reference geometry. In contrast, the conventional C20S variant reveals an increased loss grade of power than the reference variant due to the longer path of contact and the helix angle [3].

Figure 4.9 shows the influence of the lubrication condition and different lubricant media on the load-dependent loss grade of power. For all conducted test runs, the conventional tooth geometry C20 is used under constant test conditions and a constant gear temperature of 40 °C. As expected, the losses reach the highest values at dry conditions. The use of a lubricant can drastically reduce the losses. This

Fig. 4.9 Influence of lubrication condition and lubricating media on efficiency [3]



applies to both grease and water lubrication. The lowest losses are achieved by using oil as a lubricant [3].

The lubricant film separating the surfaces of the mating tooth flanks reduces friction in the tooth contact and thus increases efficiency. In dry-running operation, however, solid-body friction occurs, which results in losses due to the higher friction coefficient.

For experimental determination of the thermal operating limit in dry running, the drive power is increased incrementally until the respective test gear fails due to thermal damage such as melting. The results of the investigations are shown in Fig. 4.10. All tests are run in dry condition in a plastic-steel gear pairing. It is clearly visible that by applying low loss geometry, a significant increase in performance with regard to thermally induced damage can be achieved compared to conventional tooth geometries. By using the moderate low loss geometry LL30, an increase of nearly 60% compared to conventional design can be obtained. Geometry LL40 achieves an increase of more than 70% compared to the conventional C20 gear design.

In addition to efficiency and maximum transferable power, the occurring abrasive wear is also investigated experimentally. Here, the different geometries are examined on the test rig, and the wear progress is determined and evaluated gravimetrically. It can be observed that especially the loss-optimized variants tend to form wear notches in the dedendum flank area. This notch can lead to impermissible stress conditions during further operation, which can ultimately lead to a shear fracture of the gears in the dedendum flank area. Fig. 4.11 shows the comparison of the average mass wear rates of the different gear geometries investigated. The plastic wheels made of PA12G are each paired with a steel pinion in dry running. The tests

Fig. 4.10 Thermal power limit for different gear geometries [3]

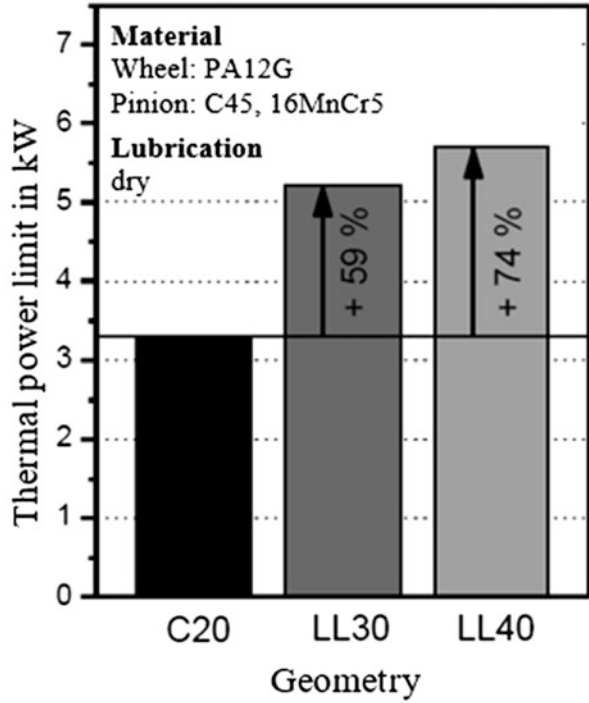


Fig. 4.11 Influence of gear geometry on wear behavior [3]

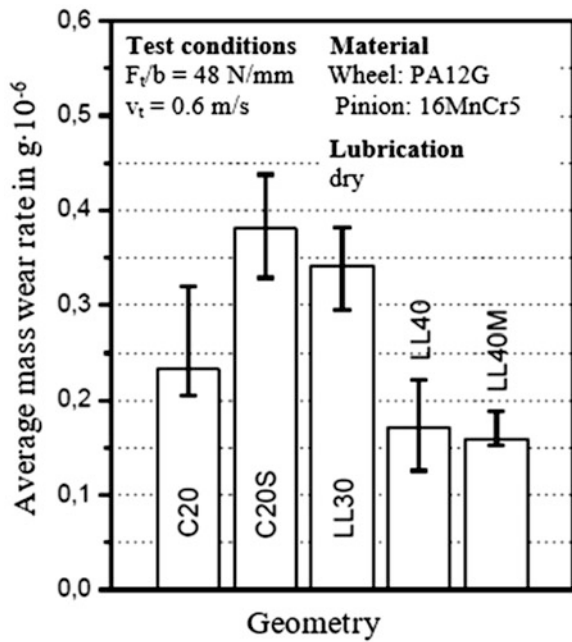
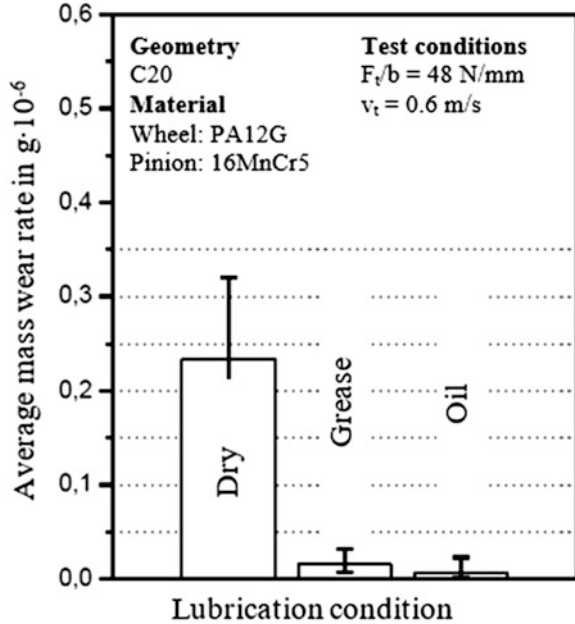


Fig. 4.12 Influence of lubrication condition on wear behavior [3]



performed show an approximately linear wear progression. Compared to the conventional geometry C20, the two variants C20S and LL30 show considerably higher wear rates. In contrast, the wear rate of the extremely loss-optimized test variant LL40 shows significantly lower wear characteristics. Gear geometry LL40M is largely identical to LL40 and is only characterized by reduced gear backlash.

The influence of the lubrication conditions on the wear behavior is shown in Fig. 4.12. The investigations are carried out with gear geometry C20 in the combination PA12G wheel and 16MnCr5 pinion. The measurements confirm the expectations of a significant reduction in wear by using a lubricant. In contrast to the test runs in dry running and with grease lubrication, the wear coefficient of the oil-lubricated variant has to be determined tactilely, since the amounts of wear are on the one hand significantly lower than in dry running and on the other hand an increase in mass could also be determined due to interactions between oil and plastic wheel [3].

Low loss gears are advantageous with regard to the thermal operating behavior since frictional losses and the resulting gear temperatures can be reduced by the loss-optimized gear geometry. Especially for dry running plastic gears, the thermal power limit can be increased by applying low loss geometry. Disadvantageous, however, are higher bearing loads resulting in higher bearing losses compared to operation with conventional gear geometry. Furthermore, the lower contact ratio results in an increased dynamic response, which can have a negative effect on the noise behavior of the gears. Moreover, more design space is required in order to achieve a load carrying capacity comparable to standard gears [13].

4.1.3.3 Tooth Root Load Carrying Capacity

The tooth root load carrying capacity of plastic gears is highly influenced by load induced deflections during operation. Since the Young’s modulus of thermoplastic gear materials is about one hundredth of that of steel gear materials and strength is about one tenth of that of steel, the load induced deflections are about ten times higher on plastic gears than on steel gears. The current guideline for plastic gear design VDI 2736 [5] is strongly oriented on the calculation approaches of steel gears [8]. When applying this VDI-guideline, the essential aspect of the increase in the actual contact ratio of plastic gears under load and the associated reduced tooth root stress is neglected compared to the undeformed gear. Test results confirm the strong influence of the deflections on the tooth root load capacity [10], which is not sufficiently taken into account by the current VDI-guideline.

Extensive experimental investigations are carried out to evaluate the influence of load-induced deflections on the tooth root load carrying capacity. The experimental investigations are accompanied by theoretical work. The aim is to integrate the deflection influences, which have not been considered so far, into the calculation method according to VDI 2736 [5], and to modify the calculation method accordingly. Table 4.7 shows the geometrical parameters of a theoretical study in which the influence of the number of teeth on the deflections under load and the actual contact ratio is evaluated. In [14], a method to calculate the actual contact ratio and the corresponding tooth root stress of plastic gears (ACORARS \triangleq **A**ctual **C**ontact **R**atio **R**oot **S**tress) is proposed. ACORARS considers the load-dependent deflections of plastic gears by calculating the actual contact ratio under load and the effect of load sharing of several tooth pairs on the corresponding tooth root stress. The iterative procedure requires implementation in a computer program. A simplified approach to calculate the actual contact ratio and the resulting tooth root stress for standard profile tooth geometries is introduced in [11].

The load-induced increase in contact ratio $\Delta\varepsilon_w$ is calculated according to Eq. (4.11) as the difference between the actual contact ratio and the “nominal” transverse contact ratio:

$$\Delta\varepsilon_w = \varepsilon_{\alpha,w} - \varepsilon_{\alpha} \tag{4.11}$$

$$\Delta\varepsilon_{zi}(z_1, z_2) = 0.15 \cdot \sqrt{z_1} \cdot (z_2/z_1)^{0.1} \tag{4.12}$$

Table 4.7 Main geometry data for variation of number of teeth calculation [10]

	Pinion	Wheel
Normal module (mm)	Variable	
Number of teeth (-)	16..96	Variable
Transmission ratio (-)	1..6	
Load $F_t/(b \cdot m_n)$ (N/mm ²)	40	
Normal pressure angle (°)	20	
Young’s modulus (N/mm ²)	210,000	1300

In Eq. (4.12), an estimation of the geometry-dependent increase in contact ratio is shown for external gears with $z_1 \leq z_2$. The increase in contact ratio is dependent of the number of teeth [14]. The actual contact ratio under load $\varepsilon_{\alpha,w}$ can be calculated using Eqs. (4.13) and (4.14) also considering the influence of the number of teeth acc. to Eq. (4.12).

$$\varepsilon_{\alpha,w} \approx \varepsilon_{\alpha} + 0.13 \cdot \sqrt{\frac{F_t/b}{(\varepsilon_{\alpha} + f_{\varepsilon\beta}) \cdot p_{et} \cdot c^j}} \cdot f_{zi} \quad (4.13)$$

$$f_{zi} = \max\left(1, \frac{\Delta\varepsilon_{zi}(z_1, z_2)}{\Delta\varepsilon_{zi}(36, 54)}\right) \quad (4.14)$$

The results of the estimation of the increase in contact ratio are shown in Fig. 4.13 for a constant load (marked as est.). Further, the results for the increase in contact ratio calculated iteratively with ACORARS (marked as ACR) are shown as well. Good correlation between the estimated values and the results according to ACORARS can be found. With increasing number of teeth, the load-induced increase in contact ratio is significant. Due to the load distribution over several pairs of teeth compared to the undeformed condition, the tooth root stress can be significantly reduced. In order to take the effects of $\varepsilon_{\alpha,w}$ into consideration when calculating the tooth root bending stresses, a modified approach to calculate the contact ratio factor Y_e is proposed according to Eqs. (4.15) and (4.16). In comparison to VDI 2736 [5], a modified contact ratio factor is used within the ACORARS approach:

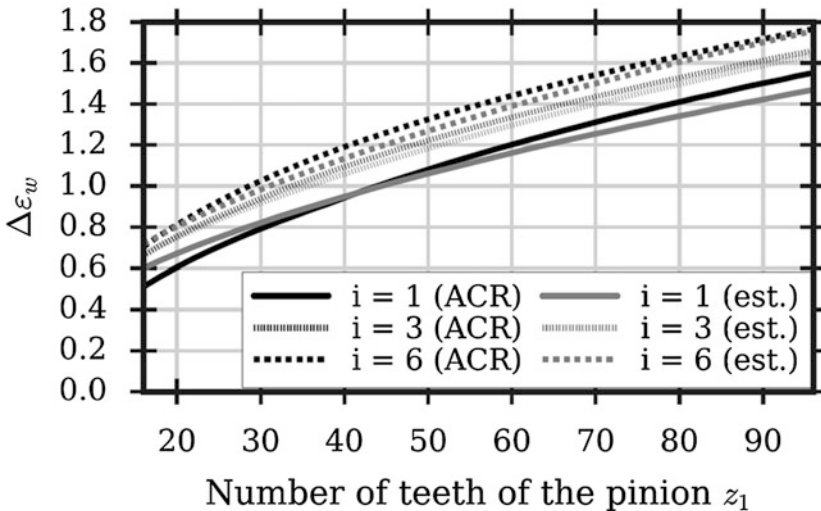


Fig. 4.13 Increase in contact ratio acc. to ACORARS for different numbers of teeth and transmission ratios [11]

$$Y_{\varepsilon,ACR} = a_{ACR} + \frac{1 - a_{ACR}}{\varepsilon_{\alpha,w}} \quad (4.15)$$

$$a_{ACR} = \max \left(\min \left((2.6 - \varepsilon_{\alpha,w}) \cdot \frac{0.25}{0.8}, 0.25 \right), 0 \right) \quad (4.16)$$

The calculation approach of the corresponding tooth root stress under consideration of load-induced deflections is shown in Eq. (4.17). The contact ratio factor Y_e is substituted by the modified contact ratio factor $Y_{\varepsilon,ACR}$:

$$\sigma_{F,mod} = K_F \cdot Y_{Fa} \cdot Y_{Sa} \cdot Y_{\varepsilon,ACR} \cdot Y_{\beta} \cdot \frac{F_t}{b \cdot m_n} \quad (4.17)$$

The field of application of this approximation basically extends to standard profiles according to DIN 867 [15] of steel-plastic spur gear pairings [11]. Since the effects of common flank profile modifications on the actual contact ratio are comparatively small in comparison to load-induced deflections, the approximation of the actual contact ratio according to Eq. (4.17) is usually adequate. The consideration of further modifications and deviations is possible via the factors K_{Fa} and $K_{F\beta}$ which are contained in K_F [5, 11].

The experimental investigations with regard to tooth root load carrying capacity of plastic gears are performed on a FZG back-to-back test rig, which is based on the standard configuration according to DIN EN ISO 14635 [12]. Fig. 4.14 shows the lubrication and cooling configuration of the test gear housing which is filled with FVA reference oil FVA3A (incl. 4% Anglamol (A99)) which is classified as a mineral oil ISO VG 100. Anglamol 99 is an extreme pressure additive based on sulfur and phosphorus components. Pipes arranged in the oil bath are fed and drained by water, allowing cooling of the oil bath. Heating cartridges in the housing walls allow heating of the oil. Furthermore, to improve temperature control performance of the system, additional oil of an external oil tempering unit is injected into the meshing gears as common for injection lubrication [11].

Fig. 4.14 Test gear housing of FZG test rig acc. to [11, 12]

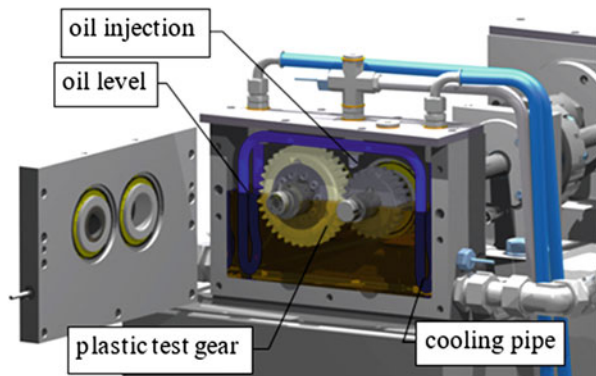


Fig. 4.15 Design of plastic gears [11]

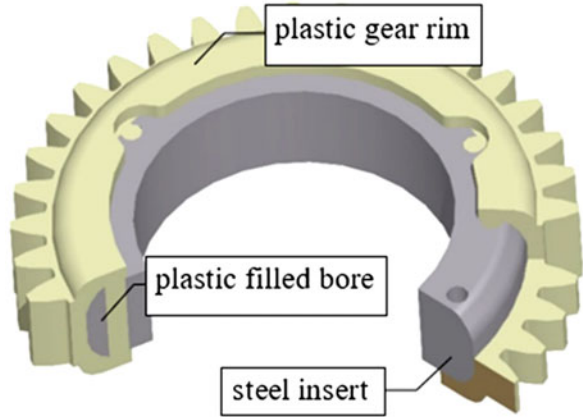


Table 4.8 Test gear geometry

Geometry	KST-A		KST-B		KST-C	
	Pinion	Wheel	Pinion	Wheel	Pinion	Wheel
Centre distance (mm)	91.5					
Normal module (mm)	1		2		3	
Normal pressure angle (°)	20		20		20	
Helix angle (°)	0		0		0	
Face width (mm)	22	20	22	20	22	20
Number of teeth (-)	72	108	36	54	24	36
Tip diameter (mm)	74.8	111.3	76.5	113.0	78.3	114.7
Transverse contact ratio (-)	1.18		1.19		1.20	

In Fig. 4.15, the design of the investigated plastic gears is shown. The gear rim is molded around a steel insert containing axial bores which are filled by plastic material during the manufacturing process, granting a form-fitting connection between both components. The steel insert enables a reliable torque transmission from the gear teeth to the test rig shaft. The gear geometries of the objected test gears are shown in Table 4.8. All subjected gear pairs feature a transmission ratio of $i = 1.5$ and a center distance of $a = 91.5$ mm. For manufacturing reasons, the plastic gears contain radii on the tip edges. The plastic test gears are paired with case carburized and ground 16MnCr5 steel pinions. To enable smoother engagement, pinions of KST-B and KST-C contain a tip relief. The flank shape of pinions of KST-A is not modified [11].

The conducted back-to-back test runs are operated under continuous torque monitoring until a “loss of drive” situation occurs due to a tooth root breakage of the plastic test gear wheel. In order to establish a constant gear temperature during the back-to-back test runs, the oil-sump temperature during testing is controlled to compensate the temperature difference $\Delta\vartheta_{tooth}$. The test runs are conducted at a constant tooth temperature of 80 °C. Fig. 4.16 shows an exemplary tooth root failure on a POM test gear of test geometry KST-B. The crack initiation of the occurring

Fig. 4.16 Exemplary tooth root fracture of a KST-B POM gear [10]

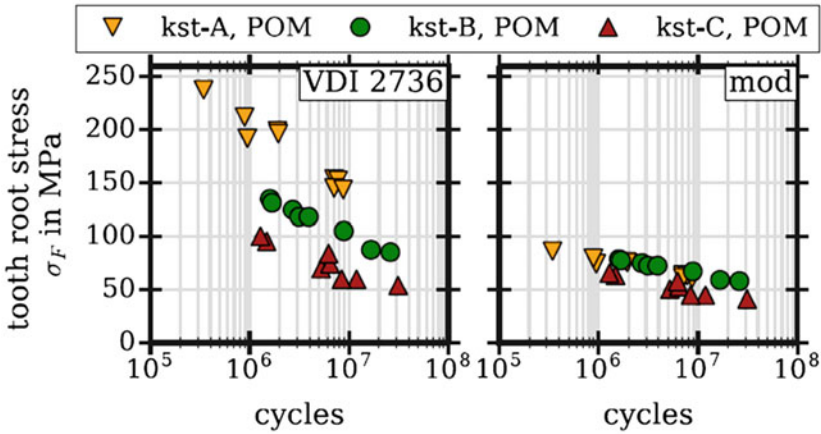


Fig. 4.17 Bearable tooth root stress acc. to VDI 2736 [5] and modified ACORARS for different POM gear geometries [11]

tooth root failures for all test runs occurs in the area of the tooth root radius. The test runs to investigate the tooth root strength of POM gears are conducted with gear geometries KST-A, KST-B, and KST-C. Test gear geometry KST-C ($m_n = 3$ mm) shows a tendency to form small cavities during the manufacturing process due to comparatively large wall thicknesses in combination with the shrinkage behavior of POM.

In Fig. 4.17 the nominal tooth root stress σ_F of all conducted test runs with different gear geometries is shown at the respective number of load cycles where the gears failed due to tooth root breakage. The tooth root stress is both calculated according to VDI 2736 [5] and according to the modified ACORARS approach which considers the effect of load-induced increase of the actual contact ratio on the occurring tooth root stress.

The calculation was conducted using the following input values: $K_F = 1.0$; $Y_{\beta} = 1.0$; $Y_{F\alpha} = 2.0$; $Y_{S\alpha} = 1.8$ [11]. The calculation of the respective tooth root stress at failure without consideration of load-induced deflections according to VDI 2736 [5] results in unrealistically high tooth root stresses for geometries with high numbers of teeth (KST-A; $z_1 = 72$; $z_2 = 108$). Furthermore, the level of bearable tooth root stresses varies for the different tooth geometries although all test gears are manufactured from the same POM material. Alternatively, a recalculation of the same experimental data with the modified and simplified ACORARS approach results in a comparable level of bearable tooth root stress for the different investigated gear geometries. The bearable tooth root stress for gear geometry KST-C reaches slightly lower values than the other investigated geometries. This effect is caused by a reduced load-bearing cross-section due to occurring cavities in the KST-C test gears. However, the good correlation of the bearable tooth root stress according to Eq. (4.17) shows that the main influence factors of load-induced deflections can be considered in an adequate accuracy [11].

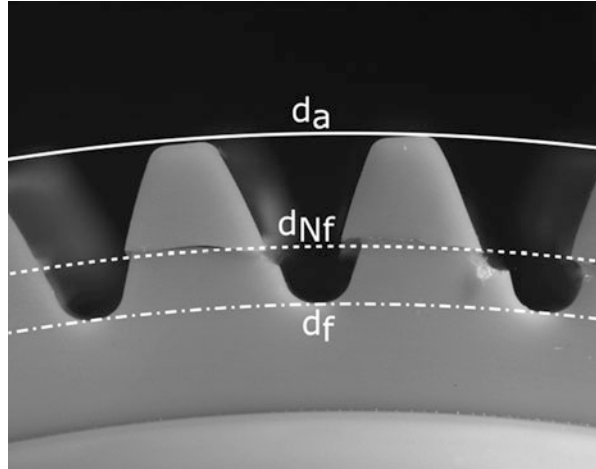
The evaluation of the test results shows that the tooth root strength calculation of plastic gears with high numbers of teeth according to VDI 2736 [5] is definitely on a conservative level. However, this may lead to an underestimation of the potential of plastic gears with high numbers of teeth with regard to their tooth root load carrying capacity due to the negligence of the elasto-kinematic effect of load-induced increase of the actual contact ratio and the resulting load distribution on further teeth.

Theoretical and experimental research has been conducted in order to consider the load-induced effects of tooth deflections on the tooth root load carrying capacity which are neglected in current design guidelines such as VDI 2736 [5]. Based on VDI 2736 [5], a modified calculation approach for the determination of the tooth load carrying capacity has been developed and contributes to a more precise design of plastic gears.

4.1.3.4 Flank Load Carrying Capacity

Operation of plastic gears under oil-lubricated conditions and the use of high-performance materials allow a significant increase of the transmitted power compared to dry running or grease-lubricated systems. The generation of a lubrication film between meshing teeth leads to a separation of the tooth surfaces and to a reduction of the occurring friction losses. Furthermore, the generated heat during operation can be dissipated effectively by means of the lubricant. This leads to lower tooth temperatures of oil-lubricated plastic gears at identical drive power in comparison with dry running and to higher tooth flank strength due to cooling effects. Experimental investigations with oil-lubricated plastic gears show that typical flank failure modes such as wear and melting can be prevented under sufficient lubricating conditions. However, fatigue damages such as pitting on the active tooth flank become more relevant [16]. However, current design guidelines for plastic gears such as VDI 2736 [5] only contain tooth flank strength numbers for a limited number of materials.

Fig. 4.18 Flank shear fracture at a PEEK gear [10]



Polyetheretherketone (PEEK) is a high-performance plastic that is particularly suitable for use at higher temperatures and higher power levels. Investigations on the tooth root load carrying capacity [10] indicate a comparatively high tooth root strength. However, pitting damages occur with regard to the tooth flank load carrying capacity. The calculation approach for determining the tooth flank carrying capacity of plastic gears according to VDI 2736 [5] is shown in Eqs. (4.6) to (4.8). The calculation approach is based on the assumption that the maximum flank pressure is present in the area of single tooth contact.

The load-induced deflections of plastic gears, however, may cause meshing interferences which lead to local pressure peaks in the area of premature and posterior meshing. These meshing errors can have a negative effect on the flank load carrying capacity of the respective plastic gears. Fig. 4.18 shows an exemplary flank fracture that is caused by high flank pressures due to meshing interference in the area of posterior meshing. Adequate measures to reduce high flank pressures such as a tip relief have to be applied in order to ensure high flank load carrying capacity and to establish reliable strength data for new thermoplastic materials such as PEEK according to VDI 2736 [5] [16].

Profile modifications on the mating steel pinion are experimentally investigated in order to avoid undesired flank damages in the area of posterior meshing. The experimental investigations are run on a FZG back-to-back test rig as shown in Fig. 4.14 using oil injection into the gear mesh. The investigations are performed using an ISO VG 100 reference mineral oil (FVA 3A [17]) and test gear geometry KST-C as shown in Table 4.8. The PEEK plastic gear is paired with a modified steel pinion (case carburized 16MnCr5). The steel pinion features a tip relief of $C_\alpha \approx 400 \mu\text{m}$ in order to avoid undesired flank fractures due to posterior meshing. The applied tip relief is dimensioned using the program system RIKOR [18]. RIKOR is suitable to calculate load and pressure distributions of gears and used to optimize the microgeometry of the investigated gears. The aim of the

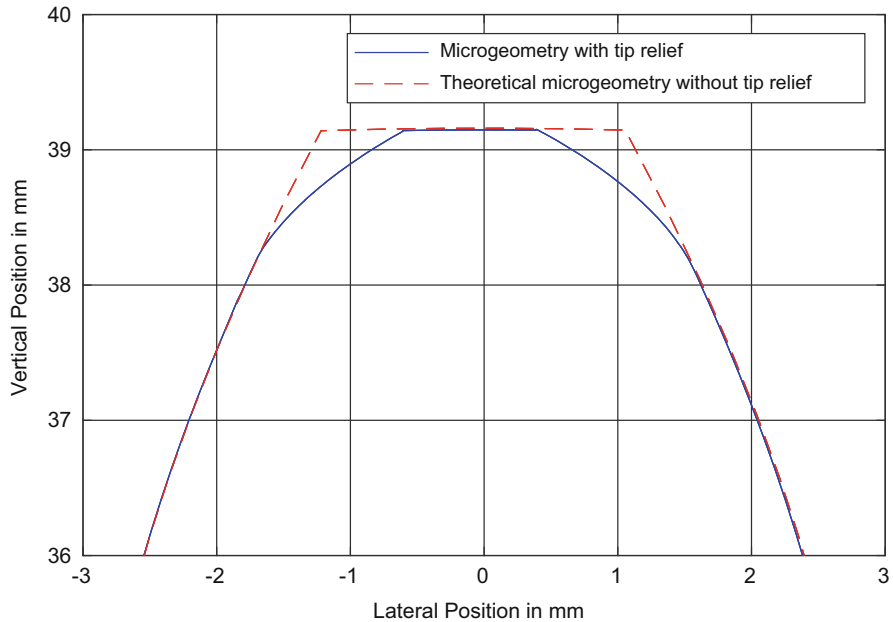


Fig. 4.19 Microgeometry of the steel pinion, pitch diameter $d = 72$ mm [16]

calculations carried out here is to completely relieve the load on the dedendum flank area of the plastic wheel by means of a flank modification on the steel pinion.

The profile modification of the steel pinion is illustrated in Fig. 4.19. In contrast to the conventional, unmodified microgeometry of the steel pinion, the modified geometry with the applied tip relief guarantees that the sharp tooth tip of the steel pinion will not engage with the dedendum flank area of the driven plastic gear during posterior meshing. This measure effectively reduces the maximum flank stress and prevents the plastic gear from undesired flank fractures.

The test runs to evaluate the flank load carrying capacity of the test gears are performed at a uniform oil temperature of $80\text{ }^{\circ}\text{C}$ at different torque levels. The test runs are stopped regularly for optical inspection of the flank condition and the damage development.

Table 4.9 shows the development stages of pitting on an exemplary plastic test gear. The damages appear in the area of single tooth contact in the dedendum flank area of the PEEK gear. As the number of load cycles increases, the flank area damaged by pitting also increases steadily, so that the active flank area is gradually disrupted. Visually, there is a large resemblance to the pitting common on steel gears. Also, the pitting appears preferably in areas of high Hertzian flank pressure and negative specific sliding speeds.

Figure 4.20 shows an enlarged view of an exemplary pitting damage on a test wheel. In addition, the beginning of the path of contact “A,” the position of the pitch point “C,” and the end of contact “E” are also shown.

Table 4.9 Development of pitting damages on a plastic wheel, $T_2 = 43\text{Nm}$, $\vartheta_{\text{oil}}=80\text{ }^\circ\text{C}$ [16]

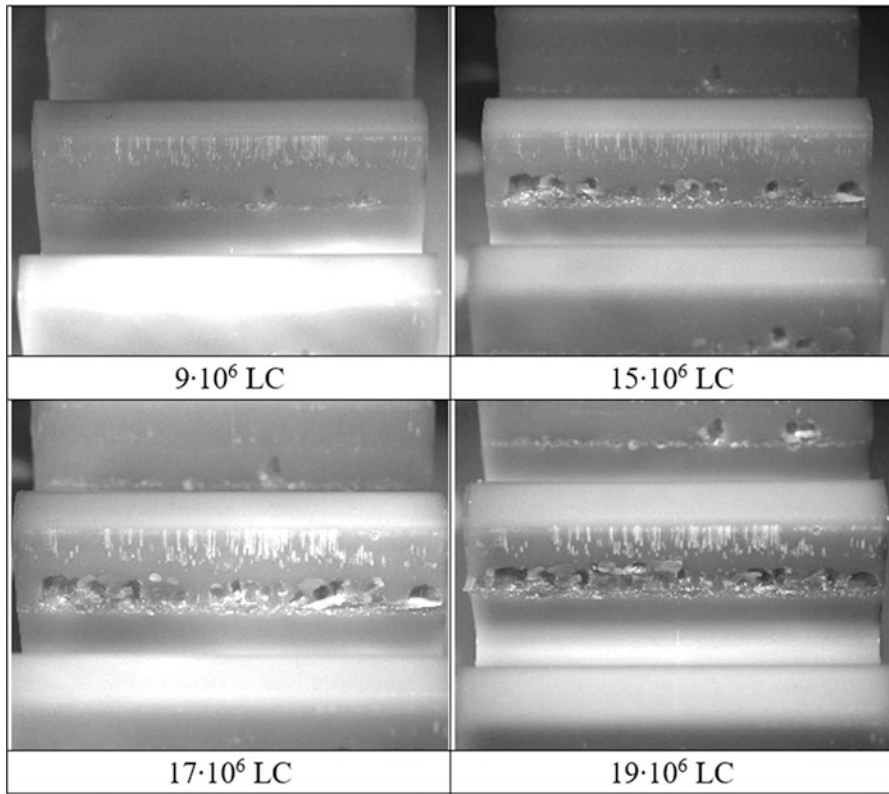
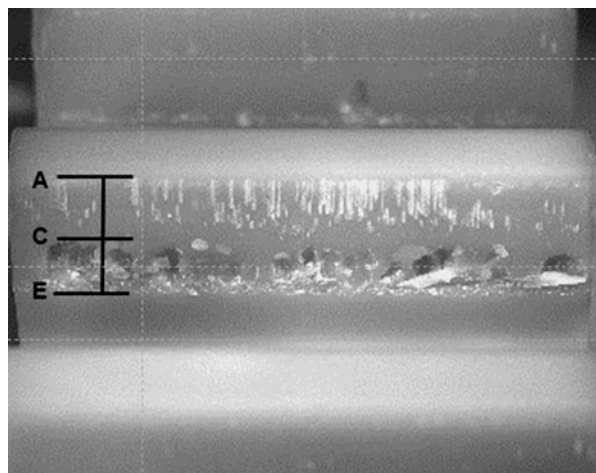


Fig. 4.20 Exemplary pitting damages including positions A, C, and E at gear flank [16]



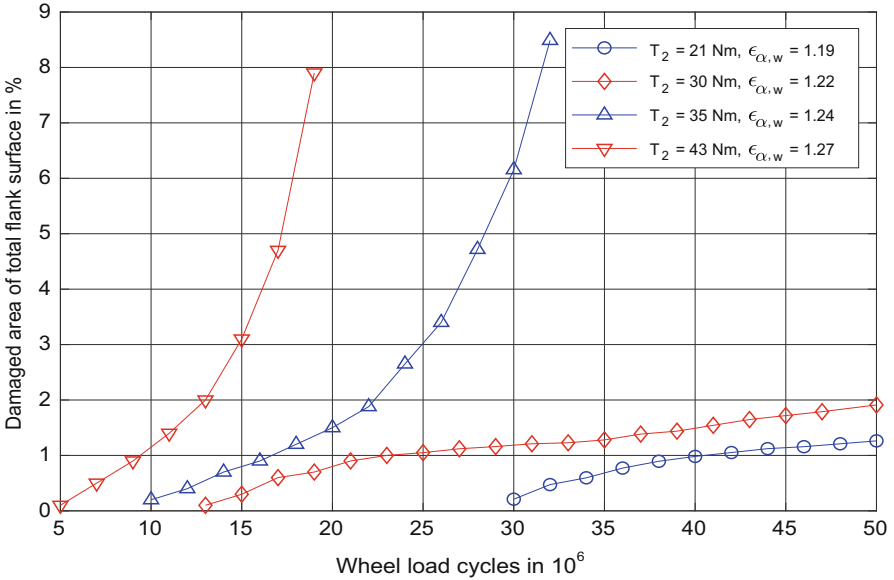


Fig. 4.21 Development of pitting damaged active flank area of the plastic wheel for different torque levels, $\vartheta_{Oil} = 80$ [16]°C

The pittings are located preferably in the dedendum flank area below the pitch point “C” where negative specific sliding and high Hertzian pressure affect the flank surface.

In Fig. 4.21, the development of the active flank surface of the plastic wheel that is damaged by pitting is illustrated. Depending on the number of load cycles, the corresponding proportion of the flank surface damaged by pittings is evaluated for different torque levels.

For the investigations performed herein, a critical damaged area of the total active flank surface of the plastic wheel of 2% is identified as the boundary between progressive and linear/degressive damage development. Therefore, a value of 2% pitting damage area is defined as the respective failure criterion for the flank load carrying capacity investigations. The flank area damaged by pitting increases progressively for high torque levels. Below the critical damage area, the development is linear/degressive [16].

The test runs for the evaluation of the pitting lifetime are run to a maximum number of $50 \cdot 10^6$ wheel load cycles and considered as passed specimen or until the failure criterion of 2% damage area is reached. Fig. 4.22 shows the evaluation of the pitting fatigue data derived from the experimental data shown in Fig. 4.21. The flank pressure σ_H is calculated according to VDI 2736 [5]. The S-N-curve for PA66 is also shown for a safety factor of $S_H = 1.0$ and a flank temperature of $\vartheta_{flank} = 90$ °C according to VDI 2736 [5]. The literature values for PA66 and the strength data of PEEK have approximately the same gradient. However, the bearable flank pressure of PEEK determined herein reaches noticeably higher values than PA66. The

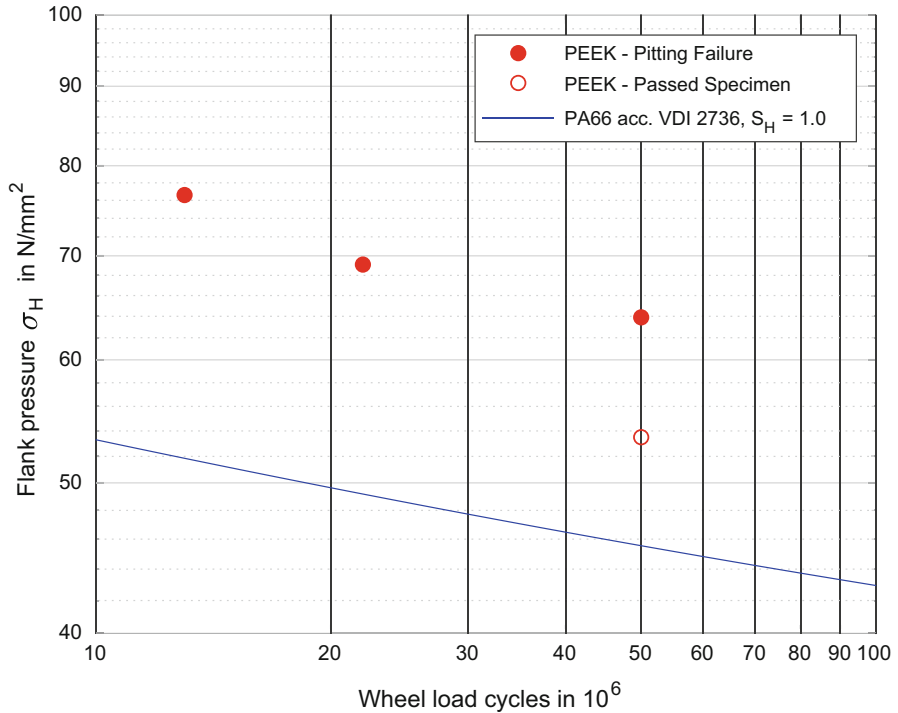


Fig. 4.22 PEEK pitting failure data, $\vartheta_{Oil} = 80\text{ }^\circ\text{C}$, PA66 S-N-curve for reference [16]

suitability of PEEK for high-performance applications, particularly for environments of higher ambient and operation temperatures, can be confirmed by the herein performed investigations [16].

In order to evaluate the flank load carrying capacity of thermoplastic materials, consequently adequate measures to reduce meshing interference, which can lead to undesired flank fractures, have to be taken. Experimental investigations show the generation of pitting damages at PEEK gears in the area of high Hertzian pressure and negative specific sliding. Based on the damage progression, criteria for the evaluation of flank load carrying capacity were derived, and first results on the flank load carrying capacity of PEEK gears were presented. These investigations are also necessary for other thermoplastic materials in order to obtain the strength numbers required for the design of plastic gears.

4.1.3.5 Tribology

In addition to the experimental investigation of the operating behavior and load carrying capacity of plastic gears in the back-to-back gear test rig, fundamental investigations of the tribological behavior of plastic materials can be carried out in a

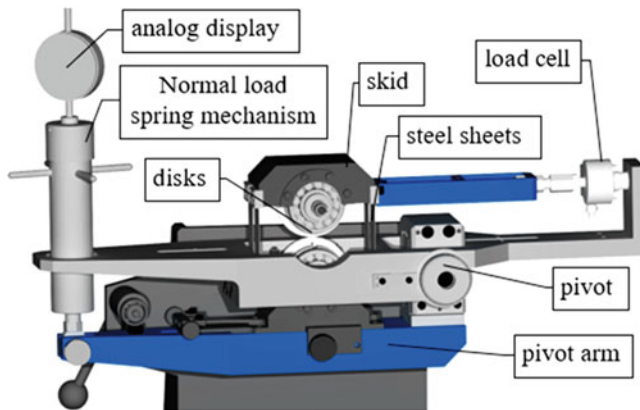


Fig. 4.23 FZG twin disk test rig [19]

twin-disc test rig. The focus of the investigations is the characterization of the friction and temperature behavior as well as the viscoelastic behavior of thermoplastic materials. The experimental investigations are supplemented by accompanying theoretical considerations of the thermo-elastohydrodynamically lubricated (TEHL) contact.

The experimental tribological investigations are carried out using an FZG twin disk test rig as shown in Fig. 4.23. Two cylindrical disks (80 mm in diameter, 20 mm in width) are mounted onto two axially parallel shafts that can be driven independently by two electric engines. Speed of the electric engines can be continuously varied. The upper disk is mounted on a skid which is connected to the test rig frame by thin steel sheets. The skid is supported laterally by a load cell which measures frictional forces as reaction forces of the skid. The lower disk is mounted at the pivot arm. Normal contact force can be applied by the normal load spring mechanism via the pivot arm. In order to investigate lubricated contacts, the test rig features an oil injection system which feeds the contact zone with temperature-controlled lubricant. The temperature of the upper disk is continuously measured using thermal sensors which are applied approximately 5 mm below the disk surface. Additionally, oil inlet temperature, surface velocities and frictional forces are continuously monitored. The coefficient of friction μ in the contact zone as well as the sum velocity v_{Σ} and the sliding velocity v_g can be calculated by Eqs. (4.18) to (4.20):

$$\mu = \frac{F_R}{F_N} \quad (4.18)$$

$$v_{\Sigma} = v_1 + v_2 \quad (4.19)$$

$$v_g = v_1 - v_2 \quad (4.20)$$

The investigated disks are made of extruded homopolymeric POM and wet polished to a mean surface roughness value of $Ra < 0.2 \mu\text{m}$. The corresponding

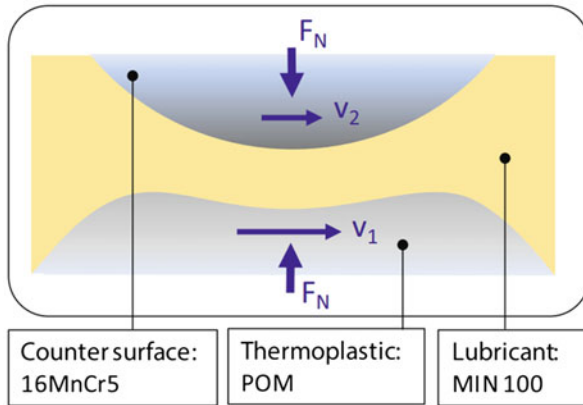


Fig. 4.24 Schematic representation of the investigated TEHL contact setup [19]

Table 4.10 Operating conditions of TEHL investigations [19]

Pairing	Normal line load	Hertzian pressure	Hertzian semi-width	Sum-velocity	Oil injection temperature	Sliding speed
	w	p_H	b_H	v_Σ	ϑ_{oil}	v_g
	N/mm	N/mm ²	mm	m/s	°C	m/s
16MnCr5-16MnCr5	100	428.5	0.149	8.00	40	3.43
16MnCr5-POM		69.6	0.823			

steel disks are machined from 16MnCr5 that are ground and polished resulting in a mean surface value of $Ra < 0.1 \mu\text{m}$. As a lubricant, plain mineral oil ISO VG 100 without additives is used. A schematic illustration of the contact setup is shown in Fig. 4.24.

The experimental investigations of the TEHL contact are accompanied by theoretical studies. For this purpose a modified TEHL simulation model [19] is used to characterize the thermoplastic TEHL contact. The tribosimulation is used to compare the general behavior of the plain steel-steel TEHL contact and the hybrid steel-thermoplastic TEHL contact. The loading conditions are in a typical range for thermoplastic contacts and are shown in Table 4.10. Due to the significantly lower Young’s modulus of POM in comparison to 16MnCr5, the corresponding Hertzian pressure in the hybrid steel-plastic contact is only 16% of the Hertzian pressure obtained in a plain steel-steel contact at identical normal load. The Hertzian semi-width of the plastic-steel contact is significantly larger than the respective half-width of a plain steel-steel contact.

The resulting hydrodynamic pressure distribution of both steel-steel and steel-plastic contact is shown in Fig. 4.25. The loading conditions shown in Table 4.10 apply, while the oil injection temperature is set to 60 °C. The abscissa of the diagram is normalized to the Hertzian semi-width b_H . As expected, the calculated

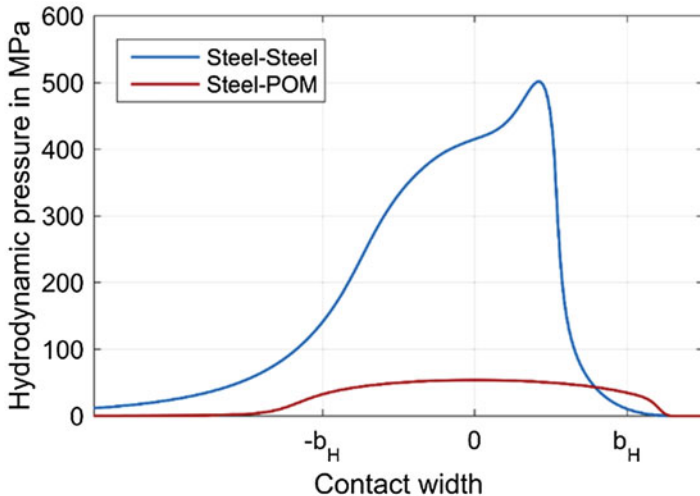


Fig. 4.25 Comparison between steel-steel and steel-POM TEHL contact [19]

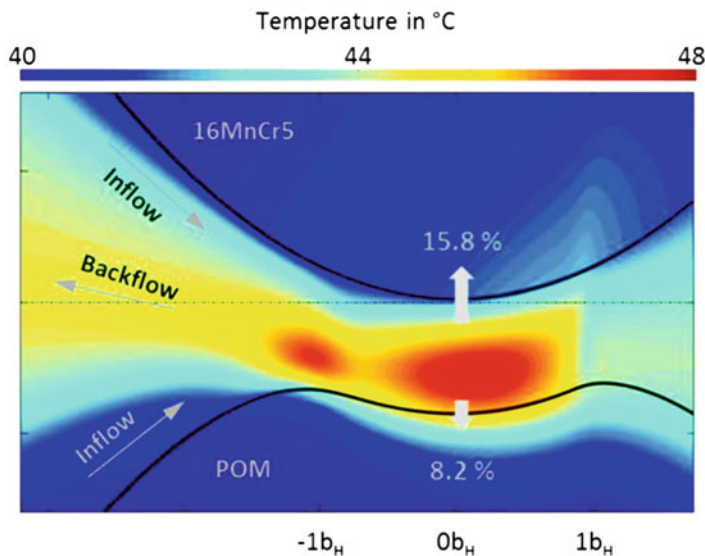


Fig. 4.26 Temperature distribution in the thermoplastic-steel TEHL contact in deformed configuration (gap height adjusted for visualization purpose) [19]

hydrodynamic pressure in the steel-POM contact is significantly lower than the respective hydrodynamic pressure obtained in the plain steel-steel contact.

Figure 4.26 shows the calculated temperature distribution of the steel-POM TEHL contact according to the loading conditions shown in Table 4.10. The considered heat sources include compression and shearing of the lubricant. While

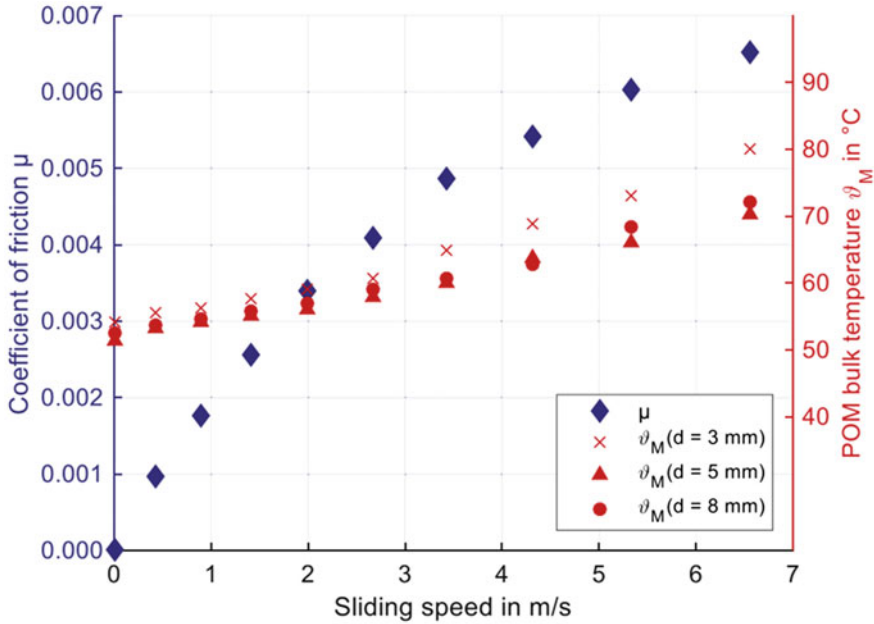


Fig. 4.27 Measured friction curve and POM bulk temperatures in 3, 5, and 8 mm depth of POM-steel TEHL contact [19]

shear heating can be obtained predominantly in the middle of the contact, positive pressure gradients lead to heating in the contact inlet zone, and negative pressure gradients lead to a heat sink in the contact outlet zone [19]. The temperature gradient within the POM material appears steep in normal direction to the surface due to the low thermal inertia of POM. The generated heat is accumulated at the POM surface. The analysis of the heat fluxes in the contact zone shows that the POM body accumulates approximately 8% of the generated heat in the contact. However, the maximum temperature rise of approximately 8 K in Fig. 4.26 shows discrepancies to the experimentally measured bulk temperatures as shown in Fig. 4.27. This may result from viscoelastic effects, which are an additional heat source and are not considered in the herein conducted simulations.

Figure 4.27 shows experimental results conducted on the twin disk test rig. The friction behavior and the measured quasi-stationary bulk temperatures in different material depths are evaluated. The coefficient of friction is averaged by three measurements at the testing conditions shown in Table 4.10. The sliding speed is increased continuously from 0 up to 6.55 m/s. Both coefficient of friction and bulk temperature rise nearly linearly with increasing sliding speed up to approximately 3.5 m/s. With higher sliding speeds, the bulk temperature rises more quickly due to the low heat conduction properties of thermoplastics. Generally, a low coefficient of friction is obtained for the conducted measurements. This effect is due to the low lubricant pressure viscosity. Increasing sliding speeds cause higher shear friction and

shear heating in the lubricant which results in a further decrease of the lubricant viscosity results in a low friction increase with increasing sliding speeds.

The basic tribological investigations provide important insights into the frictional behavior of thermoplastics. The determination of coefficients of friction serves primarily to evaluate the thermal operating behavior and to understand the wear behavior. The results thereby contribute significantly to material characterization.

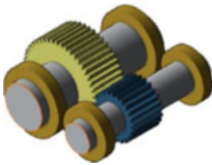
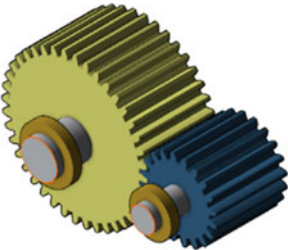
4.1.4 Challenges for the Future Application of Plastic Gears

The high-temperature dependency and the low strength properties compared to steel still pose a great challenge for the use of plastic gears. Especially in applications with higher power, there are still limits. However, the continuous development and the increased use of simulative design methods allow a more precise design and calculation of the stresses as well as of the resulting service life of thermoplastic components. One example is the use of multiphysical material models in which the complete life cycle from injection molding to friction, wear, and another tooth damage can be considered.

However, the use of such material models requires a reliable database of different thermoplastic materials with comprehensive information on material behavior and service life. At present, this information is not available in sufficient detail. The determination of material characteristics is also not sufficiently standardized at the current state of the art. For example, there are currently a large number of different test rig concepts for determining characteristic data, such as for evaluating the tooth root and tooth flank load capacity. A standardization of the execution and evaluation of tests for the determination of characteristic properties contributes decisively to the comparability and reliability of material characteristics. This is particularly important in view of the large number of different plastics available on the market. Another challenge is the use of fiber reinforcements. The influence of different fibers on the operating behavior and the load carrying capacity is currently the subject of research and cannot yet be sufficiently considered in the presently available design guidelines. With regard to a further increase in performance and an extension of the range of applications of plastic gears, the use of different fiber reinforcements offers enormous potential.

Increasing transferable power and the development of new high-performance applications are generally accompanied by larger component sizes. Here, production-related limits are set by the injection molding process. Material shrinkage and the risk of the formation of defects are production-related risks. In view of new requirements in the area of condition monitoring, sensors and other electronic components are increasingly being integrated into gear wheels. An integral design of plastic gears with integrated sensors for condition monitoring enables safe operation of the plastic components. The development of methods for condition monitoring and the production of highly integral plastic components are currently the subject of research.

Table 4.11 Challenges in direct material substitution

		Steel/Steel	Plastic/Plastic
			
i	(-)		2
m_n	(mm)	0.6	1.5
b/m_n	(-)		20
$m_{nPlastic}/m_{nSteel}$	(-)		2.5
$a_{Plastic}/a_{Steel}$	(-)		2
$Vol_{Plastic}/Vol_{Steel}$	(-)		10
S_H	(-)	1.20	1.25
S_F	(-)	1.74	1.40
Load parameters			
Min. load cycles	(-)		$50 \cdot 10^7$
P	(kW)		1

With respect to saving resources and the increasing importance of CO₂ neutral products, requirements for the environmental sustainability of plastic components will become increasingly important in the future. At present, only a small proportion of engineering plastics is recycled or not recycled at all, while production is very energy- and resource-intensive. The recirculation and recycling of plastic components and the development of bio-based and biodegradable technical materials have hardly been researched so far and has to be considered in the near future.

Despite all the progress made, the direct substitution of steel gears by plastic is associated with enormous challenges. The following example, shown in Table 4.11, illustrates the difficulties that can arise when simply changing the material from steel to a thermoplastic.

As an example, a hypothetical application in a 1 kW oil-lubricated gearbox is used, which is operated at a material temperature of approximately 50 °C. The demonstration of the tooth root and tooth flank load carrying capacity is to be provided for an exemplary service life of 50 million load cycles. The reference gear made from case hardened steel (16MnCr5) is operated at a transmission ratio of $i = 2$ and features a design size of $m_n = 0.6$ mm.

The calculation of the load carrying capacity of the reference steel/steel pairing according to ISO 6336 [9] results in a safety factor of $S_H = 1.20$ and $S_F = 1.74$ for the flank and tooth root load carrying capacity. All load factors are set to $K_i = 1.0$ for the performed calculation of the load carrying capacity.

The dimensions of a gear pairing made of polyamide for the same power output and the same required service life differ fundamentally from the steel design due to the very different strength properties between steel and plastic. The plastic gear design is calculated according to VDI 2736 [5]. Similar to the calculation of the exemplary steel gears, all load factors are set to $K_i = 1.0$. In order to achieve a certain geometric comparability between steel and plastic gear design, an identical face-width/normal-module-ratio $b/m_n = 20$ is applied. The resulting plastic gears are significantly larger than the corresponding steel gears. The safety factors for flank and tooth root load carrying capacity are in the same range compared to the reference steel gears. While the center distance and normal module approximately double, the volume of the plastic gears increases approximately by a factor of ten compared to the steel reference gears. At such an increase in size, the mass of the plastic gears already exceeds the mass of the steel gears, so that any weight benefits of the plastic are eliminated.

The design example shows that a direct substitution of steel by plastic is not in any situation beneficial. Rather, a plastic-oriented design has to be realized under consideration of the possibilities in production and the material properties in order to utilize plastic components in gearboxes profitably.

Therefore, further research is still needed to fully exploit the potential of thermo-plastic gears. In addition to the research work mentioned above regarding mainly the thermal operating behavior and load carrying capacity, there is also great potential in the optimization of the injection molding process [20].

Further potential for optimization lies in the modification of the tooth geometry to improve the load carrying capacity [21, 22], since the injection molding process offers a high degree of design freedom. At present, there are hardly any studies available on helical plastic gears. Nakamura [23] performs investigations on the load carrying capacity of helical plastic gears. However, there is still a need for further research in this topic. In the context of thermal operating behavior, increasingly complex thermal calculation models are being developed using the finite element method in order to predict the tooth temperatures accurately [24].

In addition to experimental and theoretical research work, it is also advisable to promote and further develop standardization processes in the field of plastic gear design. Besides more complex methods for the calculation and design of gears such as the finite element method, standards are very beneficial and indispensable, especially in an early stage of development. Standardized processes as known from the steel gear sector [8, 9] can provide a considerable contribution for gear designers.

4.2 Conclusion

Plastics are increasingly used due to their lightweight construction potential and the possibility of cost-effective mass production by injection molding. The development of new materials and the constant advancement of calculation and simulation

methods enable the use of plastic gears at ever higher drive powers. The high-temperature dependency of the material properties and the low strength have, however, a negative effect and limit the possibilities of plastic gear applications. Knowledge of the material behavior during operation is essential for the safe design of plastic components. In this context, comprehensive theoretical and experimental investigations of the operating behavior and load carrying capacity of plastic gears make an important contribution to a deeper understanding of thermoplastic materials. In addition to the investigation of tooth root and flank load capacity, the temperature behavior and the wear behavior and alternative gear geometries are also investigated. Basic tribological investigations provide helpful information about the lubricated steel-plastic contact. The present work provides a comprehensive insight into current research in the field of plastic gears and shows the possibilities and limits of the use of plastic gears. The presented results can find a direct way into practical application. In addition to results on the thermal operating behavior of different materials and tooth geometries, a method for calculating the tooth root load carrying capacity is also presented, which takes into account influences that have not been taken into account so far and consequently improves the calculation accuracy. The practical research results thus support the gear designer at an early stage of gear development and can be used as a useful source of information.

References

1. Gunter Erhard: *Construction with plastics* (in German: Konstruieren mit Kunststoffen). Carl Hanser Verlag, München, 4th edition (2008).
2. VDI 2736 Sheet 1: *Thermoplastic gear wheels - Materials, material selection, production methods, production tolerances, form design* (in German: Thermoplastische Zahnräder - Werkstoffe, Werkstoffauswahl, Herstellverfahren, Herstellgenauigkeit, Gestalten) (2014).
3. Fürstenberger, M.: *Operating behavior of loss-optimised plastic gears - losses, temperatures, load carrying capacity and dynamic operating behavior* (in German: Betriebsverhalten verlustoptimierter Kunststoffzahnräder - Verzahnungsverluste, Temperaturen, Tragfähigkeit und dynamisches Betriebsverhalten). P.Hd. Thesis, TU München (2013).
4. Hachmann, H., & Strickle, E. (1966). Polyamides as gear materials (in German: Polyamide als Zahnradwerkstoffe). *Konstruktion*, 18, 3.
5. VDI 2736 Sheet 2: *Thermoplastic gear wheels - Cylindrical gears - Calculation of the load-carrying capacity* (in German: Thermoplastische Zahnräder - Stirnradgetriebe Tragfähigkeitsberechnung) (2014).
6. Blok, H. (1937). Measurement of temperature flashes on gear teeth under E.P. conditions. In *Proceedings of the general discussion on lubrication and Lubricants*.
7. Takanashi, S.; Shoji, A.: On the temperature rise in the teeth of plastic gears. *International Power Transmission & Gearing Conference* (1980).
8. DIN 3990 Part 1–5: Calculation of load capacity of cylindrical gears (in German: Tragfähigkeitsrechnung von Stirnrädern) (1987).
9. ISO 6336:2016: Calculation of load capacity of spur and helical gears (2016).
10. Hasl, C.: *Tooth load carrying capacity of plastic gears* (in German: Zur Zahnfußtragfähigkeit von Kunststoffstirnrädern). P.Hd. Thesis, TU München (2019).

11. Hasl, C., Illenberger, C. M., Oster, P., Tobie, T., & Stahl, K. (2018). Potential of oil-lubricated cylindrical plastic gears. *Journal of Advanced Mechanical Design, Systems and Manufacturing*, 1, 12.
12. DIN ISO 14635-1: Gears - FZG test procedures - Part 1: FZG test method A/8.3/90 for relative scuffing load-carrying capacity of oils (in German: Zahnräder – FZG-Prüfverfahren – Teil 1: FZG-Prüfverfahren A/8,3/90 zur Bestimmung der relativen Fresstragfähigkeit von Schmierölen) (2006).
13. Hinterstoiber, M.: *Optimization of the efficiency of spur gears* (in German: Zur Optimierung des Wirkungsgrades von Stirnradgetrieben). P.Hd. Thesis, TU München (2014).
14. Hasl, C., Oster, P., Tobie, T., & Stahl, K. (2016). Method for calculating the actual contact ratio under load for plastic spur gears (in German: Verfahren zur Berechnung der Überdeckung unter last von Kunststoffstirnrädern). *Forschung im Ingenieurwesen.*, 80, 111.
15. DIN 867: Basic rack tooth profiles for involute teeth of cylindrical gears for general engineering and heavy engineering (in German: Bezugsprofile für Evolventenverzahnungen an Stirnrädern (Zylinderrädern) für den allgemeinen Maschinenbau und den Schwermaschinenbau) (1986).
16. Illenberger, C. M., Tobie, T., & Stahl, K. (2019). Flank load carrying capacity of oil-lubricated high performance plastic gears. *Forschung im Ingenieurwesen*, 83(3), 545–552.
17. Schilling, M.; *Ege: Reference oils - Reference oils for bearings, gear and clutch investigations - Data collection for mineral oils* (in German: Referenzöle - Referenzöle für Wälz- und Gleitlager, Zahnrad- und Kupplungsversuche - Datensammlung für Mineralöle) FVA-Book Nr. 180, Forschungsvereinigung Antriebstechnik e.V. (FVA), Frankfurt am Main (1985).
18. Weinberger, U.; Fingerle, A.; Otto, M.; Stahl, K.: *RitzelKORrektur*, Frankfurt am Main (2018).
19. Maier, E., Ziegltrum, A., Lohner, T., & Stahl, K. (2017). Characterization of TEHL contacts of thermoplastic gears. *Forschung im Ingenieurwesen*, 81, 317.
20. Schubert, D.; Hertle, S.; Drummer, D.: *Influence of process-related microstructures on the tooth root load carrying capacity of POM spur gears* (in German: Einfluss prozessbedingter Gefügestrukturen auf die Zahnfußtragfähigkeit von POM-Stirnrädern). *Konstruktion* 03/19 (2019).
21. Hlebanja, G., Hribersek, M., Erjavec, M., & Kulovec, S. (2019). Durability investigation of plastic gears. In *6th International BAPT Conference "Power Transmissions 2019"* (p. 287).
22. Trobentar, B., Kulovec, S., Hlebanja, G., & Glodez, S. (2020). Experimental failure analysis of S-polymer gears. *Engineering Failure Analysis.*, 111, 104496.
23. Nakamura, M.; Atsushi, K.; Moriwaki, I.: *Performance of injection-molded plastic helical gears finished by hot rolling*. Proceedings of the ASME 2011 International Engineering Technical Conferences & Computers and information in Engineering Conference (2011).
24. Raghuraman, N., Houser, D., & Wright, H. (2019). Numerical thermal 3D model to predict the surface and body temperature of spur and helical plastic gears. In *American Gear Manufacturers Association Fall Technical Meeting*.
25. Hasl, C., Liu, H., Oster, P., Tobie, T., & Stahl, K. (2017). Method for calculating the tooth root stress of plastic spur gears meshing with steel gears under consideration of deflection-induced load sharing. *Mechanism and Machine Theory.*, 111.

Chapter 5

Application of Task-Based Conceptual Design Method for Gear Chamfering Mechanisms



Hrayr V. Darbinyan

5.1 Introduction

The growing demand in novel consumer products and continuous progress of metalworking and machine-building technologies are driving the development of appropriate design and verification methodologies and other technical guidelines. The post-industrial era and especially the ever-spread digitization have heavily influenced the methodical support on such engineering activities as design and development of new products and techniques. Referring to traditional and classic mechanical design, one can state growing interest in finding ways of novel approaches for design better matching to the up-to-date demands of quick market response, raised efficiency and broader service of design methodologies, and the tendency of unification of different aspects of mechanical design on a unified basis. The analysis step of mechanical design, for instance, which is preceding the conceptual design phase, is essential in terms of consideration of previous knowledge and is putting the basis of design to create a novel product. Further steps of embodiment design, engineering verification, feasibility and manufacturing confirmation, parametric design and optimization, post design testing adjustment, and justification phases are completing the whole design cycle. Generally remaining on different methodical bases, all those phases are following a single aim to create a novel product with qualified and competitive features. Gear design and manufacturing is a specific and outstanding area of machine building and engineering in general where broad involvement of theory, practice, evaluation, production, and all the other milestones specific for any engineering product is more specific for the gear engineering.

H. V. Darbinyan (✉)

Olympia Tools International, Shanghai Kunjek Hand Tool and Hardware Co. Ltd., Shanghai, China

For this reason, consideration of gear chamfering process as a necessary step of gear chamfering technology is quite typical and characteristic for performing and presenting three unified methodologies. The task-based concept design method was firstly developed for the case of concept design with advantageous features and later extended for one preceding and another following the methods of analysis of a mechanical object and for parametric design and optimization. The current study aims to describe analysis of gear chamfering methods followed by conceptual design of novel devices and ending with parametric design. All three steps are introduced as organized on a single methodical base with the usage of newly developed means of visualization and presentation of those methodologies that are enabling and simplifying accessibility of the proposed method.

5.1.1 Task-Based Design Review

5.1.1.1 Task-Based Conceptual Design

Conceptual design is the most challenging and less understood step of general mechanical design. The difficulties of its description and formulization are coming from first from the nature of conceptual design implying search of a novel structure with novel properties among the great number of candidate solutions. The second reason is the individual nature of the designing process depending on design tradition, skill, and experience of the designer. Design process being attractive and creative by its definition may bring the designer more results and satisfaction when being organized in a way to free the designer from the routine task of checking a large number of options with necessary efforts of visualization. Combinational methods widely used for novel structure solution search are useful for the automatic organization of search process with minimum human involvement. However, they are providing solutions for a key or primary function only suggesting modifications within fixed topology with randomly generated accompanying functions with a high probability of negative features among them. This fact of consideration of a primary function in combinational search dramatically lowers its methodical ability. Any design process is valued for providing a multifunctional solution but not appreciated for the fact of generation from a single topology. For the past few decades, due to growing demand on fresh products with advantageous proprieties and because of wider application of digital technologies, the challenge of better organization of conceptual design process becomes more actual, and this demand was satisfied by several approaches and methodologies. The task-based design methods can be conventionally divided into methods based on mostly on human participation or on computer-aided methods with minimum involvement of human factor. Some examples for the second group of task-based design methodologies are quite successful when directing a designer to organize a new product development with novel properties [1–5]. Trendy and classical methods [6, 7] of splitting mechanical components from functional ones have apparent abstraction and visualization means and

require consideration of a large number of candidate solutions in an attempt to isolate a workable and optimal one. An original publication [8] is using analyses of the vast engineering database as a source for a novel product design, where the search trend implies consideration of either combination of various movements of basic links or direct search of solutions among existing solutions. Insufficient level of abstraction and visualization narrows the opportunities of processing and getting optimal results among mechanical means having required functions and properties. Any design methodology can be evaluated by the number of essential design tasks considered during a mechanism synthesis process and distribution of those tasks along with steps of conceptual design. Having more tasks involved provides broader and full satisfaction of design aim with the maximum number of demanded properties of a novel product. Concluding one may state that concept design methods are mostly serving a single design target and using vast nomenclature of design tools, they rarely show direct dependence between the function and mechanical category, thus misleading the designer from the search task-based and efficient solution.

5.1.1.2 Task-Based Analyses of Mechanical Objects

Analyses of a mechanical object are preceding the synthesis and parametric design phases, and any new solution is analyzed against the prior art and known prototypes to avoid a reproduction of known solutions. General overview [9, 10] of analyses of a mechanical object shows that they are mostly separated approaches for different embodiments of the mechanical objects, and those approaches are not methodically connected. Every method has its own specific rules and laws for analyses, creating a systematic disadvantage because the modification from one embodiment to the other one should be done on the same systematic basis and using the same toolset. Another shortcoming or methodical difficulty should be seen in the absence of a model or of etalon mechanism which can serve as a guide or as a merit for comparing different structures following to the same task of design for a better understanding. The mechanical object should have the ability to be modified structurally and functionally to allow the designer to find the hidden properties of the structure. This act of recognizing an object will significantly win and will be much useful if organized on a function-based way. The analyzing methods are lacking in such an approach which is hiding the properties and the source of features the object may have because they are not connecting the structural properties with functional properties. Based on those mentioned above, we may conclude that the analysis method should obtain the same toolset and methodology as the conceptual design methodology and parametric design methodology have.

5.1.1.3 Task-Based Parametric Design and Optimization

A classical approach of mechanical design implies consecutive implementation of the chain including an establishment of the task, accomplishment of conceptual

design, dealing with parametric design and optimization, technological assurance, including manufacturing and assembling, and finally post design verification and acceptance by the end user. Traditionally the mentioned components of the design process are methodically separated from each other having their own rules of self-organization and implementation. Despite this fact, attempts of methodical merger and unification, especially for the conceptual and parametric steps, can be found [11]. A tendency of further focusing on such unification can be observed, which is logically accommodated in the idea of simplification of design tools on the one hand and the growing involvement of digital technologies in the mechanical design process on the other. In a classical approach for the parametric design [12], an organization of optimum search process is based on consideration of some schematic or other visualized graphical presentations containing variables subject to definition or optimization, a set of constraints limiting the range of some variables and a target function(s) subject to be numerical satisfaction. The structural-graphical support for organizing the parametric design process in some cases is even missing. In the instances of its presence, the structure cannot necessarily explain and arrange solution of the target function, saying less about secondary but still essential functions. A novel method of conceptual design [13] implies the application of a set of methodical tools that allows firstly to set the task and manage and monitor the whole process of task-based design starting from the creation of models including essential components of the future mechanism.

Appropriately modified methodical tools are applicable for the organization of the next parametric design and optimization process with usage of the same structure formation rules which are specific for concept design. Those tools are upgraded to a level to have the possibility of presentation and description of design parameters (variables) subject to definition and optimization. They are using the perceptive level of structural and graphical visualization. Once the conceptual design cycles are arranged in a way to support the concept quantified evaluation process, the parametric design cycles are ending in calculative structures and schemas making possible and facilitating composition of equations and resolving them against challenged parameters of conceptual design. As a major design tool applicable for conceptual design phase, the grant DOF (degree of freedom) action is also practiced for the parametric design, where the functional meaning of such actions is in duplication of parametric relations lowering the DOF of the structure or making the grant DOF actions mechanically possible. Parametric models built in such way are applicable not only for solving parametric optimization tasks but are workable also for force analyses of mechanisms [13]. On the background of enormous heritage for methodologies of conceptual and parametric design, for example [14, 15], the author's decades-long mechanical design experience for various mechanical devices (machine and hand tools, home and leisure appliance products, etc.) has proved the workability and efficiency of self-developed methodology for conceptual and parametric design against the firstly mentioned ones. Simultaneous consideration of function and mechanism, application of unified synthesis and analyses tools, various visualization means, and usage of same modification tools for mechanical and functional sets can be related to the advantageous features of the suggested unified

conceptual and parametric design methodology. That's worthy to note that methodical arsenal of conceptual design fits and satisfies the needs and requirements of structure analyses – a step that precedes the conceptual design and stores its resources.

5.1.1.4 Novel Task-Based Conceptual and Parametric Design Method

Mainly explained by growing market interest and demand for new products, the issue of development and application of effective methods of conceptual design has turned into a high-priority problem. Several methodologies for mechanical design and guidelines are developed through the latest decades. A novel task-based conceptual design method [16] developed upon long-term experience of various mechanical devices is based on simultaneous consideration of both mechanical and functional sets once those sets are appropriately modified to conditions best matching design requirements and best providing conditions for getting a novel current solution for a single or functional set and continuing the search of remained design tasks in an identical way. A localized set of function and mechanism is considered a design model. The key model may have different contents depending on step, level, and scale of design task. The method has confirmed its efficiency not only for resolving tasks of conceptual design but also is workable for some tasks of parametric design [13].

5.1.1.5 Tasks and Objectives

The present study has a task and objectives to improve organization and visualization of all three steps of mechanical design: for analyses and conceptual and parametric design. This objective is going to be reached by usage of universal graphs which can serve of the three steps and are including necessary structural, function, and parametric data essential and ready for a step-by-step processing. The further objective of current study is to review and put on a single basis the three steps of mechanical design and organize analyzing, synthesizing, and calculative methodically unified formats using the available methodical and modification tools developed for the case of conceptual design.

5.1.2 Theoretical Background of Current Chapter

5.1.2.1 Author's Experience

From the early stages of author's experience in mechanical design, it has been noticed efficiency and practical value of mechanical-functional composition and decomposition when modifying some original structure into an upgraded one to

develop a fresh and previously not existing design that satisfies some set of pre-given functions or challenging tasks.

Also based on design experience, it was first found that the decomposition unit could be variable and differing in contents, and that's a challenge or design task in the establishment of the complexity of this unit, and, secondly, any act of decomposition is implemented for some purpose – the task or sub-task of design. In an ultimately exaggerated case, the components at a higher degree of decomposition could be imagined and named as “**construction bricks**” as the smallest size of mechanical unit firstly given in an unbiased order with a design task to organize proper physical-mechanical-kinematical order of their connection in a way to satisfy a set of pre-given functions, features, or properties of a novel structure.

5.1.2.2 “Construction Bricks”

Those units are formed as a result of structural decomposition based on the consecutive application of elementary links and elementary movements (sliding and revolute). The general structural decomposition and breakdown into “construction bricks” stimulate designer's imagination by the huge number of design opportunities. It is challenging him or her with the necessity to consider-accept-reject one by one all the options which most probably turns designers' activity into a not creative and time-consuming one. On the other hand, the evaluation and consideration process for the case of task-based design should have an outcome defined by the achievement and implementation of a specific function(s), so manipulation and processing of functional data is a must condition. From this point, the arrangement and management of functional data should be provided to assure evaluation of a specific design solution from the functional standpoint. Analogously with above, a mentioned set of “construction bricks” originally given and generated along design process functions tend to grow in numbers and thus make difficult their consideration. The same relates to a separate set of functional variables as well which are considered simultaneously with a set of “construction bricks.” This circumstance explains the limited scope of application and low efficiency of some design methodologies which are letting the designer analyze a vast number of candidate solutions before the designer comes to unacceptable results with the limited number of achieved functions. And this circumstance also prompts the apparent solution or direction about the organization of design process through a certain level of decomposition of “design bricks” on the one hand and a certain level of decomposition of involved functions and by following the must condition of assigning a certain set of functions to any action of decomposition of the mechanical means on the other. Also based on long-term design experience, it was noticed that generation of a daughter function from the parent function has methodical similarity to the act of growth or multiplication of newly involved or generated mechanical links from the original link. This fact implies the possibility of development and application of the unified methodology of processing and arrangement of both mechanical and functional data.

5.1.2.3 Building of a Mechanism

Origination of a novel link from the existing one can be described in a particular case by well-known action of granting a degree of freedom. Anyhow the birth of a new link shouldn't be limited by the necessity of mobility or the second link relative to the first or basic one but should be viewed at a broader context, accepting that any relation between two mechanical links can be the reason for some function (positive, negative, not expected, assisting, secondary, any). Ignoring this relation may reflect negatively on the completeness of the task of the design process and considering of which may provide a more comprehensive and full design process. At this point, the "links" category should be defined, depending on the needs of the design process and setting the efficiency and possibility of analyzing or synthesizing action. In the most common case, the links are the same as the physical links or rigid bodies with no elasticity. In more uncommon cases, the link can be interpreted as a human body, some environment (e.g., air, liquid, machine oil, etc.), or links having elasticity (e.g., springs) and requiring some additional sub-links for explaining the mobility or functionality of a spring. And in the most abstract case, a link can be represented as a mechanical sum of a set of links with no mobility between them or as a result of kinematical trajectory once generated or activated or followed by a set of necessary movements and then frozen at a stage after a definite set of moves has been implemented. All the commonality of movements, frozen movements, mutual influencing, and contacting could be generalized into one category of relation between the links. This relation is directly defining the character of link mobility against another one and is defining the function implemented as a result of such relation.

Worthy of mentioning that the links can be connected by three kinds of connections or relations:

First is the classic case of the kinematical joint.

Second is a conventional relation for the case with the link should be connected for some function so the function is given but the character of the kinematical connection is unknown. In this case the edge of the graph used for structure description is representing not a kinematical joint but the function.

Third case goes for the character of contact of a relation between the formation element of surface tracking tool and the surface of the chamfer. Depending on kinematical diagram and type of applicable tool the gear chamfering process may be described as one or two parametric surface reproduction.

5.1.2.4 Visualization

A design model with two links as vertices of a graph and an edge between them representing the mobility of links and the function implemented by such connection has and stores practical and methodical resource for task-based conceptual design, feature analyses, and parametric design and optimization. It should be noted that

generally any mechanical device intended to be used purposely to implement an action to simplify or make more comfortable the human job or enlarge the scope of human power and accessibility is composed of generalized links composing a closed chain. From this point, the idea of two link/one function model is not complete and should be completed by an additional parallel edge having two meanings: firstly this edge contains additional links of parallel chain necessary to get a close loop for the purpose mentioned above, and, secondly, this extra edge represents the new set of functions, that should be added to the original task functions to allow evaluating the composed mechanical functional model thoroughly. Worthy to note that additional edge directly adds the number of links, and simplicity feature is to be considered directly per number of links and kinematical or other relations inserted by the involvement of the new edge. It should be noted that in both cases when connecting the second link to the first one and with coming back to the first link using a third one, the same procedure of choosing the source link and the target link and connecting those two links via mobility or by type of relation, in general, is implemented.

Connection of two links should provide a closed loop with the last edge labelled by symbol γ which stands for general relation of the previous link of a closed-loop to the first link and bears the physical meaning of a generalized contact. Touching the fingers of user to the handles of a hand tool or contacting of cutting edge of a work tool to the processed surface of a workpiece may serve as examples of the edge γ . Any link is subject to further disintegration as well as any group of set of links is subject to uniting and grouping. A methodical demand of composition and decomposition requires all the actions to be done on a functional basis.

5.1.2.5 Composition of Models

The idea of the model takes a central and essential place in the suggested conceptual design method as a mean for concentrating on design task and focusing on the resolution of a separate task or function. Having the flexibility or being built per needs of the design process, it may address to main design target and be checked against the remained requirements or secondary functions. With the same success, it may collect requirements consecutively and be shaped in a way to address a set of requirements. In the following example of the development of gear chamfering mechanisms, the model is constructed according to the first principle. The accuracy of chamfer surface reproduction is targeted as a main requirement, and the nominal model checks the other conditions of efficiency, flexibility, tool, and kinematical simplicity in further qualitative and quantitative evaluation.

5.1.2.6 Synthesis Tools and Design Cycles

Method of decomposition into “construction bricks” extremely limits the scope and size of applicable design tools set, thus simplifying and unifying the synthesis

process. A set of “construction bricks” as a unit of a higher level having confirmed features can be involved in the composition process if those features are known from design history and database. Such unit should be preliminary decomposed or composed to a necessary level of applicability. Those cases are typical for synthesizing actions where the connection of two links is just a procedure of completing a well-known standard kinematical structure (a four-bar mechanism, for instance) with well-known properties and functions. A design procedure organized in a way as mentioned above could be repeated in a cycling manner. It can be composed as a set of methodically identical cycles, where the periods are arranged in an order with gradual involvement of required design tasks functions, starting from the main or the most important one and ending with secondary functions.

5.1.2.7 Modification Formats: Synthesis

Once the advantages and features of suggested conceptual design are explained, we can step forward to the creation of standard-based formats which could be further used for the conceptual and parametric design and analyses. First, we approach the synthesis format consisting of task planning, implementation, and evaluation steps.

At task planning step, original two links are considered connected in a way to implement the given function. If the physical nature of the connection is not precise, then the links are connected virtually just planning the implementation.

Next step of implementation is organized by a set of synthesizing tools, realizing composition and decomposition of the mechanical object or original two links once the mechanical product is not developed yet.

Two main tools for providing a pre-given function are the composition and decomposition of mechanical components, and both procedures are carried out on a function-based manner. Under composition or decomposition, we may understand granting DOF or freezing DOF actions and specific modification of mechanical category when a solid link can be presented as a set of some links connected in a way to compose the named link. The primary approach of conceptual design implies consideration of a set of links in an attempt to implement a pre-given function. So, the synthesis development format should include the first stage of primarily given links and the second stage of modifying those links into the state to either satisfy a pre-given function or to plan the satisfaction of the pre-given function. As a result of this procedure, we may have consecutively arranged links as an open mechanical chain, or we may have a close loop as a result of completing the open-chain by the last or final link, so the final circuit is composed. So far as every step of modification is accompanied by the emergence of secondary or lower-tier functions then, for an overall evaluation, the preliminary given set of tasks should be gradually added by those emerged functions. The best or the most convenient visualization mean to describe this process is the presentation by means of graphs, where vertices are for links and edges are for kinematic joints or planned functions and edges connect vertices as representations of kinematical or other joints. The format is divided into fragments where the pre-given function is planned and where the pre-given function

is implemented. Implementation of the pre-given functions can be provided by simple granting of degree of freedom where another link having the freedom against the base link may have mobility and necessary movements to implement the pre-given function.

What is specific for the suggested conceptual design method is that each step may be satisfied by one or more pre-planned functions or every function should be satisfied at consecutive steps. According to the third case, implementation of one function already includes specific level and status or other functions provided by the same topology which need either qualitative or quantitative evaluation per the present contents of the developed structure. This circumstance is specific for the below-considered example of the development of gear chamfering mechanisms (Sects. 1.3, 1.4, and 1.5).

Another synthesis scenario is to build a model granted by all required functions or features as a result of decomposing the physical diagram. Decomposition should be done to a state comparable with the model at the same structural basis and judge about presence or absence of the necessary features.

So, the synthesis format should include all the mentioned possibilities to allow the designer to plan the implementation of the pre-given function one by one by decomposing the set of functions into main one and secondary ones and following the instructions already described to get the pattern for implementation of those functions. Once the pre-given functions and the accompanying functions are figured out, they are subject of evaluation and decision-making about acceptance or rejection. A single cycle of synthesis process is completed when the pre-given function at the current stage is achieved, and the next functions are planned and delivered to the following design cycle list. The synthesis process is completed when all the pre-given, accompanying, and negative functions are satisfied.

5.1.2.8 Modification Formats: Analyses

The above-described structure of synthesis format can be reversed into analyses format if the necessary modification and decomposition is started from the real physical object instead of task of planning in synthesis format. Secondly, the analyses format is finished with decomposed 3D and 2D models with necessary graphs for their description and indication of revealed functions. Analogously to the synthesis format, a single topology may contain and provide several functions so a single level of modification can be enough for evaluation of not one but a set of functions. The decomposed topology later is used for grouping or regrouping links for description or evaluation of quantitative functions as velocity or efficiency which don't require an additional topology but are requiring set of grouped links, kinematical joints between those links, and parameters for describing quantitatively those movements. The analyses format is successfully workable also for database consideration and usage so that an existing solution can serve as example for prior art object of competitions. As well they can serve as bank of accumulated knowledge subject to proper modification prior using ready solutions for the needs of synthesis and

conceptual design. The analyses format can generate models with needed and positive properties which can serve as the base or start point for synthesis instead of concept design from scratch.

Alternatively, the same target can be reached using the database that is using the previous knowledge with the direct involvement of definite structure and a certain set of functions.

5.1.2.9 Modification Formats: Parametric Design

Analyses of design knowledge, mechanism guidebooks and structural solutions databases is an important and necessary premise for creating of a new product – a mechanism, a tool, a machine tool or a consumer product. Successful solution of this objective assures the success of not repeating the mistakes or previous knowledge acting in a way not to create a bicycle and formulate the task for the development of a new competitive product. The mentioned objective sounds with and is present in the objective of evaluation of new solutions and in the aim of comparative analysis and setting the goals and tasks for the synthesis of a new product with economically valid features. As well it is valid for the case of patent analyzes when that's necessary to evaluate a new solution or to assess the novelty of a patent-pending structure by revealing advantageous features and qualitative novelty from the prior art and known prototypes.

Firstly, the approach will allow for revising the object under consideration not only from the point of its physical appearance but from the point of its contents.

Secondly, this step may substantially win from the point of description and explanation or from a descriptive and explanatory point of view as a counterweight to narrative and not descriptive methods can be explained using existing or specifically developed graphic or visualization means.

Thirdly, the method of modification of a physical object will give a chance to reveal and review new, positive, hidden positive, hidden negative functions and provide a full-scale outlook for the object being under consideration. For the same time, some views or images or status of the modified object may serve as models and virtual mechanisms for full-scale evaluation of the existing product and for the precise formulation of original conditions for creating or synthesizing of a new product.

The procedure for general design, conceptual design, analyses, and parametric design is summarized in Figs. 5.1, 5.2, and 5.3, correspondingly.

5.1.3 Analyses of Gear Chamfering Methods

Three of almost a dozen known gear chamfering methods and devices are going to be analyzed in this paragraph to figure out the ability of each of them to address six characteristics that are specific to these devices. Choice and description of those

Fig. 5.1. General design flowchart

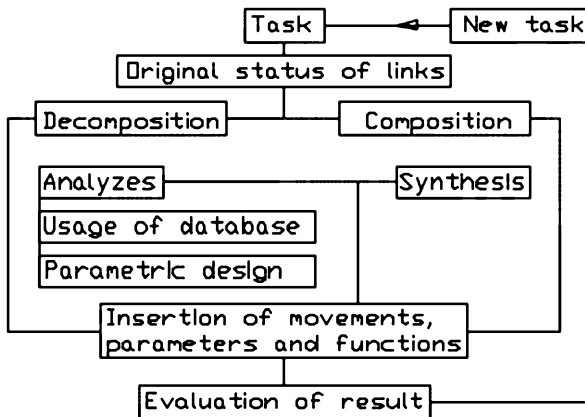
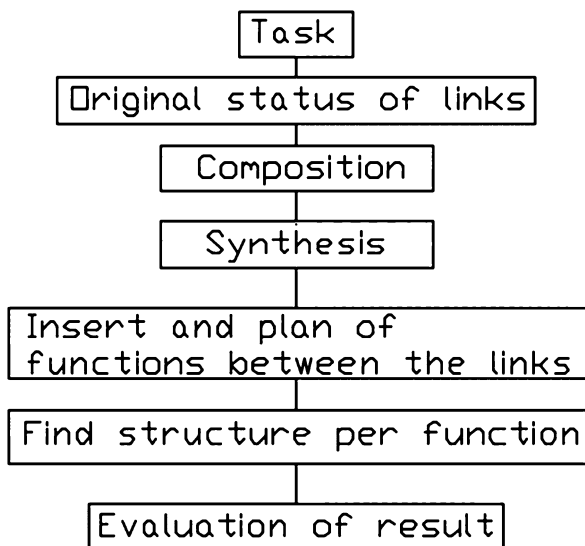


Fig. 5.2. Flowchart for synthesis



specific functions are presented in the Sect. 1.3.1. As it was mentioned earlier, the analyses should be run in a comparative manner having a merit mechanism (model) combining in itself the specific characteristics of gear chamfering process. A model with theoretical point tool is used for reproduction of chamfer surface along toothed (or any other) pattern. Description of the point model is presented in Sect. 1.3.2. Once the point model is built, and the evaluation criterion are worked out, a single cycle of analysis can be implemented by the steps below:

- Building a point model (3D and 2D) as a merit for evaluating features of a gear chamfering method and mechanism taking into consideration main criteria of geometric accuracy of chamfer surface.

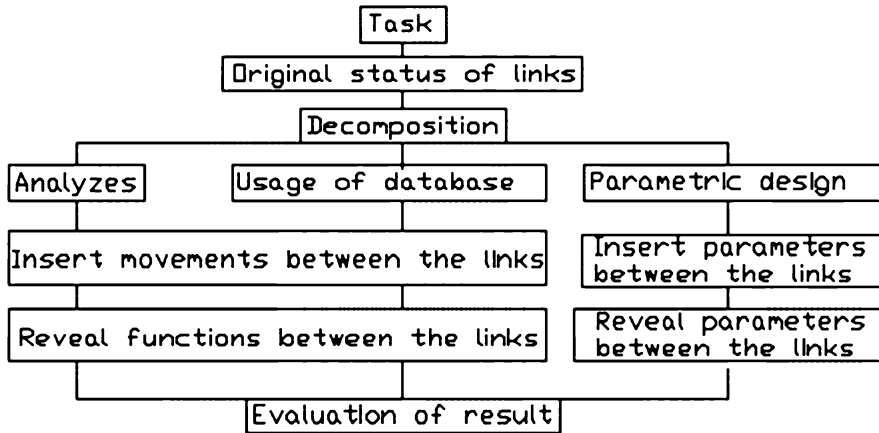


Fig. 5.3. Flowchart for analyses, database, and parametric design

- Setting procedure for evaluation of the point model features.
- Composing the general structural-functional graph of point model with the indication of links, functions, and movement parameters.
- Separation of specific sub-chains from the general graph for qualitative and quantitative evaluation of point model features.
- Comparison of contents (structure) and value (the ability of function implementation) of a specific sub-chain with appropriate sub-chain of the point model.
- Quantified evaluation of a feature based on a proper set of links and movement parameters provided by and grouped out from the general graph (quantitative characteristics).
- Quantified assessment and making a conclusion about the ability of every sub-chains to implement the function predefined by the point model and recording an appropriate weight coefficient (qualitative characteristics).

After setting analyses format, the next action should be building of the point model for side-by-side comparison with known gear chamfering methods/mechanisms.

5.1.3.1 Set of Functions Describing Gear Chamfering Methods

Coming to the chamfering methods and mechanisms, we need to formulate six basic features which are describing this kind of devices. **Firstly**, these mechanisms should be **accurate** that means they should assure accurate duplication or tracking of both carcass lines of chamfer surface – the guide line and the generating line. Accuracy of those lines means precise duplication for the guide line and stability of shape and position of the chamfering triangle for the generating line.

The **efficiency** of chamfer surface reproduction means the speed of surface tracking by a tool of both carcass lines. Evaluation of this feature doesn't require any update or further development of the point model; so far, all the necessary components and parameters are included in it. The third feature subject to evaluation and revealing is the tool **simplicity**.

The point model can be described as a model holding a tool of **zero degrees of complexity**. The feature of **flexibility** defines the method's ability to track guide lines of different shapes and generating lines with different value, angle, and direction. From this view the point model has highest flexibility because of presence in it of five degrees of freedom.

Kinematical simplicity shows how a method is qualified to include a smaller number of components with simple kinematical connections between them. For the point model, kinematical simplicity is at zero levels because of the highest number of degrees of freedom. And the last merit specific for a chamfering method is the level of **energy consumption** defined by the character of processing a steel gear: by chip removal or by plastic deformation. For the case of a point model it's at a lower level because it has no ability of metal processing. Despite this disadvantage, the point model can be used as a merit for analyzing the main features of existing gear chamfering mechanisms. After analyzing of the mentioned characteristics, each method has got an evaluation score based on decomposition analyses (except criteria of **energy consumption**).

5.1.3.2 Construction of a Point Model as Merit for Analyzing Gear Chamfering Methods (Table 5.1)

First important feature characterizing a chamfering method is the ability of the method to duplicate a geometrically accurate chamfer surface. That means those chains should assure duplication or tracking of both surface composition lines: the guide line and the generating line as the carcass for tracking a 3D surface of a chamfer along the toothed pattern. The guide line of a toothed pattern is coinciding with its toothed pattern by itself. And the accuracy of the generating line means the stability and constancy of the three pages of chamfer generating triangle against the toothed pattern.

The normal page is directed perpendicularly to the toothed pattern, the axial page is parallel to the axis of the gear, and the hypotenuse of the triangle is the generating line of the chamfer surface by itself. Creation of sub-mechanisms for guide line and generating line and creation of the whole mechanism of gear chamfering model are based on the consecutive application of elementary movements or primitive movements in a way to be responsible for a specific function.

This action is planned in Table 5.1-1-4 where firstly it is set the general requirement of surface formation (Table 5.1-1), then it is specified to accuracy issue (Table 5.1-2), and this requirement in its turn is subdivided into accuracy requirements for the guide line (Table 5.1-3) and generating line (Table 5.1-4). In the most simple and theoretical way, any complicated pattern included the toothed

Table 5.1 Format of point model synthesis for chamfer surface generation

Point Model for Chamfer Surface Generation -W=1.0			
Set of Challenged Functions with Weight Coefficients for Importance			
F ₁ :Accuracy - 0.25	F ₁₁ :Guide Line Accuracy- 0.13	F ₄ :Tool Simplicity- 0.1	
F ₂ :Efficiency- 0.3	F ₁₂ :Generate Line Accuracy- 0.12	F ₅ :Kinematic Simplicity- 0.1	
F ₃ :Flexibility- 0.1	F ₂₁ :Guide Line Efficiency- 0.15		
	F ₂₂ :Generate Line Efficiency-0.15		
	F ₃₁ :Guide Line Flexibility- 0.05		
	F ₃₂ :Generate Line Flexibility-0.05		F ₆ :Energy Consumption-0.1 (Total-1.0)
Development of Point Model			
Task Planning			
F ₀ : Functions in General	F ₁ : Accuracy	F ₁₁ : Guide Line Accuracy	F ₁₂ : Generate Line Accuracy
1	2	3	4
Task Solution			
F ₁₁ : Guide Line Accuracy		F ₁₂ : Generate Line Accuracy	
5	6		
General Solution Graph		Function Breakdown	
7	$F_A = (F_{11}, F_{21}, F_{31}, F_5)$ $F_B = (F_{11}, F_{21}, F_{31}, F_5)$ $F_C = (F_{12}, F_{22}, F_{32}, F_4, F_5)$ $F_D = (F_{12}, F_{22}, F_{32}, F_4, F_5)$ $F_E = (F_{12}, F_{22}, F_{32}, F_4, F_5)$		
	$F_0 = (L_0, L_3, L_4, L_5 L_3, L_4, L_5) == f(x, y, z, x, \phi, R)$		
3D Model		2D Model	
8	9		

(continued)

Table 5.1 (continued)

Graphs for Feature Explanation and Evaluation	
<p>F_{11}: Accuracy of Guideline Reproduction</p> <p>10</p>	<p>F_{12}: Accuracy of Generating Line Reproduction</p> <p>11</p>
Set of Links and Parameters Involved	
$F_{11} = (L_0, L_1, L_4) = f(x, y)$ (2)	$F_{12} = (L_0, L_2, L_4, L_3) = f(z, \phi, R)$ (3)
Evaluation of Synthesized Functions	
0.13	0.12
<p>F_{21}: Efficiency of Guideline Reproduction</p> <p>13</p>	<p>F_{22}: Efficiency of Generating Line Reproduction</p> <p>14</p>
Evaluation of Synthesized Functions	
0.15	0.15
<p>F_{31}: Flexibility of Guideline Reproduction</p> <p>12</p>	<p>F_{32}: Flexibility of Generating Line Reproduction</p> <p>13</p>
Evaluation of Synthesized Functions	
0.05	0.05
<p>F_4: Tool Simplicity</p> <p>14</p>	<p>F_5: Kinematic Simplicity</p> <p>15</p>
Evaluation of Synthesized Functions	
$F_4 = L_0(\emptyset)$ (10)	$F_5 = (L_0, L_1, L_2, L_3, L_4, L_5) = f(x, y, z, \phi, R)$ (11)
0.15	0.1

Table 5.1 (continued)

(continued)

pattern can be reproduced by a set of functionally connected movements, like sliding movements along axis X and Y . In a simple combination of two sliding links L_1 and L_2 , relative axis L_0 is satisfying reproduction of the guide line (Tables 5.1-8 and 9).

As it is mentioned above, the graphs are organized as closed loops where the starting is for the toothed pattern or work gear (L_0) and the end link belongs to the surface tracking tool which is bringing back the chain of vertices with original point belonging to the toothed pattern. Edge γ is symbolizing contact of surface tracking point L_5 with chamfer surface subject to reproduction. The edge γ in all the graphs is simulating contact of point L_5 to the chamfer. The symbol γ has more general interpretation of any relation between the links different from a conventional kinematical joint.

The last link of the model is a slider containing a point which is tracking the toothed surface; for that reason, the developed model can be called a **point model**. Table 5.1 includes the necessary steps and actions for the creation and evaluation of the point model. The overall weight score or coefficient of the point model is equal to 1 because of the model setting the standards for gear chamfering mechanism and despite the fact of having theoretical nature with no metal processing ability. The three chamfering methods (using an end mill, comb mill, and plastic deformer as a tool) subject to analyses are for physical processing, so the appropriate adjustments for weight coefficients are done allowing side-by-side comparison:

1. Evaluation of efficiency of processing is done by grouping the necessary parameters from Tables 5.1-4 and 5) for guide line sub-chain and from Tables 5.1-10 and 11 for generating model and based on this set is calculated the velocity of reproduction of both lines.
2. F_{31} as flexibility, the functional relation $f(x, y) = 0$ allows the reproduction of any pattern, and relation (z, φ, R) permits reproduction of any chamfering triangle (F_{32}) hypotenuse.
3. The simplicity of point model tool F_4 can be evaluated as at zero complexity or at highest (max) simplicity because of its theoretical point nature.
4. With kinematic simplicity F_5 , the model has the highest complexity level because of the maximum number of functional movements concentrated in the point model.

Tables 5.1(1-4) is showing the planning step of the construction of the point model.

Tables 5.1-5, 6, and 7 is for the task solution step, including to separate composition of graphs for providing the guide line (Table 5.1-5) and generating line (Table 5.1-5) accuracy.

Table 5.1-8 is for the general structural-functional graph with generalized and combined edges for several functions, when the same structure can perform several and combined functions. The edges of the graph first are showing the planned functions and then after consecutive connection of the links and defining the kinematical joints between them.

Table 5.1-9 is for the composed 3D model as a result of synthesizing action with indications of links and kinematical joints, while Table 5.1-10 is for 2D presentation of the 3D model.

Tables 5.1-15 are for review of features of all the functions subject to implementation by the point model. Evaluation of each function is considered at two levels either **qualitative** when the presence of links with appropriate connections are enough to confirm function or **quantitative** when besides the presence of the links the type of connection between them and derivatives is needed for feature evaluation.

Table 5.1-8 is for the edges of the graph first showing the planned functions and then after consecutive connection of the links and defining the kinematical joints between them.

5.1.3.3 Mathematical and Physical Connections between Revealed Parameters of Gear Chamfering Methods

Presented formats have the methodical ability for mathematical and physical connections between the parameters to provide ways for the description of the tooth surface. First, they contain necessary data for describing the position of the endpoint of a radius vector tracking the chamfering surface being supported by them by the set of elementary movements. The elementary movements are the sliding and revolutionary movements around and along three coordinate axes. These movements can be easily described by 4 x 4 matrices, each of them having a single variable parameter. On the other hand, this method of description correctly sounds with the methodical representation of structures where the links are either physical objects with zero dimensions or the links are solidified or frozen results of fixed movements.

5.1.3.4 End Mill Gear Chamfering Method Analyses (Table 5.2)

The tool has the highest flexibility per guide line (Table 5.2-9) and lowest fixed flexibility for the generating line (Table 5.2-11) because of the concentration of all the three movements in the solid conical body of the end mill. The fixed parameters are shown in bold to emphasize their fixed and frozen nature (Table 5.2-11). Compared with the point model, additional freedom is granted for simulating the presence of minimal radius for end mill R_o needed for providing necessary different from zero velocity of metal cutting (Table 5.2-2). Kinematical simplicity (Table 5.2-15) is at an average level due to involvement in the proper sub-chain part of total surface tracking movements. Comparison is done by side-by-side comparison of a current method and the point model.

The simplest way for making chamfer of a longer toothed pattern is the application of end mill which is practically applicable for large module gears having enough space between two neighbor teeth to allow placing a small end mill inside. The

format for analyzing gear chamfering mechanisms starts with the composition of a 3D model consisting of decomposed sliding and rotary links revealed behind the physical model and allowing the description of the features of the mechanism under consideration. The appropriate sub-mechanism or 3D model is practically the same with point model structure and contents with two major differences. **Firstly**, movements of the first two sliders can be implemented on the base of a CNC machine, for example, to provide the motion along the toothed pattern. And, **secondly**, the end mill has a minimum radius necessary for providing minimum speed of cutting or milling. One more difference is that the angle of orientation of forming triangle has two different meanings and applications. First, this angle is frozen at the value of 360° to provide the body of the end mill. This shape formation is possible when the larger side of the triangle is frozen, and second is for creation of the body of an end mill. These circumstances are defining the flexibility of the end mill method at the highest degree for the toothed guideline and the lowest flexibility degree for the chamfer generating line. Other features of the end mill mechanism are described and presented in the analyzing format in Table 5.2.

The overall rating of end mill method is 0.7 lower than that of the point model, due to limited efficiency and flexibility features.

5.1.3.5 Comb Mill Gear Chamfering Method Analysis (Table 5.3)

The next method of gear chamfering process subject to analysis is the method of a comb mill which is using a standard tool for gear processing for gear chamfering. The comb mill has cutting teeth arranged circumferentially instead of helically arranged cutting teeth of a worm gear. Physical diagram and 3D decomposed model, 2D model, and structural-functional graph are presented in an analyzing format in Table 5.3. This method is based on the separation of two functions of reproduction of the toothed pattern and application of means to provide the velocity of the main movement of cutting. The first function is implemented by a rack engaged with the teeth subject to chamfering, and second function is given to the comb mill being rotated at a speed of cutting movement and being located at a specific position relative to the axis and face of the gear. Appropriate 3D and 2D models are presented in Table 5.3. The 2D model is helping to the composition of the structural-functional graph. The graph is representing by itself a closed-loop starting from the toothed pattern and ending by the final slider of the decomposed structure of the comb mill.

This chain includes all the necessary components enough to combine them into appropriate sets for describing any required function or property of the comb mill method. Worthy to note that those components and parameters are useful and applicable for the description for qualitative as well as quantitative features of gear chamfering method. For example, the comb method is good for productivity or efficiency because of the large diameter of the comb mill. The method is relatively

Table 5.2 Functional and structural analyses of end mill method for gear teeth chamfering

Analyses of End Mill Method – W=0.7		
Physical Diagram	Decomposed 3D Diagram	
1	2	
2D Model	General graph	Function Breakdown
3	4	$ \begin{aligned} F_A &= (F_{11}, F_{21}, F_4) \\ F_B &= (F_{11}, F_{21}, F_{21}, F_5) \\ F_C &= (F_{11}, F_{21}, F_{21}, F_5) \\ F_D &= (F_{12}, F_{22}, F_{22}, F_4) \\ F_E &= (F_{12}, F_{22}, F_{22}, F_4) \\ F_G &= (F_{12}, F_{22}, F_{22}, F_4) \end{aligned} $ (1)
$F_0 = (L_0, L_1, L_2, L_3, L_4, L_5, L_6) = f(R_0, x, y, z, \varphi, R)$ (2)		
Graphs for Feature Explanation and Evaluation		
F ₁₁ : Accuracy of Guideline Reproduction per End Mill Method	F ₁₁ : Accuracy of Guideline Reproduction per Point Model	
5	6	
Set of Links and Parameters Involved		
$F_{11} = (L_0, L_1, L_2, L_2) = f(R_0, x, y)$ (3)	$F_{11} = (L_0, L_1, L_2) = f(x, y)$ (4)	
Evaluation of Analyzed Functions		
0.12	0.13	
F ₁₂ : Accuracy of Generating Line Reproduction per End Mill Method	F ₁₂ : Accuracy of Generating Line Reproduction per Point Model	

(continued)

Table 5.2 (continued)

<p>7</p>	<p>8</p>
$F_{12} = (L_0, L_4, L_5, L_6) = f(z, \varphi, R)$ (5)	$F_{12} = (L_0, L_3, L_4, L_5) = f(z, \varphi, R)$ (6)
Evaluation of Analyzed Functions	
0.12	0.12
F_{21} : Efficiency of Guideline Reproduction	F_{21} : Efficiency of Guideline Reproduction per Point Model
$V_{21} = \frac{dS}{dt} = \left(\frac{dx}{dt}, \frac{dy}{dt} \right)$ (7)	$V_{21} = \frac{dS}{dt} = \left(\frac{dx}{dt}, \frac{dy}{dt} \right)$ (8)
F_{22} : Efficiency of Generating Line Reproduction	F_{22} : Efficiency of Generating Line Reproduction per Point Model
$V_{22} = \frac{dS}{dt} = \left(\frac{dz}{dt}, \frac{d\varphi}{dt}, \frac{dR}{dt} \right)$ (9)	$V_{22} = \frac{dS}{dt} = \left(\frac{dz}{dt}, \frac{d\varphi}{dt}, \frac{dR}{dt} \right)$ (10)
F_{31} : Flexibility of Guideline Reproduction per End Mill Method	F_{31} : Flexibility of Guideline Reproduction per Point Model
<p>9</p>	<p>10</p>
$F_{31} = (L_0, L_1, L_2, L_3) = f(R_0, x, y)$ (11)	$F_{31} = (L_0, L_1, L_2) = f(x, y)$ (12)
Evaluation of Analyzed Functions	
0.05	0.05
F_{32} : Flexibility of Generating Line Reproduction per End Mill Method	F_{32} : Flexibility of Generating Line Reproduction per Point Model
<p>11</p>	<p>12</p>
$F_{32} = (L_0, L_1, L_4, L_5, L_6) = f(R_0, z, \varphi, R)$ (13)	$F_{32} = (L_0, L_3, L_4, L_5) = f(z, \varphi, R)$ (14)
Evaluation of Analyzed Functions	
0.03	0.05
F_4 : Tool Simplicity per End Mill Method	F_4 : Tool Simplicity per Point Model

(continued)

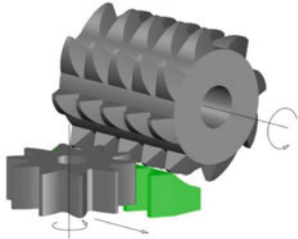
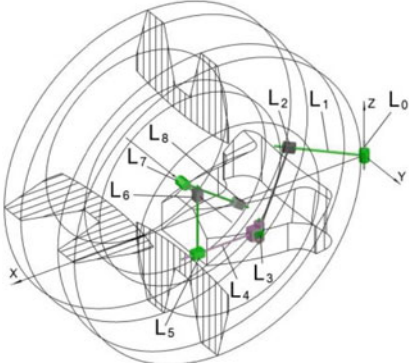
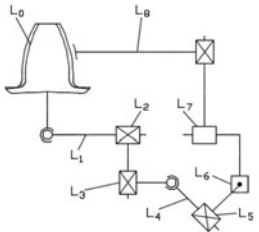
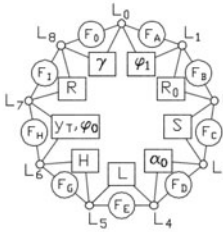
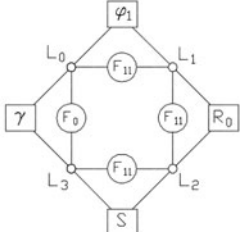
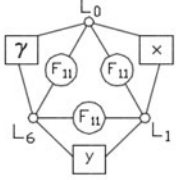
Table 5.2 (continued)

<p>13</p>	<p>14</p>
$F_4 = (L_0, L_7, L_{7A}, L_8) = f(\gamma_T, \varphi_0, R)$ (15)	$F_4 = L_0(\emptyset)$ (16)
Evaluation of Analyzed Functions	
0.03	0.15
F_5 : Kinematic Simplicity per Comb Mill Method	F_5 : Kinematic Simplicity per Point Model
<p>15</p>	<p>16</p>
$F_5 = (L_0, L_1, L_2, L_3) = f(\varphi_1, R_0, S)$ (17)	$F_5 = (L_0, L_1, L_2, L_3, L_4, L_5) = f(x, y, z, \varphi, R)$ (18)
Evaluation of Analyzed Functions	
0.03	0.1

simple, but it is not high scored for the accuracy feature and for simplicity of positioning of the tool relative to the face of the gear (Table 5.3-6). All those features can be derived from the general structural-functional graph following the 2D model in Table 5.3. The simplicity of the tool is shown by means of three decomposed sliders simulating a sliding and a circular movement. The connections between the parameters of those movements are underlining the simplicity of the tool because of the linear character of relations between those movements. Accuracy of reproduction of the chamfer surface is scored at the middle than the lower level; so far, the surface is generated as a specific and not accurately controlled cross section of the surface of comb mill by the chamfered edges of the toothed pattern (Table 5.3-5).

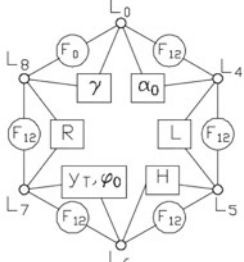
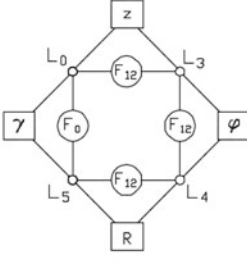
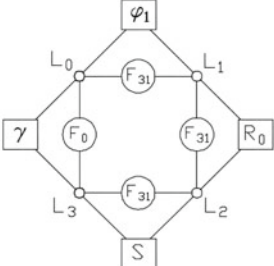
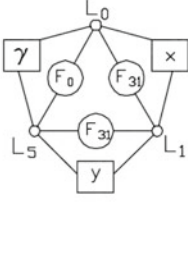
High number and concentration of decomposed links in the comb mill method's mechanism, including the fixed links responsible for tool-work gear positioning, define low accuracy of gear chamfering, with no flexibility for the chamfer's generating line. Symbolically this fact can be presented as equal to zero and the derivatives of parameters as mentioned above as constant parameters: see Table 5.3-9.

Table 5.3 Functional and structural analyses of comb mill method for gear teeth chamfering

Analyses of Comb Mill Method-W=0.72		
Physical Diagram	Decomposed 3D Diagram	
1 	2 	
2D Model	General graph	Function Breakdown
3 	4 	$ \begin{aligned} F_A &= (F_{11}, F_{21}, F_{31}, F_5) \\ F_B &= (F_{11}, F_{21}, F_{31}, F_5) \\ F_C &= (F_{11}, F_{21}, F_{31}, F_5) \\ F_D &= (F_{12}, F_{22}, F_{32}) \\ F_E &= (F_{12}, F_{22}, F_{32}, F_4) \\ F_G &= (F_{12}, F_{22}, F_{32}, F_4) \\ F_H &= (F_{12}, F_{22}, F_{32}, F_4) \\ F_I &= (F_{12}, F_{22}, F_{32}, F_4) \end{aligned} \tag{1} $
$ F_0 = (L_0, L_1, L_2, L_3, L_4, L_5, L_6, L_7, L_8) = f(\varphi_1, R_0, S, \alpha_0, L, H, y_T, \varphi_0, R) \tag{2} $		
Graphs for Feature Explanation and Evaluation		
F_{11} : Accuracy of Guideline Reproduction per Comb Mill Method	F_{11} : Accuracy of Guideline Reproduction per Point Model	
5 	6 	
Set of Links and Parameters Involved		
$ F_{11} = (L_0, L_1, L_2, L_3) = f(\varphi_1, R_0, S) \tag{3} $	$ F_{11} = (L_0, L_1, L_2) = f(x, y) \tag{4} $	
Evaluation of Analyzed Functions		
0.12	0.13	
F_{12} : Accuracy of Generating Line Reproduction per Comb Mill Method	F_{12} : Accuracy of Generating Line Reproduction per Point Model	

(continued)

Table 5.3 (continued)

<p>7</p> 	<p>8</p> 
<p>$F_{12} = (L_0, L_4, L_5, L_6, L_7, L_8) = f(\alpha_0, L, H, \gamma_T, \varphi_0, R)$ (5)</p>	<p>$F_{12} = (L_0, L_2, L_4, L_5) = f(z, \varphi, R)$ (6)</p>
<p>Evaluation of Analyzed Functions</p>	
<p>0.05</p>	<p>0.12</p>
<p>F_{21}: Efficiency of Guideline Reproduction</p>	<p>F_{21}: Efficiency of Guideline Reproduction per Point Model</p>
<p>$V_{21} = \frac{dS}{dt} = \left(\frac{d\varphi_1}{dt}, \frac{dS}{dt} \right)$ (7)</p>	<p>$V_{21} = \frac{dS}{dt} = \left(\frac{dx}{dt}, \frac{dy}{dt} \right)$ (8)</p>
<p>F_{22}: Efficiency of Generating Line Reproduction</p>	<p>F_{22}: Efficiency of Generating Line Reproduction per Point Model</p>
<p>$V_{22} = \frac{dS}{dt} = \left(\frac{dL}{dt}, \frac{dH}{dt}, \frac{d\gamma_T}{dt}, \frac{d\varphi_0}{dt}, \frac{dR}{dt} \right) = 0$ (9)</p>	<p>$V_{22} = \frac{dS}{dt} = \left(\frac{dz}{dt}, \frac{d\varphi}{dt}, \frac{dR}{dt} \right)$ (10)</p>
<p>F_{31}: Flexibility of Guideline Reproduction per Comb Mill Method</p>	<p>F_{31}: Flexibility of Guideline Reproduction per Point Model</p>
<p>9</p> 	<p>10</p> 
<p>$F_{31} = (L_0, L_1, L_2, L_3) = f(\varphi_1, R_0, S)$ (11)</p>	<p>$F_{31} = (L_0, L_1, L_2) = f(x, y)$ (12)</p>
<p>Evaluation of Analyzed Functions</p>	
<p>0.05</p>	<p>0.05</p>
<p>F_{32}: Flexibility of Generating Line Reproduction per Comb Mill Method</p>	<p>F_{32}: Flexibility of Generating Line Reproduction per Point Model</p>

(continued)

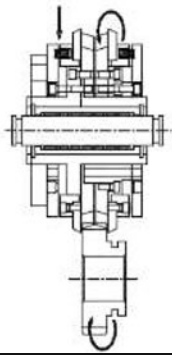
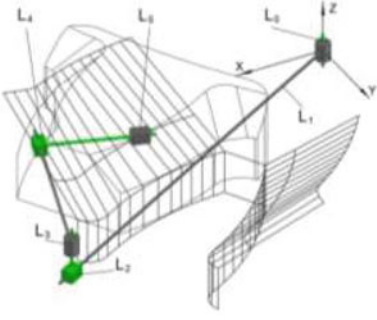
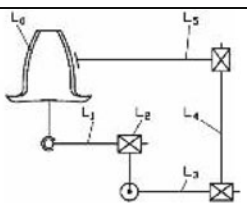
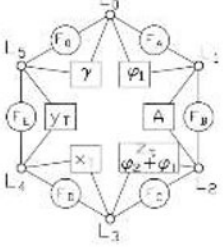
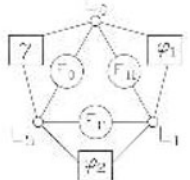
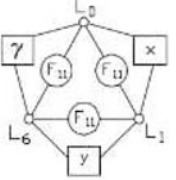
Table 5.3 (continued)

<p>11</p>	<p>12</p>
$F_{32} = (L_0, L_4, L_5, L_6, L_7, L_8) = f(\alpha_0, L, H, y_T, \varphi_0, R) \quad (13)$	$F_{32} = (L_0, L_2, L_4, L_5) = f(z, \varphi, R) \quad (14)$
Evaluation of Analyzed Functions	
0.03	0.05
F_4 : Tool Simplicity per Comb Mill Method	F_4 : Tool Simplicity per Point Model
<p>13</p>	<p>14</p>
$F_4 = (L_0, L_7, L_{7A}, L_8) = f(y_T, \varphi_0, R) \quad (15)$	$F_4 = L_0(\emptyset) \quad (16)$
Evaluation of Analyzed Functions	
0.03	0.15
F_5 : Kinematic Simplicity per Comb Mill Method	F_5 : Kinematic Simplicity per Point Model
<p>15</p>	<p>16</p>
$F_5 = (L_0, L_1, L_2, L_3) = f(\varphi_1, R_0, S) \quad (17)$	$F_5 = (L_0, L_1, L_2, L_3, L_4, L_5) = f(x, y, z, \varphi, R) \quad (18)$
Evaluation of Analyzed Functions	
0.03	0.1

5.1.3.6 Plastic Deformer Gear Chamfering Method Analyses (Table 5.4)

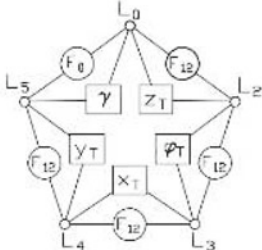
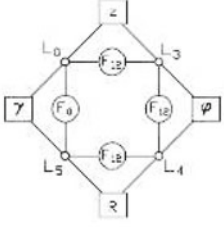
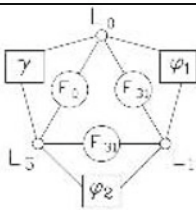
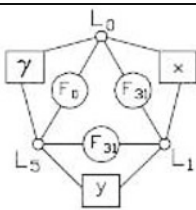
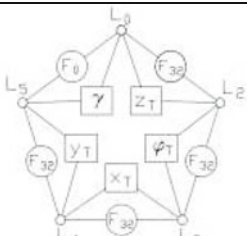
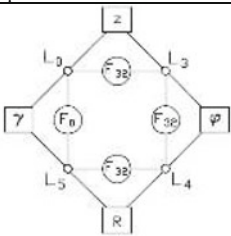
The next method subject to analyzing is the method of plastic deformation which would be considered the most progressive and effective way of gear chamfering in modern gear chamfering techniques. The disadvantage of plastic deformer is in its

Table 5.4 Functional and structural analyses of plastic deformer method for gear teeth chamfering

Analyses of Plastic Deformer Method-W=0.75		
Physical Diagram	Decomposed 3D Diagram	
1 	2 	
2D Model	General graph	Function Breakdown
3 	4 	$F_A = (F_{11}, F_{21}, F_{31}, F_{51})$ $F_B = (F_{11}, F_{21}, F_{31}, F_{51})$ $F_C = (F_{11}, F_{21}, F_{31}, F_{32}, F_4, F_5)$ $F_D = (F_{12}, F_{22}, F_{32}, F_4, F_5)$ $F_E = (F_{12}, F_{22}, F_{32}, F_4, F_5)$ (1)
$F_0 = (L_0, L_1, L_2, L_3, L_4, L_5) = f(\varphi_1, \varphi_2, x_T, y_T, z_T, \varphi_T, x_T, y_T)$ (2)		
Graphs for Feature Explanation and Evaluation		
F_{11} : Accuracy of Guideline Reproduction per Plastic Deformer Method	F_{11} : Accuracy of Guideline Reproduction per Point Model	
5 	6 	
Set of Links and Parameters Involved		
$F_{11} = (L_0, L_1, L_5) = f(\varphi_1, \varphi_2, x_T, y_T)$ (3)	$F_{11} = (L_0, L_1, L_2) = f(x, y)$ (4)	
Evaluation of Analyzed Functions		
0.12	0.13	
F_{12} : Accuracy of Generating Line Reproduction per Plastic Deformer Method	F_{12} : Accuracy of Generating Line Reproduction per Point Model	

(continued)

Table 5.4 (continued)

<p>7</p> 	<p>8</p> 
$F_{12} = (L_0, L_2, L_3, L_4, L_5) = f(z_T, \varphi_T, x_T, y_T)$ (5)	$F_{12} = (L_0, L_3, L_4, L_5) = f(z, \varphi, R)$ (6)
Evaluation of Analyzed Functions	
0.12	0.12
F_{21} : Efficiency of Guideline Reproduction	F_{21} : Efficiency of Guideline Reproduction per Point Model
$V_{21} = \frac{dS}{dt} = \left(\frac{d\varphi_1}{dt}, \frac{d\varphi_2}{dt} \right)$ (7)	$V_{21} = \frac{dS}{dt} = \left(\frac{dx}{dt}, \frac{dy}{dt} \right)$ (8)
F_{22} : Efficiency of Generating Line Reproduction	F_{22} : Efficiency of Generating Line Reproduction per Point Model
$V_{22} = \frac{dS}{dt} = \left(\frac{dz_T}{dt}, \frac{d\varphi_T}{dt}, \frac{dx_T}{dt}, \frac{dy_T}{dt} \right)$ (9)	$V_{22} = \frac{dS}{dt} = \left(\frac{dz}{dt}, \frac{d\varphi}{dt}, \frac{dR}{dt} \right)$ (10)
F_{31} : Flexibility of Guideline Reproduction per Plastic Deformer Method	F_{31} : Flexibility of Guideline Reproduction per Point Model
<p>9</p> 	<p>10</p> 
$F_{31} = (L_0, L_1, L_5) = f(\varphi_1, \varphi_2, x_T, y_T)$ (11)	$F_{31} = (L_0, L_1, L_5) = f(\varphi_1, \varphi_2, x_T, y_T)$ (12)
Evaluation of Analyzed Functions	
0.03	0.05
F_{32} : Flexibility of Generating Line Reproduction per Plastic Deformer Method	F_{32} : Flexibility of Generating Line Reproduction per Point Model
<p>11</p> 	<p>12</p> 
$F_{32} = (L_0, L_2, L_3, L_4, L_5) = f(z_T, \varphi_T, x_T, y_T)$ (13)	$F_{32} = (L_0, L_2, L_4, L_5) = f(z, \varphi, R)$ (14)
Evaluation of Analyzed Functions	
0.05	0.05
F_4 : Tool Simplicity per Plastic Deformer Method	F_4 : Tool Simplicity per Point Model

(continued)

Table 5.4 (continued)

<p>13</p>	<p>14</p>
$F_4 = (L_0, L_2, L_3, L_4, L_5) = f(z_T, \varphi_T, x_T, y_T) \quad (15)$	$F_4 = L_0(\emptyset) \quad (16)$
Evaluation of Analyzed Functions	
0.12	0.15
F ₅ : Kinematic Simplicity per Plastic Deformer Method	F ₅ : Kinematic Simplicity per Point Model
<p>15</p>	<p>16</p>
$\bar{F}_5 = (L_0, L_1, L_5) = f(\varphi_1, \varphi_2, x_T, y_T) \quad (17)$	$\bar{F}_5 = (L_0, L_1, L_2, L_3, L_4, L_5) = f(x, y, z, \varphi, R) \quad (18)$
Evaluation of Analyzed Functions	
0.07	0.1

complexity due to the concentration of a large number of elementary movements. The focus of parameters is also the reason for the complicated processing surface this tool has, being the reason for difficult manufacturing and maintenance. The method is quite simple from the kinematical point, including less number of movements needed for reproduction of a chamfer along the toothed pattern.

3D composition of the model reveals necessary sub-chains for describing essential properties of the gear chamfering mechanism. The guide line and generating line reproduction sub-mechanisms are separated from each other, giving a chance to reproduce different gears of the same module. What is remarkable to the generating line sub-chain, it reveals and shows clearly that concentration of large number of frozen movements in the body of plastic deformer is lowering the flexibility of the tool and making complicated its manufacturing and maintenance. Those frozen movements in the generating line sub-chain are indicated on the fixed character of the chamfering triangle, which is limiting the flexibility of the method (Table 5.4 (1-4)).

5.1.3.7 Short Conclusions on Analyses

Some short conclusions are summarizing the experience of analysis of four gear chamfering methods and setting objectives for further study:

1. Decomposition is practically useful for revealing the hidden and not apparent functions which are necessary for the full-scale understanding of the values and resources of a specific gear chamfering method.
2. Three-level visualization of structural means (physical diagram-3D-2D) is providing step-by-step decomposition of a particular method. It is ending by a graph containing all the necessary set of sliders and revolution units which are connected by movement parameters and linked to each other on a functional basis. This set of data is essential and sufficient for any per demand combination for the description of qualitative and quantitative features of a specific gear chamfering method.
3. A point model is useful for visualizing main features of gear chamfering mechanism and serves as a merit for setting objectives and creating a set of practical gear chamfering mechanisms having the fundamental properties of the point model.

5.1.4 Synthesis of Gear Chamfering Mechanisms


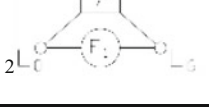
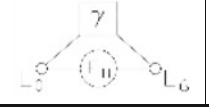
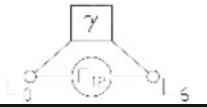
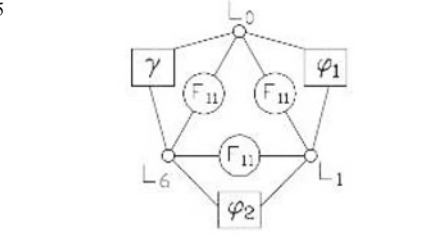
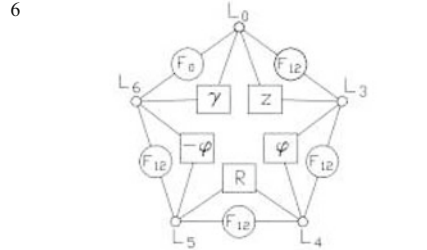
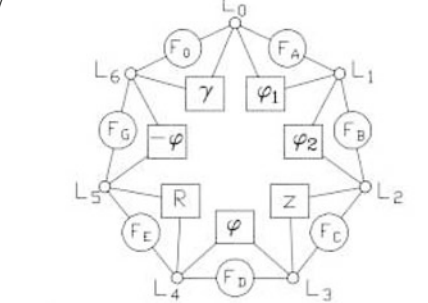
The analyzing format based on the point model can be modified into further formats for synthesizing new structures and for parametric design and optimization, keeping the main features of the task-based conceptual design. Listing here the main elements of task-based conceptual design we can point out. Synthesis of gear chamfering mechanisms includes the following steps and basic components:

- The synthesis process is started by indication or choice of two original links for the gear chamfering mechanisms – they are the work gear and the tool gear.
- At the next step, the basic function is inserted between the two links as a relation.
- Decomposition of the inserted function to sub-functions upon the necessity.
- The satisfaction of the challenging tasks by either granting a degree of freedom or using database resources.
- Doing the necessary decomposition of the database resources before its application.
- Organization of repeatable synthesis cycles and visualization of this process.
- Consideration of different design scenarios.
- Development and insertion of an evaluation mechanism.

5.1.4.1 Construction of a Linear Model for Synthesizing Gear Chamfering Methods (Table 5.5)

As stated in Sect. 1.3.2, the point model has no resource of practical implementation of metal processing and chip removal. Hence a further linear model should be synthesized for addressing this essential feature of a chamfering method.

Table 5.5 Format of linear model synthesis for chamfer surface reproduction

Linear Model for Chamfer Surface Reproduction-W=0.87			
Set of Challenged Functions with Weight Coefficients for Importance			
F ₁ :Accuracy - 0.2	F ₁₁ :Guide Line Accuracy- 0.1 F ₁₂ :Generate Line Accuracy- 0.1	F ₄ :Tool Simplicity- 0.12	
F ₂ :Efficiency- 0.3	F ₂₁ :Guide Line Efficiency- 0.15 F ₂₂ :Generate Line Efficiency- 0.15	F ₅ :Kinematic Simplicity- 0.1	
F ₃ :Flexibility- 0.1	F ₃₁ :Guide Line Flexibility-0.05 F ₃₂ :Generate Line Flexibility-0.05	F ₆ :Energy Consumption- 0.05 (Total-0.87)	
Development of Linear Model			
Task Planning			
F ₀ : Functions in General	F ₁ : Accuracy	F ₁₁ : Guide Line Accuracy	F ₁₂ : Generate Line Accuracy
1 	2 	3 	4 
Task Solution			
F ₁₁ : Guide Line Accuracy		F ₁₂ : Generate Line Accuracy	
5 		6 	
General Solution Graph		Function Breakdown	
7 		$ \begin{aligned} F_A &= (F_{11}, F_{21}, F_{31}, F_{51}) \\ F_B &= (F_{11}, F_{21}, F_{31}, F_{51}) \\ F_C &= (F_{12}, F_{22}, F_{32}, F_{52}) \\ F_D &= (F_{12}, F_{22}, F_{32}, F_{52}) \\ F_E &= (F_{12}, F_{22}, F_{32}, F_{52}) \\ F_G &= (F_{12}, F_{22}, F_{32}, F_{52}) \end{aligned} \tag{1} $	
$ F_0 = (L_0, L_1, L_1, L_1, L_2, L_1, L_6) = f(\varphi_1, \varphi_2, z, \varphi, R, -\varphi, x_T, y_T) \tag{2} $			
2D Model		2D Extended Model	

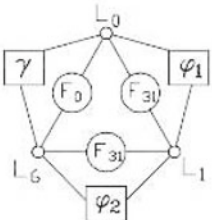
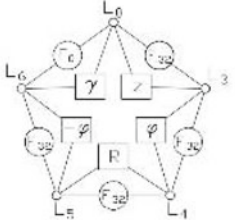
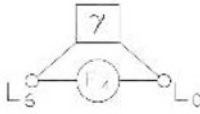
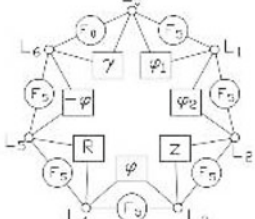
(continued)

Table 5.5 (continued)

<p>8</p>	<p>9</p>
<p>3D Model</p>	
<p>10</p>	
<p>Graphs for Feature Explanation and Evaluation</p>	
<p>F₁₁: Accuracy of Guideline Reproduction</p>	<p>F₁₂: Accuracy of Generating Line Reproduction</p>
<p>10</p>	<p>11</p>
<p>Set of Links and Parameters Involved</p>	
<p>$F_{11} = (L_0, L_1, L_2, L_6) = f(\varphi_1, \varphi_2, x_T, y_T)$ (3)</p>	<p>$F_{12} = (L_0, L_2, L_4, L_5, L_6) = f(z, \varphi, R, -\varphi)$ (4)</p>
<p>Evaluation of Synthesized Functions</p>	
<p>0.1</p>	<p>0.1</p>
<p>F₂₁: Efficiency of Guideline Reproduction</p>	<p>F₂₂: Efficiency of Generating Line Reproduction</p>
<p>$F_{11} = (L_0, L_1, L_2, L_6) = f(\varphi_1, \varphi_2, x_T, y_T)$ (5)</p>	<p>$F_{12} = (L_0, L_2, L_4, L_5, L_6) = f(z, \varphi, R, -\varphi)$ (6)</p>
<p>$V_{21} = \frac{dS}{dt} = \left(\frac{d\varphi_1}{dt}, \frac{d\varphi_2}{dt} \right)$ (7)</p>	<p>$V_{22} = \frac{dS}{dt} = \left(\frac{dz}{dt}, \frac{d\varphi}{dt}, \frac{dR}{dt} \right)$ (8)</p>
<p>Evaluation of Synthesized Functions</p>	
<p>0.1</p>	<p>0.1</p>
<p>F₃₁: Flexibility of Guideline Reproduction</p>	<p>F₃₂: Flexibility of Generating Line Reproduction</p>

(continued)

Table 5.5 (continued)

<p>12</p> 	<p>13</p> 
$F_{31} = (L_0, L_1, L_2, L_6) = f(\varphi_1, \varphi_2, x_T, y_T) \quad (9)$	$F_{32} = (L_0, L_2, L_4, L_5, L_6) = f(z, \varphi, R, -\varphi) \quad (10)$
Evaluation of Synthesized Functions	
0.05	0.05
F_4 : Tool Simplicity	F_5 : Kinematic Simplicity
<p>14</p> 	<p>15</p> 
$F_4 = L_6(x_T, y_T) \quad (11)$	$F_5 = (L_0, L_1, L_2, L_3, L_4, L_5, L_6) = f(\varphi_1, \varphi_2, x_T, y_T) \quad (12)$
Evaluation of Synthesized Functions	
0.1	0.05

A linear model of gear chamfering mechanism is a developed state of the point model. The idea of the linear model is coming from application or usage of a line as a cutting edge of a metalworking tool, so granting it the metal processing ability upon implementation of necessary relative movements against the work gear. That's obvious that using a curved line instead of point should change the structure of point model accordingly because a curved line doesn't indifferently position against the work gear and the chamfer surface. Modification of the point model is done in two steps: for guide line sub-chain and for generating line sub-chain. The point model includes links for inter-perpendicular movements along axis X and Y for tracking the point along the toothed pattern. This model is not applicable for the case of the toothed gear because two inter-perpendicular movements along axis X and Y are not workable for the case of reproduction of toothed pattern and gear engagement. Gearing is requiring rotational movement for at least one element of toothed pair. In a classic gear engagement, both gears are rotational, and this fact is setting premises of reproduction of one gear by the other. So, the first modification of the point model relates to the sub-chain of the guide line reproduction mechanism. Construction of this sub-chain is shown in Table 5.5 organized in a way to allow the designer to follow every step of the conceptual design of gear chamfering mechanism on a functional or task-based basis. Two original links are enabling the

growth of the set of elementary movements resulting in the reproduction of the first toothed pattern by the other. The work gear pattern fixed to the ground link is methodically assumed to be the same as the toothed gear subject to chamfering. At this step, the link L_3 further called a leading gear is granted by necessary movements which are sufficient for the reproduction of a guide line on the work gear. From the topological point of view, the guide line reproducing sub-units for the point model and end linear model is identical.

Next task of conceptual design (Table 5.5-4) relates to the composition of a sub-unit of generating triangle, and already developed several functions and solutions from the point model are going to be used here. Usage of generating line chain from point model (Table 5.4-5) means that orientation of the triangle plane in normal to the chamfer surface and both movements in normal and axial directions are valid. The choice of the direction of the normal movement is decided by the position of normal in the point of contact of leading gear and the work gear. That is also the place to note that the curved line L_6 selected as a cutting line (edge) of the tool in the developed gear chamfering mechanisms is subject to further decomposition in the coordinate system linked to the last element of guideline sub-chain. The parameter of the orientation of the generating triangle in a plane perpendicular to the guideline will change the position of generating line from his normal to the guide line. This de-orientation will happen because the leading gear should be duplicated and transferred to the end link of the triangles' sub-mechanism to be able to take part and implement generation and processing of all the chamfer surface along the entire guide line. To keep tool gear curved pattern in previous position against the leading gear, the cutting edge of the tool gear should be re-oriented on the same angle of orientation according to the orientation angle of sub-chain for generating triangle. Granting this new movement to the cutting edge to the basic structure of the point model is completing now into the structure of the linear model. Compared with the point model, one can notice the topological identity between point and linear models and with an additional degree of freedom necessary for triangle re-orientation. Comparing the number of degrees of freedom between point and linear models, one can notice a higher complexity of the linear model. So, after confirmation of the positive features of the linear model inherited from the point model, other unfavorable functions are challenged, which are subject to further satisfaction and solution. Basic requirements to the chamfering mechanisms listed for the point model are repeatedly listed in Table 5.5. The high **accuracy** score of the point model can be passed to the linear model for both guide line and generating line.

The efficiency of reproduction of the chamfer surface by the linear model can be provided by directing the main cutting speed along the longer guide line of the toothed pattern and directing the slower rate of feeding along the short edge of generating triangle hypotenuse.

Tool simplicity should be rated as an advantageous feature because of the concentration of a smaller number of elementary movements in the body of the cutting tool. The set of primary movements (describing the complexity of the cutting tool) are separated from the general functional-structural graph and form the basic structure of the linear model for presenting and evaluating the qualitative

characteristics of the linear model. The mentioned (Table 5.5-7) set of elementary movements in the frozen status is equivalent to the shape of a standard gear with straight teeth when chamfering a straight tooth gear and to the form of a bevel gear when chamfering a bevel gear. More advantages of the cutting tool (tool gear) are becoming thus visible. Firstly, manufacturing of the tool requires standard technology of gear processing, and secondly the maintenance, more specifically, the sharpening of such tool gear, needs a pure refreshment of the face by flat grinding.

Synthesis plan implemented in Table 5.5 includes the steps below:

- Plan the sub-chain for guide line.
- Plan the same for generating line.
- Implement chain for guide line.
- Compose the general graph.
- Create an extended model for reduction of the degree of freedom.
- Reveal conical kinematic surface for the reproduction of generating line.

Comments and results of actions implemented in Table 5.5 are listed below:

- Accuracy is defined by the accuracy of the toothed pattern reproduction.
- Accuracy depends on fixation and activation of parameters included in the sub-chain of generating triangle.
- Flexibility is defined by gear transmission of a large set of work gears having the same module with the tool gear.
- Several evaluations of flexibility for generating line are possible.
- Tool synthesis is defined by using a linear cutting edge for gear chamfer processing by chip removal.
- According to the design task and depending on the simplicity of two sub-chains, different combinations of frozen and granted movements are possible.
- Further breakdown of L_0 (work gear) is needed for its detailed description. See Sect. 1.5 Parametric Design for sub-mechanism of L_0 and its graph.

5.1.4.2 Using the Database for Completing Linear Model

On the way of simplification of the kinematical diagram based on the linear model, a task should be challenged for minimizing the excessive number of degrees of freedom. The search of such mechanisms from the database or their reinvention can be organized by equipping the current basic structure of the linear model by additional sliders composing an extra generating triangle as it is shown in Table 5.5-9. The cutting edge being now connected to the connecting rod of a four-bar mechanism with additional movement along the axis of toothed gear will be able to keep its normal position to specific areas or fragments of the toothed pattern. The number of degrees of freedom can be reduced by connecting the normal and axial movements or the cutting edge when a standard chamfer angle is required or by the flexible connection of those two movements when the angle of chamfer angle is needed to be variable. The linear model with extra constructed parallelogram mechanism is serving as a base for the development of a series of gear chamfering

mechanisms. The developed extended linear model (Table 5.5-11) contains all the necessary parameters and content of required links for providing different qualitative and quantitative features of gear chamfering mechanisms. It also has the resource of reinventing or reengineering its structure into well-known structures and mechanical solutions from the database but for the satisfaction of tasks specific for the current (e.g., gear chamfering) conceptual design. Oppositely the known mechanisms from the database can be modified using the links implementing exclusively elementary movements into sub-chains and parallel chains for equipping as the linear model as well as the chamfering mechanisms constructed on the base of the linear model.

5.1.4.3 Mathematical Expressions

Set of the parameters revealed due to the linear model are allowing to compose mathematical expressions for describing the curves of guideline and surface of chamfer and chamfer surface. They are also enabling to organize a parametric design and optimization process for minimizing the maximum height of micro-roughness as it will be shown in Sect. 1.5. Those regulations and connections are listed in the linear model format presented in the Table 5.5. The linear model, as it was mentioned earlier, is serving as a base for creation of several gear chamfering mechanisms.

5.1.4.4 Gear Chamfering Mechanism: Gear Engagement + Equidistant Tracking (Table 5.6)

Before going detailed description of synthesized gear chamfering mechanisms, the 3D model of connecting rod sub-mechanism should be developed from decomposed sliders as shown in Table 5.5-10. Easy to notice that the leading gear and the cutting gear are remaining parallel permanently being rotated around axis shifted from each other on the value of angle of chamfering triangle re-orientation. Thus, the axis of lead gear and work gear is being moved on the amount of equidistant radius R .

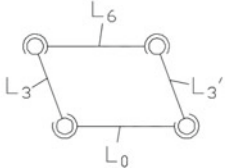
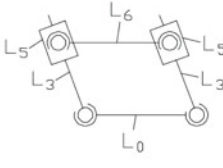
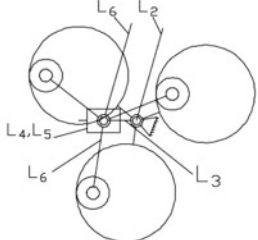
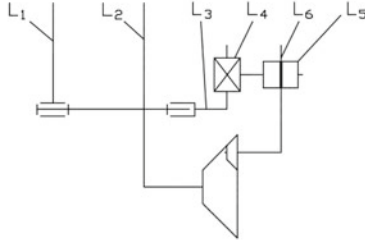
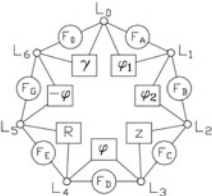
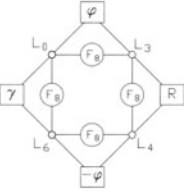
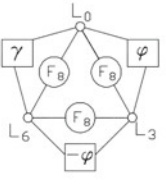
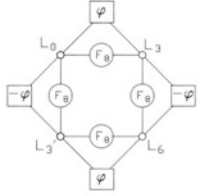
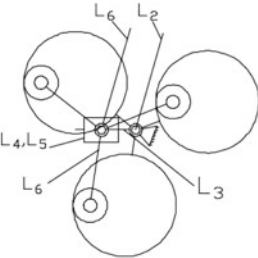
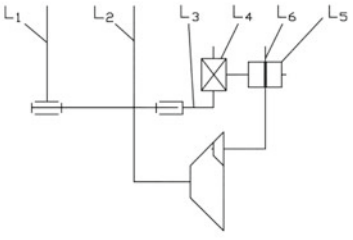
Such a mechanism can be re-invented if the trajectory of the end slider could be turned into a solid internal conical surface fixed to the lead gear. In its turn, the decomposed sliders are forming external conical surfaces attached to the leading gear and contacting with the abovementioned outer conical surface. Many other embodiments based on the extended linear model of gear chamfering mechanisms can be developed; anyhow, we will stop on two of them. The solution with internal and external conical gears is shown in Table 5.6-7. At this stage, the next challenge of ground link choice should be satisfied. In an option according to Table 5.6-7, the link holding the axis of rotation for work gear and tool gear serves as a ground link, so the lead gear and a tool gear are forming a standard gear transmission, while the work gear has a feed movement directed in the normal direction to a specific fragment of the toothed pattern of the work gear. In the solution (Table 5.6-7), a fixed chamfering angle is equal to the half of the angle of the conical surface at the

Table 5.6 Format for synthesis of gear chamfering mechanism for full toothed pattern

Synthesis of Gear Chamfering Mechanism for Full Toothed Pattern –W=0.82			
Set of Challenged Functions with Importance of Weight Coefficients			
F ₁ :Accuracy -	0.2	F ₁₁ :Guide Line Accuracy- 0.1 F ₁₂ :Generate Line Accuracy- 0.1	F ₄ :Tool Simplicity- 0.12
F ₂ :Efficiency-	0.3	F ₂₁ :Guide Line Efficiency- 0.15 F ₂₂ :Generate Line Efficiency- 0.15	F ₅ :Kinematic Simplicity- 0.07
F ₃ :Flexibility-	0.08	F ₃₁ :Guide Line Flexibility-0.03 F ₃₂ :Generate Line Flexibility-0.05	F ₆ :Energy Consumption-0.05 (Total-0.82)
Usage of Linear Model with Advantageous Features			
General Graph		Function Breakdown	
		$F_A = (F_{11}, F_{21}, F_{31}, F_{51})$ $F_B = (F_{11}, F_{21}, F_{31}, F_{51})$ $F_C = (F_{12}, F_{22}, F_{32}, F_{52})$ $F_D = (F_{12}, F_{22}, F_{32}, F_{52})$ $F_E = (F_{12}, F_{22}, F_{32}, F_{52})$ $F_G = (F_{12}, F_{22}, F_{32}, F_{52})$	
$F_0 = (L_0, L_1, L_1, L_1, L_2, L_1, L_6) = f(\varphi_1, \varphi_2, z, \varphi, R, -\varphi, x_T, y_T)$		(1)	
Linear Model as Original State of Synthesis			
2D Extended Model		3D Model	
Task 1: Reduce DOF for Chamfer Generating Line Chain (F ₇): Task 2: Use or Synthesize Chain for Gear Pattern Reproduction Task			
F ₇ : Regrouping the Links	F ₇ : Planning of Task1	F ₇ : Planning and Solution of Task 2	F ₇ :Solution of Task1
Kinematic Solution for F ₇ : Two options: Use database or synthesize			

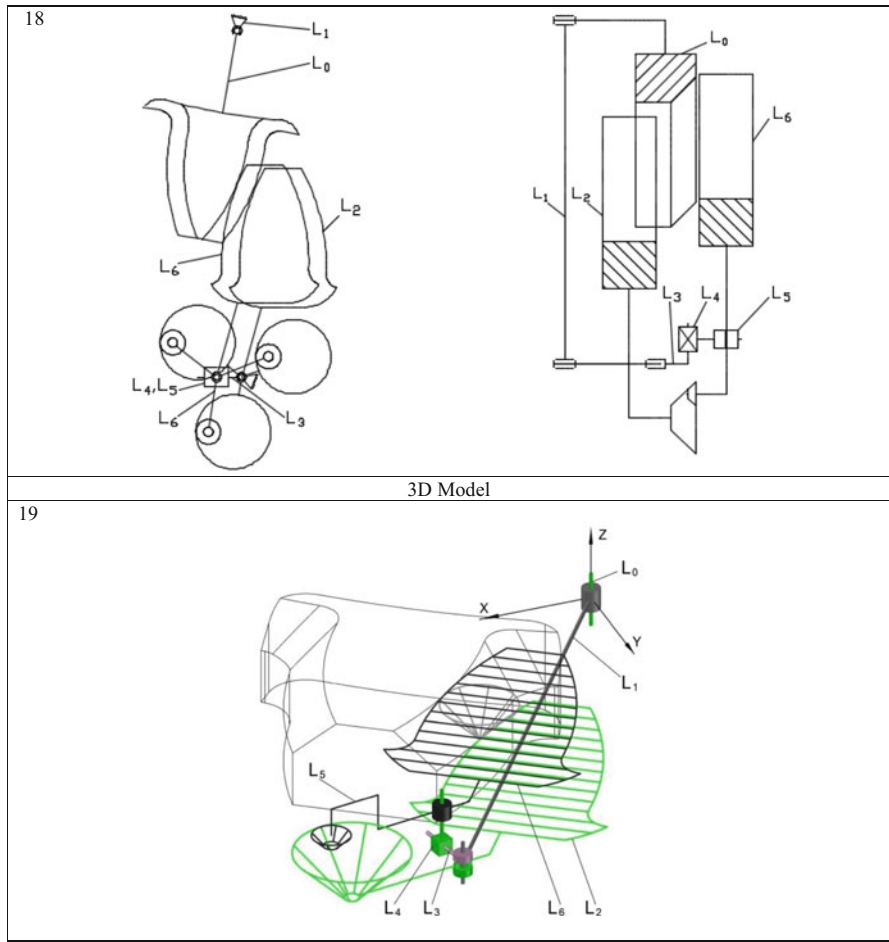
(continued)

Table 5.6 (continued)

<p>8</p> 	<p>9</p> 		
<p>10</p> 	<p>11</p> 		
<p>F₈: Reduce DOF for Chamfer Generating Line Chain: Task Planning and Graph Solution</p>			
<p>F₈: Regrouping the Links</p>	<p>F₈: Concentration on Task-1</p>	<p>F₈: Concentration on Task-2</p>	<p>F₈: Graph Solution</p>
<p>12</p> 	<p>13</p> 	<p>14</p> 	<p>15</p> 
<p>Kinematic Solution for F₈</p>			
<p>16</p> 	<p>17</p> 		
<p>F₉: Combination of Guide Line and Generating Line Chains: Kinematic Solution for F₉ 2D Models</p>			

(continued)

Table 5.6 (continued)



top. This solution will be further used for parametric design and optimization for feeding direction to satisfy the requirement of limitation of the maximum height of micro-roughness on the chamfer surface along the guide line (see Sect. 1.5).

The work gears are driven away from the fixed axis of the lead gear in a specific direction relative to toothed pattern of the work gear. If the chamfer is needed to be processed on the neighbor profiles, only then the feed movement has a fixed path, and it is reciprocated for serving both patterns (Table 5.6-7).

Plan of synthesizing mechanism #1 on the base of the linear model includes the steps as listed:

- The original state of synthesis, base structure, planning, and solution.
- Composing sub-chains from database resources and by freezing movements for creating of the conical surface of chamfer tracking triangle.
- Combining of chains and getting conceptual design solution for mechanism #1.

5.1.4.5 Gear Chamfering Mechanism: Gear Engagement + Helical Movement (Table 5.7)

Another simplified solution of gear chamfering mechanism can be obtained by using the specific property of the two involutes of a basic circle are equidistant. This fact is allowing to organize the feeding movement using a pure rotation of the cutting gear against the lead gear. The pattern reproduction function can be easily implemented by meshing the two lead and work gears, thus maximally simplifying the mechanism into a simple pair of engaged lead gear and work gear. The tool gear in such mechanism is arranged coaxially with the lead gear and has the rotational feeding movement as a simple rotation around the common axis (Tables 5.7-18 and 19).

The axial movement of the tool gear is mechanically connected with the rotational feeding movement that's reducing the number of controllable variables and parameters. The last structure of gear chamfering mechanism can be separated from the general structural-functional chain of the linear model, and its synthesis path is followed in Table 5.7.

An example of simplified linear model implementation is shown in Table 5.7. Here the work gear is fixed, and a faceplate equipped with several work gears is running around the centrally located lead gear in a planetary movement. The work gear is connected to a feeding chain which drives it in a reciprocated feed movement around the lead gear axis. The entire set of chamfer surface tracking movements are present including the axis shifting of the tool gear due to conical inserts between the lead gear and work gear which are acting as cams.

5.1.5 Parametric Design of Gear Chamfering Mechanisms

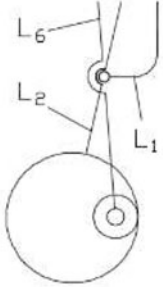
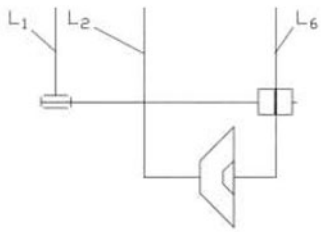
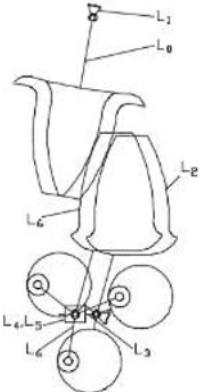
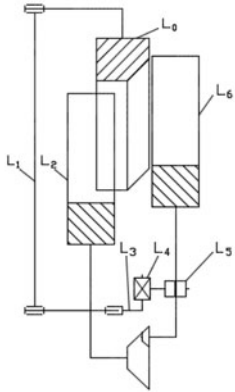
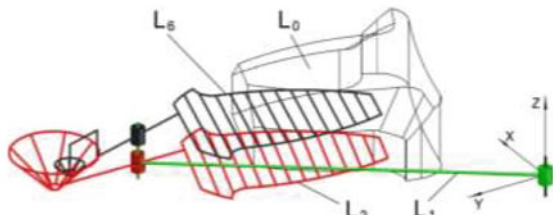
The parametric design format keeps the same methodical structure with concept design and analyses formats: firstly, the task is formulated of definition of a design parameter of gear chamfering mechanism which is responsible for chamfer surface quality. The search of parameter is started by composing a calculative scheme which in its turn depends on already developed basic 3D and 2D models of gear chamfering mechanism which are now subject of further decomposition for setting a proper calculative diagram. So far definition of the challenged parameter is connected with intersection of two curves, one the kinematical contour of tool gear and the other

Table 5.7 Format for synthesis of gear chamfering mechanism for two sides of toothed profile

Synthesis of Gear Chamfering Mechanism for Two Sides of Toothed Profile-W=0.83			
Set of Challenged Functions with Importance of Weight Coefficients			
F ₁ :Accuracy - 0.18	F ₁₁ :Guide Line Accuracy- 0.08	F ₁₂ :Generate Line Accuracy- 0.1	F ₄ :Tool Simplicity- 0.12
F ₂ :Efficiency- 0.3	F ₂₁ :Guide Line Efficiency- 0.15	F ₂₂ :Generate Line Efficiency- 0.15	F ₅ :Kinematic Simplicity- 0.08
F ₃ :Flexibility- 0.1	F ₃₁ :Guide Line Flexibility- 0.05	F ₃₂ :Generate Line Flexibility- 0.05	F ₆ :Energy Consumption-0.05(Total-0.83)
Usage of Linear Model with Advantageous Features			
General Graph		Function Breakdown	
		$ \begin{aligned} F_A &= (F_{11}, F_{21}, F_{31}, F_{51}) \\ F_B &= (F_{11}, F_{21}, F_{31}, F_{51}) \\ F_C &= (F_{12}, F_{22}, F_{32}, F_{52}) \\ F_D &= (F_{12}, F_{22}, F_{32}, F_{52}) \\ F_E &= (F_{12}, F_{22}, F_{32}, F_{52}) \\ F_G &= (F_{12}, F_{22}, F_{32}, F_{52}) \end{aligned} \tag{1} $	
$F_0 = (L_0, L_1, L_1, L_1, L_2, L_1, L_6) = f(\varphi_1, \varphi_2, z, \varphi, R, -\varphi, x_T, y_T)$		$\tag{2}$	
Linear Model as Original State of Synthesis			
2D Extended Model		3D Model	
F ₇ :Shorten Chain for Chamfer Generating Line Chain: Task Planning and Graph Solution			
F ₇ : Plan the Task	F ₇ : Plan the Task	F ₇ : Plan the Task	
Kinematic Solution for F ₇ : Two options: Use database or synthesize			

(continued)

Table 5.7 (continued)

<p>8</p> 	<p>9</p> 
<p>F₉:Combination of Guide Line and Shortened Generating Line Chains into a Single Mechanism: Kinematic Solution for F₉</p>	
<p>2D Models</p>	
<p>18</p> 	
<p>3D Model</p>	
<p>19</p> 	

kinematical curve of a point of work gear in reversed movement; so further decomposition of basic 3D model relates to creating of virtual mechanisms for reproduction of such curves. Those mechanisms will include the necessary set of parameters enough to be included in proper equations and get the challenged parameter as a result of solution of those equations.

5.1.5.1 Task of Parametric Design and Optimization

The visualized arrangement of formats developed for the conceptual design and analyses phases can be further extended to the step of parametric design and optimization of a gear chamfering mechanism. The same method of the composition and decomposition of mechanical and functional categories, being used for modification, composition, and decomposition, previously applied for synthesis and analyses of gear chamfering mechanism can be modified and used now for parametric design needs. Those methods can be used for revealing the basic set of parameters for composing equations and solving them. The graph visualization method can further be utilized for producing intermediate calculative diagrams. And the technique of virtual mechanisms may serve for the composition of sub-mechanisms for revealing the hidden and necessary parameters.

5.1.5.2 Classical Approach of Parametric Design

The classical approach of parametric design and optimization embraces the construction of a combined functional expression containing the main or several essential target functions including in it the whole set of variable parameters defining the entire range of variables as a boundary of search and parametric design [12]. The functional is subject of analysis within the whole range of variables, and the behavior of the target function is evaluated according to the fact of approaching or distancing of the current functional value from preliminary defined nominal target. Despite its classical nature and wide and general application, this approach implies compilation or variable parameters inside the main functional that provides the connection between variables without the possibility of obvious and blatant evaluation and demonstration of the physical meaning of the variables. Traditionally this methodology of the parametric design was built on the search and building of most efficient mathematical methods, following the development of numerical methods which are keeping their scientific and calculative and usefulness value for mechanics. Nowadays this approach has an alternative in terms of usage of digital and computerized techniques for the solution of equations, which has an enormous computing resource giving a chance to the designer to concentrate more on the revealing and optimization of new qualitative values of a novel mechanism. Thus, the designer has the opportunity to save on the development of mathematical models more concentrating on mechanical properties of the new design.

5.1.5.3 Alternative Approach of Parametric Design

Now coming to the alternative or the suggested methodology, we may draw parallels and make a comparison between conceptual design and parametric design methodologies. If in the case of conceptual design the links are related in the way to provide

the demanded function and then in the case of parametric design the links are related by the kinematical joints exclusively, then the links can be described as cases of kinematical embodiments with frozen parameters.

In the case of conceptual design, the number of links is growing per design task demand, and reduction of that number is organized as an attempt to provide a qualitative feature or function. In the case of parametric design, such growth or reduction may be planned in an effort for revealing, describing, and defining of new or additional parameters. Such action is the same as the freezing or thawing the links this time organized for the needs of parametric design. Such approach grants the designer a possibility to find the location of each parameter in several or in the general calculative scheme, to get the opportunity of building sub-structures per demand for discovering, defining, and optimizing the necessary parameters. The designer also gets the chance of establishing connections between the parameters, for reducing the number of unknown values, for instance, assuring the opportunity of setting a convenient design environment and visualizing the way of grouping and composing equations for resolution of unknown parameters. Once the computing schemas are established, the main calculative load is transferred on digital methods and techniques.

5.1.5.4 Procedure of Suggested Parametric Design

The current methodology of conceptual design, as it will be shown below, is applicable also for the building of well-known mechanisms for tracking of famous curves as involutes, cycloids, and epicycloids.

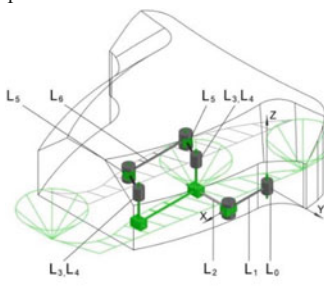
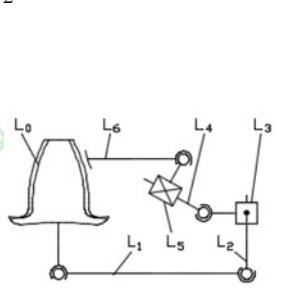
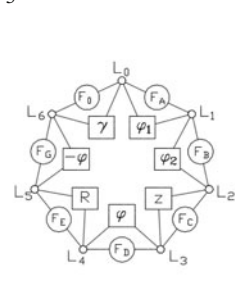
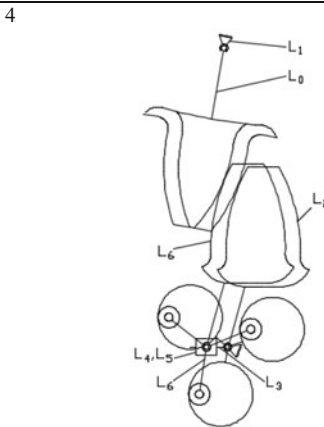
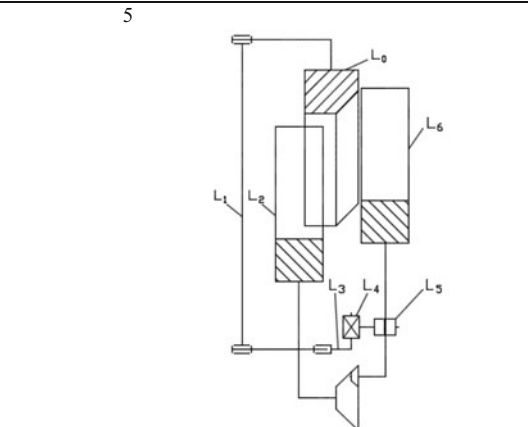
It is as well applicable for the parametric synthesis of newly developed mechanisms for reproduction of chamfered surfaces along toothed patterns of gears, following the specific requirement of quality of chamfer surface. Those requirements are limiting the maximum height of inconsistency or micro-roughness along both guide line and generating line of the chamfer surface of the toothed pattern.

Table 5.8 presents a format of parametric design with the objective of minimization of the maximum height of surface micro-roughness. This objective is planned and solved as an intersection of two trajectories.

First is the trajectory inversed movement of a specific original point on the height of micro-roughness of the work gear. And the second is the kinematical contour of the tool gear. The coordinates of the intersection point are allowing to define the direction of normal feed on the tool gear, which is presenting by itself the solution and searched value of parametric design. If described by trajectories, the intersection point is the common point of two paths. If defined by radius vectors, the intersection point is the equality of two radius vectors in the same system of Cartesian coordinates. And if represented by structural-functional graphs, modified for the parametric design case, then the intersection point is the equality of two edges of two graphs.

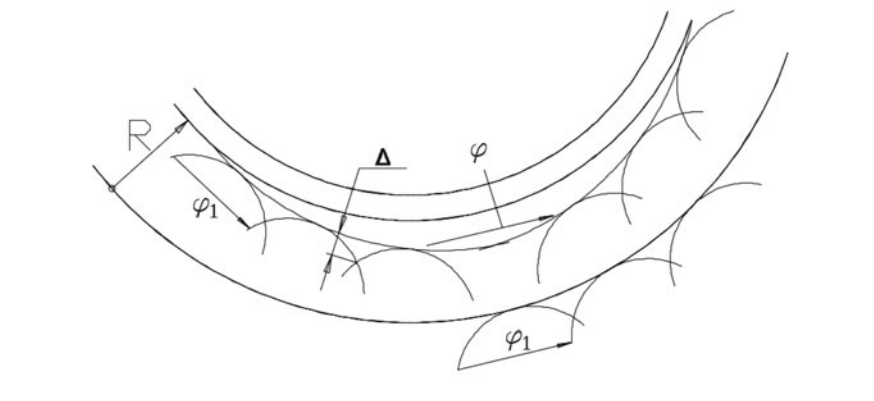
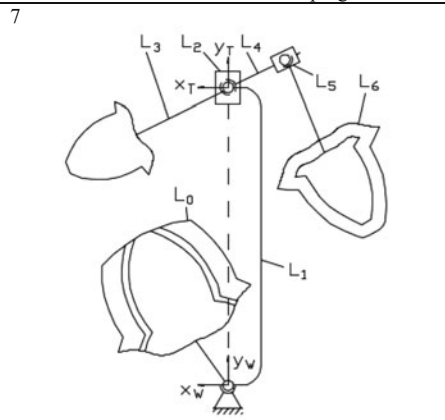
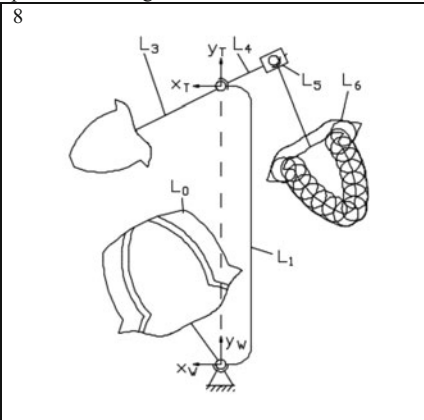
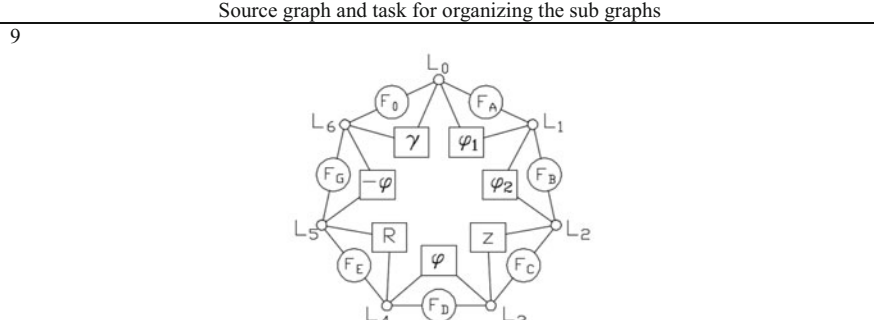
Those graphs are visualizing the contents of the parameters and are showing the origination of the sub-mechanisms and equations.

Table 5.8 Format for parametric design for orientation angle of a gear chamfering mechanism

Definition of Orientation Angle of a Gear Chamfering Mechanism		
Task of parametric design: define order of changing the value of parameter f in a way to limit maximum height of micro roughness of the chamfer surface		
Original Data for Parametric Design		
3D model	2D model	General Graph
1 	2 	3 
Kinematic solution of mechanism		
4 	5 	
Formation of micro roughness along the guide line of chamfer surface		
6		

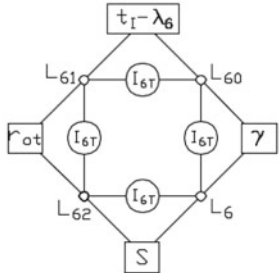
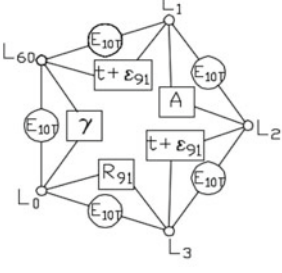
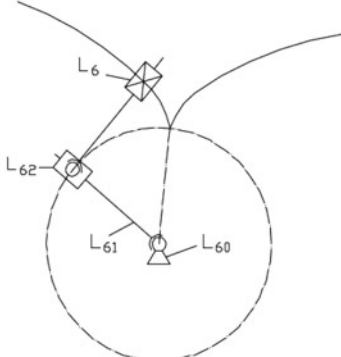
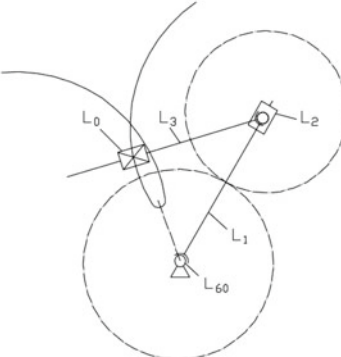
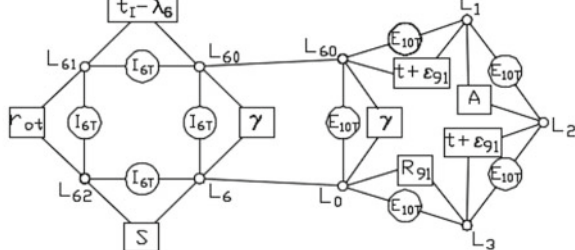
(continued)

Table 5.8 (continued)

	
<p>Task Planning</p>	
<p>Find intersection point of top point of work gear in a reversed movement against tool on the work tools' involute curve (10 epicycloid x 6 involute)</p>	
<p>Links and parameters involved</p>	
<p>$F_0 = (L_0, L_1, L_2, L_3, L_4, L_5, L_6) = f(R_0, x, y, z, \phi, R)$ (1)</p>	
<p>Modification and development of necessary graphs for finding the intersection point</p>	
<p>Grouping the links for parametric design</p>	
<p>7</p> 	<p>8</p> 
<p>Source graph and task for organizing the sub graphs</p>	
<p>9</p> 	

(continued)

Table 5.8 (continued)

<p>Graph for link L_6 – tool gear</p>	<p>Graph for work gear L_0 reversed epicycloid movement</p>
	
<p>Sub mechanism for involute pattern of link L_6 – tool gear</p>	<p>Sub mechanism for work gear L_0 reversed epicycloid movement</p>
<p>12</p> 	<p>13</p> 
<p>Equation of involute 10 according sub graph 10</p> $x_{10} = A \cos(t + \theta_{91}) - R_{91} \cos\left(\frac{A}{R_{dd}} + \theta_{91}\right) \quad (2)$ $y_{10} = A \sin(t + \theta_{91}) - R_{91} \sin\left(\frac{A}{R_{dd}} + \theta_{91}\right) \quad (3)$	<p>Equation of epicycloid 6 according sub graph 6</p> $x_6 = r_{mT} [\cos(t_e - \lambda_6) + t_e \sin(t_e - \lambda_6)] \quad (4)$ $y_6 = r_{mT} [\sin(t_e - \lambda_6) - t_e \cos(t_e - \lambda_6)] \quad (5)$
<p>Graph resolution of intersection point of curves 6 and 10</p>	
<p>14</p> 	
<p>Equality of radius vectors of curves 6 and 10</p> $R_{61} = R_{101} \quad (6)$	<p>Equality of Cartesian coordinates of curves 6 and 10</p> $x_{10} - y_{10} = x_6 - y_6 \quad (7)$
<p>Definition of polar coordinates of intersection point T_1</p>	
$R_{61} = \sqrt{x_{61}^2 + y_{61}^2}, \quad \lambda_{61} = \arctg \frac{y_{61}}{x_{61}} \quad (8)$	

(continued)

Table 5.8 (continued)

Definition of angle for normal feed direction	
$\varphi = 90^\circ + \arctg \frac{dy_{e1}}{dx_{e1}} \tag{9}$	
Chart for choosing the direction of normal feed depending on revolutions of work gear	
15	
Trajectory Chart	
16	

5.1.5.5 Surface Micro-Roughness

At this point, an additional requirement of surface microroughness should be considered and satisfied so far as the developed new kinematical diagram for gear chamfering mechanism implies the formation of step like irregularities along the hypotenuse of the generating triangle and irregularities shaped by neighboring arcs along the guideline of the chamfer surface. The micro-roughness can be described as a result of limited numbers of waves where each wave has a summarizing surface of several continuous positions of the cutting edge on them. The number of the waves and the number of the steps should be defined and calculated in a way not to allow

the max height of the micro-roughness to become higher than a standard limited value from standard requirements to the surface quality.

5.1.5.6 Procedure of Implementation of Suggested Parametric Design (Table 5.8)

The synthesized mechanism (Table 5.6) is subject to parametric design, so its 2D and 3D models and general structural-functional graph are serving as start point data for such study. Parametric design of gear chamfering mechanism is done for definition of parameter φ_1 for defining the orientation of normal feed movement of the tool gear in normal direction to a specific point of work gear toothed pattern.

The question is to provide such a direction of normal feed movement of work gear that will correspond to the intersection point of the kinematical contour of work gear to intersect the point T_I .

The intersect point T_I is defined by the intersection of two curves – circumference of outer top gear diameter and involute contour 9, limiting the maximum height of micro-roughness according to the surface quality standard.

The intersection of two curves should be defined to find the common point of the kinematical contour of tool gear which will pass through point T_I on the work gear. The first curve is the kinematical contour of tool gear, and the second curve is the epicycloid trajectory of point T_I in a reversed movement against fixed tool gear.

This definition should be planned, organized, and implemented by the development of two sub-mechanisms.

The first mechanism is for tracking an epicycloid trajectory of point T_I , and the second one is responsible for tracking the kinematical contour of tool gear, which is presenting an involute curve by itself.

For the composition of sub-mechanisms, the set of links should be grouped from the original structural solution of gear chamfering mechanism (Table 5.6).

After regrouping, a further decomposition of Link $L6$ (tool gear) is needed for description of involute 6 – kinematical contour of tool gear.

Further decomposition provides the basic set of parameters, sufficient for the composition of both challenged curves (involute 6 and epicycloid 9). The formation of equations can be accomplished by using radius vectors combined through a product of matrices as well as by putting equality of Cartesian coordinates of both curves or in another more excellent way. Proper graphs are accompanying and explaining the steps of further decomposition and process of revealing the parameters. Numerical methods are implementing the resolution of unknown parameter φ_1 . The result of the definition of parameter φ_1 is shown on graph (Tables 5.8-15) where the horizontal axis is for the number of work gear revolutions which are needed to process chamfer on all the teeth before having the necessity to redirect and change the direction of normal feed movement. And the vertical axis is for the angular value of orientation of normal feed movement plane measured against the fixed inter-axis line.

5.2 Concluding Remarks

1. A successful attempt has been accomplished to keep systematic unity when applying the methods of task-based concept design for mechanism analyses and parametric design.
2. For conceptual design, links are related in a way to provide the functions, while for analyses, the proper structure is decomposed in a way to explain the present features. Reverse order of identical actions confirms methodical unity of both procedures.
3. For the parametric design, the decomposition action adopted from conceptual design is applied for the further decomposition of links as per the needs of parametric design. The methods of conceptual design identically organize the composition of sub-mechanisms for composing equations containing the challenged parameters subject to resolution.
4. The category of the model keeps its general task concentration meaning for synthesis and analysis cases. For the parametric design case, a model defines a set of parameters having content and connection between them sufficient for finding the solution for unknown parameter.
5. Visualization of all three processes significantly wins by application of graphs storing and presenting the necessary information for each activity: the contents of links, the connections between the links, the reason of function for having a proper set of connections, and the visualized possibility of planning and implementing of various tasks of mechanical design.

References

1. Chiou, S.-J., & Kota, S. (1999). Automated conceptual Design of Mechanisms. *Mechanism and Machine Theory*, 34, 467–496. [https://doi.org/10.1016/S0094-114X\(98\)00037-8](https://doi.org/10.1016/S0094-114X(98)00037-8).
2. Paredis, C. J. J., & Khosla, P. K. (1993). Synthesis Methodology for Task Based Reconfiguration of Modular Manipulator Systems. In *Proceedings of 6th International Symposium on Robotic Research, Hidden Valley, PA*.
3. Arlitt, R., Van Bossuyt, D. L., Stone, R. B., & Tumer, I. Y. (2017). The function-based Design for Sustainability Method. *Journal of Mechanical Design*, 139, 041102–041103.
4. Pozhbelko, V. (2015). A unified structure of mechanical system with simple and multiple joints: Multiloop structural synthesis, DOF-analysis and isomorphic identification. In *Proceedings of 14th world congress in mechanism and machine science, vol2* (pp. 779–788). Taiwan: Taipei.
5. Kota, S., & Chiou, S. J. (1992). *Conceptual Design of Mechanisms Based on computational synthesis and simulation of kinematic building blocks, research in engineering design, vol. 4* (pp. 75–87, NY). Springer Verlag.
6. Freudenstein, F., & Maki, E. R. (1979). The creation of mechanisms according to kinematic structure and function. *Environment and Planning B*, 6, 375–391. <https://doi.org/10.1068/b060375>.
7. Hong-Sen, Y. (1992). A methodology for creative mechanism design. *Mech Mach Theory*, 27 (3), 235–242.
8. Pahl, G., & Beitz, W. (1995). *Engineering design, a systematic approach*. NY: Springer.

9. Brinker, J., & Corves, B. (2015). A survey on parallel robots with Delta-like architecture. In *Proceedings of 14th world congress in mechanism and machine science, vol2* (pp. 753–770). Taiwan: Taipei.
10. Ashari, M. F., et al. (2014). *Production of white pepper using integrated mechanical and enzymatic solutions in an automated machine, Key Engineering Materials, Advanced Design and Manufacture V* (Vol. 572, pp. 305–307).
11. Spitznagel, K. L., & Tesar, D. (1979). Multiparametric optimization of four Bar linkages. *Journal of Mechanical Design, 101*, 386–391. <https://doi.org/10.1115/1.3454070>.
12. Rao, A. R., Scanlan, J. P., & Keane, A. J. (2007). Applying multiobjective cost and weight optimization to the initial Design of Turbine Disks. *Journal of Mechanical Design, 129*(12), 1303–1310. <https://doi.org/10.1115/1.2779899>.
13. Sargysan, Y. L., & Darbinyan, H. V. (2015). Unified Task Based Conceptual and Parametric Design Methodology. In *In Proceedings of 14th World Congress in Mechanism and Machine Science* (Vol. 2, pp. 806–811). Taiwan: Taipei.
14. Angeles, J. (2006). The Design of Novel Prismatic Drive for a three-DOF parallel-kinematics machine. *Journal of Mechanical Design, 128*(4), 710–718.
15. Georgiopoulos, P., Kim, H. M., & Papalambros, P. Y. (2006). Analytical target setting: An Enterprise context in optimal product design. *Journal of Mechanical Design, 128*(1), 4–13.
16. Darbinyan, H. V. (2011). Task based conceptual design method. In *Proceedings of 13th world congress in mechanism and machine science* (p. A23–559). Mexico: Guanajuato.

Chapter 6

A Brief Overview of the Evolution of the Scientific Theory of Gearing



Stephen P. Radzevich

6.1 Introduction

Gears are the means by which power is transferred from source to application. Gears and gear transmissions are extensively used in the nowadays industry. Gearing and geared transmissions drive the machines of modern industry. Gears move the wheels and propellers that transport us over the sea, on the land, and in the air. Transmission and transformation of rotation from an input shaft to an output shaft is the main purpose of gearing of all kinds. A sizeable section of industry and commerce in today's world depends on gearing for its economy, production, and livelihood. No doubt gearing of all kinds will be extensively used in the future.

It should be realized here that there are two different considerations when the state of the art of gearing is discussed. Gear design, and gear manufacture, that is based on common sense of smart handicrafts and on accumulated practical experience is one of the two. An engineering approach that is based on scientific accomplishments in the theory of gearing is the other one.

Taking into account the incompleteness and the inconsistency of the nowadays knowledge in the theory of gearing, an in-depth investigation into the gear kinematics and the gear geometry has been undertaken in the recent years by the author.

This chapter of the book is written in the following manner. At the beginning, a brief overview of the pre-*Eulerian* period of the gear art is done. Then, the fundamental accomplishments in the “*scientific*” theory of gearing are identified, and a name of the corresponding key contributor (s) is associated (where possible) with each of the accomplishments. As the overall number of the “*fundamental*” accomplishments in the scientific theory of gearing is limited, and it is not large, the overall number of the fundamental contributors to the “*scientific*” theory of gearing is also limited. Irrespective of many other researchers (not mentioned in this section of the book) that have also contributed a lot to the field of gearing, they cannot be regarded as the “*fundamental contributors*” to the “*scientific*” theory of gearing.

S. P. Radzevich (✉)
Mechanical Engineering, Sterling Heights, MI, USA

Most of the results of the research that has been carried out are discussed in the monograph [1]. The fundamentals of the proposed scientific theory of gearing are based on the key accomplishments in the gear kinematics, and the gear geometry. With that said, it makes sense to begin the discussion with a brief overview of the evolution of the scientific theory of gearing. This will help us to identify what is already done in the field, where we are now, and what has to be done in the future.

Such an analysis has to be carried out in order to credit every accomplishment in the scientific theory of gearing with the name of the key contributor. In the meantime, not all the achievements in the field of gearing can be attributed with a right name of a gear researcher. A gear researcher who has contributed significantly to the theory of gearing deserves to be credited with a corresponding scientific result.

Several achievements in the theory of gearing cannot be credited to right persons. For example, the names of the key contributors for (a) the condition of contact of the tooth flanks and (maybe this accomplishment is NOT exactly from gearing but from another area of the theory of machines and mechanisms) (b) equal base pitches are not known. A few more achievements in this regard can be mentioned. It is desirable to get the appropriate names identified.

The aforementioned, as well as other accomplishments, are vital to the scientific theory of gearing. It is desirable to know who was the first to come up with these meaningful results, as well as in what way these results have been achieved.

The main goal of the book chapter titled “A Brief Overview of the Evolution of the Scientific Theory of Gearing” is to briefly outline “all” the known fundamental accomplishments in the scientific theory of gearing and to credit right gear researchers with the corresponding scientific achievements in the field, that is, an effort is undertaken aiming to associate each of the fundamental accomplishments in the scientific theory of gearing with the name of the corresponding gear researcher who contributed a particular accomplishment. In order to mention all the key researchers in the field and to miss none of them, the following approach is adopted below.

First, all (with no exclusions) the fundamental accomplishments to the scientific theory of gearing are listed in a chronological order.

Second, a name of a key gear researcher is associated with each of the accomplishment, that is, the name of a researcher who was the first either to discover or to contribute the most to a particular accomplishment in the scientific theory of gearing. For example, Leonhard Euler is credited with the application of the involute of a circle for the gear tooth profile, as he was the first to prove that the involute tooth profile fits the best the needs the gear tooth geometry, regardless of the involute of a circle is known¹ long before Euler has made his discovery in 1760.

In addition to that, a few huge mistakes committed in the past by the gear researchers when investigating gears are also mentioned in order to better understand the theory and to properly value those scientists who contributed much to the

¹The involute of a circle was first proposed by *Philippe de la Hire* in 1696, and it was later in the eighteenth century when *Leonhard Euler* proposed the involute curve as a viable tooth profile.

scientific theory of gearing. Mistakes of this type can be referred to as the “key mistakes” in the theory of gearing. Following the adopted approach, it is helpful to separate the names of the principal contributors to the scientific theory of gearing from those who contributed less to the subject, and, moreover, from those who committed mistakes that significantly affected the evolution of the theory of gearing.

The results of the research carried out by the author, and a few papers earlier published by the author [2–4], are extensively used in this section of the book. Other sources are extensively used as well [5, 6], and others. The consideration begins with ancient gear designs that are created only due to common sense and ends with the modern scientific theory of gearing.

Tons of sources were investigated prior to making a possible representation of the principal accomplishments in the scientific theory of gearing in a chronological order. A limited number of the sources were selected for a more detailed analysis. These sources are summarized in [1]. The reported analysis is based mostly on the results of the research listed in [1].

The scientific theory of gearing is the foundation of gear design, production, inspection, and application of gears. Below in this chapter of the book, the purpose, principal features, and evolution of the gear theory are discussed.

Prior to beginning the discussion on the scientific theory of gearing, it makes sense to clarify the meaning of the term “scientific theory.” As it is understood from the text below, a “scientific theory” has to be based on a few postulates (on a limited input information), which the entire theory can be derived from. The fewer the total number of the postulates, the more powerful scientific theory can be derived, and vice versa. In the case of the scientific theory of gearing, the minimum required input information is limited to:

- (a) A disposition of an input shaft relative to an output shaft.
- (b) Input rotation.
- (c) Input torque.
- (d) Output rotation (or output torque).

The entire analytical description of gearing, the kinematics and the geometry of gearing, the elements of gear dynamics, and so forth, can be derived from the clauses (a) through (d).

All the results in a scientific theory of gearing are interconnected with one another. An additional information on gearing (if any) can also be incorporated into the analysis. With that said, it is clear now that all the earlier developed so-called theories of gearing (proposed by T. Olivier (1842) [7], Ch. Gochman (1886) [8], F. Litvin (2004), D. Dooner (2012), as well as numerous others) cannot be referred to as “scientific theories of gearing,” as they represent just a collection of scientific/engineering results that are independent from one another, are not interconnected with one another, and do not form a self-consistent theory.

The art and science of gearing have their roots before the Common Era. Yet many engineers and researchers continue to delve into the areas where improvements are necessary, seeking to quantify, establish, and codify methods to make gears meet the ever-widening needs of advancing technology.

Despite gears and geared transmissions are investigated for a long while, the nowadays knowledge of the gear theory is poor and is completely insufficient. Moreover, the author is doubtful that all the principal accomplishments in the theory of gearing are known to all the gear researchers, those who are actively involved in the research in the field.

Motivation: The necessity of “cleaning” of the gear science from incorrect, wrong, and loosely statements, as well as from other inconsistencies, is the main reason to write this section of the book.

The bottom line is as follows: All the principal accomplishments in the theory of gearing have to be identified, and a gear researcher, who has contributed significantly to the theory of gearing, deserves to be credited with the corresponding scientific result.

Those who don’t know their own history have no chance for success in the future.

6.1.1 Main Periods in the Evolution of the Theory of Gearing

Gears are used to transmit and transform a rotation from an input shaft to an output shaft. Depending on a particular application, gearing has to meet certain additional requirements, namely, high accuracy of transmission of rotation and high power density², which have to be ensured by gears.

The development and investigation of gearing with a constant angular velocity ratio³ (i.e., gearing for which the equality $\omega_p/\omega_g = \text{const}$ is valid) is one of the main goals of the scientific theory of gearing [1]. Gearing with a constant angular velocity ratio (or gearing with a pre-specified function of the angular velocity ratio) is commonly called “geometrically accurate gearing,” or “ideal gearing,” or just “perfect gearing,” for simplicity. More generally, the design of gearing with a prescribed function of the angular velocity ratio (i.e., (a) non-circular gearing with a constant center-distance, (b) non-circular gearing with a variable center-distance, (c) gearing with a variable shaft angle, and (d) gearing with a variable center-distance, and a variable shaft angle simultaneously) is also covered by the scientific theory of gearing.

Many efforts were undertaken in the past by hundreds of researchers aiming for the development of the “theory of gearing.” However, not many of them have really contributed to the theory.

Below in this chapter of the book, the evolution of gearing from the earliest times to the present day is concisely discussed with the emphasis on the “theory of gearing.” The consideration is mainly focused on the kinematics of gear pairs, the

²The term “*power density*” is commonly used as an equivalent to the term “*power-to-weight ratio*” (this concept deserves to be investigated more carefully).

³In a more general sense, that is, when non-circular gears are taken into account, use of “*perfect gearing*” makes possible an exact function of the pre-specified angular velocity ratio.

geometry of the interacting tooth surfaces, as well as on some other kinematic and geometric aspect of gears and gearing pairs.⁴ The following rule is adopted in this section of the book: first, all principal contributions to the scientific theory of gearing are identified. Second, the names of the scientists who contributed these accomplishments are named. Following this rule, not many gear researchers are credited with the fundamental contributions to the field of gearing – only those who were the first to obtain a fundamental result of the research in the field.

As it was earlier (circa 2012) proposed by the author [1, 2, 9, 10], the evolution of the theory of gearing falls into three periods, namely:

- (a) Pre-Eulerian period of the gear art.
- (b) The time of the fundamental contribution by L. Euler.
- (c) Post-Eulerian period of the theory of gearing.

The principal accomplishments in the scientific theory of gearing are considered below in a chronological order in alignment with the just mentioned three periods of the evolution. It is believed that all (or, at least, almost all) principal accomplishments are covered in the paper.

6.1.1.1 Pre-Eulerian Period of Evolution of the Gear Art

The earliest account of gears comes from ancient Chinese and Greek literature. Because of force-multiplying properties of gears, early engineers used them for hoisting heavy loads such as building materials. The mechanical advantage of gears was also used for ship anchor hoists and catapult pre-tensioning.

The earliest written descriptions of gears are said to have been made by Aristotle [5] in the fourth century B.C. It has been pointed out that the passage attributed by some to Aristotle, in “Mechanical Problems of Aristotle” (ca. 280 B.C.), was actually from the writings of his school. In the passage in question, there was no mention of gear teeth on the parallel wheels, and they may just as well have been smooth wheels in frictional contact. Therefore, the attribution of gearing to Aristotle is most likely incorrect. The real beginning of gearing was “probably” with Archimedes, who in about 250 B.C. invented the endless screw turning a toothed wheel, which was used in engines of war. Archimedes also used gears to simulate astronomical ratios. The Archimedean were early forms of the wagon mileage indicator (odometer) and the surveying instrument. These devices were “probably” based on “thought” experiments of Heron of Alexandria (ca. 60 A.D.), who wrote on theoretical mechanics and the basic elements of mechanisms.

In the Ancient times, transmission and transformation of a rotation were the only purpose of gearing. The quality of rotation of the output shaft, that is, smoothness of its rotation, was out of importance in the earliest designs of gears. Therefore, it was a common practice to build pin gears made up of wood, the gear tooth profile

⁴The evolution of the geared mechanisms is out of the scope of this chapter of the book.

geometry was not considered at all, and pin gears successfully met all the requirements of that time.

Judging from the history books is one thing. Finding hard evidence of actual gears is another. The biggest problem in finding archeological evidence of gears is that early gear materials were not built to last. Gears manufactured at this time were probably made of bronze. When bronze tools and mechanical pieces broke, they were simply melted down and refashioned into something else.

The oldest surviving relic containing gears is the Antikythera mechanism⁵, named for the Greek island near which the mechanism was discovered in a sunken ship in 1900. The mechanism is not only the earliest relic of gearing⁶ but is also an extremely complex arrangement of epicyclic differential gearing. The mechanism is identified as a calendrical Sun and Moon computing mechanism and is dated to about 87 B.C.

The Antikythera mechanism (see Fig. 6.1) is the oldest⁷ known artifact consisting gears. Here, an image of the original Antikythera mechanism is shown in Fig. 6.1,a.

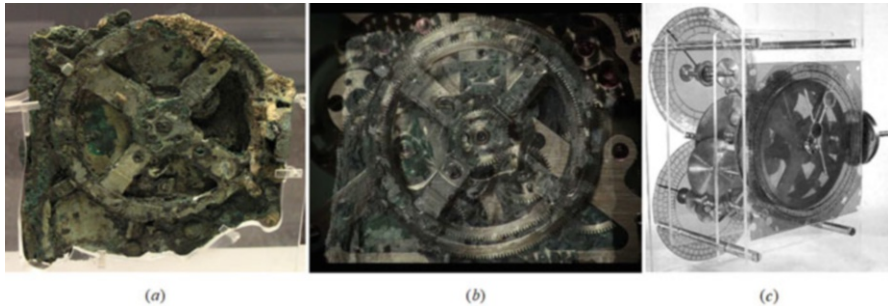


Fig. 6.1 The *Antikythera mechanism* (100 BC to 205 BC)

⁵The artifact was recovered in 1900–1901 from the [Antikythera shipwreck](#) off the Greek island of [Antikythera](#). Its significance and complexity were not understood until decades later. Believed to have been designed and constructed by Greek scientists, the instrument has been dated either between 150 and 100 BC, or, according to a more recent view, at 205 BC. This precious example of antique genius complexity grade was so high that artefacts of a similar complexity and workmanship did not reappear for a millennium and a half, when mechanical astronomical clocks were built in Europe.

⁶The *South-pointing chariot* (invented in the fifth century BC) is another known device that contains gears. Unfortunately, only numerous nowadays designed *reconstructions* (not *replicas*) of the *South-pointing chariot* are known, and no original artifact remained.

⁷The earliest known reference to a gear was around 50 A.D.; *Hero of Alexandria*, through the “[Book of Song](#),” suggests that the [South-pointing chariot](#) may have employed [differential](#) gears as early as the reign of the [Zhou Dynasty](#) (1045–256 BC) of [China](#) (Radzevich, S.P, *Dudley's Handbook of Practical Gear Design and Manufacture*, 3rd ed., Boca Raton, FL: CRC Press, 2016, 629 pages.). However, no artifact of the [South-pointing chariot](#) is discovered so far. Only nowadays designed *reconstructions/simulations* are known. Therefore, in the meantime, the [South-pointing chariot](#) cannot be considered as a relic of a mechanism with gears.

Fig. 6.2 Old-style gears made out of wood



Fig. 6.1,b illustrates the Antikythera mechanism overlapped with the image of its replica. A 3D image of a similar overlap is depicted in Fig. 6.1,c. The device has more than 30 gears, although some scientists suggested as many as 72 gears, with teeth formed through equilateral triangles.

Commonly gears of early design were made out of wood with cylindrical pegs and were often lubricated with animal fat grease. An example of old-style gears made of wood is depicted in Fig. 6.2.

Gears were used in wind and water wheel machinery for decreasing or increasing the provided rotational speed for application to pumps and other powered machines. An early gear arrangement is used to power textile machinery. The rotational speed of a water or horse-drawn wheel was typically too slow to use, so a set of wooden gears was needed to be used to increase the speed to a usable level.

In gearing of old designs (see Figs. 6.1 and 6.2, and others), no special care was taken of the geometry of the interacting tooth surfaces of the gears. Practical men were able by various empirical means to get gears adequate for their needs, at least until the early nineteenth century, when the mathematician's work was translated into practical language. Purely empirical solutions for the form of gear teeth can only be accounted for by the fact that gears operated at "low speeds" and under "small loads." No theory of gearing was necessary to design old-style gears as the rotations were low, and there were no constraints on power density of the gearing. Common sense was the only tool used by the smart ancient craftsmen when designing and manufacturing the gears.

The art of gearing was carried through the European Dark Ages, appearing in Islamic instruments such as the geared astrolabes that were used to calculate the positions of the celestial bodies. Perhaps the art was relearned by the clock- and instrument-making artisans of fourteenth-century Europe, or perhaps some crystalizing ideas and mechanisms were imported from the East after the crusades of the eleventh through the thirteenth centuries.

It appears that an English abbot of St. Alban's monastery, born Richard of Wallingford in 1330 A.D., reinvented the epicyclic gearing concept. He applied it to an astronomical clock that he began to build and that was completed after his death.

A mechanical clock of a slightly later period was conceived by Giovanni de Dondi (1348–1364). Diagrams of this clock, which did not use differential gearing, appear in the sketchbooks of Leonardo da Vinci, who designed geared mechanisms himself [11].

Numerous famous names have indicated their interest to gears and gear drives. Leonardo da Vinci (1452–1519), Albrecht Dürer (1471–1528), Robert Hooke⁸ (1635–1703), and numerous others can be mentioned in this regard.

Numerous designs of gearing are discussed in the famous book by Leonardo da Vinci [11]. In 1967, two of Leonardo da Vinci's manuscripts, lost in the National Library in Madrid since 1830, were rediscovered [11]. One of the manuscripts, written between 1493 and 1497 and known as "Codex Madrid I" [11], contains 382 pages with some 1600 sketches. Included among this display of Leonardo's artistic skill and engineering ability are his studies of gearing. Among these are tooth profile designs and gearing arrangements that were centuries ahead of their "invention."

Albrecht Dürer⁹ is credited with discovering the epicycloidal shape (ca. 1525).

For a long while, the most accurate gears were produced by clockmakers and instrument makers. Questions of exact tooth form, pressure angle, and strength did not enter into the designs of the clockmakers and instrument makers.

Contemporary gears for the uniform transmission of power and rotation are based in much on the application of mathematical curves discovered by scientists in the sixteenth and seventeenth centuries, in the design of teeth flanks. In the period 1450 to 1750 the mathematics of gear tooth profiles and theories of geared mechanisms became established.

Mathematicians turned their attention to gear tooth profile only in the seventeenth century. Girard Desargues (1591–1661), Philippe de La Hire (1640–1718) [12], and Charles Camus (1699–1768) [13] are the names of the most prominent contributors to the gear science in the pre-Eulerian period of evolution of the gear theory.

⁸In 1666, *R. Hooke* demonstrated for *The Royal Society* a model of gearing that he has invented earlier. Later on the gearing of this kind *Hooke* described in his 1674 book *Lectiones Cutlerianae*. The gearing of this particular kind is nowadays known as *White's gearing*. May be this is somehow associated with Mr. *Christopher White* of London who manufactured a microscope for *R. Hooke*.

⁹**Albrecht Dürer** (May 21, 1471–6 April 6, 1528), a [German painter, printmaker, mathematician, engraver, and theorist](#)

Desargues, de La Hire, and Camus have summarized the main accomplishments in the field of gearing in the pre-Eulerian period of time. The results of the research obtained by these scientists are very close to the origin of the scientific theory of gearing.

In particular, the first record on the use of cyclic curves as the tooth profile of a gear is related to Gerard Desargues¹⁰. Desargues' work on gearing is known mostly from the records made by his student Philippe de la Hire¹¹. A treaty on epicycloids and their usage in mechanics is discussed in his book [12]. Philippe de la Hire was the first to describe the use of epicycloids for gears that ensured (as he loosely meant) a uniform transmission of rotation. De la Hire considered the involute as the best among exterior cycloids, since he recognized that it is the special case in which the generating circle's radius is infinite. He also noted that the involute tooth gives the teeth of the corresponding rack as having straight sides. It took 150 years before this principle found practical application.

The first major contribution to the geometry of gear wheels came from France. Charles Etienne Louis Camus¹² is the first mathematician to work the theory of gear teeth into a systematic and general theory of mechanism.

Camus was close to discover the “conjugate action law” for the case of parallel-axes gearing [13]. He showed that in order to get as output a uniform angular velocity, it is necessary to shape the two teeth so that they can be generated like epicycloids by rolling one and the same curve on two different circles.

Charles Camus was the first [13] who formulated the condition that, in his opinion, has to be fulfilled for a pair of gears to be able transmitting a rotary motion smoothly. According to Camus, this condition is formulated as follows:

If, in a uniform rotation, power is to be transmitted via a pair of teeth, then the normal to the teeth flanks at the contact point (within the path of contact) must pass through the pitch point.

Another formulation of that same condition by other researchers is represented in the form:

If an auxiliary curve is rolling on the pitch circles of circular gears, any point attached to this curve traces conjugate profiles.

This sounds similar to the fundamental theorem of gearing known nowadays (see below in this chapter of the book). Camus' principle of gearing is illustrated with 1733 schematic (see Fig. 6.3). In this schematic, the path of contact, namely, a curved line segment¹³ KBC , and the line of action at different angular configurations

¹⁰**Girard Desargues** (February 21, 1591–September 1661) was a [French mathematician](#) and engineer.

¹¹**Philippe de la Hire** (March 18, 1640–April 21, 1718) was a [French](#) physicist, astronomer, [mathematician](#), and engineer.

¹²**Charles Étienne Louis Camus** (August 25, 1699–February 2, May 4, 1768) was a [French mathematician](#) and [mechanician](#)

¹³The line of action, KBC , cannot be a curve, as a force acts only along a straight line, that is, along a straight line of action, and not along a curve.

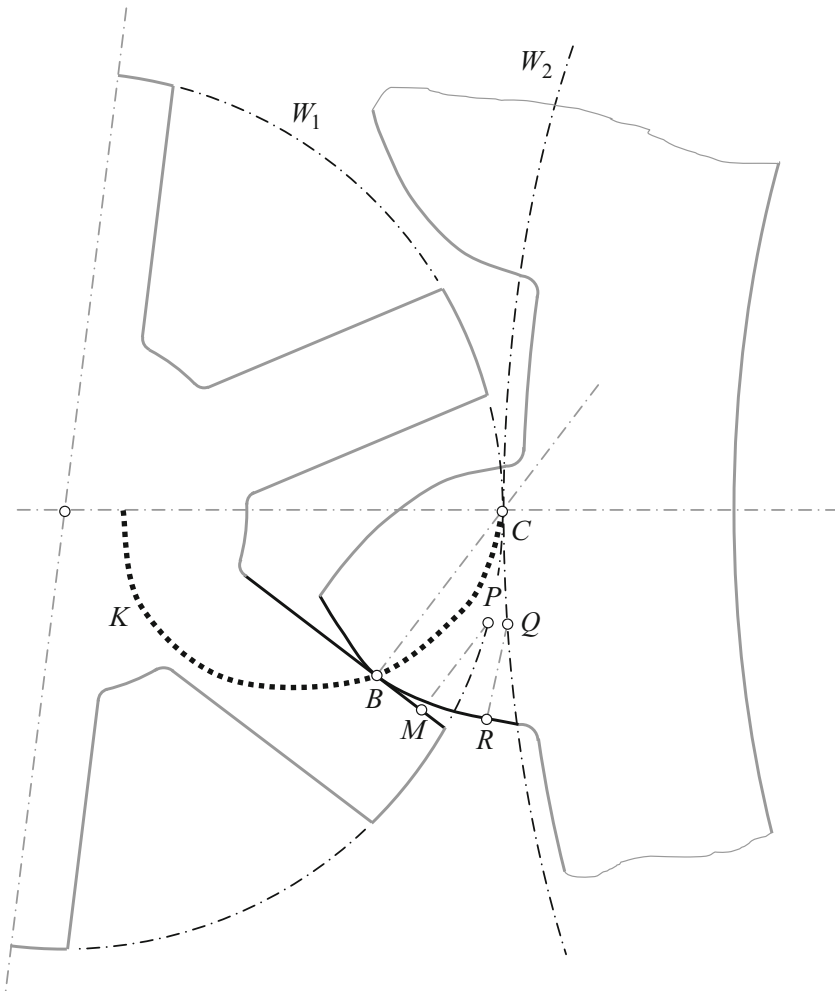


Fig. 6.3 Illustration of *Camus'* gearing principle (1733)

of the mating gears, that is, BC , MP , and RQ , do not align to one another.¹⁴ The schematic (see Fig. 6.3) reveals that Camus did not realize the difference between the “path of contact” and the “line of action.” Camus loosely assumed that the line of

¹⁴It is instructive to note here that the schematic shown in Fig. 6.3 is a kind of mistake because of the following reasons. First, the path of contact is an envelope to consecutive positions of the instant line of action. Therefore, it is not permissible that the line of action, BC , intersects the path of contact, KBC . The path of contact must be in tangency with the line of action, BC . Second, when numerous instant lines of contact are through the pitch point C , then no enveloping curve (i.e., no path of contact) can be constructed. A few more reasons for infeasibility of gearing shown in Fig. 6.3 are to be mentioned.

action, LA , in geometrically accurate gearing can be shaped in a form of an arbitrary planar curve (as illustrated in Fig. 6.3), which is incorrect.

Despite Camus was close to discover the fundamental theorem of gearing, he did not succeed doing that. As it is shown below in this chapter of the book, for gears that operate on parallel shafts, the only feasible case is when both the “path of contact” and the “line of action” are straight lines that align with one another, as it is observed in involute gearing.

Therefore, it is incorrect to grant Camus with the discovery of the “conjugate action law.”

Camus repeated much of de La Hire’s work, although he added many important elements of his own. He gives a detailed analysis of the teeth desirable for the combination of a spur and lantern gear.

Camus did, however, correct de La Hire in that he recognized the fact of sliding of even the epicycloidal teeth one upon the other and said that this phenomenon is one of the principal sources of friction and wear in gearing.

The action of engaged teeth relative to the line of centers is discussed, and he points out that the action is best when engagement takes place after the working face of the driving tooth has passed the line of centers, that is, during the receding action.

Camus goes on to consider the problem of the minimum number of teeth and that of the proper form for the ends of the teeth. He deals with true bevel gears and uses the rolling-cone principle for their analysis. But he considers only the case of interaction of a crown and a bevel gear.

Camus does not consider the involute tooth at all. Although he analyzes trains of gears, he says nothing of the form of teeth required in a series of three or more gears. This can probably be accounted for by the fact that he had only clockwork in mind. The mills of this era seldom had trains of more than two gears engaged.

Clearly, Camus had the basis for a theory of mechanism of gear teeth, but it was not systematically and completely worked out, as in R. Willis [14].

Despite the mathematicians began investigating some curves aiming for their application for the purpose of gearing, no foundations in the theory of gearing has been made at that time.

The condition of contact of the interacting tooth flanks is the only contribution to the scientific theory of gearing attained in the pre-Eulerian period of the gear art. The initially proposed for mechanics of machines in a more general sense, the condition of contact of two machine elements can also be implemented with respect to gears. This condition is schematically illustrated in Fig. 6.4.

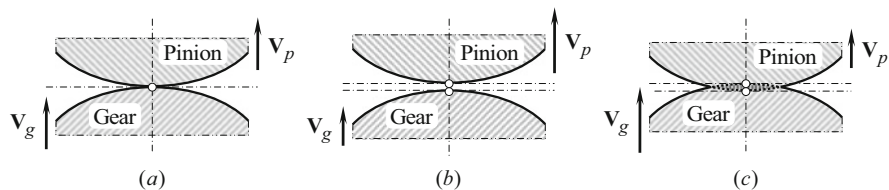


Fig. 6.4 Condition of contact of a gear and a mating pinion tooth flank: (a) perfect contact, $V_g = V_p$, (b) separation of the tooth flanks occurs, $V_g < V_p$, and (c) interference of the tooth flanks occurs, $V_g > V_p$

In order to fulfill the condition of contact, the contact point, both of a gear and a mating pinion's tooth flanks, has to travel with an equal velocity along the common perpendicular, that is, the equality $\mathbf{V}_g \equiv \mathbf{V}_p$ has to be valid (see Fig. 6.4,a). In this scenario, the relative velocity is zero ($\mathbf{V}_{rel} = 0$). In a case $\mathbf{V}_g < \mathbf{V}_p$, the relative velocity is of a positive value ($\mathbf{V}_{rel} > 0$), and the components 1 and 2 separate from one another (see Fig. 6.4,b). Inversely, in a case $\mathbf{V}_g > \mathbf{V}_p$, the relative velocity is of a negative value in this scenario ($\mathbf{V}_{rel} < 0$), and the components 1 and 2 interfere into one another (Fig. 6.4,c). None of these two scenarios are permissible in geometrically accurate gearing.

The condition of contact is important to the theory of gearing. Unfortunately, it is not known who should be credited with this important accomplishment (it is likely this is because the condition of contact has been discovered for a more general case of mechanical engineering, and not for the purposes of gears).

Accomplishments in the field of gearing and gear art in the pre-Eulerian period of evolution of the gear art are briefly summarized immediately below:

- Various primitive designs of wooden gearing were developed with the purpose to transmit a rotary motion between two shafts.
- Gears that operate (a) on parallel shafts, namely, parallel-axes gearing; (b) on intersected shafts, namely, intersected-axes gearing; and (c) on crossed shaft, namely, crossed-axes gearing, are already known in pre-Eulerian period of evolution of the gear art.
- All the early designs of gearing operate at low rotations and transmit a low torque.
- No tooth flank geometry was taken into account, first of all because of the absence of necessity of doing that: Low-power-density wooden gears that operate at low rotations met the current customer requirements of that time.
- It became clear that the performance of a gear pair depends on a specific tooth profile of the mating gears, namely, teeth wear in gearing depends on the actual shape of a gear and a mating pinion tooth.
- Mathematicians indicated an interest to a special tooth profile of a gear and a mating pinion that allows the lowest tooth flank wear.
- Epicycloid is investigated as a potential candidate that can be used to shape the gear teeth, and epicycloidal tooth flank geometry was proposed for gearing that operates on parallel shafts.
- It was realized at that time that in gearing with epicycloidal geometry of the gear teeth, a rotation cannot be transmitted smoothly – with a constant angular velocity ratio.
- Involute of a circle was known at that time. However, there was no understanding that this curve best meets the needs of gearing.

The gearing that was common in the pre-Eulerian period of evolution of the gear art are far from being referred to as “perfect gearing” as they are not capable of transmitting a rotary motion smoothly. Geometrically inaccurate gears (those feature variable angular velocity ratio) are still in use even in the nowadays industry in cases when the rotations are low, and the transmitted power is low as well.

6.1.1.2 The Time when the Fundamental Contribution by L. Euler Has Been Done – The Origin of the Scientific Theory of Gearing

The interest of mathematicians (at the beginning of Desargues, de La Hire, and Camus, and later on of Euler) seems to have come from a desire to increase efficiency and reduce wear in mills of various types where, although the speeds were low, the load was not substantial. Indirectly, these problems were associated with the quality of the transmitted rotation, that is, with the smoothness of rotation of the output shaft. It could happen that the problem of design of geometrically-accurate gears can be traced back to this period of time.

It was Leonhard Euler¹⁵ (1707–1783), a famous scientist (born in Switzerland), whom the origin of the scientific theory of gearing can be traced back to. In the first half of the 1750s, L. Euler (Fig. 6.5) has proved that involute of a circle is the best planar curve that fits to shape a gear tooth profile in geometrically accurate parallel-axes gearing [15]. The main contribution by L. Euler to the scientific theory of gearing is outlined in his two papers [15, 16].

In Euler's first paper (see Fig. 6.6) on gears [15] (written in the first half of the 1750s), he proved that in gearing, the tooth profile sliding is inevitable. As for the shape of the teeth, Euler in this paper did not succeed in going beyond what was already done by Camus. However, Euler's second paper (see Fig. 6.7) [16] (written presumably 10 years later) is very original.

Fig. 6.5 Leonhard Euler
(1707–1783)



¹⁵**Leonhard Euler** (April 15, 1707–September 18, 1783) was a pioneering Swiss [mathematician](#) and [physicist](#)

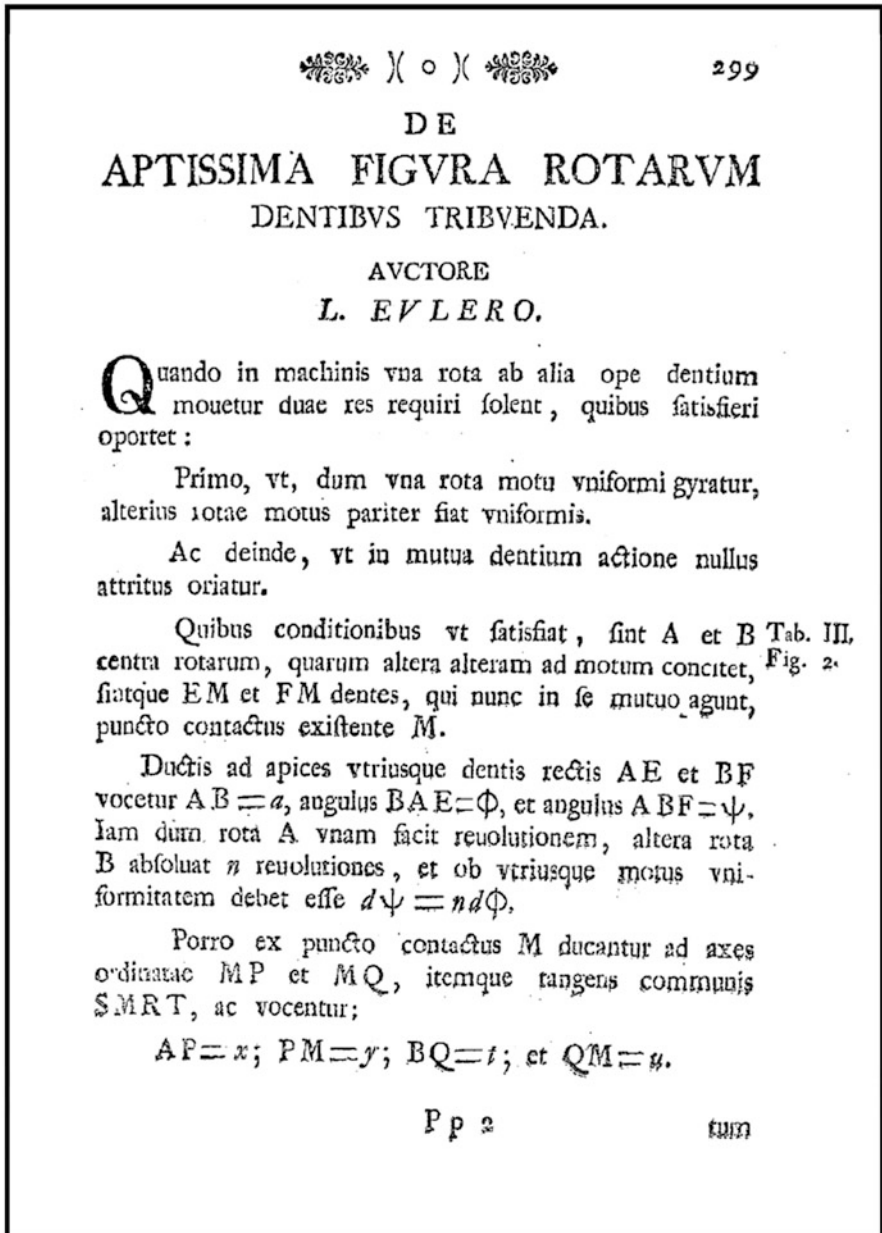


Fig. 6.6 Title page of the paper by Euler, L. (1754-55), "De Aptissima Figure Rotarum Dentibus Tribuenda" ("On Finding the Best Shape for Gear Teeth"), in: *Academiae Scientiarum Imperiales Petropolitanae, Novi Commentarii*, t. V, pp. 299-316

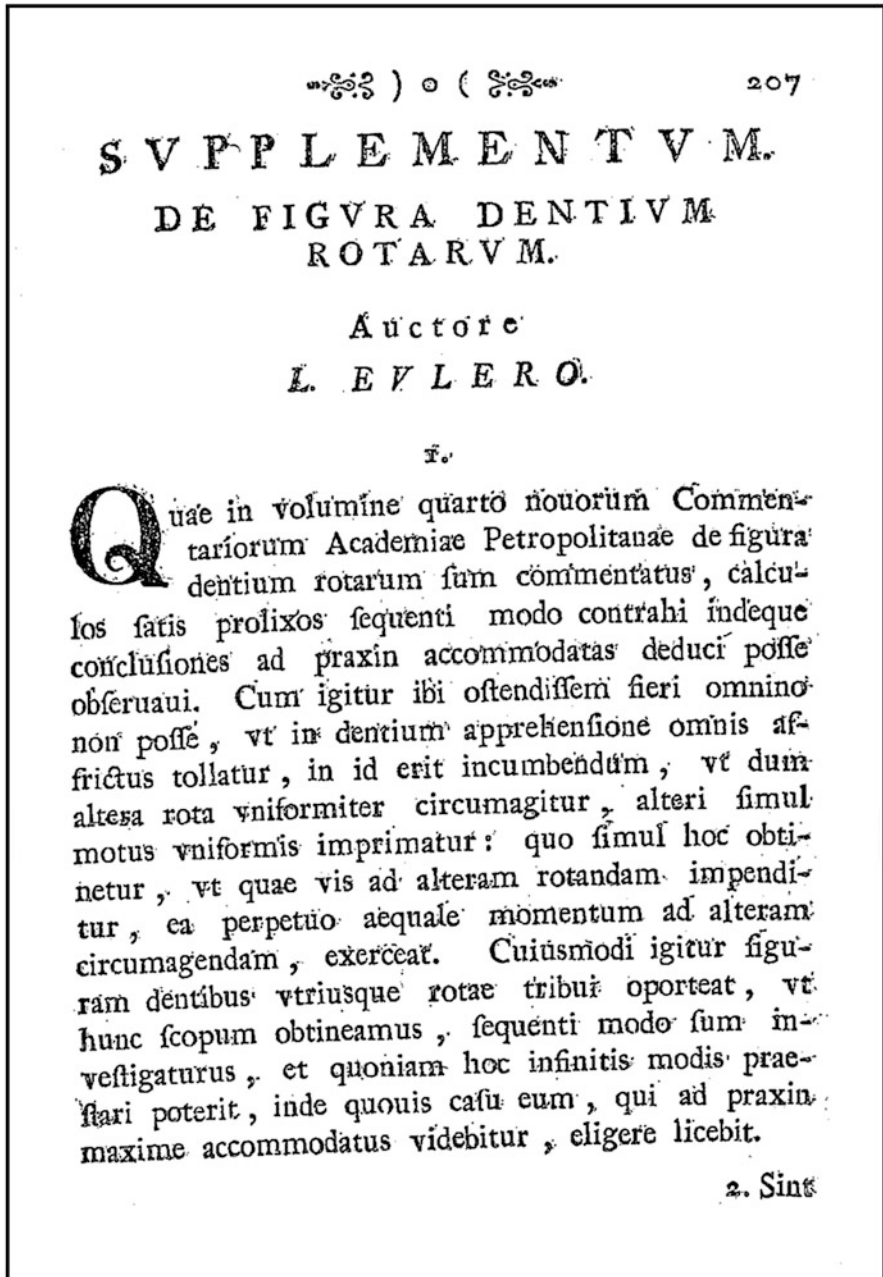


Fig. 6.7 Title page of the paper by Euler, L., "Supplementum. De figura dentium rotarum". In: *Novi Comm. Acad. Sc. Petropol.* 1767. (Originally published in *Novi Commentarii academiae scientiarum Petropolitanae* 11, 1767, pp. 207-231)

Involute Tooth Profile for Parallel-Axes Gearing

It is proven in these papers [15, 16] that in parallel-axes gearing the involute of a circle¹⁶ is the only planar curve that minimizes friction between mating gear teeth, and, therefore, involute tooth profile is the only kind of tooth profile that should be used to design conjugate gear pairs. In these papers [15, 16], Euler also shows the grasp and precision of his great mathematical mind. He specifically states the conditions:

- Uniform rotary motion of both gears.
- In the mutual action of the teeth “nullus atritus oriatur,” no interference between the mating teeth flanks (however, a gap between the mating teeth flanks, that is, equality of base pitches of the mating gears, is not considered yet).

The following conclusion can be drawn from the discussion above:

Conclusion 1: The scientific theory of gearing originated from Euler’s two famous papers on the geometry of the ideal shape of gear teeth [15, 16] in parallel-axes gearing.

Conclusion 2: The scientific theory of gearing is tightly connected with the application of an involute of a circle to shape gear teeth in parallel-axes gearing. Despite the fact that involute of a circle was known to mathematicians long before the time, when L. Euler has carried out his research on the shape gear teeth, it was L. Euler who proposed to use involute of a circle in the design of geometrically accurate (i.e., perfect) parallel-axes gearing.

By now, the kinematics and geometry of parallel-axes involute gearing are investigated so extensively that there is no need to discuss here gearing of this particular design more in detail, as it is trivial and is outlined in textbooks on machine and mechanisms theory.

The Euler-Savary Formula

Euler’s papers on gear wheels [15, 16] are part of a development that started essentially with the investigation of the ordinary cycloid: the curve described by a point on the circumference of a circle when this circle rolls without slipping on a straight line [17]. In this paper [16] Euler derived a formula that is equivalent to the Euler-Savary formula¹⁷ in the nowadays interpretation. It is remarkable that although Euler was merely studying a very specific subject, gear wheels, the Euler-Savary¹⁸ formula belongs from a modern point of view to planar theoretical

¹⁶Invention of the involute tooth profile, which best fits the practical needs of the industry, is commonly credited to *Leonhard Euler* (1707–1783).

¹⁷The consequences from the *Euler-Savary formula* (the *involute tooth profile*, and the *conjugate action law*) are important to the theory of gearing, while the formula itself is of less importance.

¹⁸**Felix Savary** (October 4, 1797–July, 15, 1841) was a [French mathematician](#) and [mechanician](#)

kinematics and has general validity. Euler in this context also discovered the so-called involute gearing, nowadays the most popular form of gearing.

When a planar motion is considered at a particular instant of time, a modern kinematician thinks of a particular position of a moving axode in relation to a stationary axode. The point where the two curves touch each other is the “instantaneous center of rotation” (or the “pitch point,” in other terminology). Clearly, an arbitrary point P of the moving plane describes a curve in the stationary plane. At a particular moment under consideration, point P coincides with a particular point of the curve that it traces. The tangent to the curve in this particular point can be constructed easily by means of the pitch point. How about the center of curvature at this particular point? Nineteenth-century kinematicians have extensively studied the relation between the points of the moving plane and the corresponding centers of curvature of their trajectories in the stationary plane. This particular relation has many properties.

Refer to Fig. 6.8,a, where an arbitrary configuration of two interacting planar curves is shown. The stationary axode is π_1 . The moving axode is π_2 . The point O at which the two axodes touch each other is the instantaneous center of rotation or pitch point at the moment that we are considering. The k_2 is a curve in the moving plane. The k_1 is the envelope in the stationary plane of the set of positions in the stationary plane of k_2 . In the position under consideration, the curves, k_1 and k_2 , touch each other at the point C . The points N_1, N_2, M_1 , and M_2 are, respectively, the centers of curvature of the planar curves k_1, k_2, π_1 , and π_2 , corresponding to the points C and O . Let θ be the angle between the common tangent to the axodes and the common perpendicular at C to the curves k_1 and k_2 . Then the following expression is valid:

$$\left(\frac{1}{ON_1} - \frac{1}{ON_2} \right) \cdot \sin \theta = \frac{1}{OM_1} - \frac{1}{OM_2} \quad (6.1)$$

This is the Euler-Savary formula or theorem. The variables ON_1, ON_2, OM_1 , and OM_2 correspond to the directed line segments and are signed values. The pitch point, O , is the origin of a Cartesian coordinate system with pr as positive x -axis and pn as positive y -axis. Similarly, O is also the origin of a Cartesian coordinate system $O\xi\eta$ with directed line segment OC defining the positive direction of the ξ -axis. The two systems have the same orientation. As for the signs of the variables in the Euler-Savary formula, ON_i is positive if moving from O to N_i is a move in the direction of the ξ -axis. OM_i is positive if moving from O to M_i is a move in the direction of the x -axis.

A modern proof of the Euler-Savary formula was given in 1970 by G.R. Veldkamp [18].

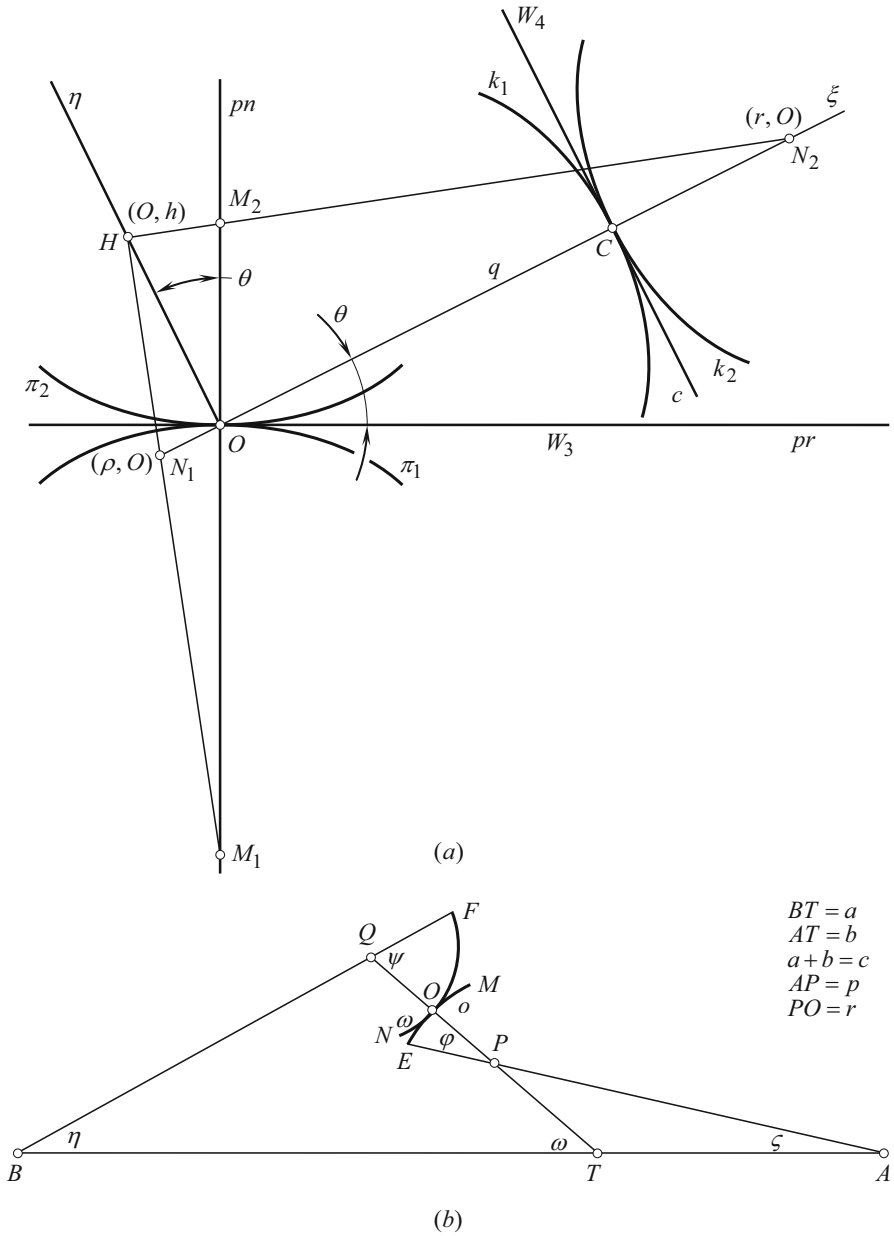


Fig. 6.8 The schematics used by *L. Euler* for the derivation of the involute gear tooth profile. (Adapted from: Euler, L. "Supplementum. De Figura Dentium Rotarum". *Novi Commentarii adacemiae Petropolitanae* 11, 1767, pp. 207-231. (E330, *Opera omnia*, 17, pages 196-219). [29])

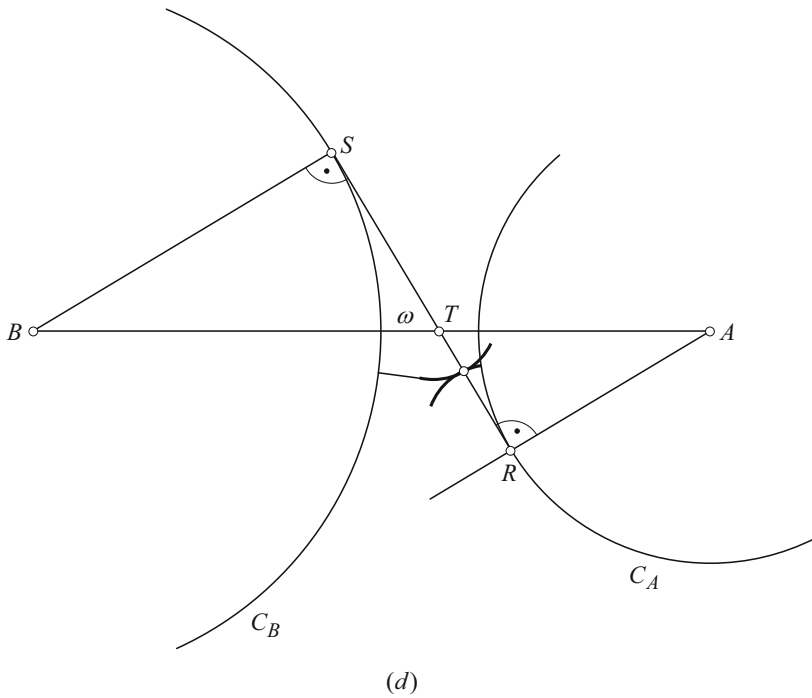
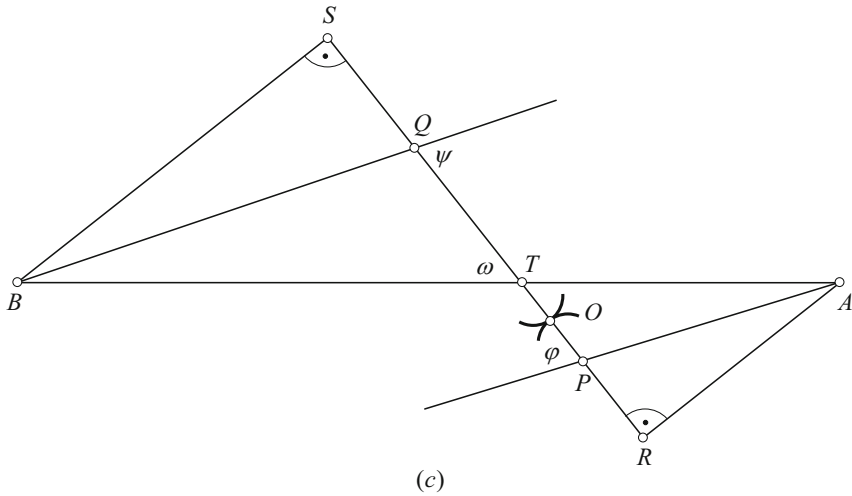


Fig. 6.8 (continued)

Leonhard Euler and the Euler-Savary Formula

In the first paper on gears [15] (written in the first half of the 1850s), and in the second paper [16], written presumably 10 years later, Euler didn't investigate general planar motion at a particular instant of time. Instead, he investigated the

form of the teeth of gear wheels. The general validity of the formula that he discovered is an accidental spin-off of his research. This arises because, in general, just as for first and second order properties, a planar motion at a particular instant can be represented by a circle rolling without slipping on another circle. This is exactly what we are dealing with when we have planar circular gear wheels fulfilling the Euler's condition of a constant velocity ratio.

Euler started with Fig. 6.8,b. The points A and B are the centers of the two wheels. The curves, EOM and FON , are the two profiles of the teeth of the wheels. O is the point where the two profiles touch and the line perpendicular to the tangent in O cuts AB in the point T . When the gear wheels rotate, a moment M_A about the center A yields a moment M_B about the center B . It is easy to see that at the instant of time under consideration, the ratio of these two moments equals BT/AT . Euler argues that the condition of a constant velocity ratio implies that the ratio of these two moments must be constant, which leads to a kinematic result: The common normal in the point where the profiles touch each other intersects AB in a stationary point T . From a modern point of view, point T is the pole of the motion of the two gear wheels with respect to each other. The axodes of the two gear wheels are two circles, one of which is centered at A and another one is centered at B . The two circles touch one another at point, T . Euler has proved a kinematic result by means of a dynamic argument.

After making clear that the point T is stationary, Euler determined several relations between the parameters depicted in Fig. 6.8,b, and differentiated them. He basically considered a slight change in the position of the two profiles with respect to each other, using the fact that the common normal intersects the center-distance, AB , always at the stationary point T . After some calculations are executed, this reveals that the ratio of the angular velocities, $d\eta/d\xi$, is equal to the ratio TA/TB . For an arbitrary configuration of the profiles, Euler then derives the following expression that enabled him, in principle, to calculate the actual value of the radius of curvature ρ' of the profile NOM out of the parameters of profile EOM :

$$\rho' = c \cdot \cos \omega - r - p \cdot \cos \varphi - \frac{b^2 \cdot \cos \omega \cdot d(p \sin \varphi)}{c \cdot d(p \cdot \sin \varphi) - a^2 \cdot d\varphi \cos \omega} \quad (6.2)$$

The explanation for the parameters in Eq. (6.2) can be found in Fig. 6.8,b.

In a particular configuration, one can assume, without loss of generality, that the profile EOM is a circle and that the center of curvature of the profile NOM coincides with Q . Then, the equalities, $dp = 0$ and $\rho' = OQ$, are valid. Moreover, if the foot points of the perpendiculars, from, respectively, A and B , on the line PQ (see Fig. 6.8,c), are designated as R and S , then it can be shown that Eq. (6.2) implies:

$$RT \cdot SQ \cdot TP + ST \cdot RT \cdot TQ = 0 \quad \text{or} \quad \frac{RT \cdot TP}{RP} + \frac{ST \cdot TQ}{SQ} = 0 \quad (6.3)$$

This is Euler’s version of the Euler-Savary formula¹⁹. It can be shown that Eq. (6.3) is equivalent to Eq. (6.1).

The Euler-Savary formula has an amazing interpretation. It turns out that when p coincides with R , then Q coincides with S . And naturally Euler considered the possibility that this is the case during entire motion. The profiles then are involutes of the circles C_B and C_A (see Fig. 6.8,d). At this moment involute gearing has been discovered [17].

In Fig. 6.9, a schematic of the equivalent three bar mechanism that is used nowadays for the derivation of Euler-Savary formula is shown. In particular, a formula for the calculation of an actual value of the radius of curvature, ρ_p , is derived

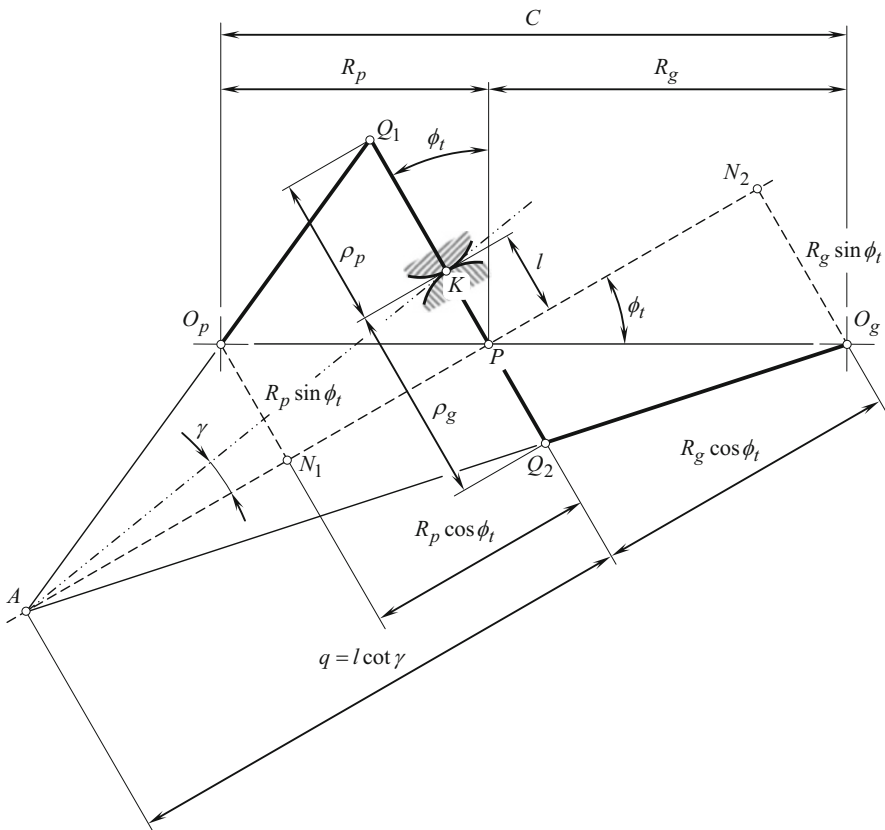


Fig. 6.9 Schematic of the equivalent three bar mechanism that is used nowadays for the derivation of Euler-Savary formula

¹⁹**Félix Savary** was the first to derive the Euler-Savary formula in its modern form. Savary’s proof can be found in: *Leçons et cours autographiés, Notes sur les machines*, par le professeur F. Savary, Ecole Polytechnique, 1835–1836 (unpublished lecture notes; available in the Bibliothèque Nationale in Paris).

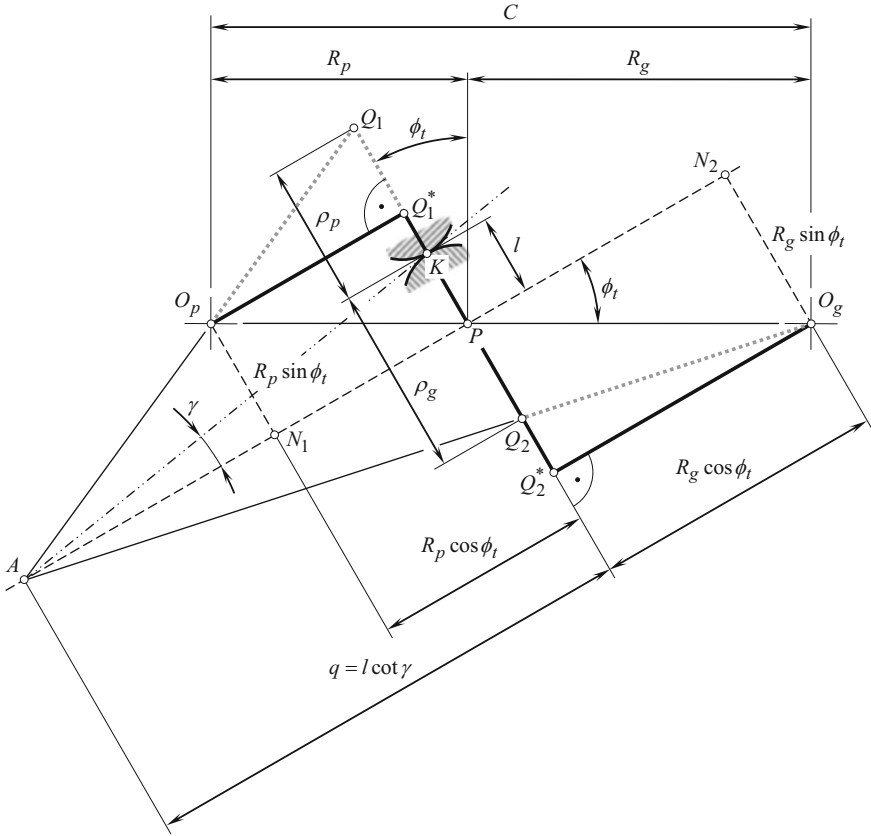


Fig. 6.10 Schematic of the equivalent three bar mechanism that is used nowadays for the derivation of an involute gear tooth profile

based on the similarity of the triangles $\triangle AQ_1P$ and $\triangle AO_1N_1$. A formula for the calculation of an actual value of the radius of curvature, ρ_g , is derived based on the similarity of the triangles $\triangle AO_2N_2$ and $\triangle AQ_2P$.

A reduced case of the equivalent three bar mechanism that is used nowadays for the derivation of an involute gear tooth profile is depicted in Fig. 6.10. The joints are located at points Q_1^* and Q_2^* , instead of points Q_1 and Q_2 correspondingly.

The proposed parallel-axes involute gearing with zero axes misalignment/displacement by L. Euler deserves to be referred to as “Eulerian gearing,” or simply as “ E_u -gearing”:

Definition 6.1. Eulerian gearing (or just E_u -gearing, for simplicity) is a kind of parallel-axes involute gearing that features zero axes misalignment/displacement.

Such a terminology can be used for science purposes; similar to that are the terms “Newtonian fluid,” “absolutely rigid body,” and “absolutely black body” that can be easily found in the public domain.

Despite the invention of the involute tooth profile is of critical importance, at the time of L. Euler the difference between the line of action and the path of contact in a gear pair has been not understood in detail. This is, in much, because in the case of parallel-axes gearing, both the lines, namely, the line of action, LA , and the path of contact, P_c , are straight line segments that align to one another. Later on, this inconsistency in interpretation of involute gearing became the root cause of many mistakes when gearing of other designs were proposed and investigated. The main reason for that is as follows.

For gearing that operates on parallel shafts, involute tooth profile is the only tooth geometry under which the tooth flanks (a) are enveloping to one another and (b) are conjugate to each other (or, in other words, they are “reversibly enveloping profile,” or just “ R_e -profile,” for simplicity [19]). Epicycloidal tooth flanks of the mating gears are enveloping to each other, but they are not conjugate to one another – they are not a type of “ R_e -surfaces.”

The principle of common tangent has been detailed by Euler. He specifically points out the need for the proper design of gear teeth to avoid friction and wear and indicates this application for clocks. Most clockmakers, however, ignored this, if they ever heard of it. Euler’s treatment of gear teeth was very general and was carried out by the application of principles of analytic geometry using both differential calculus and integral calculus. He set up mathematical expressions for gears to move without friction between their teeth (actually for a minimum value of friction). Then, he set up expressions for gears to move with uniform motion.

L. Euler and F. Savary together have devised an analytical method for determining the curvature centers of gear teeth flanks.

The importance of the “conjugate action law” worked out by L. Euler (gears designed according to this law have a steady speed ratio) became correctly realized much later.²⁰

For over a century the invention of involute tooth profile was not used in practice. The industrial revolution in Britain in the eighteenth century saw an explosion in the use of metal gearing. A science of gear design and manufacture rapidly developed through the nineteenth century. The invention and the beginning of application of steam and gas turbines that operate at high rotations and produce lots of power immediately turns the attention of engineers to involute gearing.

It should be stressed here that the concept of the “gear/pinion base pitch” (linear base pitch), as well as the concept of the “operating base pitch” (linear operating base pitch) in a parallel-axes gear pair was not known to L. Euler.

²⁰There is no evidence on whether or not Euler stressed [15, 16], on the difference between the line of action, LA , and the path of contact, P_c .

6.1.2 Accomplishments in the Theory of Gearing in the Time of the Fundamental contribution by L. Euler Are Briefly Summarized Immediately below

- It is proven by L. Euler in the mid of the eighteenth century that involute tooth profile meets the best the requirements of parallel-axes gearing.
- The fundamental theorem of parallel-axes gearing was known due to Euler and Savary.
- There is no evidence that a difference between the line of action, LA , and the path of contact, P_c , was realized by Euler and Savary, as in cases of parallel-axes gearing these two lines align to each another.
- No significant accomplishments at that time are done in the area of intersected-axes, as well as crossed-axes gearing.

The invention of involute tooth profile for parallel-axes gearing is one of the cornerstone accomplishments in the scientific theory of gearing. This achievement is referred to as the beginning of the scientific theory of gearing.

6.1.2.1 Post-Eulerian Period of Evolution of the Theory of Gearing

Since the time when L. Euler carried out his research on involute gearing, scientific theory of gearing got a significant impulse. Numerous contributions to the scientific theory of gearing have been done in the post-Eulerian period of evolution of the gear theory [1, 2, 9, 10]. Principal accomplishments in the scientific theory of gearing are outlined below in a chronological order [1].

Robert Willis and the Fundamental Theorem of Parallel-Axes Gearing

In the nineteenth century, a profound investigation of mechanisms in general sense has been undertaken by Robert Willis²¹. In his 1841 book [14] titled “Principles of Mechanisms,” R. Willis compiled the lectures for his students and knowledge about gears which could be used in practice. In the book, gearing was discussed by the author to the best extent possible in his time.

Despite the “fundamental theorem of parallel-axes gearing” was known to L. Euler, and to F. Savary, this theorem got an extensive recognition in Europe due to publication of the famous book by Robert Willis [14]. Because of this the “fundamental theorem of parallel-axes gearing” is often referred to as the “Willis’ theorem.” The latter is incorrect.

²¹**Reverend Robert Willis** (February 27, 1800–February 28, 1875), an [English](#) academic, was a professor at Cambridge.

The “fundamental theorem of gearing” is known now mostly due to the 1841 book by R. Willis [14]:

Fundamental theorem of parallel-axes gearing (according to R. Willis): The angular velocities of the two pieces are to each other inversely as the segments into which the “line of action” divides the line of centers, or inversely as the perpendiculars from centers of motion upon the line of action.

Nowadays, the “fundamental theorem of parallel-axes gearing” is commonly referred to as “Camus-Euler-Savary fundamental theorem of gearing” (or as “CES–theorem of gearing,” for simplicity).

As already stressed in this chapter of the book, in parallel-axes gearing, the line of action, LA , and the path of contact, P_a , represent two different straight lines that align with one another. The “fundamental theorem of parallel-axes gearing” gives an insight to make a difference between these two lines, LA and P_a . Unfortunately, in the meantime, this difference is not realized by most of the gear researchers.

Generalizing “CES–theorem of gearing” to a case of spatial gearing, one can come up with a conclusion (~2008, Prof. S.P. Radzevich), according to which:

Conclusion 3: Two smooth regular surfaces that travel in relation to one another are called “conjugate surfaces” if and only if the surfaces contact each other along a line, and a common perpendicular through every point of the line of contact intersects the axis of instant rotation of the surfaces.

And further:

Conclusion 4: Two (spatial) curves within two smooth regular surfaces that travel in relation to one another are called “conjugate curves” if and only if the curves are always in (point) contact, and a common perpendicular through contact point intersects the axis of instant rotation of the surfaces.

A Mistake Committed (1842) by Theodore Olivier

The necessity of the theory of gearing for the needs of gear practitioners is realized for a long while. It is likely the 1842 book by Th. Olivier [7] is the first book ever titled as Theory of Gearing. This book by Th. Olivier is followed by the 1852 book by E. Sang [20], then by the 1886 master thesis by H.I. Gochman [8], as well as by numerous other books on the topic, published later on.

The research in the field of theory of gearing has been significantly affected by Theodore Olivier²². As early as 1842 a monograph by Th. Olivier on the theory of gearing [7] was published. This monograph is the first monograph ever to be titled Geometric Theory of Gearing (“Théorie Géométrique des Engrenages”). Therefore, it is incorrect to claim that F. Litvin is the author of the “first book on the theory of gearing,” as some gear experts loosely do.

It is a right point to mention here that in the research undertaken by Th. Olivier, graphical methods developed in descriptive geometry are extensively used.

²²**Theodore Olivier** (January 21, 1793–August 5, 1853), a French mathematician and engineer

In his 1842 book [7], Th. Olivier proposed two principles for generating tooth flanks of the gear teeth. These principles are commonly referred to as the first and the second “Olivier’s principles of generating of enveloping surfaces.” Later on, both these principles got an extensive usage by gear scientists. Instead, he considered the tooth flanks, \mathcal{G} and \mathcal{P} , just the enveloping surfaces (i.e., insufficient).

In a general case of gear meshing, both the principles proposed by Th. Olivier are incorrect, as the condition of conjugacy of the interacting tooth flanks of a gear, \mathcal{G} , and a mating pinion, \mathcal{P} , is not taken into account (the condition of conjugacy is just ignored).

The violation of the condition of conjugacy of the tooth flanks is a huge mistake committed by Th. Olivier.

Both Olivier’s principles are valid just in reduced cases, when the traveling surfaces allow for sliding over themselves, and the sliding occurs in the direction of the enveloping motion. In these reduced cases, the principles by Th. Olivier are getting useless. Therefore, there is no reason in applying “Olivier’s principles” for the purpose of generation of conjugate tooth flanks in a gear pair.

Due to the mistake committed by T. Olivier, no geometrically accurate gears can be designed, and only approximate gears can be designed instead. There is no chance to anticipate any significant improvements if gears are designed following “Olivier’s principles.” Therefore, Th. Olivier cannot be considered as a contributor to the scientific theory of gearing as his accomplishments are a kind of mistake that has negatively affected further development of the gear science.

Later on, that same mistake was committed (1886) by Ch. Gochman [8], the Russian researcher of gears and gearing. This mistake is also observed in all the books by F. Litvin (1914–2017), V.A. Shishkov [21], G.I. Shevel’ova [22], as well as in many other books by authors who adopted Olivier’s approach.²³

Miscellaneous Improvements to the Gear Art

The proposed curved tooth configuration by A.C. Semple²⁴ in the first half of the nineteenth century (1848) captured the interest of many mechanical engineers and inventors.

The second ever known monograph on the theory of gearing has been published in 1852 by E. Sang [20]. This book, titled *A New General Theory of the Teeth of Wheels*, is nothing more rather than a compilation of the known achievements in the field of gearing. No contribution to the theory of gearing has been done by E. Sang [20].

²³It is likely Dr. *Fraifeld* [23] is among those most affected (influenced) with the two “*Olivier principles*.” Generating (hobbing) of gears for “*Novikov gearing*” is another example where ignorance of the condition of conjugacy resulted in insufficient accuracy of the machined gears.

²⁴US Patent No. 5.647, *Rack and Pinion*, Amzi C. Semple, June 27, 1848

Among the experts in the field of gearing in that period of time, the name of Thomas Tredgold²⁵ should be mentioned as well. As a gear person he is mostly known for his proposed approximation of bevel gears (i.e., of intersected-axes gears) by appropriate cylindrical gears (i.e., by parallel-axes gears). The proposed approximation, that is, the so-called Tradgold approximation, significantly simplifies the calculation of bevel gearing in engineering practice.

The Research Carried out by Chaim Gochman

In 1886 a new effort to evolve the theory of gearing was undertaken by Chaim Gochman²⁶. In his master's thesis, he converted the results earlier obtained by Th. Olivier (who used graphical methods for solving problems in the field of gearing) into that same results obtained by means of the methods developed in analytical geometry [8]. As it is claimed on page 7 in the research by Ch. Gochman [8], no new scientific results are contributed by Gochman to those already obtained by Olivier [7]. The interested reader is referred to [4] for details on this research.

In his master's thesis [8], Ch. Gochman loosely considered the tooth flanks of a gear and a mating pinion only as surfaces enveloping to one another. The requirement of conjugacy of the mating tooth flanks was ignored, which is a huge mistake. The fulfillment of the condition of contact is sufficient only in the cases when “no” rolling motion is observed. Otherwise, this condition needs to be complemented with (a) the condition of conjugacy and (b) the equality of a gear base pitch and its mating pinion base pitch to the operating base pitches of a gear pair [1].

It must be clearly realized that the terms “conjugate surfaces” and “enveloping surfaces” are not equivalent to one another: all conjugate surfaces are enveloping to each other, but NOT vice versa, that is, not all enveloping surfaces are conjugate to one another. In detail, the committed mistake is discussed by Professor S. Radzevich [4].

The bottom line of this discussion is as follows: there is no chance to develop a scientific theory of gearing based only on the condition of contact of a gear and a mating pinion's tooth flanks, and ignoring:

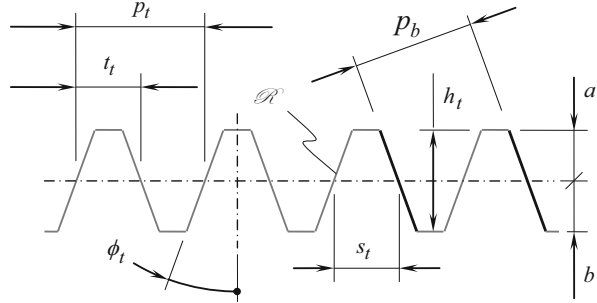
- (a) The condition of conjugacy of the interacting tooth flanks.
- (b) Equality of base pitches of a gear and a mating pinion to operating base pitch of the gear pair, and so forth.

The direction of evolution of the gear theory that strictly follows the Olivier-Gochman approach represents the dead end in the evolution of the theory of gearing.

²⁵**Thomas Tredgold** (August 22, 1788–January 28, 1829), an English engineer and author

²⁶**Chaim I. Gochman** (1851–1916), a Russian mechanician (Novorossiysk University, Odessa, now in Ukraine)

Fig. 6.11 Base pitch, p_b , in a basic rack, \mathcal{R}



Equality of Base Pitches in Geometrically Accurate Parallel-Axes Gearing

The interaction of tooth flanks, \mathcal{G} and \mathcal{P} , of a gear and a mating pinion to a certain extent can be construed as that in a cam mechanism, especially in cases when just one pair of teeth is engaged in mesh. It is common in gearing that two or even more pairs of teeth are engaged in mesh at that same time. In order to make multiple engagements possible, base pitches in interacting tooth flanks, \mathcal{G} and \mathcal{P} , have to be equal to one another; therefore, fulfillment of an equality $p_{b.g} = p_{b.p}$ is a must in geometrically accurate parallel-axes gearing. Here, $p_{b.g}$ and $p_{b.p}$ are base pitches (see Fig. 6.11) of a gear and a mating pinion, correspondingly. Only involute gears feature base pitch, and only involute gear pairs are capable of transmitting a uniform rotary motion smoothly from a driving shaft to a driven shaft. No other gear tooth profiles are capable of ensuring that. Gears with non-involute tooth profile feature no base pitches. Therefore, as in non-involute gear pairs, base pitches do not exist, of course, they cannot be equal, and, ultimately, the gear pair is not capable of transmitting a uniform rotation smoothly.

The condition according to which base pitches of a gear and its mating pinion in a geometrically accurate gear pair have to be equal to one another is an important contribution to the scientific theory of gearing. Unfortunately, no name of a gear researcher is known who was the first to derive this significant accomplishment in the theory of gearing. Moreover, even the exact date when this accomplishment was attained also is not known. Hopefully, in the future, both the name and the date of the invention will be identified.

Tooth Flank Geometry in Geometrically Accurate Intersected-Axes Gearing

For over a century involute parallel-axes gearing was the only kind of gearing for which perfect geometry of the tooth flanks (namely, the involute tooth profile) was known. The desirable geometry of the tooth flanks neither in intersected-axes gearing, nor in crossed-axes gearing, was known for over a century.

It was George Barnard Grant (1849–1917) who proposed (January 14, 1887) a correct method of generation of the tooth flanks in geometrically accurate intersected-axes gearing [24].

Grant’s achievement got no extensive application in the industry, as for a long while (and even nowadays) the industry was satisfied with approximate gears that are easier and cheaper in production.

On the author’s opinion, G. Grant underestimated his contribution to the scientific theory of gearing. Moreover, there is no evidence that Grant’s achievement is properly valued even in nowadays gear community.

Shishkov Equation of Contact, $\mathbf{n} \cdot \mathbf{V}_\Sigma = 0$

The “condition of contact” of the interacting tooth flanks of a gear, \mathcal{G} , and a mating pinion, \mathcal{P} , is the first scientific result of fundamental importance that can be used in the foundation of the scientific theory of gearing. The “condition of contact” is also known as the “enveloping condition” or “law of contact.” The contact condition states that:

Condition of contact: At every point of contact of the tooth flanks of a gear, \mathcal{G} , and a mating pinion, \mathcal{P} , the projection of the relative velocity vector onto the common perpendicular to the interacting tooth flanks is zero.

The condition of contact of two interacting tooth flanks in a gear pair is known for centuries. Per the author’s opinion, this important condition was already known to Camus (1733) [13] or even to Desargues.

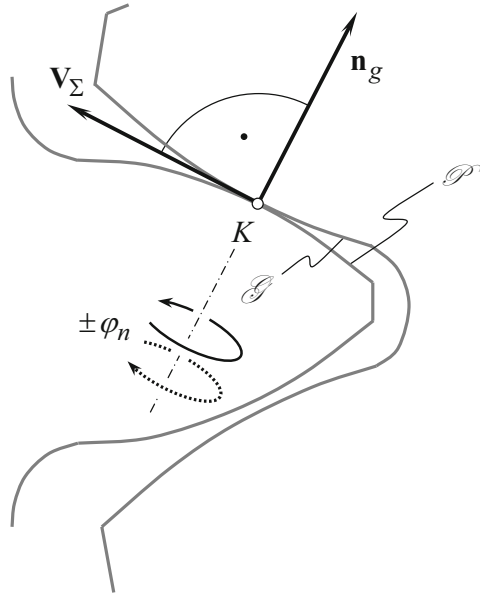
As the theory of gearing evolves, new requirements to the theory arose. Since the time when the gear scientists started realizing the importance of the “condition of contact,” the forms of its representation were different. In particular, the condition of contact (see Fig. 6.12) required an analytical representation. Numerous attempts were undertaken to derive an appropriate equation that reflects proper condition of contact of a gear, \mathcal{G} , and a mating pinion’s, \mathcal{P} , tooth flanks.

Without going into details of the analysis of this particular problem,²⁷ it should be stressed here that finally the condition of contact is represented in the form of the dot product of the unit vector of the common perpendicular, \mathbf{n} , at point of contact of the tooth flanks, \mathcal{G} and \mathcal{P} , and the instant velocity vector, \mathbf{V}_Σ , of the resultant relative motion of the tooth flanks, \mathcal{G} and \mathcal{P} . The dot product has to be equal to zero:

$$\mathbf{n} \cdot \mathbf{V}_\Sigma = 0 \quad (6.4)$$

²⁷For details, the interested reader is referred to the paper by the author: Radzevich, S.P., “Briefly on the Kinematic Method and on the History of the Equation of Contact in the Form of $\mathbf{n} \cdot \mathbf{V} = 0$,” In: *Theory of Mechanisms and Machines*, 2010, No. 1. Vol. 15, pp. 42–51. <http://tmm.spbstu.ru>

Fig. 6.12 Permissible instantaneous relative motions in gearing



This was Prof. V.A. Shishkov who proposed (in 1940s–early 1950s, and not later 1948²⁸) Eq. (6.4) to describe the condition of contact of two tooth flanks, \mathcal{G} and \mathcal{P} , [21, 25].

Here, \mathbf{n} is the unit vector of the common perpendicular, and \mathbf{V}_Σ is the linear velocity vector of the instantaneous resultant motion of the gear and the mating pinion.

Equation (6.4) is based on the fact that at common point(s) (points of contact, in other words), the linear velocity vector of the instantaneous resultant motion of the gear and the mating pinion, \mathbf{V}_Σ , and the unit vector of the common perpendicular, \mathbf{n} , have to be perpendicular to one another.

As it follows from the research undertaken by Prof. Radzevich [3], Prof. Shishkov is the first to represent the condition of contact of two smooth regular surfaces in the form of dot product $\mathbf{n} \cdot \mathbf{V}_\Sigma = 0$ of the unit vector of a common perpendicular, \mathbf{n} , by the vector of the velocity of the relative motion of the interacting surfaces at a point of their contact. The equation of contact in the form $\mathbf{n} \cdot \mathbf{V}_\Sigma = 0$ is known as “Shishkov equation of contact” [1, 3], and others.

The “Shishkov equation of contact” is a valuable contribution to the scientific theory of gearing. Nowadays, this equation is extensively used by many gear researchers. Unfortunately, this equation is often loosely supposed to be an equation of conjugacy, which is not correct.

The interested reader may wish to go to [3] for more details on “Shishkov equation of contact.”

²⁸It could happen that the equation of contact, $\mathbf{n} \cdot \mathbf{V} = 0$, can be found out even in earlier (before 1948) publications by Professor V.A. Shishkov – in his earlier papers, PhD thesis, and so forth.

Principal Planes and Reference Systems Associated with Gearing

For a gear pair with a specified set of the design parameters, a corresponding vector diagram for the rotation vectors (as well as for the torques) can be constructed. Several principal directions are associated with a gear pair. These directions are defined by the rotation vectors of a gear, and a mating pinion, the instant rotation vector, and by the center-line. Use of the principal directions allows for construction of a set of principal planes, and principal reference systems associated with a gear pair. By means of the principal planes and principal reference systems, analysis of gearing of all kinds gets significantly simpler.

The set of principal planes is comprised of “pitch-line plane” (or just “ P_{ln} -plane,” for simplicity), “center-line plane” (or just “ C_{ln} -plane,” for simplicity), “normal plane” (or just “ N_{ln} -plane,” for simplicity), and the plane of action, PA . All these planes are shown in Fig. 6.13:

“Pitch-line plane” is the plane through the axis of instant rotation, P_{ln} , and the center-line, \mathcal{C} , of the gear pair.

“Center-line plane” is the plane through the center-line, \mathcal{C} , of the gear pair perpendicular to the pitch line, P_{ln} .

“Normal plane” is the plane through the plane-of-action apex, A_{pa} , perpendicular to the center-line, \mathcal{C} , of the gear pair.

“Plane of action” is the plane through the axis of instant rotation (the pitch line), P_{ln} , at a transverse pressure angle, $\phi_{t,\omega}$, with respect to the center-line, \mathcal{C} , of the gear pair.

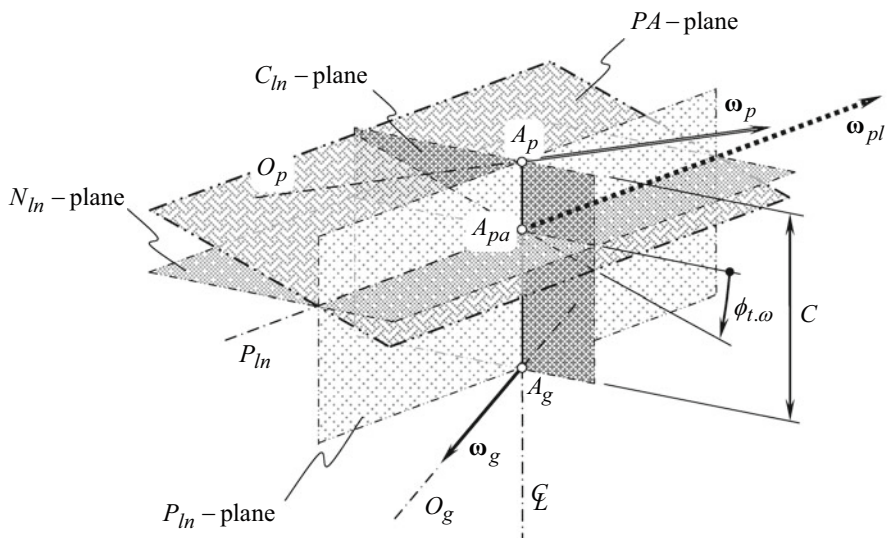


Fig. 6.13 Principal planes associated with a gear pair: the pitch-line plane (the P_{ln} -plane), the center-line plane (the C_{ln} -plane), the normal plane (the N_{ln} -plane), and the plane of action (the PA -plane)

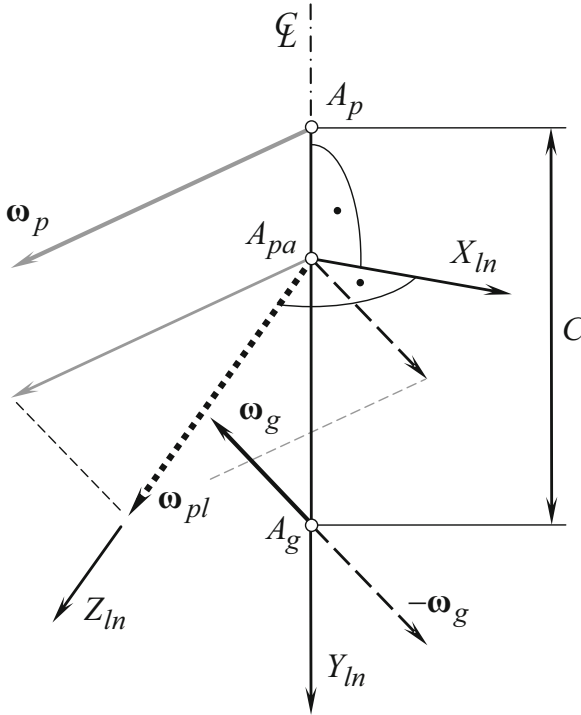


Fig. 6.14 Principal reference system $X_{ln}Y_{ln}Z_{ln}$ associated with a gear pair

A set of principal reference systems is associated with the vector diagram of a gear pair as shown Fig. 6.14. The rotation vectors, ω_g and ω_p , of a gear and its mating pinion are at a certain center-distance, C , and they cross one another. Points A_g and A_p are the points of intersection of the gear axis of rotation, O_g , and the pinion axis of rotation, O_p , correspondingly, with the centerline, \mathcal{L} . The point A_g is referred to as the “gear apex,” and the point A_p is referred to as the “pinion apex.” The vector of instant rotation, ω_{pl} , of the pinion in relation to the gear is a vector through the point A_{pa} . This point is located within the centerline, \mathcal{L} . The point A_{pa} is referred to as the “plane-of-action apex.”

Ultimately, five reference systems are introduced:

- The main reference system, $X_{ln}Y_{ln}Z_{ln}$, associated with the gear pair.
- The stationary gear reference system, $X_g, {}_sY_g, {}_sZ_g, {}_s$.
- The gear reference system, $X_gY_gZ_g$.
- The stationary pinion reference system, $X_p, {}_sY_p, {}_sZ_p, {}_s$.
- The pinion reference system, $X_pY_pZ_p$.

These reference systems are referred to as the “principal reference systems” associated with a gear pair.

Contact Geometry: Indicatrix of Conformity $Cnf_R(\mathcal{G}/\mathcal{P})$ at Point of Contact of Tooth Flanks

In order to analytically described the degree of conformity at a point(s) of contact of the tooth flanks, \mathcal{G} and \mathcal{P} , a planar characteristic curve was proposed by S. Radzevich [26], late 1970s–at the beginning of 1980s. This characteristic curve is commonly referred to as the “indicatrix of conformity, $Cnf_R(\mathcal{P} \mapsto \mathcal{G})$.” The indicatrix of conformity is derived on the premise of “Dupin indicatrices,” $Dup(\mathcal{G})$ and $Dup(\mathcal{P})$, of the tooth flanks, \mathcal{G} and \mathcal{P} , at a point of their contact.

The equation of the “indicatrix of conformity, $Cnf_R(\mathcal{G}/\mathcal{P})$ ” at a point of contact of a gear tooth flank, \mathcal{G} , and a mating pinion tooth flank, \mathcal{P} , is defined of the following structure (see Fig. 6.15):

$$\begin{aligned}
 Cnf_R(\mathcal{G}/\mathcal{P}) &\Rightarrow r_{cnf}(\varphi, \mu) \\
 &= r_g(\varphi) \operatorname{sgn} R_g(\varphi) + r_p(\varphi, \mu) \operatorname{sgn} R_p(\varphi, \mu) \quad (6.5)
 \end{aligned}$$

Here, R_g and R_p are the radii of normal curvature of a gear and a mating pinion’s tooth flanks; and $r_p = \sqrt{R_p}$; μ is the angle of local relative orientation of the tooth flanks, \mathcal{G} and \mathcal{P} , at a point K of their contact; and φ is the angular parameter of the indicatrix of conformity, $Cnf_R(\mathcal{G}/\mathcal{P})$.

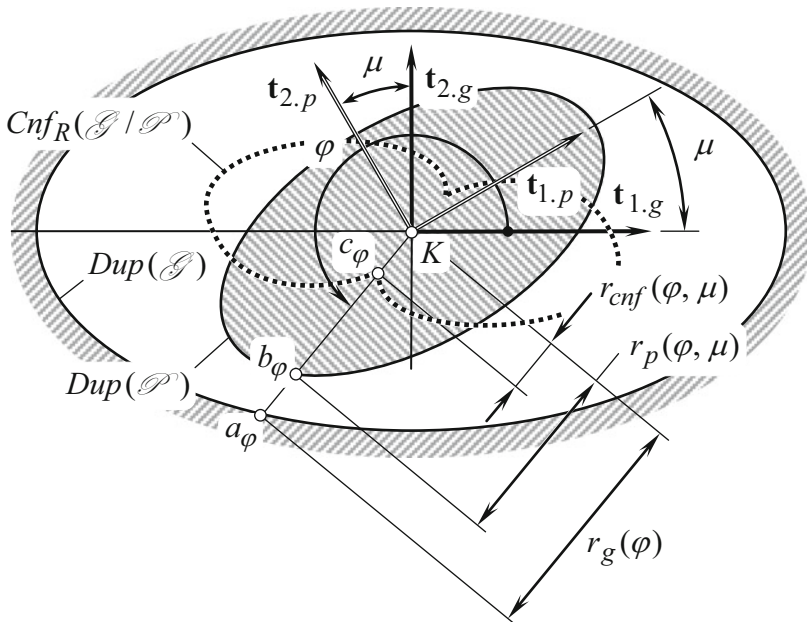


Fig. 6.15 On the definition of the indicatrix of conformity, $Cnf_R(\mathcal{P} \mapsto \mathcal{G})$, at point of contact of tooth flanks, \mathcal{G} and \mathcal{P} . (After Prof. S.P. Radzevich: Radzevich, S.P., *Differential-Geometric Method of Surface Generation*, Dr.Sci. Thesis, Tula, Tula Polytechnic Institute, 1991, 300 pages)

Indicatrix of conformity, $Cnf_R(\mathcal{G}/\mathcal{P})$, at a point of contact of two interacting tooth flanks, \mathcal{G} and \mathcal{P} , is vital for designing perfect gear pairs, and, especially, for solving a problem of synthesizing a most favorable gear pair for a particular application.

Condition of Conjugacy $\mathbf{p}_m \times \mathbf{V}_m \cdot \mathbf{n}_g = 0$ of Interacting Tooth Flanks for Gearing of all Kinds

The condition of conjugacy²⁹ of two interacting tooth profiles of a gear and a mating pinion is a bit tricky. Informally, the condition of conjugacy can be interpreted in the following manner.

Assume that a profile of one member of a gear pair is given. Then, the tooth profile of the mating member of the gear pair can be generated as an envelope to consecutive positions of the first member in its motion in relation to the second member. Then assume that the tooth profile of the second member of a gear pair is known, and the tooth profile of the first member of the gear pair is generated as an envelope to consecutive positions of the second member in its motion in relation to the first member. Then, compare the obtained tooth profiles of the first member of the gear pair with its original profile. If they are identical to one another, then the interacting tooth flanks are conjugate to one another. Otherwise, the interacting tooth flanks are not conjugate to one another.

The condition of conjugacy of interacting surfaces is more robust than the enveloping condition. All conjugate surfaces are enveloping to one another, but not vice versa – not all enveloping surfaces are conjugate.

In parallel-axes gearing, the problem of conjugacy of the tooth profiles/flanks has been solved in the eighteenth century (~1760) by L. Euler.

In involute gearing (see Fig. 6.16), the line of action, LA , and the path of contact, P_c , align to one another at every point of contact, K , of the tooth flanks \mathcal{G} and \mathcal{P} of the gear and the pinion, correspondingly. This is possible as both the line of action LA and the path of contact P_c are straight lines through the pitch point, P , at transverse pressure angle, ϕ_t , to a perpendicular to the center line. This feature of involute gearing is the root cause of confusion as the line of contact and the path of contact are commonly not distinguished from one another in intersected-axes gearing, as well as in crossed-axes gearing.

At around 2008, condition of conjugacy of the tooth flanks, \mathcal{G} and \mathcal{P} , in intersected-axes gearing, and in crossed-axes gearing was formulated by Prof. S. Radzevich. To be conjugate, the tooth flanks, \mathcal{G} and \mathcal{P} , have to be designed so as:

- (a) To retain the instant line of action, LA_{inst} , within the plane of action.
- (b) To ensure that the straight line, LA_{inst} , intersects the axis of instant rotation, P_m , at every angular configuration of the gears when they rotate.

²⁹Conjugate tooth profiles/surfaces are also known as “reversibly-enveloping” profiles/surfaces (or just as R_e -profiles/surfaces, for simplicity) [19].

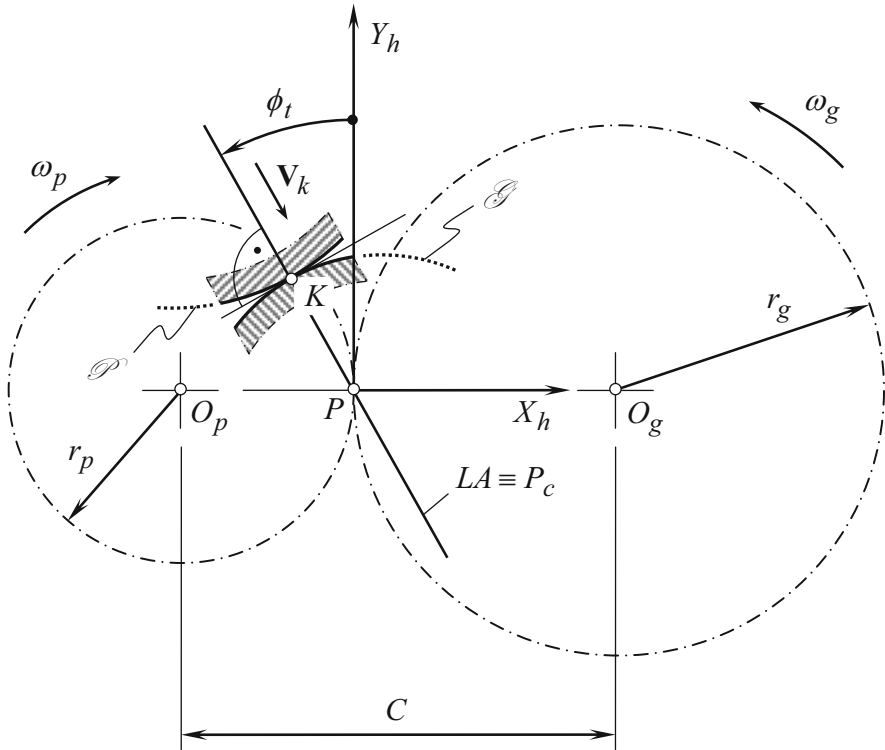


Fig. 6.16 The line of action, LA , and the path of contact, P_c , in an involute gearing

Later on, the condition of conjugacy of a gear, \mathcal{G} , and a mating pinion's, \mathcal{P} , tooth flanks is described analytically by Prof. S. Radzevich (2017) in the form of a triple scalar product $\mathbf{p}_{ln} \times \mathbf{V}_m \cdot \mathbf{n}_g = 0$.

The condition of conjugacy of the tooth flanks, \mathcal{G} and \mathcal{P} , of a gear and its mating pinion is of critical importance when designing gears for high-power-density gear pairs, as well as of gear pairs for low-noise/noiseless transmissions.

Angular Base Pitches: Operating Angular Base Pitch in a Gear Pair

In order to transmit a rotary motion between two shafts, at certain periods of time more than one pair of teeth needs to be engaged in mesh simultaneously. To meet this requirement base pitches of the mating gears must be equal to one another. This fundamental requirement³⁰ is known only for the cases of perfect parallel-axes gearing with zero axis misalignment.

³⁰It is a right point to mention here that the author failed trying to identify the name of a gear researcher who should be credited with this fundamental requirement in the theory of gearing.

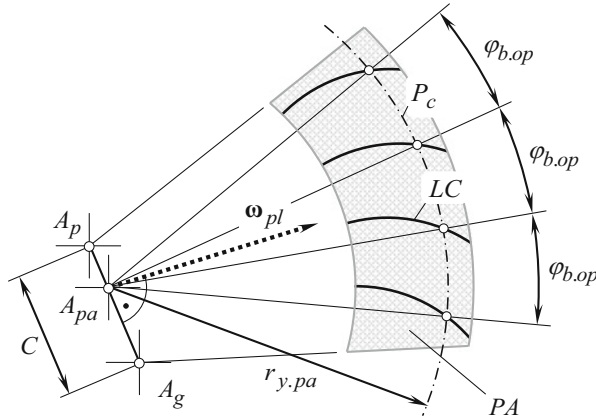


Fig. 6.17 On the concept of equal angular base pitches of a gear and a mating pinion to operating angular base pitch of a gear pair. (After Prof. S.P. Radzevich: Radzevich, S.P., *Theory of Gearing: Kinematics, Geometry, and Synthesis*, 2nd Edition, revised and expanded, CRC Press, Boca Raton, FL, 2018, 934 pages)

The earlier discussed in this chapter of book the concept on equal linear base pitches of a gear and a mating pinion in geometrically accurate parallel-axes gearing is evolved (Prof. S. Radzevich, circa 2008 [1]) to the most general case, that is, to the case of crossed-axes gearing (intersected-axes gearing is viewed here as a reduced case of C_a -gearing). For this purpose, a “concept of angular operating base pitch of a gear pair, $\varphi_{b.op}$ ” is introduced. A gear angular base pitch, $\varphi_{b.g}$, has to be equal to $\varphi_{b.op}$, and the pinion angular base pitch, $\varphi_{b.p}$, also has to be equal to $\varphi_{b.op}$:

$$\begin{cases} \varphi_{b.g} \equiv \varphi_{b.op} \\ \varphi_{b.p} \equiv \varphi_{b.op} \end{cases} \quad (6.6)$$

The concept of equal angular base pitches of a gear and a mating pinion to an operating angular base pitch in the gear pair is illustrated in Fig. 6.17.

The “condition of equality of base pitches” of two mating gears [see a set of Eq. (6.6)] is a valuable contribution to the scientific theory of gearing. This condition is used when designing precision gearing of all kinds.

Crossed-Axes Gearing with Line Contact between the Tooth Flanks (R-Gearing)

A problem of geometrically accurate parallel-axes gearing with line contact between the tooth flanks has been solved by L. Euler, who proposed (circa ~1760) involute gear tooth profile (or, in other words, “ E_u -gearing”). A problem of perfect intersected-axis gearing with line contact between the tooth flanks has been solved

by G. Grant, who proposed (1887) a method of generation of perfect bevel gear tooth flank. Gearing of this design is referred to as “ G_r -gearing”). For the first time ever, the problem of geometrically accurate crossed-axes gearing with line contact between the tooth flanks (the so-called R -gearing) has been solved (~ 2008) by Radzevich [1]. Tooth flank \mathcal{G} of a gear (and of a mating pinion \mathcal{P}) in crossed-axes gearing of this design is generated by a line of contact, LC_{des} , of a desirable geometry that travels together with the plane of action, PA , when the gears rotate. The tooth flanks, \mathcal{G} and \mathcal{P} , are viewed as a locus of the desirable line of contact, LC_{des} , considered in a corresponding reference system. The interested reader is referred to [1] for more detail description of the principal features of design of R -gearing.

Scientific Classification of Gearing

An extensive use of vector representation of gear pairs made possible the development of a scientific classification of vector diagrams of gear pairs (Prof. S. Radzevich, circa 2008 [1]). Vector diagrams of gear pairs with constant values of the center-distance, C , the crossed-axes angle, Σ , and the gear ratio, u , the so-called $C\Sigma u$ -constant gear pairs, as well as the so-called $C\Sigma u$ -variable gear pairs, are covered by the classification. The classification of the gear pairs was further evolved to a scientific classification of gear pairs themselves.

Geometrically Accurate Real Gearing

On the premise of the recent accomplishments in the scientific theory of gearing, a novel gear system is developed by Prof. S. Radzevich at around ~ 2008 [1]. This gear system is commonly referred to as S_{pr} -gearing. If gears in a S_{pr} -gear pair are manufactured to the tolerances for the gear accuracy, then the gear pair is insensitive to the axes misalignment that does not exceed the tolerances for the axes' misalignment. This means that the angular base pitch of the gear, and that of the mating pinion, are remained equal to the operating base pitch of the gear pair as long as the axes misalignment is within the tolerance band for the deviations.

Generalized Form of Equation of Conjugacy of Interacting Tooth Flanks: For Gearing of all Kinds

The considered in this section of the book condition of conjugacy (see Fig. 6.18) of the interacting tooth flanks of a gear and a mating pinion, \mathcal{G} and \mathcal{P} , provides a verbal description of the requirements to be meet by conjugate tooth flanks. Recently (2017), an equation of conjugacy of the tooth flanks, \mathcal{G} and \mathcal{P} , was derived (Prof. S. Radzevich, circa 2008 [1]):

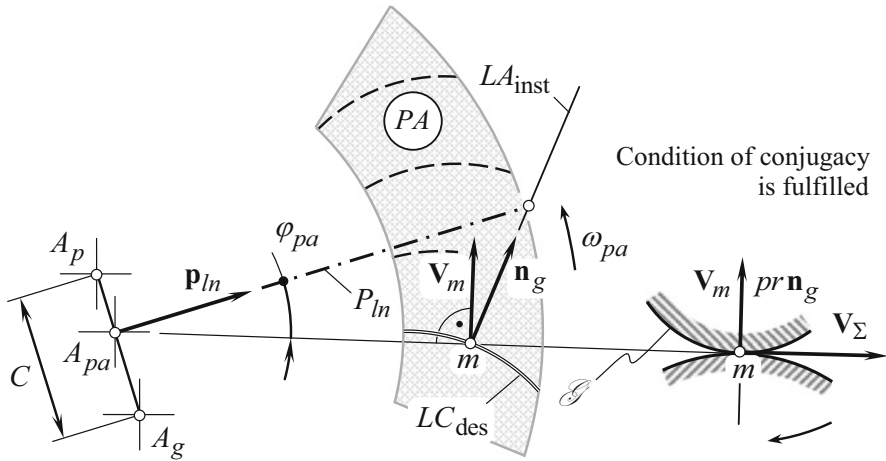


Fig. 6.18 On derivation of equation of conjugacy, $\mathbf{p}_{ln} \times \mathbf{V}_m \cdot \mathbf{n}_g = 0$, of the tooth flanks, \mathcal{G} and \mathcal{P} . (After Prof. S.P. Radzevich: Radzevich, S.P., *Theory of Gearing: Kinematics, Geometry, and Synthesis*, 2nd Edition, revised and expanded, CRC Press, Boca Raton, FL, 2018, 934 pages)

$$\mathbf{p}_{ln} \times \mathbf{V}_m \cdot \mathbf{n}_g = 0 \quad (6.7)$$

Here the following are designated (see Fig. 6.18):

\mathbf{p}_{ln} is the unit vector along the axis of instant rotation, P_{ln} .

\mathbf{V}_m is the linear velocity vector of a point of a desirable line of contact, LC_{des} , between the tooth flanks \mathcal{G} and \mathcal{P} .

\mathbf{n}_g is the unit vector of a common perpendicular at point of contact of the tooth flanks \mathcal{G} and \mathcal{P} .

If the condition of conjugacy [i.e., specified by Eq. (6.7)] is fulfilled at every point of a desirable line of contact, LC_{des} , the gear pair designed this way is capable of transmitting smoothly an input steady rotation to the output shaft.

Accomplishments in the theory of gearing in the post-Eulerian period of evolution of the theory of gearing are briefly summarized immediately below:

- The fundamental theorem of parallel-axes gearing (i.e., the “Camus-Euler-Savary fundamental theorem of gearing”) is formulated. Later on, this theorem was published in the book by Robert Willis [14], and sometimes is loosely referred to as “Willis fundamental theorem of gearing,” which is incorrect.
- The importance of the “condition of contact” between two interacting tooth flanks (i.e., the “enveloping condition”) is realized; various forms of representation of this important condition, both verbal and analytical, are known at that time.
- Investigation into intersected-axes and crossed-axes gearing started at this time.
- A huge mistake in the interpretation of the interaction between the tooth flanks of mating gears has been committed by T. Olivier [7] (1842), and repeated by C. Gochman [8] (1886). All the research in the field of gearing in the years since 1842 through the recent years are significantly affected by this mistake.

- Prof. Shishkov proposed to represent the earlier known condition of contact of the interacting tooth flanks of a gear and a mating pinion in the form of the dot product $\mathbf{n} \cdot \mathbf{V}_\Sigma = 0$. This equation of contact is a key equation in the kinematic method of surface generation. Commonly, this equation is referred to as “Shishkov equation of contact,” $\mathbf{n} \cdot \mathbf{V}_\Sigma = 0$.
- The condition of conjugacy of interacting tooth flanks of a gear and a mating pinion is not understood, and in most cases this important condition is ignored. This is a consequence of the mistake committed by T. Olivier in the nineteenth century.
- The requirement according to which the base pitches of a mating gear and its mating pinion are construed only in part, and only for the case of perfect parallel-axes gearing. The concept of the operating base pitch of a gear pair is not realized at all.

The “fundamental theorem” of parallel-axes gearing and the “contact condition” (i.e., the “enveloping condition”) can be considered as the main contribution to the scientific theory of gearing attained at this time.

In the period until the end of the nineteenth century, the development of the tooth flank profile geometry was more or less completed for the case of parallel-axes gearing. Since that time, involute gearing prevailed as the most advantageous shape of the gear teeth flanks.

6.1.3 Other Contributions to the Field of Geometrically Accurate Gearing

Regardless of unavailability of the scientific theory of gearing till the beginning of the twenty-first century, gear practitioners on their own have proposed numerous designs of geometrically accurate gearing.

6.1.3.1 Grant Bevel Gearing

In this regard, the invention [24] by George Grant³¹ (see Fig. 6.19) should be mentioned first of all. The use of the invention [24] allows generating bevel gear tooth flanks for geometrically accurate intersected-axes gearing. This is due to that in one of the possible applications of the invention, “. . . the rolling cone is increased in size until its center angle is ninety degrees, and it becomes a plane circle. Its element

³¹**George Barnard Grant** (December 21, 1849–August 16, 1917) is considered one of the founders of gear-cutting industry in the USA (*Grant* established a gear-cutting machine shop in Charlestown, Massachusetts. When this business expanded, he moved the workshop to Boston, expanded it, and named it the *Grant Gear Works*. From this extremely successful establishment evolved the *Philadelphia Gear Works* and the *Cleveland Gear Works*. *George Grant* even wrote several very successful books on the subject, for example, *A Treatise on Gear Wheels*; *A Handbook on the Teeth of Gears, Their Curves, Properties and Practical Construction*, and so forth).

45 cone with a circular base; but there are many curves that would act as its base without altering the principle of its operation. When the rolling cone is increased in size until its center angle is ninety degrees, it becomes a plane circle. Its element will form an epicycloidal surface as before; but it is now called an “involute” surface. The involute surface is a special case of the epicycloidal surface, differing from it principally in the valuable feature that it will allow a variation in the center distance of the shafts of spur-gears, 55 or in the angle between the shafts of bevel-gears; without affecting the uniformity of the motion transmitted.

In the figures, the gear-blank 19 is held by a gear-spindle 20, that is supported by the frame 25 and oscillated by the index-wheel 60 21. The index-wheel receives a slow feeding motion by means of the pinion 22.

Fig. 6.19 The essential of the *G. Grant's* invention [U.S. Pat. No. 407.437. *Machine for Planing Gear Teeth.* G.B. Grant (1887)]

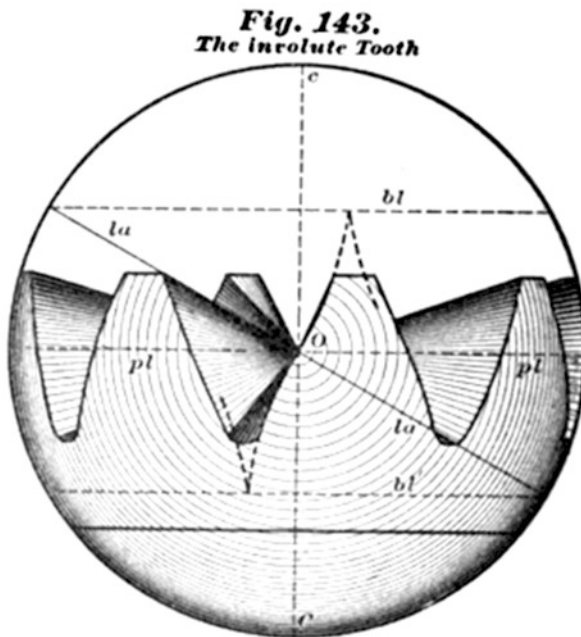


Fig. 6.20 The involute tooth flank in a bevel gear according to G. Grant [see Fig. 143 in: Grant, G.B., *A Treatise on Gear Wheels*, 6th edition, Philadelphia Gear Works, Inc., Philadelphia, 1893, 105 p.]

will form an epicycloidal surface as before, but it is now called an “involute” surface” (see Fig. 6.19). Therefore, the bevel gear tooth flanks are generated by the describing method adopted to the case of intersected-axes gearing, that is, bevel gearing. This is a significant scientific achievement by G. Grant in the field of scientific theory of gearing. Fig. 6.20 is a good evidence of perfect tooth flank

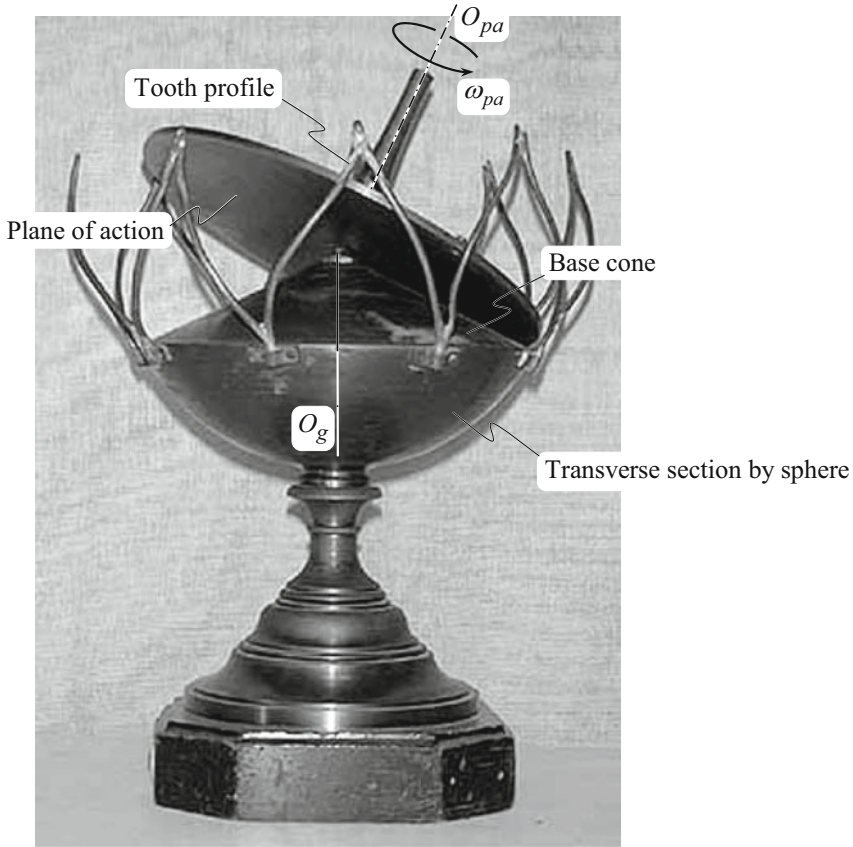


Fig. 6.21 Demonstration of principal features of meshing in a bevel gear pair

geometry in a bevel gear, correctly realized by G. Grant at the end of the twenty-first century. An elementary device (see Fig. 6.21) was used in the past to demonstrate the principal features of meshing in a bevel gear pair.

The contribution by G. Grant is incomplete, as he proposed only a method of generation of tooth flanks of a gear for intersected-axes gear pairs (I_a -gearing). The concept of the “gear/pinion angular base pitch,” as well as the concept of the “operating angular base pitch” of a gear pair, was not known to G. Grant.

However, G. Grant was a gear practitioner, and not a researcher, and (per the author’s personal opinion) he did not properly value this as his accomplishment, which is of significant importance to the scientific theory of gearing. In addition, in the time of G. Grant, there was no necessity in more accurate bevel gears compared to those produced by the gear generating method. Because of this, the invention by G. Grant was forgotten for over a century.

6.1.3.2 Contribution by Professor N.I. Kolchin

In the mid of the twentieth century, an interesting analytical research in gearing (in bevel gearing in particular) has been undertaken by Professor A.I. Kolchin of the USSR [27]. Professor A.I. Kolchin analytically described the results discovered and known in the public domain before his book was published. However, his contribution to the theory of gearing was important as a profound mathematical analysis of gears has been started from his research [27].

6.1.3.3 Novikov Conformal Gearing

In the late 1940s and at the beginning of 1950s, an extensive research work in the field of gearing has been carried out by Dr. M.L. Novikov³² in Moscow, at Military Aviation Engineering Academy. Ultimately, a novel design of high-performance gearing was proposed [28, 29]. Later on, the results of the research were summarized in the doctoral thesis [30] and in the monograph [31] by Dr. M.L. Novikov.

The proposed design of gearing features “to-convex-to-concave” contact between the interacting tooth flanks of a gear and a mating pinion. The gear designer is free to design the rest of the gear and the pinion tooth profiles.

When Professor M.L. Novikov carried out his research in the field of conformal gearing, he loosely assumed that in order to transmit a uniform rotary motion, the gear teeth do not need to have special shapes, such as the involute of a circle. He meant that, if a gear is made helical, then the helix itself can ensure uniform angular motion and tooth profiles can then be chosen with a view to minimizing contact stresses. This is a bit confusing: in order to transmit a rotation smoothly, the mating tooth profiles must be either involute or, in a degenerate case, they can feature the “involute tooth point” geometry.

“Novikov gearing” is a type of helical gearing that has a zero length of the field of action, that is, the equality $Z_a = 0$ is valid in “Novikov gearing” (this entails a zero transverse contact ratio, $m_p = 0$, in “Novikov gearing”). The equality of the base pitch of the gear and the pinion, to the operating base pitch of the gear pair, is the principal feature of “Novikov gearing” that distinguishes it from helical non-involute gearing of other types.

It is customary to associate “Novikov gearing”³³ with the patent “Gear Pairs and Cam Mechanisms Having Point System of Meshing” [29]. Evidence can be found out in scientific literature revealing the unfamiliarity of the gear community around the world with this original publication [29] on “Novikov gearing” (see Appendix H

³²**Mikhail L. Novikov** (March 25, 1915–August 19, 1957), a famous Soviet gear researcher

³³The first pair of “*Novikov gearing*” made of aluminum alloy (a pre-prototype) was cut on April 25, 1954, by a disk-type mill cutter. For testing, 15 gear pairs were machined in the summer of 1954 by the disk-type mill cutter. Hobs for cutting gears for “*Novikov gearing*” were proposed later on by Professor V.N. Kudr’avtsev (as early as in 1956) – this is a huge mistake committed by Professor V. N. Kudr’avtsev to cut gears for “*Novikov gearing*” by hobs.

for details). As early as 1955, before the invention application was filed, a doctoral thesis [30] on the subject had been defended by M.L. Novikov. The author's familiarity with the practice of defending the doctoral thesis adopted in the former Soviet Union allows an assumption that the concept of "Novikov gearing" had been proposed in the late 1940s. After M.L. Novikov was granted with the patent [29], a monograph by him was published [31]. The concept of "Novikov gearing" is discussed in detail in the two aforementioned valuable sources [30, 31]. Unfortunately, none of them are quoted by the gear experts in Western countries and in the USA. This makes it possible a conclusion that gear experts around the world are not familiar with these two valuable sources of information on "Novikov gearing."

Formally, in "Novikov gearing," the tooth flanks have circular arc profile. Actually, as it has been shown later by Professor S.P. Radzevich [32] that "Novikov conformal gearing" is a reduced type of involute gearing in which the involute tooth profile is shrunk to a point, and the rest of the tooth profiles are shaped in the form of a circular arc. Because of this, "Novikov conformal gearing" is a kind of geometrically accurate gearing (a reduced type of involute gearing) that is capable of transmitting a steady rotation smoothly.

6.1.3.4 Contribution by Professor V.a. Gavrilenko

An extensive research in the field of gearing in the 1930s through the 1960s has been carried out by Professor V.A. Gavrilenko³⁴. He spent decades on extensive research in the field of gearing, particularly in the geometrical theory of involute gearing. In the author's opinion, the most systematic discussion on involute gearing ever can be found in the monograph by V. Gavrilenko [33]. Unfortunately, the fundamental monographs by V. Gavrilenko are not known for the most of gear experts neither in Europe nor in the USA.

6.1.3.5 Contribution by Jack Phillips

An intensive research into spatial involute gearing was undertaken by Prof. J.R. Phillips³⁵ [34] who is credited with a new look and in in-depth understanding of the kinematics and the geometry of involute gearing with crossing axes of rotation of driving and of driven gears.

³⁴*Vladimir A. Gavrilenko* (June 21, 1899–June 6, 1977), Doctor (Engineering) Sciences and Professor of Mechanical Engineering (Bauman State Technical University, Moscow, Russia)

³⁵*Jack Raymond Phillips* (July 18, 1923–January 11, 2009), a famous Australian gear expert (mechanician)

6.1.3.6 Contribution by Walton Musser

In the late 1950s, Walton Musser³⁶ proposed a novel kind of transmission, the so-called harmonic drive. Although this invention revolutionized the theory of “machines and mechanisms,” harmonic drive is not a kind of gear drives in the sense considered in this monograph (gear drives consist of three components, namely, driving gear, driven gear, and the gear housing, while harmonic drive consists of four elements: a wave generator, flex-spline, stationary ring-gear, and the housing). This is the only reason why harmonic drives are not discussed in this monograph; this kind of transmission is out of the scope of the book.

Accomplishments in the field of gearing in that period of time are briefly summarized as follows:

- A breakthrough invention in the field of intersected-axes gearing has been made by G. Grant. He proposed a Machine for Planing Gear Teeth (U.S. Pat. No. 407.437, [24]) that is capable of machining perfect straight bevel gears. The geometry of a straight bevel gear tooth flank (that is equivalent to the involute of a circle in cases of parallel-axes gearing) is proposed by G. Grant for the case of intersected-axes gearing.³⁷
- A novel design of conformal gearing was proposed by Dr. M. Novikov [29].

Grant’s invention [24] is an important contribution to the theory of gearing. Novikov’s invention completely aligns with the well-developed theory of parallel-axes involute gearing, as “Novikov conformal gearing” is a reduced case of involute gearing.

6.1.4 Developments in the Field of Approximate Gearing³⁸

To meet the current needs of the industry, practical gear engineers proposed numerous approximate designs of gearing. Initially when the designs were proposed, it loosely assumed that each of them is capable of transmitting a rotation smoothly. Unfortunately, it was shown later on that they do not meet all the requirements perfect gears needs to meet.

³⁶**Walton Clarence Musser** (April 5, 1909–June 8, 1998), a famous American inventor; he is the inventor of the “*harmonic drive*” (1957).

³⁷Per the author’s opinion, *G. Grant* did not realize the importance of his invention. In the time of *Grant*, the industry was fulfilled with the available on the market approximate gears; no interest to precision (and more costly) bevel gears was indicated by the industry at that time.

³⁸For more in detail discussion on manufacture of gears for approximate gearing, the interested reader may wish to go to Chap. 1 “Gears: Brief Notes on the History of Methods of Machining Gears and of Design of Gear Cutting Tools” in the book: Radzevich, S.P., *Gear Cutting Tools: Science and Engineering*, CRC press, Boca Raton, Florida, 2017, 606 pages.

6.1.4.1 Samuel Cone Double-Enveloping Worm Gearing

First rudimentary “double-enveloping” worm gear drive was known since the times of Leonardo da Vinci [11]. Nowadays double-enveloping worm gearing was proposed as early as in 1891 by Dr. Friedrich Wilhelm Lorenz³⁹ of Germany. In his invention Dr. Lorenz proposed methods to generate the worm and the gear of the double-enveloping worm-gear drive, and then he had received two patents for these accomplishments. A bit later (at a round 1920) and independently a similar double-enveloping worm gearing was proposed by Mr. Samuel Cone⁴⁰ of the USA. Wilhelm Lorenz and Samuel Cone understood very well the advantages of the drives they had invented, particularly, the increased load capacity due to the higher contact ratio in comparison with that of conventional worm-gear drives. Although the geometry of Lorenz and Cone’s drives differs, both types offer this advantage.

Double-enveloping worm gearing is an example of approximate gearing as it does not meet all three fundamental laws of gearing [1].

6.1.4.2 Approximate Bevel Gearing

Early accomplishments in the field of bevel gearing are tightly connected with the name of William Gleason⁴¹. In 1874, his invention of the straight bevel gear planer for the production of bevel gears with straight teeth substantially advanced the progress of gear making.

The early part of the twentieth century was the beginning of the automotive industry, which required a broader application of bevel gears to transform rotation and power between intersected axes. In the 1920s, automotive industry designers also needed (a) a gear drive to transform motions and power between crossed axes and (b) a lower location for the driving shaft. The Gleason Works engineers met these needs with pioneering developments directed at designing new types of gear drives and the equipment and tools to generate the gears for these drives.

The proposed designs of bevel gears in the nowadays industry are examples of approximate gearing as they are developed and manufactured based on application of the imaginary straight-sided crown gear (basic crown rack). Because of this, nowadays bevel gears of all kinds, that is, straight bevel gears, skew bevel gears, spiral bevel gears, and others, both face-milled and face-hobbed, do not meet all three fundamental laws of gearing [1].

³⁹**Friedrich Wilhelm Lorenz** (1842–1924), Doctor of Engineering, inventor, and founder of the *Lorenz Company*

⁴⁰**Samuel I. Cone** (1842–1924), a civilian machinist and draftsman, an American inventor of double-enveloping worm gearing

⁴¹**William Gleason** (1836–1922), founder of *The Gleason Works*, Rochester, NY

6.1.4.3 Approximate Crossed-Axes Gearing

The concept of the gearing that operates on crossing shafts can be traced back to the times of Leonardo da Vinci [11].

The need for more accurate and quieter running gears became obvious with the advent of the automobile. Although the hypoid gear was within our manufacturing capabilities by 1916, it was not used practically until 1926, when it was used in the Packard automobile. The hypoid gear made it possible to lower the drive shaft and gain more usable floor space. By 1937 almost all cars used hypoid-gearing rear axles.

The success with the design, manufacture, and application of the contemporary crossed-axes gearing is credited in much to two famous gear experts, namely, Nikola Trbojevich (also known as Nicholas Terbo) and Ernest Wildhaber.

Nikola Trbojevich, a world-known research engineer, mathematician, and inventor, was a nephew and friend of Nikola Tesla. Mr. Trbojevich⁴² held nearly 200 US and foreign patents, principally in the field of gear design.

Mr. Trbojevich's most notable work that brought him international recognition was the invention of the "Hypoid gear." First published in 1923, it was a new type of spiral bevel gear employing previously unexploited mathematical techniques. The "Hypoid gear" is used on the great majority of all cars, trucks, and military vehicles today. Together with his invention of the tools and machines necessary for its manufacture, the "Hypoid gear" became an integral part of the final drive mechanism of automobiles by 1931. Its effect was immediately apparent in that the overall height of rear-drive passenger automobiles was reduced by at least four inches.

Ernest Wildhaber⁴³ is one of the most famous inventors in the field of gear manufacture and design. He is granted with 279 patents on gearing, some of which have a broad application in the gear industry because of his work as an engineering consultant for The Gleason Works. The hypoid gear drive is one of the most famous inventions by Dr. Wildhaber. He proposed different pressure angles for the driving and coast tooth sides of a hypoid gear, which allowed him to provide constancy of the tooth top-land.

The proposed designs of crossed-axes gears in the nowadays industry are examples of approximate gearing as they are developed and manufactured based on application of the imaginary crown gear with straight-sided profile (basic crown rack). Because of this, nowadays crossed-axes gears of all types, both face-milled and face-hobbed, do not meet all three fundamental laws of gearing [1].

⁴²**Nikola John Trbojevich** (May 21, 1886–December 2, 1973), also known as *Nicholas J. Terbo*, a world-known research engineer, mathematician, and inventor, held the basic patent for the *Hypoid Gear*.

⁴³**Ernest Wildhaber** (1893–1979), Doctor of Engineering, h.c., Inventor, and consultant for *The Gleason Works*

6.1.4.4 Face Gearing

Face gearing can be viewed as a reduced case either of intersected-axes gearing, or of crossed-axes gearing when the pitch cone angle increases to the right angle. All known designs of face gearing, both intersected-axes gearing and crossed-axes gearing, are approximate gearing as they do not meet all three fundamental laws of gearing [1]. The face cutting technique used to produce there crossed-axes gears is supplied by these three companies (The Gleason Works, Klingelnberg-Oerlikon, Yutaka Seimitsu Kogyo, LTD) is based upon an empirical and manufacturing technology that predates the World War II.

Accomplishments in the field of gearing in that period of time can be briefly summarized as follows:

- Double-enveloping (approximate) gearing was proposed by Wilhelm Lorenz of Germany (1874), and a bit later (at a round 1920) by Samuel Cone of the USA.
- Design of and methods for machining of approximate hypoid gearing were proposed by Nikola Trbojevich, and later on improved by Ernest Wildhaber, both of the USA.
- Face gearing are widely used in the design of Fellow's gear shaping machines.

The most significant contributions to the field of gearing at that time are made in the field of approximate gearing: to their design and production.

6.1.5 *Theory of Gearing at the Beginning of the Twenty-First Century: State of the Art*

It should be stated here from the very beginning that no self-consistent (or potentially self-consistent) scientific theory of gearing is developed by the beginning of the twenty-first century (by the year of ~2010).

Among others, a self-consistent scientific theory of gearing must possess two important properties.

First, it must cover all known designs of gears and gearing with no exclusion.

Second, it must cover all (with no exclusion) unknown yet designs of gears and gearing, that is, the theory must possess the property to predict novel designs of gears and gearing.

All the books published so far under the title "Theory of Gearing" [starting from the first (1841) book by Théodore Olivier [7], and ending with the latest publications in the field – by the year of ~2010] consist no scientific theory of gearing. These books cannot be referred to as a "theory of gearing"; rather they are collections of known achievements in the field of gearing, having no ability to predict novel unknown designs of gears and gearing.

No doubt, a scientific theory of gearing is necessary to the gear researchers and practical engineers as it is a powerful tool for the development of novel designs of

gears and gearing with a prescribed performance. Such a scientific theory of gearing can be developed now. With that said, it is important to revise the earlier obtained accomplishments in the field of gearing and identify those of them that can be useful in the development of the fundamental scientific theory of gearing.

6.1.6 Favorable Approximate Gearing

Easier manufacture is the principal advantage of approximate gearing over perfect gearing. Due to this advantage approximate gears will be used in the industry for a long while.

A theory of favorable approximate gearing can be (and will be) developed on the premises of the scientific theory of gearing [1]. Only in such a scenario approximate gear pairs with favorable design parameters can be designed.

6.1.7 Accomplishments in the Field of “Non-circular” Gearing

The most general case of non-circular gears with the crossing axes of rotation is analyzed. For the analysis, a reference system, associated with gear pair in a natural way, is used [the axes of the reference system are along:

- (a) The axis of instant rotation, P_{ln} .
- (b) The center-distance, \mathcal{C} .
- (c) Perpendicular to these two directions, P_{ln} and \mathcal{C}].

In the analysis, the center-distance C , the crossed-axes angle Σ , and the gear ratio u , are assumed variable. In particular cases, one or two variable parameters considered of a constant value. Under such the assumption, a classification of perfect $C\Sigma u$ -gearing is developed (S. Radzevich, ~2017) [1].

6.1.8 Tentative Chronology of the Evolution of the Theory of Gearing

Summarizing the above discussion, the benchmarking achievements in the theory of gearing are schematically outlined in Fig. 6.22.

The proposed chronology begins with an analysis of what was done in pre-Eulerian period of evolution of the gear art. Contributions to the field of gearing by Desargues, de la Hire, and Camus comprise the pre-Eulerian period of evolution of the theory of gearing. In the schematic (see Fig. 6.22), number “0” is assigned to the pre-Eulerian period evolution of the theory of gearing.

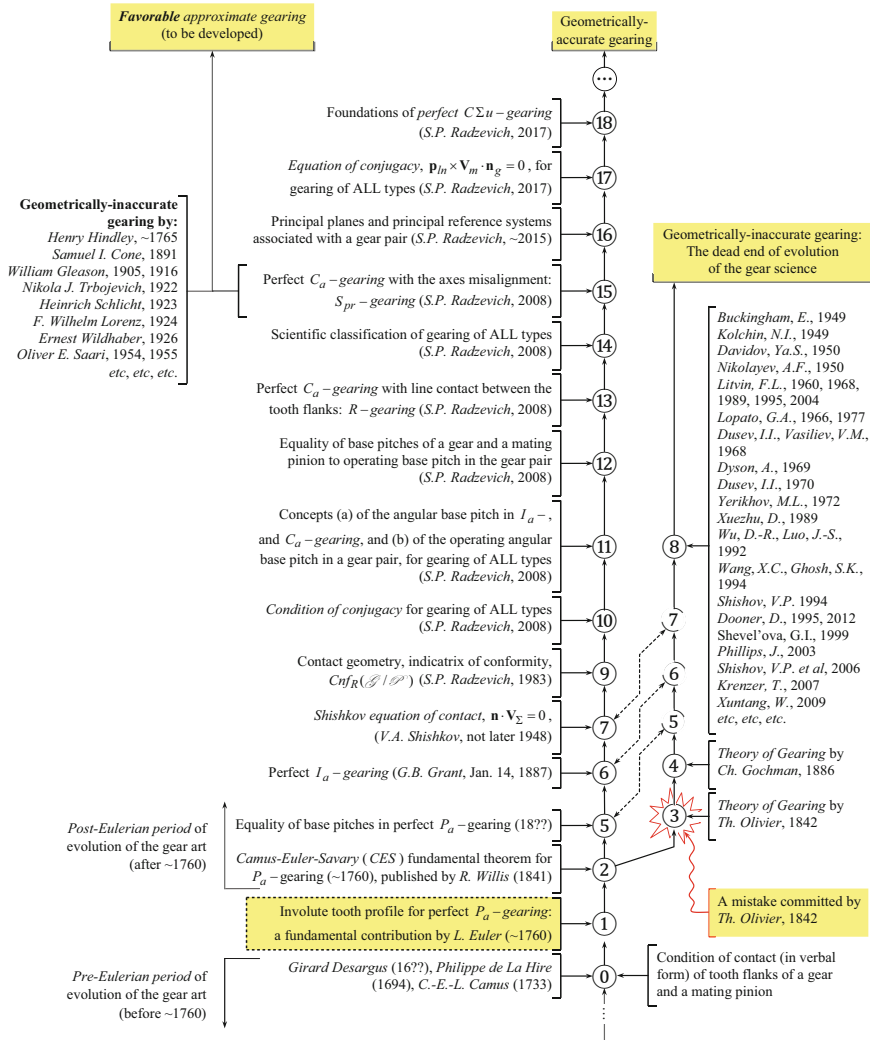


Fig. 6.22 Tentative chronology of evolution of the scientific theory of gearing

The pre-Eulerian period of evolution of the gear art is followed by the time when the fundamental contribution to the theory of gearing was made by L. Euler. The latter is considered as the origin of the scientific theory of gearing.

Invention of involute gearing⁴⁴ by L. Euler (1760) is a benchmarking achievement in the theory of gearing. Per the author's opinion, the origin of the "scientific

⁴⁴It needs to be stressed here that *involute of a circle* itself was known long before the invention of involute gearing by L. Euler.

theory of gearing” has to be associated with this accomplishment. In the schematic (see Fig. 6.22), number “1” is assigned to the invention of involute gearing by L. Euler.

The rest of the items in Fig. 6.22 correspond to the principal accomplishments in the theory of gearing that follow the contribution by L. Euler. Where possible, the names of the researchers and dates are associated with the corresponding accomplishments.

The next step in the development of the theory of gearing has been made by L. Euler and F. Savary who are granted with the “fundamental theorem of gearing” (along with Ch. Camus). Later on, in 1841, this theorem has been published in the book by R. Willis [14]. Number “2” is assigned in the schematic (see Fig. 6.22) to the achievement in the scientific theory of gearing. The “Camus-Euler-Savary fundamental theorem of gearing” is valid only for parallel-axes gearing.

In 1842 a huge mistake has been committed by T. Olivier who proposed his version of the theory of gearing based just on the enveloping condition of conjugacy of the interacting tooth flanks of a gear and a mating pinion. The condition of conjugacy of the tooth flanks is not taken into account by T. Olivier. This event is labeled as “3” in the schematic (see Fig. 6.22).

A “parallel” line (the items #3 through #8) corresponds to a wrong way of the evolution of the gear theory. The mistake committed by T. Olivier [7] (1842), and repeated by C. Gochman [8] (1886), significantly impaired further fundamental developments in the theory of gearing (“4,” “8,” and others in Fig. 6.22). Only approximate gears can be designed following this way. This is the dead end of evolution of the gear science.

The accomplishments in the theory of gearing labeled as “5” through “7” are applicable in both branches, that is, (a) in the “dead end” of the theory⁴⁵ (“4,” “8,” and others in Fig. 6.22), as well as (b) in the way that leads to the self-consistent scientific theory of gearing [1] (“5” through “14,” and others in Fig. 6.22). No perfect intersected-axes and crossed-axes gearing can be designed following this way. No correct tooth flank modification in parallel-axes gearing is possible – only trial and error method can be used to determine the parameters of the tooth flank modification.

The condition that requires equal base pitches of a gear and its mating pinion (only in cases of parallel-axes gearing) is known for a long while (note, the “operating base pitch” of a gear pair is not known yet). Per the author’s estimate, this requirement, that is, item “5” in Fig. 6.22, is known since the mid of the nineteenth century. Unfortunately, in the meantime it is not possible to identify the name of the gear scientist who should be credited with this significant accomplishment in the scientific theory of gearing.

Spherical involute in perfect bevel gearing (item “6” in Fig. 6.22) is known since 1887.

⁴⁵It is a right point to stress here that the “*dead end*” in the diagram in Fig. 6.22 means that no “*perfect*” I_a - and C_a -gearing are possible; no “*correct*” tooth flank modification in P_a -gearing is possible; and trial and error method is dominated.

“Shishkov equation of contact” (item “7” in Fig. 6.22) deserves to be mentioned here, as use of this equation makes possible significant simplifications of the kinematic method of surface generation, especially in cases when both the contact perpendicular, \mathbf{n} , and the instant linear velocity vector, \mathbf{V}_Σ , can be determined with no derivatives of equations of the tooth flanks, \mathcal{G} and \mathcal{P} , as well as the parameters of the kinematics of a gear pair.

Conditions of contact of the interacting tooth flanks, \mathcal{G} and \mathcal{P} , are investigated analytically, and an equation of the indicatrix of conformity, $Cnf_R(\mathcal{G}/\mathcal{P})$, at point of contact of tooth flanks of a gear, \mathcal{G} , and a mating pinion, \mathcal{P} , (item “9” in Fig. 6.22) is derived [26, 35–37], and others.

Equation of conjugacy $\mathbf{p}_m \times \mathbf{V}_m \cdot \mathbf{n}_g = 0$ (item “17” in Fig. 6.22) of the interacting tooth flanks, \mathcal{G} and \mathcal{P} , is derived by Prof. S.P. Radzevich (2017).

Then, the below-listed accomplishments were contributed by Professor S. Radzevich in around 2008:

- Condition of conjugacy of the tooth flanks for gear pairs of all types (item “10” in Fig. 6.22), including intersected-axes gear pairs and crossed-axes gear pairs.
- The concepts of (a) “base pitch” in intersected-axes gear pairs, and crossed-axes gear pairs, and (b) the “operating base pitch” in gear pairs of all types (item “11” in Fig. 6.22).
- The equality of base pitches of a gear and its mating pinion to the “operating base pitch” in gear pairs of all types (item “12” in Fig. 6.22).
- Design of geometrically accurate crossed-axes gearing with line contact between the tooth flanks, \mathcal{G} and \mathcal{P} , that is, R -gearing (item “13” in Fig. 6.22).
- A scientific classification of vector diagrams of gear pairs of all types (item “14” in Fig. 6.22).
- Design of perfect (crossed-axes) gearing insensitive to the axes misalignment, that is, S_{pr} -gearing (item “15” in Fig. 6.22).
- Principal planes and principal reference systems associated with a gear pair are introduced by Professor S. Radzevich in around 2015.
- Equation of conjugacy $\mathbf{p}_m \times \mathbf{V}_m \cdot \mathbf{n}_g = 0$ (item “17” in Fig. 6.22) of the interacting tooth flanks, \mathcal{G} and \mathcal{P} , is derived by Prof. S.P. Radzevich (2017).

A theory of favorable approximate gearing will be developed in the future. The discussed scientific theory of gearing is a reliable foundation for the theory of favorable approximate gearing to be developed.

It should be realized that the diagram in Fig. 6.22 is tentative. More accomplishments in the scientific theory of gearing and the corresponding gear researcher’s names can be added in Fig. 6.22 if a more in detail investigation into the evolution of the scientific theory of gearing will be undertaken. Only the key (the fundamental) achievements in the scientific theory of gearing are included in the diagram (see Fig. 6.22) in its current stage.

Generally speaking, geometrically accurate gear pairs of any kind can be designed based on the scientific theory of gearing.⁴⁶

⁴⁶Theory of gearing can be viewed as a kind of “road map” that helps the user traveling from one point (location) to another point (location) in a most efficient way.

The listed accomplishments form the foundation of the “self-consistent scientific theory of gearing” (Radzevich, S.P., 2012, 2018).

The proposed chronology (see Fig. 6.22) is open for further improvements. Constructive recommendations, comments, and concerns appreciated.

6.1.9 On Other Efforts that Pertain to the Evolution of the Scientific Theory of Gearing

The author has turned his interest to the evolution of the gear science about a decade ago [3, 38].

Despite gears are extensively used in the industry of many industrially developed countries, not much accomplishments to the theory of gearing are contributed to this end. No accomplishments to the theory of gearing are contributed in the recent years in North America (including the USA and Canada), in Europe (including Germany, Austria, as well as the rest of European countries), and in Asian countries (including, but not limited to China, Taiwan, Japan, and South Korea). In Australia, only the 2003 book by Jack Phillips on General Spatial Involute Gearing [34] deserves to be mentioned in this regard. Production of quality gears in the industry is based in much on the accumulated experience, and not on the means and methods derived from the theory of gearing. Even lead companies in the field of gear design and manufacture indicate poor familiarity with the latest achievements in the theory of gearing. An article [39], as well as many others, is a perfect illustration of poor familiarity of the gear community with the latest achievements in the theory of gearing.

In the recent years, numerous papers on the history of gearing (both in English and in Russian languages) have been authored/co-authored by Babichev, Barmina, Lagutin, Volkov, and others of Russia. All these publications are available in the public domain. A claim on the so-called Russian school of theory of gearing has been aggressively made by the authors. It should be stressed here that all these publications are focused not on the principal accomplishments in the scientific theory of gearing.

The discussion in this section of the book, along with the results of the earlier performed retrospective analysis on the history of evolution of the scientific theory of gearing [1, 2], reveals that this aggressive claim has been made with no sufficient validity. Are there significant accomplishments to the scientific theory of gearing (made by representatives of the so-called Russian school of theory of gearing) that are not taken into account (and not indicated in the chart shown in Fig. 6.22)? Feel free to name them, if any! An appropriate comment will be helpful for the enhancement of our understanding of the evolution of the scientific theory of gearing.

In the published papers and monographs authored even by the leading Soviet/Russian gear researchers, there is no evidence of understanding of the kinematics and geometry of the following:

- (a) Novikov gearing (Novikov gearing is missed by Soviets due to their poor professionalism in the theory of gearing; gear experts from Western countries contributed zero to gearing of this particular design) [40].
- (b) Spiroid gearing⁴⁷ (and geometrically accurate worm gearing in a more general sense).
- (c) Perfect intersected-axes and (more generally) crossed-axes gearing.
- (d) Perfect gears with the axes misalignment, and so forth.
- (e) Still making no difference between enveloping surfaces and conjugate surfaces.
- (f) They are not capable of demonstrating that the so-called gearing⁴⁸ proposed by a charlatan V.V. Stanovskoi (<http://www.ec-gearing.ru/company.php>) is a fake.
- (g) For decades [for over “50 (!) years in the theory and practice of gearing”], they carry out a meaningless research on gearing with a “closed line of contact that shrinks” when the gears rotate.

A few more to mention. What can be expected from the less experienced gear researchers of Russia?

Prof. Ya.S. Davidov, one of the Soviet “coryphaeus” in the field of gearing, in his “Memories . . .” correctly compared all the Russian gear theoreticians with the “swamp” (<http://referat.znate.ru/text/index-8600.html>). A following dialog took place between Prof. F.L. Litvin and Prof. Ya.S. Davidov, when they were discussing the features of “Novikov gearing”: “In one of the conversations with me F.L. Litvin very correctly compared the work of Novikov to the rock thrown into the swamp and caused a stirring of water” (It is likely the comparison of the gear community in the Soviet Union/Russia with a “swamp” makes sense). Can someone ignore this opinion of two well-known Soviet/Russian gear researchers (of Prof. F.L. Litvin, and Prof. Ya.S. Davidov), when they have compared all the Russian gear theoreticians with the “swamp”? This comparison is one more evidence that the claim on the so-called special “Russian school of theory of gearing” is at least doubtful, if not to say more.

The just made conclusion has to be taken into account when the readers meet the meaningless term “Russian school of theory of gearing” (as well as similar terms introduced by Russians in the recent years: “classical school of theory of gearing” and “the gold age of theory of gearing”). In the meantime, experienced readers are skeptical with that and are commonly having a laugh when they read about the so-called Russian school of theory of gearing [9].

⁴⁷After about 40 (!) PhD theses and 5 (!) Dr. Sci theses are defended by these people, how is it permissible to ask a question: “What do we know about spiroid gearing”? What did you do all this time?

⁴⁸Amazingly, but this stupid “gearing” is supported by two doctors of sciences (Dr. *Scherbakov, N. R.*, the chairperson of “*Geometry*” department, and Dr. *Bubenchikov, A.M.*, the chairperson of “*Theoretical Mechanics*” department, both of Tomsk State University, Russia) *who are granted with scientific degree of Dr.Sci. in mathematics and physics.*

6.2 Concluding Remarks

In this chapter of the book a brief overview on the evolution of the scientific theory of gearing is carried out.

All (or, at least, almost all) the principal accomplishments in the scientific theory of gearing are identified and are briefly overviewed in the chapter. The discussion begins with the consideration of the earliest designs of gears. The evolution of the theory of gearing falls into three periods, namely, pre-Eulerian, Eulerian, and post-Eulerian periods of the gear art. The scientific theory of gearing is originated in the Eulerian period of the gear art. Then, the developments in the field of perfect gearing are considered. The contributions by G. Grant, Professor N. Kolchin, Professor M. Novikov, Professor V. Gavrilenko, and others are covered in this discussion.

The developments in the field of approximate gearing is another consideration in this chapter of the book. Here S. Cone double-enveloping worm gearing, approximate bevel gearing, approximate crossed-axes gearing, as well as face gearing are briefly discussed.

A brief summary of the principal accomplishments in the theory of gearing achieved by the beginning of the twenty-first century is provided. The condition of contact of the interacting tooth flanks of a gear and pinion, condition of conjugacy of the interacting tooth flanks of a gear and pinion, and condition of equality of base pitches of the interacting tooth flanks of a gear and pinion are covered in this discussion.

To the best of the author's knowledge, all the principal accomplishments are covered in this text. Where possible, the accomplishments are attributed with corresponding names of the gear researchers, and dates when the contribution has been done.⁴⁹ These accomplishments form the foundation of the self-consistent scientific theory of gearing (proposed by Radzevich, S.P. circa 2008 [1]). The scientific theory of gearing is not threatened with destruction, but only superstructure and development are expected (every scientific theory features this property).

Ultimately, a tentative chronology of the evolution of the theory of gearing is proposed.

Among others, the discussion is aimed to initiate an in-depth investigation in the field of the origins of the scientific theory of gearing.

More names of the gear researchers deserve to be mentioned. However, consideration in this section of the book is limited to the evolution only of the theory of gearing. Therefore, the number of names of the researchers is limited only to those who contributed to the kinematics and the geometry of gearing.

⁴⁹Except of the contributions by *L. Euler*, the contributions by other members of the *Hall of Fame* at the *Gear Research Center* (The University of Illinois at Chicago) are out of the scope of the *scientific theory of gearing*, and, thus, are not discussed here.

Brief critical comments on the so-called Russian school of theory of gearing are outlined.

A comprehensive research on the evolution of the theory of gearing is necessary to be undertaken in the nearest future. It is needed that the research be based on in-depth study of the original scientific works of all principal investigators of the topic. The history of engineering is not less important than the engineering itself. The better we know the past, the better we can predict the future.

The discussion in this chapter of the book is helpful for better understanding of the fundamental principles of gearing.

References

1. Radzevich, S. P. (2018). *Theory of Gearing: Kinematics, Geometry, and Synthesis, 2nd Edition, revised and expanded* (p. 934). Boca Raton, FL: CRC Press. [First Edition: Radzevich, S.P., *Theory of Gearing: Kinematics, Geometry, and Synthesis*, CRC Press, Boca Raton, Florida, 2012, 743 pages].
2. Radzevich, S. P. (2015). A Brief Overview on the Evolution of the Scientific Theory of Gearing: A Preliminary Discussion. In *Proceedings of International Conference on Gears 2015, October 5–7, 2015* (pp. 1035–1046). Garching (near Munich), Germany: Technische Universität München (TUM).
3. Radzevich, S. P. (2010). Concisely on Kinematic Method and about History of the Equation of Contact in the Form $n.v=0$. *Theory of Mechanisms and Machines*, 1(15), 42–51. <http://tmm.spbstu.ru>.
4. Radzevich, S. P. (2011). On Master Thesis: Gochman, Ch.I., Theory of Gear Teeth Engagement, Generalized and Developed by Implementation of Mathematical Analysis. *Theory of Mechanisms and Machines*, 17(1), 33–43. http://tmm.spbstu.ru/01_2011.html.
5. Coy, J. J., Townsend, D. P., & Zaretsky, E. V. (1985). *Gearing, NASA reference publication 1152, AVSCOM, technical report 84-C- 15* (p. 76).
6. Woodbury, R. S. (1958). *History of the Gear-Cutting. A Historical Study in Geometry and Machine* (p. 135). The M.I.T. Press.
7. Olivier, T. (1842). *Théorie Géométrique des Engrenages destinés à transmettre le mouvement de rotation entre deux axes ou non situés dans un même plan, (Geometric Theory of Gearing)* (p. 118). Paris: Bachelier.
8. Gochman, C. I. (1886). *Theory of gear teeth engagement* (p. 229). Odessa (Ukraine): Generalized and Developed by Implementation of Mathematical Analysis.
9. Radzevich, S. P. (2019). A Brief Overview on the Evolution of Gear Art: Design and Production of Gears, Gear Science, Chapter 11, pp. 418–485. In S. P. Radzevich (Ed.), *Advances in Gear Science and Manufacture* (p. 570). Boca Raton, FL: CRC Press.
10. Radzevich, S. P. (2019). Principal Accomplishments in the Scientific Theory of Gearing. In *Proceedings of the 6th International BAPT Conference Power Transmissions 2019, 19–22.06.2019 Varna, Vol. 1: Design, Analysis, Simulation, and Optimization* (pp. 7–18). Varna: Balkan Association of Power Transmissions.
11. da Vinci, L. (1974). *The Madrid Codices, Volume 1, 1493, Facsimile Edition of Codex Madrid 1, original Spanish title: Tratado de Estatica y Mechanica en Italiano*. McGraw Hill Book Company.
12. de la Hire, P. (1694). *Mémoires de Mathématique et de Physique, Impr.* Paris: Royale.

13. Camus, C.-É.-L. (1733). *Sur la figure des dents des rouës, et des ailes des pignons, pour rendre les horloges plus parfaites*. Paris: History de l'Académie royale des sciences.
14. Willis, R. (1841). *Principles of mechanisms, designed for the use of students in the universities and for engineering students generally* (p. 446). London: John W. Parker, West Stand, Cambridge: J. & J.J. Deighton.
15. Euler, L. De Aptissima Figura Rotarum Dentibus Tribuenda (On Finding the Best Shape for Gear Teeth). In *Academiae Scientiarum Imperiales Petropolitae, Novi Commentarii, 1754–55, t. V* (pp. 299–316). (E249 in Opera omnia II, 17, pages 119–135).
16. Euler, L. (1767). Supplementum. De Figura Dentium Rotarum. *Novi Commentarii adacemiae Petropolitanae, 11, 207–231*. (E330, Opera omnia, 17, pages 196–219).
17. Koetsier, T. (2007). Euler and Kinematics, pages 167–194. In R. E. Bradley & C. E. Sandifer (Eds.), *Leonhard Euler: Life, Work and Legacy, Series: Studies in the History and Philosophy of Mathematics, Volume 5* (p. 534). Amsterdam: Elsevier.
18. Veldkamp, G. R. (1970). *Kinematica* (pp. 70–72). Amsterdam: Scheltema & Holkema.
19. Radzevich, S. P. (2013). *Geometry of surfaces: A practical guide for mechanical engineers* (264 pages). Chichester: Wiley.
20. Sang, E. (1852). *A new general theory of the teeth of wheels, a&C black* (p. 257). Edinburgh: North Bridge.
21. Shishkov, V. A. (1948). *Elements of kinematics of gear tooth flank generation and gear meshing, in: Theory and computation of gears* (Vol. 6, p. 123). LONITOMASH: Leningrad.
22. Shevel'ova, G. I. (1999). *Theory of surface generation and of contact of moving bodies* (494 pages). MosSTANKIN: Moscow.
23. Fraifeld, I. A. (1948). *Cutting tools that work on generating principle* (p. 252). Mashgiz: Moscow.
24. U.S. Pat. No. 407.437. Machine for Planing Gear Teeth. /G.B. Grant, Filed: January 14, 1887 (serial No. 224,382), Patent issued: July 23, 1889.
25. Shishov, V. P. (1994). *Theory, mathematical foundations, and synthesis of high-power-density gearing for industrial transportation, Doctoral Thesis* (p. 580). Luhansk: East Ukrainian State University. [In Russian].
26. Radzevich, S. P. (1991). *Differential-geometric method of surface generation, Dr.Sci. Thesis* (p. 300). Tula: Tula Polytechnic Institute.
27. Kolchin, N. I. (1949). *Analytical calculation of planar and spatial gearing* (p. 210). Mashgiz: Moscow.
28. Nieman, G. (1961). *Novikov gear system and other special gear systems for high load carrying capacity* (p. 47). Berichte: VDI.
29. USSR Pat. No. 109,113. Gear Pairs and Cam Mechanisms Having Point System of Meshing. / M.L. Novikov, National Classification 47h, 6; Filed: April 19, 1956, published in Bull. of Inventions No.10, 1957.
30. Novikov, M. L. (1955). *Fundamentals of geometric theory of gearing with point meshing for high power density transmissions, Doctoral Thesis*. Military Aviation Engineering Academy (MAEA): Moscow.
31. Novikov, M. L. (1958). *Gearing of gears with a novel type of teeth meshing* (p. 186). Moscow: Published by Zhukovskii Aviation Engineering Academy.
32. Radzevich, S. P. (2015). High-Conformal Gearing: A new look at the concept of Novikov gearing. In *Proceedings of International Conference on Gears 2015, October 5–7, 2015* (pp. 457–470). Garching: Technische Universität München (TUM).
33. Gavrilenko, V. A. (1969). *Fundamentals of the theory of involute gearing* (p. 432). Mashinostroyeniye: Moscow.
34. Phillips, J. (2003). *General spatial involute gearing* (498 pages). New York: Springer.
35. Radzevich, S. P. (2017). *Gear cutting tools: Science and engineering* (2nd ed., p. 606). Boca Raton Florida: CRC Press.

36. USSR Pat. No. 1,185,749, A Method of Sculptured Surface Machining on Multi-Axis NC Machine./S.P. Radzevich, Int. Cl. B23c 3/16, Filed: October 24, 1983.
37. USSR Pat. No. 1,249,787, A Method of Sculptured Surface Machining on Multi-Axis NC Machine./S.P. Radzevich, Int. Cl. B23c 3/16, Filed: December 27, 1984.
38. Radzevich, S. P. (2011). Experience gained from reading master's thesis by Ch.I. Gochman Theory of gearing, generalized and evolved by analysis. *Theory of Machines and Mechanisms*, 9(1), 33–43. http://tmm.spbstu.ru/17/radzevich_17.pdf.
39. Stadtfeld, H. J. (2019). *Why are Today's Hypoids the perfect crossed-axes gear pairs?* (pp. 42–50). Gear Solutions magazine.
40. Radzevich, S. P. (2020). *High-Conformal Gearing: Kinematics and Geometry, 2nd edition* (p. 550). Elsevier. ISBN 9780128212240. [1st edition: Radzevich, S.P., *High-Conformal Gearing: Kinematics and Geometry*, 1st edition, CRC Press, Boca Raton, Florida, 2015, 332 pages. ISBN 9781498739184].

Further Readings

- Babichev, D. T., Lagutin, S. A., & Barmina, N. A. (2016). Overview of the Works of the Russian School of Theory of and the Geometry of Gearing. Part 1. Origins of the Theory of Gearing, and its Heyday Time in 1935–1975. *Theory of Mechanisms and Machines*, 14(№3 (31)), 101–134.
- Babichev, D. T., Lagutin, S. A., & Barmina, N. A. (2017). Overview of the Works of the Russian School of Theory of and the Geometry of Gearing. Part 2. Development of the Classical Theory of Gearing and Establishment of the Theory of Real Gearing in 1976–2000. *Theory of Mechanisms and Machines*, 15(№3(35)), 86–119.
- Babichev, D. T., Lagutin, S. A., & Barmina, N. A. (2020). Russian School of the Theory and Geometry of Gearing. Part 2. Development of the Classical Theory of Gearing and Establishment of the Theory of Real Gearing in 1976–2000, pages 1–46. In V. I. Goldfarb, E. Trubachov, & N. Barmina (Eds.), *New Approaches to Gear Design and Production, (Mechanisms and Machine Science, Book 81)* (p. 529). Springer. ISBN-13: 978–3030349448, ISBN-10: 3030349446.
- Babichev, D. T., & Volkov, A. E. (2015). History of Evolution of the Theory of Gearing. *Journal of Scientific and Technological Development*, № 5(93), 25–42.
- Crosher, W. P. (2014). *A gear chronology: Significant events and dates affecting gear development* (p. 260). Xlibris Corporation.
- da Vinci, L. (1974). *The Madrid codices, volume 1, 1493, facsimile edition of codex Madrid I, original Spanish title: Tratado de Estatica y Mechanica en Italiano*. McGraw Hill Book Company.
- de la Hire, P. (1694). *Mémoires de Mathématique et de Physique, Impr.* Paris: Royale.
- de Solla Price, D. (1974). Gears from the Greeks. The Antikythera Mechanism: A Calendar Computer from ca. 80 B. C. *Transactions of the American Philosophical Society*, 64(7), 1–70.
- Dong, X. (1989). *Theoretical Foundation of Gear Meshing*. Beijing: China Machine Press.
- Dudley, D.W., The evolution of the gear art, AGMA (American Gear Manufacturers Association), 1969.
- Dooner, D. B. (2012). *Kinematic Geometry of Gearing*, 2nd Ed., John Wiley & Sons, Inc., New York, 512 p. ISBN 13: 9781119950943, ISBN 10: 1119950945.
- Dooner, D. B., Seireg, A. A. (1995). *The Kinematic Geometry of Gearing. A Concurrent Engineering Approach*, John Wiley & Sons, Inc., NY, 450p.
- Dürer, A. (1525). *Underweysung der Messung mit dem Zirckel und Richtscheit* (pp. 6–17).

- Field, J. V., & Wright, M. T. (1985). The early history of mathematical gearing. *Endeavour*, 9(4), 198–203.
- Gear History – where do gearboxes originate? APEX DYNAMICS, <https://www.apexdyna.nl/en/news/gear-history/>.
- Goldfarb, V.I., What we know about Spiroid gearing, in: Proceedings of the International Conference on Mechanical Transmissions, China, Vol. 1, Science Press, 2006, pp. 19–26.
- History of Gears, Nordex, Inc., <https://nordex.com/about/history/>.
- History of Gears. (2017). UGEARS mechanical models. Aug., 04. <https://ugears.online/blogs/news/history-of-gears>.
- Klingelberg, J. (2015). *Bevel Gear: Fundamentals and Applications, 1st ed.* (p. 325). Springer Vieweg., 2016 edition.
- Korostelev, L. V. (1964). *Geometric and kinematic indicators of the bearing capacity of spatial gearing, Dr.Sci. Thesis* (p. 48). Moscow: Stankin.
- Krenzer, T. (2007). *The bevel gear* (p. 252).
- Lagutin, S. A. (2018). 50 years in the theory and practice of gearing. *IOP Conference: Materials Science and Engineering*, 393(012001), 10. <https://doi.org/10.1088/1757-899X/393/1/012001>.
- Lagutin, S. A., Barmina, N., & NA. (2016). Prof. F.L. Litvin: Contribution to the Formation of the Russian School of the Theory of Gearing. In V. Goldfarb & Barmina (Eds.), *Theory and Practice of Gearing and Transmissions, Mechanisms and Machine Science 34* (pp. 19–36). Springer International Publishing Switzerland.
- Lewis, M. J. T. (1993). Gearing in the ancient world. *Endeavour*, 17(3), 110–115.
- Lewis, W. (1893). Investigations of the Strength of Gear Teeth. In *Proc. Of Engineers Club of Philadelphia* (pp. 16–23).
- Maddison, F. (1985). Early mathematical wheelwork: Byzantine calendrical gearing. *Nature*, 314, 316–317.
- Nikolayev, A. F. (1950). A diagram of screw and its application to the determination of conjugated ruled surfaces with line contact. *Proceedings of Seminar on the Theory of Mechanisms and Machines, Academy of Sciences of the USSR, Institute of Machine Science*, 10(37), 52–106.
- Nikolayev, A. F. (1953). *Kinematic principles of the theory of spatial gearing, Doctoral Thesis* (p. 48). Moscow: Stankin.
- de Sola, P. D. J. (1959). On the origin of clockwork, perpetual motion devices and compass. *United States National Museum Bulletin*, 218, 81–112.
- de Sola, P. D. J. (1974). Gears from the Greeks. The Antikythera Mechanism: A Calendar Computer from ca. 80 B.C. *Transactions of the American Philosophical Society New Series*, 64(7), 1–70.
- Shishov, V. P., Nosko, P. L., & Fil, P. V. (2006). *Theoretical Foundations of Synthesis of Gearing* (p. 408). Luhansk: East Ukrainian State University Publishers.
- Silich, A. A. (2013). *Cylindrical Novikov gearing* (p. 100). LAP Lambert Academic Publishing.
- Silich, A. A. (2016). *Novikov gearing: Geometrical calculation of cylindrical gearing, Monograph* (p. 79). Tiumen: Publisher of the Tiumen' Institute of Industry.
- Silich, A. A. (1999). *The development of a geometrical theory of Design of Novikov Gearing, and of the tooth flanks generation process, Doctoral Thesis* (p. 534). Kurgan: Kurgan State University.
- Stadtfeld, H. J. (2014). *Gleason bevel gear technology: Basics of gear engineering and modern manufacturing methods for angular transmissions* (p. 503). NY: The Gleason works.
- Volkov, A. E., & Babichev, D. T. (2014). History of gearing theory development. In *25th working meeting of IFToMM permanent Commission for Standardization of terminology on MMS, Saint-Petersburg, Russia, June 23–29* (pp. 71–102).
- Vullo, V. (2020). *Gears: A Concise History, Series: Springer series in Solid Structural Mechanics, Vol. 12* (Vol. XVI, p. 246). Springer International Publishing, 110 b/w illustrations. eBook ISBN 978-3-030-40164-1, DOI: 10.10007/978-3-030-40164-1, Hardcover ISBN 978-3-030-40163-4.
- Wang, X. C., & Ghosh, S. K. (1994). *Advanced theories of hypoid gears, studies in applied mechanics* (Vol. 36, p. 341). Amsterdam: Elsevier.

- Willis, R. (1841). *Principles of mechanisms, designed for the use of students in the universities and for engineering students generally* (p. 446). West Stand, London, Cambridge: John W. Parker, J. & J.J. Deighton.
- Woodbury, R. S. (1958). *History of the Gear-Cutting. A Historical Study in Geometry and Machine* (p. 135). The M.I.T. Press.
- Wu, D.-R., & Luo, J.-S. (1992). *A geometric theory of conjugate tooth surfaces* (p. 204). Singapore: World Scientific.
- Xuntang, W. (2009). *Principle of gearing*. Xi'an: Xi'an Jiaotong university.

Chapter 7

Hyperboloid-Type Hobs: Design, Manufacture, and Application



Valentyn Nastasenko

7.1 Introduction

Scientific and technological progress requires constant updating of equipment and technologies, various machines and mechanisms being the basis [1, 2]. Gears are an important component used in many machines and mechanisms, especially in turbines, machine tools, devices, appliances, automobiles, tractors, material handling machinery, and other types of equipment. As the requirements for technical and economic indicators of these technical systems are constantly growing, there is an increasing need to improve the accuracy and smoothness of the gears, rotation speeds, and powers transmitted by them. At the same time, requirements for accuracy, quality, and processing performance of gears are constantly increasing, which should be met in a timely manner, with maximum values of technical and economic indicators. The solution to these problems is associated with the improvement of technological processes, equipment, and tools for the manufacture of gears.

Currently, various methods are used for the manufacture of gears. The main ones are as follows: precision casting, rolling of gear teeth by plastic deformation, the use of 3D printing, and cutting, which is most widely used.

This is explained by the fact that gears require the use of materials of high strength, as well as high quality and precision of the tooth profile machining. Tolerances for high-precision gears their relative position and direction are from 10 to 3–4 μm . Therefore, the use of the above methods has significant limitations:

1. Precision casting—by scope of application, nomenclature and number of gears, the use of materials and the accuracy of obtaining the gear tooth profile;

V. Nastasenko (✉)

Kherson State Maritime Academy, Kherson, Ukraine

2. Tooth rolling—by materials, processing accuracy, and the need for specific expensive equipment;
3. 3D printing—by the used materials, their strength and accuracy of these processes.

It should be noted that the current trends of replacing the manufacturing processes of products with 3D printing in gear processing are not applicable yet since 3D printers do not provide the ability to control the jet of molten metal with high precision. Metal deforms when cooled and distorts the profile of gear teeth. These errors are superimposed on the accuracy errors of the applied 3D printers. If the method of spraying with metal powder is used, then for bonding it requires welding of the powder spray grains in the points of contact. This is technically possible when the powder spray is heated to a temperature of about 1000°C. However, such a compound is loose and requires pressing or strong kinetic acceleration and impact of grains, preferably in a deep vacuum (similar to the kinetic ion bombardment method when applying wear-resistant coatings [3]). It complicates the equipment used and spikes the gear cost process. Prospects for improving 3D printers are associated with great a technical difficulty, which increases the cost of their design and puts off the creation of high-precision (3–4 μm) 3D printing systems to the indefinite future.

Therefore, the most common and promising method of processing gears in the next 10–20 years will be cutting processes, due to their high accuracy, relative low cost, and wide versatility. Among these processes, a number of basic ones are outlined as follows:

1. processing of gears by copying inter-tooth space with cutting broaches and their blocks;
2. processing of gear teeth by copying and unit single of division used the disk and end tools;
3. processing of gear teeth by continuous rolling with hobs, shavers, and worm grinding wheels.

Broaching is an expensive method because it is associated with the need for a large number of broaches, their profile depending on the pitch and the number of machined gear teeth. Quite complex and expensive equipment is also used. Therefore, this method is cost-effective mainly in mass production. Of the rolling broaching [4] makes the tool universal, however, for multi-tooth wheels, its length increases significantly and increases with the increase in the size of the teeth of the machined wheel. The complexity and dimensions of the equipment used in this case increase sharply. Therefore, for more than 40 years of development, the method is not widely used. However, there is experience with its use for small gears with small tooth sizes.

The processing of gear teeth by disk and end mills and grinding wheels is used in single and small-scale production [5]. This is connected with the low productivity of the process due to the need for a single division and performing idling return strokes. However, the high accuracy of the design and manufacture of tools (especially the end ones) has expanded the opportunities of their application for machining high-

precision gears [6]. Constraining factors of such processing: (1) the need for expensive CNC machines with high-precision servo systems and technologies and adjusting of their motion, which are programmed for 8–9 types; (2) the problem of increasing tool life is aggravated, which leads to the need to equip it with materials from hard alloys and reduce cutting modes (productivity) [7]. These factors significantly limit the use of this method for high-performance finishing of multi-toothed gear rims of medium and large modules without the regrinding of tools [8].

Gear processing with worm cutting tools has been widely used in serial and large-scale production [5] since it provides high productivity, which is second only to broaching, and high accuracy (up to 3rd degree), which is second only to processing on CNC machines and the end tool. However, with increasing accuracy of worm cutting tools and machine tools used for them, a reserve is created for processing gears of the third and higher degrees of accuracy. The versatility of the use of worm gear cutting tools for processing any number of gear teeth is their important additional advantage. Therefore, the solution to the problem of increasing their accuracy and performance is an urgent and important scientific and practical task [8]. Moreover, the combination of the division and break-in chains simplifies the machine tools by 10–20%, adequately decreasing their cost and increasing accuracy. Since on modern CNC hobbers the rigid kinematic connection of the main motion and break-in chains generating a worm gear it is possible to replace, with servo systems with CNC and separate drive, this expands their prospects for the multiple of worm gear cutter mill processing [9].

Herewith, combined processing is recognized as the most preferable—obtaining a gear blank by 3D printing with minimal allowances for subsequent finishing machining with worm tools, which requires their development.

The solution of these problems is the main goal of the work performed. Its scientific novelty is the rationale for the most appropriate designs of worm gear cutting tools and their manufacturing technologies and equipment for their production.

7.1.1 Accuracy and Performance of Hyperboloid-Type Hobs

Currently, it is real and economically feasible to process gears to the third degree of accuracy with deviations of the profile and tooth pitch within 3–4 microns. It is also possible to perform gear processing of the second and first degrees of accuracy with an end tool on CNC machines. However, the high technical costs of its implementation narrow the scope of their economically viable application only for special types of products, for example, high-speed turbines, multipliers, high-precision gearboxes, machine tools, and devices.

Worm tools (milling cutters, shavers, and grinding wheels) provide the possibility of machining gears up to the third degree of accuracy. Among them, worm cutters (hobs) are most widely used. Worm shewing is used mainly for worm gears, and grinding is used for gears with small tooth sizes, where a significant increase in the

diameter of the circle is possible, which compensates for errors by reducing the angle of elevation of the helix of the main worm.

By technical and economic efficiency indicators, the hobs are most effective for processing gears of 8 ... 5th degree of accuracy. However, the high technical and economic performance of worm milling prompts its use to further improve the accuracy and productivity of gear processing, which is possible in three following basic ways (Fig. 7.1) [8]:

1. improving the accuracy of designing and production of tools;
2. increasing tool wear resistance;
3. increasing the number of turns.

If the first two ways are given great attention, there is lack of attention—to the third way. This is explained by the fact that with an increase in the number of approaches, the accuracy of processing the gear teeth profile decreases due to an increase in its faceting and distortion of the tool teeth profile. The load on the tool teeth is also growing due to an increase in the cross section of the cut chips. Therefore, it is necessary to solve these problems, which clarifies the tasks set. In full, their solution is possible only through the use of systematic methods of searching for new technical solutions [10], which is the basis for further work. Given that worm tools excels disk and end tools in terms of durability, and due to the continuity of the process—in terms of productivity, therefore, is advisable to refuse using the latter.

However, an effective concept for improving and developing worm milling cutters is currently lacking. This confirms the general identity of the designs of rough and finishing worm mills [11]. They differ only in the size of the dividing diameter, the number of racks and the accuracy and quality of manufacture although their working conditions are different. Since traditional solutions for well-known worm mills have practically exhausted their technical and economic capabilities [12], development of new directions for their design and a concept for improving them are therefore required.

7.1.1.1 Design Concept of Hyperboloid-Type Hobs

Currently, theories of designing gears and tooth profiles are receiving great attention [13]. Sections 1–6 of this monograph are also devoted to the improvement of such meshing.

However, in the end, the real profile of the machined gear is formed by the profile of the tool teeth, the parameters of its installation in the working bodies of the machine and the shaping movements that the machine performs [14]. Therefore, the initial concept for designing gears is the use of a method based on a combination of these parameters.

For example, varying the different installation options for the cutters allows getting three main worm types when turning [5], which significantly affect the shape of the profile of their threads and the conditions of their operation:

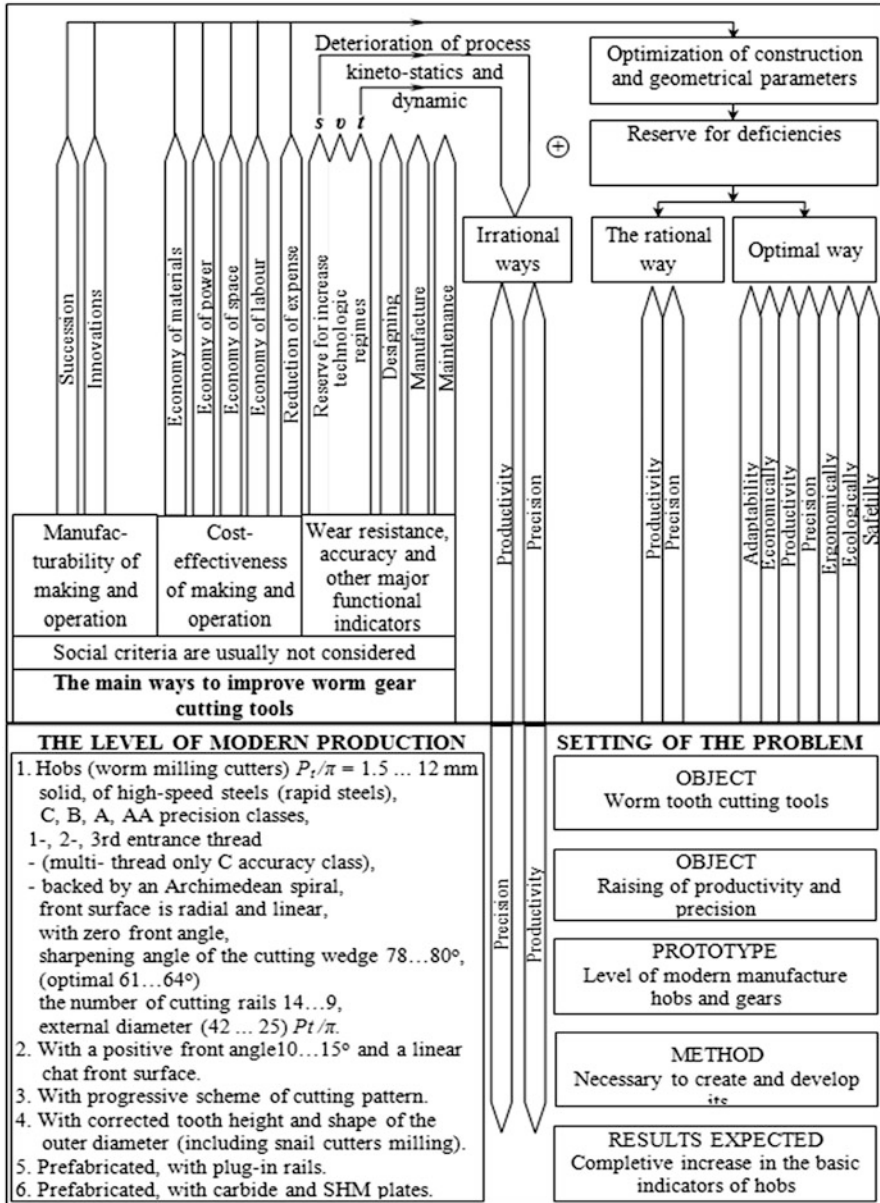


Fig. 7.1 General block diagram of the improvement of worm gear cutting tools

- Archimedean ZA (their geometric characteristics are the Archimedean spiral in the cross section of the worm and the straight profile of the turns in their axial section);

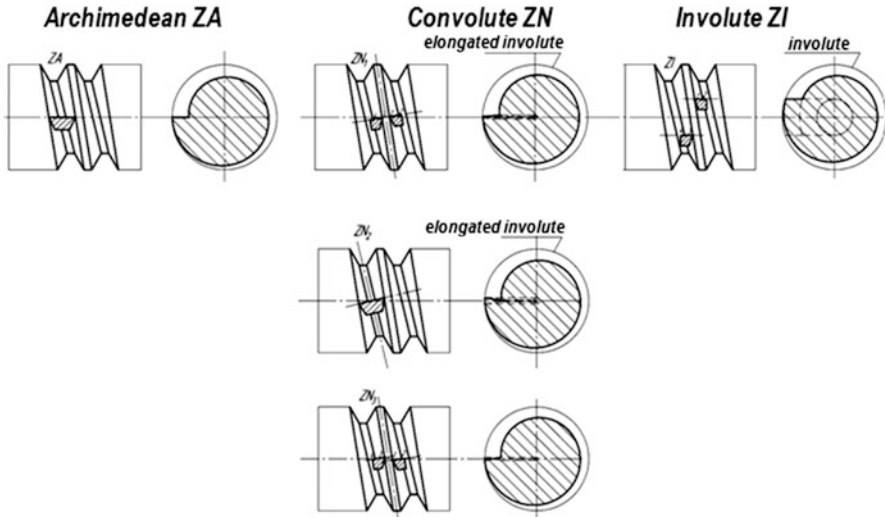


Fig. 7.2 Types of main worms obtained by turning with incisors of sharpen

- Convolute ZN (their geometric characteristics are the elongated involute in the cross section of the worm and three straight profile turns: ZN1—in the section normal to the thread turns, ZN2—in the section normal to the cavity between turns, ZN3—in section on the axial, normal to the right and left thread profiles);
- Involute ZI (their geometric characteristics in the cross section are the involute from the diameter of the design cylinder and the straight profile of the thread along a helical line tangent to the surface of the design cylinder).

All of the listed types of main worms, which are formed by the cutting edges of the cutters and their installation options, are shown in Fig. 7.2.

Since these main worm types are the basis for the design of worm tools, the initial concept of the helical movement of the generating curves should be applied to them. Such a technique in the countries of the former USSR was proposed by G.G. Inozemtsev [15] and was developed in the works of P.R. Rodin [16], S.I. Lashnev [17], G.N. Kirsanov [18], and other scientists.

As early as at the stage of formation of the main worms (Fig. 7.2), errors arise due to the helical shape of their threads and the installation parameters of the tool. They are the largest for Archimedean worms ZA since the cutter is installed in the axial plane of the worm, and the threads are formed in relation to it at the angle of their rise. Therefore, the larger this angle is, the greater is the difference in the directions of the axial and helical lines of the worm and the higher the error in the formation of the profile of its threads. This type is applicable only to single-start, low-precision worms. To increase it, correction of the profile of the right and left cutting edges of the cutter is required. Another disadvantage is the different size of the lateral rear angles at these edges, which complicates their design and technology of manufacturing and regrinding.

For convolute ZN worms, these errors are reduced since the cutter is installed at an angle to the axial plane in the direction of the helix of the worm at an angle of its rise. For ZN1 and ZN2 types of worms, these errors are almost identical since the cutting edges of the cutter are equally placed relative to the axial plane of the worm. For ZN3 worms, these errors are reduced since the deviations of the cutting edge of the cutter from the axial plane of the cutter are minimal. However, all these errors increase with an increase in the angle of the rise of the main worm helix, which is typical for multi-start structures.

For involute ZI worms, the cutting-edge placement parameters are selected so that an involute worm thread profile is formed. However, an increase in accuracy compared to ZN3 worms is not significant, and the technology for their manufacture is significantly complicated. Therefore, the ZI type of worms is not widely used for the manufacture of worm gear cutting tools and is rarely used for the manufacture of high-precision worm gear pairs since their wear, even at the breaking-in stage, eliminates the advantages of such pairs. More important factors for worm gears are the conditions for the formation and holding of the oil wedge in the worm and gear teeth pair.

It should also be noted that the linear profile of the cutting edges of the cutters is unacceptable for all types of high-precision worms since it exactly coincides with the line profile of the turns of the worm only on helical lines located on the diameter of the initial cylinder, on which the angle of elevation of their turns is determined. Above and below this diameter, the helical shape of the worm threads leads to the curvature of their profile, which must be taken into account by adjusting the profile of the cutting edges of the cutter. These deviations are negative (inside the edge) for the sections forming the thread head and positive (outside the edge) for the sections forming the thread root. The larger is the angle of the thread rise, the greater is the difference in positive and negative deviations, or the higher are the resulting errors of the threads, if the profile correction is not performed.

In addition, the method of screw movement of the forming curves requires the elimination of the following disadvantages: (1) the mismatch of the planar initial contour of the tool rail to the real tool contour formed by the producing surface of the screw form; (2) inconsistencies of the forming curves for the front and backed back surfaces; (3) transformation of profiles of tools of the first order (worm cutters, shavers, and grinding wheels), and second order (cutters, and grinding wheels that form the tool of the first order), the conditions of their editing and running during regrinding.

Therefore, for further improvement of profiling accuracy, the method of screw movement of the forming curves began to become more complicated to increase the accuracy of profiling due to the accurate determination of these curves on the profile of tools of the first and second order [14]. At the same time, the profile of its teeth is definitively formed by two helical surfaces: (1) the front, (2) the backed-off one, which is performed to maintain the profile of the milling cutter tooth after regrinding along its front surface. Thus, no matter how precisely the worm backed-off cutter is designed, the real shape of the cutting edge of its teeth will be obtained when the working bodies of the machine move two forming curves: (1) a curve formed by

helical and reciprocating movement of the working surface of the backed-off tool when it comes in contact with back surface of the cutter tooth; (2) a curve formed during the helical movement of the working surface of the grinding wheel during its contact with the front surface of the cutter tooth. In this case, the theoretical forms of the generating curves of instruments of the second order are replaced by technological curves obtained on the basis of simple types of movements [19]—in a straight line or along an arc of a circle, and in special cases—along an Archimedean spiral or involute, which introduces its errors. A theoretically accurate profile of the manufacturing surface of second-order tools can be obtained on CNC machines programmed by 8–9 types of movements. However, this option is acceptable in special cases of production and unacceptable in serial, large-scale, and mass production, due to significant technical and economic costs.

It should also be taken into account that when performing a backing-off surface of the cutter teeth, it is impossible to obtain their accurate profile along the entire length of this surface.

This is caused by decrease in tooth size from the initial cross section of original milling cutter outer diameter to the final section of the sharpen one, the of which is smaller than the original. This is explained by the fact that due to the need to obtain a rear angle, the back surface of the teeth is made in an Archimedean spiral. Therefore, the direction of the generatrix of the backing curve does not coincide with the direction generatrix of the front sharpening surface of the tooth. Since the mismatch in the direction of the generatrix curves grows toward the end of the tooth, therefore, the errors caused by it grow. Errors appear when the rack is turned by a tangent to the helical line of the main worm. In order to reduce errors, the relieved cutter should be turned in the plane parallel to the front surface of the milling cutter tooth, along which it is regrind (convolute worms ZN). The relieved surface being grinded compared to backing with the cutter, which leads to an increase in errors after regrinding. When grinding the back surface of the milling cutter tooth with a disk or conical end grinding wheel, they are set by a tangent to the backing curve. Therefore, their generating surface does not coincide more distinctly with the direction of the generatrix of the front tooth surface being grinded compared to backing with the cutter, which leads to an increase in errors. These errors increase with an increase in the angle of inclination of the rack to the worm axis, which is typical with an increase in the number of threads.

These errors can be eliminated by transforming (lengthening) the profile of the backed-off tool in time of its movement along the back of the backed-off teeth and returning to its original length on the tops of the following teeth. However, it is still difficult to implement technically. Therefore, the backed-off cutters are profiled according to the design section associated with half the length of the ground part of the backed-off surface from the top of the tooth. Thus, milling cutters that are new and worn after regrinding are the least accurate, but have opposite errors. The most accurate milling cutters are ground at half the length of backed-off surface, which is made on the surface backed by a cutter.

When sharpening milling cutter teeth with a conical grinding wheel along the front surface of the helical shape, errors also arise which are eliminated by replacing the rectilinear shape of its generatrix with the convex curvilinear form. The

parameters of this curvature depend on the diameter of the initial cylinder of the milling cutter and the inclination angle of its teeth front surface (the latter grows in multiple-thread milling cutters). However, the value of such a truing is also not constant for the backed-off milling cutters, since with regrinding, their outer diameter decreases, which causes appropriate errors. When truing the worn-out grinding wheel, its diameter decreases, which changes the conditions for its conjugation with the front surface and introduces additional errors. A theoretically accurate profile of the generating surface of a grinding wheel can be obtained on grinding machines by equipping them with a CNC truing tool programmed for three types of movements [20]. However, this option is acceptable only in special cases of grinding milling cutters for the production of highly precise gears and is unacceptable in serial, large-scale, and mass production, due to significant technical and economic costs.

The performed analysis allows us to conclude that the theoretical profile of the milling cutter tooth is formed in the section normal to its thread and is transformed depending on the diameter of the initial cylinder, the angle of its helical line rise, the type of main worm, the selected backing curve, the size of the rear angle, and the parameters of the helical front surface. Further, real technological errors of manufacturing worm milling cutters are additionally superimposed on it. They are minimized by increasing the accuracy and rigidity of machine tools, tools of the second order and the technological system of machine-tool-device-tool-workpiece. At the stage of profiling milling cutters, they are considered absolutely accurate and rigid. Therefore, its errors are neglected since the correct choice of a machine tool and technological system allows them to be reduced to 2–4 microns. Another limitation adopted in the work performed is the development of worm tools for processing involute gears and their modifications. In this case, errors in the profiling of tool rack are excluded since the rack tooth profile is adopted instead, shown in Fig. 7.3.

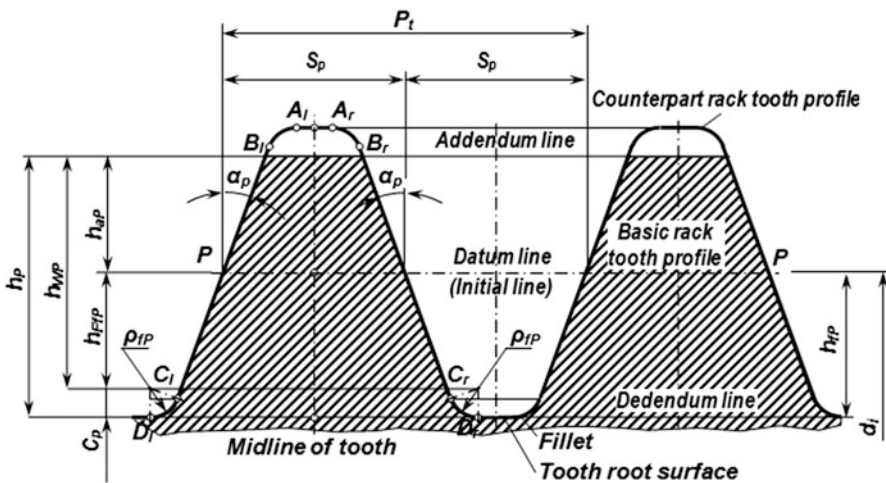


Fig. 7.3 The initial profile of the gear rack for processing gears with an involute tooth profile

However, in high-precision design techniques (and in this work), the transition from the flat initial profile of the tool rack to the real tool profile formed by the helical surface generating, it is taken into account.

In this case, the tool surface is a theoretically accurate surface that meets the nominal surface of a product at circular, transverse, and longitudinal feeds implemented in machine engagement during the processing of a gear product by break-in method.

Tool profile—refers to a flat figure obtained by plane section of a tool surface.

Rolling around method (centroid enveloping)—is characterized by circular and transverse feeds, in which the initial straight rack rolls without sliding along the bottom line (centroid) of a product.

The basic worm—represents a geometric helical surface formed by a rack with a given profile of its teeth and the type of its helical movement, which differs from a real worm in the absence of deviations of the outer and inner diameters, profile of threads, helix pitch, type of helical surface, and other geometric and design parameters composing this worm.

The data presented allow concluding that in order to reduce the errors of worm milling cutters; it is advisable to exclude the processes of their teeth backing and their front surface regrinding. In addition to affecting the accuracy of milling cutters, regrinding reduces the center-to-center distance in a “milling cutter—cut gear” pair, which can also be a source of tooth processing errors, especially when machining worm wheels.

These factors, in conjunction with the previously adopted concept of forming the profile of the milling cutter teeth by the method of helical movement of the generating curves of tools of the second order, allow us to consider the concept of their profiling to be finally developed. It should be borne in mind that worm milling cutters are the most complex tools in terms of the number of surfaces that form their teeth, compared to shavers that have no backed-off surfaces, and compared to grinding wheels that do not have backed-off and front surfaces. Therefore, the developed concept can be automatically applied for their profiling, when excluding missing surfaces.

7.1.1.2 Errors of Profiling of Hyperboloid-Type Hobs

Errors associated with the generation of the helical surface of the main worm, helical front surface, and helical backed-off surface of the teeth are absent in other types of cutting tools, except for the screw ones. Therefore, they are referred to as “organic” errors, inevitably associated with their profiling and manufacturing. Since other types of errors associated with the formation of mounting and supporting surfaces are characteristic of other types of tools that are widely known and well-studied, further attention in this work is given to organic errors worm cutting.

The arising of the organic errors of the main worm is due to the transformation of the original tool rack when it is applied to the surface of the initial worm cylinder (Fig. 7.4).

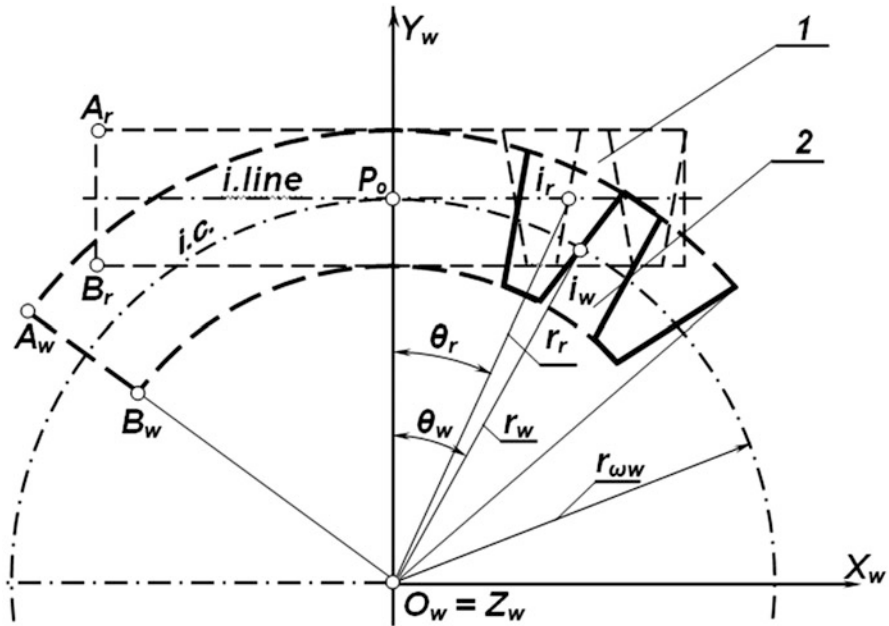


Fig. 7.4 Transformation of the rack profile during the transition to the cylindrical surface of the main worm

When cylindrical worms are formed by the initial gear rack 1 with the profile height $A_r B_r$, its initial line *i.l.* is combined with the initial circle *i.c.* of the main worm in the profiling point P_o . The rack is turned normal at an angle of the helical line rise of the main worm. This rack hangs over the cylindrical surface of the main worm and does not coincide with it. Therefore, it hangs over the cylindrical surface of the main worm and does not coincide with it. The larger is the turning angle, which is typical for multiple-thread milling cutters, the greater is this mismatch. The current point i_r on the profile of the initial gear rack is determined by the radius vector r_r and the angle of its inclination θ_r . When moving to a cylindrical worm, rack 1 forms a helical profile 2 with a height of $A_w B_w$, and the current point i_r of rack profile, having followed the path $i_r i_w$ along the involute, will take a new position i_w , determined by the radius vector r_w and its angle of inclination θ_w . It will adequately distort the parameters of the thread profile compared with tooth profile of the initial rack. Actual distortions of the initial rack profile and the worm threads profile are shown in Fig. 7.5.

The transformation of the right and left profiles of worm threads was obtained with the helical movement of the linear profile of the gear rack, which has a right $A_r B_r$ and a left $A_r B_r$ side. The fixed coordinate system of the worm $O_w X_w Y_w Z_w$ is adopted as the initial one for the helical movement, and the moving coordinate system $O'_w X'_w Y'_w Z'_w$ is connected with it, performing translational helical motion P_w relative to the fixed system when turning for the current angle Ψ_w . The coordinate

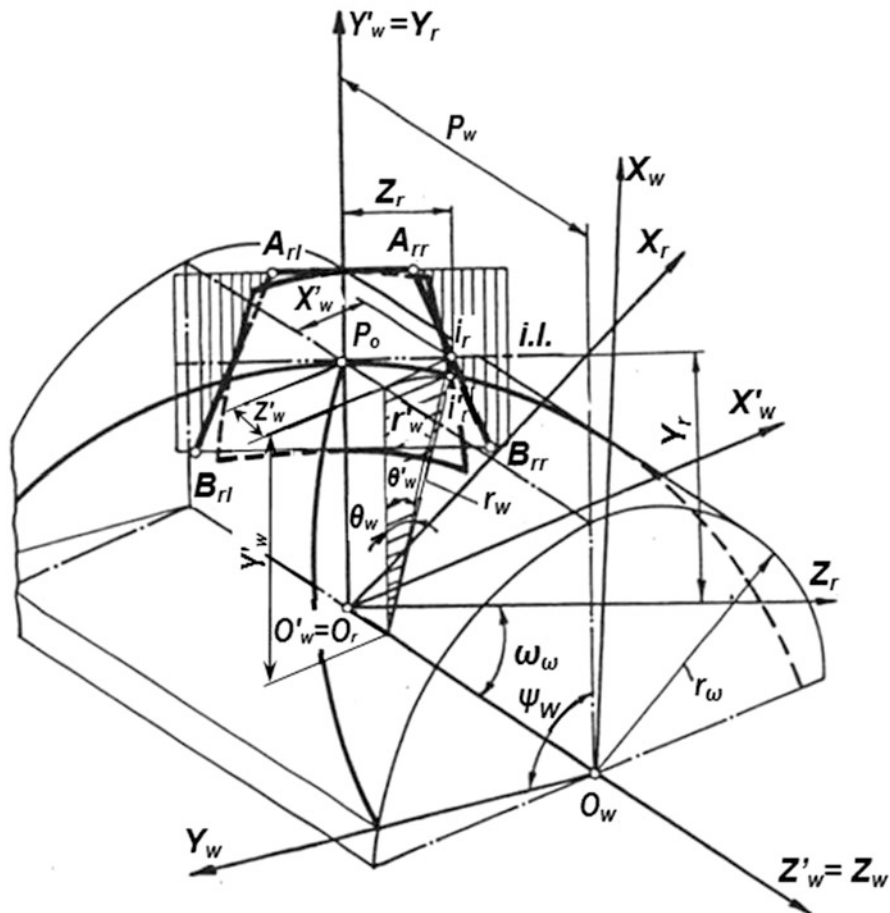


Fig. 7.5 Actual transformation of the rack tooth profile during the transition to the cylindrical surface thread of the main worm

system of the $O_r X_r Y_r Z_r$ rack is connected to the moving coordinate system and is turned in it for the lead angle τ of the main worm helical line. Initial line *i.l.* of a rack with a profiling point P_o is connected with the operating pitch cylinder of the main worm of radius r_w . The current point i_r of the rack profile in its coordinate system is determined by the $X_r Y_r Z_r$ parameters, and in the moving coordinate system of the worm it is determined by the $X'_w Y'_w Z'_w$ parameters, radius vector r'_w , and its turn angle θ'_w . On the worm, the current point will occupy the position i_w with the radius vector r_w and its turn angle θ_w . The curvature of the worm's thread profile relative to the rack tooth profile has deviations: on the right side, into the body at the top, from the body at the root, and on the left side, from the body at the top, into the body at the root. These curvatures increase with an increase in the angle of elevation of the main spiral line of the worm, which is typical for an increase in the number of its thread.

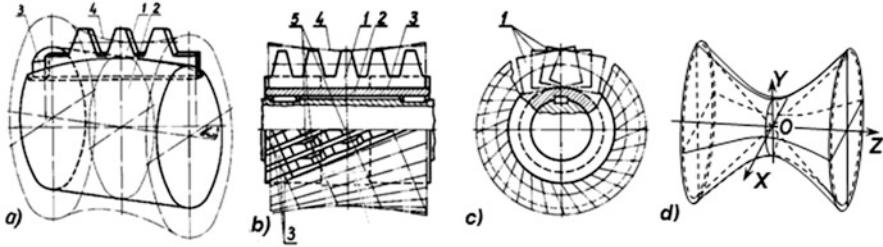


Fig. 7.6 The formation of hyperboloid worms with gear racks positioned normally to their threads

In a worm milling cutter, similar transformations also occur during the formation of a helical front and backed-off tooth back surfaces that fold. As a result of such transformations, two-thread milling cutters are used only for rough machining of cylindrical gears, and 3- and 4-thread milling cutters are practically not used, except for cases of machining worm gears.

The traditional way to reduce the errors in the transformation of worm threads profile is associated with a decrease in its lead angle to 2° . It is possible with an increase in the initial diameter of the main worm by 40–50% compared to rough milling cutters and a decrease in the number of their threads to 1. This way is used for the rest of the finishing worm tools—shavers and grinding wheels, which increases their size and weight indicators, and also requires the use of gearing machines tools of a heavier series (from a larger size range), which increases their cost and reduces the efficiency of the tooth cutting process. However, a 2° angle is too large for worm tools that process gears of more than third degree of accuracy, which limits the possibility of their use or requires reducing this angle by further increasing the diameter of the main worm.

However, the analysis of the scheme presented in Fig. 7.4 showed that if the initial state of the rack is preserved without its transformation onto the cylindrical surface of the main worm, then distortions in the teeth profile of the main worm rack and threads can be eliminated. This technique is the basis of the proposed concept for the development of high-precision worm gear cutting tools.

Designs of worms and worm milling cutters are shown in Fig. 7.6. The basic racks 1 are placed on the cylindrical surface 2 of the main worm in the grooves 3 at an angle ω normally to its threads. The initial lines of such racks form a hyperboloid worm since they describe the linear surface of a one-sheet hyperboloid (Fig. 7.6.b). The teeth 5 of such milling cutters will also form threads of a one-sheet hyperboloid (Fig. 7.6.c)

The scheme for the formation of the threads profile of the hyperboloid main worm is shown in Fig. 7.7.

The basic gear rack profile 1 with the teeth of $A_r B_r$ height, which have a right $A_{rr} B_{rr}$ and a left $A_{rl} B_{rl}$ sides, contacts the initial line $i.l.$ in the profiling point P_o with an initial circle $i.c.$ of radius r_{owc} of the cylindrical main worm, or with an initial circle of radius r_{owh} of the hyperboloid main worm. This circle is its neck, and to the right and left of it the diameter of the hyperboloid worm increases, forming a

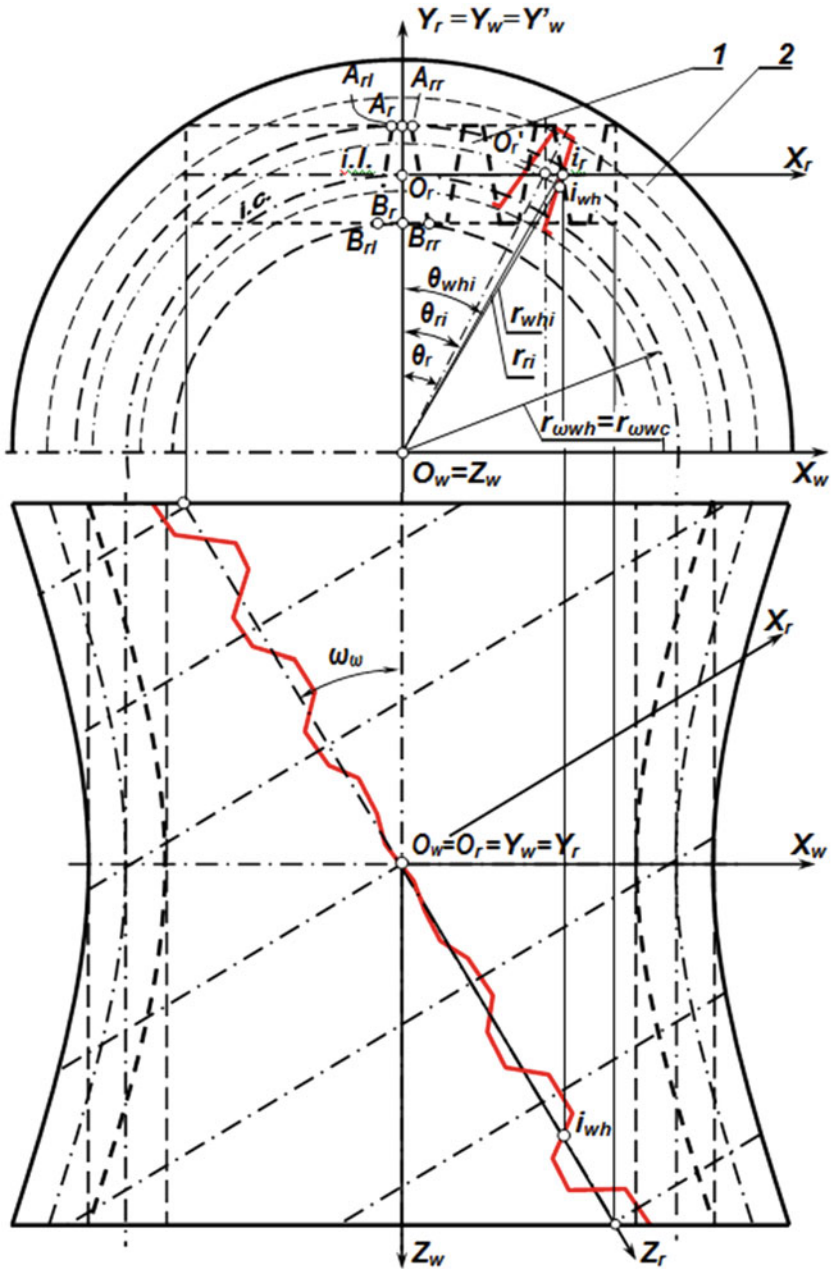


Fig. 7.7 Scheme for the formation of the threads profile of the hyperboloid main worm

hyperbola in the longitudinal axial section. The fixed coordinate system $O_w X_w Y_w Z_w$ is connected with these worms, the $O_w Z_w$ axis of which is aligned with their longitudinal axis, and the $O_r X_r Y_r Z_r$ coordinate system is connected with the rack, in which the $O_r Z_r$ axis is turned relative to the $O_w Z_w$ axis at an angle ω normal to the helical line of the main worm. The $O_r Y_r$ and $O_w Y_w$ axes coincide and pass through the P_o profiling point.

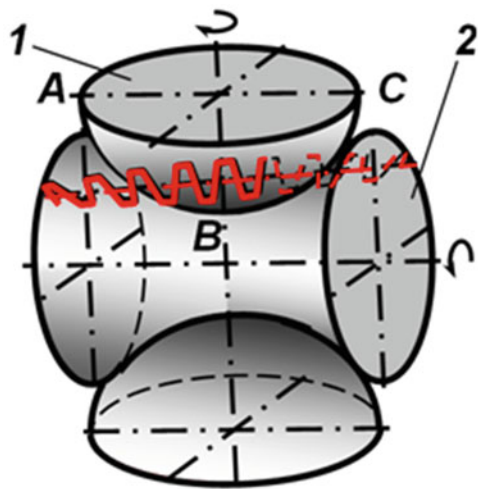
Due to the rotation of the $O_r Z_r$ axis, the radial axes of the rack teeth turn for an angle θ_{ri} and fan out with a right and left incline relative to the $O_r Y_r$ axis. In this case, the current point i_r of the basic rack profile with the radius vector r_{ri} and its turn for the angle θ_{ri} , on the hyperboloid surface of the worm, takes the position i_{wh} with the radius vector r_{whi} and its turn for the angle θ_{whi} , forming an inclined profile of the worm threads in its longitudinal direction. The larger the angle ω of the rack incline, which is typical for multiple-thread worms, the greater the radial incline of its profile. However, the errors of the profile on the thread surface of the main worm do not exceed that of the single-thread worm of ZA, ZN, ZI types. By this method, high-precision execution of multiple-thread worms is possible, and on their basis—the production of multiple-thread worm gear cutting tools.

In addition to a one-sheet hyperboloid, the formation of two-sheet ones is possible (Fig. 7.8).

A one-sheet hyperboloid has a number of advantages: it provides a larger coverage sector of the external gear rim of a cutting tool, reduces the load on the milling cutter tooth when cutting the allowance. It provides a reserve for increasing the productivity of gear processing. Their coverage sector significantly exceeds the coverage sector by cylindrical worms and tools, but it is inferior to globoid worms and tools (Fig. 7.9).

It should be noted that for globoidal worm gears and gear cutting tools, extensive experience in their manufacture and operation has been accumulated. Its analysis showed that despite the advantages in gear teeth contact, which unloads worm

Fig. 7.8 The main types of rotation hyperboloids: 1—two-sheet; 2—one-sheet



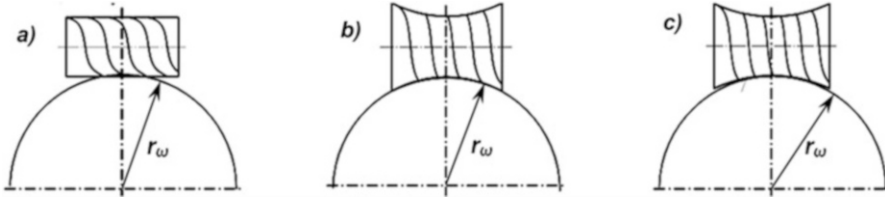


Fig. 7.9 Worm pairs with various types of worms: (a) cylindrical, (b) globoid, (c) hyperboloid

threads and worm tool teeth during operation, they are not widely used. This is explained by the increasing complexity and cost of their manufacture, as well as their sensitivity to axial errors of the installation relative to the gear symmetry axis.

Hyperboloid worms and tools are also difficult to manufacture. However, due to the incomplete coincidence of their surface with the surface of the conjugating gear, these worms are less sensitive to axial errors, and hyperboloid tools, due to the crossing of their axes and the axes of the machined gears, allow axial movement. This provides an opportunity for their wider use, and also it allows distributing teeth wear along the full length of the tool.

Thus, it can be concluded that the main way to reduce the organic errors of worms and worm gear tools is to switch to hyperboloid versions. Therefore, it is necessary to overcome the problems and contradictions that arise during their manufacture. Since other main are similar to cylindrical worms and tools, which are well studied, In that work so only the general possibilities of their reduction and the associated contradictions are considered. They take into account the recommendations of the most powerful system method for finding new technical solutions: Algorithm of Inventive Problem Solving (AIPS) developed by G.S. Altshuller [21]. According to it, the resolution of contradictions is possible in space and time (such an example is given for backing tools). On this basis, the list of errors and possible ways of their reduction is made (Table 7.1).

Since, in comparison with cylindrical worm gear cutting tools, the complexity and laboriousness of manufacturing hyperboloid, especially worm cutters milling and shavers, increase significantly, therefore, in addition to the effect of increasing their accuracy, additional recovery of these costs is required. It is possible by increasing the productivity of tools, which presents the further goal of the work performed.

7.1.1.3 A way to increase productivity of machining by means of hyperboloid-type hobs

In full, the tasks of increasing the productivity of worm gear cutting tools have not yet been solved. Despite their advantages (the continuous process of dividing and generating, which eliminates the presence of idle and reverse motion, accompanying the processing with disk and end gear cutting mills), there appeared works [7],

Table 7.1 Systematization of errors and contradictions in improving the accuracy of worm gear cutting tools and ways to eliminate them

The main factors causing errors	The main ways to eliminate errors	The main contradictions > <
I. Technological errors of manufacturing		
<ol style="list-style-type: none"> 1. Non-concentricity, misalignment and non-perpendicularity of the base surfaces. 2. Warping after heat treatment and redistribution of stresses along the keyway, turns of the worm, chip grooves and other transition surfaces. 3. Deviations of the helix pitch of the main worm and chip grooves. 4. Radial and face runout of the backed surfaces of tooth. 5. Own tooth profile modification at his backing and regrinding. 	<p><i>In time variation</i> - Is not found yet.</p> <p><i>In space variation</i> - limited to known traditional ways:</p> <ol style="list-style-type: none"> 1. Improvement of equipment and tooling. 2. Execution of keyway at the end of the housing. 3. Reducing depth or eliminating chip grooves and other surfaces. 	<p><i>Depend on</i></p> <ul style="list-style-type: none"> - the tool design, the used equipment, tooling, and tools of the 2nd order. - With single-treaded axial gearing, the distortions are similar on each gear tooth; with multiple-treaded one, they depend on the multiplicity of the number of treaded of hobs and gear teeth.
II. Technological errors of operational		
<ol style="list-style-type: none"> 1. Errors of installation and fixing of tools of the 1st order. 2. Deformation of teeth and body during cutting. 3. Wear of cutting blades. 4. Technology of performance re-sharpen. 5. Reducing the outer diameter and running conditions tools of the 1st order after re-sharpen or dressing of tools of the 2st order. 6. Faceting and undulation during processing, etc. 	<ol style="list-style-type: none"> 1. Optimization of accuracy, size and shape of base surfaces, reliability of basing and fastening. 2. Improvement of the modes v, s, t and tool material. 3. Optimization of the design and geometry of the hobs cutter teeth. 	<p><i>Depend on:</i></p> <ul style="list-style-type: none"> - processing conditions and modes v, s, t; - design of tools of the 1st and 2nd order, used equipment and tooling

proving the impossibility of achieving more high productivity in them. This is explained by the fact that when processing gear rims with a large number of teeth, the sector of their coverage with a worm tool increases significantly. This increases the number of teeth involved in operation and the load on the gear cutting machine tool, which forces to reduce processing modes. However, this drawback is not inherent with worm tools, but with used machines tools. The second factor is the ability to more easily equip disk and end mills with more high-performance carbide tool materials. In the design of finishing worm milling cutters and shavers, such possibilities are limited, and they are mainly made of high-speed steels. Therefore,

after the parameters of the required power are attained, rigidity and strength of the machine, tooling, tools, machined gear and equipping of worm tools with hard alloys, they provide higher performance than disk and end ones. It is not only due to the elimination of idling but also due to the participation in operation of a larger number of cutting teeth.

It should be noted that the problem of increasing the productivity of worm gearing is complex [22] because it is associated with a large number of limiting factors, overcoming of which is impossible in traditional ways. This requires a rejection of stereotypical approaches. The elimination of these shortcomings is a further goal of the work performed.

The first of the existing stereotypes is associated with the opinion that increasing the durability of cutting materials, applying wear-resistant coatings, improving the geometry of the cutting wedges, etc. improves productivity. In fact, they increase the tool life, which can be used for two ways: (1) reduce the consumption of cutting tools, (2) increase productivity. Since the share of the transferred value of the tool in the cost of manufactured products is 10–15%, therefore, even with an increase in their durability by two times and a reduction in tool consumption by 50%, the resulting effect will be 5–7.5%. However, a real increase in durability for tools that are already close to the pinnacle of excellence usually does not exceed 15–20%, which reduces the above economic effect to 2–3%. With an increase in processing productivity by two times, the effect will be about 50% of the cost of the manufactured products, or three to five times higher than from a reduction in tool consumption at the highest indices of its durability. Therefore, it is preferable to use the second way—increase productivity (P) processing.

It is possible to actually increase P in six main ways: (1) by increasing the cutting depth t , (2) feeding s , (3) cutting speed v , (4) by dividing the cutting path, (5) by reducing the time for idling and auxiliary motion, (6) by reducing the time for installation and removal of parts.

In case of worm cutting gearing, the growth of t is limited by the height of the wheel tooth. Its division is used only for roughing. For the remaining five ways, their implementation is possible with restrictions. For example, increasing the feed leads to a decrease in the quality of processing, and the cutting speed v sharply reduces the tool life.

With worm gear cutting tools, all of these next ways are possible.

For example, in hobs dividing of the cutting path is possible when two to four tools are installed from different sides of the machined gear. However, the complexity of creating, maintenance, and the cost of such equipment increase significantly. Reduction of idling is possible due to the batch processing of a gear, which has long been carried out, so a new increase in the possibilities of this way is limited. In addition, batch processing for multi-toothed gears of the middle and large module is not used (due to limitations in the milling cutter wear resistance and durability, or in the accuracy of gearing). Reducing the time for approaching, penetration, exiting, and withdrawal of tools largely depends on its outer diameter, which requires its reduction. However, it is impractical due to a decrease in the accuracy of hob.

Thus, the main factor is the processing modes, which require their more detailed analysis. However, the problems are complex.

According to the well-known normative for calculating cutting conditions during gear milling of hob [23], the value of P is determined by dependence (7.1), according to which its growth depends on the magnitude of the main machine time $t_{m.m.t.}$ and is ensured by an increase in feed per rotation of the machine table $s_{r.t.}$, the rotational speed of a milling cutter n_h and the number of its threads k , as well as a decrease in the cutting plunge $l_{c.p.}$, cutting length $l_{c.l.}$, over run $l_{o.r.} = 2 \dots 5$ mm, and number of teeth z_g of the machined gear.

$$P = \frac{1}{t_{m.m.t.}} = \frac{s_{r.t.} n_h k}{(l_{c.p.} + l_{c.l.} + l_{o.r.}) z_g} (\text{min}^{-1}) \quad (7.1)$$

However, as it follows from Eq. (7.2), for the same feed on the tooth s_r , the of threads number of hob k , and the number of gear teeth z_g cut, as 2 influencing factors, is excluded in the transformed dependence (7.3) to determining P . This indicates a disadvantage of the known method [23]:

$$s_{r.t.} = \frac{s_t z_h z_g}{k} \quad (7.2)$$

$$P = \frac{1}{t_{m.m.t.}} = \frac{s_t z_h z_g n_h k}{(l_{c.p.} + l_{c.l.} + l_{o.r.}) z_g k} (\text{min}^{-1}) \quad (7.3)$$

Considering that the cutter rotational speed n_h is determined by the dependence (7.4), and the cutting length $l_{c.l.}$ —by the dependence (7.5), we finally obtain the dependence (7.6) to determine P :

$$n_h = \frac{1000v}{\pi D_{ah}} \quad (7.4)$$

where v is the gear hobbing speed, m/min, and D_{ah} is the outer diameter of the hob, mm.

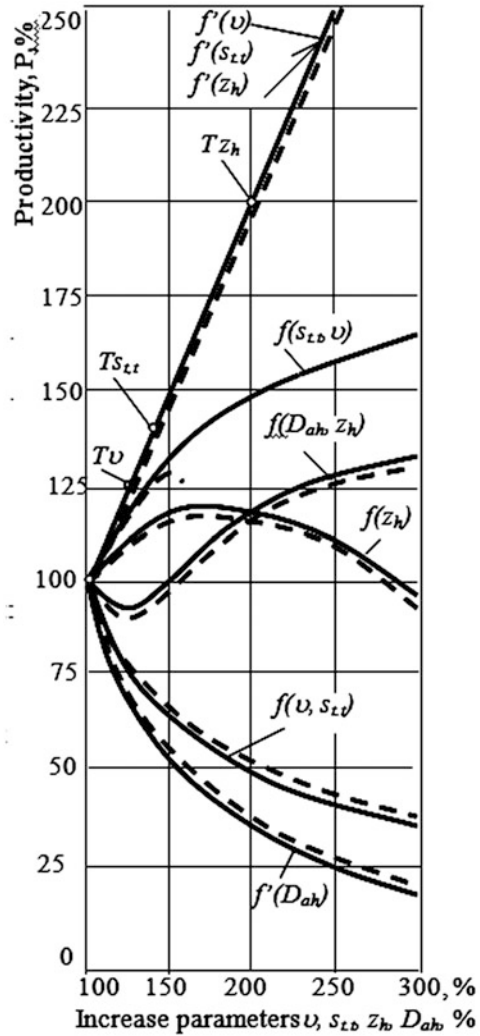
$$l_{Bp} = \sqrt{h_{t.g.} (D_{ah} - h_{t.g.})} (\text{mm}) \quad (7.5)$$

here $h_{t.g.}$ is the height of the machined gear tooth, mm.

$$P = \frac{1}{t_{m.m.t.}} = \frac{1000 s_t z_h v}{\pi D_{ah} \left[\sqrt{h_{t.g.} (D_{ah} - h_{t.g.})} + l_{c.l.} + l_{o.r.} \right]} (\text{min}^{-1}) \quad (7.6)$$

Thus, the factors finally affecting P , within the framework of the dependence (7.6), it is cutting speed v , feed per tooth s_r , number of cutter racks of hob z_h , its outer diameter D_{ah} , and tooth height of gear $h_{t.g.}$. Herewith, the growth of P according to the dependences (7.2) and (7.5) is not limited by anything, as shown in Fig. 7.10—by straight lines. It is also a drawback of the normative [23].

Fig. 7.10 The influence of the main technological cutter parameters ($v, s_{r,t}$) and design parameters hob (z_h, D_{ah}) on the productivity (P) of worm cutting gearing: $f'(v), f'(s_{r,t}), f'(z_h)$ —without considering tool wear time T ; at points—decrease in tool wear time $T/2$; solid line—multiple-start worm milling; dotted line—single-start worm milling.



However, these straight lines do not reflect the real possibilities of increasing productivity since the limiting factor is the wear time T of the hob in minutes, which should be no less than the machine cutting gearing time, determined for the selected cutting speed v according to the dependence (7.7) [24]:

$$v = \frac{C_v}{T^{0.3} (s_{r,t})^{0.5} \left(\frac{P_t}{\pi}\right)^{0.1} HB^{1.25}} \tag{7.7}$$

where C_v is the norm coefficient of cutting speed, P_t is tooth pitch, mm, HB is Brinell hardness for a non-hardened gear machined wheel.

Dependence (7.7) allows analyzing the influence of cutting conditions on the performance of worm cutting gear hob. It follows from this that an increase in cutting speed by two times leads to a decrease in the tool wear time T of milling cutters to 10 times, and increase in feed to three times. To reduce T by two times, it is enough (7.1) to increase the cutting speed v by 1.26 times, (7.2) to increase the feed per tooth s_t by 1.43 times. The influence of the durability of worm cutters on the real possibilities of increasing their productivity is also shown in Fig. 7.10.

However, to eliminate a decrease in T , a combination of these modes is possible. These are explained by the varying degrees of influence of the feed and speed on the amount of heat generated during cutting, so their combination is possible without increasing tooth wear. At $T^{0.3} = \text{const}$, it follows from the dependence (7.8) that an increase in cutting speed v by a factor of n is compensated by a decrease in feed s_t in n^2 times:

$$T^{0.3} = \frac{C_v}{nv \left(\frac{s_t}{n^2}\right)^{0.5} \left(\frac{P_t}{\pi}\right)^{0.1} HB^{1.25}} \quad (7.8)$$

Then, with all else being equal, we obtain not growth, but a decrease in productivity from the initial value (i) to a new value (v) in $\frac{1}{n}$ times (7.9):

$$\Delta P_v = \frac{P_v}{P_i} = \frac{nv}{v} = \frac{(s_t)^{0.5}}{n^2 (s_t)^{0.5}} = \frac{1}{n} \quad (7.9)$$

An increase in the feed s_t by factor of n decreases the durability less significantly and at $T^{0.3} = \text{const}$ is compensated by a decrease in cutting speed v in \sqrt{n} times (7.10):

$$T^{0.3} = \frac{C_v}{\frac{v}{\sqrt{n}} (ns_t)^{0.5} \left(\frac{P_t}{\pi}\right)^{0.1} HB^{1.25}} \quad (7.10)$$

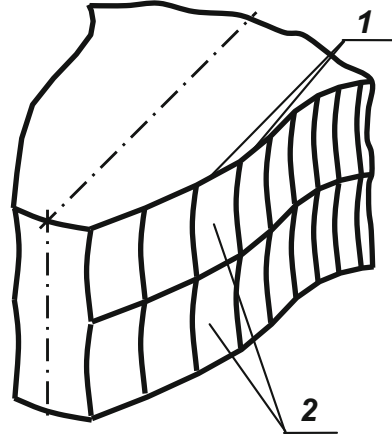
Then, with all else being equal, we obtain an increase in productivity by a factor of \sqrt{n} times (7.11):

$$\Delta P_v = \frac{P_v}{P_i} = \frac{v}{v\sqrt{n}} = \frac{n(s_t)^{0.5}}{(s_t)^{0.5}} = \sqrt{n} \quad (7.11)$$

However, an increase in feed per tooth s_t increases the machining waviness h_z along gear teeth – the height of macro-irregularities along the arc of the exit of milling cutter teeth in the direction of its feed along the gear central axis (Fig. 7.11), which is unfavorable for the finishing of high-precision gears:

Analysis of the impact of the structural parameters of milling cutter on the gear worm milling performance allows obtaining the dependence (7.6).

Fig. 7.11 The formation of faceting and undulation in the processing of gears by hobs



For standard milling cutters with a constant outer diameter, an increase in the number of racks z_h by a factor of n reduces by a factor of n , the amount of material being cut, which makes it possible to increase the feed rate s_t by a factor of n . However, at the same time, the number of tooth regrinding decreases by a factor of n^2 , and the cutter consumption increases within the same range, which is equivalent to a decrease in their total durability. Then, at $T^{0.3} = \text{const}$, an increase in the number of racks z_h and the feed on the tooth s_t practically does not give an increase in productivity P_{zh} in comparison with the initial P_{zhi} (7.12):

$$P_{zh} = \frac{1000ns_tnz_hv}{\pi D_{ah} \left[\sqrt{h_{t.g.}(D_{ah} - h_{t.g.})} + l_{c.l.} + l_{o.r.} \right] n^2} = P_{zhi} \quad (7.12)$$

An increase by a factor of n of the initial outer diameter D_{ahi} of hob leads to an increase in the cutting speed by a factor of n , which will reduce the milling cutter durability; therefore. For $T^{0.3} = \text{const}$, it will be necessary to reduce v by a factor of n . However, it is possible to increase the number of racks z_h by a factor of n with a constant feed s_t on its tooth, which will increase the feed per 1 milling cutter revolution by a factor of \sqrt{n} . Disadvantages: the dimensions of hob and the consumption of tool material on them, the dimensions of the machine, the power spent on cutting, and the length of cutting plunge and over run, the proportion of which is $\approx 10\%$ of machine time and their decrease with gear batch processing. With an increase in the number of hobs threads, it increases by 2–5% since the angle of intersection of its axis with the axis of the machined gear increases. Therefore, the performance P_{Dah} in comparison with the initial P_{Dahi} will increase by the value of (7.13):

$$P_{Dah} = \frac{1000\sqrt{n}s_t\pi n z_h \frac{v}{n}}{\pi D_{ah} \left[\sqrt{h_{t.g.}(D_{ah} - h_{t.g.})} + l_{c.l.} + l_{o.r.} \right]} \approx (0.9 \dots 0.85)\sqrt{n}P_{Dahi} \quad (7.13)$$

An increase in the number of milling cutter racks z_h by its 1 thread reduces the faceting of the product tooth (Fig. 7.11).

Since the dependence (7.6) includes the cutting length $l_{c,L}$, which depends on the specific processing conditions, it cannot be accurately taken into account in the generalized dependence. However, when processing single products, this way leads to the greatest decrease in productivity, therefore it is necessary to apply batch processing of gears, if this is allowed by the accuracy of the gears and the durability of milling cutters.

Thus, we can conclude that an increase in milling cutter diameter and the number of its racks provides a real effect of increasing the productivity of gear processing; however, this way worsens the size and mass parameters of milling cutters and the equipment used. Therefore, it is necessary to search for other ways, which is the further goal of the work performed.

Among the parameters considered above, the number of hobs threads was not taken into account. Currently, the use of multiple-thread hobs is constrained by a decrease in their accuracy, which grows with an increase in the number of threads (Fig. 7.4). Therefore, they are applied for roughing, and only in some cases, for semi-finished machining of gears with the number of teeth $z > 25$, in the presence of sufficiently rigid and high-speed gear milling machine tools [5]. However, in [25–27], the possibility of increasing the productivity of multiple-thread gearing is denied, which is associated with incomplete consideration of factors [28]. For example, in [29] it was shown that cutting factors that are optimal at the macro level may not be optimal at the micro and nanoscale, which requires a deeper analysis of them. The elimination of this drawback proposed in [28] is considered below.

In [5, 23], it was shown that multiple-thread worm milling continues to be used and provides a real increase in productivity, despite the deterioration of individual parameters of cutting mode, taken into account by correction factors [5]. At the same time, in addition to the feed and cutting speed, the restrictions are associated with the highest permissible table rotation frequency according to the ratings of a machine tool, as well as with the minimum possible number of cut teeth. However, these shortcomings can be eliminated in two ways: (1) by improving machine tools, (2) by improving tools.

The first way is possible through the use of machines with a separate drive for table rotation and for a spindle with a milling cutter, where a worm pair is eliminated of table, and the synchronization of their rotation is provided by the CNC. However, this way goes beyond the scope of the research and is not further considered.

Within the first way, a detailed analysis of multiple-thread hobs processing is required. It was shown in [25–27] that an increase in the productivity of multiple-thread hobs is considered to be the result of an increase in the diameter and number of hobs cutter racks z_h , rather than the number of threads k . This conclusion is based on the following considerations:

1. Single and multiple-thread hobs, identical in size, material, tooth shape, and body, have approximately the same cutting ability, durability, rigidity, and vibration resistance, so they do not allow unequal cutting forces.

2. It was experimentally established [30] that the approximate equality of cutting forces during multiple-thread hobbing (MTH) and single-thread hobbing (STH) takes place at the same minute feeds, which is possible in case of a decrease in feed per table revolution $s_{r.t.}$ in proportion to the number of threads k .
3. Since the feed per table rotation $s_{r.t.}$, per hob revolution $s_{r.h.}$ and per hobs tooth s_t are connected by the dependence (7.2); therefore, similar cutting conditions are ensured when the feeds per hob tooth s_t are equal, and for an equal number of hobs racks z_h —by the equality of feeds per hobs rotation $s_{r.h.}$. Then, to maintain the cutting forces identical to STH, with MTH, there is a need to reduce the feed $s_{r.t.}$ by a factor of k ; therefore, its performance will be equal to STH, which is consistent with the elimination of k in the dependence (7.6).

However, in practice with two-thread processing, the need to reducing the feed $s_{r.t.}$ makes up 20–30%, and not by two times [5]. This is due to the fact that with equal feeds $s_{r.t.}$, an increase of the thickness of the allowance cut by each tooth of the multiple-thread hobs by a factor of k is *observed*. However, there is a slight increase in cutting forces (only by 1.4–2.5% for two-thread and by 4.6–7.5% for three-thread milling cutters [30]). This is explained by the fact that when generating gear teeth, the thickness of the allowance cutoff by the teeth of a single-thread milling cutter is insignificant, especially during finishing. Therefore, a different degree of influence of the cut thickness and the radius of curvature of cutting edges on chips shrinkage occurs, which leads to a relative decrease in cutting forces and the amount of heat generated [31]. With a sufficiently high sharpness of the cutting edges (for example, in carbide materials, the radius of their self-sharpening is 10 μm), a change in the chip's shrinkage conditions will slightly affect the deformation and the strength of its separation. This is the second effect (first is overall increase in tool wear time) from the use of carbide materials for equipping hobs, which further develops the proposed concept of their improvement.

Thus, the disproportionate increase in the number of hobbing threads and the increase in cutting forces is the first reserve for their optimization. The second reserve is the optimization of faceting and undulation of the machined gear teeth. With an increase in the number of hobs racks, a reduction in faceting and undulation becomes redundant for machining gears with predetermined accuracy parameters for the profile of their teeth [32]. Then the increase in the number of racks is more appropriate to distribute on several hob threads. With the same value of feed per a hob tooth, their strength and rigidity are maintained, and the easiest way to increase the strength of the body and the attachment elements of a hob is possible by increasing their size. The increase in the number of threads proportionally increases the feed per hob revolving and per revolving of machine table. Therefore, with an increase in the wear resistance of hob teeth, this way becomes the most effective for improving the performance of worm hobs among all the options considered above, which was first shown in [28].

This analysis allows us to conclude that to increase the accuracy of hobs, they should be hyperboloid, and to increase productivity—multi-start and multi-tooth, and also equipped with cutting materials of high wear resistance (carbide or superhard

materials) with wear-resistant coatings. These provisions further develop the original concept of improving worm cutters.

The general scheme of ways to increase the productivity of worm milling cutters and the contradictions that arise during their implementation is shown in Table 7.2.

Based on the totality of the proposed principles for the development of the original concept, we can start designing hobs as the most complex tools among other worm gear cutting tools.

Table 7.2 Comprehensive analysis of the main ways to increase productivity (P) of hobs

Factor I. Increasing the outer diameter of the hob D_{ah} :		
<p><i>Disadvantages</i></p> <ol style="list-style-type: none"> 1. Decreases P by increasing the cutting plunge path and overrun of the cutter. 2. Increases the consumption of tool material. 3. Increases power consumption and other costs of operation and maintenance due to the use of more powerful, overall and expensive equipment. 	<p><i>Advantages</i></p> <ol style="list-style-type: none"> 1. Increases the strength, rigidity, vibration resistance and heat capacity of milling cutter teeth, which serves as a reserve to increase durability or P. 2. Provides an increase in the number of cutting racks, which reduces the load on the milling cutter teeth, increasing their durability and reducing faceting of the product tooth. 3. Reduces undulation along the product tooth. 4. At the same cutting speed, it reduces the rotational speed, which improves the table dynamics. 	
<i>Ways to eliminate the shortcomings (1, 2, 3) and their capabilities.</i>		<i>Contradictions > <</i>
1, 2, 3. Limitation of D_{ah} by performance and equipment dimensions.	<ol style="list-style-type: none"> a) Indirect influence on the increase P through T, b) Direct influence through $l_{c.p.}$ and $l_{o.r.}$ – to decrease P. c) Optimization of equipment dimensions. 	<ol style="list-style-type: none"> a) Increase $P > <$ durability T. b) Increase length of the overrun and penetration $> <$ increase in the number of racks z_h and T.
Overcoming the contradictions:	In time	a) At the time of penetration, D_{ah} must be <i>min</i> , and <i>max</i> when cutting.
	In space	a) It is possible to transfer the decision to space when creating of the conical the cut-in part hob (tangential feeds during penetration).
2. The use of prefabricated hobs	<ol style="list-style-type: none"> a) Complication process of the manufacturing. b) Complication of the operation process. 	a), b) Manufacturing costs $> <$ operating costs.
Overcoming the contradictions:	In time	a), b) It is impossible to implement this in the traditional way.
	In space	a), b) It is possible to use cheap materials when making the teeth of the milling cutters disposable, with a wear-resistant coating

7.1.2 Design features of hyperboloid-type hobs

Cylindrical worm cutting tools (hobs) were first created in England in 1862; they were preceded by the creation of disk backed-off milling cutters in 1861 in England [16]. The hobs were of integral design, having a cylindrical body with teeth located along the helical surface of the main worm. The teeth were formed by their front and backed rear surfaces. Until the 30s of the twentieth century, their basic design had not changed; only the parameters of the basic and abutment surfaces, the parameters and shapes of chip grooves, teeth front and rear surfaces, and the technology of their processing in the direction of improving the accuracy and quality of processing their body and teeth had been improved. The applied tool materials had been also improved (alloy steels were replaced by rapidly cutting tool steels), as well as methods for their heat treatment. Since the 30s of the twentieth century carbide hard tool materials began to be developed. Equipping the hobs with them dates back to 1938. Hard alloy plates were soldered onto the teeth of milling cutters of a standard design. The problems of soldering a large number of closely spaced teeth and the low quality of alloys increased the complexity of manufacturing and the stability of the productive operation of hobs. Since 1944, a number of prefabricated structures have been created with mechanical fastening in the steel rack body or individual teeth, including those equipped with hard alloy materials. This way is still developing to this day.

Development of hard alloy production processes in the 60s of the twentieth century led to the creation of monoliths hobs with a low tooth height and body dimensions—with a diameter and length of about 60 mm. Further, hobs of interlocking design with individual racks and teeth were being developed. However, the precision of multi-toothed interlocking hobs was inferior to the accuracy of solid ones; therefore, to process gears of the third degree of accuracy, solid backed hobs of rapidly cutting tool steels are used. Wherein the problems of creating high-precision equipment for teeth backing and grinding increased rapidly, which reduced the production of precision worm tools to a special and inaccessible manufacturing. Therefore, improving hobs requires a comprehensive solution to all these problems, including the creation of technologies and equipment. Their solution involves the following steps: (1) statement of the problem; (2) the search for ways and means of solving the problem; (3) solution to the problem; (4) design; (5) production; (6) operation, including repair and restoring; (7) disposal.

Among the main ways to improve worm milling cutters, the most important are outlined in the general structure of the criteria for the development of technical systems [33], which are as follows:

1. functional (general—performance, accuracy, durability, strength, reliability and life length, vibration resistance; special—versatility in terms of the number of cut teeth, etc.);
2. technological (complexity and manufacturability, technological effectiveness of operation, repair and disposal, partition into assembly units, the use of materials, their workability, etc.);

3. economic costs (for materials, equipment, tools, accessories, labor for production, operation and maintenance, for electricity and other consumables, for the preparation and launch of products, for the sale and promotion of products on the market, etc.);
4. social (safety and environmental friendliness of manufacture, operation, maintenance, repair and disposal, ergonomic use, aesthetic design, etc.).

Fourth group should be made a priority, since safety and environmental friendliness should prevail over the mere desire to get profit.

The analysis of the problems and this criterion allows adding to the concept of worm milling cutters improvement—they must be hyperboloid, multi-tooth, multiple-thread, and non-sharpening. The last factor eliminates backing and sharpening operations, as well as the equipment required for their implementation, the production and auxiliary areas occupied by it, reduces the main and auxiliary personnel, excludes equipment, tools of the second order, and other consumables and electricity to perform these works. Herewith, it is most rational to use interlocking hobs with disposable inserts platers with a wear-resistant coating on their front and rear surfaces that cannot be removed during regrinding. Removal of the coating leads to a decrease in durability between regrinding by 1.5–1.6 times. Moreover, non-sharpening platers improve the conditions for maintainability and recyclability (it is easier to replace worn inserts and parts hobs, collect hard alloy and other alloyed materials of the body and fastening elements for reuse). This increases the environmental performance associated with the extraction of raw materials and the production of tool material. Unfavorable environmental consequences of backing operations and regrinding leading to the generation of heat, abrasive dust and harmful gases, fuel consumption for the generation of electricity required for this, etc. are also eliminated.

The main criterion for developing non-sharpening hobs is to ensure their durability, which is not inferior to the total durability of multi-sharpening hobs. The main criterion for increasing their accuracy and productivity is to reduce gear faceting and undulation. The general system of their design is given in [34]. In this case, the studies performed in [32] were used, which show a change in undulation h_z and faceting h_t for various feeds per table revolution $s_{r.t.}$, number of threads k , number of milling cutter racks z_h and gear teeth z_g . Fig. 7.12 shows these changes at a single-unit ratio of tooth pitch P_t to the number π : ($P_t/\pi = 1$ mm). With an increase in this ratio, the values of undulation h_z and faceting h_t increase in direct proportion.

Analysis of Fig. 7.12 showed that for the most effective way to increase productivity by increasing z_h , and then $s_{r.t.}$, its possibilities for hobs of traditional designs are limited, especially when increasing their cutting properties. For example, carbide tool materials for milling cutters with a ratio of $P_t/\pi = 1$ mm can provide a tooth feed of up to 0.1 mm. In this case, the feed per hob revolution with the number of racks $z_h = 10$ will be 1 mm / rev. However, when machining a single-thread hob of the wheels with the number of teeth $z_g = 5$, this will lead to $s_{r.t.} = 5$ mm / rev.t., which will form an undulation $h_z = 17$ μ m, which exceeds the maximum tolerance f_f for the tooth profile error (Table 7.3) starting from the eighth degree of accuracy.

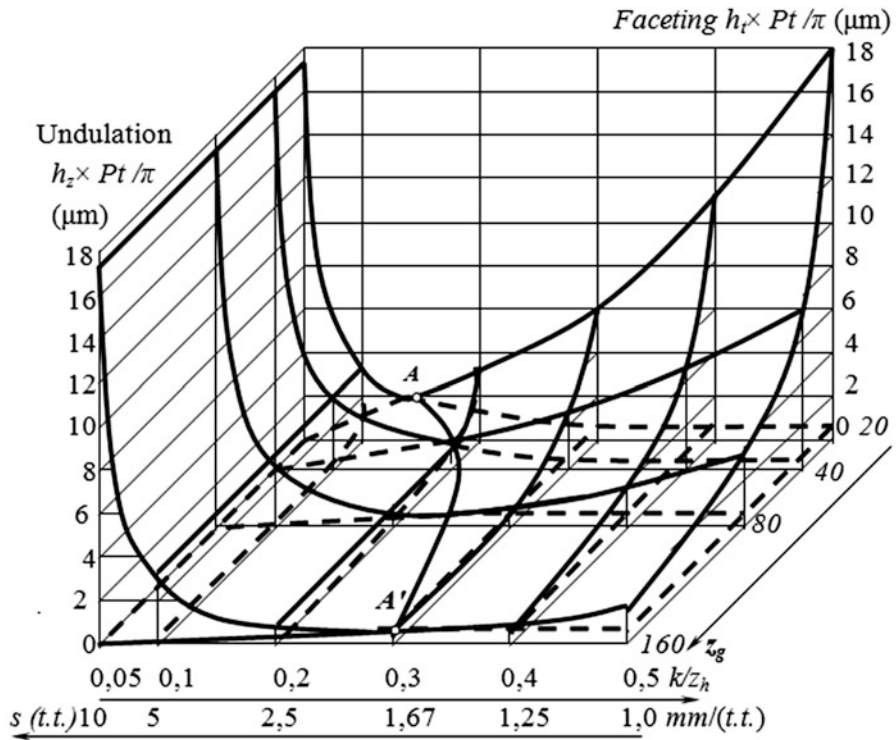


Fig. 7.12 Change in undulation h_2 and faceting h_t for various feed rates $s_{r,t}$, number of threads k , hobs racks z_h , and gear teeth z_g . Curve line AA' , its area of their minimization

Table 7.3 Characteristics of tolerances for gear profile error

Tolerance for tooth profile error f_p , μm (GOST 1643-81) Russia							
Refinement from degree to degree is ≈ 1.36 times	Degree of accuracy	Ratio of tooth pitch P_t to number π : P_t / π (mm).	Diameter of pitch circle d , (mm)				
			To 125	Over 125 to 400	Over 400 to 800	Over 800 to 1600	Over 1600 to 2000
	3	From 1 to 3.5	3.6	4.0	4.5	5.5	7.5
		Over 3.5 to 6.3	4	4.5	5.0	6.0	8.0
		Over 6.3 to 10	4.5	5.0	5.5	6.5	8.5
	4	From 1 to 3.5	4.8	5.3	6.5	8.0	11
		Over 3.5 to 6.3	5.3	6.0	7.0	9.0	11.5
		Over 6.3 to 10	6.0	6.5	7.5	9.5	12
...	
	8	From 1 to 3.5	14	18	25	36	50
		Over 3.5 to 6.3	20	22	28	40	56
		Over 6.3 to 10	22	28	36	45	63

A further increase in number of gear teeth will require a proportional reduction in of feed so $\bar{b}.ct$ and the associated feed s_g , which eliminates the use of allowance for durability from increasing the cutting properties of new materials. Since for multiple-thread hobs the feed per tooth is $s_g = ks_{r,t} / (z_h z_g)$; therefore, when the same $s_{r,t}$ for single-thread milling cutters, it can be increased in proportion to the number of threads k within the limits caused by the increase in cutting properties. However, for well-known hobs [11], the implementation of this way is difficult since an increase in the number of threads leads to a decrease in the number of their racks and to aggravation in faceting h_t (Fig. 7.12). To reduce it according to Fig. 7.12, it is possible to set the feed rate $ks_{r,t}$ and choose the optimal ratio k/z_h or vice versa, set k/z_h and select the optimal feed rate $ks_{r,t}$. The required faceting parameters for gears of the eighth degree of accuracy with 10 teeth are provided by 6 teeth per 1 milling cutter thread, and for the third degree of accuracy this value is 14 teeth. With an increase in the number of teeth z_g of the wheel, it decreases proportionally.

Faceting growth reduction is ensured by the new design of hobs [35], where zh reaches 90 and compensates for the faceting increase for high-precision gears even at 7 threads, and the total number of teeth is $\Sigma z_h = 360-500$. This allows increasing the amount of cut allowance for a tooth and makes the proposed multiple-thread hobs the most promising tool competing with broaches in performance [36].

Thus, the main advantage of multiple-thread hobs is the possibility of increasing the feed rate $sr.t$ without increasing the undulation h_z in proportion to the number of threads and the required faceting h_t due to the implementation of 12–14 teeth per 1 thread, which is especially effective for increasing productivity and accuracy of milling cutters in conditions of improving their cutting properties.

However, this raises the problem of making such a large number of teeth on the one hob thread without increasing its diameter. For this, it is necessary to solve two problems: (1) to reduce the pitch of hobs teeth; (2) to compensate for the total reduction in the durability of hobs as a result of elimination of the number of sharpening.

Further development was carried out for finishing hobs which have two main differences compared to roughing ones: (a) they cut a uniform allowance up to 0.5 mm thick along the working side surface of the gear teeth, formed after preliminary roughing or semi-finishing. With such pretreatment along the hollows of the gear teeth undercut is usually performed, which eliminates the adverse work of the tool teeth tops; (b) to reduce errors arising from the regrinding of the backed-off teeth of the milling cutters of holistic and interlocking designs, the number of sharpening is limited to 6–8.

It is easier to solve the second problem. The way to solve it is the use of disposable flat straight-shaped plates with a wear-resistant coating on all their sides, the profile being formed by the profile of the rack tooth, which transfers these inserts to the special category (Fig. 7.13).

Such inserts allow their reinstallation on the opposite side, which is equivalent to the second sharpening, and due to the grooves along the cutting edges, they allow optimal rake angles γ of front cutting surface, which increases their wear resistance in two to three times [31] and compensates from two to three of sharpening. This

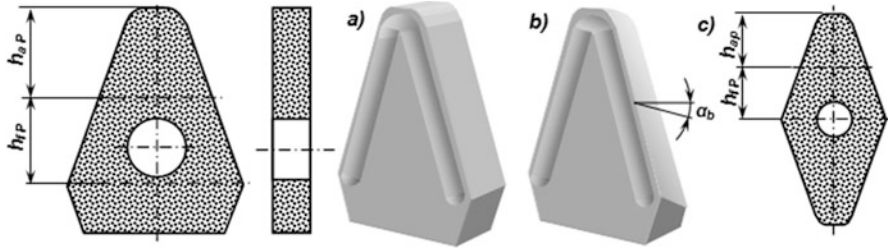


Fig. 7.13 Rational cutting insert design options for disposable hobs

requires studies on the selection of optimal rake angles, and the shape of the notches on the side of teeth, which were standard hobs, is not provided. For hobs is sharpening, with a period between sharpening T_{bet} , their total durability after 8 sharpens is $(1 + 8)T_{bet} = 9T_{bet}$. Making that for disposable inserts is equivalent to a 1.5-fold increase in durability, their total equivalent is $2 \times (2-3) \times 1.5T_{bet} = (6-9)T_{bet}$. It is also possible to use inserts with peripheral side rear angles α_s (Fig. 7.13.b). This eliminates their reinstallation; however, it improves the cutting conditions, which increases their wear resistance by up to two times [31] and compensates for the lost possibilities of reinstallations. However, this requires studies on the selection of optimal teeth peripheral relief angles, which were not provided for standard milling cutters. When inserts of the second symmetric profile are executed (Fig. 7.13.c), the number of possible reinstallations doubles, which leads to a doubling of their wear resistance equivalent of $2(6-9)T_{bet}$. However, this design option for inserts is rational for teeth with a ratio of $P_t/\pi < 4$ mm, and when it is increased to 6 mm, the first variant is rational, the equivalence of which is $(6..9)T_{bet}$. With a further increase in P_t/π , it is advisable to divide the inserts by height into 2-3 parts and alternate them through 1 or 2 teeth; however, the sharpening equivalent decreases.

When solving the first problem, it is necessary to reduce the thickness of hob tooth up to the thickness of the cutting plate and minimize the thickness of its support insert, which have of wedge form. For this, a design of hob 1 with an emphasis of the plates 2 and inserts 3 into each other is proposed (Fig. 7.14). With a flat straight shape of plates, the back angle α of hob is provided by turning the plates by front angle γ . The plates with a back angle α are installed along the radial axis of a hob, which simplifies its design. The fastening of the plates and inserts in the grooves of the hob of body is carried out by a spring 4 inserted into the hole of the plates and inserts, fixing them at of the thread end with a support element 5. With a minimum size of these plates, the spring can be placed into the hollows of the threads between the plates and inserts, as proposed in [37].

The minimum thickness of the wedge insert cartridge should ensure separating and curling of chips cut by milling cutter tooth. As it follows from the operating experience of broaching—it should be a product of 10–12 thicknesses of the cut allowance for the length of the contact of the teeth with the machined surface, which is given by the amount of feed per tooth z_g . Herewith, the placement of chips is a

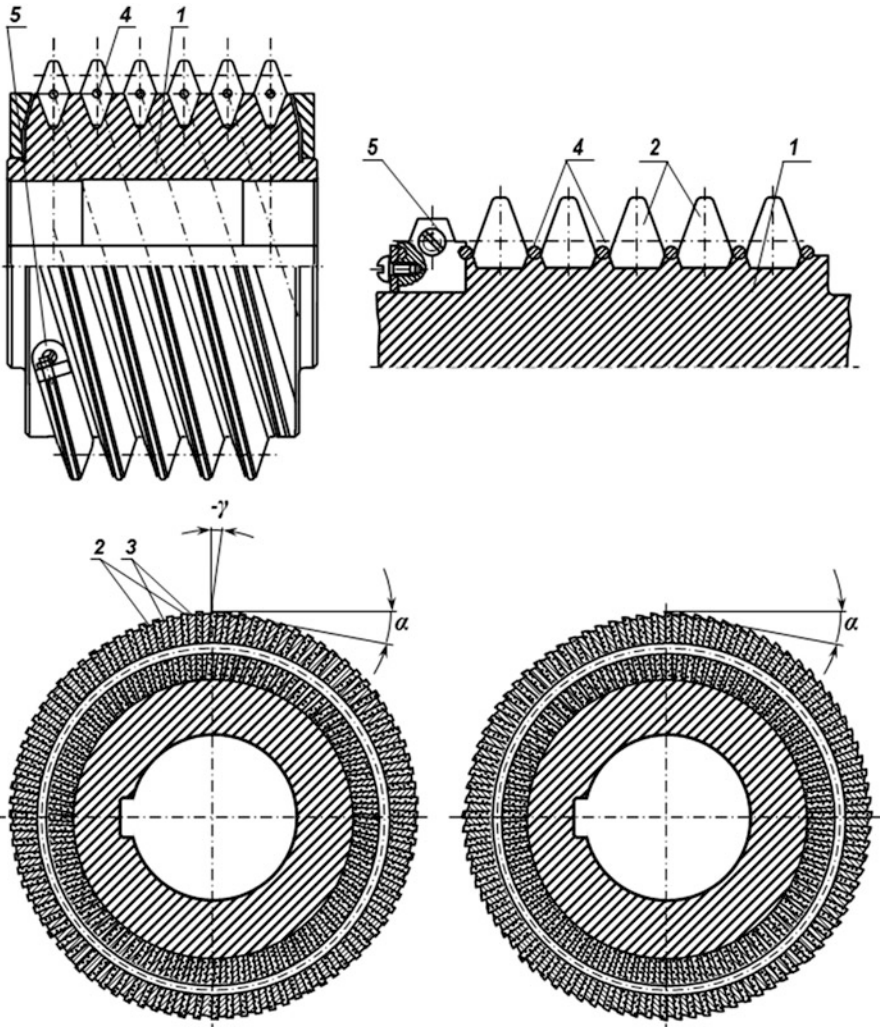


Fig. 7.14 Placement of cutting plates and inserts in the hob body

limiting factor in the application of the proposed hobs for roughing gears process. Within the allowances and feeds used for finishing gear cutting, the wedge insert thickness of 2–3 mm and the depth of the groove formed by it up to 1 mm provide the required conditions for curling, separating, and placing of chips. Then, with a standard thickness of cutting plates of 3.18 mm, the pitch of milling cutter teeth is 5.2–6 mm, and their number grows with the increase in milling cutter diameter. With a small height of machined teeth plates can be thinner by 1.5–2 times. Reducing the thickness of the cutting plates with back angles α can be performed by additional grinding after the plate’s delivery by the manufacturer. However, it is more

expedient to supply cutting plates of reduced thickness since their profile is specific and the order for them is customized, which allows modifying standard size options. With such teeth pitch and milling cutter diameter of 100 mm, their number is from 50 to 60 pieces, and according to the schemes shown in Fig. 7.14, this quantity is from 90 and more for the cutting plates of reduced thickness.

It should be noted that the design shown in Fig. 7.14 is developed for a cylindrical hobs and worm shaver, what simplifying the processing of its teeth and improving cutting properties when using inserts with optimal geometry of the cutting wedge. Their use is advisable not only for machining worm gears but also for cylindrical gears.

However, this hobs and worm shaver design does not provide the possibility of increasing the number of threads without compromising their accuracy. Although this drawback is eliminated by hyperboloid milling cutters, their production is still restrained by two factors:

1. the changed in the thickness and shape of the wedge inserts from the neck to the end of the hyperboloid milling cutter by increasing its diameter;
2. the need to extend cutting plates due to fan radial orientation of the teeth of hobs teeth (Fig. 7.7).

This creates a need for production of each wedge insert and cutting plates the first thread customized, which greatly complicates their manufacture, assembly, and operation. Performing more than one spiral turn for one thread proportionally increases the number of such inserts and cartridges, which is irrational. It should be noted that the individual production of 50–90 designs wedge inserts with a total number of more than 300 pieces becomes possible only with the development of 3D printing, which appeared in the twenty-first century. Therefore, hyperboloid hobs can be considered tools of the twenty-first century. In the twentieth century, their manufacture was almost impossible [38].

The individual profiling of the cutter plates can be excluded by the method of point profiling, in which round plates are placed on the right and left sides of the wedge inserts of milling cutter teeth along the profiling lines, of the normally to their profile (Fig. 7.15).

The main advantages of point profiling: (1) improving the accuracy of shaping by simplifying the shape of the cutting edges; (2) elimination of errors in the own profile

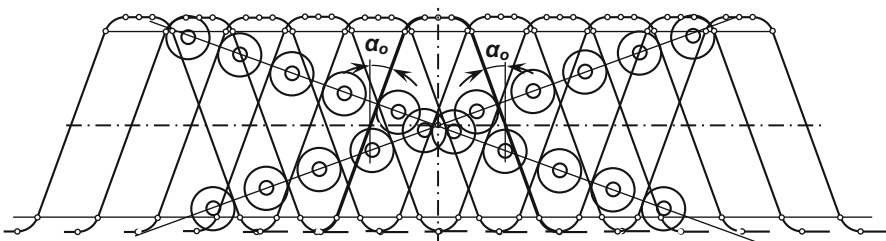


Fig. 7.15 Simplified arrangement of round plates along tooth profiling lines

of the rail due to its exclusion; (3) simplification of the shape of carbide inserts or super-hard materials and process of equipping of them the tool teeth; (4) simplification of tool designs as a whole; (5) the use of circular inserts provides the possibility to distribute the wear of cutting edges along the entire circumference of the plates, which significantly increases of the which of them equivalence of sharpening standard hobs.

However, the applicability of this method is limited by the size of the inserts and wedge insert of hob teeth.

Thus, the real accuracy of such worm milling cutters (hobs and shaver) is ensured by the accuracy of the plates and their installation parameters. For high-precision hobs and shaver, this requires the calibration of the plate's holes and the final grinding of their outer surfaces with reference to the hole. The requirements for processing wedge insert their holes, and pins inserted into the holes of plates and wedge insert are similar. For processing gears of higher than the third degree of accuracy, their selection is also required. Therefore, the complexity and cost of manufacturing hyperboloid worm tools bring them to the category of unique ones.

A large number of used plates (from 300 to 500) of hard alloys of relatively high cost additionally increase their price. When using super-hard materials, it increases even more. However, the ability to reuse the housing and replace only the cutting plates reduces these costs. The increase in productivity and accuracy of gearing most strongly reduces the unit cost of processing gears, especially when their number increases. The combination of these factors requires solving optimization problems of the cost-effectiveness using the proposed worm tools.

7.1.3 Features of manufacturing processes and requirements to equipment

In addition to the problems of designing and manufacturing the cutting part of the hyperboloid worm gear cutting tools discussed in Section 7.2, there are also problems of manufacturing the main worm and it's grooves for installing in them of cutting racks, or plates and wedge inserts. Methods for their implementation have been developed since the 70s of the twentieth century [39]. However, they were based on complex schemes of geometry shaping form and used with a large number of movements of the machine and tool. As applied to one-sheet hyperboloid worms, the scheme of the initial version of the machining implemented in the axial plane is shown in Fig. 7.16.

According to the initial scheme, the processing of a hyperboloid worm is performed with uniform rotation of the workpiece and its combination with four motions of inconstant value associated with the movement of the current center of hyperbola curvature: longitudinal and transverse feeds tool, of his offset value, alteration lengthening and orientation R_i , and angle of rotation φ_i of the tool in the axial plane. With multi-pass machining, a discrete feed to the cutting depth behind

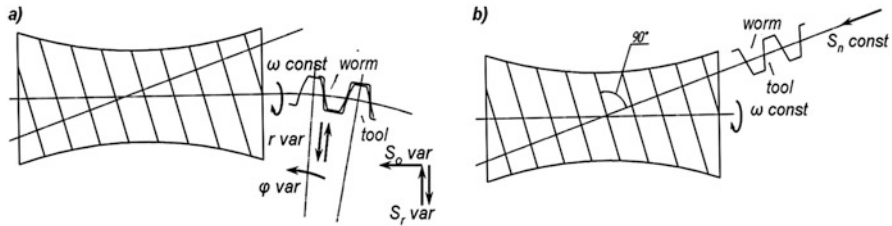


Fig. 7.16 The initial (a) and proposed (b) schemes for the generation of the hyperboloid main worm

1 pass is added to them, with the movement of the approach and retraction of tool. At multi-thread machining, a discrete rotation of the worm blank for a new thread is added. When processing the worm with milling cutters or grinding wheels, the movement of their rotation is added, it is the main movement of cutting tools of the second order.

Processing according to the original scheme requires the following:

- (a) fine-tuning the cutter tool of the second order (turning tool) to the size of the initial diameter of the main worm;
- (b) turning of the tool in the direction of the normal to the extreme point of the hyperbola, as well as its installation at the initial angle φ of turning along the normal to this point;
- (c) setting the initial lengthening of tool, which is equal to the variable radius of curvature R_i of the hyperbola at the extreme point and is associated with two current coordinates of the center of its curvature;
- (d) producing uniform rotation of the worm (the main cutting movement when cutting it with a cutter);
- (e) complex types of movements: with uniform rotation of the worm (with his coils and the pitch in the axial section based on the displacement by 1 step of the spiral per 1 revolution of the worm), coordinated uneven movements perform—turning of angle φ_i and variables the magnitude lengthening R_i , of the cutter tool, which depend on the parameters hyperbole curvature;
- (f) performing second smoothly changing caliper feeds—longitudinal and radial, forming the trajectory of the point of the current center of curvature of the hyperbola.

These parameters require processing in three ways: (1) on machines with complex kinematics of movements; (2) on CNC machines programmed for 6–8 types of movements; (3) the use of additional kinematic devices, more complex than for processing globoid worms with constant R .

Another drawback of machining hyperboloid worms in the axial plane is the mismatch of the profile of their turns and the profile of a second-order tool, both among themselves and with the profile of the initial gear rack (Figs. 7.4 and 7.7). This complicates the control of the worm profile, as well as the manufacture and control of the profile of the cutting tool of the second order. In the initial methods of

their machining, a second-order generating tool was adopted, obtained on the basis of gears conjugating with a given worm, with a specific and unique number of teeth for this worm pair, which excluded the versatility of the tool used and the machining process.

The indicated drawbacks are eliminated by manufacturing hyperboloid worms according to the method proposed in the patent [35], with an oblique feed of a second-order tool normal to the worm thread (Fig. 7.16), which simplifies the dependence of the kinematic system settings on the parameters of the worm and its hyperbola. The number of their threads is not limited herewith.

Implementation of the proposed method is possible on a conventional lathe with the initial cutter adjustment to the dividing diameter of the worm and replacing the five initial motions with two main ones: (1) uniform rotation of the worm; (2) uniform movement consistent with it with an inclined feed of the second order tool, at the rate of its shift by one pitch normal to the threads by one worm revolution. In this case, the coordination of the feed pitches and the profile parameters of the tool are provided automatically with the same motions as during the machining of cylindrical worms, therefore, it does not complicate the initial manufacturing processes.

All auxiliary motions—penetration, quick approach, and withdrawal, as well as returns for multi-pass and multiple-thread worm processing, remain the same with the original version. Matching the worm threads profile and tools of the second order with the rack teeth profile in the plane of the operational feed simplifies their manufacture and control. Implementation of the proposed method is possible by changing the worm installation angle (Fig. 7.17).

At small angles of worm inclination (up to 6°), its processing can be performed on existing equipment with the back center of the machine shifted, and the installation of cutters according to the schemes shown in Fig. 7.2 for ZN, ZN₁, and ZN₂ of main worms provides the ability to perform similar ZH, ZH₁, and ZH₂ of hyperboloid main worms (Fig. 7.18) [40]. On their basis, it is possible to manufacture hyperboloid worms of worm gears and grinding wheels for machining gears.

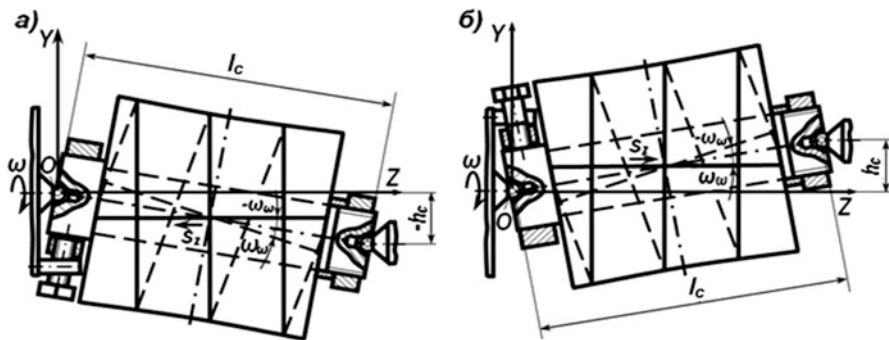


Fig. 7.17 Schematics of machining of the right-handed (a) and left-handed (b) hyperboloid worms with the front location of the support of tool with offset a cutting tool and back center of the machine

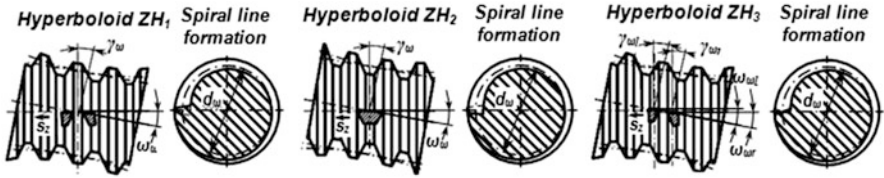


Fig. 7.18 Schemes of generating the main types of hyperboloid worms cut by second-order blade tools

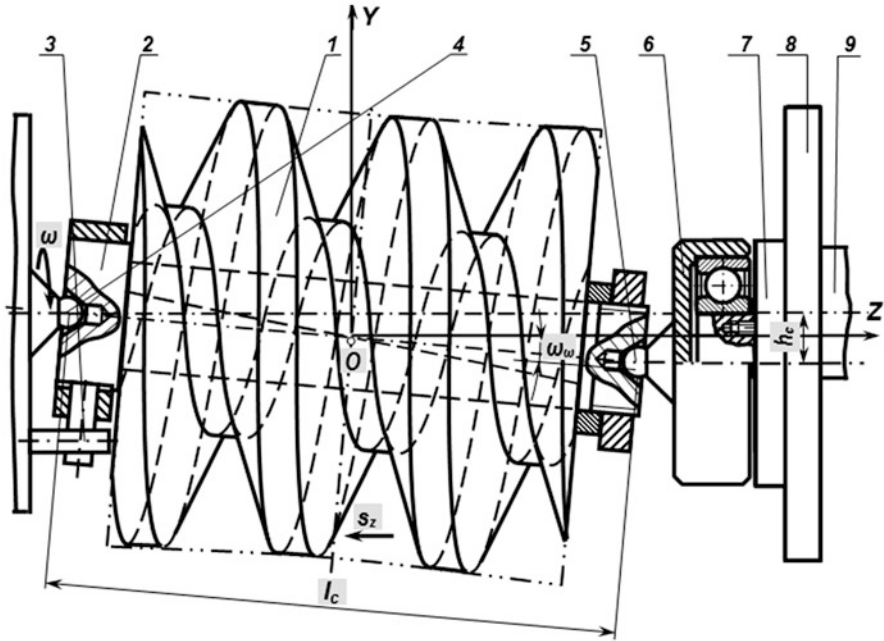


Fig. 7.19 Installation scheme of a hyperboloid worm on a mandrel with a deflection of the back center of the machine tailstock with a movable revolving center

However, for machines with a front support arrangement, a simpler version of the implementation of the above schemes in Fig. 7.17 is the deflection of the back center above the spindle axis (for example, due to pads under the tailstock), which is acceptable for processing left-hand worms. For right-hand worms, either a back center deflection below the spindle axis (the implementation of which is difficult) is required or the rear position of the machine support (which requires its substantial alteration). A more appropriate option is proposed in the patent [41] due to the use of a revolving center, which has the ability to move along vertical guides with its subsequent fixing. Herewith, its deflection is possible, both below and above the axis of the machine spindle, which provides an angle of worm threads inclination up to $\pm 12^\circ$ (Fig. 7.19).

The selection of tilt angles within 12° is due to the fact that its increase affects the reliability of worm fixation in the centers. However, it provides the machining of modern high-precision cylindrical worm milling cutters with the number of threads up to 4 since the actual angle of inclination of their threads to the worm axis is $\omega_\omega \leq 12^\circ$.

It should be noted that the installation of worms in movable revolving centers is advisable only in case of their finishing. Therefore, for 1- to 4-thread hyperboloid worms, it is proposed that rough processing of all their surfaces and threads profiles are performed according to the basic technologies for manufacturing cylindrical worms, and the hyperboloid surface and his threads profile should be cut during finishing. However, to implement this processing option, an analysis of the errors arising from this is required, which was performed in [42, 43].

The back center is displaced by a predetermined value $\pm h_c$, which depends on the helix angle $\pm\omega_\omega$ and the distance l_c between the centers (Fig. 7.17). Their accuracy depends on the accuracy of the manufacture of ball tops of the machine centers and the central holes of the worm or its mandrel. Therefore, when processing worms of high accuracy, constant monitoring and correction of the values of l_c and h_c is required. To do this, before installing the worm in the centers of the machine, a ball is introduced into both center holes of the worm or its mandrel, the diameter d_b of which is equal to the diameter of the ball tops of the front and back centers of the machine. Then, the distance l_b between the surfaces of the balls protruding from the center holes is measured, after which the value of l_c is determined by the dependence (7.14):

$$l_c = l_b - d_b(\text{mm}) \quad (7.14)$$

To displace the tool by a predetermined value $\pm h_{tool}$, depending on the helix angle $\pm\omega_\omega$ and the distance l_{tool} between the ball to center of the machine back center and hyperbola transverse axis of symmetry, it is necessary: (1) to place a ball into the right center hole of the worm or its mandrel having the diameter d_b equal to the diameter of the ball top of the machine back center; (2) to measure the distance l_b between the ball surface protruding from the center hole and the base end of the worm threads; (3) to measure the distance l_e between the ends of the worm threads; if the hyperboloid worm is symmetrical, or the distance between the right of end worm threads and the transverse plane of the neck of the hyperbola, if the hyperboloid worm is asymmetric; (4) to perform the calculation of l_{tool} according to the dependence (7.15):

$$l_{tool} = l_b - l_{be} - \frac{1}{2}(l_e + d_b)(\text{mm}) \quad (7.15)$$

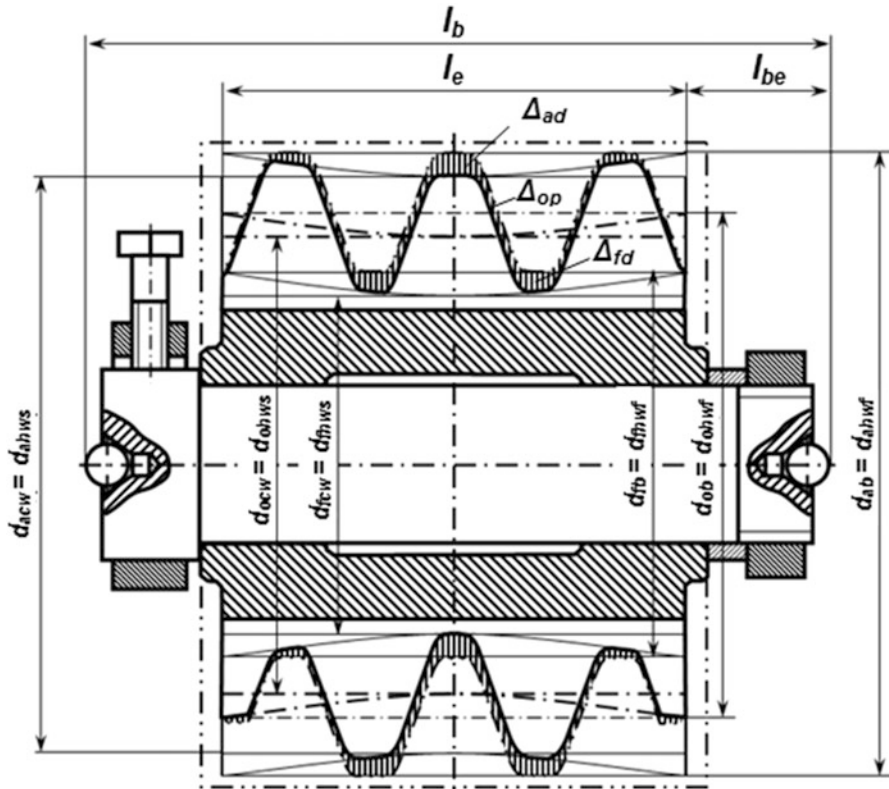


Fig. 7.20 The scheme of generating a hyperboloid worm on the basis of the workpiece of a cylindrical worm with a dedicated allowance for machining its threads profile

When using deflectable centers, the length of the mandrel or worm can be any within the working area of machine tool. Only the helix angle of ω_ω is important.

In the absence of correction of displacement (7.14), (7.15), the maximum errors of the hyperboloid surface with the sign (+) will be observable in the worms with a minimum value of l_c and maximum values of l_b and l_e , as well as with a maximum value of l_c and minimum values of l_b and l_e , which requires tightening of tolerances on these dimensions. Setting tolerances with a sign (+) for the depth of the center holes and with a sign (-) for the values of l_b and l_e , and vice versa, can partially compensate for their value.

When roughing the worms using of cylindrical technology, and then finishing them with displacement of centers, the nature of the transformation of the profile constituting the allowance for its machining is shown in Fig. 7.20.

Figure 7.2 shows that d_{ocw} , d_{acw} , and d_{fcw} are, respectively, the diameters of dividing circle (pitch circle), addendum, and dedendum circles (protrusions and troughs circles) of the base cylindrical worm, equal to the starting pitch diameters of the hyperboloid worm circles: pitch circle d_{ohws} , addendum circle d_{ahws} , and dedendum circle d_{fhw_s} ;

d_{ob} , d_{ab} , and d_{fb} are, respectively, the diameters of pitch circle, addendum, and dedendum circles of a workpiece blank, equal to the finishing diameters of the hyperboloid worm circles: pitch circle d_{ohwf} , addendum circle d_{ahwf} , and dedendum circle d_{fhw_f} ;

Δ_{ad} and Δ_{fd} are the allowances for processing inner and outer diameters, Δ_{op} is that for a thread profile.

For basic 1-, 2-, 3-, and 4-thread worms, in the range of their reference circle diameters $d_{ocw} = (16..22)P_t / \pi$ and helical part lengths $l_m = 6P_t$, the calculation results of the main parameters of blanks and allowances are shown in Table 7.4.

These errors are an allowance for the machining of hyperboloid main worms.

Milling cutters being limited up to four threads is due to the fact that when performing about 50 teeth per revolution, the number of teeth per thread is $50/4 \approx 12$, which is the limit for lobbing when machining gears with a high degree of accuracy. However, unlike the existing four-thread worm tools, the proposed ones are accurate, which provides their main advantage.

For milling cutters with a large number of teeth, for example 90, an increase in the number of threads to 7 is possible. However, for machining their bodies with a helix angle of $\omega_\omega > 12^\circ$, modernization of turning, hydroscopy, thread milling, and thread grinding machines is required, which ensures their support tilt angle ω_ω according to the patent [44]. An example of such a design of a thread grinding machine is shown in Fig. 7.21.

However, the disadvantages of such machine upgrades are as follows:

1. high complexity of their implementation,
2. in some cases, a decrease in the size of working area,
3. a certain decrease in rigidity and accuracy due to the introduction of additional machine elements. Their design, creation, and final conditioning will require significant investment of time and money. Therefore, at the first stage, it makes sense to apply the process with the displacement of the centers and rest content with 3- to 4-thread gear cutting tools.

For CNC lathes, the support upgrading is possible due to the installation of a lifting part with an individual drive 2 on it, which is connected to the drive 1 of the horizontal support motions of the through the synchronizer 3 when the carriage with the tool. Holder tool turns at the angle of the worm threads (Fig. 7.22).

Table 7.4 The main parameters of hyperboloid worms and allowances for their processing with a displacement of the back center

Starting diameters, mm d_{ohws} (mm), d_{ahws} (mm), d_{fhw} (mm),	Amount of thread of main worm z_w and angle of its elevation ω_w , (degrees)	The final diameter of the pitch circle, mm d_{ohwf} (mm)	The final diameter of the protrusion of circles d_{ahwf} (mm),	The final diameter of the trough of circles d_{fhwf} (mm),	Maximum the increase in outer diameter Δ_{ad} (μm),	Maximum the thickness increase of the turns per side Δ_{op} (μm),
$P_t/\pi = 3$ mm, outer diameter 112 mm, screw length of parts $l_e = 102$ mm, type ZN ₁ , amount of thread $z_w=1 \dots 4$						
103.0, 110.5, 95.5,	$z_w = 1,$ $\omega_w = 1^\circ 40'$	103.013	110.513	95.513	13	2.2
	$z_w = 2,$ $\omega_w = 3^\circ 20'$	103.052	110.552	95.552	52	8.9
	$z_w = 3,$ $\omega_w = 5^\circ 00'$	103.116	110.616	95.616	116	20.0
	$z_w = 4,$ $\omega_w = 6^\circ 39'$	103.206	110.706	95.706	206	35.2
$P_t/\pi = 5$ mm, outer diameter 140 mm, screw length of parts $l_e = 130$ mm, type ZN ₁ , amount of thread $z_w=1 \dots 4$						
125.5, 138.0, 113.0,	$z_w = 1,$ $\omega_w = 2^\circ 17'$	125.527	138.027	113.027	27	4.6
	$z_w = 2,$ $\omega_w = 4^\circ 33'$	125.607	138.107	113.107	107	18.3
	$z_w = 3,$ $\omega_w = 6^\circ 49'$	125.740	138.240	113.240	240	41.0
	$z_w = 4,$ $\omega_w = 9^\circ 03'$	125.927	138.427	113.427	427	73.0
$P_t/\pi = 8$ mm, outer diameter 180 mm, screw length of parts $l_e = 163$ mm, type ZN ₁ , amount of thread $z_w=1 \dots 4$						
157.0, 177.0, 137.0,	$z_w = 1,$ $\omega_w = 2^\circ 55'$	157.055	177.055	137.055	55	9.4
	$z_w = 2,$ $\omega_w = 5^\circ 49'$	157.220	177.220	137.220	220	37.6
	$z_w = 3,$ $\omega_w = 8^\circ 41'$	157.494	177.494	137.494	497	85.0
	$z_w = 4,$ $\omega_w = 11^\circ 31'$	157.876	177.876	137.876	876	149.8
$P_t/\pi = 10$ mm, outer diameter 180 mm, screw length of parts $l_e = 168$ mm, type ZN ₁ , amount of thread $z_w=1 \dots 4$						
152.0, 177.0, 127.0,	$z_w = 1,$ $\omega_w = 3^\circ 46'$	152.100	177.100	127.100	100	17.1
	$z_w = 2,$ $\omega_w = 7^\circ 30'$	152.401	177.401	127.401	401	68.6
	$z_w = 3,$ $\omega_w = 11^\circ 10'$	152.901	177.901	127.901	901	154.1
	$z_w = 4,$ $\omega_w = 14^\circ 44'$	153.598	178.598	128.598	1598	273.6

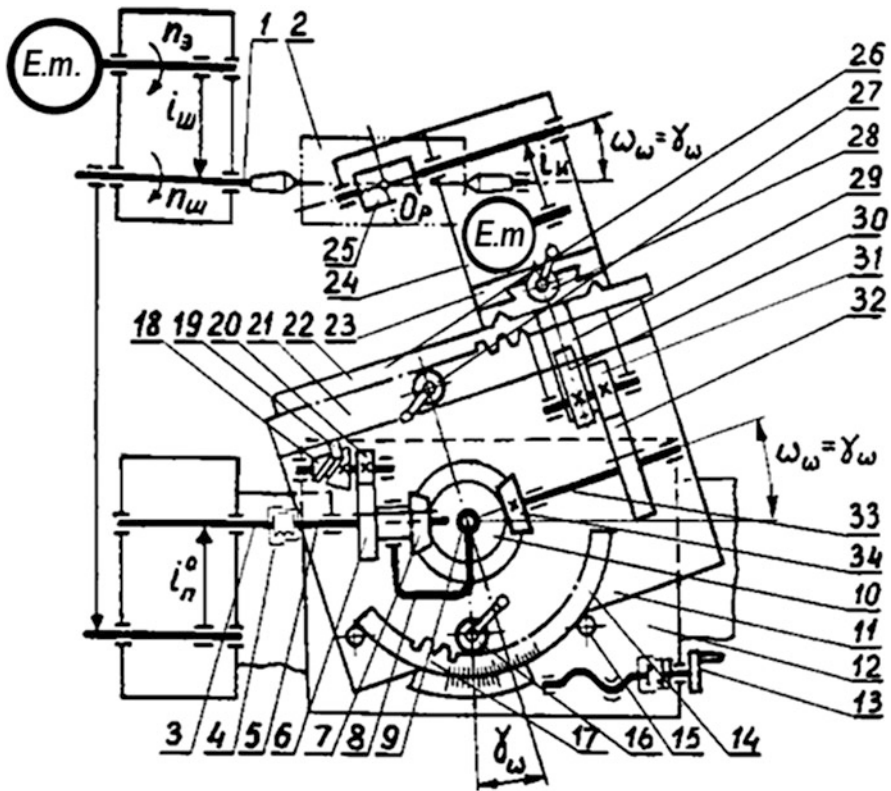


Fig. 7.21 The project of upgrading a thread grinding machine for processing hyperboloid worms

When replacing the tool holder with a grinding head with an individual drive for grinding wheel rotation, it is possible to use this machine to grind the profile of worm turns and grooves for installing cutting plates.

Among existing CNC machines, such are already available. Therefore, a real opportunity is created for the manufacture of high-precision hyperboloid worms and grinding wheels with any number of threads.

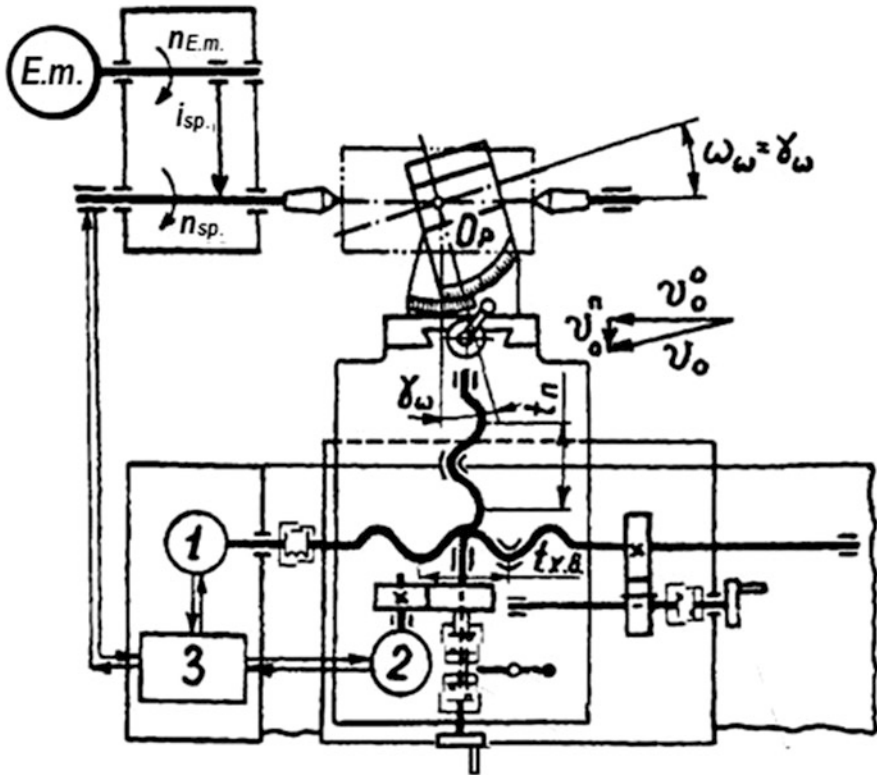


Fig. 7.22 Project of upgrading a CNC lathe for processing hyperboloid worms

7.2 Concluding Remarks

1. Worm gearing provides a sufficiently high accuracy and performance with relative simplicity, low cost, and widespread occurrence of equipment and tools, so it is a prospect for use in the coming 10–20 years, which requires their improvement.
2. The main goal of improving worm gear cutting tools (hobs and shaver) is to increase their accuracy, wear resistance, and productivity, as well as their use for processing gears of the third and higher degrees of accuracy.
3. The most effective way to increase the accuracy, wear resistance, and performance of worm gear tools is the transition to hyperboloid multiple-thread multi-tooth designs equipped with disposable carbide plates.
4. The designs of high-precision high-performance finishing hobs, worm shavers and worm grinding wheels, as well as methods and equipment for their manufacture are justified and proposed.

5. Proposed prefabricated multiple-thread and multi-tooth designs of finishing hyperboloidal hobs-worm shavers equipped with turning cutting hard alloy plates, which eliminate the need for these tools regrinding during their exploitation, are recognized as the most effective.
6. The proposed cutting plates provide the ability to generate optimal geometry of the cutting wedge and the shape of the working surfaces, which significantly increases their durability.
7. Complexity and cost of manufacturing the proposed tools increase significantly; however, they are compensated by an increase in productivity and accuracy of gear teeth machining.
8. Manufacturing of the proposed tools greatly simplifies the proposed equipment and machines, which requires further development and improvement.
9. The combination of the above data allows recommending further development, extensive research and implementation of the proposed worm gear cutting tools.
10. The final decision on the use of the proposed tools requires solving expenses optimization issues and the profit being obtained.

References

1. Uskov M.K., Parkhomenko A.A. (1980) Razvitiye teorii i praktiki sovetskogo mashinovedeniya. [The development of the theory and practice of Soviet mechanical engineering] M. Nauka. 191 S. [Russia].
2. Zubchatyye peredachi. (2016) Normativnoye obespecheniye tochnosti zubchatykh peredach na etape proyektirovaniya. [Gears. Regulatory support for gear accuracy at the designing stage] / Antonyuk i dr. Minsk. Izd-vo Belarusskaya nauka. 251 S. [Belarus].
3. Vereshchaka A.S., Tretyakov I.P. (1986) Rezhushchiye instrumenty s iznosostoykimi pokrytiyami. [Cutting tools with wear-resistant coatings] M. Mashinostroyeniye. 192 S. [Russia].
4. Kharlampiyev I.S. (1981) Obkativayushcheye protyagivaniye zub'yev zubchatykh koles. [Generating broaching of gear teeth] M. Mashinostroyeniye. 211 S. [Russia].
5. Proizvodstvo zubchatykh koles: Spravochnik (1990) [Gear manufacturing: Handbook] /S.N. Kalashnikov, A.S.Kalashnikov, G.I.Kogan i dr .; Pod obshch. red. B.A. Tayets. M. Mashinostroyeniye. 464 S. [Russia].
6. Radzevich S.P. Vinokurov I.V. (1996) Optimal'noye formoobrazovaniye vintovykh poverkhnostey postoyannogo shaga diskovogo ob'yekta. [Optimal shaping of the constant pitch helical surfaces with a disk tool] / Sovremennyye problemy mashinostroyeniya i tekhnicheskij progress. Mezhdunar. nauch.-tekhn. konf. Donetsk: DonGTU. S.191-192. [Ukraine].
7. Ternyuk N.E. (1983) Osnovy kompleksnoy optimizatsii sistem dlya proizvodstva zubchatykh koles. [Fundamentals of the comprehensive optimization of gear manufacturing systems] Dissertatsiya na soiskaniye uchenoy stepeni doktora tekhnicheskikh nauk. Khar'kov. 1983. 428 S. [Ukraine].
8. Nastasenko V.A. (1999) Development of perspective designs of worm teeth cutting tools and methods of their designing. //4th World Congress on Gearing and Power Transmission Paris, France: M.C.I. T1. P. 507-514.
9. Nastasenko V.A. (2002) Novomu pokoleniyu chervyachnykh frez novoye pokoleniye zubofreznykh stankov. [The new generation of worm milling cutters the new generation of gear milling machines] // Mashinostroyeniye i tekhnosfera XXI veka. Sb. trudov IKH

- Mezhdunar. nauch.-tekhn. konf. v g. Sevastopole. Donetsk, DonGTU, T2. –S. 164-169. [Ukraine].
10. Nastasenko V.A. (1994) Primeneniye sistemnykh metodov dlya povysheniya urovnya resheniy pri proyektirovaniy zuboreznykh instrumentov. [The use of systemic methods to increase the decision level in the design of gear cutting tools] // *Novyye tekhnologii i sistemy obrabotki v mashinostroyeniye. Mezhhregion. nauch.-tekhn. konf. Donetsk, DonGTU. S. 94-95.* [Ukraine].
 11. Spravochnik instrumental'shchika (1987) [Toolmaker handbook] /I.A.Ordinartsev, G.V. Filippov, A.I.Shevchenko i dr. Pod obshch. red. I.A.Ordinartseva. L. Mashinostroyeniye. 846 S. [Russia].
 12. Nastasenko V.A. (2001) Novaya kontseptsiya povysheniya tochnosti chervyachnykh zuboreznykh instrumentov. [A new concept for improving the accuracy of worm gear cutting tools] // *Progressivnyye tekhnologii i sistemy mashinostroyeniya. - Mezhdunar. sb. nauchnykh trudov.– Donetsk: DonGTU, Vyp. 17. S.109-114.* [Ukraine].
 13. Radzevich, S.P., *Theory of Gearing: Kinematics, Geometry, and Synthesis*, 2nd Edition, revised and expanded, CRC Press, Boca Raton, FL, 2018, 934 pages. [1st edition: Radzevich, S.P., *Theory of Gearing: Kinematics, Geometry, and Synthesis*, CRC Press, Boca Raton, Florida, 2012, 743 pages].
 14. Tsepkov A.V. (1979) Profilirovaniye zatylnykh instrumentov. [Profiling of backed tools] M. Mashinostroyeniye. 150 S. [Russia].
 15. Inozemtsev G.G. (1961) Chervyachnyye frezy s ratsional'nymi geometricheskimi i konstruktivnymi parametrami. [Worm milling cutters with rational geometric and design parameters] Saratov: Izd-vo Saratov. un-ta. 224 S. [Russia].
 16. Rodin P.R. *Metallorzhushchiye instrumenty.* (1979) [Metal cutting tools] 2-ye izd., Pererab. i dop. K. Vishcha shkola. 432 S. [Ukraine].
 17. Lashnev S.I. (1971) Formoobrazovaniye zubchatykh detaley reyechnymi i chervyachnymi instrumentami. [Geometry generation of gear parts with rack and worm tools] M. Mashinostroyeniye. 212 S. [Russia].
 18. Kirsanov G.N. (1977) Ploskostnoy metod tochnogo profilirovaniya instrumentov dlya obrabotki vintovykh poverkhnostey. [Planar method for accurate profiling of worm type tools for machining helical surfaces] / *Metallorzhushchiy i kontrol'no-izmeritel'nyy instrument. Ekspres-inform. NIImash. M. Vyp. 3. 26 S.* [Russia].
 19. Rodin P.R., Klimov V.I., Yakubson S.B. (1983) Tekhnologiya izgotovleniya zuboreznoho instrumenta. [Manufacturing technology of gear cutting tools] K. Tekhnika. 208 S. [Ukraine].
 20. Radzevich S.P. (1989) Mnogokoordinatnoye formoobrazovaniye poverkhnostey na stankakh s CHPU. [Multi-axis surface shaping on CNC machines] // *Modelirovaniye sistem, raschet elementov, formoobrazovaniye poverkhnostey, zashchitnyye pokrytiya i novoye oborudovaniye v mashinostroyeniye / Ye.I.Zhukovskiy, P.P.Lizunov, A.P.Zhukovets i dr. K. Vishcha shk. S. 200-254.* [Ukraine].
 21. Al'tshuller G.S. (1973) Algoritmn izobreteniya. [Invention Algorithmus] M. Moskovskiy rabochiy. 296 S. [Russia].
 22. Nastasenko V.A. (2003) Kompleksnaya otsenka putey povysheniya proizvoditel'nosti chervyachnykh frez. [Comprehensive assessment of ways to increase the productivity of worm milling cutters] // *Mashinostroyeniye i tekhnosfera XXI veka. Sb. trudov KH Mezhdunar. nauch.-tekhn. konf. v g. Sevastopole. Donetsk, DonGTU, T3. S. 290-297.* [Ukraine].
 23. Obshchemashinostroitel'nyye normativy rezhimov rezaniya dlya tekhnicheskikh normiruyushchikh rabot na metallorzhushchikh stankakh. CH.2. Zuboreznyye, gorizonta'l'no-rastitel'nyye, rez'bonakatnyye i otreznyye stanki. (1974) [General engineering standards of cutting conditions for the technical regulation of works on metal-cutting machines. Part 2. Gear cutting, horizontal boring, thread rolling and cutoff machines] M. Mashinostroyeniye. 200 s. [Russia].
 24. Spravochnik tekhnologa-mashinostroitelya (1985) [Guide book for a technologist-mechanical engineer] /V.B.Borisov, Ye.I. Borisov, V.N.Vasil'yev i dr. Pod red. A.G.Kosilovoy i R.K. Meshcheryakova. M. Mashinostroyeniye. 655 S. [Russia].

25. Mammano B. (1961) Perche le dentatrici a creator dovrebbero essere abbandonate // *Ingenieria meccanica*. T.10. №12. P. 23-39. [Italy].
26. Snegirev A.I. (1986) K voprosu o proizvoditel'nosti zubofrezerovaniya mnogozakhodnymi chervyachnymi frezami. [On the issue of gear milling performance with multiple-thread worm milling cutters] // *Tochnost' i proizvoditel'nost' zuboobrabatyvayushchikh stankov i instrumentov*. Mezhvuz. nauch. sb. Saratov: SPI. S. 3-9. [Russia].
27. Snegirev A.I. (1992) Analiz vozmozhnostey povysheniya proizvoditel'nosti zubofrezerovaniya uvelichivayet chislo zakhodyashchikh frezy [Analysis of the possibility of increasing the productivity of gear milling by increasing the number of milling cutter threads] // *Vestnik mashinostroyeniya*. №1. S.39-40. [Russia].
28. Nastasenko V.A. (1996) Dopolnitel'nyy analiz vozmozhnostey povysheniya proizvoditel'nosti zubofrezerovaniya uvelichivayet chislo zakhodyashchikh frezy. [Additional analysis of the possibility of increasing the productivity of gear milling by increasing the number of milling cutter threads.] / *Vestnik mashinostroyeniya*. №1. S.38-40. [Russia].
29. Mikhaylov A.N. (2009) Osnovy sinteza funktsional'no-orientirovannykh tekhnologii mashinostroyeniya [Fundamentals of the synthesis of functionally oriented engineering technologies]. Donetsk: DonNTU, 2009. 346 S. [Ukraine].
30. Malkin A.YA. (1940) Opredeleniye proizvoditel'nykh rezhimov rezaniya pri zubonarezanii. [Determination of productive cutting conditions during gear cutting] Khar'kov. 35 S. [Ukraine].
31. Bobrov V.F. (1975) Osnovy teorii rezaniya metallov. [Fundamentals of the theory of metal cutting] - M. Mashinostroyeniye. 344 S. [Russia].
32. Nastasenko V.A. (2000) Otsenka proizvoditel'nosti odnozakhodnykh i mnogozakhodnykh chervyachnykh frez v usloviyakh povysheniya rezhushchikh svoystv. [Evaluation of the performance of single-thread and multiple-thread worm milling cutters under conditions of improving cutting properties] // *Sovremennyye problemy i metodologiya proyektirovaniya i proizvodstva silovykh zubchatykh peredach*: Sb. nauch. trudy. –Tula: TGU. S. 148-151. [Russia].
33. Polovinkin A.I. (1988) Osnovy inzhenernogo tvorchestva. [Fundamentals of engineering creativity] –M. Mashinostroyeniye. 368 S. [Russia].
34. Nastasenko V.A. (2000) Chervyachnyye frezy novogo vida i ikh SAPR. [Worm milling cutters of a new type and their CAD] // *Vestnik mashinostroyeniya*. № 8. S. 28-32. [Russia].
35. Patent (2003) Rossiyskoy Federatsii na izobreteniyе № 2147496. MPK B23 F 21/16. Sbornyaz chervyachnaya freza. [Prefabricated worm cutter] Zayavka № 98104494/02 ot 10.01.98. Avt. izobr. Nastasenko V.A. // *BI* 2003. № 11 ot 20.04.2000. [Russia].
36. Nastasenko V.A. (2001) Zubonarezaniye mnogozakhodnymi chervyachnymi frezami kak al'ternativa zuboprotyagivaniyu. [Gearing with multiple-thread worm milling cutters as an alternative to gear broaching] // *STIN*. №1. S. 27-31. [Russia].
37. Nastasenko V.A. (2015) Novyy vid tverdospaynykh pruzhinno-plastinchatykh chervyachnykh sheverov i vozmozhnosti ikh izgotovleniya. [A new type of hard-alloy spring-plate worm shavers and the possibilities for their manufacturing] Seriya «Problemi mekhanichnogo privodu». Khar'kiv, № 34 (1143) S. 103-108. [Ukraine].
38. Nastasenko V.A. (1997) Chervyachnyye frezy XXI veka [Worm milling cutters of the XXI century] // *Progressivnyye tekhnologii mashinostroyeniya i sovremennost'*. Mezhdunar. nauch.-tekhn. konf. Sevastopol'- Donetsk: DonGTU. 1997. S. 176-177. [Ukraine].
39. Vitrenko A.N., Vitrenko V.A., Zuy B.S., Kirichenko I.A. Povysheniye kachestva izgotovleniya zub'yev pri obrabotke mnogozakhodnym sposobom. [Improving the quality of the gear manufacturing through machining with multiple-thread tools] / *Sovremennyye problemy mashinostroyeniya i tekhnicheskoy progress*. Mezhdunar. nauchno-tekhn. konf. Sevastopol'-Donetsk: DonGTU, 1996. -s. 41-42. [Ukraine].
40. Nastasenko V.A. (2012) Osnovnyye tipy giperboloidnykh sluzhb i sposoby ikh proizvodstva [The main types of hyperboloid worms and methods for their manufacturing] // *Progressivnyye tekhnologii i sistemy mashinostroyeniya: Mizhnarodniy zb. naukovikh prats'*. Donetsk: DonNTU, Vip. 44. S.181–188. [Ukraine].

41. Patent (2016) Rossiyskoy Federatsii na izobreteniyе № 2597933, MPK B 23 F 13/00. Sposob obrabotki giperboloidnykh chervyakov i chervyachnykh zuboreznykh instrumentov i ustroystva dlya ikh realizatsii [Method of processing hyperboloid worms and worm gear cutting tools and devices for their implementation] Zayavka № 2012138947/11 (063000) ot 11.09.12 Avt. izobr. Nastasenko V.A. // BI № 26 ot 20.09.2016. [Russia].
42. Nastasenko V.A., Podzolkov A.I. (2014) Povysheniye tekhnologichnosti izgotovleniya mnogozakhodnykh giperboloidnykh chervyachnykh instrumentov [Improving the manufacturability of multi-thread hyperboloid worm tools] // Vísnik natsíonal'nogo uníversitetu «KHPÍ». Seríya «Problemi mekhaníchnogo privodu». Kharkív,- № 31 (1074) S. 120-125. [Ukraine].
43. Nastasenko V.A. (2013) Analiz tochnosti i tekhnologichnosti izgotovleniya giperboloidnykh sistem s malym kolichestvom zakhodov [Analysis of the accuracy and manufacturability of hyperboloid worms with a small number of threads] // Progressivnyye tekhnologii i sistemy mashinostroyeniya: Mízhnarodniy zb. naukovich prats'. - Donets'k: DonNTU. Vip. 46. S.171–180. [Ukraine].
44. Patent (2003) Rossiyskoy Federatsii na izobreteniyе № 2200262. MPK V23 F 21/16. Chervyachnaya peredacha, sposob yeye izgotovleniya. [Worm gear, method of its manufacture, equipment and tools for its implementation] Zayavka № 98116838/28 ot 08.09.98. Avt. izobr. Nastasenko V.A. // BI 2003. № 7 ot 10.03.2003. [Russia].

Chapter 8

Optimal Selection of the Structural Scheme of Compound Two-Carrier Planetary Gear Trains and Their Parameters



Dimitar P. Karaivanov and Sanjin Troha

8.1 Introduction

8.1.1 Optimization of Planetary Gear Trains

8.1.1.1 General

The optimization of gear trains is a mandatory stage of the process of their design in order to increase their quality and reliability.

Gear trains are complex technical objects and their optimization can be done at different levels [1].

Meshing Optimization

There are quite detailed methods for optimizing the parameters of gear meshing; in some of them attention is paid to the design and in others to the technological factors.

In the design approach for optimization of the qualitative indicators of the meshing as an optimization criterion, the load capacity of the gears by contact stresses and bending stresses is most often used [2–7]. The influence of different geometrical parameters of the gearing is studied. In [8] a program for computer-oriented visual construction of gears is presented. The system allows optimization and creating a 3D model of the gear train in an environment of SolidWorks®.

D. P. Karaivanov (✉)

University of Chemical Technology and Metallurgy, Sofia, Sofia, Bulgaria

S. Troha

Faculty of Engineering, University of Rijeka, Rijeka, Croatia

e-mail: stroha@riteh.hr

In [9] the pitches of the gears are selected so that the gear is “accurate at nominal load,” which improves the contact of the tooth surfaces during operation.

Tooth modification is one of the most commonly used ways to increase the gears’ load capacity [10, 11] or to reduce vibration [12].

In [13] the emphasis is on the procedure for the selection of the design parameters (number of teeth, module, tooth face width) in order to optimize the planetary gear trains.

In [1] a profound study of the influence of the addendum modification of spur involute teeth on the dynamic processes in the gear trains is made, and a methodology for determining the most favorable height addendum modification is proposed. It is found that the internal dynamic load in the addendum-modified gears ($h_a^* > 1$) is lower than in the standard ones, as the lowest values are obtained at the transverse contact ratio $\varepsilon_\alpha = \text{integer}$.

In addition to the load capacity, as an optimization criterion, the efficiency is also used [14]. The optimal values of the profile shift coefficients and the number of teeth of both gears are determined. In [15] a multi-objective optimization by efficiency, transverse contact ratio, pressure angle, relative sliding, and tooth form factor are made, and their influence on the generalized criterion is determined by weight coefficients.

Within the framework of the “X-Gear” Collective Research Project (COOL-CT-2006 030433) financed by the European Commission [16], a methodology for reducing the losses in the gearing with the help of optimizing the tooth geometry has been developed. Attention is paid to the improvement of the parameters of the microgeometry (profile shifting, addendum and tooth flank modifications, etc.) and small corrections of the macrogeometry (number of teeth, module, pressure angle, tooth face width, etc). The study is focused on cylindrical planetary gear trains with helical teeth for the automotive industry and wind turbines.

It should be borne in mind that in cylindrical planetary gear trains with spur gears, the efficiency is high enough to be worth optimizing the tooth geometry in order to reduce losses. This does not prevent the possibility of looking for a way to reduce the peripheral velocity of the gear wheels and the sliding velocity in the meshing. More details on tooth geometry optimizing to reduce meshing loss can be found in [17–19].

In the technological approach, the processing modes are optimized in terms of load capacity (maximum permissible contact and bending stresses).

In [20], the negative effect on load capacity from residual stresses after gear cutting is studied. Their size depends on the degree of wear of the tool and the number of teeth of the gear and the tool (shaper cutter). These stresses are minimized by appropriate selection of the parameters of the tool.

Some authors link the technology of gear manufacturing with the technological cost [21] or labor absorption [22, 23]. In this case, the required load capacity of the gearing is considered as a fulfilled condition for all variants of the technological process. The optimal option is sought by the criterion of minimum technological cost or labor absorption.

Gear Train Elements Optimization

The rim and the disk of a gear have a significant impact on the stresses in the teeth. In [24–26] dependencies are derived geometrically and experimentally to determine the optimal thickness of the gear rim, the further increase of which does not significantly reduce the stress in the critical section of the tooth.

Gear-shafts and shafts. The bending and torsional stiffness shall be selected so as to minimize the unevenness of the load in a meshing [27] or in the parallel meshings of split torque gear trains.

Housing. Deformation of the gearbox housing also affects the load distribution, especially in heavy-duty gearboxes, where reducing deformation by thickening the walls is unacceptably material-intensive. For this reason, it is necessary to optimize the shape of the body [28–30]. Significant attention is also paid to reducing noise emission [31].

Gear train arrangement. Total mass is a common optimization criterion [32, 33]. In most cases, the independent parameters are geometric dimensions. Klein [14] proposes a methodology for minimizing gear volume because it is directly proportional to production costs, as a criterion for determining the size of the gears and selected pitting stress limit.

To minimize the dynamic phenomena in the planetary gear trains, various compensating devices are studied [34, 35]. In non-planetary cylindrical gearboxes, resonant modes are avoided by varying the number of teeth [36].

In [1] a general methodology for optimization analysis of gearboxes with cylindrical and bevel gears is proposed on the basis of a technological-economic criterion, which takes into account the complex influence of the design, technological, and economic factors. Dependencies for determining the components of the technological and economic criterion for the main elements of the gearboxes—shafts, gears, housing, and bearings—in different design and technological variants are derived.

8.1.1.2 Optimization of Planetary Gear Trains Arrangement

The pursuit of finding the optimal solution is quite natural in the process of planetary gear trains (PGTs) design.

Based on the initial data in the design (speed ratio and input torque) can be sought different technical and economic *criteria* (target parameters) for optimization—minimum dimensions, minimum mass, minimum volume, maximum efficiency, minimum production costs, etc. The control *parameters* for optimization can be:

- Number of teeth of the sun gear (mostly).
- Profile shift coefficients.
- Material and processing of gears, etc.

In specific cases, only one of the abovementioned criteria (target parameters) can be decisive for the given arrangement and only through it the optimization may be performed.

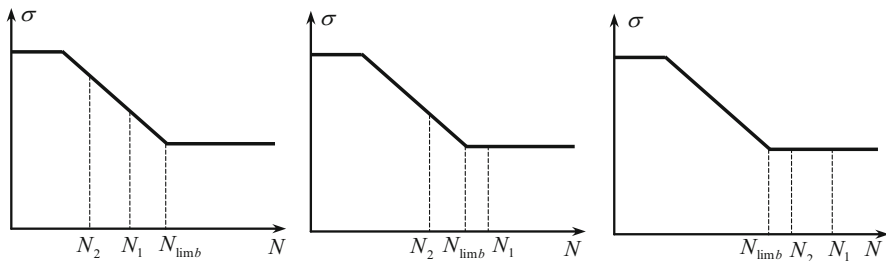


Fig. 8.1 Determination of the stress limit of sun gear 1 and planets 2 at different numbers of load cycles N_1 and N_2

In the general case, however, it is expedient to make optimization according to several criteria—multi-objective (multicriteria) optimization.

When setting the number of teeth in the optimization process, the specific limitations of the type of planetary gear—the conditions for mounting (assembly), coaxiality, and adjacency of the planets—must be taken into account, and keep in mind that these limitations can be avoided [27, 37].

One of the tendencies for PGTs optimizing is to achieve equal strength of the sun gear and planets. In this case, some specific characteristics of PGTs must be taken into account. For the most commonly used $\overline{\text{AI}}$ -PGT (with one external, one internal meshing, and an one-rim planet), these are:

- 1) In non-reversible PGTs, the teeth of the sun gear are loaded in one direction (pulsating loading), and the teeth of the planets are loaded in both directions (completely reversed loading). This fact must be taken into account when determining the bending stress limit (tooth root endurance limit) [27].
- 2) The number of load cycles of the sun gear teeth depends on the number of planets. Figure 8.1 shows the possible cases of the number of cycles N_1 and N_2 of sun gear 1 and planets 2 with respect to base number of cycles N_{limb} (at which long-life fatigue is reached—the knee of Wöhler curve). The number of cycles is determined by formulae known from the literature [27].

The characteristic for $\overline{\text{AI}}$ -PGT placement of all gears (sun gear and planets) inside the ring gear allows the optimization in size (and to a large extent in volume and mass) to be reduced to finding the minimum reference diameter of the ring gear. In this case, the load capacity of the external meshing is authoritative. Some authors accept sufficient to use the contact strength [14, 38], while others consider the bending strength too [23, 39–41].

In [23] a methodology for multi-objective Pareto optimization of $\overline{\text{AI}}$ -PGT by volume, efficiency, mass, and cost is proposed. The respective weight coefficients of the different parameters can be selected for each specific case. A minimum radial overall dimension (ring gear diameter), a maximum efficiency, and minimum clearances (backlash) are the criteria for the multi-objective Pareto optimization of a compound two-carrier PGT proposed in [42]. An arithmetic mean utility function is used.

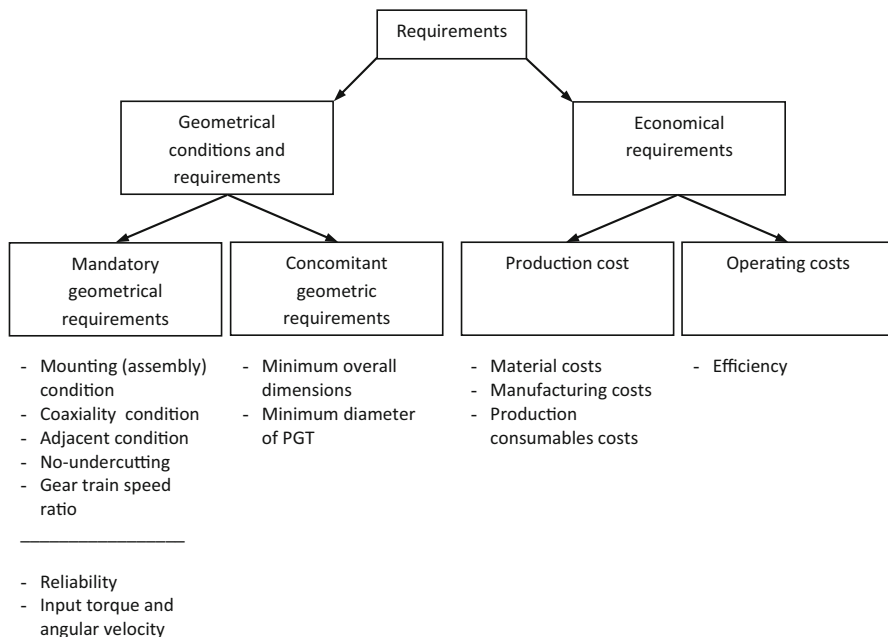


Fig. 8.2 Planetary gear train design requirements (Redrawn from [45])

It should be emphasized that in the multi-objective optimization, the convergence of the different criteria (factors) must be taken into account (Fig. 8.2). Especially at the \overline{AI} -PGT, it can be considered that when achieving a minimum radial dimension (ring gear diameter), minimum (or close to the minimum) mass and volume will be achieved. **At an engineering level, Pareto optimization can be reduced to two criteria—minimum ring gear diameter and maximum efficiency.** Some authors believe that efficiency of \overline{AI} -PGT with spur gears is high enough, and its inclusion in the optimization is only suitable for PGT with helical teeth [43].

It is worth mentioning some other more specialized work on the optimization of PGTs:

In [44] the optimization of the rim thickness of spur ring gear and planets of a simple PGT with high gear ratio is presented. The purpose of optimization is to minimize the total weight for a given power and to determine the minimum thickness of the rim of ring gear and planets. The methodology also allows to find the maximum value of the torque that the train can withstand at a given weight. A new design strategy for design, simulation, and optimization is applied to reduce weight and increase maximum transmitted torque. Tooth geometry is generated using a numerical procedure taking into account the modern manufacturing process. Accurate reproduction of working profiles and fillet curve allows for accurate calculation of contact and bending stresses. Based on a limited number of simulations, many design variants have been generated, and various optimization criteria have been implemented.

Brüser [45] uses multifactor optimization to find the optimal design-technological variant of a two-stage PGT. Fig. 18.3 shows the criteria that the designer must comply with. Of these, four have been selected for optimization purposes—housing diameter, overall dimension, production cost of sun gear, and efficiency. The arithmetic mean utility function is used.

Engineering aspects of PGTs optimization can be found in [27], and more specialized information in [13, 23, 32, 42, 46–51].

8.1.1.3 Optimization as an Element of the Structural Analysis of Planetary Gear Trains

The first step in PGTs design is choosing a structural scheme. Even with this choice, the necessary conditions for obtaining an optimal arrangement must be set. Due to the great variety of PGTs types, in their study it is appropriate to use some structural symbol representing the gear train (regardless of its arrangement) and the external shafts coming out of it. The most convenient is the representation of a simple PGT through the structural symbol of Wolf-Arnaudov. The gear train is represented by a circle, and the three external shafts—with different thickness lines, depending on the size of their torques (this avoids the need to inscribe them, which facilitates the perception of the symbol and reduces the risk of technical errors). Figure 8.3 shows the structural symbol of the most commonly used simple (single-carrier) PGT (AI according to [27, 52] or 2 K-H according to Kudryavtsev [27]). In this type of PGT, the torque of the sun gear is the smallest, the torque of the ring gear is greater, and that of the carrier is equal to their sum and is in the opposite direction [27]. This ratio is reflected in the shaft thicknesses on the structural symbol. Other simple (single-carrier) PGTs can also be successfully represented with this structural symbol, but not in all of them the carrier is with the biggest torque [27].

In the *structural analysis* the possibilities for joining several simple (single-carrier) PGTs in a compound (multi-carrier) one are investigated, and in the *optimization* the most suitable combination and its parameters are sought.

In Fig. 8.4 the possible ways of forming a compound two-carrier PGT are shown. In Fig. 8.4a the compound PGT has two single (external) shafts and two compound (one external and one internal) shafts.

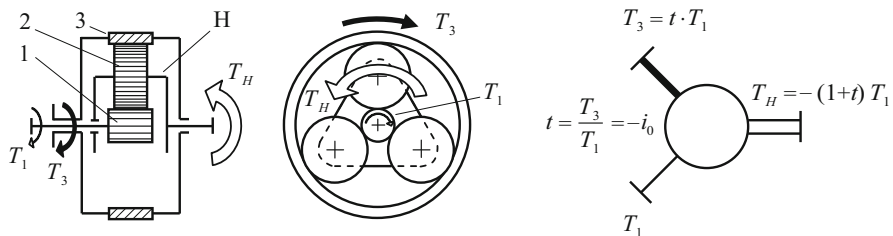


Fig. 8.3 The most common type of simple single-carrier PGT, torques at its central elements, and Wolf-Arnaudov’s symbol (1, sun gear; 2, planets; 3, ring gear; H, carrier)

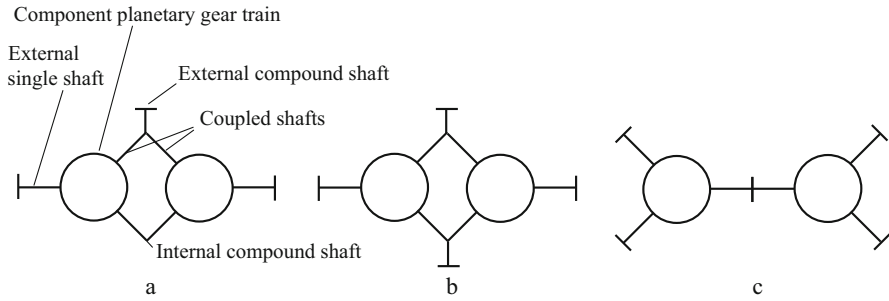


Fig. 8.4 Types of compound two-carrier PGTs: (a) With three external (two single and one compound) shafts. (b) With four external (two single and two compound) shafts. (c) With four external (single) and one internal (compound) shafts

Table 8.1 Possible ways of connecting the two component single-carrier PGTs in a compound two-carrier PGT according to Fig. 8.4a (with three external shafts)

	...1	...2	...3	...4	...5	...6
1...	11	12	13	14	15	16
2...	21 = 12	22	23	24	25	26
3...	31 = 13	32 = 23	33	34	35	36
4...	41 = 14	42 = 24	43 = 34	44	45	46
5...	51 = 15	52 = 25	53 = 35	54 = 45	55	56
6...	61 = 16	62 = 26	63 = 36	64 = 46	65 = 56	66

In the compound PGT in Fig. 8.4b all four shafts (two single and two compound) are external. The PGT in Fig. 8.4c is with four external (single) shafts and one internal (compound) shaft.

Each of the coupled shafts can be with one of the three torques (and for the \overline{AI} -PGT from Fig. 8.3 each of them can be a sun gear, a ring gear, or a carrier). In the first case (Fig. 8.4a) 36 combinations are possible (Table 8.1), 21 of which are

Table 8.2 Possible ways of connecting the two component single-carrier PGTs in a compound two-carrier PGT according to Fig. 8.4b (with four external shafts—two single and two compound)

	...1	...2	...3	...4	...5	...6
1...	11 ≡ 22	12	13 ≡ 24	14 ≡ 23	15 ≡ 26	16 ≡ 25
2...	21 ≡ 12	22 ≡ 11	23 ≡ 14	24 ≡ 13	25 ≡ 16	26 ≡ 15
3...	31 ≡ 13	32 ≡ 23	33 ≡ 44	34	35 ≡ 46	36 ≡ 45
4...	41 ≡ 14	42 ≡ 24	43 ≡ 34	44 ≡ 33	45 ≡ 36	46 ≡ 35
5...	51 ≡ 15	52 ≡ 25	53 ≡ 35	54 ≡ 45	55 ≡ 66	56
6...	61 ≡ 16	62 ≡ 26	63 ≡ 36	64 ≡ 46	65 ≡ 56	66 ≡ 55

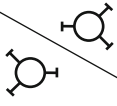
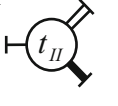
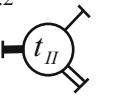
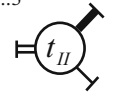
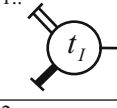
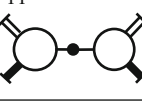
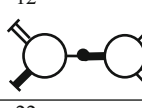
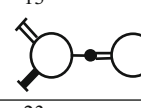
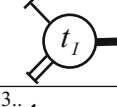
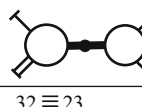
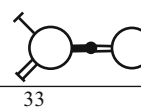
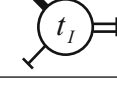
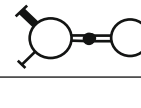
different (non-repeating) [27, 53, 54]. In the second case (Fig. 8.4b) of the 36 combinations (Table 8.2) only 12 are different (non-repeating) [27, 49, 53], and in the third case (Figure 8.4c) the different (non-repeating) schemes are only 6 [27, 53] (Table 8.3).

The main design parameter of the \overline{AI} -PGT (Fig. 8.3) is the ratio of the number of teeth of ring gear z_3 to the number of teeth of sun gear z_1 , on which ratio depends the basic speed ratio of the gear train with a fixed carrier i_0 . The basic efficiency also largely depends on this number of teeth [55–57] as well as the PGT overall dimensions (respectively, volume, mass, material consumption, and labor costs).

Generally speaking, the purpose of optimization can be to choose the structural scheme and its parameters (basic speed ratios of the component PGTs) in which the desired speed ratio is achieved with the best combination of several criteria (e.g., minimum dimensions, maximum efficiency, etc.). After this choice it is possible to proceed to optimization of the arrangement according to other parameters (e.g., the ones listed in Sect. 8.1.1.1).

There are many more combinations for three- and four-carrier PGTs, but the approach discussed in this chapter can be applied to them as well.

Table 8.3 Possible ways of connecting the two component single-carrier PGTs in a compound two-carrier PGT according to Figure 8.4c (with four single external shafts)

	..1 	..2 	..3 
1.. 	11 	12 	13 
2.. 	21 ≡ 12	22 	23 
3.. 	31 ≡ 13	32 ≡ 23	33 

8.1.2 Torque Method: An Easy Way for Planetary Gear Train Analysis

The optimization approaches proposed in this chapter are based on the torque method [27, 58]. This simple and practical method allows easy and very clear determination of the speed ratio and the efficiency. It is very appropriate for investigation of complex compound PGTs [59] as well as for optimization procedures.

The torques on the three external shafts of \overline{AI} -PGT are depicted in Fig. 8.3. They are in a strictly defined ratio, no matter what the operating mode of the gear trains is—with 1 degree of freedom (as a reducer or a multiplier) or with 2 degrees of freedom (as a division or a summation differential).

When the losses are disregarded, i.e., efficiency $\eta_0 = \eta_{13(H)} = \eta_{31(H)} = 1$, this ratio is as follows:

$$T_1 : T_3 : T_H = T_{D\min} : T_{D\max} : T_\Sigma = T_1 : t \cdot T_1 : -(1 + t)T_1 = +1 : +t : -(1 + t) \tag{8.1}$$

where:

- $T_1 \equiv T_{D\min}$ is the ideal torque on the sun gear.
- $T_3 \equiv T_{D\max}$ is the ideal torque on the ring gear.
- $T_H \equiv T_\Sigma$ is the ideal torque on the carrier.

$$t = \frac{T_3}{T_1} = \frac{T_{D \max}}{T_{D \min}} = \left| \frac{z_3}{z_1} \right| > +1 \quad (8.2)$$

is the *torque ratio* of the gear train

$\eta_0 = \eta_{13(H)} = \eta_{31(H)}$ is the basic efficiency of the PGT (with fixed carrier).

These three ideal torques are in equilibrium

$$T_1 + T_3 + T_H = T_{D \min} + T_{D \max} + T_\Sigma = 0. \quad (8.3)$$

Knowing the ideal torques on the shafts and considering which of them is input (with torque T_A and angular velocity ω_A) and output (with torque T_B and angular velocity ω_B) from the equilibrium of the ideal input and output powers

$$P_A + P_B = T_A \cdot \omega_A + T_B \cdot \omega_B = 0, \quad (8.4)$$

the gear train speed ratio (kinematic ratio) is obtained as follows:

$$i_k = \frac{\omega_A}{\omega_B} = -\frac{T_B}{T_A}. \quad (8.5)$$

When the losses are considered, i.e., the basic efficiency $\eta_0 = \eta_{13(H)} = \eta_{31(H)} < 1$, the real torques $T'_1 \equiv T'_{D \min}$, $T'_3 \equiv T'_{D \max}$, and $T'_H \equiv T'_\Sigma$ can be determined as a function of torque ratio t and basic efficiency η_0 of the PGT [27]. From the equilibrium of the real input and output powers

$$\Sigma P = P_A \cdot \eta + P_B = \eta \cdot T'_A \cdot \omega_A + T'_B \cdot \omega_B = 0 \quad (8.6)$$

the efficiency can be obtained:

$$\eta = -\frac{P_B}{P_A} = -\frac{T'_B \cdot \omega_B}{T'_A \cdot \omega_A} = -\frac{\frac{T'_B}{T'_A}}{\frac{\omega_B}{\omega_A}} = -\frac{i_T}{i_k}, \quad (8.7)$$

where:

$$i_T = \frac{T'_B}{T'_A} \quad (8.8)$$

is the so-called *torque transformation (torque transmit ratio)*.

Considering formula (8.5) at last the efficiency can be obtained by torques

$$\eta = -\frac{i_T}{i_k} = \frac{\frac{T'_B}{T'_A}}{\frac{T_B}{T_A}}. \quad (8.9)$$

Formulae (8.5) and (8.9) are very useful for optimization analysis of PGTs.

8.2 Optimal Selection of the Structural Scheme of Compound Two-Carrier Planetary Gear Trains with Three External Shafts

8.2.1 Possible Structural Schemes

Each simple PGT (with the exception of some specific types, such as uncoaxial (open) ones [27]) has three external shafts and is conveniently represented by the Wolf-Arnaudov structural symbol (Fig. 8.3). As mentioned in Sect. 8.1.1.3, depending on the way the three outer shafts of the two assembling gears are connected, 36 combinations are possible, 21 of which are non-repeating (Table 8.1.). From the various features and possibilities provided by the structural Schemes [27], for the purposes of optimization, the following will be considered here:

1. As well as the simple PGT, the compound one has three external shafts with different torques, two of which (the smaller $T_{D\min}$ and the bigger $T_{D\max}$) are unidirectional, and the torque of the third shaft T_{Σ} is opposite, equal to the sum of the other two torques $|T_{\Sigma}| = T_{D\min} + T_{D\max}$.
2. Between the torques on the three external shafts, there are the same dependencies as in the simple PGT

$$\Sigma T_i = T_{D\min} + T_{D\max} + T_{\Sigma} = 0 \text{ and } T_{D\min} < T_{D\max} < |T_{\Sigma}| \quad (8.10)$$

regardless of how the PGT works:

- With one ($F = 1$) or two ($F = 2$) degrees of freedom.
- Which is the fixed element at $F = 1$.
- What is the direction of power flow, i.e., whether the gear train operates as a reducer or multiplier at $F = 1$ or as a summation or division differential at $F = 2$.

3) Similar to simple PGT, it is convenient to define a torque ratio (the ratio of unidirectional torques $T_{D\min}$ and $T_{D\max}$), which can be called an *aligned (reduced) torque ratio* and which depends on the torque ratios t_I and t_{II} of the component PGTs

$$t_{red} = \frac{T_{D\max}}{T_{D\min}} = f(t_I, t_{II}) > 1. \quad (8.11)$$

It has been found that with this torque ratio, the speed ratios of the compound PGT for the six cases of operation with one degree of freedom ($F = 1$) are determined by the same formulae as in the simple PGT [27, 54].

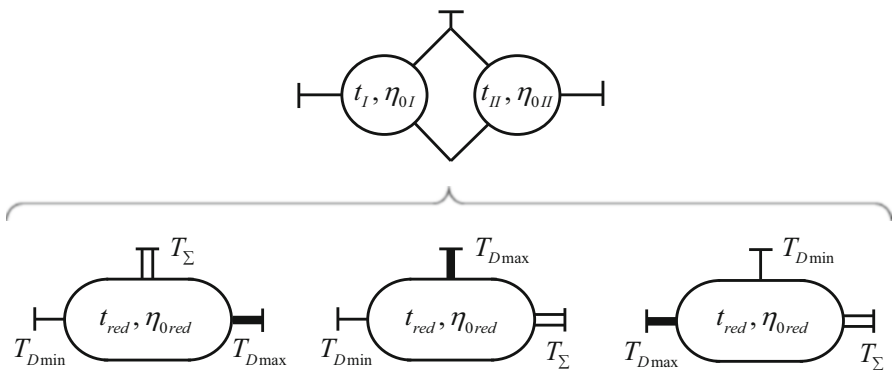


Fig. 8.5 Torques on the external shafts of compound PGTs from Table 8.1

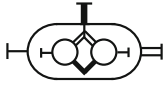
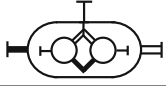
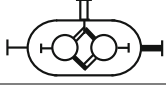
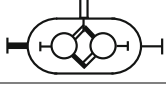
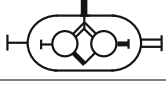
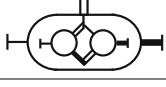
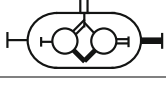
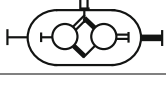
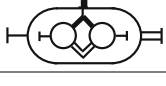
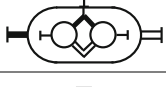
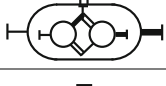
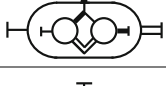

It follows from the above that when deriving formulae for $t_{red} = f(t_I, t_{II})$, for each of the structural schemes from Table 8.1, its kinematic capabilities (lower and upper limit of t_{red}) can be determined at given limits of t_I and t_{II} [54]. It should be borne in mind that in some of the structural schemes, depending on the size of the two torque ratios t_I and t_{II} , a different shaft has the least torque (T_{Dmin}), i.e., the shafts change their role in the gear, but the summation shaft (with $T_Σ$) remains the same (Fig. 8.5).

These formulae are shown in Table 8.4. Representing the dependencies in graphical form allows the designer to quickly find out which of the schemes is worth considering. Figure 8.6 shows, as an example, some of the most interesting cases.

A more detailed approach is also possible, in which the structural schemes for the six cases of operation of each PGT with $F = 1$ degree of freedom should be drawn. For the schemes from Table 8.1, it is convenient to use the designation of the input-output-(fixed) shafts with their position (according to the directions of the world) W-west (left), E-east (right), and N-north (top). For example, WE(N) means the left shaft, input; the right shaft, output; and the top shaft, fixed. These diagrams are shown in Appendix 8.1. For some schemes from the main diagonal of Table 8.1 (S11, S12, etc.) at $t_I = t_{II}$, an infinity for t_{red} is obtained ($t_{red} = ∞$ due to zero in the denominator). In this case the output shaft is immovable, and PGT is idling, i.e., the efficiency is equal to zero.

The first step of any optimization is to select the structural schemes that may provide the required speed ratio, i.e., they should have the appropriate t_{red} , and to apply the optimization procedure to them. By varying t_I and t_{II} , the plurality of combinations thereof are obtained in which the PGT can achieve the desired aligned torque ratio t_{red} . Optimization procedures are applied to this set, and the most appropriate combination of one or more criteria is sought.

Table 8.4 Determination of the aligned torque ratio t_{red} of structural schemes from Table 8.1 as a function of the torque ratios of the component PGTs t_I and t_{II}

Scheme	t_I and t_{II}	Structural symbol	$t_{red} = f(t_I, t_{II})$
S11	$t_I \geq 2 t_{II}$		$\frac{t_I - t_{II}}{t_{II}}$
	$t_{II} \leq t_I \leq 2 t_{II}$		$\frac{t_{II}}{t_I - t_{II}}$
S12	$t_I \geq 1 + t_{II}$		$\frac{t_I}{1 + t_{II}}$
	$t_I \leq 1 + t_{II}$		$\frac{1 + t_{II}}{t_I}$
S13	For every t_I and t_{II}		$t_I \cdot t_{II} - 1$
S14	For every t_I and t_{II}		$\frac{t_I \cdot t_{II}}{1 + t_{II}}$
S15	For every t_I and t_{II}		$t_I + \frac{t_I}{t_{II}}$
S16	For every t_I and t_{II}		$t_I(1 + t_{II})$
S22	$t_I \geq 1 + 2 t_{II}$		$\frac{t_I - t_{II}}{1 + t_{II}}$
	$t_{II} \leq t_I \leq 1 + 2 t_{II}$		$\frac{1 + t_{II}}{t_I - t_{II}}$
S23	For every t_I and t_{II}		$(1 + t_I) t_{II}$
S24	$t_I \geq \frac{2 + t_{II}}{t_{II}}$		$\frac{t_I \cdot t_{II} - 1}{1 + t_{II}}$
	$t_I \leq \frac{2 + t_{II}}{t_{II}}$		$\frac{1 + t_{II}}{t_I \cdot t_{II} - 1}$

(continued)

Table 8.4 (continued)

Scheme	t_I and t_{II}	Structural symbol	$t_{red} = f(t_I, t_{II})$
S25	For every t_I and t_{II}		$\frac{1 + t_I + t_I \cdot t_{II}}{t_{II}}$
S26	For every t_I and t_{II}		$t_I + t_{II} + t_I \cdot t_{II}$
S33	$t_I \geq 2 t_{II}$		$\frac{t_I - t_{II}}{t_{II}}$
	$t_{II} \leq t_I \leq 2 t_{II}$		$\frac{t_{II}}{t_I - t_{II}}$
S34	For every t_I and t_{II}		$t_I + \frac{t_I}{t_{II}}$
S35	For every t_I and t_{II}		$\frac{t_I \cdot t_{II}}{1 + t_{II}}$
S36	$t_I \geq 1 + t_{II}$		$\frac{t_I}{1 + t_{II}}$
	$t_I \leq 1 + t_{II}$		$\frac{1 + t_{II}}{t_I}$
S44	$t_I \geq t_{II}$		$\frac{t_{II} + t_I \cdot t_{II}}{t_I - t_{II}}$
S45	$t_I \geq \frac{1+t_{II}}{t_{II}-1}$		$\frac{t_I \cdot t_{II}}{1 + t_I + t_{II}}$
	$t_I \leq \frac{1+t_{II}}{t_{II}-1}$		$\frac{1 + t_I + t_{II}}{t_I \cdot t_{II}}$
S46	For every t_I and t_{II}		$\frac{1 + t_{II} + t_I \cdot t_{II}}{t_I}$
S55	$t_I \geq t_{II}$		$\frac{t_{II} + t_I \cdot t_{II}}{t_I - t_{II}}$

(continued)

Table 8.4 (continued)

Scheme	t_I and t_{II}	Structural symbol	$t_{red} = f(t_I, t_{II})$
S56	$t_I \geq \frac{2}{t_{II}-1}$		$\frac{t_I \cdot t_{II} - 1}{1 + t_I}$
	$t_I \leq \frac{2}{t_{II}-1}$		$\frac{1 + t_I}{t_I \cdot t_{II} - 1}$
S66	$t_I \geq 1 + 2 t_{II}$		$\frac{t_I - t_{II}}{1 + t_{II}}$
	$t_{II} \leq t_I \leq 1 + 2 t_{II}$		$\frac{1 + t_{II}}{t_I - t_{II}}$

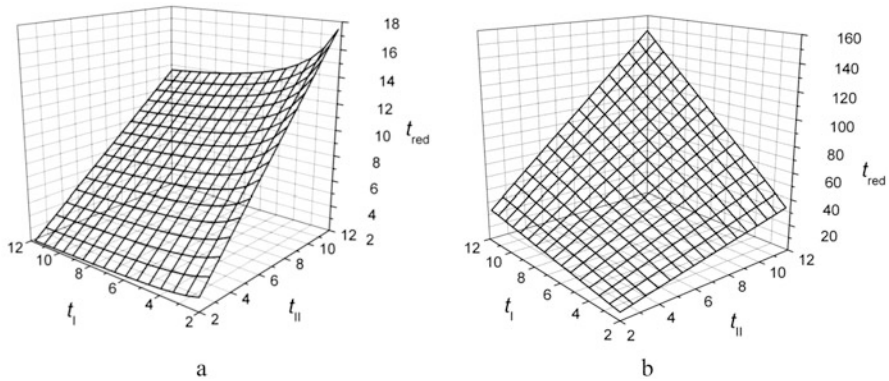


Fig. 8.6 Dependencies of t_{red} as a function of the torque ratios of the component PGTs t_I and t_{II} for several structural schemes from Tables 8.1 and 8.4: a, Scheme 15; b, Scheme 16

8.2.2 Optimization Criteria

8.2.2.1 Overall Dimensions

Compactness, one of the main advantages of PGTs, stems from both the power sharing between the planets and the fact that all the gears are located in the ring gear [27]. For this reason, for optimization purposes, it is very convenient to use the reference diameter of the ring gear as an optimization criterion for the overall PGT size.

From the load capacity of the external meshing (which is the weak point of the gear train), the smallest allowable diameter of sun gear d_1 can be determined. Practice shows that surface durability (pitting) is relevant in this case. At a torque

ratio $t = \frac{z_2}{z_1} > 3$, $z_2 > z_1$ is obtained. In this more common case, according to ISO 6336 [60] the diameter of sun gear 1 is determined as follows:

$$d_1 = \sqrt[3]{Z_H^2 \cdot Z_E^2 \cdot Z_\varepsilon^2 \cdot Z_\beta^2 \frac{2T_1}{k \left(\frac{b_H}{d_1}\right) \sigma_{HP}^2} \cdot \frac{u_{12} + 1}{u_{12}} K_A \cdot K_V \cdot K_{H\beta} \cdot K_{H\alpha} \cdot K_\gamma}, \quad (8.12)$$

where:

Z_H is the zone factor, which accounts for the influence on Hertzian pressure of tooth flank curvature at the pitch point and transforms the tangential load at the reference cylinder to normal load at the pitch cylinder.

Z_E is the elasticity factor, considering the influence of material properties—modulus of elasticity E and Poisson's ratio ν , $\sqrt{\frac{N}{\text{mm}^2}}$.

Z_ε is the contact ratio factor, considering the influence of sum length of contact line (virtual face width) because of double meshing, i.e., the influence of transverse contact ratio ε_α ($\varepsilon_\beta = 0!$)

T_1 is the torque on the sun gear 1.

k is the number of planets.

$\psi_{d1} = \frac{b_H}{d_1}$ is the face width ratio.

$u_{12} = \frac{z_2}{z_1}$ if $z_2 > z_1$, i.e., $t > 3$ (if $z_2 < z_1$, i.e., $t < 3$, the ratio $u_{21} = \frac{z_1}{z_2}$ must be used) is the teeth ratio of the external meshing.

K_A is the application factor, adjusting the nominal load F_t in order to compensate for incremental gear train loads from external sources.

K_V is the internal dynamic factor, accounting for the effects of gear tooth accuracy grade as related to speed and load. Considering meshing variable stiffness as parametric excitation too.

$K_{H\beta}$ is the face load factor, taking into account the effects of the non-uniform distribution of load over the gear face on the surface stress due to inaccuracies, deformations, and bearing clearances.

$K_{H\alpha}$ is the transverse load factor, considering the effect of the non-uniform distribution of transverse load between several pairs of simultaneous contacting gear teeth due to inaccuracies in the base pitch p_b (as well as deflection under load, profile modifications, etc.)

K_γ is the mesh load factor, considering uneven load distribution between planets due to the gears and carrier inaccuracies.

The permissible contact stress is determined as follows:

$$\sigma_{HP} = \frac{\sigma_{H \lim b} \cdot Z_{NT}}{S_{H \min}} Z_L \cdot Z_R \cdot Z_V \cdot Z_W \cdot Z_X, \quad (8.13)$$

where:

$\sigma_{H \lim b}$ is the allowable stress number—contact (pitting endurance limit).

$S_{H \min}$ is the minimum required safety factor (pitting).

Z_{NT} is the life factor for test gears for contact stress.

Z_L is the lubricant factor, which accounts for the influence of the lubricant viscosity.

Z_R is the roughness factor, which accounts for the surface roughness.

Z_v is the velocity factor, which accounts for the influence of pitch line velocity.

Z_W is the work hardening factor, which accounts for the effect of meshing with a surface hardened or similarly hard mating gear.

Z_X is the size factor, which accounts for the influence of the tooth dimensions for the permissible contact stress.

If $t = \frac{z_2}{z_1} < 3$, the case of $z_2 < z_1$ is obtained. In this case by formula (8.12), the reference diameter of planets d_2 is determined. And teeth ratio $u_{21} = \frac{z_1}{z_2}$ must be used. Despite the fact that this case is less common, it is good to take it into account in the calculations and optimization software.

Given that

$$\frac{u_{12} + 1}{u_{12} - 1} = \frac{\frac{t-1}{2} + 1}{\frac{t-1}{2} - 1} = \frac{t + 1}{t - 1}, \quad (8.14)$$

formula (8.12) can be represented as follows:

$$d_1 = K_0 \sqrt[3]{T_1 \frac{t + 1}{t - 1}}, \quad (8.15)$$

where the coefficient K_0 combines the parameters of formulae (8.12) and (8.13) independent of the structural scheme

$$K_0 = \sqrt[3]{Z_H^2 \cdot Z_E^2 \cdot Z_\varepsilon^2 \cdot Z_\beta^2 \frac{2}{k \left(\frac{b_w}{d_1}\right) \sigma_{HP}^2} K_A \cdot K_v \cdot K_{H\alpha} \cdot K_{H\beta} \cdot K_\gamma}. \quad (8.16)$$

In order to obtain comparable results, the same coefficient K_0 must be used in the analysis of all structural schemes. For example, it can be determined under the following conditions (admissions):

1. Cylindrical spur gears with involute profile without shifting are used, i.e., $Z_H = 2.5$ and $Z_\beta = 1$.
2. The gears are made absolutely accurate (without a difference between the errors in the pitch on the base circle f_{pb} , i.e., $\Delta f_{pb} = 0$); this means $K_{H\beta} = 1$.
3. The number of planets is $k = 3$ and the load is evenly distributed between them; this means $K_\gamma = 1$.
4. The influence of the external and internal dynamic load is neglected; this means $K_A = K_v = 1$.

5. The material of gears is a through hardened (tempering) wrought steel with pitting endurance limit $\sigma_{H \text{ lim } b} = 500 \text{ MPa}$ and modulus of elasticity $E = 2.1 \cdot 10^5 \text{ MPa}$; this means $Z_E = 190 \sqrt{\text{MPa}}$.
6. In all gear trains $b_H/d_1 = 0.7$, $Z_N = Z_L = Z_R = Z_V = Z_W = Z_X = 1$, and $K_{H\beta} \cdot Z_e = 1$.

After substitution in formulae (8.13) and (8.16), the following is obtained:

$$K_0 \approx 8, \sqrt[3]{\frac{1}{\text{MPa}}}.$$

Of course, the sun gear diameter can also be determined by the tooth bending strength [60]. It is important that it depends on the torque T_I and the torque ratio t of the PGT. From the kinematics of the gear train and from formulae (8.2) and (8.15) for the reference diameter of ring gear, the following is obtained:

$$d_3 = \frac{z_3}{z_1} d_1 = t \cdot d_1 = K_0 \cdot t \sqrt[3]{T_I \frac{t+1}{t-1}}. \quad (8.17)$$

The reference diameter of ring gear determined in this way can serve as a criterion for the size of the simple PGT depending on its torque ratio t (respectively basic speed ratio i_0).

In the analysis of a compound PGT, the torque on each of the sun gears of the component simple PGTs must be determined as a function of the known torque (usually this is the smallest external torque T_{min} which is an input torque for the gearbox). Using the torque method, it is not difficult to do this for the corresponding structural Scheme [54]. In order to derive these formulae, it is first good to know the relationship between the torques on the sun gears of the two component PGTs. One of these torques is the smallest torque T_{min} in the gear train in general. Table 8.5 shows the formulae for the structural schemes of the compound two-carrier PGTs with two compound and three external shafts from Table 8.1.

In Table 8.6 are defined the torques $T_{I I}$ and $T_{I II}$ on sun gears of the component PGTs as a function of the smallest external torque $T_{D \text{ min}}$ that is usually an input torque T_A when the gear train operates as a reducer.

With the help of these formulae, by varying the values of the torque ratios of the component PGTs, their influence on the dimensions of the component PGTs, and hence on the size of the compound PGT, can be determined.

8.2.2.2 Efficiency

The high efficiency of PGTs in their operation with a movable carrier is due to the fact that not all transmitted power generates losses, but only that which flows with respect to the carrier. This effect is observed only in PGTs with a negative basic speed ratio $i_0 < 0$. It can be assumed that part of the input (absolute transmitted)

Table 8.5 Determination of the torques T_{I} and T_{II} on the sun gears of component PGTs as a function of the minimal torque T_{\min} in the compound PGT and the torque ratios t_I and t_{II} of the component PGTs

11, 15, 55	12, 14	13, 16, 56
$t_I > t_{II}$ $t_I < t_{II}$ $T_{II} = T_{\min}$ $T_{II} = \frac{t_{II}}{t_I} T_{\min}$ $T_{III} = \frac{t_I}{t_{II}} T_{\min}$ $T_{III} = T_{\min}$	$t_I > 1 + t_{II}$ $t_I < 1 + t_{II}$ $T_{II} = T_{\min}$ $T_{II} = \frac{1+t_{II}}{t_I} T_{\min}$ $T_{III} = \frac{t_I}{1+t_{II}} T_{\min}$ $T_{III} = T_{\min}$	$T_{II} = T_{\min}$ $T_{II} = t_I \cdot T_{\min}$
22, 24, 44	23, 26, 46	12, 45
$t_I > t_{II}$ $t_I < t_{II}$ $T_{II} = T_{\min}$ $T_{II} = \frac{1+t_{II}}{1+t_I} T_{\min}$ $T_{III} = \frac{1+t_I}{1+t_{II}} T_{\min}$ $T_{III} = T_{\min}$	$T_{II} = T_{\min}$ $T_{II} = (1+t_I) \cdot T_{\min}$	$t_I > t_{II} - 1$ $t_I < t_{II} - 1$ $T_{II} = T_{\min}$ $T_{II} = \frac{t_{II}}{1+t_I} T_{\min}$ $T_{III} = \frac{1+t_I}{t_{II}} T_{\min}$ $T_{III} = T_{\min}$
33, 36, 66	34	35
$T_{II} = T_{\min}$ $T_{III} = T_{\min}$	$T_{II} = (1+t_{II}) T_{\min}$ $T_{III} = T_{\min}$	$T_{II} = t_{II} \cdot T_{\min}$ $T_{III} = T_{\min}$

power P_A is transmitted by the entire train (as a coupling) with the movement of the carrier—the so-called coupling power P_{coup} — and the rest is transmitted by the movement of the elements with respect to the carrier, the so-called relative (rolling) power P_{rel} (Fig. 8.7) [27].

The smaller part of input power is the relative (rolling) power; the greater is the efficiency. For the correct determination of the efficiency, it is necessary to know the direction of the relative (rolling) power that can be:

- From the sun gear 1 to the ring gear 3.
- From the ring gear 3 to the sun gear 1.

This depends on which of both elements is input (driving) and which output (driven) for the relative power. Given that the direction of the torque and the angular velocity coincides on the input element and is different on the output element, the following condition can be written with respect to the torque of the sun gear T_I and its relative angular velocity $\omega_{Irel} = \omega_1 - \omega_H$ with respect to the carrier H:

Table 8.6 Determination of the torques T_{1I} and T_{1II} on the sun gears of component PGTs as a function of the minimal external torque $T_{D\min}$ of the compound PGT

Scheme	t_I and t_{II}	Structural symbol	T_{1I} and $T_{1II} = f(t_I, t_{II}, T_{D\min})$
S11	$t_I \geq 2t_{II}$		$T_{1I} = T_{D\min}; T_{1II} = \frac{t_I}{t_{II}} T_{D\min}$
	$t_{II} \leq t_I \leq 2t_{II}$		$T_{1I} = \frac{t_{II}}{t_I - t_{II}} T_{D\min}; T_{1II} = \frac{t_I}{t_I - t_{II}} T_{D\min}$
S12	$t_I \geq 1 + t_{II}$		$T_{1I} = T_{D\min}; T_{1II} = \frac{t_I}{1 + t_{II}} T_{D\min}$
	$t_I \leq 1 + t_{II}$		$T_{1I} = \frac{1 + t_{II}}{t_I} T_{D\max}; T_{1II} = T_{D\min}$
S13	For every t_I and t_{II}		$T_{1I} = T_{D\min}; T_{1II} = t_I \cdot T_{D\min}$
S14	For every t_I and t_{II}		$T_{1I} = T_{D\min}; T_{1II} = \frac{t_I}{1 + t_{II}} T_{D\min}$
S15	For every t_I and t_{II}		$T_{1I} = T_{D\min}; T_{1II} = \frac{t_I}{t_{II}} T_{D\min}$
S16	For every t_I and t_{II}		$T_{1I} = T_{D\min}; T_{1II} = t_I \cdot T_{D\min}$
S22	$t_I \geq 1 + 2t_{II}$		$T_{1I} = T_{D\min}; T_{1II} = \frac{1 + t_{II}}{1 + t_{II}} T_{D\min}$
	$t_{II} \leq t_I \leq 1 + 2t_{II}$		$T_{1I} = \frac{1 + t_{II}}{t_I - t_{II}} T_{D\min}; T_{1II} = \frac{1 + t_I}{t_I - t_{II}} T_{D\min}$
S23	For every t_I and t_{II}		$T_{1I} = T_{D\min}; T_{1II} = (1 + t_I) T_{D\min}$
S24	$t_I \geq \frac{2 + t_{II}}{t_{II}}$		$T_{1I} = T_{D\min}; T_{1II} = \frac{1 + t_I}{1 + t_{II}} T_{D\min}$
	$t_I \leq \frac{2 + t_{II}}{t_{II}}$		Not possible if $t_I > 2$ and $t_{II} > 2$
S25	For every t_I and t_{II}		$T_{1I} = T_{D\min}; T_{1II} = \frac{1 + t_I}{t_{II}} T_{D\min}$

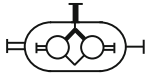
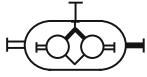
(continued)

Table 8.6 (continued)

Scheme	t_I and t_{II}	Structural symbol	T_{II} and $T_{I II} = f(t_I, t_{II}, T_{D \min})$
S26	For every t_I and t_{II}		$T_{II} = T_{D \min}; T_{I II} = (1 + t_I)T_{D \min}$
S33	$t_I \geq 2t_{II}$		$T_{II} = T_{I II} = \frac{1}{t_I} T_{D \min}$
	$t_{II} \leq t_I \leq 2t_{II}$		$T_{II} = T_{I II} = \frac{1}{t_I - t_{II}} T_{D \min}$
S34	For every t_I and t_{II}		$T_{II} = \frac{1+t_{II}}{t_{II}} T_{D \min}; T_{I II} = \frac{1}{t_{II}} T_{D \min}$
S35	For every t_I and t_{II}		$T_{II} = \frac{t_{II}}{1+t_{II}} T_{D \min}; T_{I II} = \frac{1}{1+t_{II}} T_{D \min}$
S36	$t_I \geq 1 + t_{II}$		$T_{II} = T_{I II} = \frac{1}{1+t_{II}} T_{D \min}$
	$t_I \leq 1 + t_{II}$		$T_{II} = T_{I II} = \frac{1}{t_I} T_{D \min}$
S44	$t_I \geq t_{II}$		$T_{II} = \frac{1+t_{II}}{t_I - t_{II}} T_{D \min}; T_{I II} = \frac{1+t_I}{t_I - t_{II}} T_{D \min}$
S45	$t_I \geq \frac{1+t_{II}}{t_{II}-1}$		$T_{II} = \frac{t_{II}}{1+t_I+t_{II}} T_{D \min}; T_{I II} = \frac{1+t_I}{1+t_I+t_{II}} T_{D \min}$
	$t_I \leq \frac{1+t_{II}}{t_{II}-1}$		$T_{II} = \frac{1}{t_I} T_{D \min}; T_{I II} = \frac{1+t_I}{t_I \cdot t_{II}} T_{D \min}$
S46	For every t_I and t_{II}		$T_{II} = \frac{1}{t_I} T_{D \min}; T_{I II} = \frac{1+t_I}{t_I} T_{D \min}$
S55	$t_I \geq t_{II}$		$T_{II} = \frac{t_{II}}{t_I - t_{II}} T_{D \min}; T_{I II} = \frac{t_I}{t_I - t_{II}} T_{D \min}$
S56	$t_I \geq \frac{2}{t_{II}-1}$		$T_{II} = \frac{1}{1+t_I} T_{D \min}; T_{I II} = \frac{t_I}{1+t_I} T_{D \min}$
	$t_I \leq \frac{2}{t_{II}-1}$		Not possible if $t_I > 2$ and $t_{II} > 2$

(continued)

Table 8.6 (continued)

Scheme	t_I and t_{II}	Structural symbol	T_{II} and $T_{III} = f(t_I, t_{II}, T_{D \min})$
S66	$t_I \geq 1 + 2 t_{II}$		$T_{II} = T_{III} = \frac{1}{1+t_{II}} T_{D \min}$
	$t_{II} \leq t_I \leq 1 + 2 t_{II}$		$T_{II} = T_{III} = \frac{1}{t_I-t_{II}} T_{D \min}$

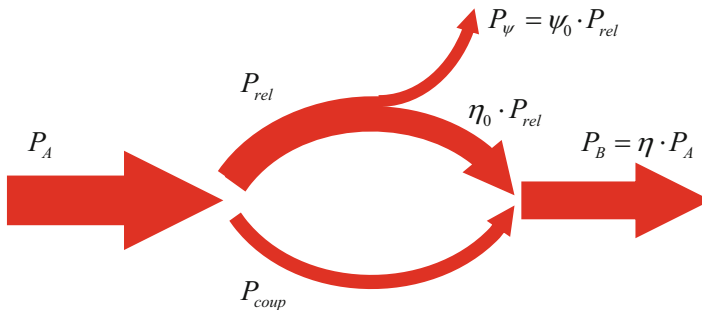


Fig. 8.7 Types of power in \overline{AI} -PGT (Redrawn from [27])

$$T_1 \cdot \omega_{1 \text{ rel}} \begin{cases} > 0 & \text{— sun gear 1 is driving (input)} \\ < 0 & \text{— sun gear 1 is driven (output)} \end{cases} \quad (8.18)$$

Depending on the direction of the relative power, the real torques are determined as follows:

Driving (input) sun gear:

$$T'_3 = \eta_0 \cdot t \cdot T'_1 < T_3 \quad (8.19)$$

$$T'_1 = \frac{1}{\eta_0} \cdot \frac{T'_3}{t} > T_1 \quad (8.20)$$

Driven (output) sun gear:

$$T'_3 = \frac{1}{\eta_0} \cdot t \cdot T'_1 > T_3 \quad (8.21)$$

$$T'_1 = \eta_0 \cdot \frac{T'_3}{t} < T_1 \quad (8.22)$$

The correct determination of the torques can be easily checked by means of the equilibrium condition

$$T'_1 + T'_3 + T'_H = 0. \quad (8.23)$$

In the above formulae η_0 is the basic efficiency of the simple PGT in work with fixed carrier H

$$\eta_0 = 1 - \psi_0, \quad (8.24)$$

where ψ_0 is the basic loss factor.

For the purposes of first approximation comparative analysis, it is sufficient to assume some value of the basic efficiency $\eta_{0I} = \eta_{0II}$, the same for all Schemes [54]. However, when compiling computer programs, the influence of some factors on the basic efficiency can be taken into account. For example, [61] recommends determining the meshing loss factor by one of the known formulae [27], [63]

$$\psi_0 = (1 + k_B + k_S + k_C) \cdot \psi_{z_0} \quad (8.25)$$

where:

ψ_0 is the basic loss factor.

ψ_{z_0} is the meshing loss factor.

$k_B = 0.06 \div 0.07$ is the coefficient of planet bearing loss.

$k_S = 0.09 \div 0.01$ is the coefficient of sealing loss.

$k_C = 0.25 \div 0.02$ is the coefficient of churn and crushing loss.

The values on the left are for the high-speed stage [62].

With sufficient accuracy for engineering practice, meshing loss factor can be determined as follows [63]:

$$\psi_{z_0} = \frac{z_3 + z_1}{z_3 - z_1} \left(\frac{0.15}{z_1} + \frac{0.2}{z_3} \right). \quad (8.26)$$

On the basis of experimental studies [27, 64], it was found that in practice there is an equality of the meshing losses in $\overline{\text{AI}}$ -PGT (i.e., deviation of less than 5%), in the transmission of relative power P_{rel} from the sun gear 1 to the ring gear 3 and vice versa. This means

$$\psi_{z_{13(H)}} \approx \psi_{z_{31(H)}} = \psi_0 \quad (8.27)$$

For *basic efficiency* η_0 the following is obtained:

$$\eta_{13(H)} \approx \eta_{31(H)} = \eta_0 = 1 - \psi_0 \quad (8.28)$$

In order to be able to compare different structural schemes by efficiency, it is convenient to use their *aligned (reduced) efficiency* η_{red} , determined when working with a fixed summation shaft.

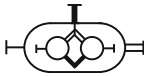
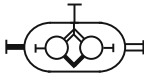
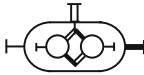
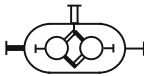
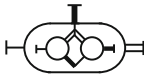
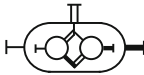
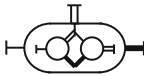
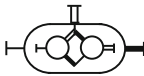
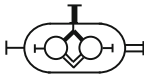
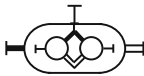
For all structural schemes from Table 8.1, the aligned (reduced) efficiency is determined as a function of the torque ratios t_I and t_{II} of the component PGTs and of their basic efficiencies η_{0I} and η_{0II}

$$\eta_{red} = f(t_I, t_{II}, \eta_{0I}, \eta_{0II}) \tag{8.29}$$

taking into account the change in the role of their shafts (Table 8.7).

For the optimal choice of structural scheme by efficiency, it is sufficient to determine the scheme with the highest aligned (reduced) efficiency without looking for the efficiency at six cases of gear operation.

Table 8.7 Determination of the aligned efficiency η_{red} of structural schemes from Table 8.1 as a function of the torque ratios t_I and t_{II} and basic efficiencies η_{0I} and η_{0II} of the component PGTs (see t_{red} from Table 8.4)

Scheme	t_I and t_{II}	Structural symbol	$\eta_{0red} = f(t_I, t_{II}, \eta_{0I}, \eta_{0II})$
S11	$t_I \geq 2 t_{II}$		$\eta_{0red} = \frac{\frac{\eta_{0I} \cdot t_I}{1 - \eta_{0II}}}{\frac{t_I - t_{II}}{t_I}}$
	$t_{II} \leq t_I \leq 2 t_{II}$		$\eta_{0red} = \frac{\frac{\eta_{0II} \cdot t_{II}}{t_I - \eta_{0II} \cdot t_{II}}}{\frac{t_I - t_{II}}{t_I}}$
S12	$t_I \geq 1 + t_{II}$		$\eta_{0red} = \frac{\frac{\eta_{0I} \cdot t_I}{1 + \eta_{0II}}}{\frac{t_I}{1 + t_{II}}}$
	$t_I \leq 1 + t_{II}$		$\eta_{0red} = \frac{\frac{1 + \eta_{0II} \cdot t_{II}}{t_I}}{\frac{t_I}{1 + t_{II}}}$
S13	For every t_I and t_{II}		$\eta_{0red} = \frac{\eta_{0I} \cdot \eta_{0II} \cdot t_I \cdot t_{II} - 1}{t_I \cdot t_{II} - 1}$
S14	For every t_I and t_{II}		$\eta_{0red} = \frac{\frac{\eta_{0I} \cdot \eta_{0II} \cdot t_I \cdot t_{II}}{1 + \eta_{0II} \cdot t_{II}}}{\frac{t_I \cdot t_{II}}{1 + t_{II}}}$
S15	For every t_I and t_{II}		$\eta_{0red} = \frac{\eta_{0I} \cdot t_I + \frac{\eta_{0I} \cdot t_I}{\eta_{0II}}}{t_I + \frac{t_I}{\eta_{0II}}}$
S16	For every t_I and t_{II}		$\eta_{0red} = \frac{\eta_{0I} \cdot t_I (1 + \eta_{0II} \cdot t_{II})}{t_I (1 + t_{II})}$
S22	$t_I \geq 1 + 2 t_{II}$		$\eta_{0red} = \frac{\frac{\eta_{0I} \cdot t_I}{1 + \eta_{0II}}}{\frac{t_I - t_{II}}{1 + t_{II}}}$
	$t_{II} \leq t_I \leq 1 + 2 t_{II}$		$\eta_{0red} = \frac{\frac{1 + \eta_{0II} \cdot t_{II}}{t_I}}{\frac{1 + \eta_{0II} \cdot t_{II}}{1 + t_{II}}}$

(continued)

Table 8.7 (continued)

Scheme	t_I and t_{II}	Structural symbol	$\eta_{0red} = f(t_I, t_{II}, \eta_{0I}, \eta_{0II})$
S23	For every t_I and t_{II}		$\eta_{0red} = \frac{(1+\eta_{0I} \cdot t_I) \eta_{0II} \cdot t_{II}}{(1+t_I)t_{II}}$
S24	$t_I \geq \frac{2+t_{II}}{t_{II}}$		$\eta_{0red} = \frac{\eta_{0I} \cdot \eta_{0II} \cdot t_I \cdot t_{II} - 1}{t_I \cdot t_{II} - 1}$
	$t_I \leq \frac{2+t_{II}}{t_{II}}$		Not possible if $t_I > 2$ and $t_{II} > 2$
S25	For every t_I and t_{II}		$\eta_{0red} = \frac{1+\eta_{0I} \cdot t_I + \eta_{0I} \cdot \eta_{0II} \cdot t_I \cdot t_{II}}{\eta_{0II} \cdot t_{II} + 1 + t_I + t_I \cdot t_{II}}$
S26	For every t_I and t_{II}		$\eta_{0red} = \frac{\eta_{0I} \cdot t_I + \eta_{0II} \cdot t_{II} + \eta_{0I} \cdot \eta_{0II} \cdot t_I \cdot t_{II}}{t_I + t_{II} + t_I \cdot t_{II}}$
S33	$t_I \geq 2 t_{II}$		$\eta_{0red} = \frac{\eta_{0I} \cdot t_I - \frac{\eta_{II}}{\eta_{0II}}}{\frac{\eta_{II}}{t_I - t_{II}} - \frac{\eta_{0II}}{t_{II}}}$
	$t_{II} \leq t_I \leq 2 t_{II}$		$\eta_{0red} = \frac{\frac{\eta_{0I} \cdot t_{II}}{t_I} - \eta_{0II} \cdot t_{II}}{\frac{\eta_{II}}{t_I - t_{II}} - \frac{\eta_{0II}}{t_I - t_{II}}}$
S34	For every t_I and t_{II}		$\eta_{0red} = \frac{\eta_{0I} \cdot t_I + \frac{\eta_{0II}}{t_{II}}}{t_I + \frac{1}{t_{II}}}$
S35	For every t_I and t_{II}		$\eta_{0red} = \frac{\eta_{0I} \cdot \eta_{0II} \cdot t_I \cdot t_{II}}{1 + \eta_{0II} \cdot t_{II} + 1 + t_{II}}$
S36	$t_I \geq 1 + t_{II}$		$\eta_{0red} = \frac{\frac{\eta_{0I} \cdot t_I}{1 + \frac{\eta_{0II}}{\eta_{0I}}} - \frac{\eta_{0II}}{1 + t_{II}}}{\frac{\eta_{0II}}{1 + t_{II}}}$
	$t_I \leq 1 + t_{II}$		$\eta_{0red} = \frac{1 + \eta_{0II} \cdot t_{II}}{\frac{\eta_{0II}}{t_I} - \frac{1 + t_{II}}{t_I}}$
S44	$t_I \geq t_{II}$		$\eta_{0red} = \frac{\eta_{0II} \cdot t_{II} + \frac{\eta_{0II}}{\eta_{0I}} \cdot t_I \cdot t_{II}}{\frac{\eta_{0II}}{t_{II}} - \eta_{0II} \cdot t_{II} - \frac{t_{II} + t_I \cdot t_{II}}{t_I - t_{II}}}$
S45	$t_I \geq \frac{1+t_{II}}{t_{II}-1}$		$\eta_{0red} = \frac{\eta_{0I} \cdot \eta_{0II} \cdot t_I \cdot t_{II}}{1 + \eta_{0I} \cdot t_I + \eta_{0II} \cdot t_{II}}$
	$t_I \leq \frac{1+t_{II}}{t_{II}-1}$		$\eta_{0red} = \frac{1 + \frac{\eta_{II}}{\eta_{0II}} - \frac{\eta_{0II}}{t_I}}{\frac{\eta_{0II}}{1 + t_I + t_{II}} - \frac{\eta_{0II}}{t_I \cdot t_{II}}}$

(continued)

Table 8.7 (continued)

Scheme	t_I and t_{II}	Structural symbol	$\eta_{0red} = f(t_I, t_{II}, \eta_{0I}, \eta_{0II})$
S46	For every t_I and t_{II}		$\eta_{0red} = \frac{\frac{1+\eta_{0II} \cdot t_{II} \cdot \frac{\eta_{0II}}{\eta_{0I}} \cdot t_I \cdot \eta_{0I}}{\frac{\eta_{0I}}{\eta_{0II}}}}{\frac{1+t_{II} \pm t_I \cdot \eta_{0I}}{t_I}}$
S55	$t_I \geq t_{II}$		$\eta_{0red} = \frac{\frac{\eta_{0I} \cdot \eta_{0II} + \frac{\eta_{0II}}{\eta_{0I}} \cdot t_I \cdot \eta_{0I}}{\frac{t_I}{\eta_{0I}} - \eta_{0II} \cdot t_{II}}}{\frac{t_I + t_I \cdot \eta_{0I}}{t_I - t_{II}}}$
S56	$t_I \geq \frac{2}{t_{II}-1}$		$\eta_{0red} = \frac{\frac{\eta_{0I} \cdot \eta_{0II} \cdot t_I \cdot t_{II} - 1}{1 + \eta_{0II} \cdot t_{II}}}{\frac{t_I \cdot t_{II} - 1}{1 + t_I}}$
	$t_I \leq \frac{2}{t_{II}-1}$		Not possible if $t_I > 2$ and $t_{II} > 2$
S66	$t_{II} \geq 1 + 2 t_{II}$		$\eta_{0red} = \frac{\frac{\eta_{0I} \cdot t_I \cdot \frac{\eta_{0I}}{\eta_{0II}}}{1 + \frac{\eta_{0I}}{\eta_{0II}}}}{\frac{t_I - t_{II}}{1 + t_{II}}}$
	$t_{II} \leq t_I \leq 1 + 2 t_{II}$		$\eta_{0red} = \frac{\frac{1 + \eta_{0II} \cdot t_{II}}{t_I} - \eta_{0II} \cdot t_{II}}{\frac{1 + t_{II}}{t_I - t_{II}}}$

8.2.2.3 Reduced Backlash

In some cases, the backlash in a PGT reduced to the input shaft may be important. The impact openings in reversing, for example, depend on it [65]. The same applies to the reduced stiffness.

In order to obtain comparable results for all structural schemes, the following simplification assumptions must be made:

- In all gears of all structural schemes, there is the same backlash (clearance) along the path of contact j'_z (Fig. 8.8).
- All gears are without profile shifting or modifications.
- All planet bearings are with the same radial clearance j_B .

From Fig. 8.8 it is seen that instead of a backlash along the path of contact j'_z it is possible to work with a backlash along the reference circle j_z , the relation between which can be assumed $j_z = j'_z \cdot \cos \alpha_w$ where α_w is the pressure angle.

Due to the clearances in the meshings and in the planet bearings, in PGT with two fixed shafts the third can rotate at an angle φ (φ_1 for sun gear, φ_3 for ring gear, and φ_H for carrier), which is the clearance reduced to the corresponding shaft (backlash).

If j'_{z12} is the backlash in the mesh of the sun gear 1 with the planets 2 and j'_{z23} is the backlash in the mesh of the planets 2 with the ring gear 3 (Figure 8.9a), it can be assumed that the tooth of the sun gear moves along the path of contact at a distance $j'_{z12} + j'_{z23} = 2 j'_z$. This is more convenient to express by moving along the reference circle $2 j_z$. Then because of the clearance in the bearings j_B , the tooth in question

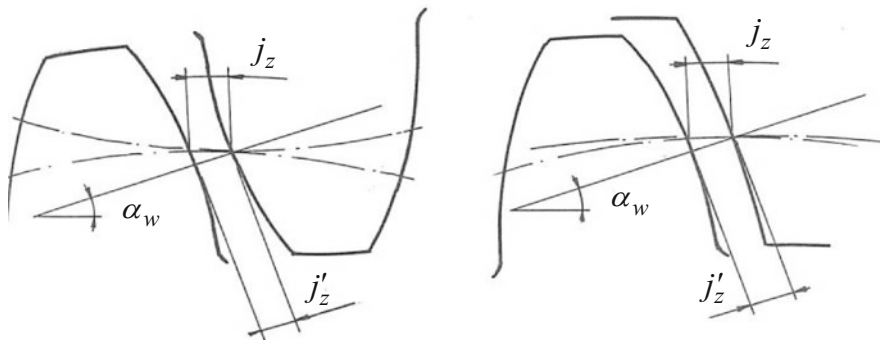


Fig. 8.8 Backlash in the meshing

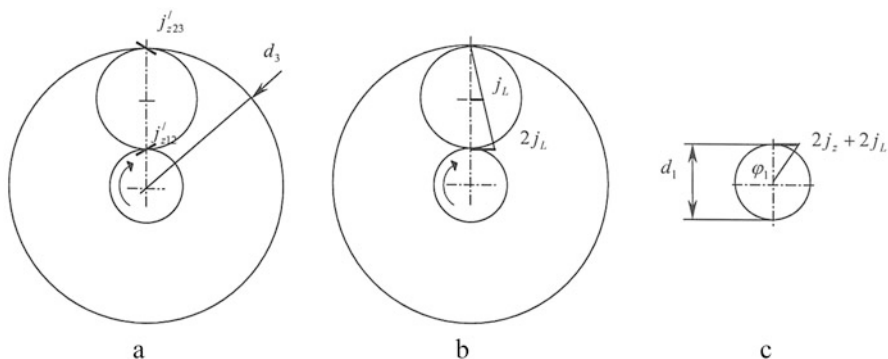


Fig. 8.9 Determination of the backlash of sun gear ϕ_1 in case of fixed ring gear 3 and carrier H (c) due the backlash in mesh (a) and the planet bearings clearance (b)

moves $2j_B$ along the reference circle (Fig. 8.9b). The all rotation of the sun gear ϕ_1 is determined in Figure 8.9c

$$\tan \phi_1 = \frac{2j_z + 2j_B}{\frac{d_1}{2}} \tag{8.30}$$

The angle ϕ_1 is small enough to assume that $\phi_1 = \tan \phi_1$. Then the reduced backlash can be represented as follows:

$$\phi_1 = \frac{4(j_z + j_B)}{d_1} \tag{8.31}$$

In a similar way, dependencies for the backlash reduced to the ring gear ϕ_3 and to the carrier ϕ_H can be obtained:

$$\varphi_3 = \frac{4(j_z + j_B)}{t \cdot d_1} = \frac{\varphi_1}{t} = i_{31(H)} \cdot \varphi_1, \tag{8.32}$$

$$\varphi_H = \frac{4(j_z + j_B)}{(1+t)d_1} = \frac{\varphi_1}{1+t} = i_{H1(3)} \cdot \varphi_1, \tag{8.33}$$

or

$$\varphi_H = \frac{t}{1+t} \varphi_3 = i_{H3(1)} \cdot \varphi_3. \tag{8.34}$$

Assuming that the output shaft is locked with a clearance allowing rotation (backlash) at an angle ξ_i , for each of the three above-considered cases, the reduced backlash can be determined by the formulae given in Table 8.8.

For the study of compound PGTs it is necessary to determine the reduced backlash taking into account the connections between the shafts of component PGTs.

Backlash reduced to a single external shaft (Fig. 8.10).

Firstly, the backlash φ_{bII} in the second PGT is determined, i.e., backlashes are reduced to the shaft *bII* forming the internal compound shaft *b*. Then the backlash φ_a of the input shaft is determined by the formulae in Table. 8.6; consider that $\xi_{bI} = \varphi_{bII}$.

Backlash reduced to a compound external shaft (Fig. 8.11).

In this case, the two component PGTs must be considered together. The rotation of the compound shaft can be represented as the sum of two angles

$$\varphi_d = \varphi'_d + \varphi^*_d, \tag{8.35}$$

where:

φ'_d is the angle (φ_{dI} or φ_{dII}) at which the backlash of one component PGT is completely removed.

φ^*_d is the angle at which the remaining backlash in the other PGT is removed.

The remaining backlash φ^*_d is removed simultaneously, both directly from the external compound shaft $\varphi_{d'}$ and through the internal compound shaft of the PGT whose backlash has already been removed $\varphi_{d''}$

$$\varphi^*_d = \frac{1}{\frac{1}{\varphi_{d'}} + \frac{1}{\varphi_{d''}}}. \tag{8.36}$$

For each structural scheme (Table 8.1) after applying the dependencies from (8.31) to (8.34) and from Table 8.6, by formulae (8.35) and (8.36) the backlashes reduced to the external compound shaft can be obtained.

Backlash reducing in a particle structural scheme

Determination of the backlash for structural scheme 15 from Table 8.1 is considered as an example, but the logic is the same for an arbitrary structural scheme.

Table 8.8 Reduced backlash to the input shaft φ_i in the case of output shaft locked with backlash ξ_i

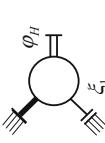

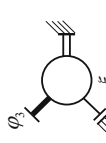

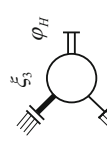

As a reducer (reduce the speed)		As a multiplier (multiply the speed)
	$\varphi_{1H} = \varphi_1 + i_{1H} \cdot \xi_H = \varphi_1 + (1 + t)\xi_H$	 $\varphi_{H1} = \varphi_H + i_{H1} \cdot \xi_1 = \varphi_H + \frac{1}{1+t}\xi_1$
	$\varphi_{13} = \varphi_1 + i_{13} \cdot \xi_3 = \varphi_1 + t \cdot \xi_3$	 $\varphi_{31} = \varphi_3 + i_{31} \cdot \xi_1 = \varphi_1 + \frac{1}{t}\xi_1$
	$\varphi_{3H} = \varphi_3 + i_{3H} \cdot \xi_H = \varphi_3 + \left(1 + \frac{1}{t}\right) \cdot \xi_H$	 $\varphi_{H3} = \varphi_H + i_{H3} \cdot \xi_3 = \varphi_H + \frac{1}{1+t}\xi_3$

Fig. 8.10 Backlash reduced to a single external shaft

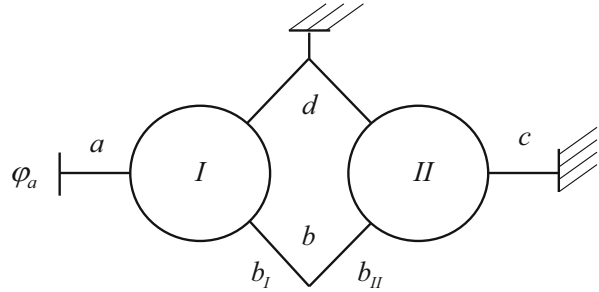
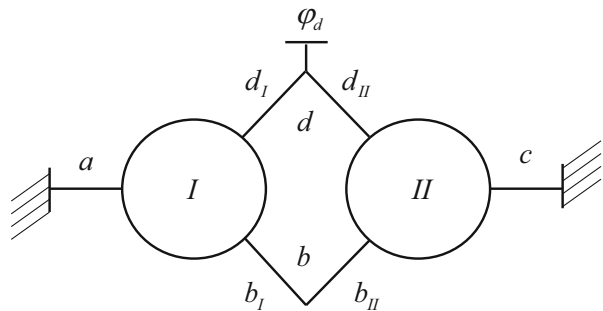


Fig. 8.11 Backlash reduced to a compound external shaft



Backlash reduced to the shaft a (Figure 8.12a)

The backlash in the second component PGT reduced to the ring gear is determined by formula (8.32)

$$\varphi_{3II} = \frac{4(j_z + j_B)}{t_{II} \cdot d_{1II}}. \tag{8.37}$$

The backlash in the first component PGT reduced to the sun gear at fixed carrier and locked with clearance $\xi_3 = \varphi_{3II}$ ring gear is determined by Table 8.6

$$\varphi_a = \varphi_{1I} + t_I \cdot \varphi_{3II}, \tag{8.38}$$

where:

φ_{1I} is the rotation of sun gear caused by clearances in the first PGT, determined by formula (8.31)

$$\varphi_{1I} = \frac{4(j_z + j_B)}{d_{1I}}. \tag{8.39}$$

After substitution in the corresponding formula in Table 8.6, for the reduced backlash the following is obtained:

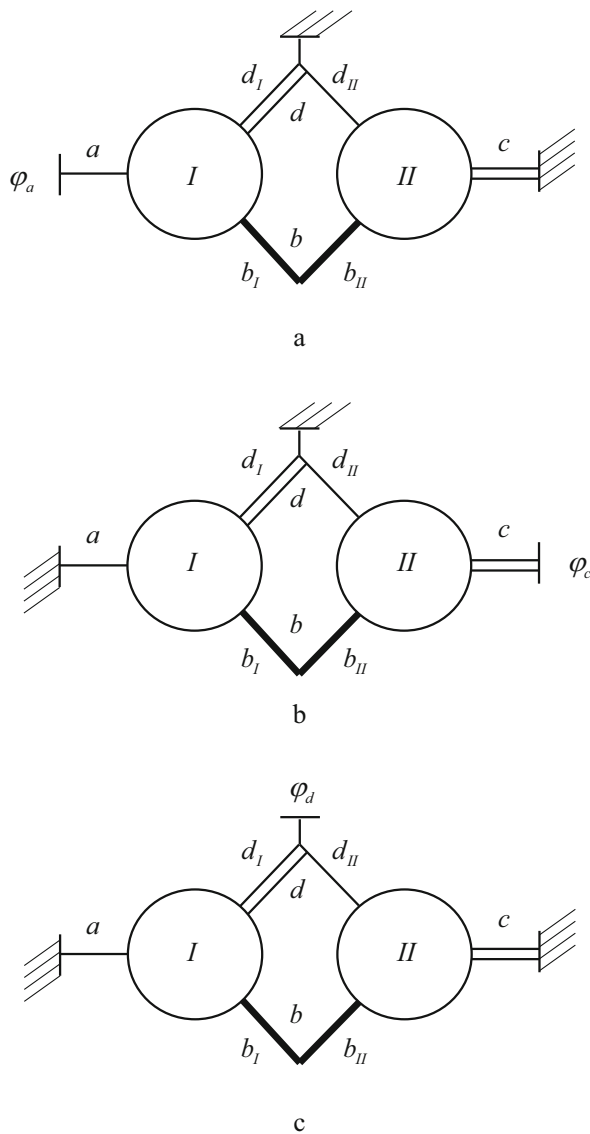


Fig. 8.12 Determination of reduced backlash in the compound two-carrier PGT arranged according to Scheme 15 from Table 8.1: (a) Backlash reduced to the single external shaft a . (b) Backlash reduced to the single external shaft c . (c) Backlash reduced to the compound external shaft d

$$\varphi_a = \frac{4(j_z + j_B)}{d_{1I}} + \frac{t_I}{t_{II}} \cdot \frac{4(j_z + j_B)}{d_{1II}}. \quad (8.40)$$

Backlash reduced to the shaft c (Figure 8.12b)

The backlash in the first component PGT reduced to the ring gear is determined by formula (8.32)

$$\varphi_{3I} = \frac{4(j_z + j_B)}{t_I \cdot d_{1I}}. \quad (8.41)$$

The backlash in the second component PGT reduced to the carrier at fixed sun gear and locked with clearance $\xi_3 = \varphi_{3I}$ ring gear is determined by Table 8.6:

$$\varphi_c = \varphi_{HII} + \frac{t_{II}}{1 + t_{II}} \cdot \varphi_{3I}, \quad (8.42)$$

where:

φ_{HII} is the rotation of carrier caused by clearances in the second PGT, determined by formula (8.24)

$$\varphi_{HII} = \frac{4(j_z + j_B)}{(1 + t_{II})d_{1II}}. \quad (8.43)$$

After substitution in the corresponding formula in Table 8.6, for the reduced backlash the following is obtained:

$$\varphi_c = \frac{4(j_z + j_B)}{(1 + t_{II})d_{1II}} + \frac{t_{II}}{1 + t_{II}} \cdot \frac{4(j_z + j_B)}{t_I \cdot d_{1I}}. \quad (8.44)$$

Backlash reduced to the shaft d (Figure 8.12c)

The backlashes in the two component PGTs, reduced to the shafts forming the compound one, are determined: reduced to the carrier of the first PGT by formula (8.33) and to the sun gear of the second PGT by formula (8.31)

$$\varphi_{dI} = \frac{4(j_z + j_B)}{(1 + t_I)d_{1I}}; \quad \varphi_{dII} = \frac{4(j_z + j_B)}{d_{1II}}. \quad (8.45)$$

In order to apply formula (8.35), it must be determined which of the two rotations is smaller (φ'_d). For this purpose, the sizes of the diameters of the sun gears must be determined by formula (8.15)

$$d_{1I} = K_0 \sqrt[3]{T_{1I} \frac{t_I + 1}{t_I - 1}}; \quad d_{1II} = K_0 \sqrt[3]{T_{1II} \frac{t_{II} + 1}{t_{II} - 1}}. \quad (8.46)$$

From the kinematic analysis and Table 8.5, it is known that for Scheme 15 T_{1I} is the smallest external torque and input torque, when operating as a reducer, i.e., $T_{1I} = T_{D\min} = T_A$, and T_{1II} is obtained as follows:

$$T_{1II} = \frac{t_I}{t_{II}} T_{1I}. \quad (8.47)$$

Substituting formula (8.47) into formula (8.46) for the sun gears diameters, the following is obtained:

$$d_{1I} = K_0 \sqrt[3]{T_{1I} \frac{t_I + 1}{t_I - 1}}, \quad d_{1II} = K_0 \sqrt[3]{T_{1I} \frac{t_I(t_{II} + 1)}{t_{II}(t_{II} - 1)}}. \quad (8.48)$$

After substituting formula (8.48) into formula (8.45) and comparing, it is established that for each t_I and $t_{II} \in [2 \div 12]$, the inequality $\varphi_{dI} > \varphi_{dII}$ is valid. Then the rotation of the input shaft by formula (8.35) is as follows:

$$\varphi_d = \varphi_{dI} + \varphi^*, \quad (8.49)$$

where φ^* is determined by formula (8.36)

$$\varphi_d^* = \frac{1}{\frac{1}{\varphi_d'} + \frac{1}{\varphi_d''}} \left| \begin{array}{l} \varphi_d' = \varphi_{dII} - \varphi_{dI} \\ \varphi_d'' = \frac{\varphi_d'}{t_{II}} i_{h3I} = \frac{\varphi_d'}{t_{II}} \cdot \frac{t_I}{1 + t_I} \end{array} \right. \quad (8.50)$$

After substitution for φ_d , the following is obtained:

$$\varphi_d = 4(j_z + j_B) \left[\left(\frac{1}{d_{1II}} - \frac{1}{(1 + t_I)d_{1I}} \right) \frac{t_I}{t_I + t_{II} + t_I \cdot t_{II}} + \frac{1}{(1 + t_I)d_{1I}} \right]. \quad (8.51)$$

After processing the formulae (8.40), (8.42), and (8.51), for the backlash reduced to the three external shafts, the following is obtained:

$$\varphi_a = 4(j_z + j_B)A_{15}, \quad (8.52)$$

$$\varphi_c = 4(j_z + j_B)A_{15} \frac{t_{II}}{t_I + t_I \cdot t_{II}}, \quad (8.53)$$

$$\varphi_d = 4(j_z + j_B)A_{15} \frac{t_{II}}{t_I + t_{II} + t_I \cdot t_{II}}, \quad (8.54)$$

where the constant A_{15} is

$$A_{15} = \frac{t_I \cdot d_{1I} + t_{II} \cdot d_{1II}}{t_{II} \cdot d_{1I} \cdot d_{1II}}. \quad (8.55)$$

From Table 8.4 it is seen that the aligned (reduced) torque ratio of Scheme 15 is

$$t_{red} = t_I + \frac{t_I}{t_{II}} = \frac{t_I + t_I \cdot t_{II}}{t_{II}}. \quad (8.56)$$

Then for the backlash reduced to the three outer shafts, it is

$$\varphi_a = 4(j_z + j_B)A_{15}, \quad (8.57)$$

$$\varphi_c = \frac{\varphi_a}{t_{red}}, \quad (8.58)$$

$$\varphi_d = \frac{\varphi_a}{1 + t_{red}}. \quad (8.59)$$

The constant A_{15} can be expressed as a function of the torque ratios (t_I and t_{II}) and the smallest of the torques on the external shafts $T_{D \min}$, which for this scheme is the torque of the shaft of the sun gear of the first component PGT ($T_{D \min} \equiv T_{1I}$)

$$A_{15} = \frac{t_I \sqrt[3]{\frac{t_I+1}{t_I-1}} + t_{II} \sqrt[3]{\frac{t_I(t_{II}+1)}{t_{II}(t_{II}-1)}}}{K_0 \cdot t_I \cdot t_{II} \sqrt[3]{T_{D \min} \frac{t_I(t_I+1)(t_{II}+1)}{t_{II}(t_I-1)(t_{II}-1)}}}. \quad (8.60)$$

Backlash reducing in structural schemes from Table 8.1

For each of the structural schemes from Table 8.1, the backlashes reduced to the three external shafts by the above procedure are determined. The constants A_{ij} analogous to those determined by formula (8.60) are determined. For each of the structural schemes, the below dependencies are valid:

$$\varphi_{D \min} = 4(j_z + j_B)A_{ij}, \quad (8.61)$$

$$\varphi_{D \max} = \frac{\varphi_{D \min}}{t_{red}}, \quad (8.62)$$

$$\varphi_{\Sigma} = \frac{\varphi_{D \min}}{1 + t_{red}}, \quad (8.63)$$

where:

$\varphi_{D \min}$ is the backlash reduced to the shaft with the smallest external torque $T_{D \min}$.

$\varphi_{D \max}$ is the backlash reduced to the shaft with the biggest external torque $T_{D \max}$.

φ_{Σ} is the backlash reduced to the shaft with summation external torque T_{Σ} .

A_{ij} is an original expression peculiar to each structural scheme (Table 8.9).

t_{red} is the aligned (reduced) speed ratio of compound PGT in question (Table 8.4).

Table 8.9 Determination of constant A_{ij} in formula (8.61).

Scheme	t_I and t_{II}	Structural symbol	$A_{ij} = f(t_I, t_{II}, d_{VI}, d_{VII})$
S11	$t_I \geq 2t_{II}$		$A_{11} = \frac{t_I \cdot d_{VI} + t_{II} \cdot d_{VII}}{t_{II} \cdot d_{VI} \cdot d_{VII}}$
	$t_{II} \leq t_I \leq 2t_{II}$		$A_{11} = \frac{t_I \cdot d_{VI} + t_{II} \cdot d_{VII}}{(t_I - t_{II})d_{VI} \cdot d_{VII}}$
S12	$t_I \geq 1 + t_{II}$		$A_{12} = \frac{t_I \cdot d_{VI} + (1 + t_{II})d_{VII}}{(1 + t_{II})d_{VI} \cdot d_{VII}}$
	$t_I \leq 1 + t_{II}$		$A_{12} = \frac{t_I \cdot d_{VI} + (1 + t_{II})d_{VII}}{t_I \cdot d_{VI} \cdot d_{VII}}$
S13	For every t_I and t_{II}		$A_{13} = A_{16} = \frac{t_I \cdot d_{VI} + d_{VII}}{d_{VI} \cdot d_{VII}}$
S14	For every t_I and t_{II}		$A_{14} = \frac{t_I \cdot d_{VI} + (1 + t_{II})d_{VII}}{(1 + t_{II})d_{VI} \cdot d_{VII}}$
S15	For every t_I and t_{II}		$A_{15} = \frac{t_I \cdot d_{VI} + t_{II} \cdot d_{VII}}{t_{II} \cdot d_{VI} \cdot d_{VII}}$
S16	For every t_I and t_{II}		$A_{16} = A_{13} = \frac{t_I \cdot d_{VI} + d_{VII}}{d_{VI} \cdot d_{VII}}$
S22	$t_I \geq 1 + 2t_{II}$		$A_{22} = \frac{(1 + t_I)d_{VI} + (1 + t_{II})d_{VII}}{(t_I - t_{II})d_{VI} \cdot d_{VII}}$
	$t_{II} \leq t_I \leq 1 + 2t_{II}$		$A_{22} = \frac{(1 + t_I)d_{VI} + (1 + t_{II})d_{VII}}{(t_I - t_{II})d_{VI} \cdot d_{VII}}$
S23	For every t_I and t_{II}		$A_{23} = A_{26} = \frac{(1 + t_I)d_{VI} + d_{VII}}{d_{VI} \cdot d_{VII}}$
S24	$t_I \geq \frac{2 + t_{II}}{t_{II}}$		$A_{24} = \frac{(1 + t_I)d_{VI} + (1 + t_{II})d_{VII}}{(1 + t_{II})d_{VI} \cdot d_{VII}}$
	$t_I \leq \frac{2 + t_{II}}{t_{II}}$		Not possible if $t_I > 2$ and $t_{II} > 2$
S25	For every t_I and t_{II}		$A_{25} = \frac{(1 + t_I)d_{VI} + t_{II} \cdot d_{VII}}{t_{II} \cdot d_{VI} \cdot d_{VII}}$

(continued)

Table 8.9 (continued)

Scheme	t_I and t_{II}	Structural symbol	$A_{ij} = f(t_I, t_{II}, d_{VI}, d_{VII})$
S26	For every t_I and t_{II}		$A_{26} = A_{23} = \frac{(1 + t_I)d_{VI} + d_{VII}}{d_{VI} \cdot d_{VII}}$
S33	$t_I \geq 2t_{II}$		$A_{33} = \frac{d_{VI} + d_{VII}}{t_{II} \cdot d_{VI} \cdot d_{VII}}$
	$t_{II} \leq t_I \leq 2t_{II}$		$A_{33} = \frac{d_{VI} + d_{VII}}{(t_I - t_{II})d_{VI} \cdot d_{VII}}$
S34	For every t_I and t_{II}		$A_{34} = \frac{d_{VI} + (1 + t_{II})d_{VII}}{t_{II} \cdot d_{VI} \cdot d_{VII}}$
S35	For every t_I and t_{II}		$A_{35} = \frac{d_{VI} + t_{II} \cdot d_{VII}}{(1 + t_{II})d_{VI} \cdot d_{VII}}$
S36	$t_I \geq 1 + t_{II}$		$A_{36} = \frac{d_{VI} + d_{VII}}{(1 + t_{II})d_{VI} \cdot d_{VII}}$
	$t_I \leq 1 + t_{II}$		$A_{36} = \frac{d_{VI} + d_{VII}}{t_I \cdot d_{VI} \cdot d_{VII}}$
S44	$t_I \geq t_{II}$		$A_{44} = \frac{(1 + t_I)d_{VI} + (1 + t_{II})d_{VII}}{(t_I - t_{II})d_{VI} \cdot d_{VII}}$
S45	$t_I \geq \frac{1 + t_{II}}{t_{II} - 1}$		$A_{45} = \frac{(1 + t_I)d_{VI} + t_{II} \cdot d_{VII}}{(1 + t_I + t_{II})d_{VI} \cdot d_{VII}}$
	$t_I \leq \frac{1 + t_{II}}{t_{II} - 1}$		$A_{45} = \frac{(1 + t_I)d_{VI} + t_{II} \cdot d_{VII}}{t_I \cdot t_{II} \cdot d_{VI} \cdot d_{VII}}$
S46	For every t_I and t_{II}		$A_{46} = \frac{(1 + t_I)d_{VI} + d_{VII}}{t_I \cdot d_{VI} \cdot d_{VII}}$
S55	$t_I \geq t_{II}$		$A_{46} = \frac{(1 + t_I)d_{VI} + d_{VII}}{t_I \cdot d_{VI} \cdot d_{VII}}$
S56	$t_I \geq \frac{2}{t_{II} - 1}$		$A_{56} = \frac{t_I \cdot d_{VI} + d_{VII}}{(1 + t_I)d_{VI} \cdot d_{VII}}$
	$t_I \leq \frac{2}{t_{II} - 1}$		Not possible if $t_I > 2$ and $t_{II} > 2$

(continued)

Table 8.9 (continued)

Scheme	t_I and t_{II}	Structural symbol	$A_{ij} = f(t_I, t_{II}, d_{1I}, d_{1II})$
S66	$t_I \geq 1 + 2 t_{II}$		$A_{66} = \frac{d_{1I} + d_{1II}}{(1 + t_{II})d_{1I} \cdot d_{1II}}$
	$t_{II} \leq t_I \leq 1 + 2 t_{II}$		$A_{66} = \frac{d_{1I} + d_{1II}}{(t_I - t_{II})d_{1I} \cdot d_{1II}}$

8.2.2.4 Reduced Stiffness

Sometimes it is important to know the dynamic parameters of the transmission, including the gear train. In this case, it is advisable to take into account the possible dynamic characteristics when choosing the structural scheme. In order to study the influence of the structural scheme and its parameters on the reduced to the external shafts’ stiffness of the PGT, the shafts can be considered as perfectly rigid, and only the stiffnesses in the gearing and planet bearings can be taken into account. The analysis of real arrangements shows that the angular compliance of the shafts is not more than 5 to 10% of the compliance of the gear train [66].

It is convenient to present the stiffness in the meshing as follows [54]:

$$c_z = \frac{F_{bn}}{\Delta_z}, \tag{8.64}$$

where:

c_z is the mean value of mesh stiffness, $\frac{N}{\mu m}$.

Δ_z is the tooth deformation on the path of contact, μm .

F_{bn} is the normal load (force) in the mesh, N.

Normal force can be represented as

$$F_{bn} = \frac{2T}{d_w \cdot \cos \alpha_w}, \tag{8.65}$$

where:

T is the torque on the shaft of one of the mated gears, N.

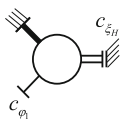
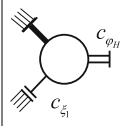
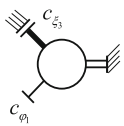
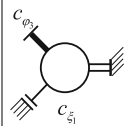
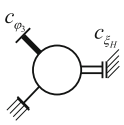
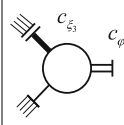
d_w is the diameter of operating circle of the gear in question. For gears without profile shifting, it is equal to the reference diameter ($d_w = d$), m.

α_w is the pressure angle.

The angle of rotation of the shaft of gear in question due to deformation Δ_c can be represented as

$$\varphi_c \approx \tan \varphi_c = \frac{2\Delta_c \cdot \cos \alpha_w}{d}. \tag{8.66}$$

Table 8.10 Reduced stiffness to the input shaft c_φ in the case of output shaft locked with stiffness c_ξ

As a reducer (reduce the speed)		As a multiplier (multiply the speed)	
	$c_{\varphi_{1H}} = \frac{1}{\frac{1}{c_{\varphi_1}} + (1+t)^2 \frac{1}{c_{\xi_H}}}$		$c_{\varphi_{H1}} = \frac{1}{\frac{1}{c_{\varphi_H}} + \frac{1}{(1+t)^2} \cdot \frac{1}{c_{\xi_1}}}$
	$c_{\varphi_{13}} = \frac{1}{\frac{1}{c_{\varphi_1}} + t^2 \frac{1}{c_{\xi_3}}}$		$c_{\varphi_{31}} = \frac{1}{\frac{1}{c_{\varphi_3}} + \left(\frac{1}{t}\right)^2 \frac{1}{c_{\xi_1}}}$
	$c_{\varphi_{3H}} = \frac{1}{\frac{1}{c_{\varphi_3}} + \left(1 + \frac{1}{t}\right)^2 \frac{1}{c_{\xi_H}}}$		$c_{\varphi_{H3}} = \frac{1}{\frac{1}{c_{\varphi_H}} + \frac{1}{\left(1 + \frac{1}{t}\right)^2} \cdot \frac{1}{c_{\xi_3}}}$

After substitution of formulae (8.64) and (8.65) in (8.66), the angular rotation of the shaft is obtained:

$$\varphi_c = \frac{4T}{c_z \cdot d^2}. \tag{8.67}$$

Then the angular stiffness $c_\varphi = \frac{T}{\varphi_c}$ is equal to

$$c_\varphi = \frac{c_z \cdot d^2}{4}. \tag{8.68}$$

After reasoning similar to those for backlashes (Sect. 2.2.3), dependencies for the stiffness reduced to the three shafts of a simple PGT with one fixed shaft and one locked with stiffness can be created (Table 8.10) [54].

Based on these dependencies, the reduced stiffness to the input shaft (external shaft with the lowest torque $T_{D \min}$) of the compound PGT can be determined. For compound PGTs in Table 8.4, the formula is [54].

$$c_{\varphi_{D \min}} = \frac{k}{8 \left(\frac{1}{c_z} + \frac{1}{c_B} \right) B_{ij}}, \tag{8.69}$$

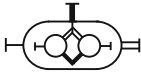
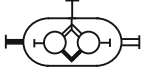

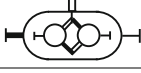
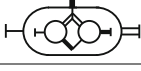

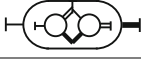

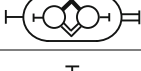
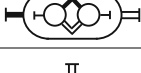

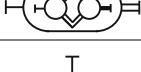



where:

k is the number of planets.

c_z and c_B are the stiffnesses in the mesh and planet bearings.

$B_{ij} = f(t_I, t_{II}, d_{1I}, d_{1II})$ is an original expression peculiar to each structural scheme (Table 8.11).

Table 8.11 Determination of constant B_{ij} in formula (8.69)

Scheme	t_I and t_{II}	Structural symbol	$B_{ij} = f(t_I, t_{II}, d_{1I}, d_{1II})$
S11	$t_I \geq 2 t_{II}$		$B_{11} = \frac{t_I^2 \cdot d_{1I}^2 + t_{II}^2 \cdot d_{1II}^2}{t_I^2 \cdot d_{1I}^2 \cdot d_{1II}^2}$
	$t_{II} \leq t_I \leq 2 t_{II}$		$B_{11} = \frac{t_I^2 \cdot d_{1I}^2 + t_{II}^2 \cdot d_{1II}^2}{(t_I^2 - t_{II}^2) d_{1I}^2 \cdot d_{1II}^2}$
S12	$t_I \geq 1 + t_{II}$		$B_{12} = \frac{t_I^2 \cdot d_{1I}^2 + (1+t_{II})^2 \cdot d_{1II}^2}{(1+t_{II})^2 \cdot d_{1I}^2 \cdot d_{1II}^2}$
	$t_I \leq 1 + t_{II}$		$B_{12} = \frac{t_I^2 \cdot d_{1I}^2 + (1+t_{II})^2 \cdot d_{1II}^2}{t_I^2 \cdot d_{1I}^2 \cdot d_{1II}^2}$
S13	For every t_I and t_{II}		$B_{13} = B_{16} = \frac{t_I^2 \cdot d_{1I}^2 + d_{1II}^2}{d_{1I}^2 \cdot d_{1II}^2}$
S14	For every t_I and t_{II}		$B_{14} = \frac{t_I^2 \cdot d_{1I}^2 + (1+t_{II})^2 \cdot d_{1II}^2}{(1+t_{II})^2 \cdot d_{1I}^2 \cdot d_{1II}^2}$
S15	For every t_I and t_{II}		$B_{15} = \frac{t_I^2 \cdot d_{1I}^2 + t_{II}^2 \cdot d_{1II}^2}{t_I^2 \cdot d_{1I}^2 \cdot d_{1II}^2}$
S16	For every t_I and t_{II}		$B_{16} = B_{13} = \frac{t_I^2 \cdot d_{1I}^2 + d_{1II}^2}{d_{1I}^2 \cdot d_{1II}^2}$
S22	$t_I \geq 1 + 2 t_{II}$		$B_{22} = \frac{(1+t_I)^2 \cdot d_{1I}^2 + (1+t_{II})^2 \cdot d_{1II}^2}{(t_I^2 - t_{II}^2) d_{1I}^2 \cdot d_{1II}^2}$
	$t_{II} \leq t_I \leq 1 + 2 t_{II}$		$B_{22} = \frac{(1+t_I)^2 \cdot d_{1I}^2 + (1+t_{II})^2 \cdot d_{1II}^2}{(t_I^2 - t_{II}^2) d_{1I}^2 \cdot d_{1II}^2}$
S23	For every t_I and t_{II}		$B_{23} = B_{26} = \frac{(1+t_I)^2 \cdot d_{1I}^2 + d_{1II}^2}{d_{1I}^2 \cdot d_{1II}^2}$
S24	$t_I \geq \frac{2+t_{II}}{t_{II}}$		$B_{24} = \frac{(1+t_I)^2 \cdot d_{1I}^2 + (1+t_{II})^2 \cdot d_{1II}^2}{(1+t_{II})^2 \cdot d_{1I}^2 \cdot d_{1II}^2}$
	$t_I \leq \frac{2+t_{II}}{t_{II}}$		Not possible if $t_I > 2$ and $t_{II} > 2$
S25	For every t_I and t_{II}		$B_{25} = \frac{(1+t_I)^2 \cdot d_{1I}^2 + t_{II}^2 \cdot d_{1II}^2}{t_{II}^2 \cdot d_{1I}^2 \cdot d_{1II}^2}$
S26	For every t_I and t_{II}		$B_{26} = B_{23} = \frac{(1+t_I)^2 \cdot d_{1I}^2 + d_{1II}^2}{d_{1I}^2 \cdot d_{1II}^2}$

(continued)

Table 8.11 (continued)

Scheme	t_I and t_{II}	Structural symbol	$B_{ij} = f(t_I, t_{II}, d_{1I}, d_{1II})$
S33	$t_I \geq 2t_{II}$		$B_{33} = \frac{d_{1I}^2 + d_{1II}^2}{t_I^2 \cdot d_{1I}^2 \cdot d_{1II}^2}$
	$t_{II} \leq t_I \leq 2t_{II}$		$B_{33} = \frac{d_{1I}^2 + d_{1II}^2}{(t_I^2 - t_{II}^2) d_{1I}^2 d_{1II}^2}$
S34	For every t_I and t_{II}		$B_{34} = \frac{d_{1I}^2 + (1+t_{II})^2 d_{1II}^2}{t_I^2 \cdot d_{1I}^2 \cdot d_{1II}^2}$
S35	For every t_I and t_{II}		$B_{35} = \frac{d_{1I}^2 + t_{II}^2 d_{1II}^2}{(1+t_{II})^2 d_{1I}^2 d_{1II}^2}$
S36	$t_I \geq 1 + t_{II}$		$B_{36} = \frac{d_{1I}^2 + d_{1II}^2}{(1+t_{II})^2 d_{1I}^2 d_{1II}^2}$
	$t_I \leq 1 + t_{II}$		$B_{36} = \frac{d_{1I}^2 + d_{1II}^2}{t_I^2 \cdot d_{1I}^2 \cdot d_{1II}^2}$
S44	$t_I \geq t_{II}$		$B_{44} = \frac{(1+t_I)^2 d_{1I}^2 + (1+t_{II})^2 d_{1II}^2}{(t_I^2 - t_{II}^2) d_{1I}^2 d_{1II}^2}$
S45	$t_I \geq \frac{1+t_{II}}{t_{II}-1}$		$B_{45} = \frac{(1+t_I)^2 d_{1I}^2 + t_{II}^2 d_{1II}^2}{(1+t_I^2 + t_{II}^2) d_{1I}^2 d_{1II}^2}$
	$t_I \leq \frac{1+t_{II}}{t_{II}-1}$		$B_{45} = \frac{(1+t_I)^2 d_{1I}^2 + t_{II}^2 d_{1II}^2}{t_I^2 \cdot t_{II}^2 \cdot d_{1I}^2 d_{1II}^2}$
S46	For every t_I and t_{II}		$B_{46} = \frac{(1+t_I)^2 d_{1I}^2 + d_{1II}^2}{t_I^2 \cdot d_{1I}^2 \cdot d_{1II}^2}$
S55	$t_I \geq t_{II}$		$B_{55} = \frac{t_I^2 d_{1I}^2 + t_{II}^2 d_{1II}^2}{(t_I^2 - t_{II}^2) d_{1I}^2 d_{1II}^2}$
S56	$t_I \geq \frac{2}{t_{II}-1}$		$B_{56} = \frac{t_I^2 d_{1I}^2 + d_{1II}^2}{(1+t_I)^2 d_{1I}^2 d_{1II}^2}$
	$t_I \leq \frac{2}{t_{II}-1}$		Not possible if $t_I > 2$ and $t_{II} > 2$
S66	$t_I \geq 1 + 2t_{II}$		$B_{66} = \frac{d_{1I}^2 + d_{1II}^2}{(1+t_{II})^2 d_{1I}^2 d_{1II}^2}$
	$t_{II} \leq t_I \leq 1 + 2t_{II}$		$B_{66} = \frac{d_{1I}^2 + d_{1II}^2}{(t_I^2 - t_{II}^2) d_{1I}^2 d_{1II}^2}$

If the reference diameters of the sun gears are determined by formula (8.15) and Table 8.5, a formula can be obtained for the stiffnesses as a function of torque ratios t_I and t_{II} of the component PGTs and several constants: the stiffnesses in the mesh c_z and bearings c_B ; the number of planets k ; meshing parameters (K_0); and the input torque $T_A \equiv T_{D \min}$ (which affects the geometric dimensions).

By varying the values of t_I and t_{II} (in the range from 2 to 12), their influence on the reduced angular stiffness c_φ can be determined. From this one can look for the most favorable combination of t_I and t_{II} (i.e., the distribution of the total speed ratio between the two planetary stages) to obtain the desired stiffness. Also it is possible to make a comparative analysis between the different structural schemes. It is appropriate to emphasize that of the above optimization criteria, the reduced stiffness is the least important for the choice of the structural scheme and its parameters. In many of the mechanisms in the transmission or in the working body, there are quite large elasticities (couplings, ropes, chains, pneumatic wheels, etc.), which minimize the impact of the elasticity of the gear.

In multi-objective optimization, other parameters can be defined (e.g., gear trains mass).

8.2.3 Multi-Objective Optimization Procedure

8.2.3.1 Optimization within One Structural Scheme

The given required total speed ratio of the compound PGT, resp. the aligned torque ratio t_{red} , can be realized at different values of the torque ratios t_I and t_{II} of the component PGTs. The purpose of optimization is to find the most suitable combination.

One of the possible approaches is to vary the values of t_I and t_{II} in a certain interval (for the considered PGT it is from 2 to 12). The variation step can be chosen small enough (e.g., 0.1) without being related to the number of teeth on the sun wheel and the ring gear (to facilitate the procedure) [54]. If desired, the number of teeth can be included by setting a value for and increasing by one tooth [49].

For each of the combinations of t_I and t_{II} , the values of the parameters used for optimization criteria are determined (ring gears diameters d_{3I} and d_{3II} , efficiency η_{red} , the reduced backlash to the input shaft $\varphi_{D \min}$). Then, by one of the known methods for multi-objective optimization, the most appropriate combination is chosen.

The case of Pareto optimization by weight coefficients [67, 68] is presented below, which the authors consider the most appropriate in this case. Other methods are also possible [69].

In [42] programs for optimal choice of the torque ratios of the component gear trains t_I and t_{II} from the standpoint of maximum efficiency and minimum overall dimensions and backlash are proposed for each of the possible structural schemes (Tables 8.1 and 8.2). All these programs contain a module which determines whether

the structural scheme has the required kinematic capabilities when changing t_I and t_{II} within a given interval in order to fulfill:

- The desired value for speed ratio $i = \frac{\omega_A}{\omega_B}$, i.e., for aligned (reduced) torque ratio of compound PGT t_{red} in case of PGT from Table 8.1.
- The desired values for the two output angular velocities ω_B and $\omega_{B\mu}$ in case of PGT from Table 8.2.
- A desired ratio between the two output angular velocities $\frac{\omega_B}{\omega_{B\mu}}$ in case of PGT from Table 8.2.

The range of t_I and t_{II} is chosen by the user and cannot go out of the previously determined values

$$2 \leq t_{I \min} \leq t_I \leq t_{I \max} \leq 12 \quad (8.70)$$

$$2 \leq t_{II \min} \leq t_{II} \leq t_{II \max} \leq 12. \quad (8.71)$$

For the structural schemes of the main diagonal of Tables 8.1 and 8.2, this check is connected with the minimum allowed values for the efficiency

$$\eta_{Br.1} \geq \eta_{\min} \quad \text{and} \quad \eta_{Br.2} \geq \eta_{\min} \quad (8.72)$$

as if $t_I = t_{II}$ in theory infinity is obtained for the speed ratio and zero for the efficiency.

The above check for the kinematic capabilities could be made by directly assigning values to t_I and t_{II} at regular intervals with no connection to a certain number of teeth.

The efficiency of the component gear train is a function of the torque ratios t_I and t_{II} and the basic efficiencies η_{OI} and η_{OII} of the component PGTs. For a more accurate reading of the influence of the structural scheme parameters on the efficiency, an approach is assumed, in which the efficiencies of the component PGTs η_{OI} and η_{OII} are determined as a function of the number of teeth of the gears in the corresponding PGT [63]

$$\eta_0 = 1 - \psi_z = 1 - \frac{z_3 + z_1}{z_3 - z_1} \left(\frac{0,15}{z_1} + \frac{0,2}{z_3} \right). \quad (8.73)$$

For this reason the following approach for determining t_I and t_{II} is used:

1. Choice of number of teeth for the sun gears of the component gear trains z_{1I} and z_{1II} .
2. Determination of minimum and maximum number of teeth of the ring gears $z_{3I} \min = t_{I \min} \cdot z_{1I}$, $z_{3II} \min = t_{II \min} \cdot z_{1II}$, $z_{3I} \max = t_{I \max} \cdot z_{1I}$, $z_{3II} \max = t_{II \max} \cdot z_{1II}$.
3. Determination of the current values of the torque ratios $t_I = \frac{z_{3I}}{z_{1I}}$ and $t_{II} = \frac{z_{3II}}{z_{1II}}$.

4. Consecutive increase in the number of teeth of the ring gear of one gear train (e.g., the second one) one tooth at a time until the maximum value (determined in p. 2) is reached.
5. Consecutive increase in the number of teeth of the other gear train (e.g., the first one) one tooth at a time, while the cycle is repeated for the second gear train (p. 3) until the maximum value (determined in p. 2) is reached.

The program allows the inclusion of fulfillment check for the additional conditions when choosing the number of teeth:

- Coaxiality condition, i.e.,

$$z_2 = \frac{z_3 - z_1}{2} = \text{int} \quad (8.74)$$

- Mounting condition

$$\frac{z_3 + z_1}{k} = \text{int} \quad (8.75)$$

In practice, the coaxiality condition is eluded by choosing appropriate corrections of the tooth meshing, which are even recommended from the standpoint of teeth bending stiffness.

The mounting condition could also be eluded [27] with appropriate design solutions.

A program is created, which determines within 3 cycles the current values of the various parameters of the component (η_{0I} , η_{0II} , d_{3I} , d_{3II}) and compound (η_{0red} , $\varphi_{D\min}$, $\eta_{Br.1}$, $\eta_{Br.2}$, $\varphi_{Br.1}$, $\varphi_{Br.2}$) planetary gear trains as a function of t_I and t_{II} .

The thus established database is used for building the graphical relations of the changes in the parameters as a function of t_I and t_{II} , which contribute to the quick orientation of the designer in the capabilities of the various structural schemes.

Due to differences in the dimensions and variations of the individual criteria, they are normalized while nondimensional quantitative measures are assumed:

$$k_i(t_I, t_{II}) = \frac{f_i(t_I, t_{II}) - f_i^{\min}}{f_i^{\max} - f_i^{\min}}$$

or

$$k_j(t_I, t_{II}) = \frac{f_j^{\max} - f_j(t_I, t_{II})}{f_j^{\max} - f_j^{\min}} \quad (8.76)$$

where:

$k_i(t_I, t_{II})$ is the normalized (nondimensional) value of the criteria with minimum values.

$k_j(t_I, t_{II})$ is the normalized (nondimensional) value of the criteria with maximum values.

$f_i(t_I, t_{II})$ and $f_j(t_I, t_{II})$ are the current values of the corresponding characteristics.

f_{\max} and f_{\min} are the extremal values of the characteristics in the given range of t_I and t_{II} .

The generalized criterion is assigned. It is expressed by a purpose function obtained from the scalar product of the vectors, the components of which are weight coefficients and nondimensional purpose evaluations

$$Z(t_I, t_{II}) = \sum_{i=1}^n \chi_i \cdot k_i(t_I, t_{II}) \quad (8.77)$$

where:

$\chi = (\chi_i)'$ is the vector of the weight coefficients, $0 < \chi_i < 1$; $\sum \chi_i = 1$.

$k = (k_i)'$ is the vector of the nondimensional purpose evaluations

$$(t_I^*, t_{II}^*) : \min_{t_{\min} \leq t_I, t_{II} \leq t_{\max}} Z(t_I, t_{II}). \quad (8.78)$$

The weight coefficients reflect the priority of each criterion. Thus, the different degree of importance of the various criteria for each particular case of gear train application is taken into account.¹

The optimal solution regarding the controlling parameters t_I and t_{II} is the one in which the purpose function (8.77) reaches its minimum value.

8.2.3.2 Optimal Choice of a Structural Scheme

Within the single-objective optimizations, the choice of the most appropriate structural scheme is reduced to the determination of the best combination of t_I and t_{II} for the chosen parameter in the various structural schemes, comparison of the parameter values, and determination of the most appropriate structural scheme (with the corresponding values of t_I and t_{II}).

In multi-objective optimization the most appropriate values for t_I and t_{II} for each of the given structural schemes are determined as well from the standpoint of the generalized criterion (8.77).

¹At the end of the twentieth century, there was a tendency toward dismissing the optimization methods with weight coefficients as subjective. Modern computer technology with its advanced dialogue mode enables the rapid simulation of different variants (with different weight coefficients) and renders these methods more flexible and suitable for various tasks, which definitely compensates the shortcomings of subjectivism and even turns it into advantage.

With first approximation one could expect the best structural scheme to be the one with the lowest value of the purpose function (8.77). For more accurate results, however, it is desirable that what is determined by the multi-objective optimization values of the individual criteria (characteristics, indices) be compared with one another. This means another normalization where (8.76) becomes

$$k_i(p_{sh}) = \frac{f_i(p_{sh}) - f_i^{\min}}{f_i^{\max} - f_i^{\min}}$$

or

$$k_j(p_{sh}) = \frac{f_j^{\max} - f_j(p_{sh})}{f_j^{\max} - f_j^{\min}} \quad (8.79)$$

where:

$k_i(p_{sh})$ is the normalized (nondimensional) value of the criteria with minimum values.

$k_j(p_{sh})$ is the normalized (nondimensional) value of the criteria with maximum values.

$f_i(p_{sh})$ and $f_j(p_{sh})$ are the current values of the corresponding characteristics obtained by multi-objective optimization of the various schemes.

f_{\max} and f_{\min} are the extremal values of the characteristics obtained by multi-objective optimization of the various schemes.

p_{sh} is the number of the structural scheme participating in the optimization.

The procedure for determining the purpose function (8.77) and its minimum value (8.78) is repeated for the thus determined nondimensional values of the criteria $k(p_{sh})$.

The process in (8.79) features the various versions of the structural schemes corresponding to the kinematic criterion (to provide the necessary ratio between the output angular velocities $\frac{\omega_B}{\omega_{B\mu}}$ in the admissible range of t_I and t_{II}).

Figure 8.13 presents the result of the optimization of all variants which provide the desired speed ratios (the most appropriate structural scheme is given in the bottom row).

The design, technological, and economic optimization methods reviewed in Sect. 1.1 can be applied to the variant chosen by the method above (according to the specific case).

A major advantage of the proposed program is the possibility to take different indices and study their dependence on the torque ratios of the component gear trains. This enables the detailed study of the various structural schemes (Fig. 8.14).

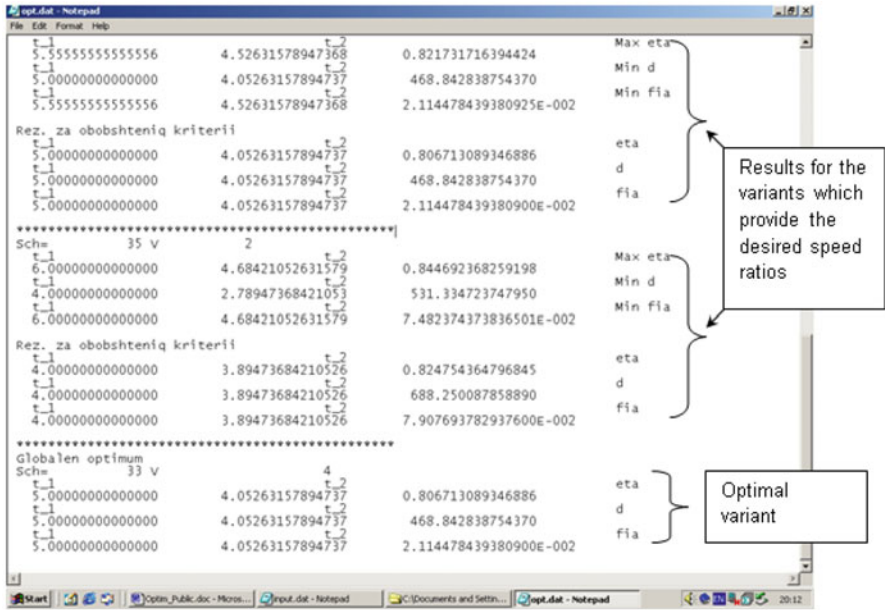
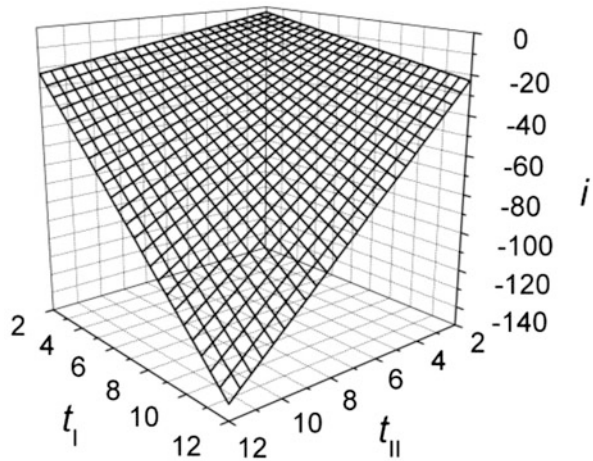


Fig. 8.13 Result of the optimization of all variants providing the desired speed ratios

Fig. 8.14 Total speed ratio as a function of torque ratios t_I and t_{II} of scheme S13WN (E)



8.3 Program 2-BRZ

Developed 2-BRZ program (software) is intended for investigation of single-speed and two-speed two-carrier PGTs. It is written in the Compaq Visual Fortran Professional Edition 6.6.0. The program has three subprograms for:

- Analysis of characteristics of arbitrary variant.
- Synthesis of all solutions that meet the set requirements.
- Evaluation of the solution.

A description of its subprogram (modules) is given below.

8.3.1 *Subprogram for PGT Characteristics Analysis*

This subprogram enables the generation of sets of different characteristics of each of the PGT variants according to the given input data in the *input* file and recording these sets in a file. This allows engineering visualization of large data sets and comprehensive analysis. In order to speed up the response of the program, there is also the possibility to obtain a reduced record of the data sets of the analyzed variant of the PGT.

Reduced record contains data on the PGT variant at given intervals of torque ratios t_I and t_{II} . These data are:

- Achievable gear ratios.
- Teeth numbers of planets.
- Planets modules.

Reference diameters of ring gears

- Ratios of reference diameters of ring gears.
- Approximate masses of gears (sun gear, ring gear, and planets) in component PGT.
- Approximate mass of gears in compound PGT.
- Calculated efficiency of compound PGT.
- Dispersion of the calculated efficiency shown by standard deviation.
- Relative speeds of planets.
- Forces on planet bearings.
- Torques on the brake shafts.

The complete set, in addition to the above data, also contains:

- Rotational speeds of all elements.
- Torques on all elements.
- Power on all elements.
- Relative (rolling) power in both component PGTs.

All the above data is accompanied by an ordered pair of torque ratios t_I and t_{II} of component PGTs so that they can be graphically represented as functions of these ratios. The program also allows the display of the interdependence of the values of

these characteristics, where one or two characteristics can form a domain and the third a codomain.

All output data of the analysis subprogram are entered in the folder *all results* of the developed program *2-BRZ*.

8.3.2 *Subprogram for PGT Variants Synthesis*

The synthesis subprogram returns as a result of all solutions (PGT variants) that meet the requirements from the *input* file of the *2-BRZ* program as well as the sets of their quantitative characteristics. The output data is written to the *results* folder and they are:

- Alphanumeric designation of the compound PGT variant.
- Corresponding torque ratios of component PGTs.
- Corresponding speed ratios.
- Numbers of teeth of ring gears of component PGTs.
- Modules of PGTs meshing.
- Ratios of reference diameters of PGTs ring gears.
- Approximate masses of gears (sun gear, ring gear, and planets) in component PGT.
- Approximate mass of gears in compound PGT.
- Relative speeds of planets.
- Dispersion characteristic of the calculated equivalent² efficiency (standard deviation).
- Possible specific circulated power.

8.3.3 *Subprogram for Evaluation of the Solution*

The solution evaluation subprogram enables the ranking of the compound PGT variants according to the criteria covered by the complex global objective function and the selection of optimal solution.

The minimum of the global objective function $Z_{gl\ min}$ gives, conditionally speaking, the optimal solution. Namely, this solution is a recommendation of a program in which the most important criteria are expressed by weight coefficients. Due to the impossibility of the mathematical model to cover all criteria that affect the quality of the solution, as well as the problem of lack of information for exact values of the weight of the criteria, it is strongly recommended to critically evaluate solutions from the aspect of criteria not covered by the mathematical model.

²*Equivalent efficiency* is calculated for two-speed PGTs on the base of efficiencies in work with both speeds (i_1 and i_2) considering relative working time of each of them.

In the output file *rank* in the *results* folder (program *2-BRZ*) with the ordinal number indicating the position of each variant of the compound PGT on the priority scale, the program system returns:

- Compound PGT variant designations with corresponding weight coefficients.
- The value of the global objective function, i.e., the quantitative evaluation of the solution.
- The corresponding torque ratios t_I and t_{II} of component PGTs.
- Achievable speed ratio of compound PGT (total speed ratio).
- Dispersion of equivalent efficiency determined by standard deviation.
- Reference Diameter of the Larger Ring Gear (Indicator for Overall Dimension of Compound PGT)
- Ratio of the reference diameters of the ring gears of larger and smaller component PGT.
- Approximate mass of gears in compound PGT.
- Rotational speed of the fastest planet.
- Modules of PGTs meshing.
- The minimum required dynamic load capacity of the most loaded planet bearing.

8.3.4 *Input Data*

So far, the possibilities of the program in the form of output are listed. In order to obtain the output data, input data must be entered. The input data is entered in the *input* file (program *2-BRZ*). Some of them will be shown in the following examples.

8.4 Examples of Selection of the Optimal Compound PGT Variant

8.4.1 *Optimal Choice of Single-Speed PGT*

In case the goal is to arrange a single-speed PGT (Table 8.1), the program will generate a set of variants of single-speed PGTs that can meet the set requirements. Each variant of this set, in the general case, has a set of ordered pairs of torque ratios t_I and t_{II} , where each individual ordered pair enables the realization of the required total speed ratio in its tolerance interval. All arranged pairs within the corresponding variant enable the realization of the required speed ratio, but with different overall dimensions of component PGTs, different efficiency, different relative speeds of planets, etc. The program can find the most acceptable ordered pair of torque ratios

guided by selected criteria. The criteria are accompanied by certain weight coefficients which describe their importance—see formula (8.77).

With a given torque on the input shaft of $T_A = 50 \text{ Nm}$, the required total speed ratio $i = 30.5 \pm 0.5$, and the number of teeth of sun gears $z_{1I} = z_{1II} = 18$, the program provides solutions. Secondary input data is not shown in this example.

The program makes it possible to compare all variants of the compound PGT with each other and to obtain a priority list of variants with their optimal parameters according to the weights of the selected criteria.

For three different combinations of weights, the program generates three files with a list of PGT variants by priority that can achieve the given total speed ratio. In Table 8.12, Table 8.13, and Table 8.14, variant designations with some basic data are listed.

From Table 8.12 it can be seen that according to this criterion the optimal variant is 66NE(W). This variant has the smallest radial dimensions $d_{3\text{max}} = 180 \text{ mm}$, but it has a relatively low degree of efficiency $\eta = 0.481$. The second variant is 26WE(N) with an ordered pair of torque ratios (6, 3.3333) which has a slightly larger dimension $d_{3\text{max}} = 195 \text{ mm}$ and a significantly higher efficiency $\eta = 0.964$.

The analysis of Table 8.13 shows that according to the criterion of the highest efficiency, the optimal variant is 26WE(N) with an ordered pair of torque ratios (4.1667, 5) and the calculated efficiency $\eta = 0.966$. The priority list shows that the

Table 8.12 Priority list of PGT variants with associated parameters obtained with weight coefficients $\chi_a = 1$, $\chi_n = 0$

Variants	Z_{gl}	t_I	t_{II}	i	η	$d_{3\text{max}}$, mm	$d_{3\text{max}}/d_{3\text{min}}$
S66NE(W)	0	3.8333	4	30	0.481	180	1.043
S26WE(N)	0,02717	6	3.3333	30.333	0.964	195	1.032
S55NE(W)	0,03261	3.6667	3.1667	30.555	0.734	198	1.069
S26WN(E)	0,04484	6	3.5	-30.5	0.964	204.75	1.083
S16WN(E)	0,04484	6.5	3.5	30.25	0.964	204.75	1
S33NE(W)	0,05299	5	5.1667	31	0.462	209.25	1.033
S16WE(N)	0,05435	6.6667	3.5	-30	0.963	210	1.025
S44NE(W)	0,0625	3.1667	3.6667	30.555	0.734	214.5	1.075
S23WN(E)	0,08016	6.6667	3.8333	30.389	0.963	224.25	1.068
S23WE(N)	0,08967	8.5	3.1667	-30.083	0.958	229.5	1.074
S13WN(E)	0,09239	8.5	3.6667	-30.167	0.959	231	1.007
S13WE(N)	0,09239	8.3333	3.6667	30.555	0.960	231	1.027
S44NE(W)	0,12228	5	4.1667	-30	0.806	247.5	1.1
S55NE(W)	0,12228	4.1667	5	-30	0.806	247.5	1.1
S22NE(W)	0,22826	4	4.1667	-30	0.461	306	1.02
S33NE(W)	0,2731	10.5	10.1667	-30.5	0.521	330.75	1.033
S66NE(W)	0,29348	9.5	9.1667	-30.5	0.538	342	1.036
S11NE(W)	0,30435	5	4.8333	30	0.465	348	1.031
S11NE(W)	0,32609	5	5.1667	-30	0.444	360	1.032
S22NE(W)	0,86957	9.1667	8.8333	30.5	0.558	660	1.038

Table 8.13 Priority list of PGT variants with associated parameters obtained with weight coefficients $\chi_d = 0, \chi_\eta = 1$

Variant	Z_{gl}	t_I	t_{II}	i	η	d_{3max}, mm	d_{3max}/d_{3min}
S26WE(N)	0	4.1667	5	31	0.966	247.5	1.886
S16WN(E)	0.00098	5	5	31	0.965	247.5	1.571
S23WN(E)	0.00098	5	5	31	0.965	270	1.714
S26WN(E)	0.00137	4.3333	5	-31	0.965	270	1.978
S23WE(N)	0.00246	5	5.1667	-31	0.964	279	1.771
S16WE(N)	0.00246	5.1667	5	-31	0.964	247.5	1.520
S13WE(N)	0.00496	5.1667	6	31	0.963	297	1.825
S13WN(E)	0.00653	5.3333	6	-31	0.962	297	1.768
S55NE(W)	0.07694	12	8.3333	30.54	0.926	432	1.28
S44NE(W)	0.07694	8.3333	12	30.54	0.926	432	1.28
S55NE(W)	0.08717	8.3333	11.8333	-30.55	0.920	426	1.262
S44NE(W)	0.08717	11.8333	8.3333	-30.55	0.920	426	1.136
S66NE(W)	0.77995	8.8333	9.1667	30.5	0.559	330	1.038
S22NE(W)	0.77995	9.1667	8.8333	30.5	0.559	660	1.038
S11NE(W)	0.80696	10	9.6667	30	0.545	696	1.031
S33NE(W)	0.81254	9.8333	10.1667	30.5	0.542	320.25	1.034
S22NE(W)	0.81955	9.1667	9.5	-305	0.538	684	1.036
S66NE(W)	0.81955	9.5	9.1667	-305	0.538	342	1.036
S11NE(W)	0.84752	10	10.3333	-30	0.524	720	1.032
S33NE(W)	0.85269	10.5	10.1667	-30.5	0.521	330.75	1.033

Table 8.14 Priority list of PGT variants with associated parameters obtained with weight coefficients $\chi_d = 0.5, \chi_\eta = 0.5$

Variant	Z_{gl}	t_I	t_{II}	i	η	d_{3max}, mm	d_{3max}/d_{3min}
S26WE(N)	0.01503	6	3.3333	30.333	0.964	195	1.031
S16WN(E)	0.02377	6.5	3.5	30.25	0.964	204.75	1
S26WN(E)	0.02431	6	3.5	-30.5	0.964	204.75	1.083
S16WE(N)	0.0295	6.6667	3.5	-30	0.963	210	1.026
S23WN(E)	0.04272	6.6667	3.8333	30.389	0.963	224.25	1.068
S23WE(N)	0.05048	7.3333	3.6667	-30.555	0.961	231	1
S13WE(N)	0.05153	8.3333	3.6667	30.555	0.960	231	1.027
S13WN(E)	0.05269	8.5	3.6667	-30.167	0.959	231	1.006
S55NE(W)	0.18314	7	5.5	30.333	0.872	283.5	1.041
S55NE(W)	0.19463	5.6667	7.1667	-30.852	0.866	290.25	1.035
S44NE(W)	0.20058	5.1667	6.5	30.063	0.863	292.5	1.144
S44NE(W)	0.21317	6.6667	5.3333	-30.666	0.857	300	1.136
S66NE(W)	0.46493	3.8333	4	30	0.481	180	1.043
S33NE(W)	0.50931	5	5.1667	31	0.462	209.25	1.033
S66NE(W)	0.55651	9.5	9.1667	-30.5	0.538	342	1.036
S33NE(W)	0.56289	10.5	10.1667	-30.5	0.521	330.75	1.033
S22NE(W)	0.59804	4	4.1667	-30	0.461	306	1.020
S11NE(W)	0.63184	5	4.8333	30	0.465	348	1.031
S11NE(W)	0.66304	5	5.1667	-30	0.444	360	1.032
S22NE(W)	0.82476	9.1667	8.8333	30.5	0.559	660	1.038

first eight mentioned variants of PGT have the same value of efficiency, so when choosing the best variant, the variant that is better according to other criteria can be chosen.

The analysis of Table 8.14 shows that taking into account both criteria with equal weights, the best choice is the variant 26WE(N) with an ordered pair of torque ratios (6, 3.3333) which has a reference diameter of radially larger ring gear $d_{3\max}=195$ mm and calculated efficiency $\eta=0.964$. In this variant, the degree of efficiency does not change significantly with all three combinations of weight coefficients.

In the same way, an optimal solution for different input data can be sought. The program will offer a list of solutions based on the criteria with which it works, and based on the list of solutions, the designer can choose the appropriate variant of the PGT, guided by criteria that are not built into the logic of the program.

8.4.2 Optimal Choice of Two-Speed PGT

Compound PGTs with two internal and four external shafts (Table 8.2) are investigated. For operating with $F = 1$ degree of freedom, the brake on one of the external shafts is needed. These PGTs are appropriate to realize two speed ratios (i_{Br1} and i_{Br2}) with two brakes (Br1 and Br2) on two external shafts. Three locations of both brakes are possible [27, 49]:

- Brakes on both compound shafts (Fig. 8.15a).
- Brakes on both single shafts (Fig. 8.15b).
- Brakes on a single and on a compound shaft (Fig. 8.15c).

All possible working modes (brakes' location and power flow direction) of all variants are checked through the optimization procedure. The variants are described by number from Table 8.2 and indication of input and output shafts (by letters according to the four directions of the world—W-west, N-north, E-east, and S-south). For example, S16NW means Scheme 16 from Table 8.2 with top (N-north) shaft as input and left (W-west) shaft as output.

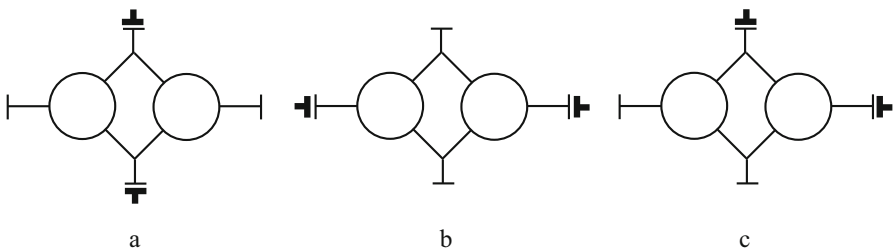


Fig. 8.15 Possible locations of both brakes at two-carrier PGT with four external shafts: a) Brakes on both compound shafts. b) Brakes on both single shafts. c) Brakes on a single and on a compound shaft

Two of more common cases of these PGT applications are investigated below.

Example A: Two-speed compound PGT with positive speed ratios

To show how the program can help set up a two-speed PGT, the following example is shown. Some relevant inputs are:

- Number of required speed ratios is 2: $9.8 \leq i_1 \leq 10$ and $3.9 \leq i_2 \leq 4$.
- Intervals of torque ratios are $2 \leq t_{I} \leq 12$ and $2 \leq t_{II} \leq 12$.
- Numbers of teeth of sun gears are $z_{1I} = 18$ and $z_{1II} = 18$.
- Relative working times with every speed ratio (i_1 and i_2) are $\alpha_{i1} = 0.7$ (70%) and $\alpha_{i2} = 0.3$ (30%).
- Input torque is $T_A = 50$ Nm and input speed is $n_A = 2850 \text{ min}^{-1}$.

Based on the 2-BRZ program, results are obtained that show the basic parameters of PGT variants that can realize the required speed ratios. Some of the basic parameters of these variants are listed in Table 8.15, Table 8.16, and Table 8.17.

Table 8.15 Priority list of solutions obtained with weighting coefficients $\chi_d = 1, \chi_n = 0$

Priority	Scheme	t_I	t_{II}	i_1	i_2	$d_{3 \text{ max}}, \text{ mm}$	η_{eq}
1.	S16WN	3	2	10	4	117	0.953
2.	S55NE	5	3	10	4	157.5	0.930
3.	S13WE	5	2	10	4	157.5	0.940
4.	S36SE	4.833	8.833	9.833	3.912	238.5	0.986
5.	S33SN	3	8.833	9.833	4	238.5	0.984
6.	S12WN	8.833	2	9.833	3.944	238.5	0.979

Table 8.16 Priority list of solutions obtained with weighting coefficients $\chi_d = 0, \chi_n = 1$

Priority	Scheme	t_I	t_{II}	i_1	i_2	$d_{3 \text{ max}}, \text{ mm}$	η_{eq}
1.	S36SE	4.833	8.833	9.833	3.912	238.5	0.986
2.	S33SN	3	8.833	9.833	4	238.5	0.984
3.	S12WN	8.833	2	9.833	3.944	238.5	0.979
4.	S16WN	3	2	10	4	117	0.953
5.	S13WE	5	2	10	4	157.5	0.940
6.	S55NE	5	3	10	4	157.5	0.930

Table 8.17 Priority list of solutions obtained with weighting coefficients $\chi_d = 0.5, \chi_n = 0.5$

Priority	Scheme	t_I	t_{II}	i_1	i_2	$d_{3 \text{ max}}, \text{ mm}$	η_{eq}
1.	S16WN	3	2	10	4	117	0.953
2.	S36SE	4.833	8.833	9.833	3.912	238.5	0.986
3.	S33SN	3	8.833	9.833	4	238.5	0.984
4.	S12WN	8.833	2	9.833	3.944	238.5	0.979
5.	S13WE	5	2	10	4	157.5	0.940
6.	S55NE	5	3	10	4	157.5	0.930

The analysis of Table 8.15, which was obtained only according to the criterion of minimum dimensions ($\chi_d = 1$), shows that the smallest radial dimensions of the larger ring gear are obtained with the S16WN variant with an ordered pair of torque ratios t_I and t_{II} (3; 2). In this case, the reference diameter of the larger ring gear is $d_{3\max} = 117$ mm. It can be seen that in this variant the mass is also the smallest. The calculated equivalent efficiency is $\eta_{eq} = 0.953$.

The analysis of Table 8.16, obtained only according to the criterion of the maximum equivalent efficiency ($\chi_\eta = 1$), shows that S36SE is the variant with the highest efficiency. The calculated efficiency is $\eta_{eq} = 0.986$, but the reference diameter of the larger ring gear is $d_{3\max} = 234$ mm—significantly larger than the reference diameter of the best variant from Table 8.15 (117 mm).

The analysis of Table 8.17 obtained according to both criteria with the same weighting coefficients ($\chi_d = 0.5$ and $\chi_\eta = 0.5$) shows that the optimal variant is S16WN, as in the case of $\chi_d = 1$ and $\chi_\eta = 0$.

It is observed that changing the weight of the criteria changes the value of the global function of the target, and thus the position of the variants in the priority list.

With two-speed PGTs, only one combination of torque ratios t_I and t_{II} can give the required speed ratios. This means that when choosing the optimal solution, they cannot vary in the search for torque ratios because otherwise the speed ratios would also change. Numerous computer syntheses of various solutions show that two-speed two-carrier PGT do not have a large number of variants that can meet the kinematic requirements. This makes it relatively easier to choose the right solution.

Example B: Reversible two-speed compound PGT

Reversible two-speed compound PGTs can provide different speeds (by absolute value) in every direction (appropriate for technological machines with slow working and fast retrieval movement) or equal speeds in both directions—mainly used in vessels [27, 47, 49–51, 70]. The second case is investigated below.

Some relevant inputs are:

- Number of required speed ratios is 2: $-4.6 \leq i_1 \leq -4.4$ and $4.4 \leq i_2 \leq 4.6$.
- Intervals of torque ratios of component PGTs are $1.4 \leq t_I \leq 6$ and $1.4 \leq t_{II} \leq 6$.
- Relative working times with every speed ratio are $\alpha_{i1} = 0.9$ (90%) and $\alpha_{i2} = 0.1$ (10%).
- Input torque is $T_A = 3000$ Nm and input speed is $n_A = 1800$ min⁻¹.

It is necessary to determine the torque ratios t_I and t_{II} , actual speed ratios i_1 and i_2 , teeth numbers of all gears, and efficiency. All component PGTs are with $k = 3$ planets.

Based on the 2-BRZ program, results are obtained that show the basic parameters of PGT variants that can realize the required gear ratios. Some of the basic parameters of these variants are listed in Table 8.18, Table 8.19, and Table 8.20. The speed ratios are indicated as i_{Br1} and i_{Br2} in dependence on the locked brake—Br1 or Br2 (Table 8.20). Marked (colored) values of efficiency are for forward speed of the boat (at which it mainly operates).

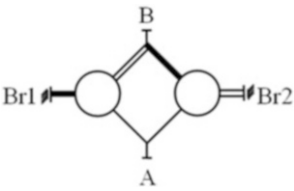
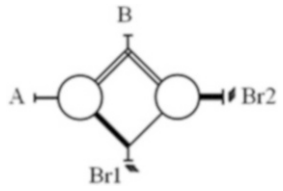
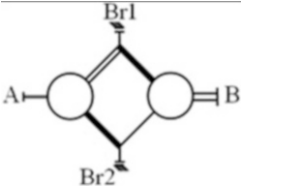
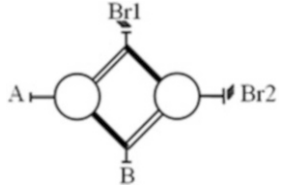
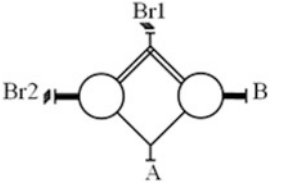
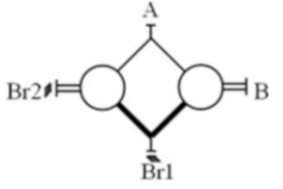
Table 8.18 Main parameters of both component PGTs

Scheme	t_I	t_{II}	z_{1I}	z_{2I}	z_{3I}	z_{1II}	z_{2II}	z_{3II}
S36SN	3.5	4.55	14	17	49	20	35	91
S16WE	1.714	1.604	42	15	72	53	16	85
S33SE	1.714	4.437	42	15	72	16	27	71
S13WN	3.5	1.553	14	17	49	47	13	73
S12WS	4.55	1.553	20	35	91	47	13	73
S55NE	1.714	3.4	42	15	72	15	18	51

Table 8.19 Speed ratios and efficiencies of compound PGTs

Scheme	i_{Br1}	i_{Br2}	η_{oI}	η_{oII}	η_{Br1}	η_{Br2}
S36SN	4.5	-4.55	0.973	0.985	0.979	0.985
S16WE	-4.464	4.407	0.976	0.978	0.962	0.976
S33SE	-4.438	4.422	0.976	0.980	0.980	0.959
S13WN	4.5	-4.436	0.973	0.973	0.979	0.934
S12WS	-4.55	4.573	0.985	0.973	0.985	0.969
S55NE	4.4	-4.475	0.976	0.974	0.980	0.924

Table 8.20 Acceptable solutions (A-input shaft; B-output shaft)

No.	Scheme	Structural scheme	No.	Mark	Structural scheme
1	S36SN		4	S13WN	
2	S16WE		5	S12WS	
3	S33SE		6	S55NE	

8.5 Concluding Remarks

This chapter discusses a method for optimal selection of a structural scheme and its parameters of compound two-carrier PGTs. The optimization methodology is based on the torque method, which makes it easy and understandable for the engineer. The optimization procedure is demonstrated on compound two-carrier planetary gear trains with three external shafts. Due to the limited volume of this chapter, the authors have not shown the peculiarities of the application of the method in other more complex two- and multi-carrier PGTs, but the main things are the same.

According to the presented methodology, an optimization procedure for selection of structural scheme and its parameters for two-speed change-gears on the base of compound two-carrier PGTs with four external shafts has been developed, details of which can be found in [42, 47, 49, 50]. Other aspects of these interesting PGTs can be found in [48, 70–72].

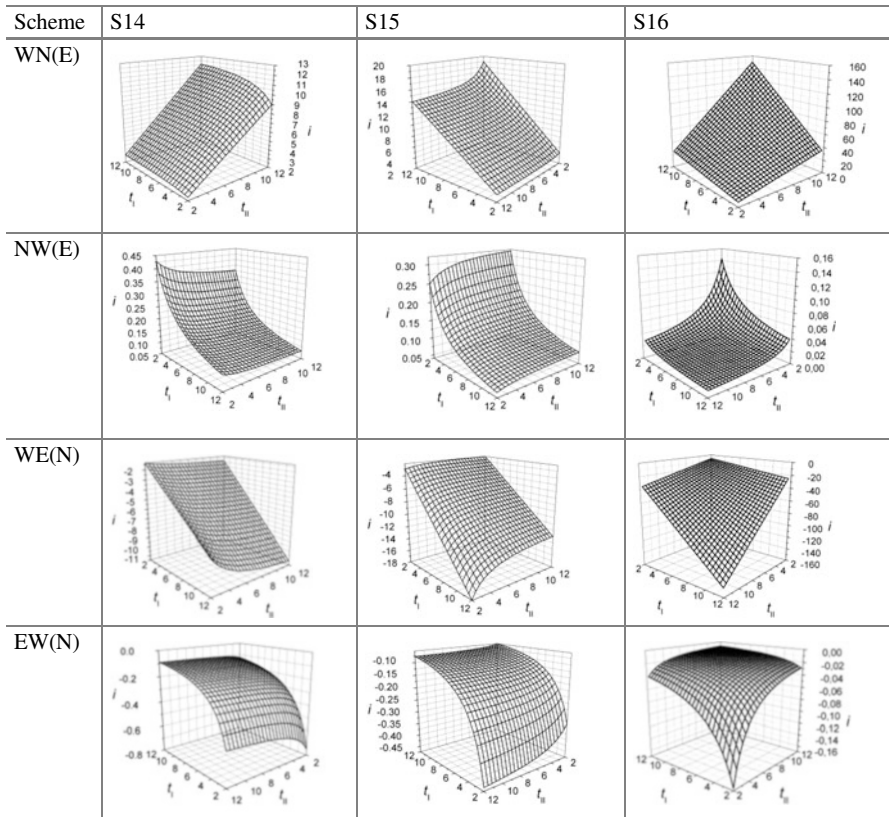
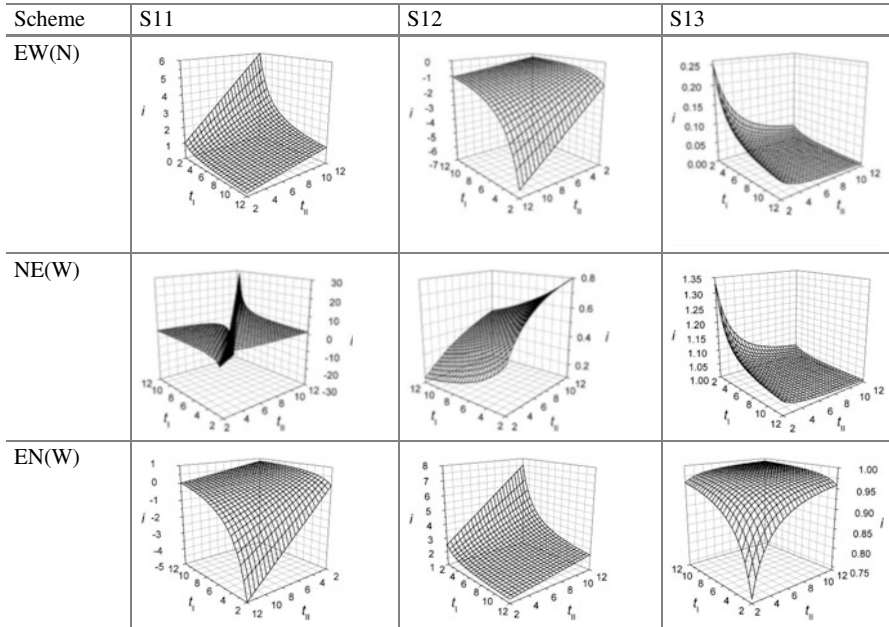
The proposed methodology is also suitable for more complex multi-carrier PGTs.

Appendix 8.1

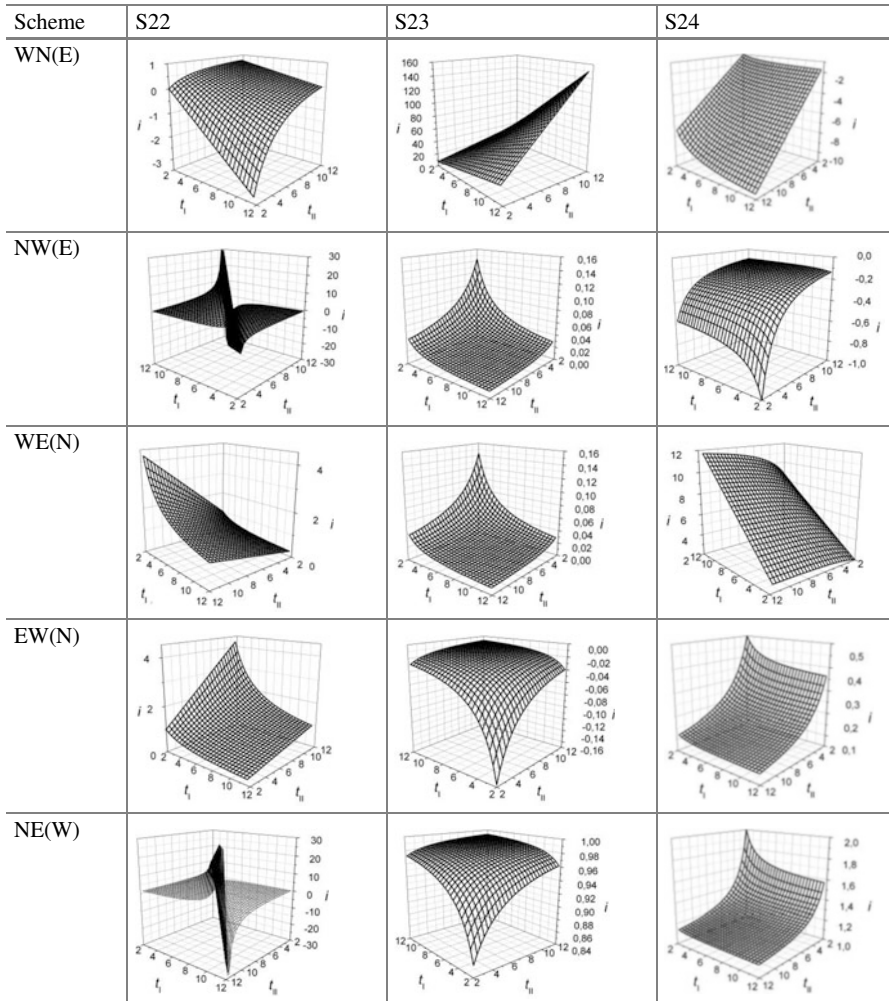
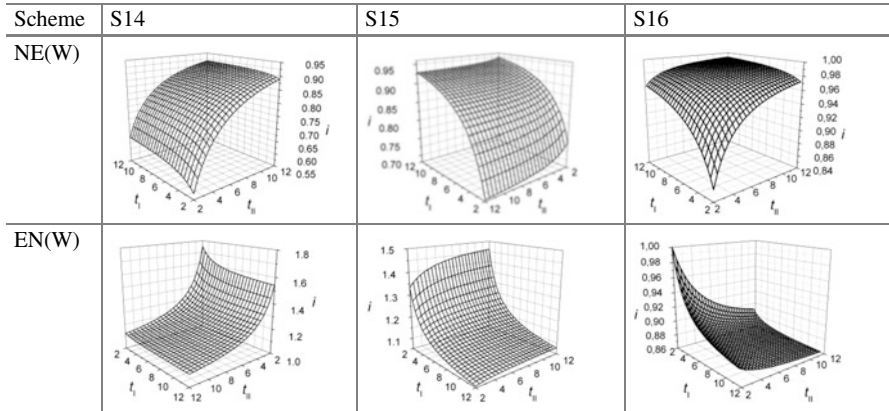
Total speed ratio i of six working modes of compound PGTs from Table 8.1 as a function of torques ratios t_I and t_{II} of component PGTs.

Scheme	S11	S12	S13
WN(E)			
NW(E)			
WE(N)			

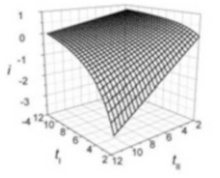
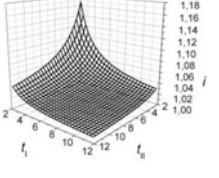
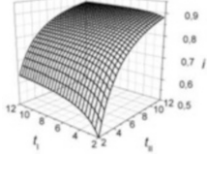
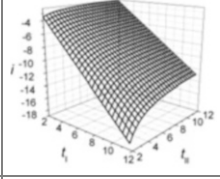
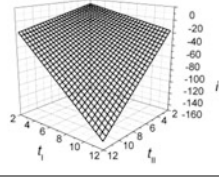
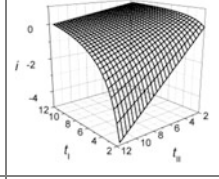
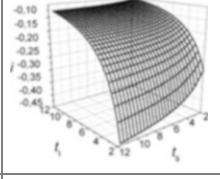
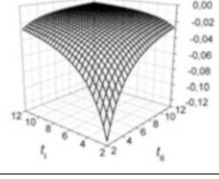
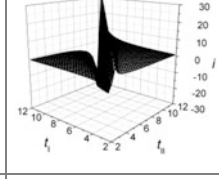
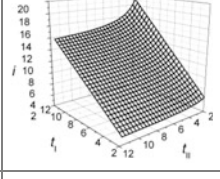
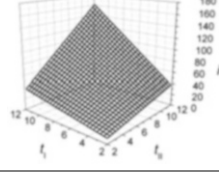
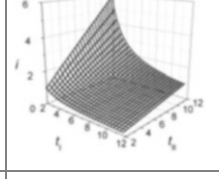
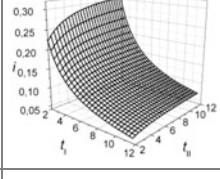
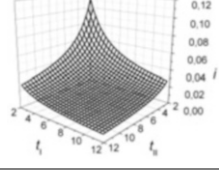
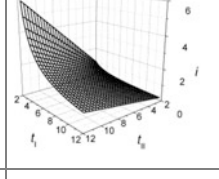
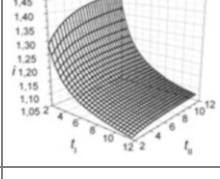
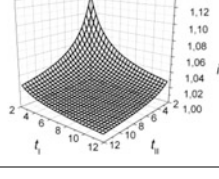
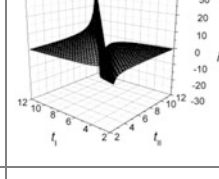
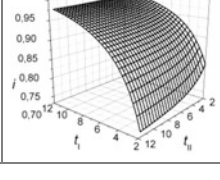
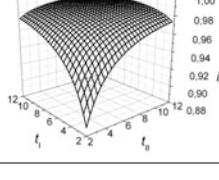
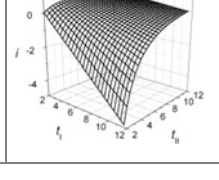
(continued)



(continued)



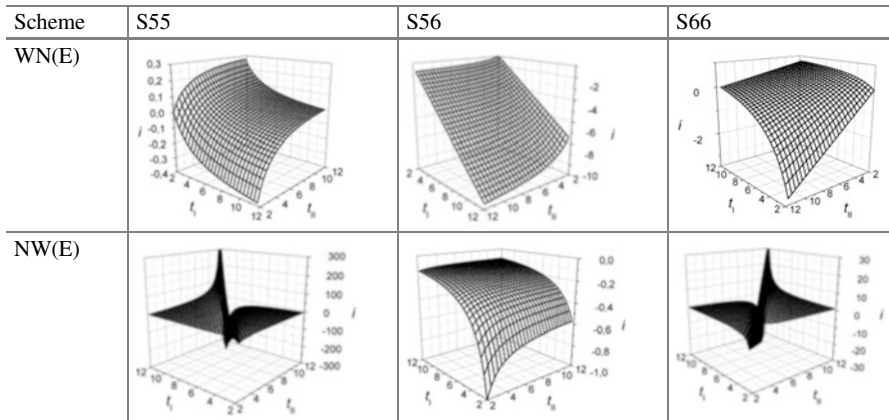
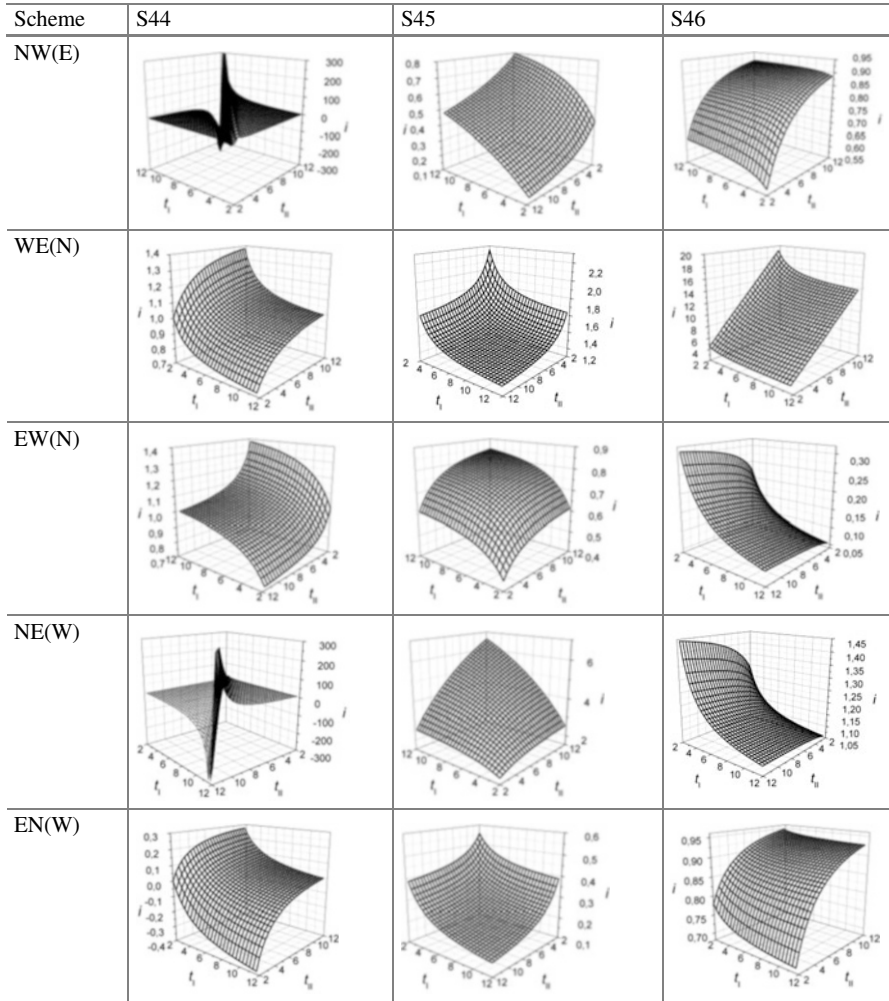
(continued)

Scheme	S22	S23	S24
EN(W)			
WN(E)			
NW(E)			
WE(N)			
EW(N)			
NE(W)			
EN(W)			

Scheme	S34	S35	S36
WN(E)			
NW(E)			
WE(N)			
EW(N)			
NE(W)			
EN(W)			

Scheme	S44	S45	S46
WN(E)			

(continued)



(continued)

Scheme	S55	S56	S66
WE(N)			
EW(N)			
NE(W)			
EN(W)			

References

1. Dimchev, G. (2000). *Geometrical and technical-economical optimization of gear trains. Habilitation Thesis.* Sofia: Technical University. (in Bulgarian).
2. Goll, S. (1980). Einfluss auf die Tragfähigkeit Zahnrad. *Maschinenbautechnik*, 86.
3. Linke, H. And G. Gayewski. Breitenlastverteilung unter besonderen Berücksichtigung bei Verzahnungen. *Maschinenbautechnik*. 1983, Nr.10.
4. Roth, K., Kollenroth, F. Zahnradsparungen mit komplementprofilen. *Konstruktion*. 1982, Nr. 3.
5. Shaker, M., T. Zou, J. Angeles, and A. Morozov. Optimization of tooth-root profile for maximum load-carrying capacity: spur and bevel gears. *CCToMM Mechanisms, Machines, and Mechatronics (M³) Symposium, Ottawa, Ontario: May 28 and 29, 2015.* http://iftomm.net/images/Documents/ConferenceProceedings/CCToMM_2015.pdf
6. Satoshi, Oda. Study on bending fatigue strength of gears. // Bull. ISME, Nr.177, 1980.
7. Zhuravlev, G.A. and G.A. Ageev. Synthesis of spur gear trains with minimal bending stresses. *Vestnik Mashinostroenia* 1982, No 2. (in Russian).
8. Stoyanov, S., A. Dobrova, and V. Dobrev. Design system for gear trains in the environment of SolidWorks®. *Proceedings of the "Power Transmissions 2006", Novi Sad, Serbia, 25–25 April 2006*, pp. 91–94.
9. Gushchin, V. G., & Ostrovskiy, G. N. (1980). Spur gear train with multidirectional deviations of the pitch of gearing. *Izvestiya VUZ Mashinostroenie, 11.* (in Russian).

10. Leistner, F. And E. Freitag. Einfluss deer Taumelabweichung auf das Tragbild bei Stirnradgetrieben. *Maschinenbautechnik*. 1979, Nr.10.
11. Teraushi, Y., H. Nadano, and N. Miaoru. On the effect of the tooth profile modification on the dynamic load of the spur gear. *Bull. ISME*, Nr. 207, 1982.
12. Ma, H., Pang, X., Feng, R., & Wen, B. (2016). Evaluation of optimum profile modification curves of profile shifted spur gears based on vibration responses. *Mechanical Systems and Signal Processing*, 70-71, 1131–1149. <https://doi.org/10.1016/j.ymssp.2015.09.019>.
13. Vulić, A. And J. Stefanović-Marinović. Design parameters for planetary gear transmissions optimization. *Proceedings of the "Power Transmissions 2006"*, Novi Sad, Serbia, 25–25 April 2006, pp. 137–142.
14. Klein, B., and Z. Li. Analytisches Verfahren zur parametrischen Optimierung von Zahnradgetrieben. *Antriebstechnik*. 1995, Nr. 3, S. 75–78.
15. Lambin, L. N. (1983). Assignment of displacement factors in the automated design of gear trains. *Vestnik Mashinostroeniya*, 6. (in Russian).
16. Karaivanov, D. (2009). X-Gear – an European project in help of gear trains manufacturers. *Machines Technologies Materials*, 3(3–4), 3–8. (in Bulgarian).
17. Concli, F., & Coenen, J. (2015). Low-lost gears for precision planetary gearboxes: Influence of the gear design on the meshing and the churning power losses. *VDI-Berichte*, 2255-1, 53–65. ISSN 0083-5560.
18. Concli, F., & Gorla, C. (2013). A new methodology for the prediction of the no-load losses of gears: CFD an experimental investigation of the efficiency of a planetary gearbox. *VDI-Berichte*, 2199-2, 1125–1137. ISSN 0083-5560.
19. Hohn, B. -R., K. Stahl and P. Gwinner. Improved efficiency for high-ratio planetary gear transmission for wind turbines – Low-loss Wolfrom transmission for wind turbines. *VDI-Berichte* 2199–2202, 2013, pp. 1113–1124. ISSN 0083-5560.
20. Kruszynski, B. Einfluss des Walzfraserverschleisses auf die Eigenspannungen von Zahnradern. *Werkstoff und Betrieb*, 1981, Nr. 9.
21. Gulya, Z. N. (1981). *Durability control of cylindrical gear wheels*. Vysshaya Shkola: Lvov. (in Russian).
22. Ponamarev, V. P., & Shchin, D. P. (1981., No. 3). Technological tolerances and dimensions determination in gear cutting process. *Vestnik Mashinostroeniya*. (in Russian).
23. Stefanović-Marinović, J. and M. Milovančević. An application of multicriteria optimization to planetary gear transmissions. *Proceedings of The International Conference Mechanical Engineering in XXI Century*, 25–28 November 2010, Niš, Serbia, pp. 133–136.
24. Norihisa, A., & Susomi, H. (1981). *Research on bending strength properties spur gears without rim*. *Bull. ISME*, Nr195.
25. Tae-Hyong, C., & Toshiyui, S. (1982). Bending stress of internal Spur Gear. *Bull. ISME*, 202.
26. Sholomov, N. M. (1984., No. 4). Stresses determination in the tooth root of thin-rim gears. *Vestnik Mashinostroeniya*. (in Russian).
27. Arnaudov, K., & Karaivanov, D. (2019). *Planetary gear trains* (p. 358). Boca Raton: CRC Press. ISBN 978-1-138-31158-5.
28. Peeken, H. and J. Widanata. Rechnerunterstutze Konstruktioin von Maschinen-gehausen zur Optimierung. *Konstruktion*. 1982, Nr. 6.
29. Pinenkamp, W. Methoden zur Konstruktion und Prufung grosser Zahnradgetrieben. Congr. mond. engrenage, Paris, 1977, Nr. 2.
30. Winter H. Gears & Gear Research. Gearing and transmissions. 1995, No. 1.
31. Ognianović, M. and S. Ćirić-Kostić. Gear disturbance energy transmission through the gear system and frequency spectrum. *Proceedings of the "Power Transmissions 2006"*, Novi Sad, Serbia, 25–25 April 2006, pp. 167–172.
32. Dinev, G. One approach for multicriteria optimization of one stage gear transmission. In *Proceedings of 6th Int. Conference RaDMI 2006, Budva, Montenegro, 13–17 September 2006* (pp. 201–206).

33. Ushakov, M. M. (1985., No. 8). Relative weight of gear trains. *Izvestiya VUZ Mashinostroenie.* (in Russian).
34. Kos, M. Bewertung der Ausgleichssysteme in Planetengetriebe. *Konstruktion*. 1981, Nr. 3.
35. Petrov, Z. V., & Prevalov, V. S. (1984). Minimization of the reduced moment of inertia of two-stage cylindrical gear trains. *Izvestiya VUZ Mashinostroenie*, 12. (in Russian).
36. Week, M., & Gold, P. (1977). *Möglichkeiten und Grenzen bei der Bestimmung des dynamischen Verhaltens von Zahnradgetrieben*. Paris: Congr. mond. engrenage.
37. Arnaudov, K., & Karaivanov, D. (2004). Raum- und Massesparende Zahnradgetriebe. In *Proceedings of the 3rd Conference about Construction, Shaping & Design*. Novi Sad (pp. 73–78).
38. Karaivanov, D. Structural analysis of coupled multi-carrier planetary gear trains – from lever analogy to multi-objective optimization. *Proceedings of the 3rd Int. Conf. on Manufacturing Engineering (ICMEN)*, 1–3 October 2008, Chalkidiki, Greece, pp. 579–588.
39. Rao, S.S. Multiobjective optimization in structural design with stochastic processes. *AIAA Journal*. 1984, 108, No. 4, pp. 1670-1678.
40. Rao, S. S., & Eslampour, H. R. (1986). Multistage multiobjective optimization of gearboxes. *Journal of Mechanisms, Transmissions, and Automation in Design.*, 108, 461–468.
41. Savsani, V., Rao, R., & Vakharia, D. (2010). Optimal weight design of a gear train using particle swarm optimization and simulated annealing algorithms. *Mechanism and Machine Theory*, 45, 531–541.
42. Troha, S., P. Petrov, and D. Karaivanov. Regarding the optimization of coupled two-carrier planetary gears with two coupled and four external shafts. *Machinebuilding and Electrical Engineering*. 2009, **LVIII** (1), pp. 49–55. ISSN 0025-455X.
43. Bozzolo, A., & Zangani, D. (2009). Development of gear drive-trains based on new materials and novel gear systems. In *Proceedings of the 3rd Int. Conf. Power Transmissions '09* (edited by A. Mihailidis), *Kallithea [Greece]* (pp. 249–253). ISBN 978-960-243-662-2.
44. Mihailidis, A. and C. Pupaza. Simulation Driven Design of Internal Gears. Multicriteria optimization of internal gears. *VDI-Berichte*, Nr. 2108, 2010, pp. 725–740.
45. Brüser, P. (1989). Optimierung von Planetengetrieben. *Antriebstechnik*, 28(2), 64–67.
46. Daoudi, K., El-M. Boudi, and M. Abdellah. Genetic Approach for Multiobjective Optimization of Epicyclic Gear Train. *Mathematical Problems in Engineering*. 2019, 9324903, 10, <https://doi.org/10.1155/2019/9324903>.
47. Stefanović-Marinović, J., S. Troha, and M. Milovančević. An application of multicriteria optimization to the two-carrier two-speed planetary gear trains. *Facta Universitatis, Series: Mechanical Engineering*. 2017, **15** (1), pp. 85–95. ISSN 0354–2025 (Print) , ISSN 2335–0164 (Online).
48. Stefanović-Marinović, J., Troha, S., Andelković, B., & Milovančević, M. (2018). Efficiency of planetary gear trains as criterion for optimal solution selection. *Machine Design.*, 3, 95–98. ISSN 1821-1259.
49. Troha, S. (2011). *Analysis of a planetary change gear train's variants*. Dissertation. Croatia: Engineering Faculty, University of Rijeka. (in Croatian).
50. Troha, S., Ž. Vrcan, D. Karaivanov, and M. Isametova. The selection of optimal reversible two-speed planetary gear trains for machine tool gearboxes. *FACTA UNIVERSITATIS, Series: Mechanical Engineering*. 2020, **18** (1), pp. 121–134. ISSN: 0354–2025 (Print), ISSN: 2335–0164 (Online).
51. Troha, S., Stefanović-Marinović, J., Vrcan, Ž., & Milovančević, M. (2020). Selection of the optimal two-speed planetary gear train for fishing boat propulsion. *FME Transactions.*, 48(2), 397–403. ISSN 1451-2092.
52. Tkachenko, B. A. (2003). *Planetary mechanisms*. Kharkov: Kharkov Aviation Institute Publ. (in Russian).
53. Arnaudov, K., & Karaivanov, D. (2001). Engineering analysis of the coupled two-carrier planetary gearing through the lever analogy. In *Proceedings of the International Conference on Mechanical Transmissions* (pp. 44–49). Chongqing, China: China Machine Press.

54. Karaivanov, D. (2000). *Theoretical and experimental studies of influence of the structure of coupled two-carrier planetary gear trains on its basic parameters. Dissertation*. Sofia: University of Chemical Technology and Metallurgy. (in Bulgarian).
55. Karaivanov, D., S. Troha, and R. Pavlova. Experimental study of the losses in a three-stage planetary gear train. *Proceedings of the 3rd Int. Conf. "Power Transmissions '09"*, edited by A. Mihailidis, Kallithea [Greece], 1–2 Oct., 2009, pp. 527–532. ISBN 978-960-243-662-2.
56. Kurth, F. (2012). *Efficiency determination and synthesis of complex-compound planetary gear transmissions. Dissertation*. Munich: Technical University.
57. Niemann, G., & Winter, H. (1995). *Maschinenelemente. Band 2. Zahnradgetriebe – Grundlagen, Stirnradgetriebe. 2. Auflage*. Berlin: Springer-Verlag.
58. Arnaudov, K., & Karaivanov, D. (2017). *Torque method for analysis of compound planetary gear trains* (p. 92). Beau Bassin [Mauritius]: LAP Lambert Academic Publishing. ISBN 978-620-2-01693-3.
59. Arnaudov, K., Alipiev, O., & Karaivanov, D. (2020). Biplanetary gear trains and their analysis through the torque method. In V. Goldfarb, E. Trubachev, & N. Barmina (Eds.), *New approaches to gear design and production* (Mechanisms and Machine Science 81) (pp. 311–322). Springer Nature Switzerland AG. ISSN 2211-0984, ISBN 978-3-030-34944-8, <https://doi.org/10.1007/978-3-030-34945-5>.
60. ISO 6336 Calculation of load capacity of spur and helical gears, 2006.
61. Karaivanov, D. Structural analysis of the coupled planetary gears with considering the efficiency of the coupling gears. *Proceedings of the 2th Int. Conf. on Manufacturing Engineering (ICMEN), Kallithea of Chalkidiki, Greece*, October 5–7, 2005, pp. 381–387. ISBN 960-243-615-8.
62. Predki, W., F. Jarhov F., and J. Kettler. Calculation method for the determination of the oil sump temperature of industrial planetary gears. *VDI-Berichte 1665–1*, pp. 507–522.
63. Karaivanov, D. and S. Troha. On the structural Analysis of Coupled Planetary Gears. *Machinebuilding and electrical engineering*. 2005, Special edition – science edition 9, pp. 76–83.
64. Müller, H. W. (1998). *Die Umlaufgetriebe – Auslegung und vielseitige Anwendungen* (2. Auflage ed.). Berlin: Springer-Verlag.
65. Karaivanov, D., & Popov, R. (2003). Experimental study on the clearances of the two-stage planetary gear. *Journal of the University of Chemical Technology and Metallurgy*, 4(XXXVIII), 1331–1338.
66. Veits, V. L., Kochura, A. E., & Martynenko, A. E. (1971). *Dynamic calculation of machines transmissions* (352 p). Leningrad: Mashinostroenie.
67. Arora, J., & Wang, Q. (2005). Review of formulations for structural and mechanical system optimization. *Structural and Multidisciplinary Optimization*, 30(4), 252–272.
68. Stoyanov, S. (2006). *Optimization of technological systems*. Tehnika: Sofia. (in Bulgarian).
69. Karaivanov, D. Handling machines gearings and their optimal choice. *Zbornik radova sa Naučno-stručnog skupa Istraživanje i razvoj mašinskih elementa i sistema JAHORINA – IRMES'2002, 2/2, Srpsko Sarajevo - Jahorina*, 19. i 20. September 2002, pp. 685–690.
70. Troha, S., D. Karaivanov, and E. Džindo. Two-speed two-carrier planetary gear trains. *7th International Scientific and Expert Conference TEAM 2015, Technique, Education, Agriculture & Management*. Belgrade, Serbia, October 15–16, 2015, pp. 538–542.
71. Troha, S., N. Lovrin, and M. Milovančević. Selection of two-carrier shifting planetary gear train controlled by clutches and brakes. *Transactions of FAMENA*. 2012, XXXVI (3), pp. 1–12. ISSN 1333-1124.
72. Troha, S., Žigulić, R., & Karaivanov, D. (2014). Kinematic operating modes of two-speed two-carrier planetary gear trains with four external shafts. *Transactions of FAMENA*, 38(1), 63–76. ISSN 1333-1124.

Chapter 9

Development of Gears from the Antiquity to the Present Time



Jože Hlebanja and Gorazd Hlebanja

9.1 Emergence of Gears

Gears soon became vital components of machines transmitting power and movement from an energy source to accomplish useful work. According to historical evidence, irrigating machines emergence might be attributed to ancient Egypt (or great river valley civilizations in general) because of human need to irrigate soil to produce needed food. This machine, called *sakia* (Fig. 9.1), used simple wooden gears (Fig. 9.2) to transmit power and rotation. At first, the ancient population irrigated soil by *swapes* or *shadufs*. Such a device consisted of a bucket on the end of a cord that hung from the long end of a pivoted boom which was counterweighted at its short end. Based on observation, they realized that they could increase capacity by tying a greater number of containers to a rope. On this basis, a paternoster-like device was gradually developed, which consists of a rope formed into a ring, with buckets (containers) attached at regular intervals, hung onto a wheel. They probably first rotated the wheel manually and thus lifted the water from the river, poured it into a trough, and irrigated the fields. The hard, manual operation was strenuous and ineffective, so later a whim was developed to replace human power with that of draught animals. The whim is composed of a horizontal gear wheel attached to a rotary vertical pillar, which the animal pulls and spins around its vertical axis, while the gear drives the paternoster via its tandem gear (Fig. 9.2) and a horizontal shaft, roughly as seen in Fig. 9.1. The shadufs and sakiyas are still in use in some parts of the world.

J. Hlebanja
University of Ljubljana, Ljubljana, Slovenia
e-mail: joze.hlebanja@siol.net

G. Hlebanja (✉)
University of Novo Mesto, Novo Mesto, Slovenia
e-mail: gorazd.hlebanja@siol.net

Fig. 9.1 Photo of a sakia
[1]



Fig. 9.2 Gearing of a sakia
[1]



It is obvious that this simple device could have been produced at the time with simple tools, which were at disposal at that time. These and similar devices used the oldest wooden gears we know as a result of human creative capacity.

Figure 9.2 shows that gear teeth were simple rounded pegs fixed in the gear wheel. The whim gear rotated slowly with a pace of the draught animals, while the speed of the paternoster wheel depended on the transmission ratio of the gears. The precision of the rotation transmission was insignificant, and uninterrupted rotation of the whim, continuously fed the soil. Through the centuries, pumping water by whim with simple gears was perfected and spread to the fields of the great rivers like the Euphrates and Tigris in Mesopotamia, the Indus and Ganges in India, and the Yellow River and Yangtze in China.

9.2 Old Greeks

Antiquity time was a fruitful era for the development of geared devices and machines. Many machines with gears were described and passed on to succeeding generations by great scholars of that era, including the Greek philosopher Aristotle (384–322 BC), a student of Plato and the teacher of Alexander the Great; *Archimedes of Syracuse* (287–212 BC), a mathematician, physicist, and engineer; and *Philo of Byzantium* (ca. ~280 BC– a. 220 BC), who was a famous engineer and mechanic.

Aristotle in his works described machines such as the pulley, crankshaft, rollers, and irrigation devices with gears. Archimedes knew the principle of leverage and cranes, as well as worm gears. So, Fig. 9.3 illustrates a winch made of a gear train and a worm for the handle. He is famous for saying: “Give me a place to stand on, and I will move the Earth,” so the ancient reports have revealed that Archimedes moved a ship weighing 4200 tons out to sea using a system of levers, pulleys, and gear trains. Philo of Byzantium was famous for a chain drive and water-lifting device consisting of a gear and a rack employing also hydraulic principles. He wrote a large

Fig. 9.3 Archimedes’ winch consisting of a gear train and a worm ended handle [2]

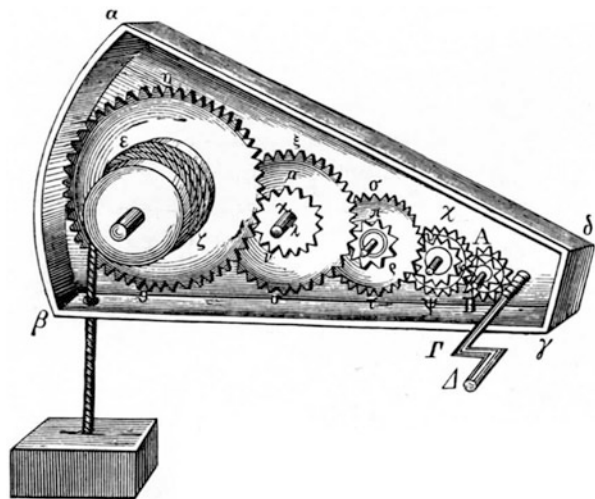




Fig. 9.4 The Antikythera mechanism: Fragment A—front and rear [4]

a technological compendium entitled *Mechanike syntaxis* (Compendium of Mechanics) consisting of nine parts, which included introduction to mathematics, mechanics, building a harbor, artillery, pneumatic principles and devices, mechanical amusements, defense preparations, siege craft, and study of cryptography [3].

The Antikythera mechanism (Fig. 9.4) was recovered in 1900–1901 from the Antikythera wreck. Its significance and complexity were not understood until decades later. The construction has been dated to the early first century BC. This precious example of antique genius complexity grade was so high that artifacts of similar complexity and workmanship did not reappear for a millennium and half, when mechanical astronomical clocks were built in Europe. All discovered parts of the mechanism are now in the National Archaeological Museum, Athens.

The true function of the Antikythera mechanism was not understood until recently, when scientists disclosed its structure and written material by contemporary methods, which include surface imaging, digital radiography (2D&3D), and computer tomography. The device is remarkable for the level of miniaturization and for the complexity of its parts and has at least 42 gears, 21 axles and shafts, and 8 pointers [5], although some scientists suggested as many as 72 gears, with teeth formed through equilateral triangles. The mechanism calculated the position of the Sun and Moon or other astronomical information such as the locations of planets, so it can be treated as an ancient analogue mechanical computer. Since the purpose was to position astronomical bodies with respect to the celestial sphere, with reference to the observer's position on the surface of the Earth, the device was based on the geocentric model [5]. Numerous models, gearings, 3D models, STL models, and simulations, were produced all over the world based on The Antikythera Mechanism Research Project (AMRP), and an example is presented in Fig. 9.5.

Fig. 9.5 The Antikythera mechanism, 3D model of the inner structure



9.3 Roman Times

The underlying mechanism of the sakia type irrigation device was used by many generations throughout Antiquity and the Middle Ages, with the gear teeth being perfected, while expanding the use of whim as a source of energy for various tasks. By expanding their rule over a large part of Europe, the Romans also spread knowledge inherited from the Greeks and Egyptians. Instead of a whim, the Romans also used the water energy of rivers or streams by a water wheel on a horizontal shaft, which drove the conical millstones on a vertical shaft by a gear pair, as illustrated in Fig. 9.6, left, as an example of *Vitruvius'* (c. 80–70 BC to c. 15 BC) engineering work. He was a Roman author, an architect, and a civil and military engineer. He wrote *The Ten Books on Architecture—De architectura*, which influenced artists and architects from the Early Renaissance onward [6]. However, Vitruvius also designed drainage systems consisting of several reverse overshot water wheels, e.g., the fragments found in Rio Tinto mines [7]. Vitruvius also designed a hodometer, consisting of a set of gears and worms, which dropped a small ball into the box for each passed mile. Vitruvius himself said that his knowledge derived from famous old Greek sources [2].

The power from the energy source—a whim or a water wheel—was transmitted by wooden gears, similar to those shown in Fig. 9.6, right, for over two thousand years without major changes. Manufacturers of such gears were always master carpenters. They shaped the water wheels and the geared wheels based on experience. According to historical sources, such gears on country mills and saws would have lasted for several decades. The Romans also used waterpower for sawing. The Roman sawmill at Hierapolis in Asia Minor from the third century incorporated a

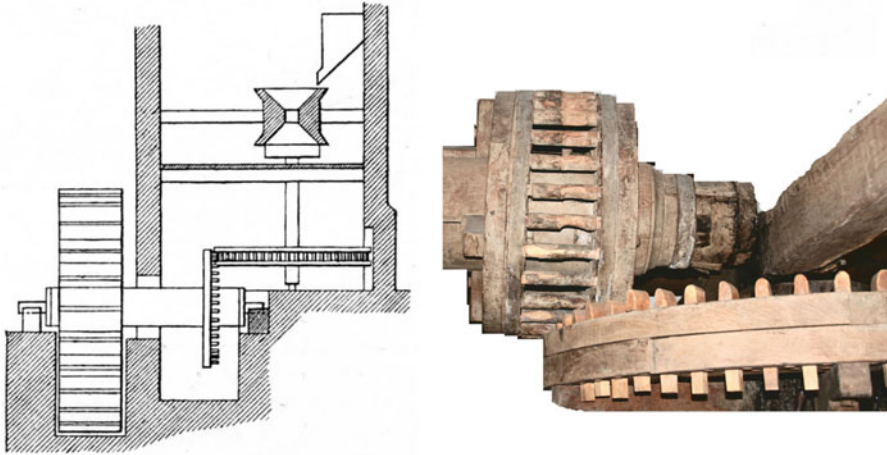


Fig. 9.6 Roman water mill, according to Vitruvius, left [2]. Appearance of wooden gears, such as those in water mills after many years of operation, right

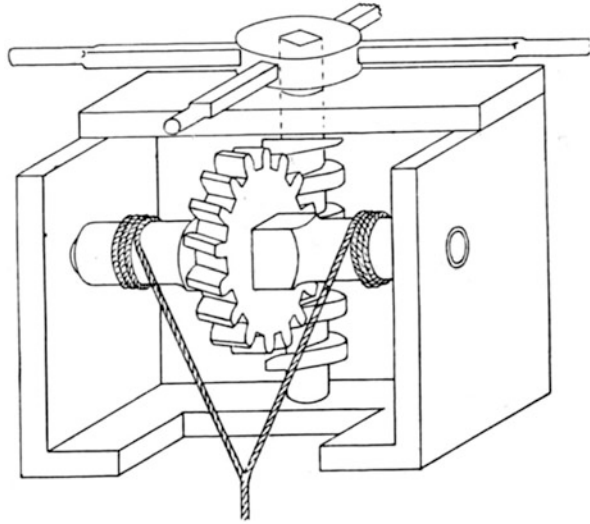
crank and connecting rod mechanism, which was used for saws cutting marble [8]. Water-driven mills and saws with wooden gears could have been found along the rivers and streams all over Europe until the beginning of the twentieth century, and some of them are preserved as examples of our technical heritage.

Heron of Alexandria (c.10–70 AD) was an ancient Greek mathematician and engineer active in his native city of Alexandria, Roman Egypt. He is considered the greatest experimenter of antiquity [9]. His numerous works start with an aeolipile, a jet engine which spins when heated. A vending machine, distributing a dose of holy water after insertion of a coin, a wind-wheel, a force pump, the Heron's fountain, and a syringe-like device are also attributed to Heron. Several variants of gear train arrangements for lifting heavy loads, such as illustrated in Fig. 9.7, are his inventions as well.

9.4 Middle Ages

In the late Middle Ages, from the thirteenth century on, mining became quite widespread. *Agricola* [10] extensively described the development of mining methods, metallurgical processes, geology, mineralogy, and according law from the earliest times to the sixteenth century in his work *De Re Metallica*. Georgius Agricola, born as Georg Bauer, 1494–1555, was a German humanist scholar, mineralogist, and metallurgist. He was broadly educated but took a particular interest in the mining and refining of metals. His work *De Re Metallica* was published in 1556, one year after his death. This 12-volume work is a comprehensive and systematic study on all available factual and practical aspects, concerning mining

Fig. 9.7 A worm winch for lifting loads [2]



and metallurgy by means of direct observation. Unrivalled in its complexity and accuracy, it served as the standard reference work for two centuries [11].

The mechanical principles of winding, ventilating, and pumping machinery described in the book were already known and old. The block and pulley, the windlass, the water wheel, the transmission of power through shafts and gear wheels, chain pumps, and piston pumps with valves were all known to the Greeks and Romans. Devices, used for lifting ore, ranged from simple man-powered windlasses to rather complex, in both direction operating water wheels. Horse-operated whims were also often, with the same working principle as ancient *sakia* as illustrated in Fig. 9.8 (left). The same applies to the water-lifting device which consists of an iron frame and three iron axles on which two pairs of drums with rundles and toothed wheels are mounted with a total reduction ratio of 36. The input axle also contains a fly wheel to facilitate action, Fig. 9.8 (right), as described in the sixth book of *De Re Metallica*.

The specialty of the machine from Fig. 9.8 (left) is the usage of a brake. A miner in the shaft pushed the vertical beam down and thus lifted the braking beam up by reverting the oscillating beam and stopped the braking wheel. This machine could have lifted ore 240 feet, and up to four horses could have rotated the whim, depending on the actual depth and loads. Nevertheless, waterpower was the limiting factor of the mine shaft depth. This did not change until the discovery of the steam engine which offered a new, powerful source of energy. Parallel to mining, craftsmanship was also thriving. Able self-taught masters honed their skills and learned how to make complex wooden gear wheels by hand, while in the meanwhile, with the advancement of metallurgy, they also began to manufacture cast iron gears. Despite the widespread use of gears to transmit movement and energy, manufacturing was still based on previous experience. The whims were also widely used in agriculture, e.g., for threshing.

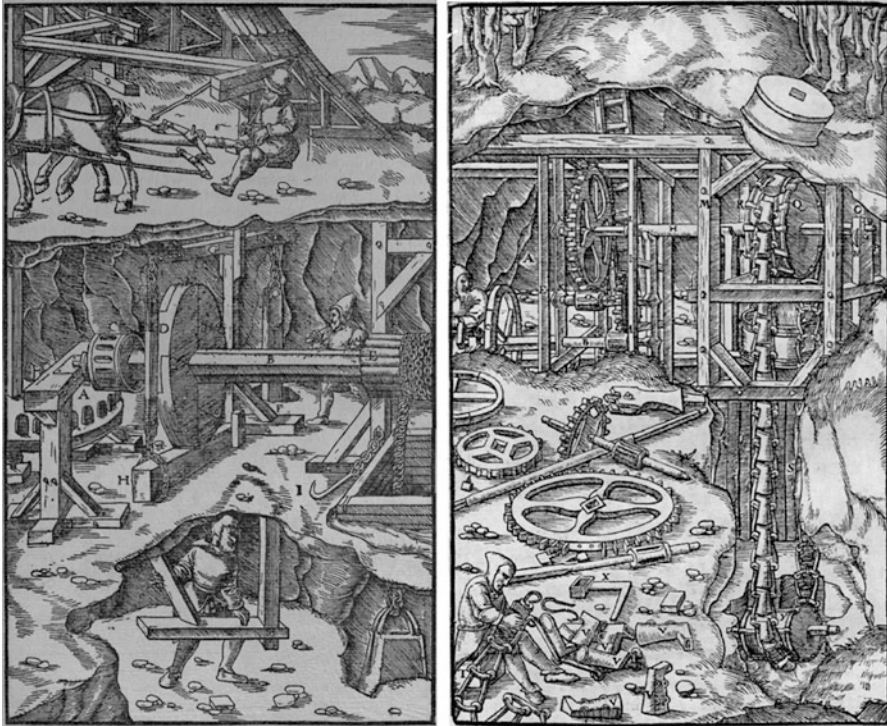
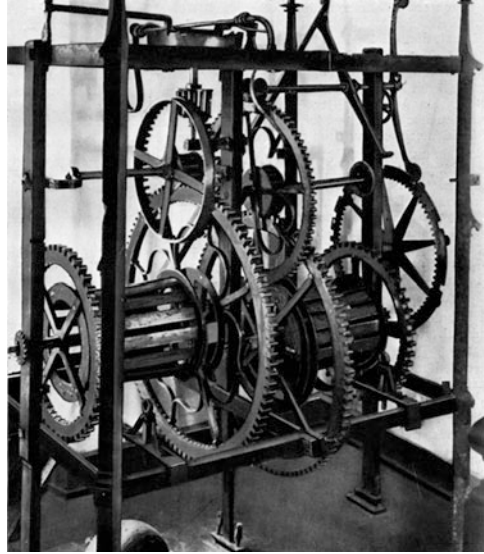


Fig. 9.8 A whim-based lifting machine. A, toothed drum which is on the upright axle; B, horizontal axle; C, drum which is made of rundles; D, braking wheel; E, drum made of hubs; F, brake; G, oscillating beam; H, short beam; I, hook (left). A water-lifting system. A, iron frame; B, lowest axle; C, fly wheel; D, smaller drum made of rundles; E, second axle; F, smaller toothed wheel; G, larger drum made of rundles; H, upper axle; I, larger toothed wheel; K, bearings; L, pillow; M, framework; N, oak timber; O, support of iron bearing; P, roller; Q, upper drum; R, clamps; S, chain; T, links; V, dippers; X, crank; Y, lower drum or balance weight (right) [10]

9.5 Mechanical Clocks

Sun dials and water clocks were introduced to Europe by the Romans and perfected by Arabs. The rare “horologes” during the Middle Ages were water powered. The word clock (from the Latin word clocca, “bell”), which gradually supersedes “horologe,” suggests that it was the sound of bells which also characterized the prototype mechanical clocks that appeared during the thirteenth century in Europe [12]. These devices were often without hands, indicating time only by bells, telling people to attend service. Churches and monasteries needed to know the precise time to perform their duties, so the first mechanical clocks were developed by monks in monasteries. The first mechanical clock with hands in Germany dated to 1304 and was situated in the Benedictine monastery of Erfurt [2]. It was driven by a weight and regulated by a simple step regulator. In that period, similar clocks appeared in

Fig. 9.9 Überlingen clock mechanism, 1540 [2]



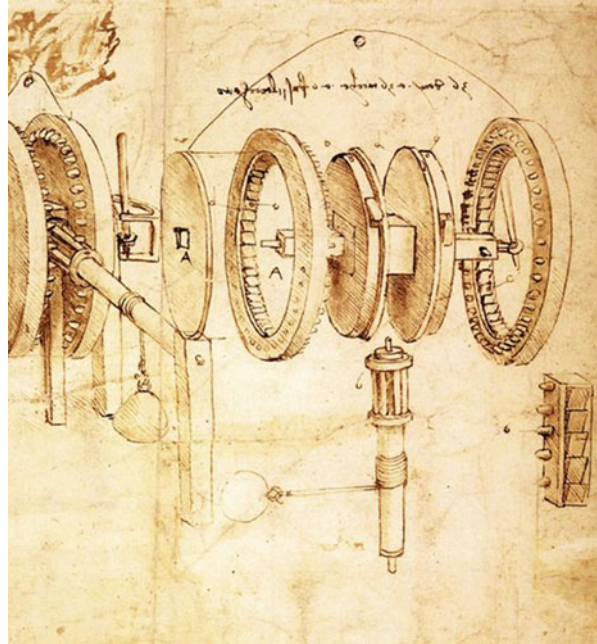
Italy, France, and England, e.g., Canterbury Cathedral installed a “great horologe” in 1292. The complexity of the geared mechanism of such clocks is represented in Fig. 9.9 showing the clock mechanism of the Überlingen cathedral tower near Bodensee [2].

The gears were from iron, and the wheels were forged and geared manually, shaped by an experienced master. The clocks of the period were powered by weights, and the introduction of springs in the fifteenth century was highly advantageous. *Christiaan Huygens* used a pendulum for clocks in 1656 [13], which increased accuracy of mechanical clocks. With an increased demand for clocks, the reputation of the clock-making profession grew, and the number of clockmakers’ guilds and masters increased, which led to the accelerated development of clocks, their miniaturization, and increased precision.

9.6 Leonardo da Vinci

Leonardo da Vinci (1452–1519) was the most famous engineer of all time. He left the legacy of his ideas of gear transmission in the form of sketches. So, he sketched numerous geared arrangements, e.g., helical gears, bevel gears, worm gears, and noncircular gears, however without precise teeth definitions. Leonardo was directly involved with the technological issues of his time and sought to find answers to questions with a pencil in his hand, drawing solutions to an issue, which could not all have been realized at the time. In any case, his sketches present solutions and reflect the technology of the time. Although Leonardo left a multitude of sketches on transmitting power and movement from one shaft to another, he did not study

Fig. 9.10 Leonardo's sketch of the geared device from "Il codice Atlantico" [2]



teeth flanks, so he did not contribute to the advancement of teeth theory. In order to give an idea of the ingenious art of sketching without redrawing, Fig. 9.10 shows an example of a mechanism as an assembly and in detail where angular and ratchet toothed wheels were used to convert back and forth movement to a concurrent rotary motion.

Agricola already described iron gears in his work *De Re Metallica*. Since its durability this already signifies the discovery of new, improved teeth flanks.

9.7 Great Scientists from the Sixteenth to the Eighteenth Century

Modern gears, which transmit power and movement uniformly, are based on the application of mathematical curves in the design of teeth flanks and discovered by great scientists in the sixteenth and seventeenth centuries, Galilei, Desargues, de la Hire, Camus, and Euler.

The first was *Galileo Galilei* (1564–1642), who, after having finished his studies in medicine, devoted his research to geometry and the mathematics of plane curves. In his 1598 treatise, he was the first to name and mathematically define curves generated by a point on a circle rolled along a straight line or along another circle of a cycloid. In addition to other laws of nature and physics, his discoveries include the

law of oscillation of the pendulum (1583) and free fall. He also improved the telescope (1609). Galileo was a professor of geometry, mechanics, and astronomy at the University of Padua until 1610. Since he was spreading and teaching heliocentric system, he was sentenced to the house arrest in 1633. During this time, he wrote works on new disciplines, now known as kinematics and strength of materials [14].

French architect and engineer *Girard Desargues* (1591–1661) was the first to use cyclic curves for practical purposes. He is also considered the predecessor of descriptive geometry and is known particularly for his work on conic sections (curves obtained by intersecting a cone with a plane). Desargues is also known for constructing a system for raising water, which he installed near Paris, using the principle of the epicycloidal wheel [15].

Some of Desargues' work is known only from the records made by his student *Philippe de la Hire* (1640–1718), French physicist, astronomer, mathematician, and engineer, who learned from Desargues all that was known about cycloids at the time. A treaty on epicycloides and their usage in mechanics was published in his 1694 book entitled *Mémoires de mathématique et de physique* [16]. *Philip de La Hire* was the first to describe the use of epicycloids for gears that ensured a uniform transmission of rotation [17]. Such a gear with a one-sided epicycloidal gearing with eight teeth is shown in Fig. 9.11 (left), while Fig. 9.11 (right) shows a pin gearing, for which de la Hire designed the correct shape of the tooth flank by generating an equidistant curve for the involute. Until recently, such gearing was used in raising mechanisms for small floodgates in water-powered sawmills. De la Hire explored the use of cycloids for the shape of teeth flanks of special gears.

In his work “*Sur la figure des dents des roués et des ailes des pignons pour rendre les horologes plus parfaits*” (1733) *Charles Etienne Louis Camus* (1699–1768), a mathematician and professor from Paris [18], discovered the conditions that have to be fulfilled for a pair of gears. This condition is defined by the following: “if, in uniform rotation, power is to be transmitted by a pair of teeth, then the normal to the teeth flanks at the contact point P (on the path of contact) must pass through the pitch point C” [2], as illustrated in Fig. 9.12, which is exactly the law of gearing known today.

This can be illustrated by a pair of cycloid gears with a rolling circle whose point P generates a hypocycloid on the pinion with a straight tooth flank, while the gear tooth flanks have the shape of an epicycloid. The teeth flanks come into contact on the path of contact where both flanks have a common tangent and normal, the latter passing through the pitch point C.

Independently of de la Hire and Camus, *Leonhard Euler* (1707 Basel–1783 St. Petersburg) sought the most advantageous shape of gear teeth flanks, and according to Jacobi, [19] in 1752 he was the first to publish a treatise on the usefulness of the involute for the shape of gear teeth flanks [20]. His concept of involute gearing shown in Fig. 9.13, left, is in common use today. Euler also discovered that the uniform transmission of power by gear teeth flanks always involves friction, which causes loss of energy. He also showed how to graphically determine the radii of curvature, which is presented for a pair of cycloid gears in Fig. 9.13, right. During

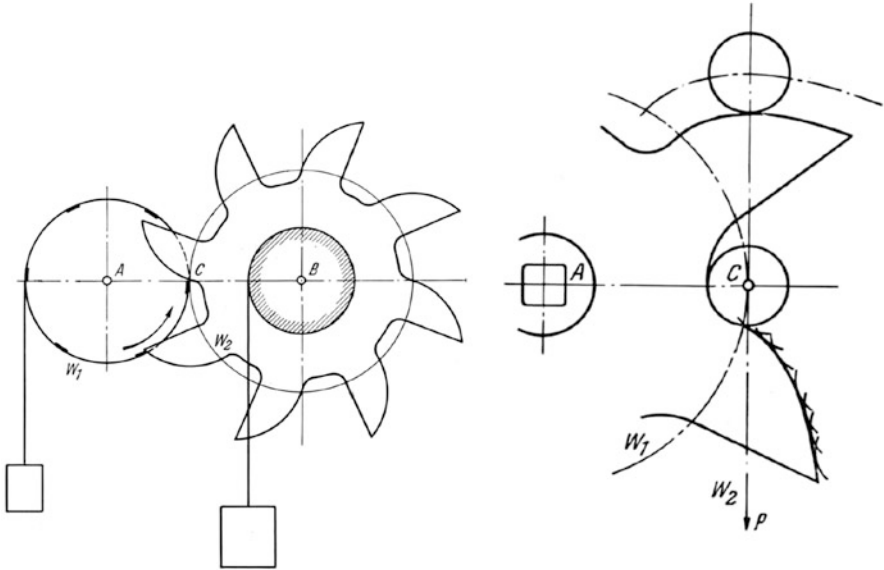
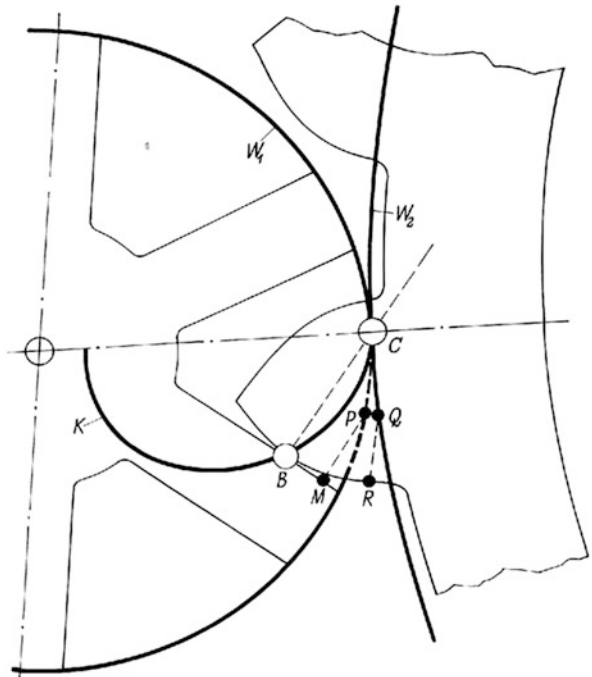


Fig. 9.11 Single-sided pin gearing (left); pin-gear rack driven by a single-sided gearing with an equidistant involute flank (right)

Fig. 9.12 Illustration of Camus' gearing principle from 1733



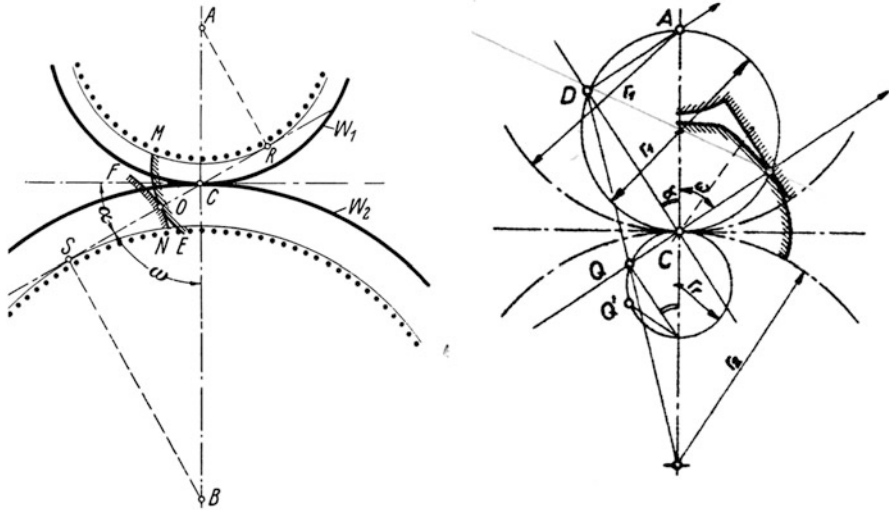


Fig. 9.13 Euler’s involute gearing (left); curvature centers of teeth flanks at the contact point in the case of a cycloid pair of teeth (right)

the rotation of the gears, the normal to teeth flanks at contact point must always pass through the pitch point C, which is why the instantaneous center of rotation is at point D, while at the same time the gear also rotates around axis O_1 , which is why the curvature center of the tooth flanks must be at contact point P, i.e., the intersection Q of the normal to the teeth flanks at the contact point and the connecting line DO_1 . Since the diameter of the rolling circle is equal to half of the pitch diameter of the big gear, the tooth flank of the big gear in this illustration has the shape of a straight line with the curvature center in infinity. Euler and Savary together devised an analytical method for determining the curvature centers of gear teeth flanks.

Christiaan Huygens (1629–1695) also had a major impact on the accelerated development of gears, when he made the pendulum clock in 1656/1657. The Huygens clock, which he patented in 1657, was very precise for its time, and with later improvements it could also display minutes as well as hours. Gears were used to transmit movement from the escapement mechanism to the handles, and weights for driving the pendulum. In the following years, Huygens also made a clock whose gear mechanism was driven by a spiral spring made of steel.

Discoveries by Galileo (doctrine of cycloids and the law of the pendulum, 1583), de la Hire (normal to the tooth flank, 1694), Camus (law of gearing, 1733), and Euler (involute gearing, 1752) can be treated as the basis for the development of contemporary gears. The era of the early development ended when the first steam engine was successfully constructed at the beginning of the eighteenth century. This was an exceptional milestone for humanity, as it was now possible to translate heat energy

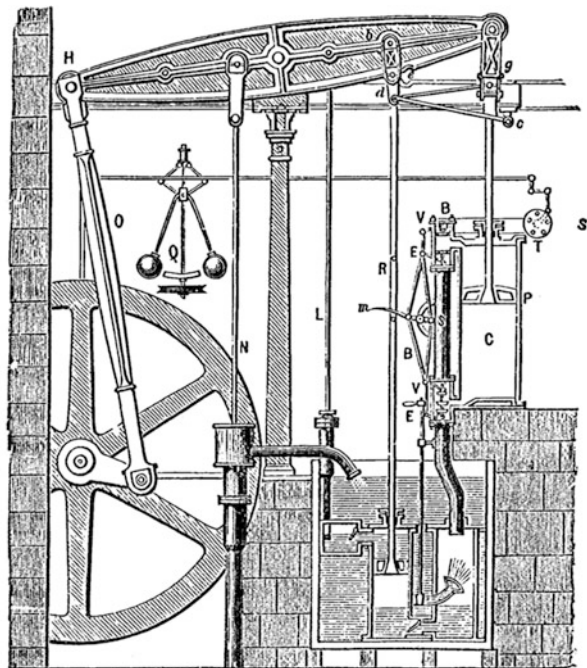
into mechanical operation based on natural laws, and marked the time when machines began to perform physical tasks previously done by people and animals.

9.8 James Watt

James Watt (1736–1819) was a Scottish inventor, mechanical engineer, and chemist who improved Thomas Newcomen’s (1712) steam engine with a design enhancement, the separate condenser (1776), which was fundamental to the changes brought by the Industrial Revolution. The separate condenser avoided huge waste of energy and radically improved the power, efficiency, and cost-effectiveness of steam engines. He adapted his engine to produce rotary motion and, thus, greatly broadened their use beyond pumping water [21]. Figure 9.14. shows the double-action steam engine, designed by Boulton and Watt, which included a centrifugal governor, yet another Watt’s invention.

The first steam engines were simple piston engines used for drawing water from the mines, and based on them a double-action rotary shaft engine was developed in 1781. In 1770, Watt introduced a unit for power based on horsepower “HP” ($1 \text{ HP} = 75 \text{ kpm/s}$), and the watt unit for measuring power was named after him ($1 \text{ W} = \text{J/s}$). He invented a centrifugal speed governor for his machines, which had “rapid” velocity for the time – 40 movements per minute – which later decreased to

Fig. 9.14 Engraving of a 1784 steam engine designed by Boulton and Watt [21]



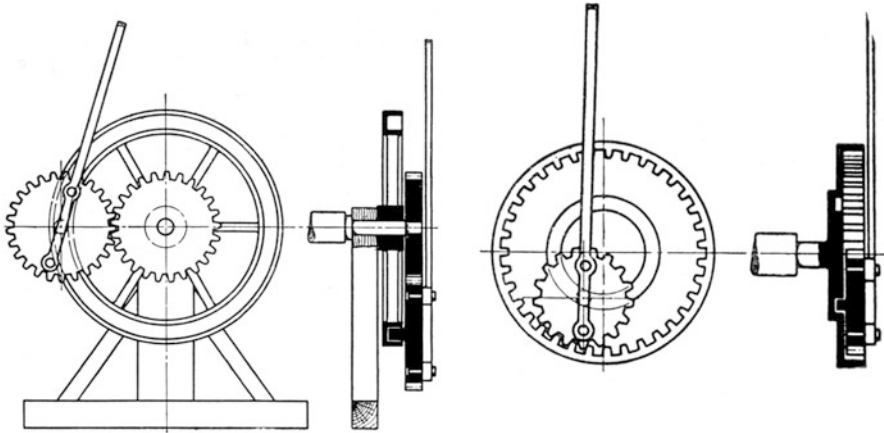


Fig. 9.15 Watt's planetary gears for the transmission of the piston movement into shank rotation: (left) for external gear pair; (right) internal gear pair [2]

30 movements per minute. Although the crank shaft was already known in Roman times, the patent was granted to Watt's opponent. Watt overcame this obstacle with planetary gears, as shown by Fig. 9.15, where a planetary gear is rigidly attached to the connecting rod of the tandem, while the sun gear is attached to the driven shaft [22] (*Encyclopædia Britannica Online*, "James Watt," 2020).

The new steam machine immediately became extremely popular, and in 1784 the Albion milling company ordered a Watt steam machine with a rotary shaft and gears. The machine, with a power of 20 PS to drive 20 mill stones, was built in 4 years, and in 1788 there was a ceremony to mark the beginning of operations. The gears had cycloid teeth flanks and were made by hand from forged iron. Watt and Rennie assessed in 1783 that teeth in corresponding gears were submitted to bending, so their calculations were adjusted accordingly. After the first successes, the development of the steam engine blossomed both in terms of construction and use. The first railways were laid on land, and the first steam ships started sailing the sea.

9.9 Electricity and Combustion Engine

The successful introduction of the Watt steam engine in the eighteenth century was followed by new successful inventions in the nineteenth century, dealing with electric power. Thus, the Belgian *Zenobe Gramme* (1826–1901) in 1870 invented the first electrical generator producing direct current. *Nikola Tesla* (1856–1943) in 1885 discovered the rotating magnetic field of alternating current. As a result of Tesla's work, the Niagara power-plant producing 3.7 MW (5000 HP) of electric energy from AC generator was connected to grid in 1895.

On the other hand, in 1861, *Nikolaus August Otto* (1831–1891) patented the first internal combustion engine running on petrol, and in 1892 *Rudolf Diesel* (1858–1913) patented the internal combustion engine running on gas, while *Karel Benz* (1844–1929) and *Gottlieb Daimler* patented an engine-driven automobile almost at the same time, at about 1887. These inventions demanded a much higher quality and loading capacity of gear transmissions. In addition to the already mentioned inventions, the discovery of the high-pressure steam turbine developed by the Swede *Gustav de Laval* (1819–1913) in 1887 and the low-pressure turbine designed by *Charles Algernon Parsons* (1854–1931) the same year should be stressed.

The enthusiasm over new sources of power and possibilities for mechanical operation gave birth to ambitious goals, which included a rack railway to the Jungfrau in Switzerland. In 1894, the entrepreneur *Adolf Guyer-Zeller* (1839–1899) was granted a license for the construction of the 9.34 km rack railway from the Kleine Scheidegg station at 2.061 meters to the Jungfrauoch summit station at 3.454 meters (Fig. 9.16).

The construction of the railway with the gauge of 1 m began in 1896 and was built in four stages. It was inaugurated in 1912. The difference in height between the upper and lower station was 1.393 m, the average operational speed was 12.5 km/h, and the average gradient 15% and maximum gradient 25% [23]. Figure 9.15 (left) shows the view of the electrical AC locomotive of 50 Hz, 500/550 V with 240 HP at the gear and a detailed view of the rack and gear of app. 70 cm, Fig. 9.15 (right), design-type Strub [2]. The successful project was remarkable at the time.

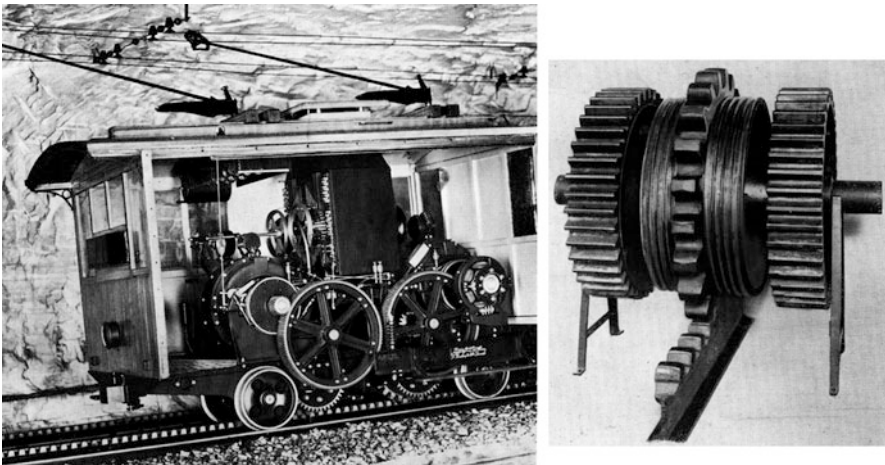


Fig. 9.16 (left) Jungfrau locomotive; (right) gear and rack

9.10 Impact to the Gear Science in the Nineteenth Century

Remarkable scientists of the eighteenth century laid the foundations and laws for designing teeth flanks, which were followed by more elaborate designs considering special machine parts for power transmission. Together with the development of energy machines came the development of processing machinery, which had specific issues regarding speed, which were overcome by gearboxes. Production demands for gears in a higher quality grade rose accordingly, but the manufacturers had limited knowledge. Due to the need for much greater loads and speeds, the gears had to be made of more durable materials, which posed the problem of manufacturing the required design of teeth flanks. This led to calls for uniform manufacturing guidelines.

Robert Willis (1800–1875) was a professor at Cambridge, who in 1841 published the book, entitled *Principles of Mechanisms* [24], where he compiled the lectures for his students and knowledge about gears which could be used in practice. At the time, gears were mostly made from cast iron, which made correcting casting-related mistakes a great problem. In 1836, Willis presented his idea on the unification of the shape of gear teeth with the gear train composed of three gears. His suggestion implies that the gears should be interchangeable, which means same pitches and same teeth sizes and an arbitrary number of gear teeth, ranging between $z = 12$ and $z = \infty$. He expressed the listed requirements with a “module,” which he designated with the letter M and defined as the quotient of the pitch t and the number π ($M = t/\pi$). He also defined pitch circles with a given number of teeth and pitch t , whose diameter was expressed with the product of the module and the number of teeth, $d_0 = M z$. He chose a uniform height of the teeth, which was equal to the module ($h = M$). Sometime later (1873), *Paul Hoppe* [25], similarly as Willis before him (Fig. 9.17, left), expressed the unification of teeth sizes with the threesome involute gear train (Fig. 9.17, right).

Willis also studied the effect of the contact angle on the shape of teeth. He found that 15° is the appropriate value when the number of teeth is limited (under-cutting when $z < 15$). The shape of gears was determined by the number of teeth z , module M , and pressure angle.

Franz Reuleaux (1829–1905) was one of the professors who were strongly involved in the development of gears. He studied the effect of the contact path on the shape of gear teeth flanks and the flank load carrying capacity. He stated, based on his research, that involute gears are the most advantageous. He became famous for his textbook *Construkteur* (1861), which focused on the topics of design in mechanical engineering and the kinematics of gear pairs.

The development of the tooth flank profile shape was completed until the end of the nineteenth century. The law of gearing, which uniformly defined the relations between the contacting teeth flanks and the path of contact, was affirmed. Based on the above, the involute gearing prevailed as the most advantageous shape of teeth flanks.

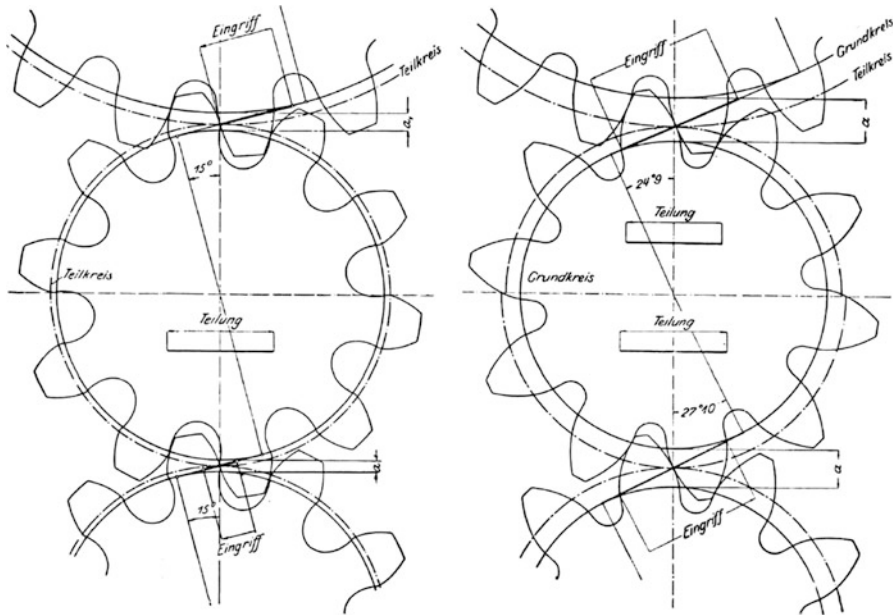


Fig. 9.17 Threesome gear train (left) after Willis; (right) after Hoppe (in [2])

9.11 Gear Manufacturing

Edward Sang (1805–1890) defined a rack as a gear with an infinite radius whose pitch circle is a straight line in his book *New General Theory of the Teeth of Wheels* (1852) [27]. And in 1861, *Carl Hermann Wiebe* (1818–1881) defined a rack for involute teeth flanks where the common normal passes through the convergence point of two involutes, always through the same point on the line connecting the axes of base circles, which also means that all contact points represent the path of contact and that the rack teeth flanks are straight [28].

The basis for manufacturing cylindrical gears by rolling with a spiral milling cutter was first constructed and patented in 1856 by German engineer *Christian Schile* in Oldham. Schile was the first to carry out the coordinated movement (rotation) of the workpiece (gear) and worm milling cutter, but he did not realize the manufacturing machine. The latter was constructed based on an American patent first in 1887 by *George Grant* (1849–1917) and in 1894 by *Julius Eduard Reinecker* (1832–1895) from Chemnitz. The Reinecker Company was the first German factory that produced machine tools for manufacturing gears by rolling with a worm milling cutter [2].

Hermann Pfauter (1854–1914) from Chemnitz substantially improved Reinecker's system of manufacturing gears with a worm milling cutter and patented the improvement in 1900, receiving the patent entitled "Pfauterverfahren." He, too,

founded a factory of machine tools for serrating gears by rolling with a worm milling cutter (*Hermann Pfauter* [29]).

Parallel to the development of gear manufacturing with a milling cutter, a gear shaper system with a straight rack tool and the Fellows gear shaper system with a circular rack tool were also developed. The gear shaper system with a straight rack was realized by Reinecker and in 1908 by *Max Maag* (1883–1960), while the gear shaper system with a circular rack was realized in 1896 by *Edwin Fellows* (1865–1945) [30].

9.12 Gear Development until 1940

At the turn of the century, the use of involute gearing was already established in general engineering and heavy industry, while cycloidal gears were mostly used in fine mechanics. Moreover, also known were effective methods for manufacturing gears either by rolling with a milling cutter or by a straight or a circular shaping (Fellows). The development of gears was closely connected to the development of energy machines at the time, which was based on emerging higher education courses in applied sciences in developed European countries that also comprised machine elements, design, and technical drawing. The knowledgeable graduates intensely worked on developing energy and processing machines, whose power, rotational speeds, and consequently complexity of gear arrangements grew rapidly. In general, the speed of energy supplying machines did not correspond to the needs of processing machines, which was resolved by gear transmissions.

Major sources of power became the quickly developing electric motors, which drove processing machines via added or built-in gears. *Werner von Siemens* (1816–1892), who built the first electric railway in 1879 [31], deserves special credit in this respect. Parsons' (1854–1931) low pressure steam turbine (1884) was also gaining importance [32]. Thus, power of anew installed devices scaled rapidly as well as the demand for appropriate gears. In power plants, steam piston engines were replaced by steam turbines, which also began driving large freight, passenger, and military ships. Steam turbines of high-power outputs (from 30.000 to 70.000 HP) and rotational speeds between 4000 and 5000 RPM were used to run propellers on big ships. Rotational speeds of the ship propeller should be substantially smaller, depending on the type of propeller, which was overcome with high-performance turbine gear transmissions.

Manufacturers of all types of vehicles became new customers of specially designed gears. The field developed quickly, so a new plant for manufacturing high-performance gears with the MAAG system was built in Friedrichshafen to satisfy the demand of the automobile and aviation industry.

Other industries also imposed new requirements for gearings, which included highly loaded but slower running gears used in transport devices and lifts, quietly operating gears used in the textile industry, high-performance printing machines, and particularly demanding high precision gears for machine tools.

The widespread use of gears required standardization, so in 1927 tools for manufacturing involute gears were standardized (DIN 867) [33] along with the prescribed modules, pressure angles, and uniform addendum size equaling the module. Gear manufacturing by rolling enabled the rack profile shifting, which furthermore enabled the improved kinematic characteristics of gears. Materials for gears changed from cast iron at the turn of the century to alloy steels in the 1930s. High-quality and stronger steel was made in electric arc furnaces. With tempering and surface heat treatment, gear teeth flanks became more durable, and gears became smaller and achieved greater load-bearing capacity. Besides steel, brass and plastic materials were used for gears in fine mechanics. Improved tools and new machinery shortened production time. Moreover, new machines and cutting tools also perfected treatment processes, such as grinding, honing, and lapping, achieving smoother teeth flank surface.

Dimensioning of gears also greatly improved in the first half of the twentieth century. In this respect, *Stephen P. Timoshenko* (1878–1972) in 1925 based on the theory of elasticity [34] improved theoretical foundations of gear teeth root strength dimensioning, whereas *Robert V. Baud* (1894–1970) in 1925 elaborated the stress state of gear teeth by the principles of photoelasticity, which was proved by Timoshenko [35]. Both highlighted that the basic factor influencing the root strength of a tooth was stress concentration on the fillet, so that a rounding between the dedendum and root circle needs to be considered.

Wear of gear flanks was recognized even before the end of the nineteenth century on the gears made of gray cast iron. When the wear and pitting damages were detected on steel gears, it was realized that this was due to flank load. Hertzian pressure, which became a measure of the tooth flank load, was formulated by *Heinrich R. Hertz* (1857–1894) in 1881. Major researchers in the field of gearings studied the application of the Hertzian equation for designing teeth flank, including *August Föppl* (1854–1924), who presented Hertz's theory for the first time to a wide circle of engineers in Munich in 1897 [35]; *Earle Buckingham* (1887–1978), who studied Hertzian equation regarding the influence of load on flank wear considering the material and the pressure angle and presented his findings to AGMA in 1926; and *Gustav Niemann* (1899–1982) who in 1938 studied the rolling strength based on Hertz's theory and depending on the surface state, hardness, and loading [25].

With the development of working and energy supplying machines, the mechanical loads and working speeds increased and thereby also the heat produced due to friction, which could have caused severe damage due to the scuffing of teeth flanks. In 1931, *Hermann Hofer* (1891–1963), who was the head of gear development at the ZF factory, suggested that the measure of scuffing risk should be the limit value $A = P n_1/b$, with P being the tangential force on the teeth, n_1 rotational speed of the pinion, and b the tooth width. With numerous tests on gears of various intended functions and loads (automobile industry—gearboxes), Hofer obtained a partial limit value A' for each test and then calculated the average limit value $A = 70,000$. This means that particular gear pairs are scuffing resistant during operation if their resistance $S_a = 70,000/A' < 1$ [25].

John O. Almen (1886–1973) was employed at GM’s (General Motors) research laboratory and defined the measure of scuffing risk load as the product $P V < PV_{\max}$, with P being the Hertzian pressure, V the sliding speed of one flank along another at a contact point, and PV_{\max} experimentally obtained value [25].

Dutch researcher *H. Blok* chose flash temperature $T_{fl,\max}$ at the most exposed point of contact for the measure of scuffing risk. Blok presented his “flash temperature” concept and equation in 1937. T_{fl} is a consequence of friction and the sliding speed of the contact surfaces. During operation, the teeth are scuffing safe if Blok’s flash temperature is lower than the permissible one determined by tests [37].

Based on these important development milestones, one can see that the development of geometric characteristic and the manufacturing of gears from the turn of the century to World War II reached a high level of industrial production in all industrially developed countries. Many new shapes were possible and could have been manufactured by advanced machinery; however, according to the current needs in terms of production and operating features, involute gears were the most appropriate. The production of gear increased along with the growing needs and the expansion of the engineering field.

Several gear types were developed depending on the position of the shafts and transmission rates, e.g., cylindrical, helical, bevel, and worm gears. During decades, the cutting technology greatly improved and was supplemented by fine machining for lower surface roughness and heat treatment. New materials, particularly alloy steel, made possible less weight and better durability, and special materials enabled production of gears operating in special atmospheric and temperature conditions. Due to higher complexity and demands, gear manufacturing faced requirements toward smaller tolerances; consequently corresponding machine tools and cutters were developed, as well as necessary measurement equipment. Standards defining gear qualities for various applications were enforced. Unfortunately, this also enabled more lethal war machinery helping effective ruination of previous achievements and welfare of our civilization during World War II. The corresponding knowledge retained, and the development soon continued with an accelerated pace in the new millennium. Some notable scientists, who contributed to new achievements and disseminated their knowledge, are professors *H. Winter* and *B.-R. Höhn* from TU Munich, *D.W. Dudley* from California, *F.L. Litvin* from the University of Illinois at Chicago, and *S.P. Radzevich* (EATON Corporation, Detroit, USA).

9.13 Need for Standardization

After World War II there was a strong need for renovation and consequently for research and development and consequently for standards in industry. In 1947, the International Organization for Standardization (ISO) was founded in London. The organization adopted *iso*, based on the Greek word *isos* (ἴσος, meaning *equal*), as the universal short form of its name [38]. ISO became a **network** of the national standards institutes, which enlarged from initially 25 to already **164 countries**, one

member per country, with a Central Secretariat in Geneva, Switzerland, that coordinates the system. And within its framework, the ISO committee TC60 for gears was founded. The ISO committee coordinates development of recommendations and standards in the field of gears, and its members come from research institutions or gear manufacturers in their countries, where all gear-related activities are conducted. Besides international, there are several national organizations dealing with gears, e.g., AGMA in the USA, BGA in the UK, VDI in Germany, IET in France, JSME in Japan, and CMSE in China. The International Federation for the Theory of Machines and Mechanisms (IFTOMM) was founded in the town of Zakopane, Poland, in 1969, initiated by professor *Artabolevsky* [39]. Its members largely focused on gear research. The foundation of the theory on elasto-hydrodynamic lubrication is among the most important developments of this later period. Regarding production, automated manufacturing of the highest-quality gears is the most prominent. The belief that involute gears are the best solution persists, and a lot of research work has been and is conducted in this context. Despite the engineering industry at the turn of the third millennium can offer almost perfect involute gears, they might not be appropriate for all tasks faced by the industry today.

9.14 New Gear Tooth Flank Shapes

The perfect, optimal shape of involute gears transmits power by the convex-convex contact. However, the intrinsic property of the involute gear is their curvature radius function in the dedendum part when approaching the base circle. Values in general are small and limit to zero at the base circle, and therefore high contact loads in this area. Additionally, for gears with low number of teeth, the dedendum flank is comparatively short, thus invoking excessive sliding and friction losses. Yet another problem is undercutting of the dedendum area. This was why numerous gear developers sought new solutions to make the teeth flanks of the driving and the driven gears fit together better.

In view of this requirement, the concave-convex pair seems an obvious solution, which was precisely what researchers and inventors suggested. Let us mention only a few, the most characteristic ones, in this paper.

In 1921, *Francis John Bostock* (1881–1943) and *Swinfen Bramley-Moore* filed a patent for the VBB gearing (Fig. 9.18), which was bought by Vickers shipbuilding company after successful tests in 1924 [25]. The VBB gearing is based on a mathematically defined curved contact path. The tests showed that flank stiffness increased three to four times. With the VBB gearing, Vickers manufactured a large number of turbine gearboxes for powers ranging between 450 and 19,000 HP and rotational speeds between 5.9 and 44.2 m/s. Despite its great initial success, VBB gearing did not survive in practice. *H.W. Harrison* reported that the reason for this was that it was too noisy during operation and the susceptibility to changes in the distance between axes.

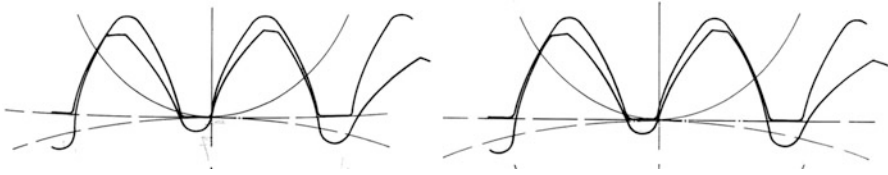
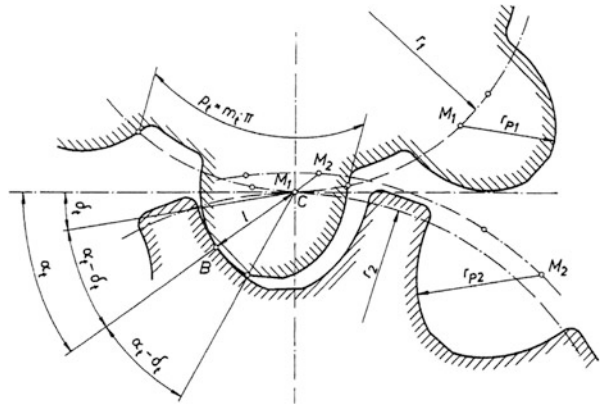


Fig. 9.18 VBB gearing (Vickers–Bostock–Bramley), (left) gear pair $z_1 = 30, z_2 = 180$; (right) $z_1 = 30, z_2 = \infty$ (rack)

Fig. 9.19 Novikov gears



Ernest Wildhaber, a development engineer at Gleason, worked along the same lines. In 1923, he designed, and in 1926 [40] a US patent was granted for a concave-convex gear pair whose flanks are in the form of arcs with the curvature center near the rolling circles. In 1955, *M.L. Novikov* designed similar pair of profiles, which he patented in 1956. [41] Working gearing has the point contact of teeth flanks and can operate only as helical gearing. The Wildhaber tooth flank profile is in normal section to the helix, while the Novikov gear profile in Fig. 9.19 is shown in the front view (in the direction of the gear axis).

Extensive research was carried out on the load-bearing capacity of WN gears. And researchers largely agree [42] that untempered WN gears have approximately three times higher flank strength than the same size involute gears, while surface-hardened or tempered involute gears are superior to WN gears. Wildhaber failed in researching his gear to such extent that would enable users to learn their qualities, so they were never included in production.

On the contrary, Soviet engineers did study Novikov gears and use them widely in oil pumps, compressors, tractors, construction machines, etc. The Russians also developed the Novikov gear with double contact, as represented on a rack in Fig. 9.20, which is defined by the Russian standard GOST 17744–72. The Chinese, who follow advancements achieved in Russia, also use Novikov double-contact gears to a great extent, prescribed by the Chinese standard JB 2940–81. However, it should be noted that gears according to Wildhaber’s patent and those according to

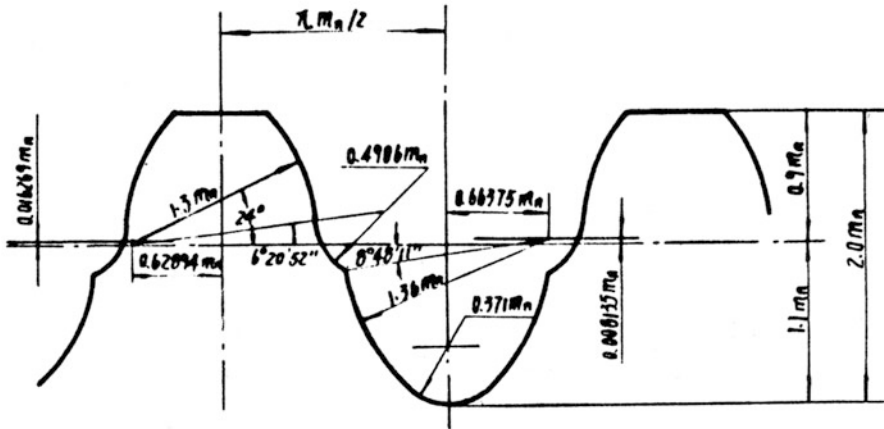


Fig. 9.20 Rack for Novikov gear with double teeth contact

Novikov's patent differ, so the naming of WN gears is inappropriate [43]. Litvin [44] stated that Wildhaber's gearing had a line-type contact and the Novikov's, a point-type contact. Also gear pairs with intersected axes and crossed axes can be designed based on the idea proposed by Novikov [14].

Another attempt is that of Hawkins, who in 2005 [45] patented non-involute gears with conformal contact. In 2009 G. and J. Hlebanja [46] proposed a new version of WN gears, UPT (uniform power transmission) gears, illustrated in Fig. 9.21. According to this proposal, the tooth flank profile is comprised of three circular arcs, with the first arc forming the addendum, the second forming the dedendum, and the third arc forming the intermediate section, which prevents the flanks from touching as they rotate around the kinematic pole C. The advantage of this solution is a simple flank geometry, which is easier in terms of tools, while the relative rotation of one gear vis-à-vis its pair is similar to the movement of the shaft in the bearing. The essential element of the UPT gears is the absence of a pitch line and the gear-teeth contact in the transverse plane. In addition, there is no sliding between the teeth flanks in the transverse plane. Power is mainly transmitted by the rolling of the teeth flanks at both contact points, with the simultaneous sliding of the teeth flanks around the pitch point C. The contact load is divided into two contact points. Better lubrication conditions can be expected because of the thicker oil-film thickness and lower heat generation. And the most important features of the UPT gears are non-intermittent sliding and power transmission. These features indicate that UPT gears can be used with heavy loads in non-stop operating condition, for example, in the power transmission of wind turbines, gear units for refinery services, and similar applications.

Despite prevailing use of involute gears, there exists a permanent need for improved gears with such features as a convex-concave contact, a stronger root, improved curvature radii, better lubrication conditions, etc. Such an attempt was implementation of a gear pair based on the curved path of contact, which implied a

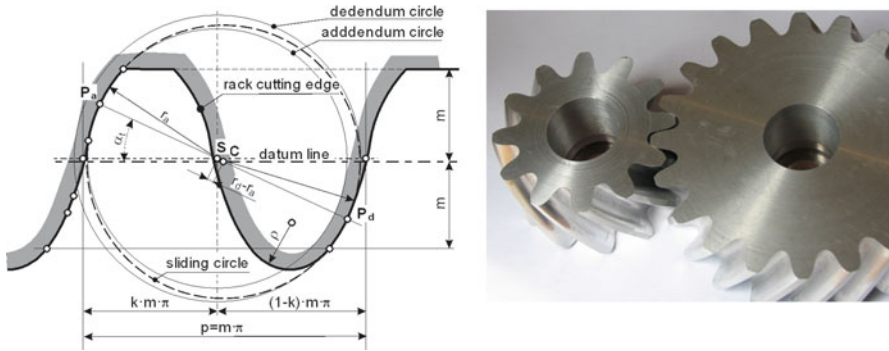
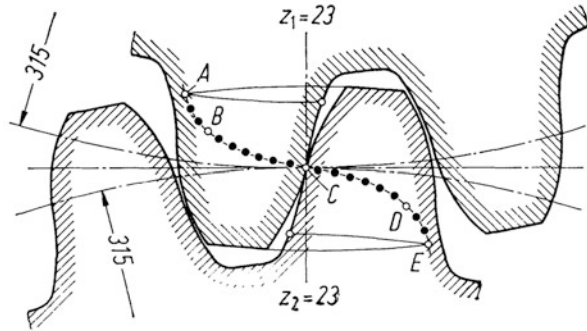


Fig. 9.21 UPT gears proposed by Hlebanja; rack profile (left); UPT gear pair with $m_n = 5$ mm; $z_1 = 12$, $z_2 = 20$ (right)

concave-convex fit of the meshing gear teeth flanks at meshing start and end zones. The path of contact is a sequence of contact points of the meshing gear pair, which transmits rotation, where each contact point complies with the law of gearing. The path of contact should also warrant sufficiently high contact ratio. The contact load in the kinematic pole C depends on the initial pressure angle α_C . The starting pressure angle α_A is limited due to the contact ratio and contact load. The condition for manufacturing gears of the same module with an arbitrary number of teeth by the same tool profile is the half-symmetrical path of contact. Gears are designed with regard to their root strength and flank durability. The path of contact shape and the root fillet influence the root thickness, whereas the flank shape essentially influences its durability. The basic factors influencing flank durability are the reduced radii of curvature and amount of sliding. So, higher radii imply lower Hertzian pressure. Also, the sliding circumstances are essentially improved in the case of convex-concave contact. The research showed that areas of the path of contact with a higher curvature imply lower sliding and higher reduced radii of curvature. Due to the necessity of the stronger oil film in the meshing start zone, the path of contact curvature in that area should be higher, and the path of contact takes on a distinctive S-form.

This tooth flank form was used in grooved roller gears for rolling mills. It was successfully installed in the Sisak rolling mill, with variations in other facilities. Gears were helical, $\beta = 28^\circ$, and transmitted 1500 kW at 80 up to 160 RPM. Material was alloy steel 30CrMoV9 [47]. The tooth profile is illustrated in Fig. 9.22. Initially, in the facility the involute gearing was installed, which suffered severe scuffing in the gear teeth dedendum and addendum areas soon after installation. S-formed gearing was an essential improvement, operating for several decades, so it was also reported in Niemann and Winter 1989 (p. 43). Experiences with the gears featuring the curved path of contact and corresponding shape led to the mathematically defined S-gear shape. Recently, *J. and G. Hlebanja* [48] presented a new method of designing gears based on the basic rack tooth profile. The simplified

Fig. 9.22 Industrial implementation for rolling mills [47]



expression that defines the positive part (where C is the origin) of a rack profile flank is:

$$y_{pi} = a_p [1 - (1 - x_{pi})^n] \quad (9.1)$$

The rack profile flank definition can be regarded as a cutting tool definition. Each rack profile then designates a single (curved) path of contact and corresponding external or internal gears with arbitrary numbers of teeth. The discussion of the S-gears is presented in Chap. 2. So, let us only briefly mention some features. The mating gears exhibit convex-concave contact in the vicinity of the contact start and contact end. The minimal teeth number of spur S-gears can be as low as four. The S-gear tooth flank profile assures higher comparative curvature radii, and thus lower contact load and higher relative velocities of the contact surfaces which imply better lubrication. Due to their S-shape, the velocity characteristics of mating gears are improved, especially in both meshing limit areas with high relative velocities and low sliding. The meshing start zone in involute gears represents potential danger of micro-pitting, whereas S-gears exhibit advantage in this context due to the thicker oil film in this area, which diminishes possibility of damage. Another important feature of the S-gears is more evenly distributed contact point density, which causes lower sliding and less power losses. The dedendum flank of pinion is not substantially smaller as that of gear addendum even for low number of teeth. Therefore, authors believe this gear type can be a successful substitute for involute gears for diverse applications, like gearboxes for wind power plants on the large scale and miniature plastic gears for various purposes.

9.15 Conclusion

Millennia ago, humans invented machines driven by animals which could perform useful work for them. Energy was transmitted by the movement of gears to those elements which perform the given task. In all periods, from the first irrigation

devices along the Nile to this day, gears have been essential composite parts of machines, transmitting energy from the source to the user. For millennia, wood was the only material available for making gears, and humans or animals the only sources of energy. Such systems are still in use in agriculture in some places of the planet. The first iron gears date back to when the steam engine became the source of power, while the use of involute machines dates back to Euler. Machines for manufacturing gears followed industrial needs of the nineteenth century and were further developed with the accelerated pace in the twentieth century. In-depth scientific work and standardization followed World War I. After World War II, Novikov gears were developed, which are widely used in Russia and China, while involute gears are preferred in the West. Further, many efforts have been made to design even better geometry. S-gears can be regarded in this way, with some features, which can cope with arising problems with new industrial applications with standardized involute gears.

One of the great names of gear science is *Darle W. Dudley*, who presented the development of gears at a conference on gears in 1988 in Zhengzhou in China, concluding his presentation with a centennial forecast [49]. The set targets have already been achieved and even exceeded in the 25 years since. Today, we can also concur that the difference in the rotational speed of energy and working machines is not overcome. This cannot be always solved by direct driving electro-motors, which means that gears and the development of the field will still be needed.

Despite systems are becoming more electrical, even mechatronic, their improved functionality with increased power consumption requires reliable mechanical sub-systems. The essential parts of such systems are various gear arrangements with increasing demands (e.g., higher power density, lower noise, lower cost, increased reliability, and service life), so the research in this area keeps pace. Results are improved materials; manufacturing methods like power skiving and 5D CNC machining; improved calculation methods and programs, e.g., KiSSsoft; guidelines for calculation of gears made of plastics and their testing methods, e.g., VDI Richtlinie 2736, parts 1 to 4; improved gear shapes; and more. So, the research interest can be observed in numerous published papers and conferences, like AGMA Fall Technical meetings or biannual VDI Conference on Gears in Garching near Munich with more than 600 participants.

References

1. Radzevich S P (2020) Personal communication.
2. Matschoß, C. (1940). *Geschichte des Zahnrades*. Berlin: VDI.
3. Rance, P. (2013, 2013). Philo of Bysantium. In R. S. Bagnal et al. (Eds.), *The Encyclopedia of Ancient History, 1st Edition* (pp. 5266–5268). Blackwell Publishing Ltd.
4. Wikipedia, s.v. “Antikythera mechanism”. Accessed 10 Jul 2020 from https://en.wikipedia.org/wiki/Antikythera_mechanism.
5. Efstathiou, K., & Efstathiou, M. (2018). Celestial gearbox. *ASME. Mechanical Engineering*, 140(09), 31–35. <https://doi.org/10.1115/1.2018-SEP1>.

6. Wikipedia, s.v. “Vitruvius”. Accessed 11 Jul 2020 from <https://en.wikipedia.org/wiki/Vitruvius>.
7. Wikipedia, s.v. “Reverse overshot water-wheel”. Accessed 11 Jul 2020 from https://en.wikipedia.org/wiki/Reverse_overshot_water-wheel.
8. Wikipedia, s.v. “List of ancient watermills”. Accessed 11 Jul 2020 from https://en.wikipedia.org/wiki/List_of_ancient_watermills.
9. Wikipedia, s.v. “Heron of Alexandria”. Accessed 11 Jul 2020 from https://en.wikipedia.org/wiki/Hero_of_Alexandria.
10. Agricola G (1556) *De Re Metallica*. Agricola G (1912) The mining magazine (transl: Hoover H C, Hoover L C). London.
11. Wikipedia, s.v. “Georgius Agricola”. Accessed 11 Jul 2020 from https://en.wikipedia.org/wiki/Georgius_Agricola.
12. Dohrn-Van Rossum, G. (1996). *History of the hour: clocks and modern temporal orders*. (transl: Dunlap T). Chicago: The University of Chicago Press. ISBN 0226155102.
13. Encyclopædia Britannica Online, s.v. “pendulum”. Accessed 12 Jul 2020 from <https://www.britannica.com/technology/pendulum>
14. Encyclopædia Britannica Online s.v. “Galileo”. Accessed 12 Apr 2020 from <https://www.britannica.com/biography/Galileo-Galilei>
15. Encyclopædia Britannica Online s.v. “Girard Desargues”. Accessed 12 Apr 2020 from <https://www.britannica.com/biography/Girard-Desargues>
16. de la Hire, P. (1694). *Mémoires de mathématique et de physique*. Royale, Paris: Impr.
17. Complete Dictionary of Scientific Biography (2008a) “La Hire, Philippe De,” Accessed 13 Jul 2020 from [Encyclopedia.com: http://www.encyclopedia.com/doc/1G2-2830902429.html](http://www.encyclopedia.com/doc/1G2-2830902429.html)
18. Complete Dictionary of Scientific Biography (2008b) “Camus, Charles-Étienne-Louis,” Accessed 13 Jul 2020 from [Encyclopedia.com: http://www.encyclopedia.com/doc/1G2-2830900770.html](http://www.encyclopedia.com/doc/1G2-2830900770.html)
19. The Euler Archive, s.v. “E249—De aptissima figura rotarum dentibus tribuenda”. Accessed 12 Jul 2020 from <http://eulerarchive.maa.org/> or <https://scholarlycommons.pacific.edu/euler/>
20. Euler, L. (1760). *Novi Commentarii academiae scientiarum Petropolitanae*, 5(1760), 299–316.
21. Wikipedia, s.v. “James Watt”. Accessed 12 Jul 2020 from https://en.wikipedia.org/wiki/James_Watt.
22. Encyclopædia Britannica Online, s.v. “James Watt”. Accessed 12 Jul 2020 from <https://www.britannica.com/biography/James-Watt>
23. Jungfrau Railway Accessed 13 Jul 2020 from <https://www.jungfrau.ch/en-gb/jungfrau-joch-top-of-europe/construction-of-the-jungfrau-railway/>
24. Willis, R. (1841). *Principles of mechanism*. Cambridge: University Press.
25. Seherr-Thoss, H. C., & Fronius, S. (1965). *Die Entwicklung der Zahnrad-technik: Zahnformen und Tragfähigkeitsberechnung*. Berlin: Springer.
26. Reuleaux, F. (1861). *Der Constructeur*. Braunschweig: Vieweg.
27. Sang, E. (1852). *A new general theory of the teeth of wheels*. Edinburgh: A&C Black.
28. Matschoß, C. (1925). *Männer der Technik: Ein biographisches Handbuch*. Berlin: VDI.
29. Hermann Pfauter Werkzeugmaschinenfabrik (1976), Ludwigsburg (Hrsg.): *Pfauter-Wälzfräsen Teil 1. 2. Auflage*. Springer, Berlin 1976, ISBN 3-540-07446-5.
30. Litvin, F. L. (1997). *Development of gear technology and theory of gearing*. Cleveland: NASA Lewis Research Center.
31. Siemens, s.v. “Siemens history, Transportation”. Accessed 13 Jul 2020 from <https://new.siemens.com/global/en/company/about/history/news/on-track.html>
32. Encyclopædia Britannica Online s.v. “Sir Charles Algernon Parsons”. Accessed 13 Jul 2020 from <https://www.britannica.com/biography/Charles-Algernon-Parsons>
33. DIN 867 (1927) Bezugsprofile für Evolventenverz. An Stirnrädern (Zylinder.) für allgem. Maschinenbau und den Schwermaschinenbau.
34. Timoshenko, S. P., & Goodier, J. N. (1951). *Theory of elasticity* (2nd ed.). New York: McGraw-Hill.

35. Linke, H. (2010). *Stirnradverzahnung, 2., vollständig überarbeitete Auflage*. Hanser.
36. Hertz, H. (1881). Über die Berührung fester elastischer Körper. *Journal für die reine und angewandte Mathematik*, 92, 156–171.
37. Blok H (1937) Measurement of temperature flashes on gear teeth under extreme pressure conditions. In: *Proceedings of general discussion lubrication 2*, institution of mechanical engineers, p 14–20.
38. ISO, “About us”. Accessed 14 Jul 2020 from <https://www.iso.org/about-us.html>
39. IFTOMM, v.s. “Historical Background”. Accessed 10 Jul 2020 from http://iftomm.net/images/Documents/About/Historical_Background.pdf.
40. Wildhaber E (1926) Helical gearing. US patent no. 1 601 750, issued 5 Oct 1926.
41. Novikov ML (1956) U.S.S.R., Patent no. 109,750, 1956.
42. Niemann, G. (1961). *Novikov gear system and other special gear systems for high load carrying capacity* (p. 47). VDI Berichte.
43. Radzevich, S. P. (2012). *Dudley’s handbook of practical gear design and manufacture* (2nd ed.). Boca Raton: CRC Press, Taylor & Francis Group.
44. Litvin, F. L., Fuentes, A., Gonzales-Perez, I., Carnevali, L., & Sep, T. M. (2002). new version of Novikov-Wildhaber helical gears: Computerized design, simulation of meshing and stress analysis. *Computer Methods in Applied Mechanics and Engineering*, 191(49–50, 6), 5707–5740.
45. Hawkins R M (2005) Non-involute gears with conformal contact. US Patent No. 6,837,123, dated 4 Jan 2005.
46. Hlebanja, G., & Hlebanja, J. (2009). Uniform power transmission gears. *J Mech Eng*, 55(7/8), 472–483.
47. Hlebanja, J. (1976). Konkav-konvexe Verzahnung Ermittlung der Zahnflanken und einige Grenzfälle. *Antriebstechnik* Jg. 15. Nr., 6, 324–329.
48. Hlebanja, J., & Hlebanja, G. (2010). Spur gears with a curved path of contact for small gearing dimensions. *VDI Berichte*, 2108, 1281.
49. Dudley, W. D. (1988). Gear technology—Past, present, and future. In *Proceedings of international conference on gearing, 5–10 Nov* (p. 1988). China: Zhengzhou.

Appendix A: Elements of Differential Geometry of Surfaces

The discussion in this book is focused primarily on the elements of theory of gear cutting tool design.

The gear and the pinion tooth flank and their motion in space in relation to one another are analytically described in a reference system. An orthogonal “*Cartesian*”¹ reference system is a major kind of reference systems that is commonly used for this purpose. Mutually perpendicular coordinate axes of a “*Cartesian*” coordinate system are conventionally labeled as X , Y , and Z .

In a “*Cartesian*” reference system, the axes can be oriented in either a left- or right-handed sense. A right-handed “*Cartesian*” reference system is preferred, and all algorithms and formulae used in this book assume a right-handed convention.

A coordinate system provides a numerical frame of reference for the three-dimensional space in which the theory is developed. Two coordinate systems are particularly useful to us: the ubiquitous “*Cartesian*” (XYZ) rectilinear system and the spherical polar (r , θ , φ) or angular system. “*Cartesian*” coordinate systems are the most commonly used, but angular coordinates are often helpful as well.

¹*René Descartes* (March 31, 1596–February 11, 1650), (Latinized form: *Renatus Cartesius*), a French mathematician, philosopher, and writer

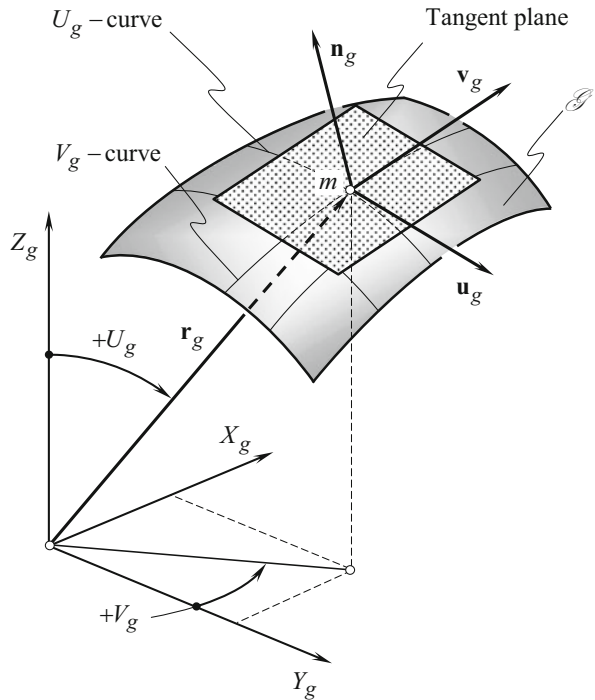
Specification of a Gear Tooth Flank

A gear tooth flank could be uniquely determined by two independent variables. Therefore, we give a gear tooth flank \mathcal{G} (see Fig. A.1), in most cases, by expressing its rectangular coordinated $X_g, Y_g,$ and $Z_g,$ as functions of two “Gaussian² coordinates” U_g and V_g in a certain closed interval³:

$$\mathcal{G} \Rightarrow \mathbf{r}_g = \mathbf{r}_g(U_g, V_g) = \begin{bmatrix} X_g(U_g, V_g) \\ Y_g(U_g, V_g) \\ Z_g(U_g, V_g) \\ 1 \end{bmatrix} \tag{A.1}$$

$$U_{1.g} \leq U_g \leq U_{2.g}; V_{1.g} \leq V_g \leq V_{2.g}$$

Fig. A.1 Principal parameters of local topology of a gear tooth flank, \mathcal{G}



²Johann Carl Friedrich **Gauss** (April 30, 1777–February 23, 1855), a famous German mathematician and physical scientist

³All the equations that are valid for the gear tooth flank, \mathcal{G} , are also valid for the pinion tooth flank, \mathcal{P} .

where:

\mathbf{r}_g is the position vector of a point of the gear tooth flank, \mathcal{G}

U_g and V_g are curvilinear coordinates (“*Gaussian coordinates*”) of the gear tooth flank, \mathcal{G}

X_g, Y_g, Z_g are “*Cartesian*” coordinates of the point of the gear tooth flank, \mathcal{G}

$U_{1.g}, U_{2.g}$ are the boundary values of the closed interval of the U_g – parameter

$V_{1.g}, V_{2.g}$ are the boundary values of the closed interval of the V_g – parameter

The parameters U_g and V_g must enter into Eq. (A.1) independently, which means that the matrix:

$$\mathbf{M} = \begin{bmatrix} \frac{\partial X_g}{\partial U_g} & \frac{\partial Y_g}{\partial U_g} & \frac{\partial Z_g}{\partial U_g} \\ \frac{\partial X_g}{\partial V_g} & \frac{\partial Y_g}{\partial V_g} & \frac{\partial Z_g}{\partial V_g} \end{bmatrix} \quad (\text{A.2})$$

has a rank 2.

Positions, where the rank is 1 or 0, are singular points; when the rank at all points is 1, then Eq. (A.1) represents a curve.

Other methods of surfaces specification are known as well. Specification of a gear tooth flank by:

- An equation in explicit form.
- An equation in implicit form.
- A set of parametric equations.

are among the most frequently used in practice methods of surfaces specification.

It is assumed here and below that any given kind of a gear tooth flank, \mathcal{G} , specification can be converted either into the vector form or into the matrix form of its specification as it is following from Eq. (A.1).

Tangent Vectors and Tangent Plane; Unit Normal Vector

The following notation is proven to be convenient in the consideration below.

The first derivatives of \mathbf{r}_g with respect to “*Gaussian coordinates*” U_g and V_g are designated as:

$$\frac{\partial \mathbf{r}_g}{\partial U_g} = \mathbf{U}_g \quad (\text{A.3})$$

$$\frac{\partial \mathbf{r}_g}{\partial V_g} = \mathbf{V}_g \quad (\text{A.4})$$

and for the unit tangent vectors:

$$\mathbf{u}_g = \frac{\mathbf{U}_g}{|\mathbf{U}_g|} \quad (\text{A.5})$$

$$\mathbf{v}_g = \frac{\mathbf{V}_g}{|\mathbf{V}_g|} \quad (\text{A.6})$$

correspondingly.⁴

The direction of the tangent line to the U_g -coordinate line through a given point m on the gear tooth flank, \mathcal{G} , is specified by the unit tangent vector \mathbf{u}_g (as well as by the tangent vector \mathbf{U}_g). Similarly, the direction of the tangent line to the V_g -coordinate line through that same point m on a gear tooth flank \mathcal{G} is specified by the unit tangent vector \mathbf{v}_g (as well as by the tangent vector \mathbf{V}_g).

The significance of the unit tangent vectors \mathbf{u}_g and \mathbf{v}_g becomes evident from the following considerations.

First, unit tangent vectors \mathbf{u}_g and \mathbf{v}_g yield an equation of the tangent plane to a gear tooth flank \mathcal{G} at a specified point m :

$$\text{Tangent plane} \quad \Rightarrow \quad \begin{bmatrix} \left[\mathbf{r}_{t,p} - \mathbf{r}_g^m \right] \\ \mathbf{u}_g \\ \mathbf{v}_g \\ 1 \end{bmatrix} = 0 \quad (\text{A.7})$$

where:

$\mathbf{r}_{t,p}$ is the position vector of a point of the tangent plane to a gear tooth flank \mathcal{G} at a specified point m

\mathbf{r}_g^m is the position vector of the point m on a gear tooth flank \mathcal{G}

Second, tangent vectors yield an equation of the perpendicular \mathbf{N}_g and of the unit normal vector \mathbf{n}_g to a gear tooth flank \mathcal{G} at a given point m :

$$\mathbf{N}_g = \mathbf{U}_g \times \mathbf{V}_g \quad (\text{A.8})$$

and

$$\mathbf{n}_g = \frac{\mathbf{N}_g}{|\mathbf{N}_g|} = \frac{\mathbf{U}_g \times \mathbf{V}_g}{|\mathbf{U}_g \times \mathbf{V}_g|} = \mathbf{u}_g \times \mathbf{v}_g \quad (\text{A.9})$$

When the order of the multipliers in Eqs. (A.8) and (A.9) is chosen properly, then the unit normal vector \mathbf{n}_g (as well as the normal vector \mathbf{N}_g) is pointed outward of the bodily side of the surface \mathcal{G} .

⁴It is right point to underline here that the unit tangent vectors \mathbf{u}_p and \mathbf{v}_p are dimensionless values as they are following from Equations (A.5) and (A.6).

Local Frame

Two unit tangent vectors \mathbf{u}_g and \mathbf{v}_g along with the unit normal vector \mathbf{n}_g comprise a local frame $\mathbf{u}_g, \mathbf{v}_g, \mathbf{n}_g$ having the origin at a current point m on a gear tooth flank \mathcal{G} . Unit tangent vector \mathbf{u}_g is perpendicular to the unit normal vector \mathbf{n}_g (i.e., $\mathbf{u}_g \perp \mathbf{n}_g$), as well as unit tangent vector \mathbf{v}_g is also perpendicular to the unit normal vector \mathbf{n}_g (i.e., $\mathbf{v}_g \perp \mathbf{n}_g$). Speaking generally, the unit tangent vectors \mathbf{u}_g and \mathbf{v}_g are not perpendicular to one another; they form a certain angle ω_g . In order to construct an orthogonal local frame, either the unit tangent vector \mathbf{u}_g in the local frame $(\mathbf{u}_g, \mathbf{v}_g, \mathbf{n}_g)$ must be substituted with a unit tangent vector \mathbf{u}_g^* , or the unit tangent vector \mathbf{v}_g in that same local frame $(\mathbf{u}_g, \mathbf{v}_g, \mathbf{n}_g)$ must be substituted with a unit tangent vector \mathbf{v}_g^* . For the calculation of the newly introduced unit tangent vectors \mathbf{u}_g^* and \mathbf{v}_g^* , the following equations can be used:

$$\mathbf{u}_g^* = \mathbf{u}_g \times \mathbf{n}_g \quad (\text{A.10})$$

$$\mathbf{v}_g^* = \mathbf{v}_g \times \mathbf{n}_g \quad (\text{A.11})$$

It is convenient to choose that order of the multipliers in Eqs. (A.10) and (A.11), which preserves the orientation (the hand) of the original local frame $(\mathbf{u}_g, \mathbf{v}_g, \mathbf{n}_g)$, namely, if the original local frame $(\mathbf{u}_g, \mathbf{v}_g, \mathbf{n}_g)$ is right-hand oriented, then the newly constructed local frame [either the local frame $(\mathbf{u}_g^*, \mathbf{v}_g, \mathbf{n}_g)$, or the local frame $(\mathbf{u}_g, \mathbf{v}_g^*, \mathbf{n}_g)$] should also be a right-hand oriented local frame, and vice versa.

It should be pointed out here that another possibility to construct an orthogonal local frame is also available. A local frame of this kind is commonly referred to as “*Darboux*⁵ frame” and is briefly considered below in this section of the book.

Unit tangent vectors \mathbf{u}_g and \mathbf{v}_g to a surface \mathcal{G} at a point m are of critical importance when solving practical problems in the field of gearing. This statement is proven by numerous examples shown below.

Fundamental forms of a Surface

Consider two other important issues concerning the gear tooth flank geometry – both relate to intrinsic geometry in differential vicinity of a current surface point m .

“*First fundamental form of a surface.*” The first issue is the so-called the first fundamental form, $\Phi_{1.g}$, of a gear tooth flank \mathcal{G} . The metric properties of a gear tooth

⁵ *Jean Gaston Darboux* (August 14, 1842–February 23, 1917), a French mathematician

flank \mathcal{G} are described by the first fundamental form, $\Phi_{1.g}$, of the surface. Usually, the first fundamental form, $\Phi_{1.g}$, is represented as the quadratic form:

$$\Phi_{1.g} \Rightarrow ds_g^2 = E_g dU_g^2 + 2F_g dU_g dV_g + G_g dV_g^2 \quad (\text{A.12})$$

Here, in Eq. (A.12) the following are designated:

s_g is the linear element on a gear tooth flank \mathcal{G} (s_g is equal to the length of a segment of a certain curve on a gear tooth flank \mathcal{G}).

E_g, F_g, G_g are fundamental magnitudes of the first order at a surface point.

Equation (A.12) for the first fundamental form, $\Phi_{1.g}$, is known from many advanced sources. In the theory of gearing, another form of analytical representation of the first fundamental form, $\Phi_{1.g}$, is proven to be useful:

$$\Phi_{1.g} \Rightarrow ds_g^2 = [dU_g \ dV_g \ 0 \ 0] \cdot \begin{bmatrix} E_g & F_g & 0 & 0 \\ F_g & G_g & 0 & 0 \\ 0 & 0 & 1 & 0 \\ 0 & 0 & 0 & 1 \end{bmatrix} \cdot \begin{bmatrix} dU_g \\ dV_g \\ 0 \\ 0 \end{bmatrix} \quad (\text{A.13})$$

This kind of analytical representation of the first fundamental form $\Phi_{1.p}$ is proposed by Prof. *S.P. Radzevich* (~2008).

The practical advantage of Eq. (A.13) is that it can easily be incorporated into computer programs when multiple coordinate system transformations are used. The last is vital for the theory of gearing.

Fundamental magnitudes of the first order, E_g, F_g, G_g , can be calculated from the set of the following equations:

$$E_g = \mathbf{U}_g \cdot \mathbf{U}_g \quad (\text{A.14})$$

$$F_g = \mathbf{U}_g \cdot \mathbf{V}_g \quad (\text{A.15})$$

$$G_g = \mathbf{V}_g \cdot \mathbf{V}_g \quad (\text{A.16})$$

Equations (A.14) through (A.16) can be represented in an expanded form:

$$E_g = \frac{\partial \mathbf{r}_g}{\partial U_g} \cdot \frac{\partial \mathbf{r}_g}{\partial U_g} = \frac{\partial X_g}{\partial U_g} \cdot \frac{\partial X_g}{\partial U_g} + \frac{\partial Y_g}{\partial U_g} \cdot \frac{\partial Y_g}{\partial U_g} + \frac{\partial Z_g}{\partial U_g} \cdot \frac{\partial Z_g}{\partial U_g} \quad (\text{A.17})$$

$$F_g = \frac{\partial \mathbf{r}_g}{\partial U_g} \cdot \frac{\partial \mathbf{r}_g}{\partial V_g} = \frac{\partial X_g}{\partial U_g} \cdot \frac{\partial X_g}{\partial V_g} + \frac{\partial Y_g}{\partial U_g} \cdot \frac{\partial Y_g}{\partial V_g} + \frac{\partial Z_g}{\partial U_g} \cdot \frac{\partial Z_g}{\partial V_g} \quad (\text{A.18})$$

$$G_g = \frac{\partial \mathbf{r}_g}{\partial V_g} \cdot \frac{\partial \mathbf{r}_g}{\partial V_g} = \frac{\partial X_g}{\partial V_g} \cdot \frac{\partial X_g}{\partial V_g} + \frac{\partial Y_g}{\partial V_g} \cdot \frac{\partial Y_g}{\partial V_g} + \frac{\partial Z_g}{\partial V_g} \cdot \frac{\partial Z_g}{\partial V_g} \quad (\text{A.19})$$

Fundamental magnitudes of the first order, E_g, F_g, G_g , are functions of the U_g - and V_g -coordinates of a point of a gear tooth flank \mathcal{G} . In general form, these relationships can be represented in the form:

$$E_g = E_g(U_g, V_g) \quad (\text{A.20})$$

$$F_g = F_g(U_g, V_g) \quad (\text{A.21})$$

$$G_g = G_g(U_g, V_g) \quad (\text{A.22})$$

It is important to point out here that fundamental magnitudes E_g and G_g are always positive (i.e., $E_g > 0, G_g > 0$), and the fundamental magnitude F_g can be equal to zero ($F_g \geq 0$). This results in that the first fundamental form, $\Phi_{1.g}$, at a point of a gear tooth flank \mathcal{G} , is always positively defined ($\Phi_{1.g} \geq 0$), and it cannot be of a negative value.

By the use of the first fundamental form, $\Phi_{1.g}$, the following major parameters of geometry of a gear tooth flank \mathcal{G} can be calculated:

- (a) Length of a curve-line segment on a gear tooth flank \mathcal{G} .
- (b) Square of a gear tooth flank \mathcal{G} portion that is bounded by a closed curve on the surface.
- (c) Angle between any two directions on a gear tooth flank \mathcal{G} .

Length, s_g , of a curve-line segment:

$$U_g = U_g(t) \quad (\text{A.23})$$

$$V_g = V_g(t) \quad (\text{A.24})$$

on a gear tooth flank, \mathcal{G} , is given by the equation:

$$s_g = \int_{t_0}^t \sqrt{E_g \left(\frac{dU_g}{dt} \right)^2 + 2F_g \frac{dU_g}{dt} \frac{dV_g}{dt} + G_g \left(\frac{dV_g}{dt} \right)^2} dt \quad (\text{A.25})$$

$$t_0 \leq t \leq t_1$$

For the calculation of square, S_g , of a gear tooth flank \mathcal{G} patch Σ , which is bounded by a closed curve on the surface \mathcal{G} , the following equation can be used:

$$S_g = \iint_{\Sigma} \sqrt{E_g G_g - F_g^2} dU_g dV_g \quad (\text{A.26})$$

Ultimately, value of the angle, ω_g , between two given directions through a certain point m on a gear tooth flank \mathcal{G} can be calculated from one of the equations below:

$$\cos \omega_g = \frac{F_g}{\sqrt{E_g G_g}} \quad (\text{A.27})$$

$$\sin \omega_g = \frac{H_g}{\sqrt{E_g G_g}} \quad (\text{A.28})$$

$$\tan \omega_g = \frac{H_g}{F_g} \quad (\text{A.29})$$

For the calculation of the discriminant, H_g , of the first fundamental form, $\Phi_{1.g}$, the following equation can be used:

$$H_g = \sqrt{E_g G_g - F_g^2} \quad (\text{A.30})$$

It is assumed here that the discriminant, H_g , is always nonnegative – that is, $H_g = +\sqrt{E_g G_g - F_g^2}$.

The first fundamental form, $\Phi_{1.g}$, represents the length of a curve-line segment, and thus it is always nonnegative – that is, the inequality $\Phi_{1.g} \geq 0$ is always valid.

The first fundamental form, $\Phi_{1.g}$, remains the same when the surface is banding. This is another important feature of the first fundamental form $\Phi_{1.g}$.

“*Second fundamental form of a surface.*” The “*second fundamental form, $\Phi_{2.g}$* ” of a gear tooth flank \mathcal{G} is another of the two abovementioned issues. The second fundamental form $\Phi_{2.g}$ describes curvature of a smooth regular surface \mathcal{G} .

Consider a point K on a smooth regular part surface \mathcal{G} (Fig. A.2). The location of the point K is specified by two coordinates U_g and V_g . A line through the point K is entirely located within the surface \mathcal{G} . A nearby point m is located within the line through the point K . The location of the point m is specified by the coordinates $U_g + dU_g$ and $V_g + dV_g$ as it is infinitesimally close to the point K . The closest distance of approach of the point m to the tangent plane through the point K is expressed by the second fundamental form $\Phi_{2.g}$. Torsion of the curve Km is ignored. Therefore, the distance a is assumed equal to zero ($a = 0$).

The second fundamental form, $\Phi_{2.g}$, describes the curvature of a smooth, regular part surface \mathcal{G} . Usually, it is represented as the quadratic form (Fig. A.2):

$$\Phi_{2.g} \Rightarrow -d\mathbf{r}_g \cdot d\mathbf{n}_g = L_g dU_g^2 + 2M_g dU_g dV_g + N_g dV_g^2 \quad (\text{A.31})$$

Equation (A.31) is known from many advanced sources.

In the theory of gearing, another analytical representation of the second fundamental form, $\Phi_{2.g}$, is proven to be useful:

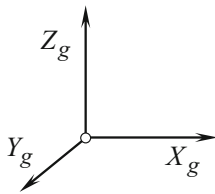
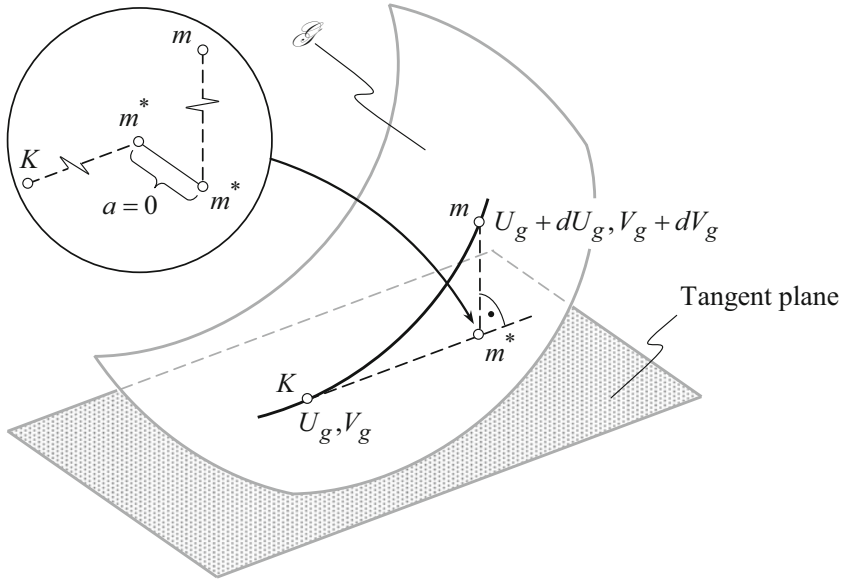


Fig. A.2 On definition of second fundamental form, $\Phi_{2.g}$, at a point of a smooth gear tooth flank, \mathcal{G}

$$\Phi_{2.g} \Rightarrow [dU_g \quad dV_g \quad 0 \quad 0] \cdot \begin{bmatrix} L_g & M_g & 0 & 0 \\ M_g & N_g & 0 & 0 \\ 0 & 0 & 1 & 0 \\ 0 & 0 & 0 & 1 \end{bmatrix} \cdot \begin{bmatrix} dU_g \\ dV_g \\ 0 \\ 0 \end{bmatrix} \quad (\text{A.32})$$

This analytical representation of the second fundamental form, $\Phi_{2.p}$, is proposed by Prof. *S.P. Radzevich* (~2008).

Similar to Eq. (A.13), the practical advantage of Eq. (A.32) is that it can easily be incorporated into computer programs when multiple coordinate system transformations are used. The last is vital for both the theory of gearing.

In Eq. (A.32), the parameters L_g, M_g, N_g designate fundamental magnitudes of the second order.

By definition, fundamental magnitudes of the second order are equal:

$$L_g = -\mathbf{U}_g \cdot \frac{\partial \mathbf{n}_g}{\partial U_g} = \mathbf{n}_g \cdot \frac{\partial \mathbf{U}_g}{\partial U_g} \quad (\text{A.33})$$

$$M_g = -\frac{1}{2} \left(\mathbf{U}_g \cdot \frac{\partial \mathbf{n}_g}{\partial V_g} + \mathbf{V}_g \cdot \frac{\partial \mathbf{n}_g}{\partial U_g} \right) = \mathbf{n}_g \cdot \frac{\partial \mathbf{U}_g}{\partial V_g} = \mathbf{n}_g \cdot \frac{\partial \mathbf{V}_g}{\partial U_g} \quad (\text{A.34})$$

$$N_g = -\mathbf{V}_g \cdot \frac{\partial \mathbf{n}_g}{\partial V_g} = \mathbf{n}_g \cdot \frac{\partial \mathbf{V}_g}{\partial V_g} \quad (\text{A.35})$$

For the calculation of the fundamental magnitudes of the second order of a smooth regular gear tooth flank G , the following equations can be used:

$$L_g = \frac{\frac{\partial \mathbf{U}_g}{\partial U_g} \times \mathbf{U}_g \cdot \mathbf{V}_g}{\sqrt{E_g G_g - F_g^2}} \quad (\text{A.36})$$

$$M_g = \frac{\frac{\partial \mathbf{U}_g}{\partial V_g} \times \mathbf{U}_g \cdot \mathbf{V}_g}{\sqrt{E_g G_g - F_g^2}} = \frac{\frac{\partial \mathbf{V}_g}{\partial U_g} \times \mathbf{U}_g \cdot \mathbf{V}_g}{\sqrt{E_g G_g - F_g^2}} \quad (\text{A.37})$$

$$N_g = \frac{\frac{\partial \mathbf{V}_g}{\partial V_g} \times \mathbf{U}_g \cdot \mathbf{V}_g}{\sqrt{E_g G_g - F_g^2}} \quad (\text{A.38})$$

Equations (A.36) through (A.38) can be represented in an expanded form:

$$L_g = \frac{\begin{vmatrix} \frac{\partial^2 X_g}{\partial U_g^2} & \frac{\partial^2 Y_g}{\partial U_g^2} & \frac{\partial^2 Z_g}{\partial U_g^2} \\ \frac{\partial X_g}{\partial U_g} & \frac{\partial Y_g}{\partial U_g} & \frac{\partial Z_g}{\partial U_g} \\ \frac{\partial X_g}{\partial V_g} & \frac{\partial Y_g}{\partial V_g} & \frac{\partial Z_g}{\partial V_g} \end{vmatrix}}{\sqrt{E_g G_g - F_g^2}} \quad (\text{A.39})$$

$$M_g = \frac{\begin{vmatrix} \frac{\partial^2 X_g}{\partial U_g \partial V_g} & \frac{\partial^2 Y_g}{\partial U_g \partial V_g} & \frac{\partial^2 Z_g}{\partial U_g \partial V_g} \\ \frac{\partial X_g}{\partial U_g} & \frac{\partial Y_g}{\partial U_g} & \frac{\partial Z_g}{\partial U_g} \\ \frac{\partial X_g}{\partial V_g} & \frac{\partial Y_g}{\partial V_g} & \frac{\partial Z_g}{\partial V_g} \end{vmatrix}}{\sqrt{E_g G_g - F_g^2}} \quad (\text{A.40})$$

$$N_P = \frac{\begin{vmatrix} \frac{\partial^2 X_g}{\partial V_g^2} & \frac{\partial^2 Y_g}{\partial V_g^2} & \frac{\partial^2 Z_g}{\partial V_g^2} \\ \frac{\partial X_g}{\partial U_g} & \frac{\partial Y_g}{\partial U_g} & \frac{\partial Z_g}{\partial U_g} \\ \frac{\partial X_g}{\partial V_g} & \frac{\partial Y_g}{\partial V_g} & \frac{\partial Z_g}{\partial V_g} \end{vmatrix}}{\sqrt{E_g G_g - F_g^2}} \quad (\text{A.41})$$

Fundamental magnitudes of the second order, L_g, M_g, N_g , are also functions of the U_g - and V_g -coordinates of a point of a gear tooth flank \mathcal{G} . In general form, these relationships can be represented in the form:

$$L_g = L_g(U_g, V_g) \quad (\text{A.42})$$

$$M_g = M_g(U_g, V_g) \quad (\text{A.43})$$

$$N_g = N_g(U_g, V_g) \quad (\text{A.44})$$

The discriminant, T_g , of the second fundamental form, $\Phi_{2.g}$, can be calculated from the following equation:

$$T_g = \sqrt{L_g N_g - M_g^2} \quad (\text{A.45})$$

We now come to the theorem, which is essential justification for considering the differential geometry of surfaces in connection with the six fundamental magnitudes. It has been proven (1867) first by *Bonnet*⁶ and may be enunciated as follows:

Theorem A.1 *When six fundamental magnitudes E_g, F_g, G_g and L_g, M_g, N_g are given, and when they fulfill the Gauss characteristic equation, and the two Mainardi⁷-Codazzi⁸ relations, they determine a gear tooth flank \mathcal{G} uniquely say as to its position and orientation in space.*

This theorem is commonly referred to as the “*main theorem in the theory of surface*,” or simply as “*Bonnet theorem*.” According to the main theorem, two surfaces that have identical first and second fundamental forms must be either congruent or symmetrical to one another.

By use of six fundamental magnitudes, all parameters of local geometry of a given part surface can be calculated.

⁶*Pierre Ossian Bonnet* (December 22, 1819–June 22, 1892), a French mathematician

⁷*Gaspare Mainardi* (June 27, 1800–March 9, 1879), an Italian mathematician

⁸*Delfino Codazzi* (March 7, 1824 – July 21, 1873), an Italian mathematician

Principal Directions on a Gear Tooth Flank

. The direction of vectors of principal directions, $\mathbf{T}_{1.g}$ and $\mathbf{T}_{2.g}$ at a point on a gear tooth flank \mathcal{G} , can be specified in terms of the ratio dU_g/dV_g . For the vectors of the first, $\mathbf{T}_{1.g}$, and for the second, $\mathbf{T}_{2.g}$, principal directions at a point m of a smooth, regular part surface \mathcal{G} , the corresponding values of the ratio dU_g/dV_g are calculated as roots of the quadratic equation:

$$\begin{vmatrix} E_g dU_g + F_g dV_g & F_g dU_g + G_g dV_g \\ L_g dU_g + M_g dV_g & M_g dU_g + N_g dV_g \end{vmatrix} = 0 \quad (\text{A.46})$$

The first principal plane section, $C_{1.g}$, is perpendicular to a gear tooth flank \mathcal{G} at a current surface point m and passes through the vector of the first principal direction $\mathbf{T}_{1.g}$. The second principal plane section, $C_{2.g}$, is orthogonal to a gear tooth flank \mathcal{G} at a current surface point m and passes through the vector of the second principal direction $\mathbf{T}_{2.g}$.

The principal directions $\mathbf{T}_{1.g}$ and $\mathbf{T}_{2.g}$ can be identified at any and all points of a smooth, regular gear tooth flank \mathcal{G} except of umbilic points and in flatten points of the surface. At umbilic points of a surface, as well as at flatten points, principal directions cannot be identified.

In the theory of gearing, it is often preferred to use not the vectors $\mathbf{T}_{1.g}$ and $\mathbf{T}_{2.g}$ of the principal directions, but, instead, to use the unit vectors $\mathbf{t}_{1.g}$ and $\mathbf{t}_{2.g}$ of the principal directions. The unit tangent vectors $\mathbf{t}_{1.g}$ and $\mathbf{t}_{2.g}$ are calculated from the equations:

$$\mathbf{t}_{1.g} = \frac{\mathbf{T}_{1.g}}{|\mathbf{T}_{1.g}|} \quad (\text{A.47})$$

$$\mathbf{t}_{2.g} = \frac{\mathbf{T}_{2.g}}{|\mathbf{T}_{2.g}|} \quad (\text{A.48})$$

correspondingly.

Unit tangent vectors $\mathbf{t}_{1.g}$ and $\mathbf{t}_{2.g}$ of principal directions at a point m on a gear tooth flank \mathcal{G} along with unit normal vector \mathbf{n}_g at that same point m comprise an orthogonal local frame $(\mathbf{t}_{1.g}, \mathbf{t}_{2.g}, \mathbf{n}_g)$. All three unit vectors $\mathbf{t}_{1.g}$, $\mathbf{t}_{2.g}$, and \mathbf{n}_g are mutually perpendicular to one another. The local frame $(\mathbf{t}_{1.g}, \mathbf{t}_{2.g}, \mathbf{n}_g)$ is commonly referred to as “*Darboux frame*.”

Curvatures at a Point of a Part Surface

The first, $R_{1.g}$, and the second, $R_{2.g}$, principal radii of curvature at a point of a gear tooth flank \mathcal{G} are measured within the first and in the second principal plane sections, $C_{1.g}$ and $C_{2.g}$, accordingly. For the calculation of values of the principal radii of curvature, the following equation is commonly used:

$$R_g^2 - \frac{E_g N_g - 2F_g M_g + G_g L_g}{T_g} R_g + \frac{H_g}{T_g} = 0 \quad (\text{A.49})$$

Remember that algebraic values of the radii of principal curvature, $R_{1.g}$ and $R_{2.g}$, relate to one another as $R_{2.g} > R_{1.g}$. In particular cases, at umbilic points on a gear tooth flank \mathcal{G} , no principal curvatures can be identified as all normal curvatures of the tooth surface \mathcal{G} at an umbilic point are equal to one another.

Another two important parameters of local topology of a gear tooth flank \mathcal{G} are:

- Mean curvature, \mathcal{M}_g .
- Intrinsic curvature (“*Gaussian curvature*” or “*full curvature*”), \mathcal{G}_g .

For the calculation of the curvatures \mathcal{M}_g and \mathcal{G}_g , the following equations are commonly used:

$$\mathcal{M}_g = \frac{k_{1.g} + k_{2.g}}{2} = \frac{E_g N_g - 2F_g M_g + G_g L_g}{2 \cdot (E_g G_g - F_g^2)} \quad (\text{A.50})$$

$$\mathcal{G}_g = k_{1.g} \cdot k_{2.g} = \frac{L_g N_g - M_g^2}{E_g G_g - F_g^2} \quad (\text{A.51})$$

The expressions for the mean curvature \mathcal{M}_g and for the “*Gaussian curvature*, \mathcal{G}_g ”:

$$\mathcal{M}_g = \frac{k_{1.g} + k_{2.g}}{2} \quad (\text{A.52})$$

$$\mathcal{G}_g = k_{1.g} \cdot k_{2.g} \quad (\text{A.53})$$

considered together yield a quadratic equation with respect to principal curvatures $k_{1.g}$ and $k_{2.g}$:

$$k_g^2 - 2\mathcal{M}_g k_g + \mathcal{G}_g = 0 \quad (\text{A.54})$$

The following formulae

$$k_{1.g} = \mathcal{M}_g + \sqrt{\mathcal{M}_g^2 - \mathcal{G}_g} \quad (\text{A.55})$$

$$k_{2.g} = \mathcal{M}_g - \sqrt{\mathcal{M}_g^2 - \mathcal{G}_g} \quad (\text{A.56})$$

are the solutions to Eq. (A.54).

Here, in Eqs. (A.55) and (A.56), the first principal curvature of a gear tooth flank \mathcal{G} at a current point m is designated as $k_{1.g}$, and $k_{2.g}$ designates the second principal curvature of a gear tooth flank \mathcal{G} at that same point m .

The principal curvatures $k_{1.g}$ and $k_{2.g}$ are the reciprocals to the corresponding principal radii of curvature $R_{1.g}$ and $R_{2.g}$:

$$k_{1.g} = \frac{1}{R_{1.g}} \quad (\text{A.57})$$

$$k_{2.g} = \frac{1}{R_{2.g}} \quad (\text{A.58})$$

The first principal curvature, $k_{1.g}$, is always larger than the second principal curvature, $k_{2.g}$, of a gear tooth flank \mathcal{G} at a current point m —that is, the inequality:

$$k_{1.g} > k_{2.g} \quad (\text{A.59})$$

is always valid.

This brief consideration of major elements of part surface geometry makes it possible the introduction of two definitions that are of critical importance for further discussion.

As it is already mentioned earlier in this section of the book, it is proven by *Bonnet* that the specification of the first and the second fundamental forms determines a unique surface if the “*Gauss’ characteristic equation*” and the “*Mainardi-Codazzi relations of compatibility*” are satisfied, and those two surfaces that have identical first and second fundamental forms are congruent.⁹ Six fundamental magnitudes determine a surface uniquely, except as to position and orientation in space.

The specification of a surface in terms of the first and the second fundamental forms is usually called the “*natural kind*” of surfaces representation. In general form, this kind of part surfaces representation can be expressed by a set of two equations:

$$\left. \begin{array}{l} \text{Natural form of a} \\ \text{surface } \mathcal{G} \text{ representation} \end{array} \right| \Rightarrow \mathcal{G} = \mathcal{G}(\Phi_{1.g}, \Phi_{2.g}) \begin{cases} \Phi_{1.g} = \Phi_{1.g}(E_g, F_g, G_g) \\ \Phi_{2.g} = \Phi_{2.g}(E_g, F_g, G_g, L_g, M_g, N_g) \end{cases} \quad (\text{A.60})$$

Equation (A.60) can be derived from Eq. (A.1). A given gear tooth flank \mathcal{G} can be expressed in both forms, namely, either by Eq. (A.19) or by Eq. (A.1).

⁹Two surfaces with the identical first and second fundamental forms might also be symmetrical. Refer to the literature – Koenderink, J.J., *Solid Shape*, The MIT Press, Cambridge, MA, 1990, 699 pages – on differential geometry of surfaces for details about this specific issue.

Illustrative Example

Consider an example of how an analytical representation of a surface in a “Cartesian” reference system can be converted into the natural representation of that same surface.

A “Cartesian” coordinate system $X_g Y_g Z_g$ is associated with a gear tooth flank \mathcal{G} as it is schematically shown in Fig. A.3.

The position vector of a point, \mathbf{r}_g , of the gear tooth flank \mathcal{G} can be represented as a sum of three vectors:

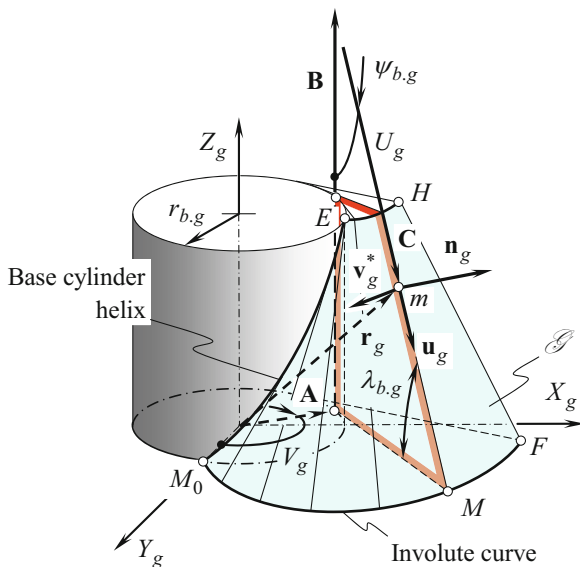
$$\mathbf{r}_g = \mathbf{A} + \mathbf{B} + \mathbf{C} \tag{A.61}$$

Each of the vectors \mathbf{A} , \mathbf{B} , and \mathbf{C} can be expressed in terms of projections onto the axes of the reference system $X_g Y_g Z_g$. Then, Eq. (A.61) casts into the equation:

$$\mathbf{r}_g(U_g, V_g) = \begin{bmatrix} r_{b,g} \cos V_g + U_g \cos \tau_{b,g} \sin V_g \\ r_{b,g} \sin V_g - U_g \sin \tau_{b,g} \sin V_g \\ r_{b,g} \tan \tau_{b,g} - U_g \sin \tau_{b,g} \\ 1 \end{bmatrix} \tag{A.62}$$

This yields the calculation of two tangent vectors $\mathbf{U}_g(U_g, V_g)$ and $\mathbf{V}_g(U_g, V_g)$, which are correspondingly equal:

Fig. A.3 Derivation of the natural form of representation of a gear tooth flank, \mathcal{G}



$$\mathbf{U}_g(U_g, V_g) = \begin{bmatrix} \cos \tau_{b,g} \sin V_g \\ -\cos \tau_{b,g} \cos V_g \\ -\sin \tau_{b,g} \\ 0 \end{bmatrix} \quad (\text{A.63})$$

$$\mathbf{V}_g(U_g, V_g) = \begin{bmatrix} -r_{b,g} \sin V_g + U_g \cos \tau_{b,g} \cos V_g \\ r_{b,g} \cos V_g + U_g \cos \tau_{b,g} \sin V_g \\ r_{b,g} \tan \tau_{b,g} \\ 0 \end{bmatrix} \quad (\text{A.64})$$

Substituting the derived vectors \mathbf{U}_g and \mathbf{V}_g into Eq. (A.14), one can come up with formulae for the calculation of the fundamental magnitudes of the first order:

$$E_g = 1 \quad (\text{A.65})$$

$$F_g = -\frac{r_{b,g}}{\cos \tau_{b,g}} \quad (\text{A.66})$$

$$G_g = \frac{U_g^2 \cos^4 \tau_{b,g} + r_{b,g}^2}{\cos^2 \tau_{b,g}} \quad (\text{A.67})$$

These expressions can be substituted directly to Eq. (A.12) for the first fundamental form $\Phi_{1,g}$ of the gear tooth flank, \mathcal{G} :

$$\Phi_{1,g} \Rightarrow dU_g^2 - 2\frac{r_{b,g}}{\cos \tau_{b,g}} dU_g dV_g + \frac{U_g^2 \cos^4 \tau_{b,g} + r_{b,g}^2}{\cos^2 \tau_{b,g}} dV_g^2 \quad (\text{A.68})$$

The derived expressions for the fundamental magnitudes E_g , F_g , and G_g [see Eqs. (A.65) through (A.67)] can also be substituted to Eq. (A.13). In this way a corresponding matrix representation of the first fundamental form $\Phi_{1,g}$ of the gear tooth flank, \mathcal{G} , can be calculated. The interested reader may wish to complete these formulae on his or her own.

The discriminant, H_g , of the first fundamental form of the gear tooth flank, \mathcal{G} , can be calculated from the expression:

$$H_g = U_g \cos \tau_{b,g} \quad (\text{A.69})$$

In order to derive an equation for the second fundamental form, $\Phi_{2,g}$, of the gear tooth flank, \mathcal{G} , the second derivatives of the position vector of a point, $\mathbf{r}_g(U_g, V_g)$, with respect to U_g - and V_g -parameters are necessary. The above derived equations for the tangent vectors \mathbf{U}_g and \mathbf{V}_g [see Eqs. (A.63) and (A.64)] make it possible the following expressions for the derivatives under consideration:

$$\frac{\partial \mathbf{U}_g}{\partial U_p} = \begin{bmatrix} 0 \\ 0 \\ 0 \\ 1 \end{bmatrix} \quad (\text{A.70})$$

$$\frac{\partial \mathbf{U}_g}{\partial V_g} \equiv \frac{\partial \mathbf{V}_g}{\partial U_g} = \begin{bmatrix} \cos \tau_{b.g} \cos V_g \\ \cos \tau_{b.g} \sin V_g \\ 0 \\ 1 \end{bmatrix} \quad (\text{A.71})$$

$$\frac{\partial \mathbf{V}_g}{\partial V_g} = \begin{bmatrix} -r_{b.g} \cos V_g - U_g \cos \tau_{b.g} \sin V_g \\ -r_{b.g} \sin V_g + U_g \cos \tau_{b.g} \cos V_g \\ 0 \\ 1 \end{bmatrix} \quad (\text{A.72})$$

Further, substitute these expressions [see Eqs. (A.70) through (A.72)] into Eqs. (A.36) through (A.38). After the necessary formulae transformations are complete, then Eqs. (A.36) through (A.38) cast into the set of formulae for the calculation of the fundamental magnitudes of the second order of the gear tooth flank, \mathcal{G} . This set of formulae is as follows:

$$L_g = 0 \quad (\text{A.73})$$

$$M_g = 0 \quad (\text{A.74})$$

$$N_g = -U_g \sin \tau_{b.g} \cos \tau_{b.g} \quad (\text{A.75})$$

Further, after substituting Eqs. (A.73) through (A.75) into Eq. (A.31), an equation for the calculation of the second fundamental form of the gear tooth flank, \mathcal{G} , can be represented in the form:

$$\Phi_{2.g} \Rightarrow -d\mathbf{r}_g \cdot d\mathbf{N}_g = -U_g \sin \tau_{b.g} \cos \tau_{b.g} dV_g^2 \quad (\text{A.76})$$

Similar to Eq. (A.68), the derived expressions for the fundamental magnitudes L_g , M_g , and N_g of the second order can be substituted into Eq. (A.32) for the second fundamental form $\Phi_{2.g}$. In this way a corresponding matrix representation of the second fundamental form, $\Phi_{2.g}$, of the surface \mathcal{G} can be derived. The interested reader may wish to complete this formulae transformation on his or her own.

For the calculation of the discriminant, T_g , of the second fundamental form, $\Phi_{2.g}$, of the gear tooth flank, \mathcal{G} , the following expression can be used:

$$T_g = U_g \sin \tau_{b.g} \cos \tau_{b.g} \quad (\text{A.77})$$

Table A.1 Fundamental magnitudes of the first and the second order of involute gear tooth flank, \mathcal{G}

$E_g = 1$	$L_g = 0$
$F_g = -\frac{r_{b.g}}{\cos \tau_{b.g}}$	$M_g = 0$
$G_g = \frac{U_g^2 \cos^4 \tau_{b.g} + r_{b.g}^2}{\cos^2 \tau_{b.g}}$	$N_g = -U_g \sin \tau_{b.g} \cos \tau_{b.g}$

The natural representation of the gear tooth flank, \mathcal{G} , can be expressed in terms of the derived set of six equations for the calculation of the fundamental magnitudes of the first E_g, F_g, G_g and of the second $L_g, M_g,$ and N_g (Table A.1).

All major elements of local geometry of the gear tooth flank, \mathcal{G} , can be calculated based on the fundamental magnitudes, E_g, F_g, G_g , of the first, $\Phi_{1.p}$, and L_g, M_g, N_g of the second, $\Phi_{2.g}$, fundamental forms. The location and orientation of the gear tooth flank, \mathcal{G} , are the two parameters that remain indefinite.

Once a part surface is represented in natural form – that is, it is expressed in terms of six fundamental magnitudes of the first and of the second order – then further calculation of parameters of a gear tooth flank \mathcal{G} becomes much easier. In order to demonstrate significant simplification of the calculation of parameters of a gear tooth flank \mathcal{G} , several useful equations are presented below as examples.

Few More Useful Equations

Many calculations of parameters of geometry can be significantly simplified by use of the first and of the second fundamental forms of a smooth, regular part surface \mathcal{G} .

For the calculation of value of radius, R_g , of normal curvature within a normal plane section through a current point m on a gear tooth flank \mathcal{G} and at a given direction the following equation can be used:

$$R_g = \frac{\Phi_{1.g}}{\Phi_{2.g}} \tag{A.78}$$

“Euler formula” for the calculation of normal curvature, $k_{\theta.g}$, at a point m in a direction that is specified by the angle, θ , can be represented as follows:

$$k_{\theta.g} = k_{1.g} \cos^2 \theta + k_{2.g} \sin^2 \theta \tag{A.79}$$

Here, in Eq. (A.79), θ is the angle that the normal plane section, C_g , makes with the first principal plane section, $C_{1.g}$. In other words, $\theta = \angle(\mathbf{t}_g, \mathbf{t}_{1.g})$; here \mathbf{t}_g designates the unit tangent vector within the normal plane section C_g .

Equation (A.79) also is a good illustration of significant simplification of the calculations when fundamental magnitudes, E_g, F_g, G_g , of the first and L_g, M_g, N_g of the second order are used.

In order to get a profound understanding of differential geometry of surfaces, the interested reader may wish to go to advanced monographs in the field. Systematic discussion of the topic is available from many sources. The author would like to turn the reader's attention to the books by [1–3] and others.

Appendix B: Applied Coordinate Systems and Linear Transformations

Consequent coordinate systems transformations can be easily described analytically with implementation of matrices. The use of matrices for the coordinate system transformation¹⁰ can be traced back to the mid of 1940s¹¹ when Dr. *S.S. Mozhayev*¹² began describing coordinate system transformations by means of matrices.

Below, coordinate system transformation is briefly discussed from the standpoint of its implementation in the theory of gearing.

Coordinate System Transformation

Homogeneous coordinates utilize a mathematical trick to embed three-dimensional coordinates and transformations into a four-dimensional matrix format. As a result, inversions or combinations of linear transformations are simplified to inversions or multiplication of the corresponding matrices.

¹⁰Matrices were introduced into mathematics by *A. Cayley* in 1857. They provide a compact and flexible notation particularly useful in dealing with linear transformations, and they presented an organized method for the solution of systems of linear differential equations.

¹¹Application of matrices for the purposes of analytical representation of coordinate system transformation should be credited to Dr. *S.S. Mozhayev* [*Mozhayev, S.S., General Theory of Cutting Tools*, Doctoral Thesis, Leningrad, Leningrad Polytechnic Institute, 1951, 295 pages]. Dr. *S.S. Mozhayev* began using matrices for this purpose in the mid of 1940s. Later on, matrix approach for coordinate system transformation has been used by *Denavit* and *Hartenberg*, as well as by many other researchers.

¹²*S.S. Mozhayev* is a Soviet scientist mostly known for his accomplishments in the theory of cutting tool design.

Homogeneous Coordinate Vectors

Instead of representing each point $\mathbf{r}(x, y, z)$ in three-dimensional space with a single three-dimensional vector,

$$\mathbf{r} = \begin{bmatrix} x \\ y \\ z \end{bmatrix} \quad (\text{B.1})$$

homogeneous coordinates allow each point $\mathbf{r}(x, y, z)$ to be represented by any of an infinite number of four-dimensional vectors:

$$\mathbf{r} = \begin{bmatrix} T \cdot x \\ T \cdot y \\ T \cdot z \\ T \end{bmatrix} \quad (\text{B.2})$$

The three-dimensional vector corresponding to any four-dimensional vector can be calculated by dividing the first three elements by the fourth, and a four-dimensional vector corresponding to any three-dimensional vector can be created by simply adding a fourth element and setting it equal to one.

Homogeneous Coordinate Transformation Matrices of the Dimension 4×4

Homogeneous coordinate transformation matrices operate on four-dimensional homogeneous vector representations of traditional three-dimensional coordinate locations. Any three-dimensional linear transformation (translation, rotation, and so forth) can be represented by a 4×4 homogeneous coordinate transformation matrix. In fact, because of the redundant representation of three-space in a homogeneous coordinate system, an infinite number of different 4×4 homogeneous coordinate transformation matrices are available to perform any given linear transformation. This redundancy can be eliminated to provide a unique representation by dividing all elements of a 4×4 homogeneous transformation matrix by the last element (which will become equal to one). This means that a 4×4 homogeneous transformation matrix can incorporate as many as 15 independent parameters. The generic format representation of a homogeneous transformation equation for mapping the three-dimensional coordinate (x_1, y_1, z_1) to the three-dimensional coordinate (x_2, y_2, z_2) is:

$$\begin{bmatrix} T^* \cdot x_2 \\ T^* \cdot y_2 \\ T^* \cdot z_2 \\ T^* \end{bmatrix} = \begin{bmatrix} T^* \cdot a & T^* \cdot b & T^* \cdot c & T^* \cdot d \\ T^* \cdot e & T^* \cdot f & T^* \cdot g & T^* \cdot h \\ T^* \cdot i & T^* \cdot j & T^* \cdot k & T^* \cdot m \\ T^* \cdot n & T^* \cdot p & T^* \cdot q & T^* \end{bmatrix} \cdot \begin{bmatrix} T \cdot x_2 \\ T \cdot y_2 \\ T \cdot z_2 \\ T \end{bmatrix} \quad (\text{B.3})$$

If any two matrices or vectors of this equation are known, the third matrix (or vector) can be calculated, and then the redundant T element in the solution can be eliminated by dividing all elements of the matrix by the last element.

Various transformation models can be used to constrain the form of the matrix to transformations with fewer degrees of freedom.

Translations

The translation of a coordinate system is one of the major linear transformations used in the theory of part surface generation. Translations of the coordinate system $X_2Y_2Z_2$ along axes of the coordinate system $X_1Y_1Z_1$ are depicted in Fig. B.1. Translations can be analytically described by the homogeneous transformation matrix of dimension 4×4 .

For an analytical description of translation along coordinate axes, the operators of translation $\mathbf{Tr}(a_x, X)$, $\mathbf{Tr}(a_y, Y)$, and $\mathbf{Tr}(a_z, Z)$ are used. These operators yield matrix representation in the form:

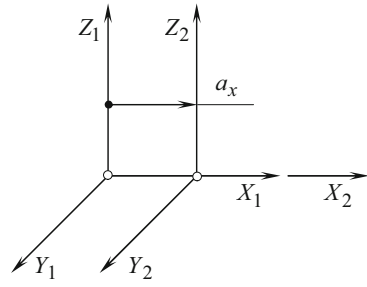
$$\mathbf{Tr}(a_x, X) = \begin{bmatrix} 1 & 0 & 0 & a_x \\ 0 & 1 & 0 & 0 \\ 0 & 0 & 1 & 0 \\ 0 & 0 & 0 & 1 \end{bmatrix} \quad (\text{B.4})$$

$$\mathbf{Tr}(a_y, Y) = \begin{bmatrix} 1 & 0 & 0 & 0 \\ 0 & 1 & 0 & a_y \\ 0 & 0 & 1 & 0 \\ 0 & 0 & 0 & 1 \end{bmatrix} \quad (\text{B.5})$$

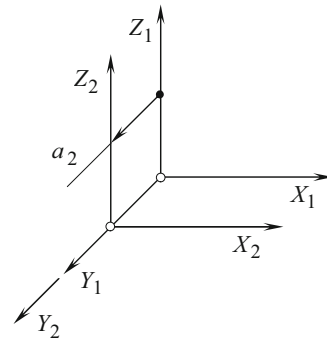
$$\mathbf{Tr}(a_z, Z) = \begin{bmatrix} 1 & 0 & 0 & 0 \\ 0 & 1 & 0 & 0 \\ 0 & 0 & 1 & a_z \\ 0 & 0 & 0 & 1 \end{bmatrix} \quad (\text{B.6})$$

Here, in Eq. (B.4) through Eq. (B.6), the parameters a_x , a_y , and a_z are signed values that denote the distance of translation along the corresponding axis.

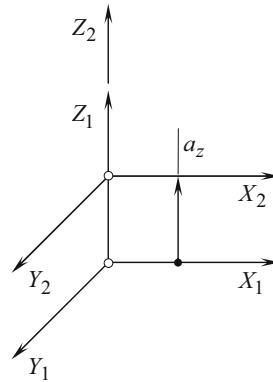
Fig. B.1 Analytical description of the operators of translations $\text{Tr}(a_x, X)$, $\text{Tr}(a_y, Y)$, $\text{Tr}(a_z, Z)$ along the coordinate axes of a “Cartesian” reference system XYZ



(a)



(b)



(c)

Consider two coordinate systems, $X_1Y_1Z_1$ and $X_2Y_2Z_2$, displaced along the X_1 -axis at a distance a_x as schematically depicted in Fig. B.1a. A point m in the reference system $X_2Y_2Z_2$ is given by the position vector $\mathbf{r}_2(m)$. In the coordinate system, $X_1Y_1Z_1$, that same point m can be specified by the position vector $\mathbf{r}_1(m)$. Then the

position vector $\mathbf{r}_1(m)$ can be expressed in terms of the position vector $\mathbf{r}_2(m)$ by the equation:

$$\mathbf{r}_1(m) = \mathbf{Tr}(a_x, X) \cdot \mathbf{r}_2(m) \tag{B.7}$$

Equations similar to Eq. (B.7) are valid for the operators $\mathbf{Tr}(a_y, Y)$ and $\mathbf{Tr}(a_z, Z)$ of the coordinate system transformation. The latter is schematically illustrated in Fig. B.1b and B.1c.

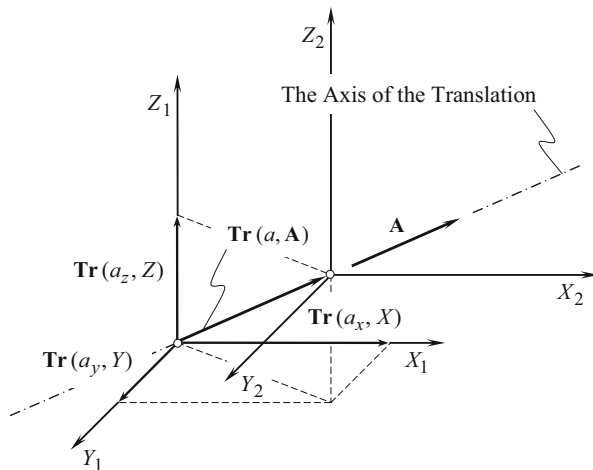
Use of the operators of translation $\mathbf{Tr}(a_x, X)$, $\mathbf{Tr}(a_y, Y)$, and $\mathbf{Tr}(a_z, Z)$ makes it possible an introduction of an operator $\mathbf{Tr}(a, \mathbf{A})$ of a combined transformation. Suppose that point, p , on a rigid body goes through a translation describing a straight line from a point p_1 to a point p_2 with a change of coordinates of (a_x, a_y, a_z) . This motion of the point, p , can be analytically described with a resultant translation operator $\mathbf{Tr}(a, \mathbf{A})$:

$$\mathbf{Tr}(a, \mathbf{A}) = \begin{bmatrix} 1 & 0 & 0 & a_x \\ 0 & 1 & 0 & a_y \\ 0 & 0 & 1 & a_z \\ 0 & 0 & 0 & 1 \end{bmatrix} \tag{B.8}$$

The operator $\mathbf{Tr}(a, \mathbf{A})$ of the resultant coordinate system transformation can be interpreted as the operator of translation along an arbitrary axis having the vector \mathbf{A} as the direct vector.

An analytical description of translation of the coordinate system $X_1Y_1Z_1$ in direction of an arbitrary vector \mathbf{A} to the position of $X_2Y_2Z_2$ can be composed from Fig. B.2. The operator of translation $\mathbf{Tr}(a, \mathbf{A})$ of that particular kind can be expressed in terms of the operators $\mathbf{Tr}(a_x, X)$, $\mathbf{Tr}(a_y, Y)$, and $\mathbf{Tr}(a_z, Z)$ of elementary translations:

Fig. B.2 Analytical description of an operator, $\mathbf{Tr}(a, \mathbf{A})$, of translation along an arbitrary axis (vector \mathbf{A} is the direct vector of the axis)



$$\mathbf{Tr}(a, \mathbf{A}) = \mathbf{Tr}(a_z, Z) \cdot \mathbf{Tr}(a_y, Y) \cdot \mathbf{Tr}(a_x, X) \quad (\text{B.9})$$

Evidently, the axis along the vector \mathbf{A} is always the axis through the origins of both the reference systems $X_1Y_1Z_1$ and $X_2Y_2Z_2$.

Any and all coordinate system transformations that do not change the orientation of a geometrical object are referred to as “*orientation-preserving transformation*” or “*direct transformation*.” Therefore, transformation of translation is an example of a direct transformation.

Rotation about a Coordinate Axis

Rotation of a coordinate system about a coordinate axis is another major linear transformation used in the theory of part surface generation. A rotation is specified by an axis of rotation and the angle of the rotation. It is a fairly simple trigonometric calculation to obtain a transformation matrix for a rotation about one of the coordinate axes.

Possible rotations of the coordinate system $X_2Y_2Z_2$ about the axis of the coordinate system $X_1Y_1Z_1$ are illustrated in Fig. B.3.

For analytical description of rotation about a coordinate axis, the operators of rotation $\mathbf{Rt}(\varphi_x, X_1)$, $\mathbf{Rt}(\varphi_y, Y_1)$, and $\mathbf{Rt}(\varphi_z, Z_1)$ are used. These operators of linear transformations yield representation in the form of homogeneous matrices:

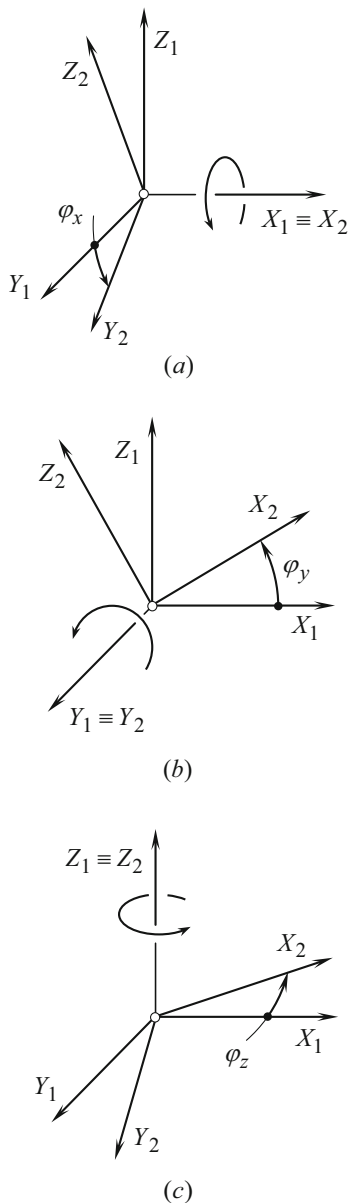
$$\mathbf{Rt}(\varphi_x, X_1) = \begin{bmatrix} 1 & 0 & 0 & 0 \\ 0 & \cos \varphi_x & \sin \varphi_x & 0 \\ 0 & -\sin \varphi_x & \cos \varphi_x & 0 \\ 0 & 0 & 0 & 1 \end{bmatrix} \quad (\text{B.10})$$

$$\mathbf{Rt}(\varphi_y, Y_1) = \begin{bmatrix} \cos \varphi_y & 0 & \sin \varphi_y & 0 \\ 0 & 1 & 0 & 0 \\ -\sin \varphi_y & 0 & \cos \varphi_y & 0 \\ 0 & 0 & 0 & 1 \end{bmatrix} \quad (\text{B.11})$$

$$\mathbf{Rt}(\varphi_z, Z_1) = \begin{bmatrix} \cos \varphi_z & \sin \varphi_z & 0 & 0 \\ -\sin \varphi_z & \cos \varphi_z & 0 & 0 \\ 0 & 0 & 1 & 0 \\ 0 & 0 & 0 & 1 \end{bmatrix} \quad (\text{B.12})$$

Here φ_x , φ_y , and φ_z are signed values that denote the corresponding angles of rotations about a corresponding coordinate axis: φ_x is the angle of rotation around the X_1 -axis (pitch) of the “*Cartesian*” coordinate system $X_1Y_1Z_1$; φ_y is the angle of rotation around the Y_1 -axis (roll), and φ_z is the angle of rotation around the Z_1 -axis (yaw) of that same “*Cartesian*” reference system $X_1Y_1Z_1$.

Fig. B.3 Analytical description of the operators of rotation $\mathbf{Rt}(\varphi_x, X)$, $\mathbf{Rt}(\varphi_y, Y)$, and $\mathbf{Rt}(\varphi_z, Z)$ about a coordinate axis of a reference system $X_1Y_1Z_1$



Rotation about a coordinate axis is illustrated in Fig. B.3.

Consider two coordinate systems $X_1Y_1Z_1$ and $X_2Y_2Z_2$, which are turned about X_1 -axis through an angle φ_x as shown in Fig. B.3a. In the reference system $X_2Y_2Z_2$, a point m is given by a position vector $\mathbf{r}_2(m)$. In the coordinate system $X_1Y_1Z_1$, that same point m can be specified by the position vector $\mathbf{r}_1(m)$. Then, the position vector $\mathbf{r}_1(m)$ can be expressed in terms of the position vector $\mathbf{r}_2(m)$ by the equation:

$$\mathbf{r}_1(m) = \mathbf{Rt}(\varphi_x, X) \cdot \mathbf{r}_2(m) \quad (\text{B.13})$$

Equations those similar to that above Eq. (B.13) are also valid for other operators $\mathbf{Rt}(\varphi_y, Y)$ and $\mathbf{Rt}(\varphi_z, Z)$ of the coordinate system transformation. These elementary coordinate system transformations are schematically illustrated in Fig. B.3b and in Fig. B.3c accordingly.

Rotation about an Arbitrary Axis through the Origin

When a rotation is to be performed around an arbitrary vector based at the origin, the transformation matrix must be assembled from a combination of rotations about the “*Cartesian*” coordinate.

Two different approaches for analytical description of a rotation about an arbitrary axis through the origin are discussed below.

Conventional Approach

Analytical description of rotation of the coordinate system $X_1Y_1Z_1$ about an arbitrary axis through the origin to the position of a reference system $X_2Y_2Z_2$ is illustrated in Fig. B.4. It is assumed here that the rotation is performed about the axis having a vector \mathbf{A}_0 as the direction vector. The operator $\mathbf{Rt}(\varphi_A, \mathbf{A}_0)$ of rotation of that kind can be expressed in terms of the operators $\mathbf{Rt}(\varphi_x, X)$, $\mathbf{Rt}(\varphi_y, Y)$, and $\mathbf{Rt}(\varphi_z, Z)$ of elementary rotations:

$$\mathbf{Rt}(\varphi_A, \mathbf{A}_0) = \mathbf{Rt}(\varphi_z, Z) \cdot \mathbf{Rt}(\varphi_y, Y) \cdot \mathbf{Rt}(\varphi_x, X) \quad (\text{B.14})$$

Evidently, the axis of rotation (a straight line along the vector \mathbf{A}_0) is always an axis through the origin.

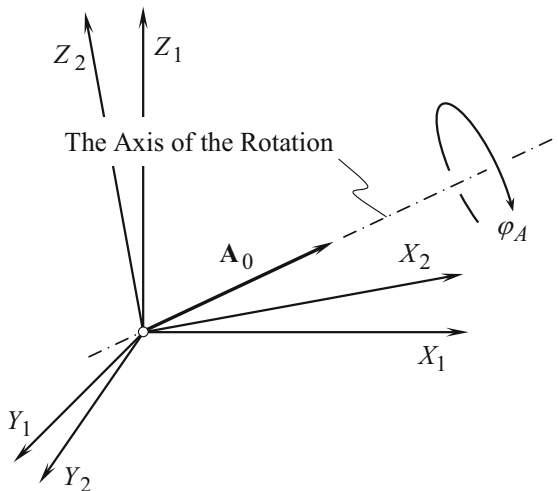
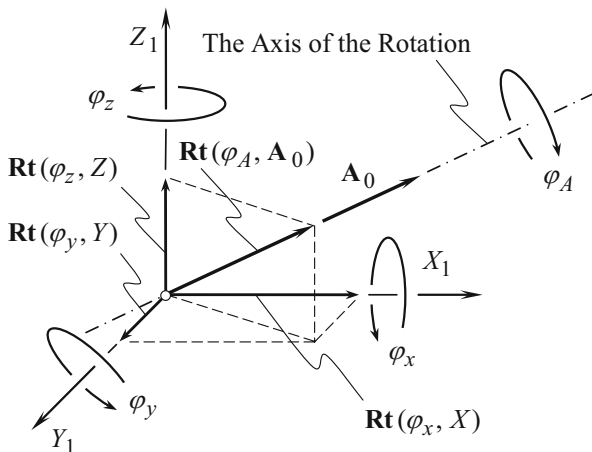
The operators of translation and of rotation also yield linear transformations of other kinds as well.

“Eulerian Transformation”

“*Eulerian transformation*” is a well-known kind of linear transformations used widely in mechanical engineering. This kind of linear transformations is analytically described by the operator $\mathbf{Eu}(\psi, \theta, \varphi)$ of “*Eulerian*¹³ *transformation*.”

¹³*Leonhard Euler* (April 15, 1707–September 18, 1783), a famous Swiss mathematician and physicist who spent most of his life in Russia and Germany

Fig. B.4 Analytical description of the operator $\mathbf{Rt}(\varphi_A, \mathbf{A})$ of rotation about an arbitrary axis through the origin of a “Cartesian” coordinate system $X_1Y_1Z_1$ (the vector \mathbf{A} is the directing vector of the axis of rotation)



The operator $\mathbf{Eu}(\psi, \theta, \varphi)$ is expressed in terms of three “Euler angles” (or “Eulerian angles”) ψ , θ , and φ . Configuration of an orthogonal “Cartesian” coordinate system $X_1Y_1Z_1$ in relation to another orthogonal “Cartesian” coordinate system $X_2Y_2Z_2$ is defined by the “Euler angles” ψ , θ , and φ . These angles are shown in Fig. B.5.

The line of intersection of the coordinate plane X_1Y_1 of the first reference system by the coordinate plane X_2Y_2 of the second reference system is commonly referred to as “line of nodes.” In Fig. B.5 the line OK is the line of nodes. It is assumed here and below that the line of nodes, OK , and the axes Z_1 and Z_2 form a frame of that same orientation as the reference systems $X_1Y_1Z_1$ and $X_2Y_2Z_2$ do.

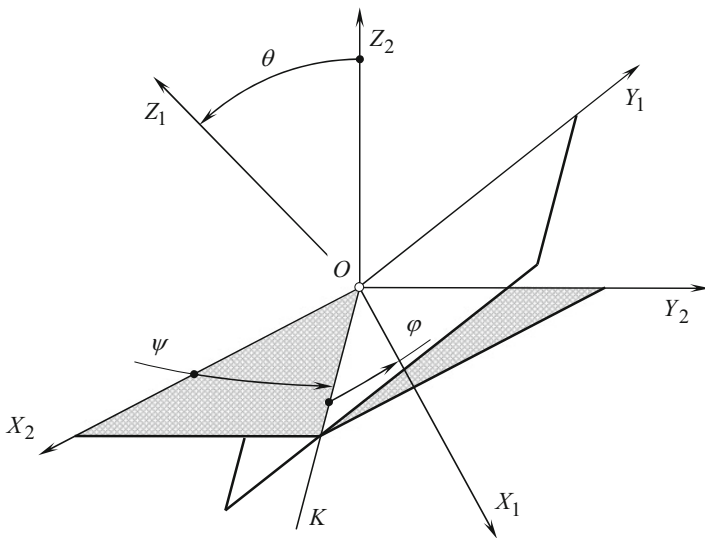


Fig. B.5 “Euler angles”

The “Euler angle, φ ” is referred to as the “angle of pure rotation.” This angle is measured between the X_1 -axis and the line of nodes, OK . The angle of pure rotation, φ , is measured within the coordinate plane X_1Y_1 in the direction of shortest rotation from the axis X_1 to the axis Y_1 .

The “Euler angle, θ ” is referred to as the “angle of nutation.” The angle of nutation, θ , is measured between the axes Z_1 and Z_2 . The actual value of this angle never exceeds 180° .

The “Euler angle, ψ ” is referred to as the “angle of precession.” The angle of precession, ψ , is measured in the coordinate plane X_2Y_2 . This the angle between the line of nodes, OK , and the X_2 -axis. The direction of the shortest rotation from the axis X_2 to the axis Y_2 is the direction in which the angle of precession is measured.

In case, when the angle of nutation is equal either $\theta = 0^\circ$ or $\theta = 180^\circ$, then the “Euler angles” are not defined.

Operator $\mathbf{Eu}(\psi, \theta, \varphi)$ of “Eulerian transformation” allows for the following matrix representation:

$$\mathbf{Eu}(\psi, \theta, \varphi) = \begin{bmatrix} -\sin \psi \cos \theta \sin \varphi + \cos \psi \cos \varphi & \cos \psi \cos \theta \sin \varphi + \sin \psi \cos \varphi & \sin \theta \sin \varphi & 0 \\ -\sin \psi \cos \theta \cos \varphi - \cos \psi \sin \varphi & \cos \psi \cos \theta \cos \varphi - \sin \psi \cos \varphi & \sin \theta \cos \varphi & 0 \\ \sin \theta \sin \varphi & -\cos \psi \cos \theta & \cos \theta & 0 \\ 0 & 0 & 0 & 1 \end{bmatrix} \tag{B.15}$$

It is important to stress here the difference between the operator $\mathbf{Eu}(\psi, \theta, \varphi)$ of “Eulerian transformation” and between the operator $\mathbf{Rt}(\psi_A, \mathbf{A}_0)$ of rotation about an arbitrary axis through the origin.

The operator $\mathbf{Rt}(\psi_A, \mathbf{A})$ of rotation about an arbitrary axis through the origin can result in that same final orientation of the coordinate system $X_2Y_2Z_2$ in relation to the coordinate system $X_1Y_1Z_1$ as the operator $\mathbf{Eu}(\psi, \theta, \varphi)$ of “Eulerian transformation” does. However, the operators of linear transformations $\mathbf{Rt}(\psi_A, \mathbf{A}_0)$ and $\mathbf{Eu}(\psi, \theta, \varphi)$ are the operators of completely different nature. They can result in identical coordinate system transformation, but they are not equal to one another.

Rotation about an Arbitrary Axis Not through the Origin

The transformation corresponding to rotation of an angle φ around an arbitrary vector not through the origin cannot readily be written in a form similar to the rotation matrices about the coordinate axes.

The desired transformation matrix is obtained by combining a sequence of elementary translation and rotation matrices. (Once a single 4×4 matrix has been obtained representing the composite transformations, it can be used in the same way as any other transformation matrix.)

The rotation of the coordinate system $X_1Y_1Z_1$ to a configuration, which the coordinate system $X_2Y_2Z_2$ possesses, can be performed about a corresponding axis that features an arbitrary configuration in space (see Fig. B.6). The vector \mathbf{A} is the direction vector of the axis of the rotation. The axis of the rotation is not a line through the origin.

The operator of linear transformation of this particular kind $\mathbf{Rt}(\psi_A, \mathbf{A})$ can be expressed in terms of the operator $\mathbf{Tr}(a, \mathbf{A})$ of translation along and of the operator $\mathbf{Rt}(\psi_A, \mathbf{A}_0)$ of rotation about an arbitrary axis through the origin:

$$\mathbf{Rt}(\varphi_A, \mathbf{A}) = \mathbf{Tr}(-b, \mathbf{B}^*) \cdot \mathbf{Rt}(\varphi_A, \mathbf{A}_0) \cdot \mathbf{Tr}(b, \mathbf{B}) \quad (\text{B.16})$$

Here, in Eq. (B.16) the following are designated:

$\mathbf{Tr}(b, \mathbf{B})$

is the operator of translation along the shortest distance of approach of the axis of rotation and origin of the coordinate system.

$\mathbf{Tr}(-b, \mathbf{B}^*)$

is the operator of translation in the direction opposite to the translation $\mathbf{Tr}(b, \mathbf{B})$ after the rotation $\mathbf{Rt}(\psi_A, \mathbf{A})$ is completed.

In order to determine the shortest distance of approach, B , of the axis of rotation (i.e., the axis along the directing vector \mathbf{B}) and origin of the coordinate system, consider the axis (\mathbf{B}) through two given points $\mathbf{r}_{B.1}$ and $\mathbf{r}_{B.2}$.

The shortest distance between a certain point \mathbf{r}_0 and the straight line through the points $\mathbf{r}_{B.1}$ and $\mathbf{r}_{B.2}$ can be calculated from the following formula:

$$B = \frac{|(\mathbf{r}_2 - \mathbf{r}_1) \times (\mathbf{r}_1 - \mathbf{r}_0)|}{|\mathbf{r}_2 - \mathbf{r}_1|} \quad (\text{B.17})$$

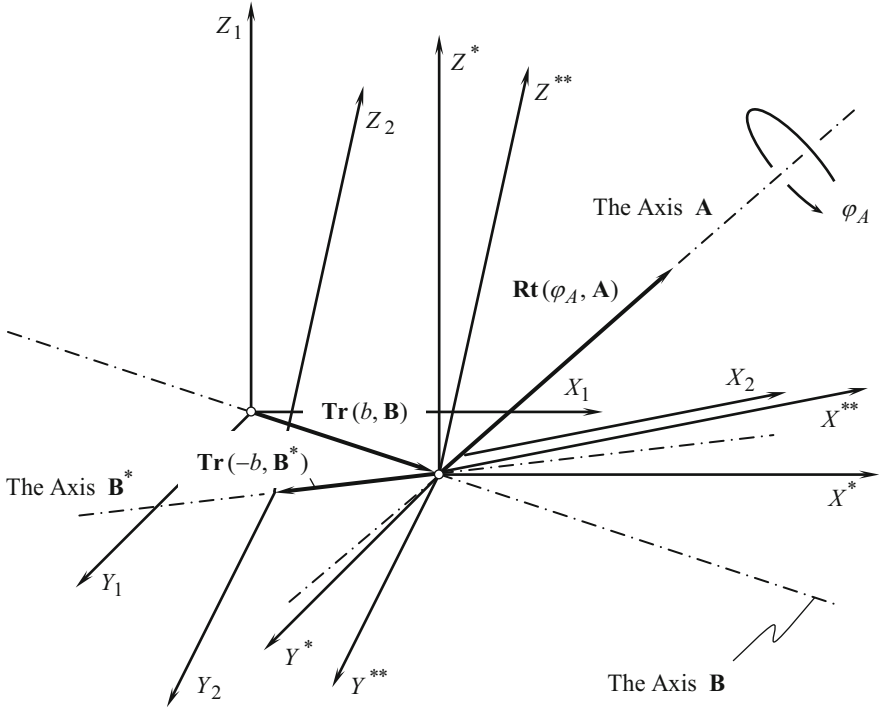


Fig. B.6 Analytical description of the operator, $\mathbf{Rt}(\varphi_A, \mathbf{A})$, of rotation about an arbitrary axis not through the origin (vector \mathbf{A} is the direct vector of the axis of the rotation)

For the origin of the coordinate system, the equality $\mathbf{r}_0 = 0$ is observed. Then,

$$B = |\mathbf{r}_1| \cdot \sin \angle[\mathbf{r}_1, (\mathbf{r}_2 - \mathbf{r}_1)] \tag{B.18}$$

Matrix representation of the operators of translation $\mathbf{Tr}(a_x, X)$, $\mathbf{Tr}(a_y, Y)$, and $\mathbf{Tr}(a_z, Z)$ along the coordinate axes, together with the operators of rotation $\mathbf{Rt}(\varphi_x, X)$, $\mathbf{Rt}(\varphi_y, Y)$, and $\mathbf{Rt}(\varphi_z, Z)$ about the coordinate axes is convenient for implementation in the theory of part surface generation. Moreover, use of the operators is the simplest possible way to analytically describe the linear transformations.

Resultant Coordinate System Transformation

The operators of translation $\mathbf{Tr}(a_x, X)$, $\mathbf{Tr}(a_y, Y)$, and $\mathbf{Tr}(a_z, Z)$ together with the operators of rotation $\mathbf{Rt}(\varphi_x, X)$, $\mathbf{Rt}(\varphi_y, Y)$, and $\mathbf{Rt}(\varphi_z, Z)$ are used for the purpose of composing the operator $\mathbf{Rs}(1 \mapsto 2)$ of the resultant coordinate system transformation. The transition from the initial “*Cartesian*” reference system $X_1Y_1Z_1$ to another

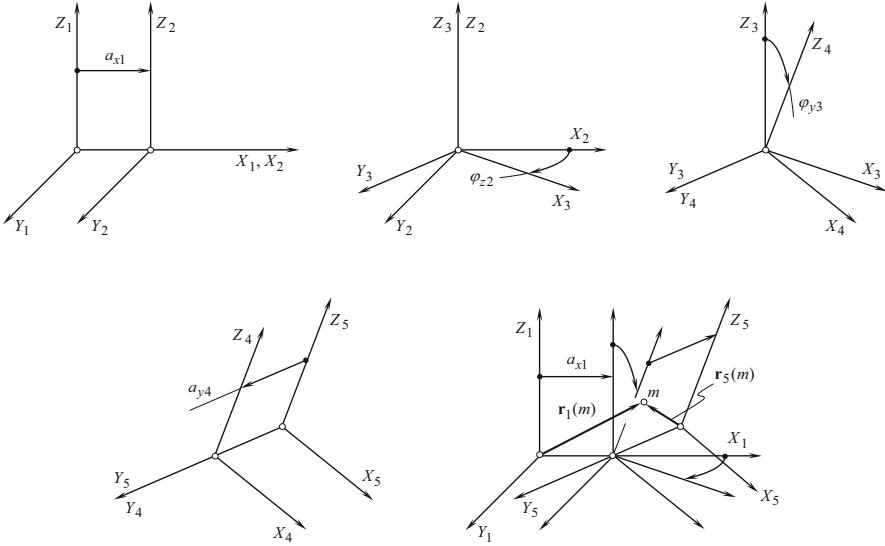


Fig. B.7 An example of the resultant coordinate system transformation, analytically expressed by the operator \mathbf{Rs} ($1 \mapsto 5$)

“Cartesian” reference system $X_2Y_2Z_2$ is analytically described by the operator \mathbf{Rs} ($1 \mapsto 2$) of the resultant coordinate system transformation.

For example, the expression:

$$\mathbf{Rs}(1 \mapsto 5) = \mathbf{Tr}(a_x, X) \cdot \mathbf{Rt}(\varphi_z, Z) \cdot \mathbf{Rt}(\varphi_x, X) \cdot \mathbf{Tr}(a_y, Y) \tag{B.19}$$

indicates that the transition from the coordinate system $X_1Y_1Z_1$ to the coordinate system $X_5Y_5Z_5$ is executed in the following four steps (see Fig. B.7):

$$\mathbf{Tr}(a_y, Y) \tag{Translation}$$

- Followed by rotation $\mathbf{Rt}(\varphi_x, X)$.
- Followed by second rotation $\mathbf{Rt}(\varphi_z, Z)$.
- And finally followed by the translation $\mathbf{Tr}(a_x, X)$.

Ultimately, the equality:

$$\mathbf{r}_1(m) = \mathbf{Rs}(1 \mapsto 5) \cdot \mathbf{r}_5(m) \tag{B.20}$$

is valid.

When the operator $\mathbf{Rs}(1 \mapsto t)$ of the resultant coordinate system transformation is specified, then the transition in the opposite direction can be performed by means of the operator $\mathbf{Rs}(t \mapsto 1)$ of the inverse coordinate system transformation. The following equality can be easily proven:

$$\mathbf{Rs}(t \mapsto 1) = \mathbf{Rs}^{-1}(1 \mapsto t) \quad (\text{B.21})$$

In the above example illustrated in Fig. B.7, the operator $\mathbf{Rs}(5 \mapsto 1)$ of the inverse resultant coordinate system transformation can be expressed in terms of the operator $\mathbf{Rs}(1 \mapsto 5)$ of the direct resultant coordinate system transformation. Following Eq. (B.21), one can come up with the equation:

$$\mathbf{Rs}(5 \mapsto 1) = \mathbf{Rs}^{-1}(1 \mapsto 5) \quad (\text{B.22})$$

It is easy to show that the operator $\mathbf{Rs}(1 \mapsto t)$ of the resultant coordinate system transformation allows for representation in the following form:

$$\mathbf{Rs}(1 \mapsto t) = \mathbf{Tr}(a, A) \cdot \mathbf{Eu}(\psi, \theta, \varphi) \quad (\text{B.23})$$

The linear transformation $\mathbf{Rs}(1 \mapsto t)$ [see Eq. (B.23)] can also be expressed in terms of rotation about an axis $\mathbf{Rt}(\varphi_A, A)$, not through the origin [see Eq. (B.16)].

Complex Coordinate System Transformation

In particular cases of complex coordinate system transformations that are repeatedly used in practice, special purpose operators of coordinate system transformation can be composed of elementary operators of translation and operators of rotation.

Linear Transformation Describing a Screw Motion about a Coordinate Axis

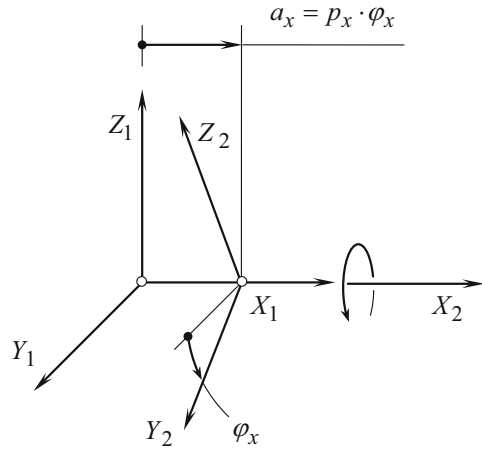
Operators for analytical description of screw motions about an axis of the “*Cartesian*” coordinate system are a particular case of the operators of the resultant coordinate system transformation.

By definition (see Fig. B.8), the operator $\mathbf{Sc}_x(\varphi_x, p_x)$ of a screw motion about X -axis of the “*Cartesian*” coordinate system XYZ is equal to:

$$\mathbf{Sc}_x(\varphi_x, p_x) = \mathbf{Rt}(\varphi_x, X) \cdot \mathbf{Tr}(a_x, X) \quad (\text{B.24})$$

After substituting of the operator of translation $\mathbf{Tr}(a_x, X)$, and the operator of rotation $\mathbf{Rt}(\varphi_x, X)$ [see Eq. (B.10)], Eq. (B.24) casts into the expression:

Fig. B.8 On analytical description of the operator of screw motion, $\mathbf{Sc}_x(\varphi_x, p_x)$



$$\mathbf{Sc}_x(\varphi_x, p_x) = \begin{bmatrix} 1 & 0 & 0 & p_x \cdot \varphi_x \\ 0 & \cos \varphi_x & \sin \varphi_x & 0 \\ 0 & -\sin \varphi_x & \cos \varphi_x & 0 \\ 0 & 0 & 0 & 1 \end{bmatrix} \tag{B.25}$$

for the calculation of the operator of the screw motion $\mathbf{Sc}_x(\varphi_x, p_x)$ about X-axis.

The operators of screw motions $\mathbf{Sc}_y(\varphi_y, p_y)$ and $\mathbf{Sc}_z(\varphi_z, p_z)$ about Y- and Z-axis correspondingly are defined in the way similar to that; the operator of the screw motion $\mathbf{Sc}_x(\varphi_x, p_x)$ is defined:

$$\mathbf{Sc}_y(\varphi_y, p_y) = \mathbf{Rt}(\varphi_y, Y) \cdot \mathbf{Tr}(a_y, Y) \tag{B.26}$$

$$\mathbf{Sc}_z(\varphi_z, p_z) = \mathbf{Rt}(\varphi_z, Z) \cdot \mathbf{Tr}(a_z, Z) \tag{B.27}$$

Using Eqs. (B.5) and (B.6) together with Eqs. (B.11) and (B.12), one can come up with the expressions:

$$\mathbf{Sc}_y(\varphi_y, p_y) = \begin{bmatrix} \cos \varphi_y & 0 & -\sin \varphi_y & 0 \\ 0 & 1 & 0 & p_y \cdot \varphi_y \\ \sin \varphi_y & 0 & \cos \varphi_y & 0 \\ 0 & 0 & 0 & 1 \end{bmatrix} \tag{B.28}$$

$$\mathbf{Sc}_z(\varphi_z, p_z) = \begin{bmatrix} \cos \varphi_z & \sin \varphi_z & 0 & 0 \\ -\sin \varphi_z & \cos \varphi_z & 0 & 0 \\ 0 & 0 & 1 & p_z \cdot \varphi_z \\ 0 & 0 & 0 & 1 \end{bmatrix} \tag{B.29}$$

for the calculation of the operators of the screw motion $\mathbf{Sc}_y(\varphi_y, p_y)$ and $\mathbf{Sc}_z(\varphi_z, p_z)$ about Y- and Z-axis.

Screw motions about a coordinate axis, as well as screw surfaces, are common in the theory of part surface generation. This makes it practical to use the operators of the screw motion $\mathbf{Sc}_x(\varphi_x, p_x)$, $\mathbf{Sc}_y(\varphi_y, p_y)$, and $\mathbf{Sc}_z(\varphi_z, p_z)$ in the theory of part surface generation.

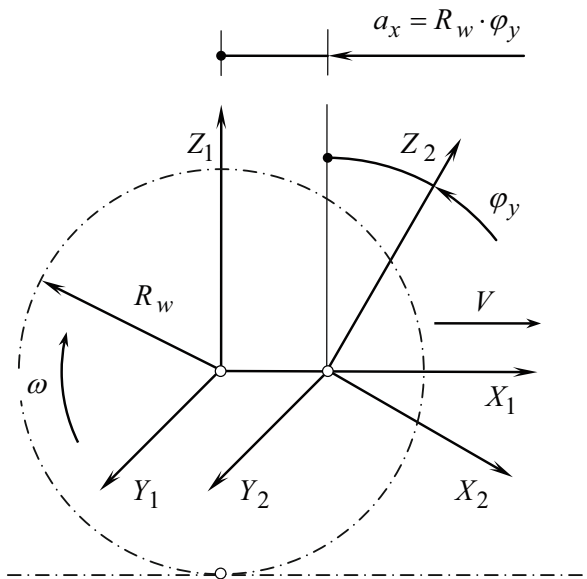
In case of necessity, an operator of the screw motion about an arbitrary axis either through the origin of the coordinate system or not through the origin of the coordinate system can be derived following the method similar to that used for the derivation of the operators $\mathbf{Sc}_x(\varphi_x, p_x)$, $\mathbf{Sc}_y(\varphi_y, p_y)$, and $\mathbf{Sc}_z(\varphi_z, p_z)$.

Linear Transformation Describing Rolling Motion of a Coordinate System

One more practical combination of a rotation and of a translation is often used in the theory of part surface generation.

Consider a “Cartesian” coordinate system $X_1Y_1Z_1$ (see Fig. B.9). The coordinate system $X_1Y_1Z_1$ is traveling in the direction of X_1 -axis. The velocity of the translation is denoted by V . The coordinate system $X_1Y_1Z_1$ is rotating about its Y_1 -axis simultaneously with the translation. The speed of the rotation is denoted as ω . Assume that the ratio V/ω is constant. Under such a scenario the resultant motion of the reference system $X_1Y_1Z_1$ to its arbitrary position $X_2Y_2Z_2$ allows interpretation in the form of rolling with no sliding of a cylinder of radius R_w over the plane. The plane is parallel to the coordinate X_1Y_1 -plane, and it is remote from it at the distance R_w . For the calculation of radius of the rolling cylinder the expression $R_w = V/\omega$ can be used.

Fig. B.9 Illustration of the transformation of rolling, $\mathbf{Rl}_x(\varphi_y, Y)$, of a coordinate system



Since the rolling of the cylinder of a radius, R_w , over the plane is performed with no sliding, a certain correspondence between the translation and the rotation of the coordinate system is established. When the coordinate system turns through a certain angle φ_y , then the translation of origin of the coordinate system along X_1 -axis is equal to $a_x = \varphi_r \cdot R_w$.

Transition from the coordinate system $X_1Y_1Z_1$ to the coordinate system $X_2Y_2Z_2$ can be analytically described by the operator of the resultant coordinate system transformation $\mathbf{Rs}(1 \mapsto 2)$. The $\mathbf{Rs}(1 \mapsto 2)$ is equal:

$$\mathbf{Rs}(1 \mapsto 2) = \mathbf{Rt}(\varphi_y, Y_1) \cdot \mathbf{Tr}(a_x, X_1) \quad (\text{B.30})$$

Here $\mathbf{Tr}(a_x, X_1)$ designates the operator of the translation along X_1 -axis, and $\mathbf{Rt}(\varphi_y, Y_1)$ is the operator of the rotation about Y_1 -axis.

The operator of the resultant coordinate system transformation of the kind [see Eq. (B.30)] is referred to as the “operator of rolling motion over a plane.”

When the translation is performed along the X_1 -axis, and the rotation is performed about the Y_1 -axis, the operator of rolling is denoted as $\mathbf{Rl}_x(\varphi_y, Y)$. In this particular case the equality $\mathbf{Rl}_x(\varphi_y, Y) = \mathbf{Rs}(1 \mapsto 2)$ [see Eq. (B.30)] is valid. Based on this equality, the operator of rolling over a plane $\mathbf{Rl}_x(\varphi_y, Y)$ can be calculated from the equation:

$$\mathbf{Rl}_x(\varphi_y, Y) = \begin{bmatrix} \cos \varphi_y & 0 & -\sin \varphi_y & a_x \cdot \cos \varphi_y \\ 0 & 1 & 0 & 0 \\ \sin \varphi_y & 0 & \cos \varphi_y & a_x \cdot \sin \varphi_y \\ 0 & 0 & 0 & 1 \end{bmatrix} \quad (\text{B.31})$$

While rotation remains about the Y_1 -axis, the translation can be performed not along the X_1 -axis but along the Z_1 -axis instead. For rolling of this kind the operator of rolling is equal:

$$\mathbf{Rl}_z(\varphi_y, Y) = \begin{bmatrix} \cos \varphi_y & 0 & -\sin \varphi_y & -a_z \cdot \sin \varphi_y \\ 0 & 1 & 0 & 0 \\ \sin \varphi_y & 0 & \cos \varphi_y & a_z \cdot \cos \varphi_y \\ 0 & 0 & 0 & 1 \end{bmatrix} \quad (\text{B.32})$$

For the cases when the rotation is performed about the X_1 -axis, the corresponding operators of rolling are as follows:

$$\mathbf{Rl}_y(\varphi_x, X) = \begin{bmatrix} 1 & 0 & 0 & 0 \\ 0 & \cos \varphi_x & \sin \varphi_x & a_y \cdot \cos \varphi_x \\ 0 & -\sin \varphi_x & \cos \varphi_x & -a_y \cdot \sin \varphi_x \\ 0 & 0 & 0 & 1 \end{bmatrix} \quad (\text{B.33})$$

for the case of rolling along the Y_1 -axis, and

$$\mathbf{Rl}_z(\varphi_x, X) = \begin{bmatrix} 1 & 0 & 0 & 0 \\ 0 & \cos \varphi_x & \sin \varphi_x & a_z \cdot \sin \varphi_x \\ 0 & -\sin \varphi_x & \cos \varphi_x & a_z \cdot \cos \varphi_x \\ 0 & 0 & 0 & 1 \end{bmatrix} \quad (\text{B.34})$$

for the case of rolling along the Z_1 -axis.

Similar expressions can be derived for the case of rotation about the Z_1 -axis:

$$\mathbf{Rl}_x(\varphi_z, Z) = \begin{bmatrix} \cos \varphi_z & \sin \varphi_z & 0 & a_x \cdot \cos \varphi_z \\ -\sin \varphi_z & \cos \varphi_z & 0 & a_x \cdot \sin \varphi_z \\ 0 & 0 & 1 & 0 \\ 0 & 0 & 0 & 1 \end{bmatrix} \quad (\text{B.35})$$

$$\mathbf{Rl}_y(\varphi_z, Z) = \begin{bmatrix} \cos \varphi_z & \sin \varphi_z & 0 & a_y \cdot \sin \varphi_z \\ -\sin \varphi_z & \cos \varphi_z & 0 & a_y \cdot \cos \varphi_z \\ 0 & 0 & 1 & 0 \\ 0 & 0 & 0 & 1 \end{bmatrix} \quad (\text{B.36})$$

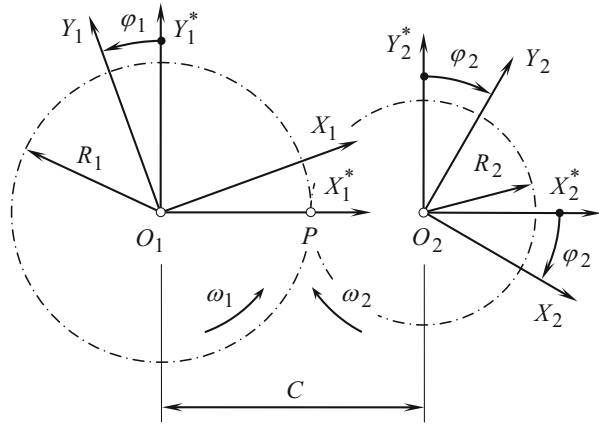
Use of the operators of rolling Eq. (B.31) through Eq. (B.36) significantly simplifies analytical description of the coordinate system transformations.

Linear Transformation Describing Rolling of Two Coordinate Systems

In the theory of part surface generation, combinations of two rotations about parallel axes are of particular interest.

As an example, consider two “*Cartesian*” coordinate systems $X_1Y_1Z_1$ and $X_2Y_2Z_2$ shown in Fig. B.10. The coordinate systems $X_1Y_1Z_1$ and $X_2Y_2Z_2$ are rotated about their axes Z_1 and Z_2 . The axes of the rotations are parallel to each other ($Z_1 \parallel Z_2$). The rotations ω_1 and ω_2 of the coordinate systems can be interpreted so that a circle of a certain radius R_1 that is associated with the coordinate system $X_1Y_1Z_1$ is rolling with no sliding over a circle of the corresponding radius R_2 that is associated with the coordinate system $X_2Y_2Z_2$. When the center-distance C is known, then radii, R_1 and R_2 , of the circles (i.e., of centrodes) can be expressed in terms of the center-distance, C , and of the given rotations, ω_1 and ω_2 . For the calculations, the following formulae:

Fig. B.10 On derivation of the operator of rolling, $\mathbf{Rr}_u(\varphi_1, Z_1)$, of two coordinate systems



$$R_1 = C \cdot \frac{1}{1 + u} \tag{B.37}$$

$$R_2 = C \cdot \frac{u}{1 + u} \tag{B.38}$$

can be used. Here, the ratio ω_1/ω_2 is denoted by u .

In the initial configuration, the X_1 and X_2 -axes align to each other. The Y_1 - and Y_2 -axes are parallel to each other. As shown in Fig. B.10, the initial configuration of the coordinate systems $X_1Y_1Z_1$ and $X_2Y_2Z_2$ is labeled as $X_1^*Y_1^*Z_1^*$ and $X_2^*Y_2^*Z_2^*$.

When the coordinate system $X_1Y_1Z_1$ turns through a certain angle φ_1 , then the coordinate system $X_2Y_2Z_2$ turns through the corresponding angle φ_2 . When the angle φ_1 is known, then the corresponding angle φ_2 is equal to $\varphi_2 = \varphi_1/u$.

Transition from the coordinate system $X_2Y_2Z_2$ to the coordinate system $X_1Y_1Z_1$ can be analytically described by the operator of the resultant coordinate system transformation $\mathbf{Rs}(1 \mapsto 2)$. In the case under consideration, the operator $\mathbf{Rs}(1 \mapsto 2)$ can be expressed in terms of the operators of the elementary coordinate system transformations:

$$\mathbf{Rs}(1 \mapsto 2) = \mathbf{Rt}(\varphi_1, Z_1) \cdot \mathbf{Rt}(\varphi_1/u, Z_1) \cdot \mathbf{Tr}(-C, X_1) \tag{B.39}$$

Other equivalent combinations of the operators of elementary coordinate system transformations can result in that same operator $\mathbf{Rs}(1 \mapsto 2)$ of the resultant coordinate system transformation. The interested reader may wish to exercise on his or her own deriving the equivalent expressions for the operator $\mathbf{Rs}(1 \mapsto 2)$.

The operators of the resultant coordinate system transformations of the kind [see Eq. (B.39)] are referred to as the “*operators of rolling motion over a cylinder.*”

When rotations are performed around the Z_1 - and the Z_2 -axis, the operator of rolling motion over a cylinder is designated as $\mathbf{Rr}_u(\varphi_1, Z_1)$. In this particular case the equality $\mathbf{Rr}_u(\varphi_1, Z_1) = \mathbf{Rs}(1 \mapsto 2)$ [see Eq. (B.39)] is valid. Based on this

equality, the operator of rolling $\mathbf{Rr}_u(\varphi_1, Z_1)$ over a cylinder can be calculated from the equation:

$$\mathbf{Rr}_u(\varphi_1, Z_1) = \begin{bmatrix} \cos\left(\varphi_1 \cdot \frac{u+1}{u}\right) & \sin\left(\varphi_1 \cdot \frac{u+1}{u}\right) & 0 & -C \\ -\sin\left(\varphi_1 \cdot \frac{u+1}{u}\right) & \cos\left(\varphi_1 \cdot \frac{u+1}{u}\right) & 0 & 0 \\ 0 & 0 & 1 & 0 \\ 0 & 0 & 0 & 1 \end{bmatrix} \quad (\text{B.40})$$

is derived.

For the inverse transformation, the inverse operator of rolling of two coordinate systems $\mathbf{Rr}_u(\varphi_2, Z_2)$ can be used. It is equal to $\mathbf{Rr}_u(\varphi_2, Z_2) = \mathbf{Rr}_u^{-1}(\varphi_1, Z_1)$. In terms of the operators of the elementary coordinate system transformations, the operator $\mathbf{Rr}_u(\varphi_2, Z_2)$ can be expressed as follows:

$$\mathbf{Rr}_u(\varphi_2, Z_2) = \mathbf{Rt}(\varphi_1/u, Z_2) \cdot \mathbf{Rt}(\varphi_1, Z_2) \cdot \mathbf{Tr}(C, X_1) \quad (\text{B.41})$$

Other equivalent combinations of the operators of elementary coordinate system transformations can result in that same operator $\mathbf{Rr}_u(\varphi_2, Z_2)$ of the resultant coordinate system transformation. The interested reader may wish to exercise on his or her own deriving the equivalent expressions for the operator $\mathbf{Rr}_u(\varphi_2, Z_2)$.

For the calculation of the operator of rolling of two coordinate systems $\mathbf{Rr}_u(\varphi_2, Z_2)$, the equation:

$$\mathbf{Rr}_u(\varphi_2, Z_2) = \begin{bmatrix} \cos\left(\varphi_1 \cdot \frac{u+1}{u}\right) & -\sin\left(\varphi_1 \cdot \frac{u+1}{u}\right) & 0 & C \\ \sin\left(\varphi_1 \cdot \frac{u+1}{u}\right) & \cos\left(\varphi_1 \cdot \frac{u+1}{u}\right) & 0 & 0 \\ 0 & 0 & 1 & 0 \\ 0 & 0 & 0 & 1 \end{bmatrix} \quad (\text{B.42})$$

can be used.

Similar to that the expression [see Eq. (B.40)] is derived for the calculation of the operator of rolling $\mathbf{Rr}_u(\varphi_1, Z_1)$ around the Z_1 - and Z_2 -axis; the corresponding formulae can be derived for the calculation of the operators of rolling $\mathbf{Rr}_u(\varphi_1, X_1)$ and $\mathbf{Rr}_u(\varphi_1, Y_1)$ about parallel axes X_1 and X_2 , as well as about parallel axes Y_1 and Y_2 .

Use of the operators of rolling about two axes $\mathbf{Rr}_u(\varphi_1, X_1)$, $\mathbf{Rr}_u(\varphi_1, Y_1)$, and $\mathbf{Rr}_u(\varphi_1, Z_1)$ substantially simplifies analytical description of the coordinate system transformations.

Coupled Linear Transformation

It is right point to notice here that a translation, $\mathbf{Tr}(a_x, X)$, along the X -axis of a “Cartesian” reference system, XYZ , and a rotation, $\mathbf{Rt}(\varphi_x, X)$, about the axis X of that same coordinate system, XYZ , obey the commutative law, that is, these two coordinate system transformations can be performed in different orders equally. It makes no difference whether the translation, $\mathbf{Tr}(a_x, X)$, is initially performed, which is followed by the rotation, $\mathbf{Rt}(\varphi_x, X)$, or the rotation, $\mathbf{Rt}(\varphi_x, X)$, is initially performed, which is followed by the translation, $\mathbf{Tr}(a_x, X)$. This is because the dot products $\mathbf{Rt}(\varphi_x, X) \cdot \mathbf{Tr}(a_x, X)$ and $\mathbf{Tr}(a_x, X) \cdot \mathbf{Rt}(\varphi_x, X)$ are identical to one another:

$$\mathbf{Rt}(\varphi_x, X) \cdot \mathbf{Tr}(a_x, X) \equiv \mathbf{Tr}(a_x, X) \cdot \mathbf{Rt}(\varphi_x, X) \tag{B.43}$$

This means that the translation from the coordinate system $X_1Y_1Z_1$ to the intermediate coordinate system $X^*Y^*Z^*$ followed by the rotation from the coordinate system $X^*Y^*Z^*$ to the finale coordinate system $X_2Y_2Z_2$ produces that same reference $X_2Y_2Z_2$ as in a case when the rotation from the coordinate system $X_1Y_1Z_1$ to the intermediate coordinate system $X^*Y^*Z^*$ followed by the translation from the coordinate system $X^*Y^*Z^*$ to the finale coordinate system $X_2Y_2Z_2$.

The validity of Eq. (B.43) is illustrated in Fig. B.11. The translation, $\mathbf{Tr}(a_x, X)$, that is followed by the rotation, $\mathbf{Rt}(\varphi_x, X)$, as shown in Fig. B.11a, is equivalent to the rotation, $\mathbf{Rt}(\varphi_x, X)$, that is followed by the translation, $\mathbf{Tr}(a_x, X)$ as shown in Fig. B.11b.

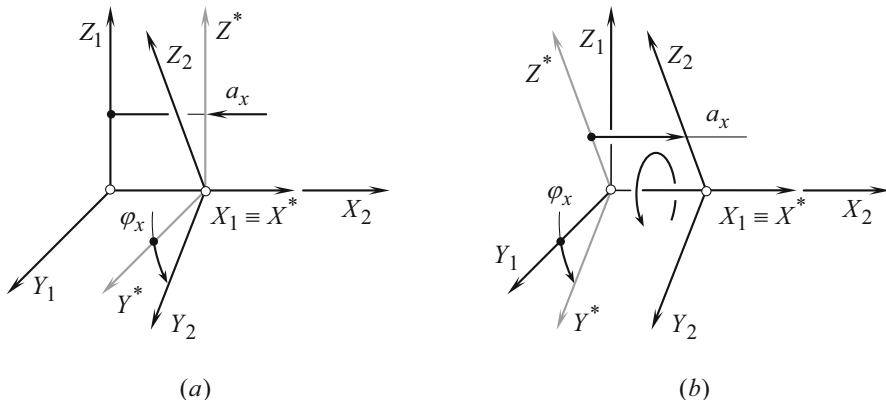


Fig. B.11 On the equivalency of the linear transformations, $\mathbf{Rt}(\varphi_x, X) \cdot \mathbf{Tr}(a_x, X)$ and $\mathbf{Tr}(a_x, X) \cdot \mathbf{Rt}(\varphi_x, X)$, in the operator, $\mathbf{Cp}_x(a_x, \varphi_x)$, of coupled linear transformation of a “Cartesian” reference system XYZ

Therefore, the two linear transformations, $\mathbf{Tr}(a_x, X)$ and $\mathbf{Rt}(\varphi_x, X)$, can be coupled into a linear transformation:

$$\mathbf{Cp}_x(a_x, \varphi_x) = \mathbf{Rt}(\varphi_x, X) \cdot \mathbf{Tr}(a_x, X) \equiv \mathbf{Tr}(a_x, X) \cdot \mathbf{Rt}(\varphi_x, X) \quad (\text{B.44})$$

The operator of linear transformation, $\mathbf{Cp}_x(a_x, \varphi_x)$, can be expressed in matrix form (see Fig. B.12a):

$$\mathbf{Cp}_x(a_x, \varphi_x) = \begin{bmatrix} 1 & 0 & 0 & a_x \\ 0 & \cos \varphi_x & \sin \varphi_x & 0 \\ 0 & -\sin \varphi_x & \cos \varphi_x & 0 \\ 0 & 0 & 0 & 1 \end{bmatrix} \quad (\text{B.45})$$

This expression is composed based on Eq. (B.4) for the linear transformation $\mathbf{Tr}(a_x, X)$ and on Eq. (B.10) that describes the linear transformation $\mathbf{Rt}(\varphi_x, X)$.

Two reduced cases of operator of the linear transformation, $\mathbf{Cp}_x(a_x, \varphi_x)$, are distinguished.

First, it could happen that in a particular case the component, a_x , of the translation is zero, that is, $a_x = 0$. Under such a scenario the operator of linear transformation, $\mathbf{Cp}_x(a_x, \varphi_x)$, reduces to the operator of rotation, $\mathbf{Rt}(\varphi_x, X)$, and the equality $\mathbf{Cp}_x(a_x, \varphi_x) = \mathbf{Rt}(\varphi_x, X)$ is observed in the case under consideration.

Second, it could happen that in a particular case the component, φ_x , of the rotation is zero, that is, $\varphi_x = 0^\circ$. Under such a scenario the operator of linear transformation, $\mathbf{Cp}_x(a_x, \varphi_x)$, reduces to the operator of translation, $\mathbf{Tr}(a_x, X)$, and the equality $\mathbf{Cp}_x(a_x, \varphi_x) = \mathbf{Tr}(a_x, X)$ is observed in the case under consideration.

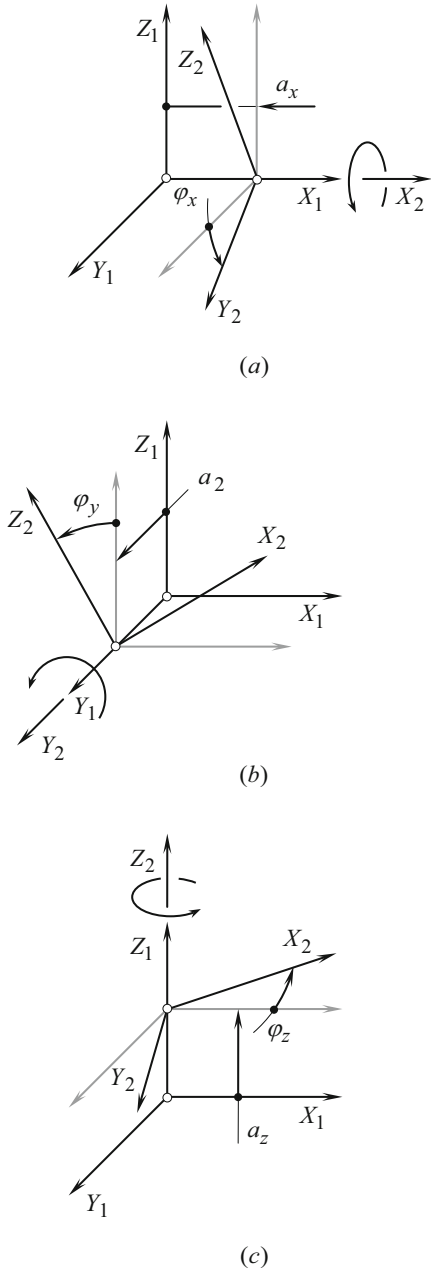
The said is valid with respect to the translations and the rotations along and about the axes Y and Z of a “*Cartesian*” reference system XYZ . The corresponding coupled operators, $\mathbf{Cp}_y(a_y, \varphi_y)$ and $\mathbf{Cp}_z(a_z, \varphi_z)$, for linear transformations of these kinds can also be composed (see Fig. B.12b, c):

$$\mathbf{Cp}_y(a_y, \varphi_y) = \begin{bmatrix} \cos \varphi_y & 0 & \sin \varphi_y & 0 \\ 0 & 1 & 0 & a_y \\ -\sin \varphi_y & 0 & \cos \varphi_y & 0 \\ 0 & 0 & 0 & 1 \end{bmatrix} \quad (\text{B.46})$$

$$\mathbf{Cp}_z(a_z, \varphi_z) = \begin{bmatrix} \cos \varphi_z & \sin \varphi_z & 0 & 0 \\ -\sin \varphi_z & \cos \varphi_z & 0 & 0 \\ 0 & 0 & 1 & a_z \\ 0 & 0 & 0 & 1 \end{bmatrix} \quad (\text{B.47})$$

In the operators of linear transformations, $\mathbf{Cp}_x(a_x, \varphi_x)$, $\mathbf{Cp}_y(a_y, \varphi_y)$, and $\mathbf{Cp}_z(a_z, \varphi_z)$, values of the translations a_x , a_y , and a_z , as well as values of the rotations φ_x , φ_y , and φ_z , are finite values (and not continuous). The linear and

Fig. B.12 Analytical description of the operators $\mathbf{Cp}_x(a_x, \varphi_x)$, $\mathbf{Cp}_y(a_y, \varphi_y)$, and $\mathbf{Cp}_z(a_z, \varphi_z)$, of linear transformation of a “Cartesian” reference system XYZ



angular displacements do not correlate to one another in time; thus, they are not screws. They are just a kind of couples of a translation along and a rotation about a coordinate axis of a “Cartesian” reference system.

Introduction of the operators of linear transformation, $\mathbf{Cp}_x(a_x, \varphi_x)$, $\mathbf{Cp}_y(a_y, \varphi_y)$, and $\mathbf{Cp}_z(a_z, \varphi_z)$, makes the linear transformations easier as all the operators of the linear transformations become uniform.

The operators of linear transformation $\mathbf{Cp}_x(a_x, \varphi_x)$, $\mathbf{Cp}_y(a_y, \varphi_y)$, and $\mathbf{Cp}_z(a_z, \varphi_z)$, do not obey the commutative law. This is because rotations are not vectors by nature. Therefore, special care should be undertaken when treating rotations as vectors – when implementing coupled operators of linear transformations in particular.

The operators of coupled linear transformations $\mathbf{Cp}_x(a_x, \varphi_x)$, $\mathbf{Cp}_y(a_y, \varphi_y)$, and $\mathbf{Cp}_z(a_z, \varphi_z)$ [see Eq. (B.45) through Eq. (B.47)] can be used for the purpose of analytical description of a resultant coordinate system transformation. Under such the scenario, the operator, $\mathbf{Rs}(1 \mapsto t)$, of a resultant coordinate system transformation can be expressed in terms of all the operators $\mathbf{Cp}_x(a_x, \varphi_x)$, $\mathbf{Cp}_y(a_y, \varphi_y)$, and $\mathbf{Cp}_z(a_z, \varphi_z)$ by the following expression:

$$\mathbf{Rs}(1 \mapsto t) = \prod_{\substack{i=1 \\ j=x,y,z}}^{t-1} \mathbf{Cp}_j^i(a_j^i, \varphi_j^i) \quad (\text{B.48})$$

In Eq. (B.48), only operators of coupled linear transformations are used.

An Example of Non-orthogonal Linear Transformation

Consider a non-orthogonal reference system $X_1Y_1Z_1$ having certain angle ω_1 between the axes X_1 and Y_1 . Axis Z_1 is perpendicular to the coordinate plane X_1Y_1 . Another reference system $X_2Y_2Z_2$ is identical to the first coordinate system $X_1Y_1Z_1$, and is turned about Z_1 -axis through a certain angle φ . Transition from the reference system $X_1Y_1Z_1$ to the reference system $X_2Y_2Z_2$ can be analytically described by the operator of linear transformation:

$$\mathbf{Rt}_\omega(1 \rightarrow 2) = \begin{bmatrix} \frac{\sin(\omega_1 + \varphi)}{\sin \omega_1} & \frac{\sin \varphi}{\sin \omega_1} & 0 & 0 \\ -\frac{\sin \varphi}{\sin \omega_1} & \frac{\sin(\omega_1 - \varphi)}{\sin \omega_1} & 0 & 0 \\ 0 & 0 & 1 & 0 \\ 0 & 0 & 0 & 1 \end{bmatrix} \quad (\text{B.49})$$

In order to distinguish the operator of rotation in the orthogonal linear transformation $\mathbf{Rt}(1 \rightarrow 2)$ from the similar operator of rotation in a non-orthogonal linear transformation $\mathbf{Rt}_\omega(1 \rightarrow 2)$, the subscript “ ω ” is assigned to the last.

When $\omega = 90^\circ$, Eq. (B.49) casts into Eq. (B.12).

Conversion of a Coordinate System Hand

Application of matrix method of coordinate system transformation presumes that both of the reference systems “ i ” and “ $(i \pm 1)$ ” are of the same hand. This means that it assumed from the very beginning that both of them are either right-hand- or left-hand-oriented “*Cartesian*” coordinate systems. In the event the coordinate systems i and $(i \pm 1)$ are of opposite hand, say one of them is the right-hand-oriented coordinate system while another one is left-hand-oriented coordinate system, then one of the coordinate systems must be converted into the oppositely oriented “*Cartesian*” coordinate system.

For the conversion of a left-hand-oriented “*Cartesian*” coordinate system into a right-hand-oriented coordinate system or vice versa, the operators of reflection are commonly used.

In order to change the direction of X_i axis of the initial coordinate system i to the opposite direction (in this case in the new coordinate system $(i \pm 1)$ the equalities $X_{i \pm 1} = -X_i$, $Y_{i \pm 1} \equiv Y_i$ and $Z_{i \pm 1} \equiv Z_i$ are observed) the operator of reflection $\mathbf{Rf}_x(Y_i Z_i)$ can be applied. The operator of reflection yields representation in matrix form:

$$\mathbf{Rf}_x(Y_i Z_i) = \begin{bmatrix} -1 & 0 & 0 & 0 \\ 0 & 1 & 0 & 0 \\ 0 & 0 & 1 & 0 \\ 0 & 0 & 0 & 1 \end{bmatrix} \quad (\text{B.50})$$

Similarly, implementation of the operators of reflections $\mathbf{Rf}_y(X_i Z_i)$ and $\mathbf{Rf}_z(X_i Y_i)$ change the directions of Y_i and Z_i axes onto opposite directions. The operators of reflections $\mathbf{Rf}_y(X_i Z_i)$ and $\mathbf{Rf}_z(X_i Y_i)$ can be expressed analytically in the form:

$$\mathbf{Rf}_y(X_i Z_i) = \begin{bmatrix} 1 & 0 & 0 & 0 \\ 0 & -1 & 0 & 0 \\ 0 & 0 & 1 & 0 \\ 0 & 0 & 0 & 1 \end{bmatrix} \quad (\text{B.51})$$

$$\mathbf{Rf}_z(X_i Y_i) = \begin{bmatrix} 1 & 0 & 0 & 0 \\ 0 & 1 & 0 & 0 \\ 0 & 0 & -1 & 0 \\ 0 & 0 & 0 & 1 \end{bmatrix} \quad (\text{B.52})$$

A linear transformation that reverses direction of the coordinate axis is an “*opposite transformation*.” Transformation of reflection is an example of “*orientation-reversing transformation*.”

Useful Equations

The sequence of the successive rotations can vary depending on the intention of the researcher. Several special types of successive rotations are known, including “*Eulerian transformation*,” “*Cardanian transformation*,” and two kinds of “*Euler-Krylov transformations*.” The sequence of the successive rotations can be chosen from a total of 12 different combinations. Even though the “*Cardanian transformation*” is different from the “*Eulerian transformation*” in terms of the combination of the rotations, they both use a similar approach to calculate the orientation angles.

RPY-Transformation

series of rotations can be performed in the order “*roll matrix, (R)*,” by “*pitch matrix (P)*,” and finally by “*yaw matrix, (Y)*.” The linear transformation of this kind is commonly referred to as “*RPY-transformation*.” The resultant transformation of this kind can be represented by the homogenous coordinate transformation matrix:

$$\mathbf{RPY}(\varphi_x, \varphi_y, \varphi_z) = \begin{bmatrix} \cos \varphi_y \cos \varphi_z + \sin \varphi_x \sin \varphi_y \sin \varphi_z & \cos \varphi_y \sin \varphi_z - \sin \varphi_x \sin \varphi_y \cos \varphi_z & \cos \varphi_x \sin \varphi_y & 0 \\ -\cos \varphi_x \sin \varphi_z & \cos \varphi_x \cos \varphi_z & \sin \varphi_x & 0 \\ \sin \varphi_x \cos \varphi_y \sin \varphi_z - \sin \varphi_y \cos \varphi_z & -\sin \varphi_x \cos \varphi_y \cos \varphi_z - \cos \varphi_y \sin \varphi_z & \cos \varphi_x \cos \varphi_y & 0 \\ 0 & 0 & 0 & 1 \end{bmatrix} \quad (\text{B.53})$$

The “*RPY-transformation*” can be used for solving problems in the field of part surface generation.

Operator of Rotation about an Axis in Space

A spatial rotation operator for the rotational transformation of a point about a unit axis $\mathbf{a}_0(\cos \alpha, \cos \beta, \cos \gamma)$ passing through the origin of the coordinate system can be described as follows, with $\mathbf{a}_0 = \mathbf{A}_0 / |\mathbf{A}_0|$ designating the unit vector along the axis of rotation \mathbf{A}_0 .

Suppose the angle of rotation of the point about \mathbf{a}_0 is θ , the “*rotation operator*” is expressed by:

$$\mathbf{Rt}(\theta, \mathbf{a}_0) = \begin{bmatrix} (1 - \cos \theta) \cos^2 \alpha + \cos \theta & (1 - \cos \theta) \cos \alpha \cos \beta - \sin \theta \cos \gamma \\ (1 - \cos \theta) \cos \alpha \cos \beta + \sin \theta \cos \gamma & (1 - \cos \theta) \cos^2 \beta + \cos \theta \\ (1 - \cos \theta) \cos \alpha \cos \gamma - \sin \theta \cos \beta & (1 - \cos \theta) \cos \beta \cos \gamma + \sin \theta \cos \alpha \\ 0 & 0 \end{bmatrix} \quad (\text{B.54})$$

$$\begin{bmatrix} (1 - \cos \theta) \cos \alpha \cos \gamma + \sin \theta \cos \beta & 0 \\ (1 - \cos \theta) \cos \beta \cos \gamma - \sin \theta \cos \alpha & 0 \\ (1 - \cos \theta) \cos^2 \gamma + \cos \theta & 0 \\ 0 & 1 \end{bmatrix}$$

Solution to a problem in the field of part surface generation can be significantly simplified by implementation of the rotational operator $\mathbf{Rt}(\theta, \mathbf{a}_0)$ [see Eq. (B.54)].

Combined Linear Transformation

Suppose a point, p , on a rigid body rotates with an angular displacement, θ , about an axis along a unit vector, \mathbf{a}_0 , passing through the origin of the coordinate system at first, and then followed by a translation at a distance, B , in the direction of a unit vector, \mathbf{b} . The linear transformation of this kind can be analytically described by the homogenous matrix:

$$\mathbf{Rt}(\theta_{\mathbf{a}_0}, B_{\mathbf{b}}) = \begin{bmatrix} (1 - \cos \theta) \cos^2 \alpha + \cos \theta & (1 - \cos \theta) \cos \alpha \cos \beta - \sin \theta \cos \gamma \\ (1 - \cos \theta) \cos \alpha \cos \beta + \sin \theta \cos \gamma & (1 - \cos \theta) \cos^2 \beta + \cos \theta \\ (1 - \cos \theta) \cos \alpha \cos \gamma - \sin \theta \cos \beta & (1 - \cos \theta) \cos \beta \cos \gamma + \sin \theta \cos \alpha \\ 0 & 0 \end{bmatrix} \quad (\text{B.55})$$

$$\begin{bmatrix} (1 - \cos \theta) \cos \alpha \cos \gamma + \sin \theta \cos \beta & B \cos \alpha \\ (1 - \cos \theta) \cos \beta \cos \gamma - \sin \theta \cos \alpha & B \cos \beta \\ (1 - \cos \theta) \cos^2 \gamma + \cos \theta & B \cos \gamma \\ 0 & 1 \end{bmatrix}$$

More operators of particular linear transformations can be found out in the literature.

Chains of Consequent Linear Transformations and a Closed Loop of Consequent Coordinate Systems Transformations

Consequent coordinate system transformations form chains (circuits) of linear transformations. The elementary chain of coordinate system transformation is composed of two consequent transformations. Chains of linear transformations play an important role in the theory of part surface generation.

Two different kinds of chains of consequent coordinate system transformations are distinguished.

First, transition from the coordinate system $X_g Y_g Z_g$ associated with the gear tooth flank, \mathcal{G} , to the local “*Cartesian*” coordinate system $x_g y_g z_g$ having the origin at a point, K , of contact of the gear tooth flank, \mathcal{G} , and of the pinion tooth flank, \mathcal{P} . This linear transformation is also made up of numerous operators of intermediate coordinate system transformations ($X_{in} Y_{in} Z_{in}$). It forms a chain of direct consequent coordinate system transformations illustrated in Fig. B.13a.

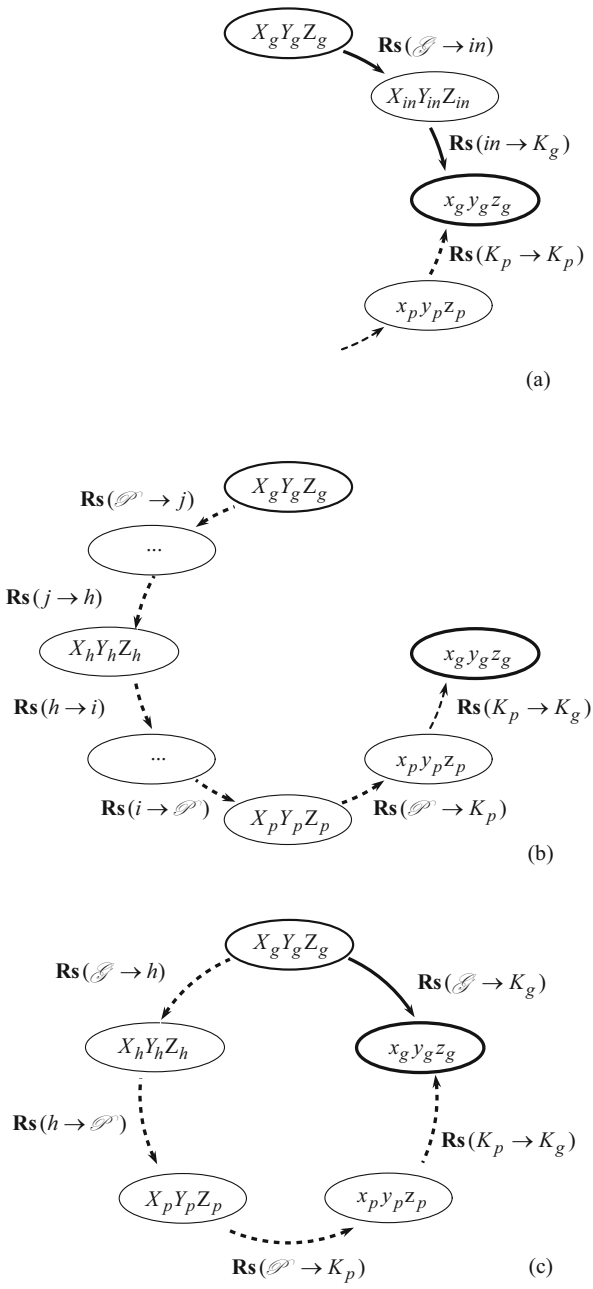
The local coordinate system, $x_g y_g z_g$, is associated with the gear tooth flank, \mathcal{G} . The operator $\mathbf{Rs}(\mathcal{G} \rightarrow K_g)$ of the resultant coordinate system transformation for a direct chain of the linear transformations can be composed using for this purpose a certain number of the operators of translations [see Eq. (B.4) through Eq. (B.6)] and a corresponding number of the operators of rotations [see Eq. (B.10) through Eq. (B.12)].

Second, transition from the coordinate system, $X_g Y_g Z_g$, to the local “*Cartesian*” coordinate system, $x_p y_p z_p$, with the origin at a point K of contact of the tooth flanks, \mathcal{G} and \mathcal{P} . The local coordinate system, $x_p y_p z_p$, is associated to pinion tooth flank, \mathcal{P} . This linear transformation is also made up of numerous intermediate coordinate system transformations ($X_j Y_j Z_j$), for example, transitions from the coordinate system $X_h Y_h Z_h$ associated with gear housing, to numerous intermediate coordinate system $X_i Y_i Z_i$. The linear transformation of this kind forms a chain of inverse consequent coordinate system transformations shown in Fig. B.13b. The operator $\mathbf{Rs}(\mathcal{G} \rightarrow K_p)$ of the resultant coordinate system transformations for the inverse chain of transformations can be composed using for this purpose a certain number of the operators of translations [see Eq. (B.4), Eq. (B.5), and Eq. (B.6)] and a corresponding number of the operators of rotations [see Eq. (B.10) through Eq. (B.12)].

Chains of the direct and of the reverse consequent coordinate system transformations together with the operator of transition from the local coordinate system, $x_p y_p z_p$, to the local coordinate system, $x_g y_g z_g$, form a closed loop (a closed circuit) of the consequent coordinate system transformations depicted in Fig. B.13c.

If a closed loop of the consequent coordinate system transformations is complete, the implementation of a certain number of the operators of translations [see Eq. (B.4), Eq. (B.5), and Eq. (B.6)] and a corresponding number of the operators of rotations [see Eq. (B.10) through Eq. (B.12)] returns a result that is identical to the input data. This means that the analytical description of a meshing process specified in the original coordinate system remains the same after implementation of the

Fig. B.13 An example of direct chain (a), of reverse chain (b), and a closed loop (c) of consequent coordinate system transformations



operator of the resultant coordinate system transformations. This condition is the necessary and sufficient condition for existence of a closed loop of consequent coordinate system transformations.

Implementation of the chains, as well as of the closed loops of consequent coordinate system transformations, makes it possible to consider the meshing process of the teeth flanks, \mathcal{G} and \mathcal{P} , in any and all of the reference systems that make up the loop. Therefore, for consideration of a particular problem of part surface generation, the most convenient reference system can be chosen.

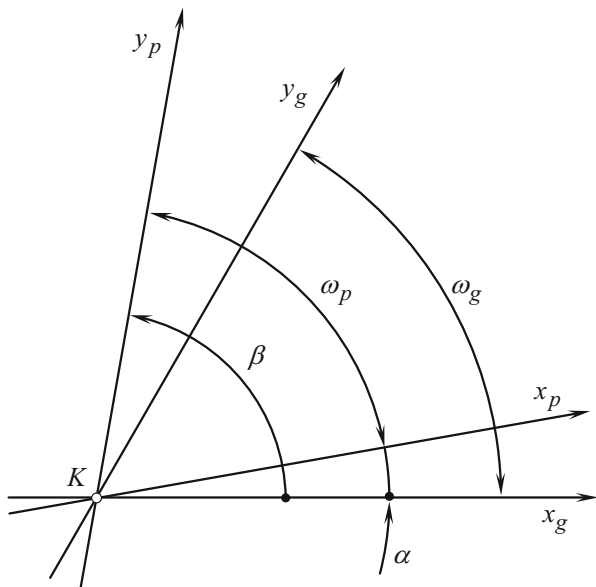
In order to complete the construction of a closed loop of a consequent coordinate system transformations, an operator of transformation from the local coordinate system, $x_p y_p z_p$, to the local coordinate system, $x_g y_g z_g$, must be composed. Usually, the local reference systems, $x_g y_g z_g$ and $x_p y_p z_p$, are the kind of semi-orthogonal coordinate systems. This means that the axis, z_p , is always orthogonal to the coordinate plane, $x_g y_g$, while the axes, x_g and y_g , can be either orthogonal or not orthogonal to each other. The same is valid with respect to the local coordinate system, $x_p y_p z_p$.

Two possible ways for performing the required transformation of the local reference systems, $x_g y_g z_g$ and $x_p y_p z_p$, are considered below.

Following the first way, the operator $\mathbf{Rt}_\omega(p \rightarrow g)$ of the linear transformation of semi-orthogonal coordinate systems (see Fig. B.14) must be composed. The operator $\mathbf{Rt}_\omega(p \rightarrow g)$ can be represented in the form of the homogenous matrix:

$$\mathbf{Rt}_\omega(p \rightarrow g) = \begin{bmatrix} \frac{\sin(\omega_p + \alpha)}{\sin \omega_p} & -\frac{\sin(\omega_g - \omega_p - \alpha)}{\sin \omega_p} & 0 & 0 \\ -\frac{\sin \alpha}{\sin \omega_p} & \frac{\sin(\omega_g - \alpha)}{\sin \omega_p} & 0 & 0 \\ 0 & 0 & -1 & 0 \\ 0 & 0 & 0 & 1 \end{bmatrix} \quad (\text{B.56})$$

Fig. B.14 Local coordinate systems, $x_g y_g z_g$ and $x_p y_p z_p$, with the origin at contact point, K



Here the following are designated:

- ω_g – the angle that makes U_g and V_g coordinate lines on the gear tooth flank, \mathcal{G}
- ω_p – the angle that makes U_p and V_p coordinate lines on the pinion tooth flank, \mathcal{P}
- α – the angle that makes the axes, x_g and x_p , of the local coordinate systems $x_g y_g z_g$ and $x_p y_p z_p$

The auxiliary angle β in Fig. B.14 is equal to $\beta = \omega_T + \alpha$.

The inverse coordinate system transformation, that is, the transformation from the local coordinate system, $x_g y_g z_g$, to the local coordinate system, $x_p y_p z_p$, can be analytically described by the operator $\mathbf{Rt}_\omega(g \rightarrow p)$ of the inverse coordinate system transformation. The operator $\mathbf{Rt}_\omega(g \rightarrow p)$ can be represented in the form of the homogenous matrix:

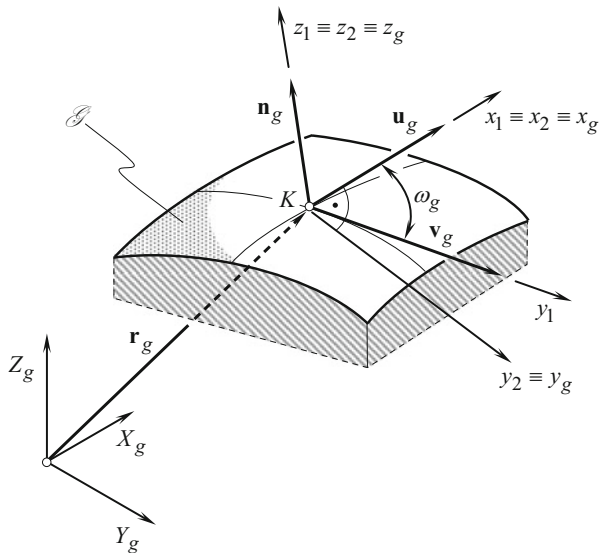
$$\mathbf{Rt}_\omega(g \rightarrow p) = \begin{bmatrix} \frac{\sin(\omega_g - \alpha)}{\sin \omega_g} & \frac{\sin(\omega_g - \omega_p - \alpha)}{\sin \omega_g} & 0 & 0 \\ \frac{\sin \alpha}{\sin \omega_g} & \frac{\sin(\omega_p + \alpha)}{\sin \omega_g} & 0 & 0 \\ 0 & 0 & -1 & 0 \\ 0 & 0 & 0 & 1 \end{bmatrix} \quad (\text{B.57})$$

Following the second way of transformation of the local coordinate systems, the auxiliary orthogonal local coordinate system must be constructed.

Let’s consider an approach, according to which a closed loop (a closed circuit) of the consequent coordinate system transformations can be composed.

In order to construct an orthogonal normalized basis of the coordinate system $x_g y_g z_g$, an intermediate coordinate system $x_1 y_1 z_1$ is used. Axis x_1 of the coordinate system $x_1 y_1 z_1$ is pointed out along the unit vector \mathbf{u}_g that is tangent to the U_g -coordinate curve (see Fig. B.15). Axis y_1 is directed along vector \mathbf{v}_g that is tangent to

Fig. B.15 Local coordinate system, $x_g y_g z_g$, associated with the gear tooth flank, \mathcal{G}



the V_g -coordinate line on the gear tooth flank, \mathcal{G} . The axis, z_1 , aligns with unit normal vector, \mathbf{n}_g , and is pointed outward the gear tooth body.

For a gear tooth flank, \mathcal{G} , having orthogonal parameterization (for which $F_g = 0$, and therefore $\omega_g = \pi/2$), analytical description of coordinate system transformations is significantly simpler. Further simplification of the coordinate system transformation is possible when the coordinate U_g - and V_g -lines are congruent to the lines of curvature on the part surface \mathcal{G} . Under such a scenario, the local coordinate system is represented by “*Darboux frame*.”

In order to construct “*Darboux frame*,” principal directions on the gear tooth flank, \mathcal{G} , must be calculated. Determination of the unit tangent vectors, $\mathbf{t}_{1.g}$ and $\mathbf{t}_{2.g}$, of the principal directions on the gear tooth flank, \mathcal{G} , is considered in Appendix A.

In the common tangent plane, orientation of the unit vector, $\mathbf{t}_{1.g}$, of the first principal direction on the gear tooth flank, \mathcal{G} , can be uniquely specified by the included angle, $\xi_{1.g}$, that the unit vector, $\mathbf{t}_{1.g}$, forms with the U_g -coordinate curve. This angle depends on both, on the gear tooth flank, \mathcal{G} , geometry, and on the gear tooth flank, \mathcal{G} , parameterization. Depicted in Fig. B.16, is the relationship between the tangent vectors \mathbf{U}_g and \mathbf{V}_g and the included angle $\xi_{1.g}$. From the Law of Sines,

$$\frac{\sqrt{G_g}}{\sin \xi_{1.g}} = \frac{\sqrt{E_g}}{\sin [\pi - \xi_{1.g} - (\pi - \omega_g)]} = \frac{\sqrt{F_g}}{\sin (\omega_g - \xi_{1.g})} \tag{B.58}$$

Here, $\omega_g = \cos^{-1}(F_g/\sqrt{E_g G_g})$.

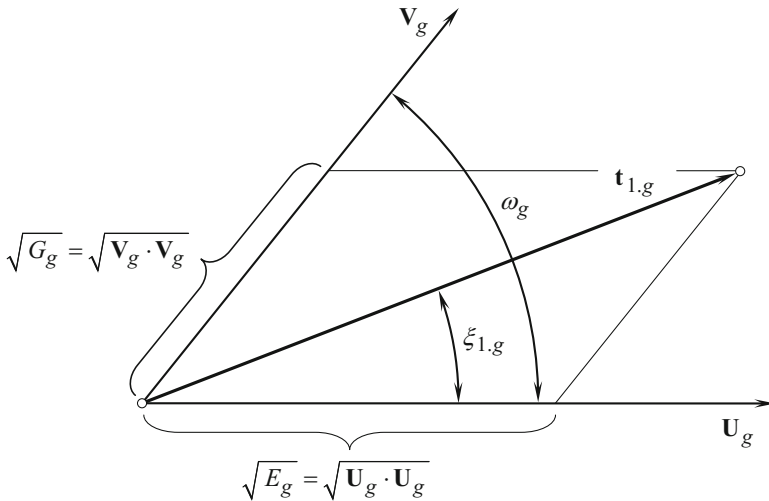


Fig. B.16 Differential relationships between the tangent vectors, \mathbf{U}_g and \mathbf{V}_g , the fundamental magnitudes of the first order, the included the angle, $\xi_{1.g}$, and the direction of the unit tangent vector, $\mathbf{t}_{1.g}$

Solving the expression above for the included angle, $\xi_{1.g}$, results in:

$$\xi_{1.g} = \tan^{-1} \frac{\sqrt{E_g G_g - F_g^2}}{E_g + F_g} \quad (\text{B.59})$$

Another possible way of constructing of orthogonal local basis of the local “*Cartesian*” coordinate system, $x_p y_p z_p$, is based on the following consideration.

Consider an arbitrary non-orthogonal and not normalized basis, $\mathbf{x}_1 \mathbf{x}_2 \mathbf{x}_3$ (see Fig. B.17a). Let’s construct an orthogonal and normalized basis based on the initial given basis, $\mathbf{x}_1 \mathbf{x}_2 \mathbf{x}_3$.

The cross product of any two of three vectors, \mathbf{x}_1 , \mathbf{x}_2 , \mathbf{x}_3 , for example, cross product of the vectors $\mathbf{x}_1 \times \mathbf{x}_2$, determines a new vector, \mathbf{x}_4 (see Fig. B.17b). Evidently, the vector, \mathbf{x}_4 , is orthogonal to the coordinate plane, $\mathbf{x}_1 \mathbf{x}_2$. Then, use the calculated vector, \mathbf{x}_4 , and one of two original vectors, \mathbf{x}_1 or \mathbf{x}_2 , for instance, use the vector, \mathbf{x}_2 . This yields a calculation of a new vector, $\mathbf{x}_5 = \mathbf{x}_4 \times \mathbf{x}_2$ (see Fig. B.17c). The calculated basis, $\mathbf{x}_1 \mathbf{x}_4 \mathbf{x}_5$, is orthogonal. In order to convert it into a normalized basis, each of the vectors, $\cos \angle (Y^{(K)}, X_n) = [\cos \angle (X^{(K)}, Y_n) \cos \angle (Z^{(K)}, Z_n) - \cos \angle (X^{(K)}, Z_n) \cos \angle (Z^{(K)}, Y_n)]$; $\cos \angle (Y^{(K)}, Y_n) = [\cos \angle (X^{(K)}, X_n) \cos \angle (Z^{(K)}, Z_n) - \cos \angle (X^{(K)}, Z_n) \cos \angle (Z^{(K)}, X_n)]$; and $\cos \angle (Y^{(K)}, Z_n) = [\cos \angle (X^{(K)}, X_n) \cos \angle (X^{(K)}, Y_n) - \cos \angle (X^{(K)}, Y_n) \cos \angle (Z^{(K)}, X_n)]$, must be divided by its magnitude:

$$\mathbf{e}_1 = \frac{\mathbf{x}_1}{|\mathbf{x}_1|} \quad (\text{B.60})$$

$$\mathbf{e}_4 = \frac{\mathbf{x}_4}{|\mathbf{x}_4|} \quad (\text{B.61})$$

$$\mathbf{e}_5 = \frac{\mathbf{x}_5}{|\mathbf{x}_5|} \quad (\text{B.62})$$

The resultant basis $\mathbf{e}_1 \mathbf{e}_4 \mathbf{e}_5$ (see Fig. B.17d) is always orthogonal, as well as it is always normalized.

In order to complete the analytical description of a closed loop of consequent coordinate system transformations, it is necessary to compose the operator \mathbf{R}_s ($K_p \rightarrow K_g$) of transformation from the local reference system, $x_p y_p z_p$, to the local reference system, $x_g y_g z_g$ (see Fig. B.13c).

In the case under consideration, the axes, z_g and z_p , align with the common unit normal vector, \mathbf{n}_g . The axis, z_g , is pointed out from the bodily side to the void side of the gear tooth flank, G . The axis, z_p , is pointed oppositely. Due to that, the following equality is observed:

$$\mathbf{R}_s (K_p \rightarrow K_g) = \mathbf{R}_t (\varphi_z, z_p) \quad (\text{B.63})$$

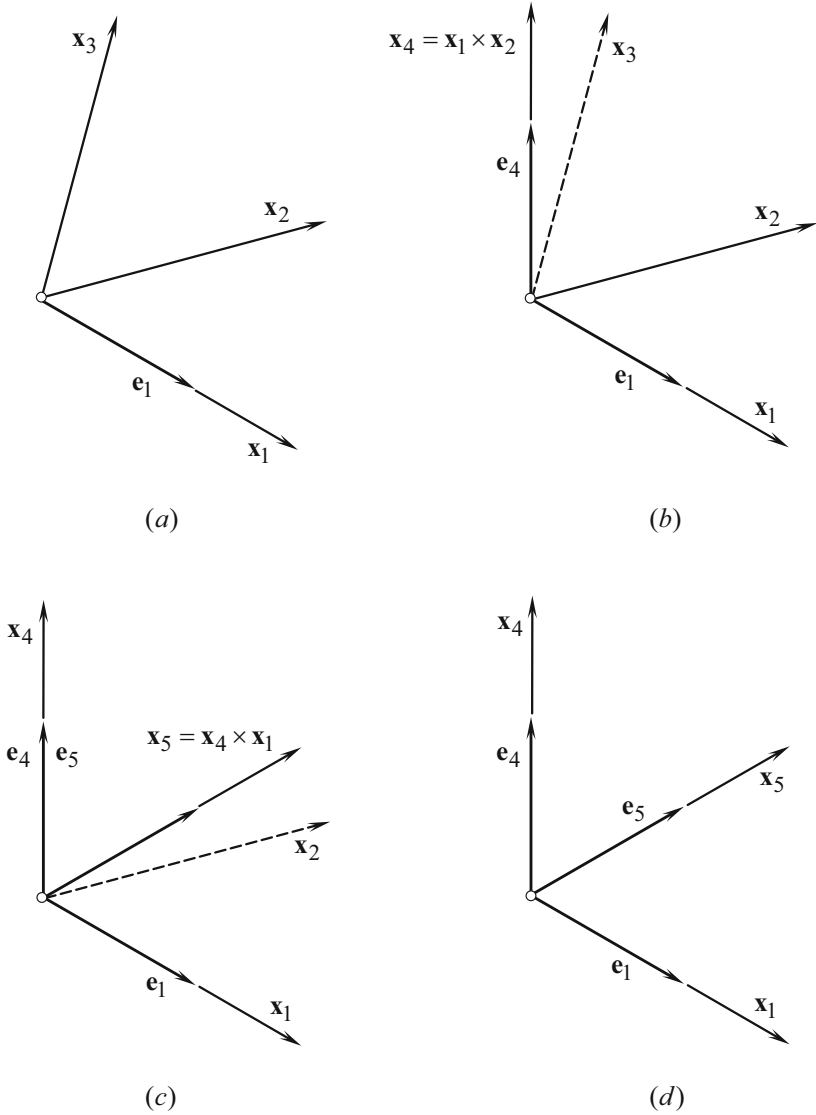


Fig. B.17 A normalized and orthogonally parameterized basis, $\mathbf{e}_1\mathbf{e}_4\mathbf{e}_5$, that is constructed from an arbitrary basis, $\mathbf{x}_1\mathbf{x}_2\mathbf{x}_3$

The inverse coordinate system transformation can be analytically described by the operator:

$$\mathbf{R}_s(K_g \rightarrow K_p) = \mathbf{R}_s^{-1}(K_p \rightarrow K_g) = \mathbf{R}_t(-\varphi_z, z_p) \quad (\text{B.64})$$

Implementation of the discussed results allows for:

- (a) Representation of the gear tooth flank, \mathcal{G} , and the pinion tooth flank, \mathcal{P} , of the form cutting tool, as well as their relative motion in a common coordinate system.
- (b) Consideration of meshing of the gear tooth flank, \mathcal{G} , in any desired coordinate systems that is a component of the chain and/or the closed loop of consequent coordinate system transformations.

Transition from one coordinate system to another coordinate system can be performed in both of two feasible directions, say in direct as well as in inverse directions.

Impact of the Coordinate Systems Transformations on Fundamental Forms of the Surface

Every coordinate system transformation results in a corresponding change to equation of the gear tooth flank, \mathcal{G} , and/or pinion tooth flank, \mathcal{P} . Because of this, it is often necessary to re-calculate coefficients of the first $\Phi_{1.g}$ and of the second $\Phi_{2.g}$ fundamental forms of the gear tooth flank, \mathcal{G} (as many times as the coordinate system transformation is performed). This routing and time-consuming operation can be eliminated if the operators of coordinate system transformations are used directly to the fundamental forms $\Phi_{1.g}$ and $\Phi_{2.g}$.

After been calculated in an initial reference system, the fundamental magnitudes $E_g, F_g,$ and G_g of the first, $\Phi_{1.g}$, and the fundamental magnitudes $L_g, M_g,$ and N_g of the second, $\Phi_{2.g}$, fundamental forms can be determined in any new coordinate system using for this purpose the operators of translation, of rotation, and of resultant coordinate system transformation. Transformation of such kind of the fundamental magnitudes, $\Phi_{1.g}$ and $\Phi_{2.g}$, becomes possible due to implementation of a formula that can be found out immediately below.

Let's consider a gear tooth flank, \mathcal{G} , that is given by equation $\mathbf{r}_g = \mathbf{r}_g(U_g, V_g)$, where $(U_g, V_g) \in \mathcal{G}$.

For the analysis below, it is convenient to use the equation of the first fundamental form, $\Phi_{1.g}$, of the gear tooth flank, \mathcal{G} , represented in matrix form:

$$[\Phi_{1.g}] = [dU_g \quad dV_g \quad 0 \quad 0] \cdot \begin{bmatrix} E_g & F_g & 0 & 0 \\ F_g & G_g & 0 & 0 \\ 0 & 0 & 1 & 0 \\ 0 & 0 & 0 & 1 \end{bmatrix} \cdot \begin{bmatrix} dU_g \\ dV_g \\ 0 \\ 0 \end{bmatrix} \quad (\text{B.65})$$

Similarly, equation of the second fundamental form $\Phi_{2,g}$ of the gear tooth flank, \mathcal{G} , can be given by:

$$[\Phi_{2,g}] = [dU_g \quad dV_g \quad 0 \quad 0] \cdot \begin{bmatrix} L_g & M_g & 0 & 0 \\ M_g & N_g & 0 & 0 \\ 0 & 0 & 1 & 0 \\ 0 & 0 & 0 & 1 \end{bmatrix} \cdot \begin{bmatrix} dU_g \\ dV_g \\ 0 \\ 0 \end{bmatrix} \quad (\text{B.66})$$

The coordinate system transformation that is performed by the operator of linear transformation $\mathbf{Rs}(1 \rightarrow 2)$ transfers the equation $\mathbf{r}_g = \mathbf{r}_g(U_g, V_g)$ of the gear tooth flank, \mathcal{G} , initially given in $X_1Y_1Z_1$, to the equation $\mathbf{r}_g^* = \mathbf{r}_g^*(U_g^*, V_g^*)$ of that same gear tooth flank, \mathcal{G} , in a new coordinate system $X_2Y_2Z_2$. It is clear that $\mathbf{r}_g \neq \mathbf{r}_g^*$.

In the new coordinate system, the gear tooth flank, \mathcal{G} , is analytically described by the following expression:

$$\mathbf{r}_g^*(U_g^*, V_g^*) = \mathbf{Rs}(1 \rightarrow 2) \cdot \mathbf{r}_g(U_g, V_g) \quad (\text{B.67})$$

The operator of resultant coordinate system transformation $\mathbf{Rs}(1 \rightarrow 2)$ casts the column matrices of variables in Eq. (B.65) and Eq. (B.66) to the form:

$$[dU_g^* \quad dV_g^* \quad 0 \quad 0]^T = \mathbf{Rs}(1 \rightarrow 2) \cdot [dU_g \quad dV_g \quad 0 \quad 0]^T. \quad (\text{B.68})$$

Substitution of Eq. (B.68) into Eq. (B.65) and Eq. (B.66) makes it possible the expressions for the fundamental forms, $\Phi_{1,g}^*$ and $\Phi_{2,g}^*$, in the new coordinate system:

$$[\Phi_{1,g}^*] = [\mathbf{Rs}(1 \rightarrow 2) \cdot [dU_g \quad dV_g \quad 0 \quad 0]^T]^T \cdot [\Phi_{1,g}] \cdot \mathbf{Rs}(1 \rightarrow 2) \cdot [dU_g \quad dV_g \quad 0 \quad 0]^T \quad (\text{B.69})$$

$$[\Phi_{2,g}^*] = [\mathbf{Rs}(1 \rightarrow 2) \cdot [dU_g \quad dV_g \quad 0 \quad 0]^T]^T \cdot [\Phi_{2,g}] \cdot \mathbf{Rs}(1 \rightarrow 2) \cdot [dU_g \quad dV_g \quad 0 \quad 0]^T \quad (\text{B.70})$$

The following equation is valid for multiplication:

$$\begin{aligned} & \left[\mathbf{Rs}(1 \rightarrow 2) \cdot [dU_g \quad dV_g \quad 0 \quad 0]^T \right]^T \\ & = \mathbf{Rs}^T(1 \rightarrow 2) \cdot [dU_g \quad dV_g \quad 0 \quad 0] \end{aligned} \quad (\text{B.71})$$

Therefore,

$$[\Phi_{1,g}^*] = [dU_g \quad dV_g \quad 0 \quad 0]^T \cdot \{ \mathbf{Rs}^T(1 \rightarrow 2) \cdot [\Phi_{1,g}] \cdot \mathbf{Rs}(1 \rightarrow 2) \} \cdot [dU_g \quad dV_g \quad 0 \quad 0] \quad (\text{B.72})$$

$$\begin{bmatrix} \Phi_{2,g}^* \end{bmatrix} = \begin{bmatrix} dU_g & dV_g & 0 & 0 \end{bmatrix}^T \cdot \{ \mathbf{R}\mathbf{s}^T(1 \rightarrow 2) \cdot \begin{bmatrix} \Phi_{2,g} \end{bmatrix} \cdot \mathbf{R}\mathbf{s}(1 \rightarrow 2) \} \cdot \begin{bmatrix} dU_g & dV_g & 0 & 0 \end{bmatrix} \quad (\text{B.73})$$

It can be easily shown that the matrices $\begin{bmatrix} \Phi_{1,g}^* \end{bmatrix}$ and $\begin{bmatrix} \Phi_{2,g}^* \end{bmatrix}$ in Eq. (B.72) and Eq. (B.73) represent quadratic forms with respect to dU_g and dV_g .

The operator of transformation $\mathbf{R}\mathbf{s}(1 \rightarrow 2)$ of the gear tooth flank, \mathcal{G} , having the first, $\Phi_{1,g}$, and the second, $\Phi_{2,g}$, fundamental forms from the initial coordinate system $X_1Y_1Z_1$ to the new coordinate system, $X_2Y_2Z_2$, results in that in the new coordinate system the corresponding fundamental forms are expressed in the form:

$$\begin{bmatrix} \Phi_{1,g}^* \end{bmatrix} = \mathbf{R}\mathbf{s}^T(1 \rightarrow 2) \cdot \begin{bmatrix} \Phi_{1,g} \end{bmatrix} \cdot \mathbf{R}\mathbf{s}(1 \rightarrow 2) \quad (\text{B.74})$$

$$\begin{bmatrix} \Phi_{2,g}^* \end{bmatrix} = \mathbf{R}\mathbf{s}^T(1 \rightarrow 2) \cdot \begin{bmatrix} \Phi_{2,g} \end{bmatrix} \cdot \mathbf{R}\mathbf{s}(1 \rightarrow 2) \quad (\text{B.75})$$

Equations (B.74) and (B.75) reveal that after the coordinate system transformation is completed, the first $\Phi_{1,g}^*$ and the second $\Phi_{2,g}^*$ fundamental forms of the gear tooth flank, \mathcal{G} , in the coordinate system $X_2Y_2Z_2$ are expressed in terms of the first, $\Phi_{1,g}$, and the second, $\Phi_{2,g}$, fundamental forms initially represented in the coordinate system $X_1Y_1Z_1$. In order to do that, the corresponding fundamental form (either the form, $\Phi_{1,g}$, or the form, $\Phi_{2,g}$) must be pre-multiplied by $\mathbf{R}\mathbf{s}(1 \rightarrow 2)$ and after that be post-multiplied by $\mathbf{R}\mathbf{s}^T(1 \rightarrow 2)$.

Implementation of Eq. (B.74) and Eq. (B.75) significantly simplifies formulae transformations.

Equations similar to those above Eq. (B.74) and Eq. (B.75) are valid with respect to pinion tooth flank, \mathcal{P} .

In case of use of the third, $\Phi_{3,g}$, and of the fourth, $\Phi_{4,g}$, fundamental forms, their coefficients can be expressed in terms of the fundamental magnitudes of the first and of the second order.

Appendix C: Contact Geometry of a Gear and a Mating Pinion' Tooth Flanks

In the theory of gearing, the kinematics of gearing is considered as the prime element of the gear pair. Other important elements of gearing are:

- (a) The shape and the geometry of the gear tooth flank, \mathcal{G} .
- (b) The shape and the geometry of the mating pinion tooth flank, \mathcal{P} (as well as numerous others).

which are considered as the secondary elements of gearing. This does not mean that the importance of the secondary elements is lower than that of the primary element. No, this is incorrect. This just means that the most favorable parameters of the secondary elements can be expressed in terms of the parameters of the prime element. Ultimately, the entire gear pair can be synthesized on the premise just of the prime element – that is, on the premise of the desirable kinematics of the gear pair. In other words, having just the desirable kinematics of the gear pair to be designed, it is possible to synthesize the rest of the design parameters of the gear pair. Only the kinematics of gearing is used for the purposes of synthesizing the best possible gear pair for transmitting the input rotation and torque.

In order to solve the problem of synthesizing the most favorable gear pair, an appropriate analytical description of contact geometry of the gear tooth flank, \mathcal{G} , and the mating pinion tooth flank, \mathcal{P} , is required. The problem of analytical description of contact geometry between two smooth regular surfaces in the first order of tangency is a sophisticated one.

Investigation of contact geometry of curves and surfaces can be traced back to the eighteenth century. In considerable detail the study of the contact of curves and surfaces has been undertaken by *J.L. Lagrange*¹⁴ in his *Theorié des Fonctions Analytiques* (1797) and *A.L. Cauchy*¹⁵ in his *Leçons sur les Applications du Calcul*

¹⁴*Joseph-Louis Lagrange* (January 25, 1736–April 10, 1813), an Italian born [born *Giuseppe Lodovico (Luigi) Lagrangia*] famous French mathematician and mechanician

¹⁵*Augustin-Louis Cauchy* (August 21, 1789–May 23, 1857), a famous French mathematician

Infinitésimal à la Geometrie (1826). Later on, in the twentieth century, an investigation in the realm of contact geometry of curves and surfaces has been undertaken by *J. Favard*¹⁶ in his *Course de Géométrie Différentielle Locale* (1957). A few more names of the researchers in the field are to be mentioned.

The results of the research obtained in the field of contact geometry of two smooth regular surfaces are widely used in the theory of gearing. The problem of synthesizing the most favorable gear pair can be solved on the premise of the analysis of topology of the contacting surfaces in differential vicinity of the point of their contact.

Various methods for analytical description of contact geometry between two smooth regular surfaces are developed by now. Latest achievements in the field are discussed in plurality of papers and monograph available in the public domain.

An in-detail analysis of known methods of analytical description of the geometry of contact between two smooth regular surfaces uncovered poor capability of known methods for solving problems in the field of designing efficient gear pairs. Therefore, an accurate method for analytical description of contact geometry between two smooth regular surfaces, \mathcal{G} and \mathcal{P} , in the first order of tangency, which fits the needs of the theory of gearing, is necessary. Such a method is worked out in this chapter.

It is convenient to begin the discussion starting from analytical description of local relative orientation of the gear tooth flank, \mathcal{G} , and the mating pinion tooth flank, \mathcal{P} . The proposed analytical description is relevant to differential vicinity of the point of contact, K , of the tooth flanks, \mathcal{G} and \mathcal{P} .

Local Relative Orientation at a Point of Contact of a Gear and a Mating Pinion' Tooth Flanks

When the gears rotate, a gear tooth flank, \mathcal{G} , and the mating pinion tooth flank, \mathcal{P} , are in permanent tangency with one another. The contacting surfaces, \mathcal{G} and \mathcal{P} , can be approximated by the corresponding quadrics as schematically illustrated in Fig. C.1. The requirement to be permanently in tangency to each other imposes a kind of restrictions on the relative configuration (location and orientation) of the tooth flanks, \mathcal{G} and \mathcal{P} , and on their instant relative motion.

In the theory of gearing, a quantitative measure of relative orientation of the gear tooth flank, \mathcal{G} , and of the mating pinion tooth flank, \mathcal{P} , is established.

Relative orientation of the point of contact of the gear tooth flank, \mathcal{G} , and of the mating pinion tooth flank, \mathcal{P} , is specified by the angle, μ , of local¹⁷ relative orientation of the surfaces. By definition, angle μ is equal to the angle that the unit

¹⁶*Jean Favard* (August 28, 1902–January 21, 1965), a French mathematician

¹⁷The surfaces orientation is “local” in nature because it relates only to differential vicinity of point, K , of contact of the tooth flanks, \mathcal{G} and \mathcal{P} .

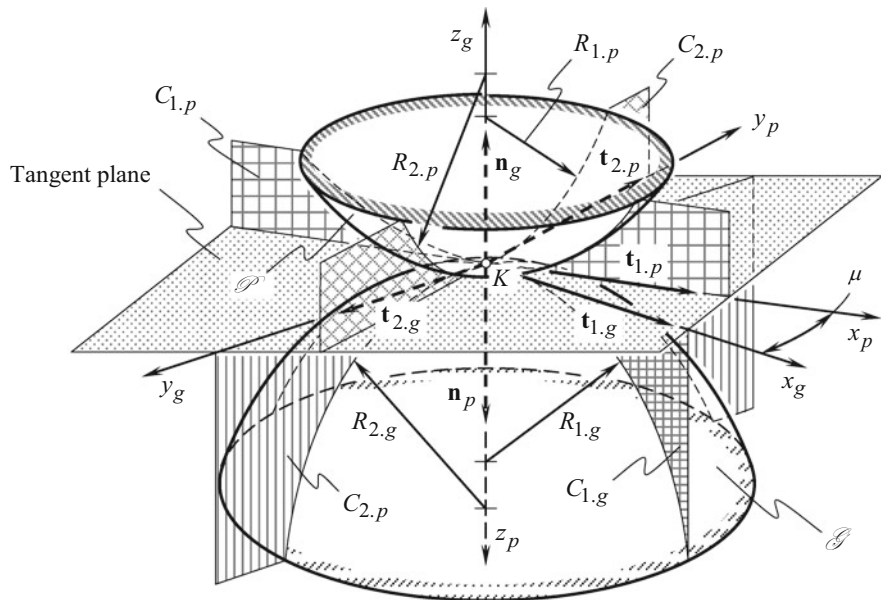


Fig. C.1 Local configuration of two quadrics tangent to a gear tooth flank \mathcal{G} and to a mating pinion tooth flank \mathcal{P} at a point K of their contact. (After S.P. Radzevich, ~2008)

tangent vector, $\mathbf{t}_{1.g}$, of the first principal direction of the gear tooth flank, \mathcal{G} , forms with the unit tangent vector, $\mathbf{t}_{1.p}$, of the first principal direction of the mating pinion tooth flank, \mathcal{P} . That same angle, μ , can also be determined as the angle that makes the unit tangent vectors, $\mathbf{t}_{2.g}$ and $\mathbf{t}_{2.p}$, of the second principal directions of the surfaces, \mathcal{G} and \mathcal{P} , at contact point, K . This immediately yields equations for the calculation of the angle, μ :

$$\sin \mu = | \mathbf{t}_{1.g} \times \mathbf{t}_{1.p} | = | \mathbf{t}_{2.g} \times \mathbf{t}_{2.p} | , \tag{C.1}$$

$$\cos \mu = \mathbf{t}_{1.g} \cdot \mathbf{t}_{1.p} = \mathbf{t}_{2.g} \cdot \mathbf{t}_{2.p}, \tag{C.2}$$

$$\tan \mu = \frac{ | \mathbf{t}_{1.g} \times \mathbf{t}_{1.p} | }{ \mathbf{t}_{1.g} \cdot \mathbf{t}_{1.p} } \equiv \frac{ | \mathbf{t}_{2.g} \times \mathbf{t}_{2.p} | }{ \mathbf{t}_{2.g} \cdot \mathbf{t}_{2.p} } \tag{C.3}$$

Here the following are designated:

$\mathbf{t}_{1.g}, \mathbf{t}_{2.g}$

- the unit vectors of principal directions on the gear tooth flank, \mathcal{G} , measured at contact point, K

$\mathbf{t}_{1.p}, \mathbf{t}_{2.p}$

- the unit vectors of principal directions on the mating pinion tooth flank, \mathcal{P} , at that same contact point, K , of the tooth flanks, \mathcal{G} and \mathcal{P}

Directions of the unit tangent vectors, $\mathbf{t}_{1.g}$ and $\mathbf{t}_{2.g}$, of the principal directions on the gear tooth flank, \mathcal{G} (as well as directions of the unit tangent vectors $\mathbf{t}_{1.p}$ and $\mathbf{t}_{2.p}$

of the principal directions on the pinion tooth flank, \mathcal{P}) can be specified in terms of the ratio dU_g/dV_g (or in terms of the ratio dU_p/dV_p in case of the pinion tooth flank, \mathcal{P}). The corresponding values of the ratio, $dU_{g(p)}/dV_{g(p)}$, are calculated as roots of the quadratic equation:

$$\begin{vmatrix} E_{g(p)} \frac{dU_{g(p)}}{dV_{g(p)}} + F_{g(p)} & F_{g(p)} \frac{dU_{g(p)}}{dV_{g(p)}} + G_{g(p)} \\ L_{g(p)} \frac{dU_{g(p)}}{dV_{g(p)}} + M_{g(p)} & M_{g(p)} \frac{dU_{g(p)}}{dV_{g(p)}} + N_{g(p)} \end{vmatrix} = 0 \quad (C.4)$$

In case of point contact of the surfaces, \mathcal{G} and \mathcal{P} , the actual value of the angle, μ , is calculated at contact point, K . If the tooth flanks, \mathcal{G} and \mathcal{P} , are in line contact, then the actual value of the angle, μ , can be calculated at every point within the line of contact.¹⁸ The line of contact of the tooth flanks, \mathcal{G} and \mathcal{P} , is commonly referred to as “characteristic line, \mathcal{E} ,” or just as “characteristic, \mathcal{E} ,” for simplicity.

Determination of the angle, μ , of local relative orientation of the tooth flanks, \mathcal{G} and \mathcal{P} , of a gear and a mating pinion is illustrated in Fig. C.1.

In order to calculate an actual value of the angle, μ , of local relative orientation of the tooth flanks, \mathcal{G} and \mathcal{P} , the unit vectors of the principal directions, $\mathbf{t}_{1.g}$ and $\mathbf{t}_{1.p}$, are employed.

Consider tooth flanks, \mathcal{G} and \mathcal{P} , in point contact, which are represented in a common reference system. The surfaces make contact at a point, K . For further analysis, an equation of the common tangent plane to the tooth flanks, \mathcal{G} and \mathcal{P} , at the contact point, K , is necessary (see Figs. C.1 and C.2).

$$(\mathbf{r}_p - \mathbf{r}_K) \cdot \mathbf{u}_g \cdot \mathbf{v}_g = 0 \quad (C.5)$$

Here:

\mathbf{r}_p is the position vector of a point of the common tangent plane

\mathbf{r}_K is the position vector of the contact point, K

\mathbf{u}_g and \mathbf{v}_g are unit vectors that are tangent to U_g - and V_g -coordinate lines on the gear tooth flank, \mathcal{G} at the contact point, K

The angle ω_g is the angle that is formed by the unit vectors, \mathbf{u}_g and \mathbf{v}_g . The actual value of the angle, ω_g , can be calculated from one of the following equations:

$$\sin \omega_g = \frac{\sqrt{E_g G_g - F_g^2}}{\sqrt{E_g G_g}} \quad (C.6)$$

¹⁸It is worthy pointing out here that in a case of line contact, relative orientation of two surfaces, \mathcal{G} and \mathcal{P} , is predetermined in “global” sense. However, the actual value of the angle, μ , of the surfaces “local” relative orientation at different points of the characteristic, \mathcal{E} , is different.

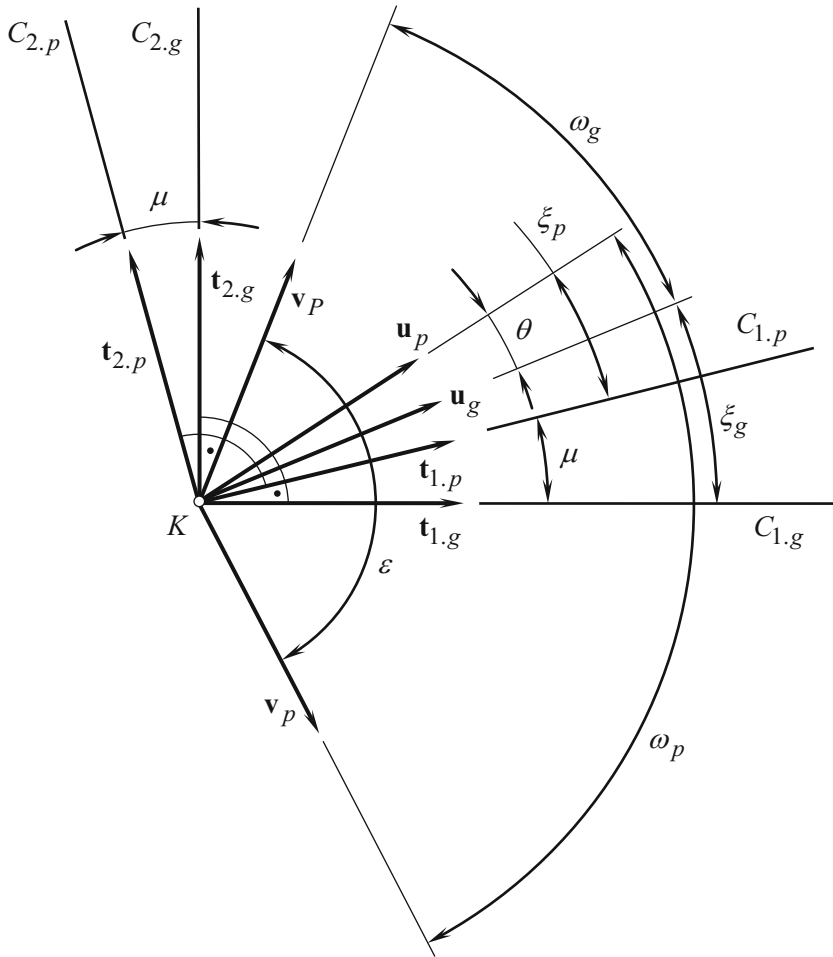


Fig. C.2 Local “relative” orientation at a point of contact of the tooth flanks of a gear, G , and a mating pinion, P , considered in a common tangent plane

$$\cos \omega_g = \frac{F_g}{\sqrt{E_g G_g}} \tag{C.7}$$

$$\tan \omega_g = \frac{\sqrt{E_g G_g - F_g^2}}{F_g} \tag{C.8}$$

Equations similar to Eq. (C.6) through Eq. (C.8) are also valid for the calculation of the angle, ω_p , at a point on the pinion tooth flank, P .

Tangent directions, \mathbf{u}_g and, to the U_g - and V_g -coordinate lines at a point on the gear tooth flank, \mathcal{G} , as well as tangent directions, \mathbf{u}_p and \mathbf{v}_p to the U_p - and V_p -coordinate at a point lines on the pinion tooth flank, \mathcal{P} , are specified in terms of the angles, θ and ε . For the calculation of actual values of the angles, θ and ε , the following equations can be used:

$$\cos \theta = \mathbf{u}_g \cdot \mathbf{u}_p \quad (\text{C.9})$$

$$\cos \varepsilon = \mathbf{v}_g \cdot \mathbf{v}_p \quad (\text{C.10})$$

The angle, ξ_g , is the angle that the first principal direction, $\mathbf{t}_{1.g}$, on the gear tooth surface, \mathcal{G} , forms with the unit tangent vector, \mathbf{u}_g (see Fig. C.2). The equation for the calculation of an actual value of the angle, ξ_g , is derived by Prof. *S.P. Radzevich*:

$$\sin \xi_g = \frac{\eta_g}{\sqrt{\eta_g^2 - 2\eta_g \cos \omega_g + 1}} \sin \omega_g \quad (\text{C.11})$$

where η_g designates the ratio $\eta_g = \frac{\partial U_g}{\partial V_g}$.

In the event $F_g = 0$, the following equality, $\tan \xi_g = \eta_g$, is observed. Here, the ratio, η_g , is equal to the root of the quadratic equation:

$$(F_g L_g - E_g M_g) \eta_g^2 + (G_g L_g - E_g N_g) \eta_g + (G_g M_g - F_g N_g) = 0 \quad (\text{C.12})$$

which immediately follows from the equation:

$$\begin{vmatrix} E_g dU_g + F_g dV_g & F_g dU_g + G_g dV_g \\ L_g dU_g + M_g dV_g & M_g dU_g + N_g dV_g \end{vmatrix} = 0 \quad (\text{C.13})$$

The equation for the calculation of actual value of the angle, ξ_g , allows for another representation. Following chain rule, $d\mathbf{r}_g$ can be represented in the form:

$$d\mathbf{r}_g = \mathbf{U}_g dU_g + \mathbf{V}_g dV_g \quad (\text{C.14})$$

By definition, $\tan \xi_g = \frac{\sin \xi_g}{\cos \xi_g}$. The functions, $\sin \xi_g$ and $\cos \xi_g$, yield representation as:

$$\sin \xi_g = \frac{|\mathbf{U}_g \times d\mathbf{r}_g|}{|\mathbf{U}_g| \cdot |d\mathbf{r}_g|} \quad (\text{C.15})$$

$$\cos \xi_g = \frac{\mathbf{U}_g \cdot d\mathbf{r}_g}{|\mathbf{U}_g| \cdot |d\mathbf{r}_g|} \quad (\text{C.16})$$

The last expressions yield:

$$\begin{aligned}\tan \xi_g &= \frac{\sin \xi_g}{\cos \xi_g} = \frac{|\mathbf{U}_g \times d\mathbf{r}_g|}{\mathbf{U}_g \cdot d\mathbf{r}_g} = \frac{|\mathbf{U}_g \times d\mathbf{r}_g|}{\mathbf{U}_g \cdot (\mathbf{U}_g dU_g + \mathbf{V}_g dV_g)} \\ &= \frac{|\mathbf{U}_g \times d\mathbf{r}_g| \cdot dV_g}{\mathbf{U}_g \cdot \mathbf{U}_g dU_g + \mathbf{U}_g \cdot \mathbf{V}_g dV_g}\end{aligned}\quad (\text{C.17})$$

By definition:

$$\mathbf{U}_g \cdot \mathbf{U}_g = E_g \quad (\text{C.18})$$

$$\mathbf{U}_g \cdot \mathbf{V}_g = F_g \quad (\text{C.19})$$

$$|\mathbf{U}_g \times \mathbf{V}_g| = \sqrt{E_g G_g - F_g^2} \quad (\text{C.20})$$

Equation (C.14) through Eq. (C.20) yield the formula:

$$\tan \xi_g = \frac{\sqrt{E_g G_g - F_g^2}}{\eta_g \cdot E_g + F_g} \quad (\text{C.21})$$

for the calculation of actual value of the angle ξ_g .

Equations similar to those above Eq. (C.11) and Eq. (C.21) are also valid for the calculation of actual value of the angle, ξ_p , that the first principal direction, $\mathbf{t}_{1.p}$, at a point on the pinion tooth flank, \mathcal{P} , forms with the unit tangent vector, \mathbf{u}_p .

The performed analysis makes possible the following equations for the calculation of the unit vectors of principal directions, $\mathbf{t}_{1.g}$ and $\mathbf{t}_{2.g}$:

$$\mathbf{t}_{1.g} = \mathbf{Rt}(\xi_g, \mathbf{n}_g) \cdot \mathbf{u}_g \quad (\text{C.22})$$

$$\mathbf{t}_{2.g} = \mathbf{Rt}\left[\left(\xi_g + \frac{\pi}{2}\right), \mathbf{n}_g\right] \cdot \mathbf{u}_g \quad (\text{C.23})$$

for the gear tooth flank, \mathcal{G} , and similar equations for the calculation of the unit vectors of principal directions, $\mathbf{t}_{1.p}$ and $\mathbf{t}_{2.p}$:

$$\mathbf{t}_{1.p} = \mathbf{Rt}(\xi_p, \mathbf{n}_g) \cdot \mathbf{u}_p \quad (\text{C.24})$$

$$\mathbf{t}_{2.p} = \mathbf{Rt}\left[\left(\xi_p + \frac{\pi}{2}\right), \mathbf{n}_g\right] \cdot \mathbf{u}_p \quad (\text{C.25})$$

for the pinion tooth flank, \mathcal{P} .

The operator of rotation $\mathbf{Rt}(\varphi_A, A_0)$ through an angle φ_A about an axis A_0 is employed for the calculation of the operators of rotation in Eq. (C.22) through Eq. (C.25).

The Second Order Analysis: Planar Characteristic Images

For a more accurate analytical description of contact geometry of the gear tooth flank, \mathcal{G} , and the pinion tooth flank, \mathcal{P} , consideration of the second order parameters is necessary. The second order analysis incorporates elements of both the first order and elements of the second order analysis. For performing the second order analysis, familiarity with “*Dupin indicatrix*” is highly desirable.¹⁹ “*Dupin indicatrix*” is a perfect start-point for consideration of the second order analysis.

Preliminary Remarks: “Dupin indicatrix”

At any point of a smooth regular gear tooth flank, \mathcal{G} (as well as at any point of a smooth regular pinion tooth flank, \mathcal{P}) a corresponding “*Dupin indicatrices*” can be constructed. “*Dupin indicatrix, Dup*(\mathcal{G})” at a point of a gear tooth flank, \mathcal{G} , and “*Dupin indicatrix, Dup*(\mathcal{P})” at a point of the pinion tooth flank, \mathcal{P} , are planar characteristic curves of the second order. They are used for graphical interpretation of the distribution of normal radii of curvature of a surface in the differential vicinity of a surface point.

“*Dupin indicatrices*” at a point of the tooth flank, \mathcal{G} (as well as at a point of the tooth flank, \mathcal{P}), are of critical importance in the theory of gearing. Generation of this planar characteristic curve is illustrated with a diagram shown in Fig. C.3.

A plane W through the unit normal vector, \mathbf{n}_g , to the gear tooth flank, \mathcal{G} , at a point, m , is rotating about the unit normal vector, \mathbf{n}_g . While rotating, the plane occupies consecutive positions, W_1, W_2, W_3 , and others. The radii of normal curvature of the line of intersection of the gear tooth flank, \mathcal{G} , by normal planes, W_1, W_2, W_3 , are equal to $R_{g, 1}, R_{g, 2}, R_{g, 3}$, and so forth. The gear tooth flank, \mathcal{G} , is intersected by a plane, Q . The plane, Q , is orthogonal to the unit normal vector, \mathbf{n}_g . This plane is at a certain small distance, δ , from the point, m . When the distance, δ , approaches zero ($\delta \rightarrow 0$), and when the scale of the line of intersection of the gear tooth flank, \mathcal{G} , by the plane, Q , approaches infinity, then the line of intersection of the gear surface, \mathcal{G} , by the plane, Q approaches to the planar characteristic curve that is commonly referred to as “*Dupin indicatrix, Dup*(\mathcal{G}).”

In differential geometry of surfaces, a surface is construed as a zero-thickness film. Because of this, “*Dupin indicatrices*” of the following five different types are distinguished in differential geometry of surfaces (see Fig. C.4):

- Elliptic (Fig. C.4a).
- Umbilic (Fig. C.4b).
- Parabolic (Fig. C.4c).

¹⁹*Pierre Charles Francois Dupin* (October 6, 1784–January 18, 1873), a French mathematician

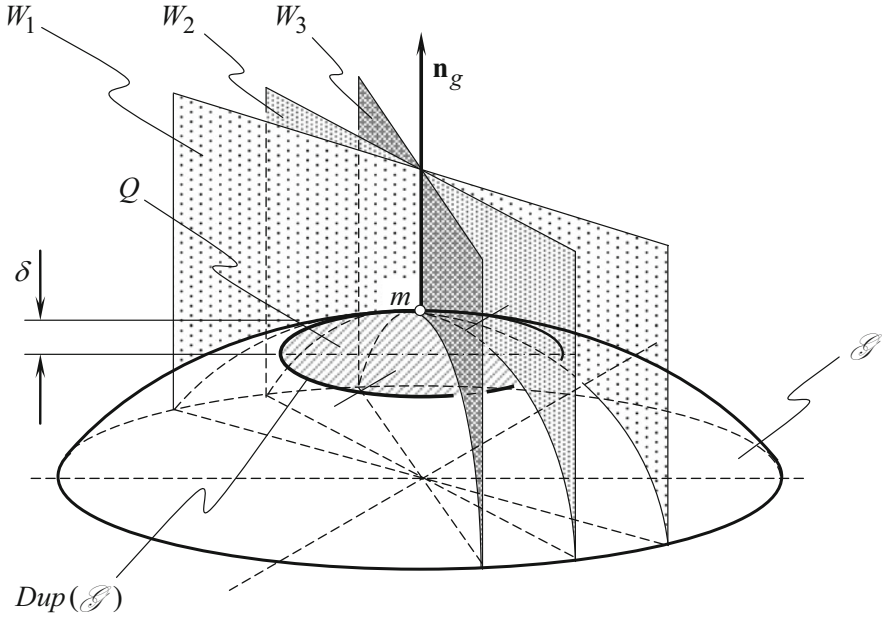


Fig. C.3 “Dupin indicatrix” at point of smooth regular gear tooth flank, G

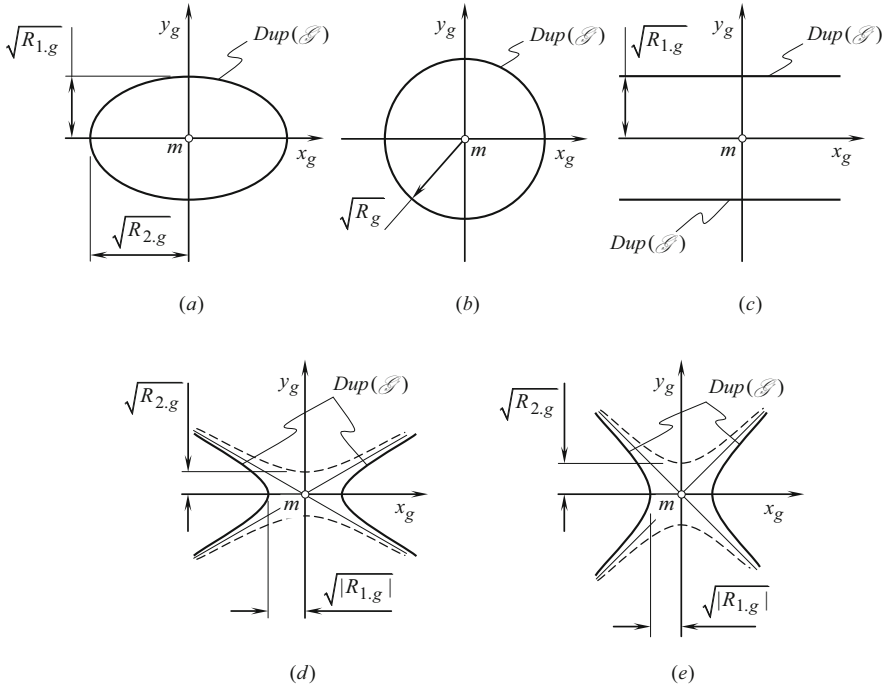


Fig. C.4 Five different types of “Dupin indicatrices, $Dup(G)$ ”, at a point, m , of a smooth regular gear tooth flank, G

- Hyperbolic (Fig. C.4d).
- Minimal (Fig. C.4e).

“*Dupin indicatrix*” for a plane local surface patch doesn’t exist. In the case of plane, all points of the “*Dupin indicatrix*” are remote to infinity.

For local surface patches having negative full curvature ($\mathcal{G}_g < 0$), phantom branches (i.e., the branches that are not intersected by a plane perpendicular to the unit normal vector, \mathbf{n}_g , to the gear tooth flank, \mathcal{G} , at a point, m) of the characteristic curve, $Dup(\mathcal{G})$, in Fig. C.4d and in Fig. C.4e are shown in dashed lines.

An easy way to derive an equation of the characteristic curve, $Dup(\mathcal{G})$, is discussed immediately below.

“*Euler formula*”:

$$k_{1.g} \cos^2 \varphi + k_{2.g} \sin^2 \varphi = k_g \quad (\text{C.26})$$

yields representation in the form:

$$\frac{k_{1.g}}{k_g} \cos^2 \varphi + \frac{k_{2.g}}{k_g} \sin^2 \varphi = 1 \quad (\text{C.27})$$

Transition from polar coordinates to “*Cartesian coordinates*” can be performed using well-known formulae:

$$x_g = \rho \cos \varphi \quad (\text{C.28})$$

$$y_g = \rho \sin \varphi \quad (\text{C.29})$$

These formulae make it possible the following expressions for $\cos^2 \varphi = x_g^2 / \rho^2$ and $\sin^2 \varphi = y_g^2 / \rho^2$. After substituting the last formulae into the above equation Eq. (C.27), one can come up with the equation:

$$\frac{k_{1.g}}{k_g} \cdot \frac{x_g^2}{\rho^2} + \frac{k_{2.g}}{k_g} \cdot \frac{y_g^2}{\rho^2} = 1. \quad (\text{C.30})$$

It is convenient to designate $\rho = \sqrt{k_g^{-1}}$. Principal curvatures $k_{1.g}$ and $k_{2.g}$ are the roots of the quadratic equation:

$$\begin{vmatrix} L_g - E_g k_g & M_g - F_g k_g \\ M_g - F_g k_g & N_g - G_g k_g \end{vmatrix} = 0 \quad (\text{C.31})$$

Substituting the calculated values of the principal curvatures $k_{1.g}$ and $k_{2.g}$ into Eq. (C.30), and after performing necessary formulae transformations, an equation²⁰ for the “*Dupin indicatrix*, $Dup(\mathcal{G})$ ” can be represented in the form:

$$k_{1.g}x_g^2 + k_{2.g}y_g^2 = 1 \tag{C.32}$$

Equation (C.32) describes a particular case of the “*Dupin indicatrix*,” which is represented in “*Darboux frame*”.²¹

The general form of equation of “*Dupin indicatrix*” at a point m of a gear tooth flank, \mathcal{G} , is often represented as:

$$Dup(\mathcal{G}) \Rightarrow \frac{L_g}{E_g}x_g^2 + \frac{2M_g}{\sqrt{E_gG_g}}x_gy_g + \frac{N_g}{G_g}y_g^2 = 1 \tag{C.33}$$

In Eq. (C.33), the characteristic curve, $Dup(\mathcal{G})$, is expressed in terms of the fundamental magnitudes, E_g , F_g , and G_g of the first, $\Phi_{1.g}$, and in terms of the fundamental magnitudes, L_g , M_g , and N_g , of the second order, $\Phi_{2.g}$, at a point of the gear tooth flank, \mathcal{G} .

Matrix Representation of Equation of “Dupin indicatrix” at Point of a Gear Tooth Flank

Like any other quadratic form, equation of “*Dupin indicatrix*” of the gear tooth flank, \mathcal{G} , can be represented in matrix form:

$$Dup(\mathcal{G}) \Rightarrow \begin{bmatrix} x_g & y_g & 0 & 0 \end{bmatrix} \cdot \begin{bmatrix} \frac{L_g}{E_g} & \frac{2M_g}{\sqrt{E_gG_g}} & 0 & 0 \\ \frac{2M_g}{\sqrt{E_gG_g}} & \frac{N_g}{G_g} & 0 & 0 \\ 0 & 0 & \mp 1 & 0 \\ 0 & 0 & 0 & 1 \end{bmatrix} \cdot \begin{bmatrix} x_g \\ y_g \\ 0 \\ 0 \end{bmatrix} = \pm 1 \tag{C.34}$$

²⁰The same equation of the “*Dupin indicatrix*” could be derived in another way. *Coxeter* considers a pair of conics obtained by expanding an equation in *Monge’s* form $z = z(x, y)$ in a “*Maclauren series*”:

$$z = z(0, 0) + z_1x + z_2y + \frac{1}{2}(z_{11}x_1^2 + 2z_{12}xy + z_{22}y^2) + \dots = \frac{1}{2}(b_{11}x^2 + 2b_{12}xy + b_{22}y^2).$$

This gives the equation $(b_{11}x^2 + 2b_{12}xy + b_{22}y^2) = \pm 1$ of the “*Dupin indicatrix*.”

²¹*Jean Gaston Darboux* (August 13, 1842–February 23, 1917), a French mathematician

In “*Darboux frame*” this equation reduces to:

$$Dup(\mathcal{G}) \Rightarrow \begin{bmatrix} x_g & y_g & 0 & 0 \end{bmatrix} \cdot \begin{bmatrix} L_g & M_g & 0 & 0 \\ M_g & N_g & 0 & 0 \\ 0 & 0 & \mp 1 & 0 \\ 0 & 0 & 0 & 1 \end{bmatrix} \cdot \begin{bmatrix} x_g \\ y_g \\ 0 \\ 0 \end{bmatrix} = \pm 1 \quad (\text{C.35})$$

It is convenient to implement matrix representation of equation of the “*Dupin indicatrix*” (see above), for instance, when investigating spatial gearings, that is, crossed-axis gearings, when multiple coordinate system transformations are required.

The equation of “*Dupin indicatrix*” can be represented in the form:

$$r_{Dup}(\varphi) = \sqrt{|R_g(\varphi)|} \cdot \text{sgn } \Phi_{2,g}^{-1} \quad (\text{C.36})$$

The last equation reveals that the position vector of a point of the “*Dupin indicatrix, Dup(\mathcal{G})*,” in any direction is equal to the square root of the radius of curvature in that same direction.²²

Degree of Conformity at Point of Contact of a Gear and a Mating Pinion's Tooth Flanks in the First Order of Tangency

For an accurate analytical description of contact geometry of the gear and the mating pinion's tooth flanks in the first order of tangency, a higher order analysis is necessary to be done.

The below-discussed method of a higher order analysis is targeting the development of an analytical description of degree of conformity of the pinion tooth flank, \mathcal{P} , to the gear tooth flank, \mathcal{G} , at a current point, K of their contact. The higher the degree of conformity of the tooth flanks, \mathcal{G} and \mathcal{P} , the closer these surfaces to each other in differential vicinity of the point, K . This qualitative (“*intuitive*”) definition of degree of conformity of two smooth regular surfaces needs a corresponding quantitative measure.

²²Similar to “*Dupin indicatrix, Dup(\mathcal{G})*,” a planar characteristic curve of another type can be introduced. An equation of this characteristic curve can be postulated in the form: $r_{Dup.k}(\varphi) = \sqrt{|k_g(\varphi)|} \cdot \text{sgn } \Phi_{2,g}^{-1}$. Application of curvature indicatrix in the form, $r_{Dup.k}(\varphi)$, makes possible avoiding uncertainty in cases of plane surface. For plane surface, the characteristic curve, $Dup(\mathcal{G})$, does not exist, while, $r_{Dup.k}(\varphi)$, exists. It shrinks to the point, m , on the gear tooth flank, \mathcal{G} .

Preliminary Remarks

Implementation of the resultant deviation, l_{cnf} (see Fig. C.5), of two smooth regular surfaces in contact for the analytical description of contact geometry of two surfaces in contact is a type of straightforward solution to the problem under consideration. This approach is proven to be computationally ineffective. However, the approach gives an insight for how an effective method for solving the problem under consideration can be developed.

As seen in Fig. C.5, three geometrical parameters are interrelated when a deviation of a surface from the tangent plane is considered in differential vicinity of a surface point. They are:

- (a) The measure of the deviation, $m_g m_g^*$, of a gear tooth flank, G , from the tangent plane, l_{cnf} .
- (b) The distance, $K m_g^*$, of a current point, m_g , from the contact point, K .
- (c) Radius of normal curvature R_g of the gear tooth flank, G , at the contact point, K .

As a consequence from this relationship among the parameters, $m_g m_g^*$, $K m_g^*$, and R_g , any one of them can be used for the purposes of quantitative evaluation of degree of conformity of the contacting tooth flanks, G and P , of the gear and the mating pinion. As it is following from Fig. C.5:

$$m_g m_g^* = R_g - \sqrt{R_g^2 - (K m_g^*)^2} \Big|_{m_g \rightarrow K} \mapsto l_{cnf} \tag{C.37}$$

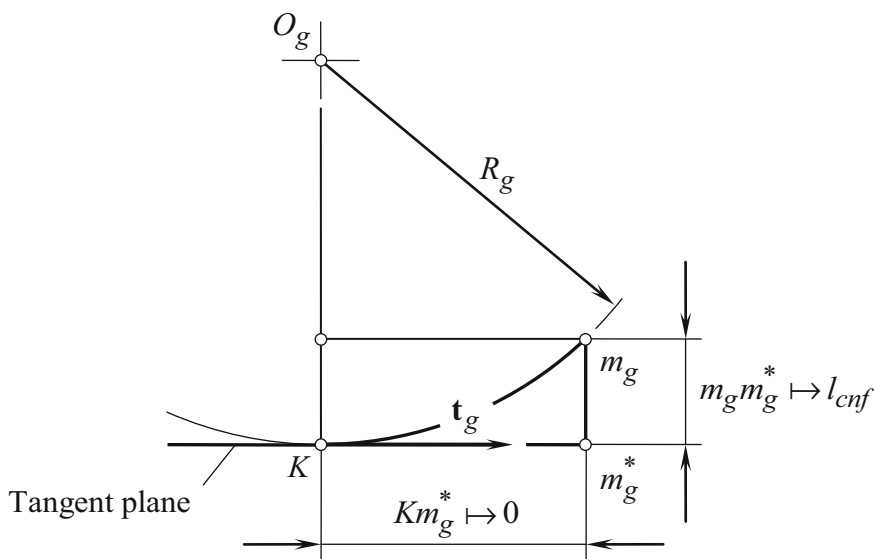


Fig. C.5 On transition from the resultant deviation, l_{cnf} , of two tooth flanks to indicatrix of conformity, $Cnf (G/P)$, at a contact point, K , between a smooth regular tooth flanks, G and P

Inversely, for the radius of normal curvature, R_g , at a point of the gear tooth flank, \mathcal{G} , the following expression is valid:

$$R_g = \frac{\left(m_g m_g^*\right)^2 + \left(K m_g^*\right)^2}{2 \cdot m_g m_g^*} \quad (\text{C.38})$$

Ultimately, one may conclude that any legitimate analytical function of normal radii of curvature, R_g and R_p , at a point of contact of the gear tooth flank, \mathcal{G} , and the pinion tooth flank, \mathcal{P} , can be used for this particular purpose.

Consider two smooth regular tooth flanks, \mathcal{G} and \mathcal{P} , in the first order of tangency that make contact at a point, K . Degree of conformity of the tooth flanks, \mathcal{G} and \mathcal{P} , can be construed as a function of radii of normal curvature, R_g and R_p , of the contacting surfaces. Radii of normal curvature, R_g and R_p , of the tooth flanks, \mathcal{G} and \mathcal{P} , are taken in a common normal plane section through the point, K . For a specified radius of normal curvature, R_g , of the tooth flank, \mathcal{G} , the degree of conformity of the tooth flanks depends upon the corresponding value of radius of normal curvature, R_p , of the pinion tooth flank, \mathcal{P} .

In most cases of gear meshing, degree of conformity at a point of contact of the tooth flanks, \mathcal{G} and \mathcal{P} , is not constant, and it is changing as coordinates of the contact point change. Degree of the surfaces conformity to one another depends on orientation of the normal plane section through the contact point, K , and changes as the normal plane section is turning about the common perpendicular, \mathbf{n}_g . This statement immediately follows from the above-made conclusion that degree of conformity at a point of contact of the tooth flanks, \mathcal{G} and \mathcal{P} , yields interpretation in terms of radii of normal curvature, R_g and R_p .

The change of degree of conformity of a gear tooth flank, \mathcal{G} , and a mating pinion tooth flank, \mathcal{P} , due to turning of the normal plane section about the common perpendicular, \mathbf{n}_g , is illustrated in Fig. C.6. Here, in Fig. C.6, just two-dimensional examples are shown, for which the same normal plane section of the gear tooth flank, \mathcal{G} , makes contact with different plane sections, \mathcal{P}^i , of the pinion tooth flank, \mathcal{P} .

In the example shown in Fig. C.6a, radius of normal curvature, R_p^1 , of the convex plane section, \mathcal{P}^1 , of the pinion tooth flank, \mathcal{P} , is positive ($R_p^1 > 0$). The convex normal plane section of the pinion tooth flank, \mathcal{P} , makes contact with the convex normal plane section ($R_g > 0$) of a gear tooth flank, \mathcal{G} . The degree of conformity of the pinion tooth flank, \mathcal{P} , to the gear tooth flank, \mathcal{G} , in Fig. C.6a is relatively low as both the contacting surfaces are convex.

Another example is shown in Fig. C.6b. The radius of normal curvature, R_p^2 , of the convex plane section, \mathcal{P}^2 , of the pinion tooth flank, \mathcal{P} , also is positive ($R_p^2 > 0$). However, its value exceeds the value, R_p^1 , of the radius of normal curvature in the first example ($R_p^2 > R_p^1$). This results in that degree of conformity of the pinion tooth flank, \mathcal{P} , to the gear tooth flank, \mathcal{G} (Fig. C.6b), is greater compared to that shown in Fig. C.6a.

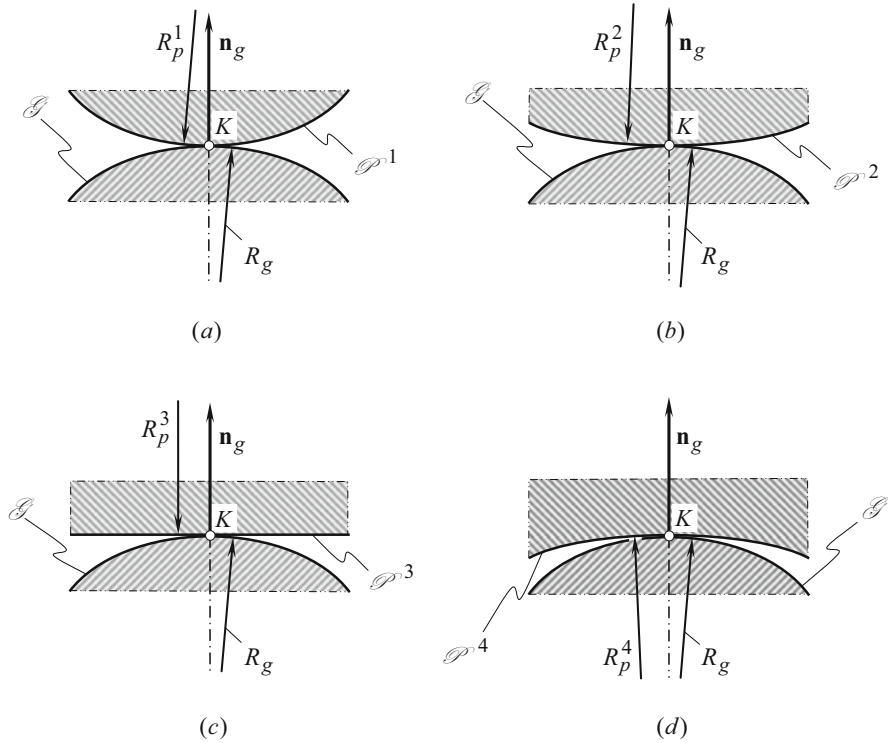


Fig. C.6 Sections of two smooth regular tooth flanks, \mathcal{G} and \mathcal{P} , in contact by a plane through the common perpendicular, \mathbf{n}_g

In the next example depicted in Fig. C.6c, the normal plane section \mathcal{P}^3 of the pinion tooth flank, \mathcal{P} , is represented with locally flattened section. The radius of normal curvature, R_p^3 , of the flattened plane section, \mathcal{P}^3 , approaches infinity ($R_p^3 \rightarrow \infty$). Thus, the inequality, $R_p^3 > R_p^2 > R_p^1$, is valid. Therefore, the degree of conformity of the pinion tooth flank, \mathcal{P} , to the gear tooth flank, \mathcal{G} in Fig. C.6c, is also getting greater.

Finally, for a concave normal plane section, \mathcal{P}^4 , of the pinion tooth flank, \mathcal{P} , that is illustrated in Fig. C.6d, the radius of normal curvature, R_p^4 , is of negative value ($R_p^4 < 0$). In this case, the degree of conformity of the pinion tooth flank, \mathcal{P} , to the gear tooth flank, \mathcal{G} , is the greatest of four examples considered in Fig. C.6.

The examples shown in Fig. C.6 qualitatively illustrate what is known intuitively regarding the different degree of conformity of two smooth regular surfaces in the first order of tangency. Intuitively one can realize that in the examples shown in Fig. C.6a through Fig. C.6d, the degree of conformity at a point of contact of two tooth flanks, \mathcal{G} and \mathcal{P} , is gradually increased.

A similar observation is made for a given pair of the tooth flanks, \mathcal{G} and \mathcal{P} , when different sections of the surfaces by a plane surface through the common perpendicular, \mathbf{n}_g , are considered (see Fig. C.7a). When rotating the plane section about the

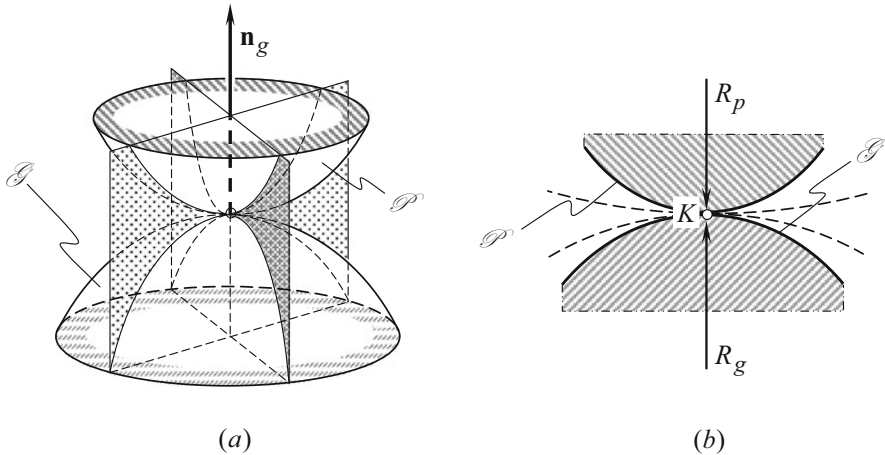


Fig. C.7 To analytical description of contact geometry of two smooth regular tooth flanks, \mathcal{G} and \mathcal{P} , of a gear and a mating pinion

common perpendicular, \mathbf{n}_g , it can be observed that the degree of conformity of the gear and the pinion tooth flanks, \mathcal{G} and \mathcal{P} , is different in different configurations of the cross-sectional plane (see Fig. C.7b).

The above examples provide an intuitive understanding of what the degree of conformity at a point of contact of two smooth regular tooth flanks, \mathcal{G} and \mathcal{P} , means. The examples cannot be employed directly for the purpose to evaluate in quantities the degree of conformity at a point of contact of two smooth regular tooth flanks, \mathcal{G} and \mathcal{P} . The next necessary step to be made up is to introduce an appropriate quantitative evaluation of the degree of conformity of two smooth regular surfaces in the first order of tangency. In other words, how can a certain degree of conformity of two smooth regular surfaces be described analytically?

Indicatrix of Conformity at Point of Contact of a Gear and a Mating pinion's Tooth Flanks

This section is aiming for the introduction of a quantitative measure of degree of conformity at a point of contact between two smooth regular surfaces. The degree of conformity at a point of contact of two tooth flanks, \mathcal{G} and \mathcal{P} , indicates how the pinion tooth flank, \mathcal{P} , is close to the gear tooth flank, \mathcal{G} , in differential vicinity of a point, K , of their contact, say how much the surface, \mathcal{P} , is “congruent” to the surface, \mathcal{G} , in differential vicinity of the contact point, K . These particular types of congruency between the contacting surfaces, \mathcal{G} and \mathcal{P} , can also be construed as the “local congruency” of the contacting surfaces.

Quantitatively, the degree of conformity at a point of contact of a smooth regular surface, \mathcal{P} , to another surface, \mathcal{G} , can be expressed in terms of the difference between the corresponding radii of normal curvature of the contacting surfaces. In order to develop a quantitative measure of the degree of conformity of the tooth flanks, \mathcal{G} and \mathcal{P} , it is convenient to implement “Dupin indicatrices,” $Dup(\mathcal{G})$ and $Dup(\mathcal{P})$, constructed at a point of contact of the gear tooth flank, \mathcal{G} , and the pinion tooth flank, \mathcal{P} , correspondingly.

It is natural to assume that the smaller difference between the normal curvatures of the surfaces, \mathcal{G} and \mathcal{P} , in a common cross-section by a plane through the common normal vector, \mathbf{n}_g , results in the greater degree of conformity at a point of contact of the tooth flanks, \mathcal{G} and \mathcal{P} .

“Dupin indicatrix, $Dup(\mathcal{G})$ ” indicates the distribution of radii of normal curvature at a point of the gear tooth flank, \mathcal{G} , as it had been shown, for example, for a concave elliptic patch of the surface, \mathcal{G} (see Fig. C.8). For a gear tooth flank, \mathcal{G} , equation of this characteristic curve in polar coordinates can be represented in the form:

$$Dup(\mathcal{G}) \Rightarrow r_g(\varphi_g) = \sqrt{|R_g(\varphi_g)|} \tag{C.39}$$

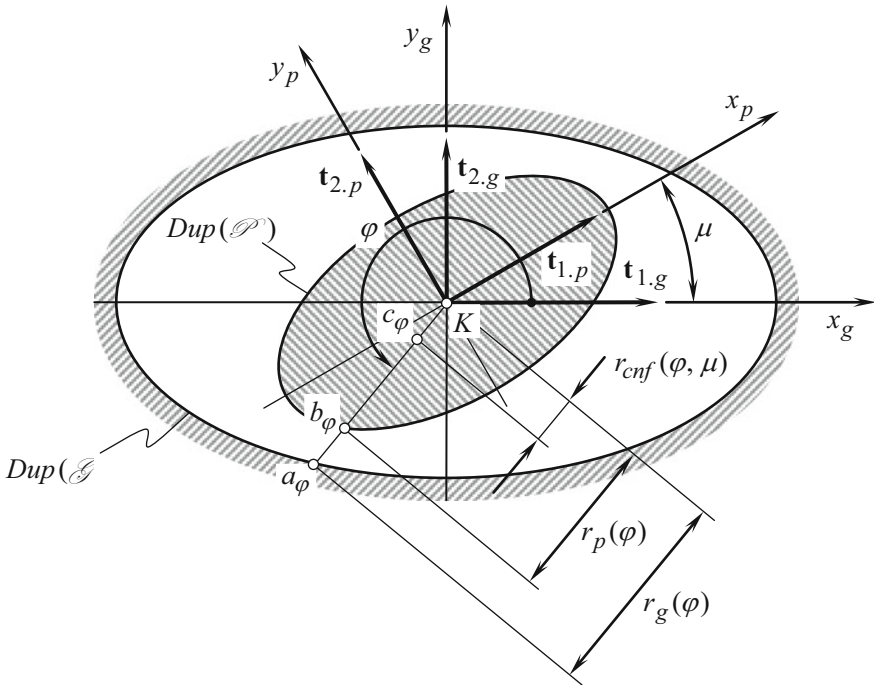


Fig. C.8 To derivation of equation of indicatrix of conformity, $Cnf_R(\mathcal{G}/\mathcal{P})$, at a point of contact of a smooth regular gear tooth flank, \mathcal{G} , and the mating pinion tooth flank, \mathcal{P} , which are in the first order of tangency

where:

r_g is the position vector of a point of the “Dupin indicatrix, $Dup(\mathcal{G})$ ” at a point of the gear tooth flank, \mathcal{G}

φ_g is the polar angle of the indicatrix, $Dup(\mathcal{G})$

The similar is true with respect to the “Dupin indicatrix, $Dup(\mathcal{P})$ ” at a point of the pinion tooth flank, \mathcal{P} , as it had been shown, for instance, for a convex elliptical patch of the pinion tooth flank, \mathcal{P} (see Fig. C.8). Equation of this characteristic curve in polar coordinates can be represented in the form:

$$Dup(\mathcal{P}) \Rightarrow r_p(\varphi_p) = \sqrt{|R_p(\varphi_p)|} \quad (C.40)$$

where:

r_p is the position vector of a point of the “Dupin indicatrix, $Dup(\mathcal{P})$ ” at a point of the pinion tooth flank, \mathcal{P}

φ_p is the polar angle of the indicatrix, $Dup(\mathcal{P})$

In the coordinate plane, $x_g y_g$, of the local reference system, $x_g y_g z_g$, the equalities, $\varphi_g = \varphi$ and $\varphi_p = \varphi + \mu$, are valid. Therefore, in the coordinate plane, $x_g y_g$, Eq. (C.39) and Eq. (C.40) cast into:

$$Dup(\mathcal{G}) \Rightarrow r_g(\varphi) = \sqrt{|R_g(\varphi)|} \quad (C.41)$$

$$Dup(\mathcal{P}) \Rightarrow r_p(\varphi, \mu) = \sqrt{|R_p(\varphi, \mu)|} \quad (C.42)$$

When degree of conformity at a point of contact of the gear tooth flank, \mathcal{G} , is greater, then the difference between the functions $r_g(\varphi)$ and $r_p(\varphi, \mu)$ becomes smaller and vice versa. The last makes valid the following conclusion:

Conclusion

The distance between the corresponding²³ points of the Dupin indicatrices, $Dup(\mathcal{G})$ and $Dup(\mathcal{P})$, constructed at a point of contact of a gear tooth flank, \mathcal{G} , and a mating pinion's tooth flank, \mathcal{P} , can be employed for the purpose of indication of the degree of conformity at a point of contact of the gear tooth flank, \mathcal{G} , and of the pinion tooth flank, \mathcal{P} , at the contact point, K .

The equation of the “indicatrix of conformity, $Cnf_R(\mathcal{G}/\mathcal{P})$ ” at a point of contact of a gear tooth flank, \mathcal{G} , and a mating pinion tooth flank, \mathcal{P} , is defined of the following structure:

²³Corresponding points of the “Dupin indicatrices,” $Dup(\mathcal{P})$ and $Dup(\mathcal{T})$, share the same straight line through the contact point, K , of the tooth flanks, \mathcal{G} and \mathcal{P} , and are located at the same side of the point, K .

$$\begin{aligned}
Cnf_R(\mathcal{G}/\mathcal{P}) &\Rightarrow r_{cnf}(\varphi, \mu) \\
&= \sqrt{|R_g(\varphi)|} \operatorname{sgn} R_g(\varphi) + \sqrt{|R_p(\varphi, \mu)|} \operatorname{sgn} R_p(\varphi, \mu) \\
&= r_g(\varphi) \operatorname{sgn} R_g(\varphi) + r_p(\varphi, \mu) \operatorname{sgn} R_p(\varphi, \mu)
\end{aligned} \tag{C.43}$$

Because the location of a point, a_φ , of the “*Dupin indicatrix, Dup(\mathcal{G})*” at a point of the gear tooth flank, \mathcal{G} , is specified by the position vector, $r_g(\varphi)$, and the location of a point, b_φ , of the “*Dupin indicatrix, Dup(\mathcal{P})*” at a point of the pinion tooth flank, \mathcal{P} , is specified by the position vector, $r_p(\varphi, \mu)$, then the location of a point, c_φ (see Fig. C.8), of the “*indicatrix of conformity, Cnf_R(\mathcal{G}/\mathcal{P})*” at a point of contact, K , of the tooth flanks, \mathcal{G} and \mathcal{P} , is specified by the position vector $r_{cnf}(\varphi, \mu)$. Therefore, the equality $r_{cnf}(\varphi, \mu) = Kc_\varphi$ is observed, and the length of the straight line segment, Kc_φ , is equal to the distance, $a_\varphi b_\varphi$.

Here, in Eq. (C.43) the following are designated:

$$r_g = \sqrt{|R_g|}$$

is the position vector of a point of “*Dupin indicatrix*” of the gear tooth flank, \mathcal{G} , at a point K of contact with pinion tooth flank, \mathcal{P}

$$r_p = \sqrt{|R_p|}$$

is the position vector of a corresponding point of the “*Dupin indicatrix*” of the pinion tooth flank, \mathcal{P}

Here, in Eq. (C.43), the multipliers $\operatorname{sgn} R_g(\varphi)$ and $\operatorname{sgn} R_p(\varphi, \mu)$ are assigned to each of the functions, $r_g(\varphi) = \sqrt{|R_g(\varphi)|}$ and $r_p(\varphi, \mu) = \sqrt{|R_p(\varphi, \mu)|}$, accordingly just for the purpose to remain the corresponding sign of the functions, that is, to remain that same sign that the radii of normal curvature, $R_g(\varphi)$ and $R_p(\varphi, \mu)$, have.

Ultimately, one can conclude that position vector, r_{cnf} , of a point of the “*indicatrix of conformity, Cnf_R(\mathcal{G}/\mathcal{P})*” can be expressed in terms of position vectors, r_g and r_p , of the “*Dupin indicatrices,*” $Dup(\mathcal{G})$ and $Dup(\mathcal{P})$.

For the calculation of a current value of the radius of normal curvature, $R_g(\varphi)$, at point of the gear tooth flank, \mathcal{G} , the equality:

$$R_g(\varphi) = \frac{\Phi_{1.g}}{\Phi_{2.g}} \tag{C.44}$$

can be used.

Similarly, for the calculation of the current value of the radius of normal curvature, $R_p(\varphi, \mu)$, at point of pinion tooth flank, \mathcal{P} , the equality:

$$R_p(\varphi, \mu) = \frac{\Phi_{1.p}}{\Phi_{2.p}} \tag{C.45}$$

can be employed.

Use of the angle, μ , of local relative orientation of the tooth flanks, \mathcal{G} and \mathcal{P} , indicates that the radii of normal curvature, $R_g(\varphi)$ and $R_p(\varphi, \mu)$, are taken in a common normal plane section through the contact point, K .

Further, it is well-known that the inequalities, $\Phi_{1.g} \geq 0$ and $\Phi_{1.p} \geq 0$, are always valid. Therefore, Eq. (C.43) can be rewritten in the following form:

$$r_{cnf} = r_g(\varphi) \operatorname{sgn} \Phi_{2.g}^{-1} + r_p(\varphi, \mu) \operatorname{sgn} \Phi_{2.p}^{-1} \quad (\text{C.46})$$

For the derivation of an equation of the “*indicatrix of conformity*, $Cnf_R(\mathcal{G}/\mathcal{P})$,” it is convenient to use the “*Euler equation*” for normal radius of curvature, $R_g(\varphi)$, at a point of the gear tooth flank, \mathcal{G} :

$$R_g(\varphi) = \frac{R_{1.g} \cdot R_{2.g}}{R_{1.g} \cdot \sin^2 \varphi + R_{2.g} \cdot \cos^2 \varphi} \quad (\text{C.47})$$

Here, the radii of principal curvature, $R_{1.g}$ and $R_{2.g}$, are the roots of the quadratic equation:

$$\begin{vmatrix} L_g \cdot R_g - E_g & M_g \cdot R_g - F_g \\ M_g \cdot R_g - F_g & N_g \cdot R_g - G_g \end{vmatrix} = 0 \quad (\text{C.48})$$

Recall, that the inequality, $R_{1.g} < R_{2.g}$, is always observed.

Equation (C.47) and Eq. (C.48) allow for expression of the radius of normal curvature, $R_g(\varphi)$, at a point of the gear tooth flank, \mathcal{G} , in terms of the fundamental magnitudes of the first order, E_g , F_g , and G_g , and of the fundamental magnitudes of the second order, L_g , M_g , and N_g .

A similar consideration is applicable for the pinion tooth flank, \mathcal{P} . Omitting routing analysis, one can conclude that the radius of normal curvature, $R_p(\varphi, \mu)$, at a point of the pinion tooth flank, \mathcal{P} , can be expressed in terms of the fundamental magnitudes of the first order, E_p , F_p , and G_p , and of the fundamental magnitudes of the second order, L_p , M_p , and N_p .

Finally, on the premise of the above-performed analysis, the following equation for the “*indicatrix of conformity*, $Cnf_R(\mathcal{G}/\mathcal{P})$ ” at a point of contact of the tooth flanks, \mathcal{G} and \mathcal{P} , can be derived:

$$\begin{aligned} r_{cnf}(\varphi, \mu) = & \sqrt{\left| \frac{E_g G_g}{L_g G_g \cos^2 \varphi - M_g \sqrt{E_g G_g} \sin 2\varphi + N_g E_g \sin^2 \varphi} \right|} \operatorname{sgn} \Phi_{2.g}^{-1} \\ & + \sqrt{\left| \frac{E_p G_p}{L_p G_p \cos^2(\varphi + \mu) - M_p \sqrt{E_p G_p} \sin 2(\varphi + \mu) + N_p E_p \sin^2(\varphi + \mu)} \right|} \operatorname{sgn} \Phi_{2.p}^{-1} \end{aligned} \quad (\text{C.49})$$

Equation (C.49) of the characteristic curve²⁴ $Cnf_R(P/T)$ is known from the late 1970s.

Analysis of Eq. (C.49) reveals that the “*indicatrix of conformity, $Cnf_R(\mathcal{G}/\mathcal{P})$* ” at a point of contact of a gear tooth flank, \mathcal{G} , and the mating pinion tooth flank, \mathcal{P} , is represented by a planar centro-symmetrical curve of the fourth order. In particular cases, this characteristic curve possesses also a property of mirror symmetry. Mirror symmetry of the indicatrix of conformity is observed, for example, when the angle, μ , of local relative orientation of the tooth flanks, \mathcal{G} and \mathcal{P} , is equal to $\mu = \pm \pi \cdot n/2$, where n designates an integer number.

It is important to notice here that even for the most general case of gearing, the position vector of a point, $r_{cnf}(\varphi, \mu)$, of the “*indicatrix of conformity, $Cnf_R(\mathcal{G}/\mathcal{P})$* ” is not dependent on the fundamental magnitudes, F_g and F_p . The independence of the “*indicatrix of conformity, $Cnf_R(\mathcal{G}/\mathcal{P})$* ” of the fundamental magnitudes, F_g and F_p , is because of the following.

Coordinate angle, ω_g , at a point of the gear tooth flank, \mathcal{G} , can be calculated from the formula:

$$\omega_g = \arccos \frac{F_g}{\sqrt{E_g G_g}} \quad (\text{C.50})$$

It is natural that the position vector, $r_{cnf}(\varphi, \mu)$, of a point of the indicatrix of conformity, $Cnf_R(\mathcal{G}/\mathcal{P})$, is not a function of the coordinate angle, ω_g . Although the position vector, $r_{cnf}(\varphi, \mu)$, depends on the fundamental magnitudes, E_g, G_g and E_p, G_p , the above analysis makes it clear why the position vector, $r_{cnf}(\varphi, \mu)$, does not depend upon the fundamental magnitudes F_g and F_p .

Two illustrative examples of the “*indicatrix of conformity, $Cnf_R(\mathcal{G}/\mathcal{P})$* ” at a point of contact of a gear tooth flank, \mathcal{G} , and a mating pinion tooth flank, \mathcal{P} , are shown in Fig. C.9. The first example (see Fig. C.9a) relates to the cases of contact of a saddle-like local patch of the tooth surface, \mathcal{G} , and of a convex elliptic-like local patch of tooth surface, \mathcal{P} . The second one (see Fig. C.9b) is for the case of contact of a convex parabolic-like local patch of the tooth surface, \mathcal{G} , and of a convex elliptic-like local patch of tooth, \mathcal{P} . For both cases (see Fig. C.9), the corresponding curvature indicatrices $Crv(\mathcal{G})$ and $Crv(\mathcal{P})$ at the point of contact of the tooth flanks, \mathcal{G} and \mathcal{P} , are depicted in Fig. C.9 as well. The imaginary (phantom) branches of the “*Dupin indicatrix, $Dup(\mathcal{G})$* ” (not labeled in Fig. C.9a) for the saddle-like local patch of the gear tooth flank, \mathcal{G} , are shown in dashed line (see Fig. C.9a).

A gear tooth flank, \mathcal{G} , and the pinion tooth flank, \mathcal{P} , can make contact geometrically; however physical conditions of their contact could be violated. Violation of the physical condition of contact results in that the bodies those bounded by the

²⁴Equation of this characteristic curve is known from:

(a) Pat. No.1249787, USSR, *A Method of Sculptured Part Surface Machining on a Multi-Axis NC Machine*, S.P. Radzevich, B23C 3/16, Filed: December 27, 1984

(b) Pat. No.1185749, USSR, *A Method of Sculptured Part Surface Machining on a Multi-Axis NC Machine*, S.P. Radzevich, B23C 3/16, Filed: October 24, 1983 (in hidden form)

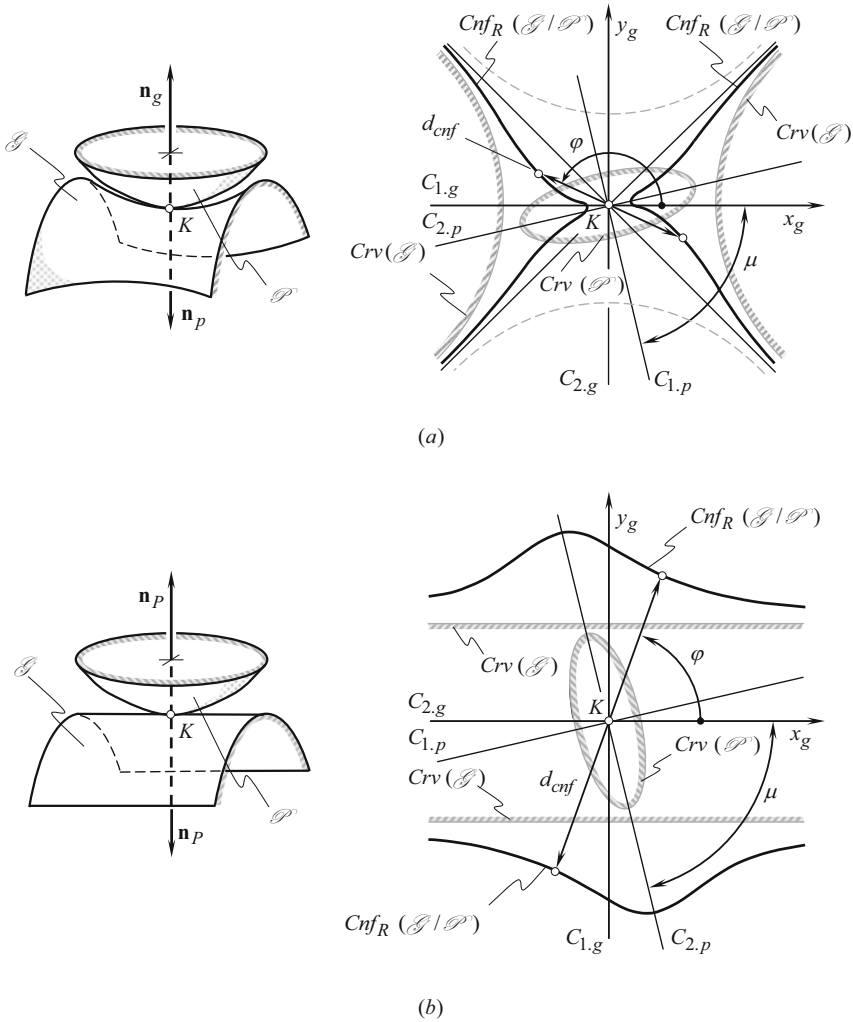


Fig. C.9 Examples of indicatrix of conformity, $Cnf_R(\mathcal{G}/\mathcal{P})$, at a point of contact, K , of a smooth regular gear tooth flank, \mathcal{G} , and a mating pinion tooth flank, \mathcal{P} , in the first order of tangency

contacting surfaces, \mathcal{G} and \mathcal{P} , interfere into one another. Implementation of the “*indicatrix of conformity, $Cnf_R(\mathcal{G}/\mathcal{P})$* ” immediately uncovers the surfaces interference if there is any. Three illustrative examples of the violation of physical condition of contact are illustrated in Fig. C.10. When correspondence between the radii of normal curvature of the contacting tooth flanks, \mathcal{G} and \mathcal{P} , is inappropriate, then the “*indicatrix of conformity, $Cnf_R(\mathcal{G}/\mathcal{P})$* ” either intersects itself (see Fig. C.10a), or all of its diameters become negative (see Fig. C.10b, c).

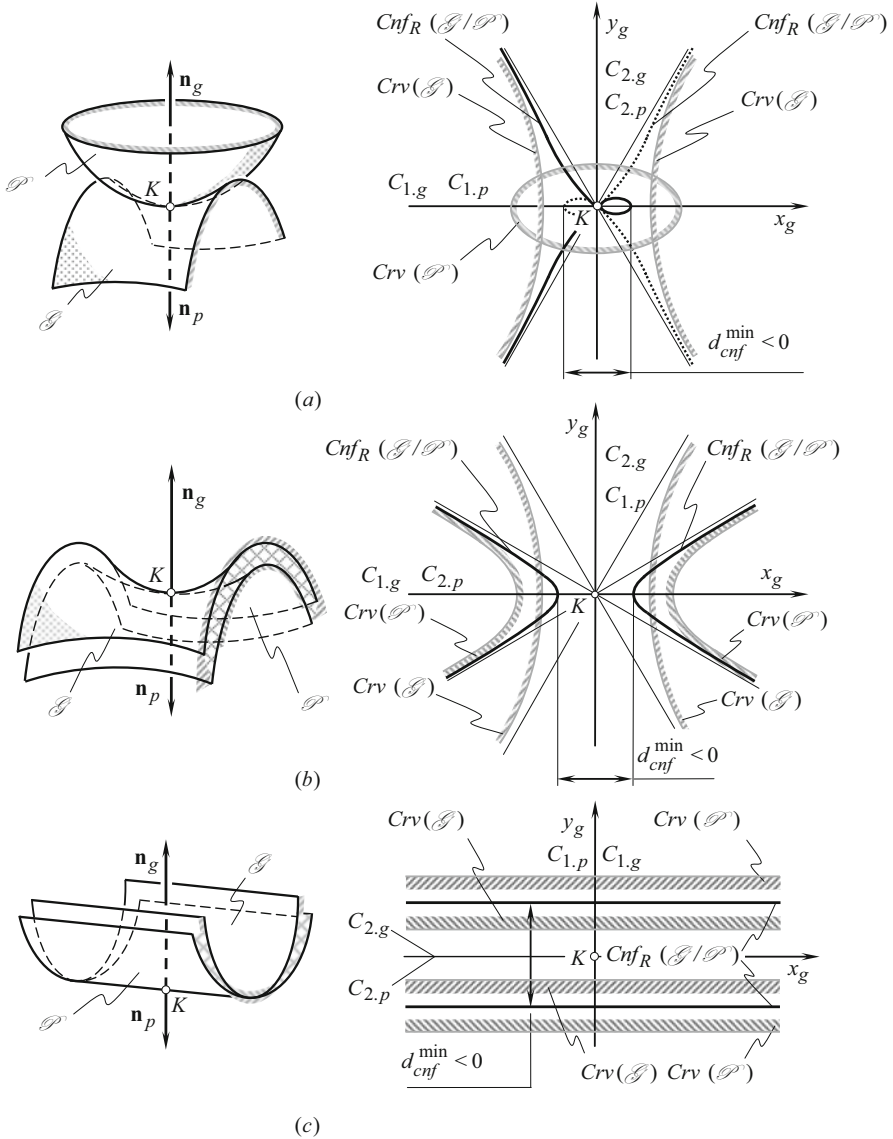


Fig. C.10 Examples of violation of physical condition of contact of a smooth regular gear tooth flank, \mathcal{G} and a mating pinion tooth flank, \mathcal{P}

Another interpretation of satisfaction and violation of physical condition of contact of two smooth regular tooth flanks, \mathcal{G} and \mathcal{P} , is illustrated in Fig. C.11. Condition of physical contact is fulfilled when all diameters of the “*indicatrix of conformity, $Cnf_R(\mathcal{G}/\mathcal{P})$* ” are positive. In this case, the gear tooth flank, \mathcal{G} , and the mating pinion tooth flank, \mathcal{P} , may contact one another like two rigid bodies do. An

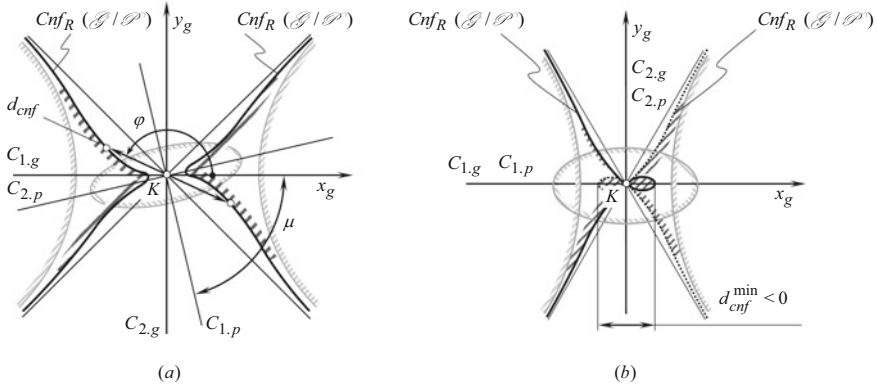


Fig. C.11 Another interpretation of satisfaction (a) and of violation (b) of condition of physical contact of a smooth regular gear tooth flank, \mathcal{G} , and the mating pinion tooth flank, \mathcal{P}

example of the “*indicatrix of conformity, $Cnf_R(\mathcal{G}/\mathcal{P})$* ” for such a case is depicted in Fig. C.11a. In cases when this planar characteristic curve has negative diameters as it is schematically shown in Fig. C.11b, physical contact between the tooth flanks, \mathcal{G} and \mathcal{P} , is infeasible.

The value of the current diameter²⁵ d_{cnf} of the “*indicatrix of conformity, $Cnf_R(\mathcal{G}/\mathcal{P})$* ” indicates the degree of conformity to each other of the gear tooth flank, \mathcal{G} , and the mating pinion tooth flank, \mathcal{P} , in a corresponding cross-section of the surfaces by normal plane through the common perpendicular. The orientation of the normal plane section with respect to the tooth flanks, \mathcal{G} and \mathcal{P} , is specified by the corresponding central angle, ϕ .

For the orthogonally parameterized gear tooth flank, \mathcal{G} , and the mating pinion tooth flank, \mathcal{P} , equation of the “*Dupin indicatrices,*” $Dup(\mathcal{G})$ and $Dup(\mathcal{P})$, simplifies to:

$$L_g x_g^2 + 2M_g x_g y_g + N_g y_g^2 = \pm 1 \tag{C.51}$$

$$L_p x_p^2 + 2M_p x_p y_p + N_p y_p^2 = \pm 1 \tag{C.52}$$

After being represented in a common reference system, use of Eq. (C.51) and Eq. (C.52) makes possible a simplified equation of the “*indicatrix of conformity, $Cnf_R(\mathcal{G}/\mathcal{P})$* ” at a point of contact of the tooth flanks, \mathcal{G} and \mathcal{P} :

²⁵Diameter of a symmetrical that possesses a property of central symmetry, curve can be defined as a distance between two points of the curve, measured along the corresponding straight line through the center of symmetry of the curve.

$$r_{cnf}(\varphi, \mu) = (L_g \cos^2 \varphi - M_g \sin 2\varphi + N_g \sin^2 \varphi)^{-0.5} \operatorname{sgn} \Phi_{2.g}^{-1} \\ + [L_p \cos^2(\varphi + \mu) - M_p \sin 2(\varphi + \mu) + N_p \sin^2(\varphi + \mu)]^{-0.5} \operatorname{sgn} \Phi_{p.T}^{-1} \quad (\text{C.53})$$

Equation (C.53) is valid for the orthogonally parameterized tooth flanks, \mathcal{G} and \mathcal{P} .

Directions of Extremum Degree of Conformity at Point of Contact of a Gear and a Mating pinion's Tooth Flanks

The directions, those along which degree of conformity at a point of contact of a gear tooth flank, \mathcal{G} , and a mating pinion tooth flank, \mathcal{P} , is extremum – that is, the degree of conformity reaches either maximal of its value or minimal of its value – are of prime importance for engineering applications. This issue is especially important for synthesizing a favorable gear pair.

The directions of extremal degree of conformity of the contacting smooth regular tooth flanks, \mathcal{G} and \mathcal{P} , that is, the directions pointed along the extremal diameters, d_{cnf}^{\min} and d_{cnf}^{\max} , of the “*indicatrix of conformity, Cnf_R(\mathcal{G}/\mathcal{P}),*” can be found from the equation of the “*indicatrix of conformity, Cnf_R(\mathcal{G}/\mathcal{P}).*” For the reader's convenience, the equation of this characteristic curve is transformed and is represented in the form:

$$r_{cnf}(\varphi, \mu) = \sqrt{|r_{1.g} \cos^2 \varphi + r_{2.g} \sin^2 \varphi|} \operatorname{sgn} \Phi_{2.g}^{-1} \\ + \sqrt{|r_{1.p} \cos^2(\varphi + \mu) + r_{2.p} \sin^2(\varphi + \mu)|} \operatorname{sgn} \Phi_{2.p}^{-1} \quad (\text{C.54})$$

Two directions within the common tangent plane are specified by the angles, φ_{\min} and φ_{\max} . These directions feature an extremum degree of conformity of the pinion tooth flank, \mathcal{P} , to the gear tooth flank, \mathcal{G} . Actually, the angles are the roots of equation:

$$\frac{\partial}{\partial \varphi} r_{cnf}(\varphi, \mu) = 0. \quad (\text{C.55})$$

It can be easily proved that in general case of contact of two smooth regular tooth flanks, \mathcal{G} and \mathcal{P} , the difference between the angles, φ_{\min} and φ_{\max} , is not equal to 0.5π . This means that the equality

$$\varphi_{\min} - \varphi_{\max} = \pm 0.5\pi n \quad (\text{C.56})$$

is not always observed, and in most cases the relationship:

$$\varphi_{\min} - \varphi_{\max} \neq \pm 0.5\pi n \quad (\text{C.57})$$

is valid (here n is an integer number). The condition [see Eq. (C.56)] $\varphi_{\min} = \varphi_{\max} \pm 0.5\pi n$ is fulfilled only in cases when the angle, μ , of local relative orientation of the contacting surfaces, \mathcal{G} and \mathcal{P} , is equal to $\mu = \pm 0.5\pi n$, and thus the principal directions, $\mathbf{t}_{1, g}$ and $\mathbf{t}_{2, g}$, of the gear tooth flank, \mathcal{G} , and the principal directions, $\mathbf{t}_{1, p}$ and $\mathbf{t}_{2, p}$, of the mating pinion tooth flank, \mathcal{P} , either aligned to each other or they are directed oppositely.

This enables one making the following statement:

Statement C.1. *In general case of contact of two smooth regular tooth flanks, the directions along which degree of conformity of the tooth flanks, \mathcal{G} and \mathcal{P} , is extremal are not orthogonal to one another.*

This statement is important for engineering applications.

The solution to equation, $\partial r_{rel}(\varphi)/\partial \varphi = 0$, returns two extremal angles, φ_{\min} and $\varphi_{\max} = \varphi_{\min} + 90^\circ$ [here $r_{rel}(\varphi)$ denotes position vector of a point of “Dupin indicatrix” at point of the surface of relative curvature]. Eq. (C.55) allows for two solutions, φ_{\min}^* and φ_{\max}^* . Therefore, the extremal difference:

$$\Delta\varphi_{\min} = \varphi_{\min} - \varphi_{\min}^* \quad (\text{C.58})$$

as well as the extremal difference:

$$\Delta\varphi_{\max} = \varphi_{\max} - \varphi_{\max}^* \quad (\text{C.59})$$

can be easily calculated.

Generally speaking, neither the extremal difference, $\Delta\varphi_{\min}$, nor the extremal difference, $\Delta\varphi_{\max}$, is equal to zero. They are equal to zero only in particular cases, say when the angle, μ , of local relative orientation of the surfaces, \mathcal{G} and \mathcal{P} , fulfills the relationship $\mu = \pm 0.5\pi n$.

Let us consider an example that illustrates the Statement C.1.

Example. As an illustrative example, let us describe analytically contact geometry of two convex parabolic patches of the contacting tooth flanks, \mathcal{G} and \mathcal{P} (see Fig. C.12). The example pertains to finishing a helical involute gear by a disk-type shaving cutter. In the example under consideration, the design parameters of the gear and of the shaving cutter, along with the specified gear and shaving cutter configuration, yield the following numerical data for the calculation. At the point, K , of the tooth flanks contact, principal curvatures of the gear tooth flank, \mathcal{G} , are equal to $k_{1, g} = 4\text{mm}^{-1}$ and $k_{2, g} = 0$. Principal curvatures of the mating pinion tooth flank, \mathcal{P} , are equal to $k_{1, p} = 1\text{mm}^{-1}$ and $k_{2, p} = 0$. The angle, μ , of local relative orientation of the tooth flanks, \mathcal{G} and \mathcal{P} , is equal to $\mu = 45^\circ$.

Two approaches can be implemented for the analytical description of the contact geometry of the tooth flanks, \mathcal{G} and \mathcal{P} . The first one is based on implementation of

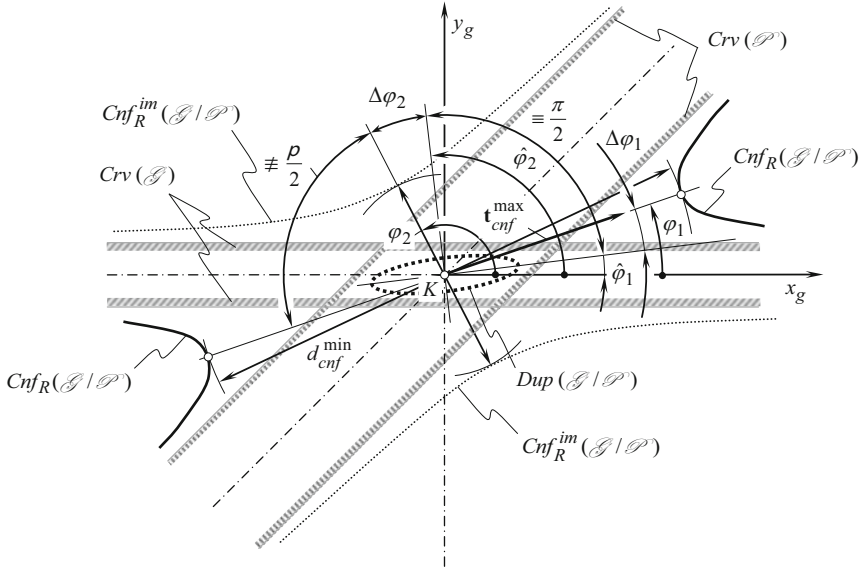


Fig. C.12 Example 5.1: Determination of the optimum instant kinematics for a gear shaving operation

“Dupin indicatrix” of the surface of relative curvature. The second one is based on the application of the “indicatrix of conformity, $Cnf_R(G/P)$ ” constructed at a contact point, K , of the interacting tooth flaks, G and P .

The first approach. In the case under consideration, normal curvature k_R of the surface of relative curvature, R , can be analytically expressed as:

$$k_R = k_{1,g} \cos^2 \varphi - k_{1,p} \cos^2(\varphi + \mu) \tag{C.60}$$

Therefore, the following equality:

$$\frac{\partial k_R}{\partial \varphi} = -2k_{1,g} \sin \varphi \cos \varphi + 2k_{1,p} \sin(\varphi + \mu) \cos(\varphi + \mu) = 0 \tag{C.61}$$

is valid for the directions of the extremum degree of conformity of the tooth flaks, G and P , at every point of their contact.

For the directions of the extremal degree of conformity at the point of contact of the gear tooth flank, G , and the mating pinion tooth flank, P , Eq. (C.61) yields the calculation of the extremal values $\varphi_{\min} = 7^\circ$ and $\varphi_{\max} = \varphi_{\min} + 90^\circ = 97^\circ$ of the angles φ_{\min} and φ_{\max} .

The direction that is specified by the angle $\varphi_{\min} = 7^\circ$ indicates the direction of the minimal diameter of the “Dupin indicatrix” of the surface of relative curvature. That same direction corresponds to the maximal degree of conformity at the point of contact of the tooth flaks, G and P . Another direction, that is specified by the angle

$\varphi_{\max} = 97^\circ$, indicates the direction of the minimum degree of conformity of the contacting tooth flanks, \mathcal{G} and \mathcal{P} , at that same contact point.

The second approach. For the case under consideration, use of Eq. (C.49) of the “*indicatrix of conformity, $Cnf_R(\mathcal{G}/\mathcal{P})$* ” at a point of contact of the gear tooth flank, \mathcal{G} , and the mating pinion tooth flank, \mathcal{P} , makes it possible the calculation of the extremal angles $\varphi_{\min}^* = 19^\circ$ and $\varphi_{\max}^* = 118^\circ$.

Imaginary branches of the “*indicatrix of conformity, $Cnf_R(\mathcal{G}/\mathcal{P})$* ” at the point of contact of the tooth flanks, \mathcal{G} and \mathcal{P} , in Fig. C.12 are depicted in dashed line.

It is important to stress the readers' attention here onto two issues.

First, the extremal angles, φ_{\min} and φ_{\max} , that are calculated using the first approach, are not equal to the corresponding extremal angles, φ_{\min}^* and φ_{\max}^* , that are calculated using the second approach. The relationships, $\varphi_{\min} \neq \varphi_{\min}^*$ and $\varphi_{\max} \neq \varphi_{\max}^*$, are generally observed.

Second, the difference, $\Delta\varphi^*$, between the extremal angles, φ_{\min}^* and φ_{\max}^* , is not equal to half of π . Therefore, the relationship, $\varphi_{\max}^* - \varphi_{\min}^* \neq 90^\circ$, between the extremal angles, φ_{\min}^* and φ_{\max}^* , is observed. In general case of contact of two sculptured surfaces, the directions of the extremal degree of conformity of the gear tooth flank, \mathcal{G} , and the mating pinion tooth flank, \mathcal{P} , are not orthogonal to one another.

The discussed example reveals that in general cases of contact of two smooth regular tooth flanks, the “*indicatrix of conformity, $Cnf_R(\mathcal{G}/\mathcal{P})$* ” can be implemented for the purpose of accurate analytical description of the contact geometry of the surfaces. The “*Dupin indicatrix*” of the surface of relative curvature can be implemented for this purpose only in particular cases of the surfaces, \mathcal{G} and \mathcal{P} , relative orientation. Application of the “*Dupin indicatrix*” of the surface of relative curvature enables only approximate analytical description of the geometry of contact of the surfaces. The “*Dupin indicatrix*” of the surface of relative curvature could be equivalent to the indicatrix of conformity only in degenerate cases of contact of the surfaces. Advantages of the indicatrix of conformity over the “*Dupin indicatrix*” of the surface of relative curvature are due to the characteristic curve, $Cnf_R(\mathcal{G}/\mathcal{P})$, which is a curve of the fourth order.

Important Properties of Indicatrix of Conformity $Cnf_R(\mathcal{G}/\mathcal{P})$ at Point of Contact of a Gear and a Mating pinion's Tooth Flanks

The performed analysis of Eq. (C.49) of the “*indicatrix of conformity, $Cnf_R(\mathcal{G}/\mathcal{P})$* ” at a point of contact of a gear tooth flank and a mating pinion tooth flank reveals that this characteristic curve possesses the following important properties:

1. “*Indicatrix of conformity, $Cnf_R(\mathcal{G}/\mathcal{P})$* ” at a point of contact of the tooth flanks, \mathcal{G} and \mathcal{P} , is a planar characteristic curve of the fourth order. It possesses the property

of central symmetry, and, in particular cases, it also possesses the property of mirror symmetry.

2. “*Indicatrix of conformity, $Cnf_R(\mathcal{G}/\mathcal{P})$* ” is closely related to the surfaces’, \mathcal{G} and \mathcal{P} , second fundamental forms, $\Phi_{2.g}$ and $\Phi_{2.p}$. This characteristic curve is invariant with respect to the kind of parameterization of the tooth flanks, \mathcal{G} and \mathcal{P} , but its equation does. A change in the surfaces’, \mathcal{G} and \mathcal{P} , parameterization leads to a change in the equation of the “*indicatrix of conformity, $Cnf_R(\mathcal{G}/\mathcal{P})$,*” while the shape and parameters of this characteristic curve remained unchanged.
3. The characteristic curve, $Cnf_R(\mathcal{G}/\mathcal{P})$, is independent of the actual value of the coordinate angle, ω_g , that forms the coordinate lines, U_g and V_g , on the gear tooth flank, \mathcal{G} . It is also independent on the actual value of the coordinate angle, ω_p , that forms the coordinate lines, U_p and V_p , on the mating pinion tooth flank, \mathcal{P} . However, parameters of the “*indicatrix of conformity, $Cnf_R(\mathcal{G}/\mathcal{P})$* ” are depending upon the angle, μ , of local relative orientation of the tooth flanks, \mathcal{G} and \mathcal{P} . Therefore, for a given pair of the tooth flanks, \mathcal{G} and \mathcal{P} , the degree of conformity of the surface varies correspondingly to variation of the angle, μ , while the pinion tooth flank, \mathcal{P} , is spinning around the unit vector of the common perpendicular.

More properties of the “*indicatrix of conformity, $Cnf_R(\mathcal{G}/\mathcal{P})$* ” at a point of contact of a gear tooth flank, \mathcal{G} , and a mating pinion tooth flank, \mathcal{P} , can be outlined.

Converse Indicatrix of Conformity at Point of Contact of a Gear and a Mating pinion’s Tooth Flanks in the First Order of Tangency

For the “*Dupin indicatrix, $Dup(\mathcal{G}/\mathcal{P})$* ” at a point of the surface of relative curvature, R , there exists a corresponding inverse “*Dupin indicatrix, $Dup_k(\mathcal{G}/\mathcal{P})$* .” Similarly, for the indicatrix of conformity, $Cnf_R(\mathcal{G}/\mathcal{P})$, at a point of contact of the tooth flanks, \mathcal{G} and \mathcal{P} , there exists a corresponding “*converse indicatrix of conformity, $Cnf_k(\mathcal{G}/\mathcal{P})$* .” This characteristic curve can be expressed directly in terms of the surfaces’, \mathcal{G} and \mathcal{P} , normal curvatures, k_g and k_p :

$$Cnf_k(\mathcal{G}/\mathcal{P}) \Rightarrow r_{cnf}^{cnv}(\varphi, \mu) = \sqrt{|k_g(\varphi)|} \cdot \operatorname{sgn} \Phi_{2.g}^{-1} - \sqrt{|k_p(\varphi, \mu)|} \cdot \operatorname{sgn} \Phi_{2.p}^{-1} \quad (\text{C.62})$$

For derivation of an equation of the “*converse indicatrix of conformity, $Cnf_k(\mathcal{G}/\mathcal{P})$* ,” the “*Euler formula*” for a surface normal curvature is used in the following representation:

$$k_g(\varphi) = k_{1.g} \cos^2 \varphi + k_{2.g} \sin^2 \varphi \quad (\text{C.63})$$

$$k_p(\varphi, \mu) = k_{1,p} \cos^2(\varphi + \mu) + k_{2,p} \sin^2(\varphi + \mu) \quad (\text{C.64})$$

Here in Eq. (C.63) and Eq. (C.64), the principal curvatures of the gear tooth flank, \mathcal{G} , are designated as $k_{1,g}$ and $k_{2,g}$, while $k_{1,p}$ and $k_{2,p}$ designate the principal curvatures of the mating pinion tooth flank, \mathcal{P} .

After substituting Eq. (C.63) and Eq. (C.64) into Eq. (C.62), one can come up with the equation:

$$\begin{aligned} r_{cnf}^{cnv}(\varphi, \mu) = & \sqrt{|k_{1,g} \cos^2 \varphi + k_{2,g} \sin^2 \varphi|} \operatorname{sgn} \Phi_{2,g}^{-1} \\ & - \sqrt{|k_{1,p} \cos^2(\varphi + \mu) + k_{2,p} \sin^2(\varphi + \mu)|} \operatorname{sgn} \Phi_{2,p}^{-1} \end{aligned} \quad (\text{C.65})$$

for the “*converse indicatrix of conformity, $Cnf_k(\mathcal{G}/\mathcal{P})$* ” at a point of contact of the tooth flanks \mathcal{G} and \mathcal{P} in the first order of tangency.

Here, in Eq. (C.65), principal curvatures $k_{1,g}$, $k_{2,g}$ and $k_{1,p}$, $k_{2,p}$ can be expressed in terms of the corresponding fundamental magnitudes E_g , F_g , and G_g of the first and L_g , M_g , and N_g of the second order of the gear tooth flank, \mathcal{G} , and in terms of the corresponding fundamental magnitudes E_p , F_p , and G_p of the first and L_p , M_p , and N_p of the second order of the mating pinion tooth flank \mathcal{P} . Following this way, Eq. (C.65) of the “*converse indicatrix of conformity, $Cnf_k(\mathcal{G}/\mathcal{P})$* ” can be cast to the form that is similar to Eq. (C.49) of the ordinary “*indicatrix of conformity, $Cnf_R(\mathcal{G}/\mathcal{P})$* ” at a point of contact of the tooth flanks, \mathcal{G} and \mathcal{P} .

It can be shown that similar to the “*indicatrix of conformity, $Cnf_R(\mathcal{G}/\mathcal{P})$* ,” the characteristic curve $Cnf_k(\mathcal{G}/\mathcal{P})$ also possesses the property of central symmetry. In particular cases of the surfaces contact, it also possesses the property of mirror symmetry. The directions of the extremal degree conformity of the gear tooth flank, \mathcal{G} , and the mating pinion tooth flank, \mathcal{P} , are orthogonal to one another only in degenerate cases of the surfaces contact.

Equation (C.65) of the “*converse indicatrix of conformity, $Cnf_k(\mathcal{G}/\mathcal{P})$* ” is convenient for implementation when:

- (a) The gear tooth flank \mathcal{G} .
- (b) The mating pinion tooth flank \mathcal{P} .
- (c) Both of them.

feature point(s) or line(s) of inflection. In the point(s) or (line(s)) of inflection, radii of normal curvature, $R_{g(p)}$ of the surface, \mathcal{G} and \mathcal{P} , are equal to infinity. Points/lines of inflection cause indefiniteness when calculating the position vector, $r_{cnf}(\varphi, \mu)$, of a point of the characteristic curve, $Cnf_R(\mathcal{G}/\mathcal{P})$. Eq. (C.65) of the “*converse indicatrix of conformity, $Cnf_k(\mathcal{G}/\mathcal{P})$* ” is free of the disadvantages of such kind, and therefore it is recommended for practical applications.

Appendix D: Closest Distance of Approach between a Gear and a Mating Pinion's Tooth Flanks

Generally, the problem of the calculation of the closest distance of approach between two smooth regular surfaces is a sophisticated and challenging. Per the author's knowledge, no general solution to the problem of calculation of the closest distance of approach between two smooth regular surfaces is available in the public domain. For the purpose of calculation of the deviation, δ_g , of the actual gear tooth flank, \mathcal{G}_{ac} , with respect to the desired (nominal) gear tooth flank, \mathcal{G}_{nom} , the problem under consideration can be reduced to the problem of computation of the closest distance of approach between two torus surfaces, Tr_g and Tr_p .

Consider a gear tooth flank, \mathcal{G} , and mating pinion tooth flank, \mathcal{P} , that initially are given in a common coordinate system, $X_h Y_h Z_h$, associated with the gear housing, as illustrated in Fig. D.1. The tooth flanks, \mathcal{G} and \mathcal{P} , are locally approximated by portions of torus surfaces, Tr_g and Tr_p , respectively. Again, not all points of the torus surfaces, Tr_g and Tr_p , can be used for the local approximation of the gear and the pinion tooth flanks, \mathcal{G} and \mathcal{P} . Only points that are located either within the biggest meridian or within the smallest meridian of the torus surface are employed for this purpose.

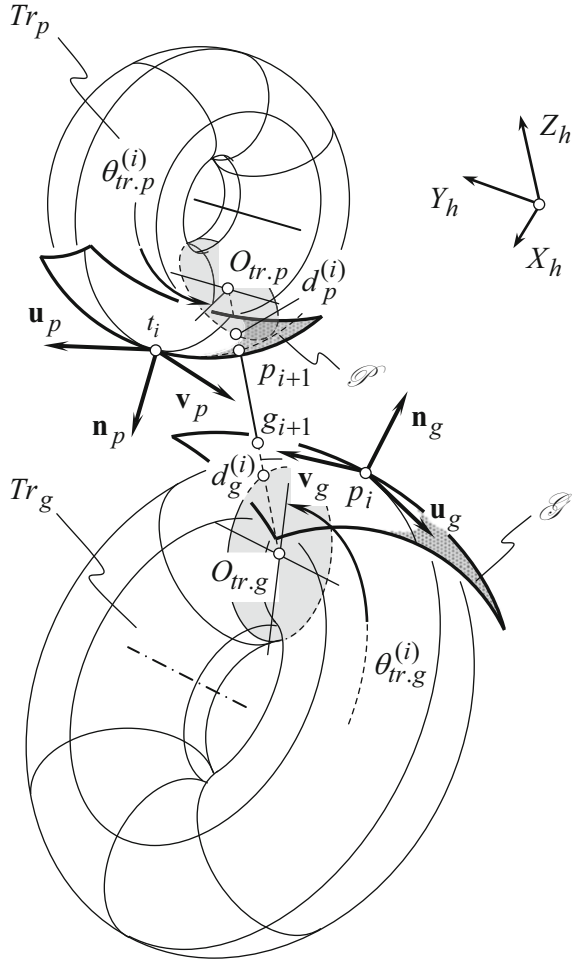
The points, K_g and K_p^* , are chosen as the first guess points on the torus surfaces, Tr_g and Tr_p . For the analysis below, it is convenient to relabel the points, K_g and K_p^* , to g_i and p_i accordingly.

For a given configuration of the torus surfaces, Tr_g and Tr_p , the closest distance of approach between these surfaces can be used as a first approximation to the closest distance of approach between the original gear and the pinion tooth flanks, \mathcal{G} and \mathcal{P} .

The closest distance of approach between the torus surfaces, Tr_g and Tr_p , is measured along the common perpendicular to these surfaces. The following equations can be composed on the premises of this property of the closest distance of approach.

Unit normal vector, \mathbf{n}_{Tr_g} , to the torus surface, Tr_g , is located within a plane through the axis of rotation of the surface, Tr_g . In the coordinate system $X_{Tr_g} Y_{Tr_g} Z_{Tr_g}$ that is associated with the torus surface, Tr_p , the equation of a plane through the axis of rotation of the torus surface, Tr_g , can be expressed in the form:

Fig. D.1 Computation of the closest distance of approach of a gear tooth flank, G , and a mating pinion tooth flank, P



$$\left[\mathbf{r}_{\tau g} - \mathbf{r}_{tr.g}^{(0)} \right] \times \mathbf{k}_{tr.g} \times \mathbf{R}_{tr.g} = 0 \tag{D.1}$$

where the following are designated:

$\mathbf{r}_{\tau g}$ is the position vector of point of the plane through the axis of rotation of the torus, Tr_g .

$\mathbf{r}_{tr.g}^{(0)}$ is the position vector of point within the plane, $\mathbf{r}_{\tau g}$ (it is assumed below that this point coincides with the origin of the coordinate system, $X_{tr.g} Y_{tr.g} Z_{tr.g}$).

$\mathbf{k}_{tr.g}$ is the unit vector of the $Z_{tr.g}$ -axis.

Equation (D.1) is expressed in terms of the radius, $\mathbf{R}_{tr.g}$. This indicates that the set of all planes through the fixed $Z_{tr.g}$ -axis forms a pencil of planes. The equation of the pencil of planes, $\mathbf{r}_{\tau g}$, in the common coordinate system, $X_h Y_h Z_h$, can be represented in the form:

$$\mathbf{r}_{\tau g}(Z_{tr.g}, V_{tr.g}, \theta_{tr.g}) = \mathbf{R}_s(Tr_g \mapsto h) \cdot \begin{bmatrix} V_{tr.g} \cdot \cos \theta_{tr.g} \\ V_{tr.g} \cdot \sin \theta_{tr.g} \\ Z_{tr.g} \\ 1 \end{bmatrix} \quad (\text{D.2})$$

The unit normal vector, $\mathbf{n}_{Tr.p}$, to the torus surface, Tr_p , is located within a plane through the axis of rotation of the surface, Tr_p . In the coordinate system, $X_{tr.p}Y_{tr.p}Z_{tr.p}$, that is associated with the surface, Tr_p , the equation of a plane through the axis of rotation of the torus surface, Tr_p , can be represented in the form:

$$\left[\mathbf{r}_{\tau p} - \mathbf{r}_{tr.p}^{(0)} \right] \times \mathbf{k}_{tr.p} \times \mathbf{R}_{tr.p} = 0 \quad (\text{D.3})$$

Here the following are designated:

$\mathbf{r}_{\tau p}$ is the position vector of point of the plane through the torus, Tr_p , axis of rotation.

$\mathbf{r}_{tr.p}^{(0)}$ is the position vector of point within the plane, $\mathbf{r}_{\tau p}$ (it is assumed below that this point coincides with the origin of the coordinate system, $X_{tr.p}Y_{tr.p}Z_{tr.p}$).

$\mathbf{k}_{tr.p}$ is the unit vector of the $Z_{tr.p}$ -axis.

Equation (D.3) is expressed in terms of the radius, $\mathbf{R}_{tr.p}$. This indicates that the set of all planes through the fixed $Z_{tr.p}$ -axis forms a pencil of planes. The equation of this pencil of planes, $\mathbf{r}_{\tau p}$, in the common coordinate system, $X_hY_hZ_h$, can be represented in the form:

$$\mathbf{r}_{\tau p}(Z_{tr.p}, V_{tr.p}, \theta_{tr.p}) = \mathbf{R}_s(Tr_p \mapsto h) \cdot \begin{bmatrix} V_{tr.p} \cdot \cos \theta_{tr.p} \\ V_{tr.p} \cdot \sin \theta_{tr.p} \\ Z_{tr.p} \\ 1 \end{bmatrix} \quad (\text{D.4})$$

A straight line through the points, $d_g^{(i)}$ and $d_p^{(i)}$, along which the shortest distance of approach, d_{gp}^{\min} , of the torus surfaces, Tr_g and Tr_p , is measured, is the line of intersection of the planes, $\mathbf{r}_{\tau g}$ and $\mathbf{r}_{\tau p}$. Therefore, this line, d_{gp}^{\min} , must be aligned with both unit normal vectors, $\mathbf{n}_{tr.g}$ and $\mathbf{n}_{tr.p}$.

In the coordinate system, $X_hY_hZ_h$, the equation for the unit normal vector, $\mathbf{n}_{tr.g}$, to the torus surface, Tr_g , yields representation in matrix form:

$$\mathbf{n}_{tr.g} = \mathbf{R}_s(Tr_g \mapsto h) \cdot \begin{bmatrix} (C_{tr.g} + \cos \varphi_{tr.g}) \cdot \cos \varphi_{tr.g} \cdot \cos \theta_{tr.g} \\ (C_{tr.g} + \cos \varphi_{tr.g}) \cdot \cos \varphi_{tr.g} \cdot \sin \theta_{tr.g} \\ (C_{tr.g} + \cos \varphi_{tr.g}) \cdot \sin \varphi_{tr.g} \\ 1 \end{bmatrix} \quad (\text{D.5})$$

where $C_{tr.g}$ designates the parameter $C_{tr.g} = 1 - \frac{R_{2.g}}{R_{1.g}}$.

Similarly, in the coordinate system, $X_h Y_h Z_h$, the equation for the unit normal vector, $\mathbf{n}_{tr.p}$, to the torus surface, Tr_p , yields matrix representation in the form:

$$\mathbf{n}_{tr.p} = \mathbf{Rs}(Tr_p \mapsto h) \cdot \begin{bmatrix} (C_{tr.p} + \cos \varphi_{tr.p}) \cdot \cos \varphi_{tr.p} \cdot \cos \theta_{tr.p} \\ (C_{tr.p} + \cos \varphi_{tr.p}) \cdot \cos \varphi_{tr.p} \cdot \sin \theta_{tr.p} \\ (C_{tr.p} + \cos \varphi_{tr.p}) \cdot \sin \varphi_{tr.p} \\ 1 \end{bmatrix} \quad (\text{D.6})$$

where $C_{tr.p}$ designates the parameter $C_{tr.p} = 1 - \frac{R_{2,p}}{R_{1,p}}$.

Evidently, the points $O_{tr.g}$, $O_{tr.p}$, $d_g^{(i)}$, and $d_p^{(i)}$ (see Fig. D.1) are located within the straight line through the centers, $O_{tr.g}$ and $O_{tr.p}$. The position vector, \mathbf{r}_{cd} , of this straight line can be calculated from the equation:

$$(\mathbf{r}_{cd} - \mathbf{r}_{cg}) \times (\mathbf{r}_{cp} - \mathbf{r}_{cg}) = 0 \quad (\text{D.7})$$

where the following are designated:

\mathbf{r}_{cg}

is the position vector of a point on the circle of a radius, $R_{tr.g}$.

\mathbf{r}_{cp}

is the position vector of a point on the circle of a radius, $R_{tr.p}$.

It is necessary that the straight line, \mathbf{r}_{cd} , be along the unit normal vectors, \mathbf{n}_{tg} and \mathbf{n}_{tp} , to the torus surfaces, Tr_g and Tr_p .

Considered together, Eq. (D.2), Eq. (D.4), and Eq. (D.7) make possible the calculation of the closest distance of approach between the torus surfaces, Tr_g and Tr_p . Then, the straight line, d_{gp}^{\min} , intersects the part surface, \mathcal{G} , and the generating surface, \mathcal{P} , of the form cutting tool at the points, g_{i+1} and p_{i+1} , correspondingly. The points, g_{i+1} and p_{i+1} , serve as the second guess to the closest distance of approach between the surfaces, \mathcal{G} and \mathcal{P} .

The cycle of the recursive calculations is repeated as many times as necessary for making the deviation of the calculation of the closest distance of approach between the surfaces, \mathcal{G} and \mathcal{P} , smaller than the maximal permissible value.

There is an alternative approach for the calculation of the closest distance of approach between two torus surfaces. The direction of the unit normal vector to an offset surface to, Tr_g , is identical to the direction of the unit normal vector, $\mathbf{n}_{tr.g}$, to the torus surface, Tr_g . This statement is also valid for the unit normal vector $\mathbf{n}_{tr.T}$ to the torus surface, Tr_p . This property of the unit normal vectors, $\mathbf{n}_{tr.g}$ and $\mathbf{n}_{tr.p}$, can be used for the modification of the method of calculation of the closest distance of approach between two torus surfaces.

The equation of the circle of radius, $R_{tr.g}$, yields matrix representation:

$$\mathbf{r}_{cg}(\theta_{tr.g}) = \mathbf{Rs}(\mathcal{G} \mapsto h) \cdot \begin{bmatrix} R_{tr.g} \cdot \cos \theta_{tr.g} \\ R_{tr.g} \cdot \sin \theta_{tr.g} \\ 0 \\ 1 \end{bmatrix} \quad (\text{D.8})$$

The equation of the circle of radius, $R_{tr.p}$, can be analytically described in the similar way:

$$\mathbf{r}_{cp}(\theta_{tr.p}) = \mathbf{Rs}(\mathcal{P} \mapsto h) \cdot \begin{bmatrix} R_{tr.p} \cdot \cos \theta_{tr.p} \\ R_{tr.p} \cdot \sin \theta_{tr.p} \\ 0 \\ 1 \end{bmatrix} \quad (\text{D.9})$$

The distance, d_{gp} , between two arbitrary points on the circles, $\mathbf{r}_{cg}(\theta_{tr.g})$ and $\mathbf{r}_{cp}(\theta_{tr.p})$, equals:

$$d_{gp}(\theta_{tr.g}, \theta_{tr.p}) = | \mathbf{r}_{cg}(\theta_{tr.g}) - \mathbf{r}_{cp}(\theta_{tr.p}) | \quad (\text{D.10})$$

The distance, d_{gp} , is minimal for a specific (optimal) combination of the parameters, $\theta_{tr.g}$ and $\theta_{tr.p}$. The favorable values of the parameters, $\theta_{tr.g}$ and $\theta_{tr.p}$, can be calculated on solution of the set of two equations:

$$\frac{\partial}{\partial \theta_{tr.g}} \mathbf{r}_{cg}(\theta_{tr.g}) = 0 \quad (\text{D.11})$$

$$\frac{\partial}{\partial \theta_{tr.p}} \mathbf{r}_{cp}(\theta_{tr.p}) = 0 \quad (\text{D.12})$$

On the solution of Eq. (D.11) and Eq. (D.12), the optimal values, $\theta_{tr.g}^{(opt)}$ and $\theta_{tr.p}^{(opt)}$, can be determined. These angles specify the direction of the closest distance of approach of the torus surfaces, Tr_g and Tr_p .

Following this method, the three-dimensional problem of calculation of the closest distance of approach of two torus surfaces is reduced to the problem of calculation of the closest distance of approach between two circles. Under a certain scenario, the last approach could possess an advantage over the previous approach.

Convergence of the disclosed algorithms for the computation of the closest distance of approach between two smooth regular surfaces is illustrated in Fig. D.2. The computation procedure is convergent regardless of the actual location of the first guess points on the surfaces, \mathcal{G} and \mathcal{P} .

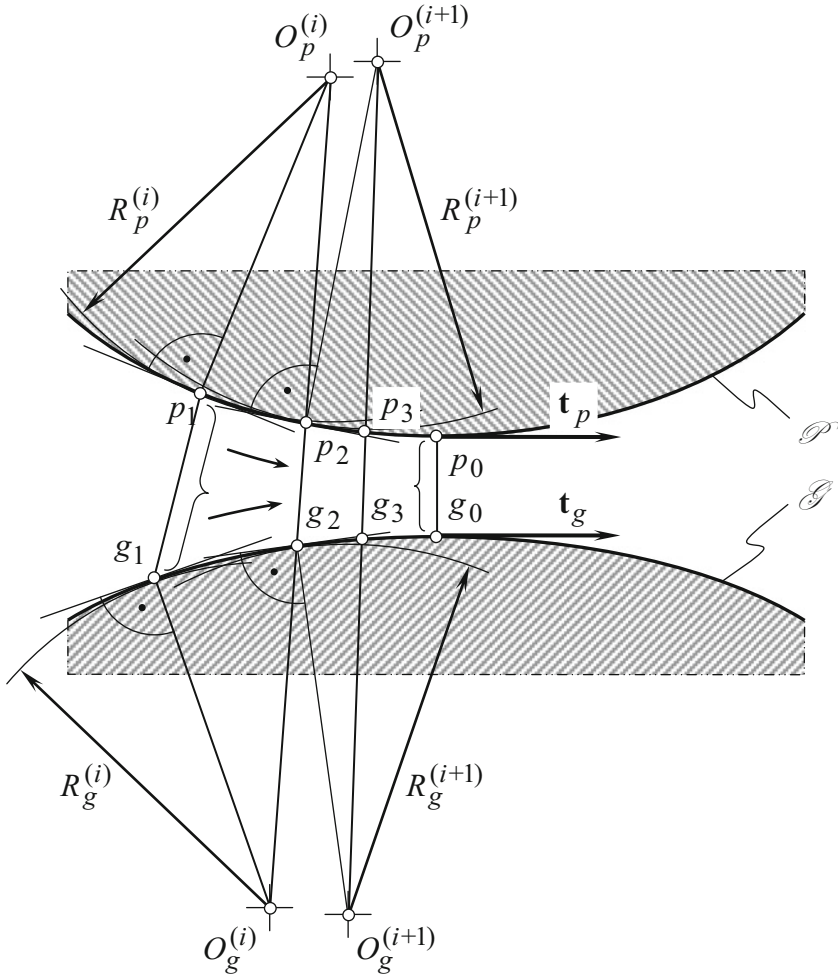


Fig. D.2 Convergence of the methods of computation of the closest distance of approach of a gear tooth flank, \mathcal{G} , and a mating pinion tooth flank, \mathcal{P}

It is instructive to draw attention here to the similarities between the disclosed iterative method for the computation of the closest distance of approach between two smooth regular surfaces, and between the “*Newton-Raphson’s method*,” the iterative method of chords, and so forth. Many similarities can be found out on this comparison.

Appendix E: On Inadequacy of the Terms “Wildhaber-Novikov Gearing” and “W-N Gearing”

“*Wildhaber Helical Gearing*” (US Patent 1,601,750, 1923) and “*Novikov Gearing*” (S.U. Patent No. 109,113, 1956) are briefly discussed below aiming to illustrate inadequacy of the terms “*Wildhaber-Novikov Gearing*” and “*W-N Gearing*.” As it follows from the discussion, helical gearing proposed by Dr. *E. Wildhaber* must be referred to as “*Wildhaber Helical Gearing*,” or so. Helical gearing proposed by Dr. *M. Novikov* must be referred to as “*Novikov Gearing*,” or so. The extensively used terms “*Wildhaber-Novikov Gearing*” and “*W-N Gearing*” are meaningless, and commonly are used by poorly knowledgeable people.

The “Wildhaber Helical Gearing”

Helical gearing with circular arc tooth profile (US Patent 1,601,750) targets an improved power capacity of the gear pair. The invention relates to the tooth shape of gears, which run on parallel axes, and may be applied to helical gears, such as single helical gears and double helical gears or herringbone gears.

The purpose of the invention is threefold:

1. To provide helical gearing with an improved tooth contact, so as to lessen surface stresses and wear.
2. To provide helical gearing, which is capable of rapid and accurate production, and which may be ground without difficulty, if so desired.
3. To provide accurate gearing of circular tooth profile.

The invention is illustratively exemplified in the accompanying drawings, in which Fig. E.1a is a side elevational view of the proposed gear showing parts thereof in section; Fig. E.1d is a normal sectional view if Fig. E.1a, is taken on the lines 2–2 of the latter figure; Fig. E.1g is a side elevational view of a pair of gears constructed in accordance with the invention; Fig. E.1h is a sectional view taken through a pair of gears; Fig. E.1b and E.1c are sectional views of milling cutters used in the

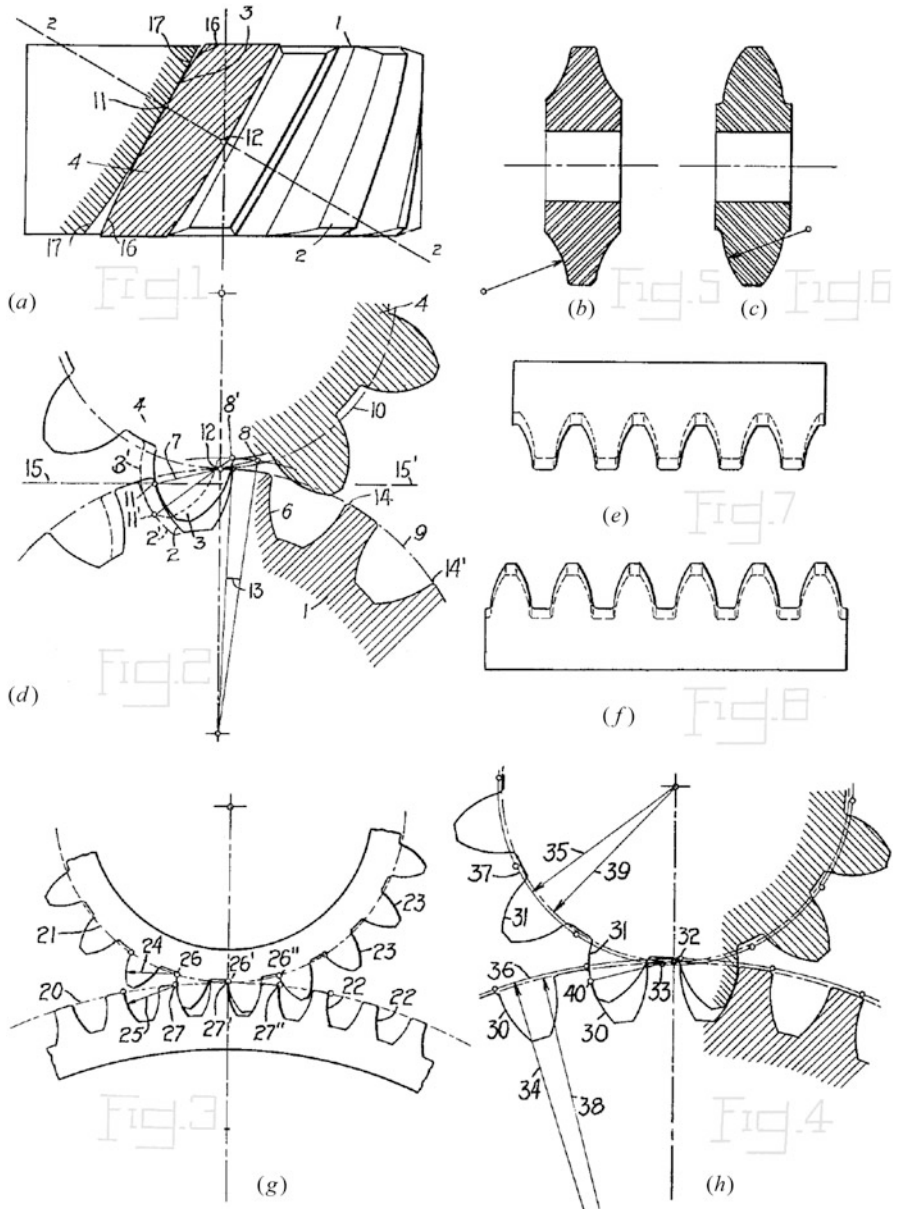


Fig. E.1 Helical Gearing. (After E. Wildhaber., US Patent 1,601,750, Patented: October 5, 1926, Filed: November 2, 1923)

manufacture of gear of the proposed design; Fig. E.1e and E.1f are elevational views of corresponding tools of rack shape, to be used in reciprocating machines for cutting helical gears in accordance with the invention; Fig. E.1k and E.1l are side elevational views of the improved gear showing a pair of grinding wheels in different operating

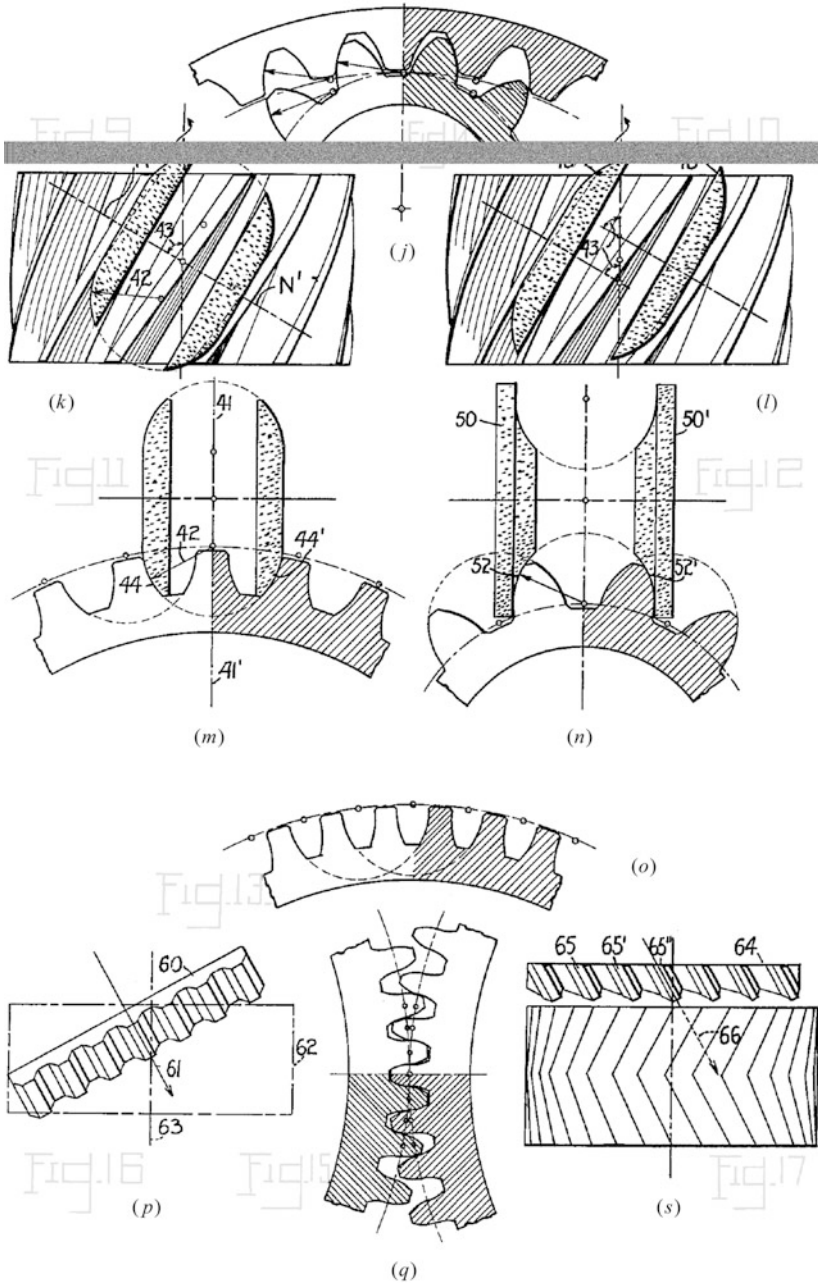


Fig. E.1 (continued)

positions, the wheels being set to grind opposite tooth surfaces; Fig. E.1m is a view of a gear taken in normal section and showing the grinding wheels in operation position; Fig. E.1n is a view of a mate pinion showing the grinding wheels in operating position; Fig. E.1o is a view of modified form of gear made in accordance with the invention; Fig. E.1j is a sectional view taken through an internal gear and its pinion; Fig. E.1 is a normal section through helical teeth of composite outline, constructed from the invention; Fig. E.1p is a view of reciprocating tool of rack shape in operating position; and Fig. E.1s is a view of a modified type of reciprocating tools, in position to start a cut on a herringbone gear.

Referring to the drawings, and particularly to Fig. E.1a and E.1d, 1 denotes a helical gear having teeth 2 in contact with the teeth 3 of a mating pinion 4. In order to clearly illustrate the degree of contact between the teeth of the gear and pinion, the tooth 4 is shown in section in Fig. E.1a.

It is customary to analyze helical gearing with reference to a normal section, that is, line 2–2 of Fig. E.1a, line 2–2 being normal to the helix of the pitch circle. Fig. E.1d illustrates the said normal sect. 2–2 for both pinion 4 and gear 1.

It has been assumed as an example that the tooth profiles 6 of gear 1 are circular arcs of radii 7 and centers 8, in the shown normal section. Centers 8 are situated close to the pitch circle 9 of the gear.²⁶ The corresponding teeth of pinion 4 are so shaped as to allow rolling of the pitch circles 9 and 10 on each other, as well known to those skilled in the art.

When the gear tooth 2 is in the position shown, in Fig. E.1a and E.1d, and its center at 8, then it contacts with tooth 3 at point 11, which may be determined by a perpendicular to tooth 2 through point 12, point 12 being the contact point between the two pitch circles 9 and 10. The said perpendicular is in the present case the connecting line between point 12 and center 8 of the tooth profile.

Another position 2' of the gear tooth and 3' of the corresponding pinion tooth are shown in dotted lines in Fig. E.1d. The tooth profiles contact here at a point 11', which can be determined like point 11. It will be noted that the contact point has traveled from 11 to 11' during a small angular motion of the gears.²⁷ The contact point has passed practically over the whole active profile during a turning angle 13 of the gear, which angle corresponds to a fraction only of the normal pitch 14, 14'. The said normal pitch equals the circle pitch of the shown normal section.

In gearing now in use, however, the tooth outline and the tooth proportions are so selected that the contact of corresponding normal profiles lasts for an angle, which, as a rule, corresponds to more than one full pitch.

²⁶Centers 8 need to be situated along the line of action, *LA*, that is a must. Otherwise, the condition of contact ($\mathbf{n} \cdot \mathbf{V}_{\Sigma} = 0$) is violated.

²⁷Once the contact point has traveled from 11 to 11' during a small angular motion of the gears, this immediately reveals that the transverse contact ratio, m_p , in the “Wildhaber’s Helical Gearing” is greater than 0, that is, $m_p > 0$, which is not permissible.

In gearing according to the invention, the contact point between two normal profiles passes over the whole active profile during a turning angle, which corresponds to less than one half the normal pitch, and usually to much less than that.

Gearing, designed according to the invention, allows the teeth to come into better contact with each other, inasmuch as the tooth surfaces remain much closer to each in a direction perpendicular to the contact line between two mating gears. This is illustrated by a section taken in direction of lines 15, 15' of Fig. E.1d. In Fig. E.1a the lateral profile 16 of tooth 3 and profile 17 of tooth 2 of said section are shown to contact at point 11, and to remain close to each other on their whole length. The same holds true for other sections, taken parallel to section 15, 15'.

Close contact between teeth is well known to reduce wear and to improve the efficiency of the gears.

Although a circular arc is shown as the normal tooth profile of gear 1, in Fig. E.1d, it will be understood that this is not the only shape to affect the stated purpose, of increasing the speed, at which the contact point travels over the tooth profile of a normal section. As a rule, however, the shape can be approximated by a circle, whose center is close to the pitch center.

The gearing according to the present invention is strictly a gearing for helical teeth. It would not be advisable on straight teeth, on account of the explained short duration of contact between tooth profiles. This would cause intermittent action, whereas on helical gears similar parts of the teeth are always in contact, on account of the twisted nature of the tooth surfaces.

Figure E.1g may be considered as a view taken in the direction of the axes of a pair of gears. The tooth profiles are the circles in a section, which is perpendicular to the axes. The gear is provided with helical teeth, with working faces below the pitch circle 20, while the pinion teeth have working faces above the pitch circle 21 only. The working profiles 22 of the gear are concave and circular, and their centers are substantially situated on the pitch circle 20. The convex working profiles 23 of the pinion are also of circular shape. Their radii 24 are substantially the same as the radii 25 of the mate profiles. The centers 26, 26', 26'' are similarly situated on pitch circle 21. Profile centers 27, 27', 27'' of pitch circle 20 and profile centers 26, 26', 26'' of pitch circle 21 correspond to each other. They coincide during the mesh, which takes place on the whole tooth profile at once.

Figure E.1g may also be considered as a section perpendicular to the helical teeth and shows then the normal tooth profiles.

Figure E.1h shows a refinement of the preferred embodiments of the invention. It is a normal section through the helical teeth, but can also be considered as a section perpendicular to the axes. Corresponding profiles 30 and 31 are circular, as in Fig. E.1g, but in this case the radius of the concave circular profile 30 is made a trifle larger than the radius of the convex circular profile 31. Consequently, the profile centers 32 and 33 do not exactly coincide during the mesh. The radii 34 and 35 of the circles 36 and 37, constituted by the profile centers 32 and 33 respectively, are not accurately identical with the pitch radii 38 and 39 of the two gears. The sum of the radii 34 and 35 is a trifle larger than the sum of the pitch radii. The radii 34 and 35 are so selected that the main tooth pressure runs about in a direction 33, 40.

The slight difference of the radii of profiles 30 and 31 facilitates the tooth contact and allows for small errors in making and assembling.

Figure E.1b and E.1c show a pair of milling cutters for milling gear teeth. The cutter may be applied in the usual manner, their axis being inclined in correspondence with the tooth inclination, that is, with the helix angle of teeth. It will be found that the cutters to be inclined for an angle, which is a trifle smaller than the helix angle in the pitch circle, for producing most accurate results.

In Fig. E.1e and E.1f a pair of rack-shaped cutters is shown.²⁸ These cutters are for use in a reciprocating machine. The teeth of these tools are relieved inwardly, in the usual manner, as evident by the dotted lines.

The convex grinding wheels shown in Fig. E.1k are illustrated in their operating positions, in a view which is taken perpendicular to the axis of the gear blank as well as to the axis of the grinding wheels, that is, in a view along the gear radii 41, 41' of Fig. E.1m. The wheels which are to produce concave circular teeth profiles in a normal section are of convex circular profile, its radius 42 being the same as the radius of the concave circular profile. The grinding wheels are inclined for an angle 43, which equals the helix angle of the teeth, in the pitch circle. The wheels grind along their profiles indicated in dotted lines 44 and 44', which are located in a normal section. As shown in Fig. E.1k, the two grinding wheels are coaxially arranged with respect to each other.

The device shown in Fig. E.1l corresponds to that shown in Fig. E.1k, with the exception that the grinding wheels 45 and 46 are not coaxially arranged. Although the arrangement shown in Fig. E.1k imposes certain restrictions on the tooth design, it is frequently preferred. The arrangement of Fig. E.1l is advantageous, when grinding wheels are not free to run out, for instance, when they must clear against a shoulder, or in the case of herringbone teeth.

Referring particularly to Fig. E.1m, a normal section is illustrated and taken along lines N, N' of Fig. E.1k. In this view, the axis of the coaxially arranged grinding wheels is situated in the said normal section. The wheels grind along the profiles 44 and 44' of the shown normal section, while the blank performs a translator motion in the direction of its axis, and, in timed relation thereto, a turning motion about its axis. In other words, the blank is screwed past the grinding wheels.

Figure E.1n discloses a normal section through the teeth of the mating gear or pinion. Grinding wheels 50 and 50' are provided with concave circular profiles 52 and 52' with which they grind the convex gear teeth.

It will be understood that milling cutters might be used instead of the grinding wheels shown in Fig. E.1k through Fig. E.1n and also that grinding wheels of a shape shown in Fig. E.1b and E.1c might be used, if so desired.

The teeth ground according to Fig. E.1k, E.1m, and E.1n are preferably so designed that the centers of opposite tooth arcs 44 and 44' and 52 and 52',

²⁸Conformal gears cannot be cut by rack cutters, and, more generally, they cannot be machined in any gear generating process.

respectively, in Fig. E.1n coincide. In Fig. E.1m and E.1n, the tooth arcs of every third tooth side have a common center.

The tooth arcs of every fifth tooth side have a common center in the normal section shown in Fig. E.1o.

In Fig. E.1m the common center of opposite tooth arcs of alternate teeth is situated on the centerline of the intermediate tooth. The corresponding pinion shows convex circular profiles, of which opposite tooth sides of adjacent teeth have common centers in the middle of the intermediate tooth space.

The normal section shown in Fig. E.1j shows an internal gear and its mate pinion, constructed in accordance with the concave tooth profiles. In external gears similarly preference is given to providing the larger gear with concave tooth profiles.

The normal section through a pair of helical gears shown in Fig. E.1q discloses opposite tooth profiles, the addendum being convex and the dedendum concave.

A rack-shaped planing tool is illustrated in operating position in Fig. E.1p. Tools of this kind have been shown in another view in Fig. E.1e and E.1f. The reciprocatory tool 60 moves in the direction 61, at an inclination, which equals the helix angle of the teeth. Gear 62, with its axis 63, is shown in dotted and dash lines. In order to cut the proper tooth shape, gear blank 62 after every cut is slightly fed in a rolling generating motion with respect to a rack which is embodied by tool 60.

Another reciprocatory tool 64 is shown in Fig. E.1s, the tool in this case being provided with stepped teeth 65, 65', 65'' which allow it to clear shoulders, and herringbone teeth. The tool moves in the direction 66 of the helical teeth, which cuts.

Other ways of producing gearing according to the invention, that is, hobbing, planing with a pinion cutter, rolling, and casting, may be contemplated, but it is not deemed necessary at this time to give a detailed explanation of the mechanism used in connection therewith.

Briefly stated, the invention consists in providing helical gearing of such profile that the tooth contact passes rapidly over the normal profile of the teeth. This has been found to result in close contact between helical mate teeth. In a direction at right angles to the contact line, the mate teeth recede from each other only slightly, and thus provide a tooth contact, which is not very far from surface contact.

It is claimed²⁹ the “*Wildhaber's gearing*” features a non-zero transverse contact ratio ($m_p > 0$) and a non-zero face contact ratio $m_F > 0$. The total contact ratio, m_t , is greater than one ($m_t \equiv m_p + m_F > 1$).

The “*Wildhaber's gearing*” (see Fig. E.1) does not meet the condition of contact. The condition of conjugacy of the tooth flanks and the condition of equality of the base pitches of the gear and the pinion to the operating base pitch are not fulfilled in this design of gearing. This immediately yields a conclusion that “*Wildhaber's gearing*” is not workable at all.

Tons of the research papers and book on “*Wildhaber's gearing*” are available in the public domain.

²⁹Wildhaber, E., *Helical Gearing*, US Patent 1,601,750, Patented: October 5, 1926, Filed: November 2, 1923

The “Novikov Gearing”

“*Novikov Gearing*” is an example of conformal helical gearing. For a long while *Novikov*’s patent (S.U. Patent No. 109,113, 1956) was not available to most of the gear experts.

Known designs of gearing, those featuring point system of meshing, feature low contact strength and are not widely used in practice.

The contact strength of known designs of gearing with a line system of meshing, including the widely used involute gearing, is limited.

The proposed gearing³⁰ (S.U. Patent No. 109,113) features higher contact strength due to favorable curvatures of the interacting tooth flanks. Under equivalent contact stress, similar dimensions, and comparable remaining design parameters, greater circular forces are permissible by the proposed gearing. Lower sensitivity to manufacturing errors and to deflections under the load is the other advantage of the proposed gearing.

The proposed gearing can be designed either with parallel, intersecting, or crossing axes of rotations of the gears. External gearing as well as internal gearing of the proposed system of meshing is possible. The tooth ratio of the proposed gearing can be either of constant value or it can be variable, and time dependent. The proposed concept of gearing can be utilized in the design of cam mechanisms.

In Fig. E.2, possible tooth profiles in the cross-section of tooth flanks by a plane that is perpendicular to the instant axis of relative rotation through the current point of contact are illustrated.

Here, the point of intersection of the planar cross-section by the axis of instant relative rotation is denoted by P .

O_1 and O_2 are the points of intersection of the planar cross-section by the axes of the gear and the pinion.

A is the point of meshing (in its current location).

PA denotes the line of action.

$\mathcal{D}A\mathcal{D}$ is the circle centered at point P which corresponds to the limit case of the tooth profiles (in the case the profiles are aligned to each other).

Several curves, BAB , represent examples of the tooth profiles of one of the mating gears. The curves BAB are arbitrary smooth curves, which are located inside of the circular arc $\mathcal{D}A\mathcal{D}$ (i.e., the arcs are located within the bodily side of the limit tooth flank of one of the gears). The curves BAB are located close to the circular arc $\mathcal{D}A\mathcal{D}$, and they feature high degree of conformity to the circular arc.

Several curves, CAC , represent examples of the tooth profiles of the second of the mating gears. The curves CAC are arbitrary smooth curves, which are located outside of the circular arc $\mathcal{D}A\mathcal{D}$ (i.e., the arcs are located within the bodily side of the limit tooth flank of another of two gears). The curves CAC are also located close

³⁰Pat. No. 109,113, (USSR). *Gear Pairs and Cam Mechanisms Having Point System of Meshing*. / M.L. Novikov, National Classification 47 h, 6; Filed: April 19, 1956, published in Bull. of Inventions No.10, 1957

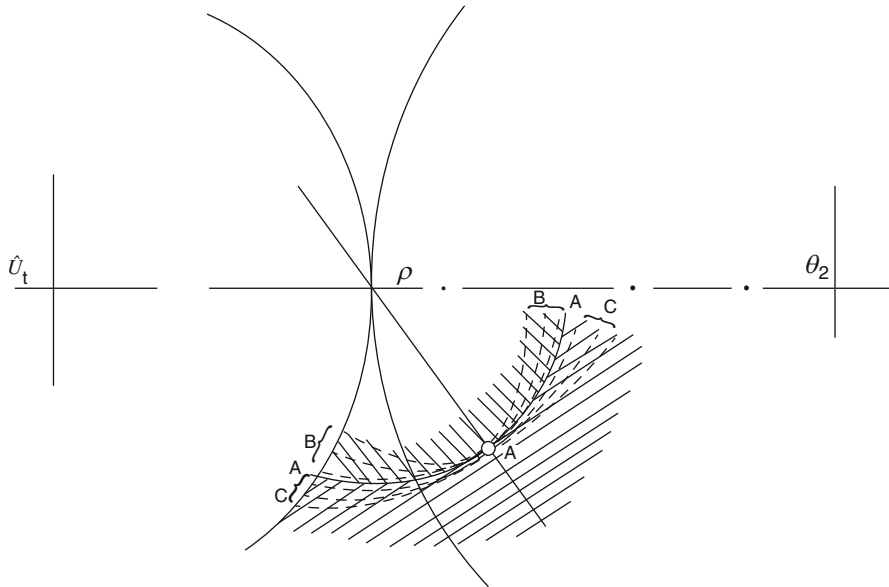


Fig. E.2 Helical gearing (After Dr. M. Novikov, Pat. No. 109,113, (USSR). *Gear Pairs and Cam Mechanisms Having Point System of Meshing.* / National Classification 47 h, 6; Filed: April 19, 1956, published in Bull. of Inventions No.10, 1957.)

to the circular arc $\mathcal{D}\mathcal{A}\mathcal{D}$, and they feature high degree of conformity to the circular arc.

The entity of the invention is disclosed below in detail.

The location and orientation either of a straight path of contact or a smooth curved path of contact is specified in space in which the location and orientation of the axes of rotations of the gear and the pinion are given. The path of contact is located reasonably close to the axis of instant relative rotation of the gears. Either constant or time-dependent (smoothly varying in time) speed of motion of the contact point along the path of contact is assigned. A coordinate system is associated with the gear, and a corresponding coordinate system is associated with the pinion. In the coordinate systems the moving contact point traces the so-called contact lines.³¹ One of the “*paths of contact*” is associated with the gear and another one is associated with the pinion. Certain smooth regular surfaces through the “*pseudo-paths of contact*” can be used as the tooth flanks of the gear and the pinion. The following requirements should be fulfilled in order for the surfaces to be used as the tooth flanks:

- At every location of the contact point, the tooth flanks should have a common perpendicular, and thus the requirements of the main theorem of meshing should be satisfied.

³¹The “*contact line*” is a term used by Dr. M.L. Novikov. Actually, the “*contact line*” is the “*pseudo-path of contact*.”

- The curvatures of the tooth profiles should correspond to each other.
- No tooth flanks interference occurs within the working portions of the surfaces.

The proposed tooth flanks fulfill the above-listed requirements and allow for high contact strength of the gear teeth.

Consider a plane through the current contact point, which is perpendicular to the instant axis of relative rotation. Then, two circular arcs are constructed. The circular arcs are centered at points within the straight line through the pitch point and the contact point. The arcs centers are located close to the pitch point. The constructed circular arcs can be considered an example of the tooth profiles of the gear and the pinion. The tooth flanks are generated as loci of the tooth profiles constructed for all possible locations of the contact point. The working portion of one of two tooth flanks is convex, while the working portion of another tooth flank is concave (in the direction toward the axis of instant relative rotation). In a particular case, the radii of tooth profiles could be of the same magnitude and equal to the distance from the contact point to the axis of instant relative rotation. The centers of both profiles in this particular case are located at the axis of instant relative rotation. Under such a scenario, point meshing reduces to a special line meshing. This would require an extremely high accuracy of the center distance and independence of it from operation conditions, which is impractical. Point meshing is preferred when designing tooth profiles. A small difference between the radii of curvature of the tooth profiles is desirable. It should be kept in mind that during run-in period of time, point meshing of the gear teeth will transform to the abovementioned *locally line* meshing of the tooth profiles. However, the theoretical point contact of the tooth flanks will be retained.

Tooth profiles can differ from the circular arcs. However, the tooth profiles of other geometries (those always passing through the contact point) should be located (for one gear) within the interior of the abovementioned circular arc profile that centers at the point within the axis of instant relative rotation as shown in Fig. E.2. For another gear, the tooth profile should be located outside the circular arc.

The law of motion of the contact point (i.e., speed of the point and its trajectory) should be chosen so as to minimize the friction and wear losses. The friction and wear losses are proportional to the relative sliding velocity in the gear mesh. Therefore, it is desirable to reduce the sliding velocity as much as possible. For this purpose, the path of contact should be located not far from the axis of instant relative rotation. On the other hand, a too-close location of the path of contact to the axis of instant relative rotation is also not desirable as that reduces the contact strength of the gear tooth flanks. In addition, it is recommended to ensure favorable angles between the common perpendicular (along which the tooth flanks of one of the gears act against the tooth flank of another gear) and between the axes of rotations of the gears.

Opposite sides of tooth profiles are designed in a similar manner to that just discussed. Tooth thicknesses and angular pitch are assigned to ensure the required bending tooth strength.

The face width of the gear or the length of the gear teeth should correlate to their pitch to ensure the required value of the face contact ratio. Gear pairs can feature either one point of contact (when working portions of the tooth flank contact each

other just in one point, excluding the phases of the teeth re-engagement), or they can feature multiple contact points when the tooth flanks contact each other at several points simultaneously.

For parallel axis gear pairs, it is preferred to use a straight line as the path of contact, which is parallel to the axes of rotations of the gear and the pinion. The speed of the contact point along the straight path of contact can be of constant value. In this particular case, the radii of curvature of the tooth profiles in all cross-sections by planes are equal to each other. Tooth flanks in this case are regular screw surfaces. Gears that feature tooth flanks of such the geometry are easy for manufacture, and they can be cut on machine tools available on the market.

An example of parallel axis gearing with limit geometry of the tooth profiles is illustrated in Fig. E.2. Point contact of the tooth flanks in this particular case is transformed to almost line contact of the tooth flanks. The curved contact line is located across the tooth profile. When axial thrust in the gear pair is strongly undesirable, herringbone gears can be used instead.

“*Novikov gearing*” (see Fig. E.2) meets the condition of contact, as well as it meets the condition of conjugacy of the tooth surfaces, and the condition of equality of the base pitches of the gear and the pinion to the operating base pitch. “*Novikov gearing*” is a type of perfect gearing.³² “*Novikov gearing*” is the only feasible type of gearing with point contact of the tooth flanks that is capable of transmitting a rotation smoothly. As it is clear now, “*Novikov gearing*” is a reduced type of involute gearing.

The invention by *Novikov* got no expansive investigation, as “*Wildhaber Gearing*” did. The inadequacy of the terms “*Wildhaber-Novikov Gearing*” and “*W-N Gearing*” is disclosed in several scientific papers and monographs “*Novikov Gearing*,” available in the public domain.

References

1. doCarmo, M.P., *Differential Geometry of Curves and Surfaces*, Englewood Cliffs, NJ: Prentice-Hall, 1976, 503p.
2. Eisenhart, L.P., *A Treatise on the Differential Geometry of Curves and Surfaces*, London, Dover Publications, Inc., 1909; New York, reprint 1960, 474p.
3. Struik, D.J., *Lectures on Classical Differential Geometry*, 2nd Edition, Addison-Wesley Publishing Company Inc., Massachusetts, 1961, 232p.

³²It needs to be noticed here that Dr. *E. Wildhaber* did not recognize the difference between “*Novikov gearing*” and the helical gearing proposed by him. This conclusion immediately follows from the *Wildhaber*’s statement: “I may say also that it gives me satisfaction to see the original concept vindicated through the Russian reinvention and effort and through subsequent efforts and articles.” This *Wildhaber*’s statement can be found on page 949 in the paper by T. Allan [Allan, T., “Some Aspects of the Design and Performance of Wildhaber-Novikov Gearing,” *Proc. Inst. MecE. Engrs, Part I*, v. 179, n. 30, 1964/1965, pp. 931–954.] (see the *Communications* section). Other evidences in this concern are also known.

Index

A

- Aligned (reduced) efficiency, 361
- Aligned (reduced) torque ratio, 349
- Angular base pitches, 267, 268
- Antikythera mechanism, 408, 409
- Approximate gearing
 - concave axial profiles, 41
 - convex axial profile, 41
 - evaluation, 23
 - feature straight axial profile, 42
 - generic surfaces, 22, 23
 - geometrically accurate gearing, 22
 - geometries of axial profile
 - analytical description, 23, 24
 - angular parameter, 25
 - circular-arc axial profile, 30, 34
 - consecutive positions, 23
 - conventional machine tools, 37
 - convex circular-arc axial profiles, 32
 - Darboux frame, 25, 27, 32, 34
 - feature axial profile, 32
 - Gauss parameter, 25
 - gear generic surfaces, 27, 34
 - geometries, 37
 - hyperbolas, 23
 - hyperbolic arc segment, 28
 - hypoid gearing, 28
 - local reference system, 25
 - methods, 29
 - principal directions, 26
 - rotation vector, 25
 - straight-line axial profile, 28
 - straight-line segment, 27, 31, 34
 - unit tangent vectors, 26, 27
 - implementation, 43, 45, 46, 48

- machining/generating process, 42
- rotation vectors, 22

B

- Broaching, 294, 295, 322
- 2-BRZ program (software)
 - characteristics analysis, 385, 386
 - input data, 387
 - single- and two-speed two-carrier, 384
 - solution evaluation, 386, 387
 - variants synthesis, 386

C

- Camus' gearing principle, 416
- Cartesian coordinate system, 249
- Center-distance, 2, 3, 8, 9, 14, 16
- Center-line plane, 263
- Charles Etienne Louis Camus, 241, 415
- Classification of gear pairs, 22
- Combined processing, 295
- Conceptual design, 184, 185, 190
- Condition of conjugacy, 266, 267
- Condition of contact, 261
- Condition of equality of base pitches, 268
- Conformal kinematic pairs, 111
- Conjugate action law, 241, 243, 255
- "Construction bricks", 188, 190
- Contact geometry, 265
 - curves, 96
 - Dupin indicatrix, 97
 - indicatrix of conformity, 97, 98, 100
 - surfaces, 96
- Convex functional surfaces, 106, 129

Convex-to-concave contact, 122
 Convex-to-hyperbolic, 125
 Coupling power, 357
 Crossed-axes angle, 3, 5, 14, 16, 22
 Crossed-axes gearing, 244, 256, 260, 266, 268,
 269, 278, 279, 282, 283, 285, 286
 Cutting wedges, 310

D

Data acquisition (DAQ), 75
 da Vinci, L. (1452–1519), 413, 414
 Decomposition, 211
 Design process, 189, 239
 Development of gears
 Antikythera mechanism, 408, 409
 antiquity time, 407, 409, 410
 discoveries
 by Camus, 415
 by de la Hire, 415
 by da Vinci, 413, 414
 by Desargues, 415
 by Euler, 415, 417
 with electric power, 419
 emergence, 405–407
 gear science in the nineteenth century, 421
 grooved roller gears for rolling mills, 429
 internal combustion engine, 420
 intrinsic property, involute gear, 426
 Jungfrau locomotive, 420
 mating gears, 430
 mechanical clocks, 412, 413
 Middle Ages, 410, 411
 until 1940
 cutting technology, 425
 dimensioning, 424
 involute gearing, 423
 ISO committee TC60, 426
 manufacturers, 423
 national organizations, 426
 sources of power, 423
 standardization, 424
 wear, gear flanks, 424
 at ZF factory, 424
 Novikov gears, 427, 428
 patented non-involute, 428
 path of contact, 429
 rack profile flank, 430
 Roman times, 409, 410
 S-gears, 430
 UPT gears, 428, 429
 VBB gearing, 426, 427
 Watt's invention, 418, 419

WN gears, 427, 428
 word clock, 412
 Dupin indicatrices, 265

E

Efficiency, 356, 357, 360–362
 chamfer surface reproduction, 196
 Electric motors, 423
 Emergence, gears, 405–407
 Energy consumption, 196
 Euler-Savary formula
 bar mechanism, 254
 configuration, 252
 conjugate action law, 255
 constant velocity ratio, 252
 fundamental contribution, 256–271
 gear/pinion base pitch, 255
 gear wheels, 248
 interpretation, 255
 invention, 255, 256
 operating base pitch, 255
 parallel-axes gearing, 254, 255
 parameters, 252
 planar curves, 249
 planar motion, 249, 251
 principle, 255
 tooth geometry, 255
 variables, 249
 wheels, 252
 Euler's involute gearing, 417

F

Fiber reinforcements, 146
 Flexibility, 196
 Four gear chamfering methods, 211
 Fundamental theorem of parallel-axes
 gearing, 256
 FZG (Gear Research Centre) efficiency
 test rig, 159

G

Gear chamfering mechanisms
 accurateness, 195
 chamfering methods, 199
 classical approach, parametric design, 224
 comb mill, 201, 204
 conceptual design, parametric design, 225
 database, linear model, 216, 217
 edge γ , 199
 efficiency, 196

- end mill, 200, 201
- features, 195
- flexibility, 196
- gear engagement and equidistant tracking, 217, 220
- gear engagement and helical movement, 221
- general requirement, surface formation, 196
- kinematical simplicity, 196
- linear model, 214, 215
- mathematical and physical connections, 200
- mathematical expressions, 217
- parametric design and optimization, 221, 223, 224
- physical processing, 199
- plastic deformation, 207, 210
- point model, 199
- procedure, parametric design, 225
- simplicity, 196
- surface composition lines, 196
- surface micro-roughness, 229
- synthesis, 211, 216
- synthesized mechanism to parametric design, 230
- tool simplicity, 215
- Gear chamfering, 184, 193–195
- Gear design and manufacturing, 183
- Gear generic surfaces
 - actual value, 40
 - axial plane, 37
 - configurations, 40
 - coordinate system transformation, 38, 39
 - Darboux frame, 37
 - geometries, 41
 - interpretation, 40
 - local reference system, 39
 - reference system, 38
 - rotation, 37
 - unit tangent vector, 38–40
- Gearing
 - achievements, 234
 - analysis, 234
 - application, 234
 - art and science, 235
 - bevel gearing, 277
 - chronological order, 234, 235
 - classification, 1
 - crossed-axes gearing, 278
 - design, 233
 - development, 1
 - double-enveloping worm gearing, 277
 - efforts, 284, 285
 - evolution
 - angular velocity ratio, 236
 - development and investigation, 236
 - kinematics, 236
 - periods, 237
 - rotation, 236
 - face gearing, 279
 - favorable approximate gearing, 280
 - field, 1
 - foundation, 235
 - geometry, 233, 235
 - in-depth analysis, 1
 - industry and commerce, 233
 - “key mistakes”, 235
 - kinematics, 233
 - manufacture, 233
 - motivation, 236
 - non-circular, 280
 - origination, 2
 - parallel-axes gearing, 248
 - post-Eulerian period
 - angular base pitches, 267, 268
 - Chaim Gochman, 259
 - condition of conjugacy, 266, 267
 - contact geometry, 265
 - equality, 260
 - equation of conjugacy, 269–271
 - gear art, 258
 - parallel-axes gearing, 256, 257
 - principal planes, 263, 264
 - reference systems, 263, 264
 - scientific classification, 269
 - Shishkov equation of contact, 261, 262
 - Theodore Olivier, 257, 258
 - tooth flank, 260, 261, 269
 - practical application, 2
 - pre-Eulerian period
 - Antikythera mechanism, 238
 - clockmakers, 240
 - condition of contact, 244
 - cyclic curves, 241
 - descriptions, 237
 - epicyclic gearing concept, 240
 - epicycloidal shape, 240
 - epicycloids, 241
 - equal velocity, 244
 - evidence, 238
 - exterior cycloids, 241
 - field, 244
 - force-multiplying properties, 237
 - frictional contact, 237
 - geometry, 241
 - instrument makers, 240
 - line of action, 242, 243
 - mathematicians, 240
 - mechanical advantage, 237
 - mechanical clock, 240

Gearing (*cont.*)

- numerous designs, 240
 - path of contact, 242, 243
 - rolling-cone principle, 243
 - rotary motion, 241
 - rotation, 237
 - theory of mechanism, 243
 - road map, 1
 - state of the art, 279
 - tentative chronology, 280, 282–284
 - transformation, 233
 - transmissions, 233, 236
- Gear manufacturing, 422, 423
- Gear milling of hob, 311
- Gear pair
- advantage, 20
 - complementary degrees-of-freedom
 - fundamental design parameters, 6, 7
 - mechanical devices, 6
 - noncircular gears, 6
 - crossed-axes gearing, 2, 18
 - geometry, 21
 - kinds of gearing, 2
 - lines of contact, 18
 - planar curves, 21
 - plane-of-action apex, 20
 - pseudo-straight crossed-axes, 20
 - screw surfaces, 20
 - straight-line segments, 20
 - tooth flanks, 20, 21
 - vector diagrams
 - angle, 5, 6
 - application, 3
 - center-distance, 3
 - conventional design, 5
 - crossed-axes, 3, 5, 6
 - rotation vectors, 3, 5
- Gear processing
- constraining factors, 295
 - with worm cutting tools, 295
- Gears
- art of gearing, 240
 - gearing of old designs, 239
 - machines and mechanisms, 293
 - machining high-precision gears, 295
 - methods for manufacture, 293
 - processing gears, 294
 - wind and water wheel machinery, 239
- Gear vector diagrams
- classification, 7, 8
 - one-degree-of-freedom, 11–13
 - three-degree-of-freedom, 9
 - two-degree-of-freedom, 10, 11
 - zero-degree-of-freedom, 13, 14, 16–18

- Generic gear surface, 25, 30, 34, 37, 43, 44
- Geometric Theory of Gearing, 257
- Geometrically accurate gearing, 236
 - Gavrilenko, V.A., 275
 - grant bevel gearing, 271
 - Kolchin, N.I., 274
 - Musser, W., 276
 - Novikov conformal gearing, 274, 275
 - Phillips, J.R., 275
- Glass/carbon fibers, 146

H

- Harmonic drive, 276
- Helicon gearing, 46
- High-molecular polyethylene of high density (PE-HD), 145
- Hyperbolic-to-hyperbolic, 125
- Hyperboloid-type hobs
 - accuracy and performance
 - Archimedean spiral, 300
 - backed-off cutters, 300
 - backing-off surface, cutter teeth, 300
 - on CNC machines, 295
 - convolute ZN worms, 299
 - designing gears and tooth profiles, 296
 - design of worm tools, 298
 - errors of profiling, 302–305, 307–309
 - high-precision worms, 299
 - installation options, 296
 - involute ZI worms, 299
 - method of screw movement, 299
 - “milling cutter—cut gear” pair, 302
 - performed analysis, 301
 - processing gears, 301
 - productivity of machining, 308–317
 - profiling accuracy, 299
 - sharpening milling cutter teeth, 300
 - stage of formation, 298
 - technical and economic indicators, 296
 - tool surface, 302
 - working bodies, 299
 - worm gear cutting tools, 297
 - worm milling cutters, 296
 - worm tools, 295
 - auxiliary motions, 327
 - back center deflection, 328
 - CNC lathes, 331, 334
 - cylindrical technology, 330
 - design features
 - advantage, point profiling, 324
 - applied tool materials, 318
 - carbide tool materials for milling cutters, 319

- cylindrical hobs and worm shaver, 324
 - development of technical systems, 318
 - disk backed-off milling cutters, 318
 - faceting growth reduction, 321
 - hard alloy production, 318
 - hyperboloid milling cutters, 324
 - individual profiling, cutter plates, 324
 - MTHs, 321
 - non-sharpening hobs and platers, 319
 - placement, cutting plates, 323
 - rational cutting insert design, 322
 - reinstallations, 322
 - safety and environmental friendliness, 319
 - sharpening, 321
 - super-hard materials, 325
 - technologies and equipment, 318
 - thickness, cutting plate, 322
 - worm milling cutters improvement, 319
 - disadvantages, machine upgrades, 331
 - drawback, machining hyperboloid worms, 326
 - finishing machining, 327
 - generation, hyperboloid main worm, 326
 - implementation, proposed method, 327
 - longitudinal and transverse feeds tool, 325
 - milling cutters, 331
 - parameters, hyperboloid worms and allowances, 332
 - processing, 326
 - rough processing, 329
 - second-order blade tools, 328
 - transverse axis of symmetry, 329
 - worm inclination, 327
- I**
- Ideal gearing, 236
 - Indicatrix of conformity, 97–99, 265
 - Instantaneous center of rotation, 249
 - Internal combustion engine, 420
 - Intersected-axes gearing, 244, 260, 266, 268, 271, 276, 279
 - Involute gearing, 415, 421, 423, 429
 - Involute gears, 51, 52, 54, 58, 67, 428
 - Iron gears, 414
- K**
- Kinematic pairs
 - analysis, 94, 95
 - classifications, 92, 137–139
 - concave surfaces, 102
 - conformity criterion
 - bearing capacity, 121
 - “convex-to-concave” contact, 120
 - degree of conformity, 121
 - 3D-plot, 119, 120
 - functional surfaces, 118, 119
 - high-conformal contact, 117, 120, 121
 - indicatrix of conformity, 120
 - normalized design parameters, 118
 - operating load, 118
 - plane section, 117, 118
 - definition, 102
 - degree of freedom, 102
 - design, 94, 95
 - features, 94
 - functional surfaces, 100, 101
 - gearing, 90
 - high-conformal point-contact, 115–117, 122, 123, 125, 127
 - instantaneous kinematics (mobility), 95
 - interacting functional surfaces, 93
 - locally-line-contact, 111, 112, 114
 - locally surface-to-surface contact, 114, 115
 - machine theory, 90
 - mechanisms, 90
 - morphological matrix, 102
 - motion of elements, 91
 - physical constraints, 104
 - simple machine, 89
 - surface-to-surface contact, 92, 93, 135–137
 - true-point-contact, 104, 106, 108, 109, 111
- Kinemematical simplicity, 196
- L**
- Line-contact kinematic pairs
 - high-conformal point-contact, 134
 - locally surface-to-surface contact, 132, 133
 - true-line-contact, 129–131
 - Load carrying capacity, plastic gears
 - frictional wear load carrying capacity, 153
 - tooth flank load carrying capacity, 152, 169, 172
 - tooth root load carrying capacity, 152, 153, 163, 165, 168
 - Locally-line-contact, 111, 112, 114
- M**
- Machine-building technologies, 183
 - Machining high-precision gears, 294
 - Mechanical design
 - author’s experience, 187, 188
 - Mechanical object analysis, 185

- Metalworking, 183
- Modern gears, 414
- Modification, 191
- Modification formats
 - analyses, 192, 193
 - parametric design, 193
 - synthesis, 191, 192
- Multi-objective optimization procedure
 - approach, 380
 - coaxiality condition, 381
 - efficiency, 380
 - generalized criterion, 382
 - kinematic capabilities, 380
 - nondimensional purpose evaluations, 382
 - nondimensional quantitative measures, 381
 - parameters, 381
 - Pareto optimization, 379
 - speed ratio, 379
 - structural scheme
 - advantage, 383
 - characteristics, 383
 - desired speed ratios, 383, 384
 - kinematic criterion ratio, 383
 - nondimensional values, 383
 - normalization, 383
 - single-factor optimizations, 382
 - values, 379
 - weight coefficients, 382
- Multiple-thread hobbing (MTH), 315, 316, 321

- N**
- Normal plane, 263
- Novel task-based conceptual design method, 187
- Novikov gears, 427, 428
- “Nullus a tritus oriatur”, 248

- O**
- Optimal compound PGT variant
 - single-speed, 387–390
 - two-speed, 390–392
- Organic errors, 302

- P**
- Parametric design
 - and optimization, 186
- Perfect gearing, 236
- Pinion apex, 264
- Pitch-line plane, 263
- Plane-of-action apex, 263, 264

- Planetary gear trains (PGTs)
 - advantages, 353
 - backlash
 - compound external shaft, 366, 368
 - input and output shaft, 366
 - meshings, 364, 365
 - particle structural scheme, 366
 - ring gear, 365, 368
 - shaft, 370–372
 - single external shaft, 368
 - structural schemes, 364, 372
 - sun gear, 365
 - characteristics, 342
 - contact ratio factor, 354
 - control parameters, 341
 - design requirements, 343
 - determination, torques, 358
 - efficiency, 356, 357, 360–362
 - elasticity factor, 354
 - elements optimization, 341
 - face load factor, 354
 - internal dynamic factor, 354
 - kinematic capabilities, 350
 - kinematics, 356
 - load capacity, 353
 - meshing optimization, 339, 340
 - mesh load factor, 354
 - multifactor optimization, 344
 - multi-objective optimization, 342
 - optimal solution, 341
 - permissible contact stress, 354
 - PGT, 343
 - purposes of optimization, 349
 - quality, 339
 - reduced stiffness, 375, 376, 379
 - reliability, 339
 - stress limit, 342
 - structural analysis, 344–346
 - structural schemes, 355
 - technical and economic criteria, 341
 - tooth geometry, 343
 - torque method, 347, 348, 356
 - torque ratios, 353
 - torques, 350
 - transverse load factor, 354
 - Wolf-Arnoudov structural symbol, 349
 - zone factor, 354
- Planocentric gearboxes, 53
 - backlash, 75, 76
 - gradual development, 73, 74
 - influence of geometric tolerances, 79, 80
 - kinematic circumstances, 71, 72
 - kinematic error, 77, 78

- planet gears, 69
 - routout, 81–84
 - single pitch deviation, 81–84
 - stiffness, 75, 76
 - Plastic gears, 52, 53
 - automotive sector, 145
 - challenge for use, 178
 - design and calculation methods
 - frictional wear load carrying capacity, 153
 - tooth flank load carrying capacity, 152, 153
 - tooth root load carrying capacity, 152
 - tooth temperature, 149–151
 - drive unit, e-bikes, 145
 - fields of application, 149
 - gear temperature, 154
 - humidity, 146
 - manufacturing, 148
 - mechanical properties, 146
 - motion transmission in actuators, 145
 - temperature distributions, 155
 - thermal behavior, 149, 155–157
 - tooth root load carrying capacity, 163, 165, 168
 - tooth temperatures, 154
 - tribological behavior, 174–178
 - Polyamide (PA), 52, 145
 - Polybutylene terephthalate (PBT), 52, 146
 - Polyetheretherketone (PEEK), 52, 146, 169, 170, 172, 173
 - Polyoxymethylene (POM), 52, 145
 - Polytetrafluoroethylene (PTFE), 146
 - Powder spray, 294
 - Precision casting, 293
 - Principal reference systems, 264
- R**
- Rolling broaching, 294
 - Roman water mill, 410
 - Rotary motion, 241, 244, 248, 260, 267, 274
 - Rotation vector, 3, 5, 14, 16, 17, 22, 25
- S**
- Self-consistent scientific theory of gearing, 284, 286
 - Semi-conformal kinematic pairs, 106
 - Servo motors (SM), 75
 - S-gear geometry
 - analytical approach, 59, 60
 - contact analysis, 67
 - convex-concave contact, 51
 - E-gear pair, 64
 - higher quality, 51
 - intrinsic property, 51
 - loading capacity, 51
 - manufacturing, 61, 62
 - planocentric gear boxes, 53
 - plastic gears, 52, 53, 60
 - plastic materials, 68
 - steel-POM gear pair, 64
 - temperature, 65, 67
 - temperature-time dependency, 64
 - temperature-time diagram, 68
 - testing arrangement, 62, 63
 - thermoplastic gears, 64
 - transmit power, 51
 - wear detection, 69, 70
 - Shishkov equation of contact, 261, 262
 - Single-sided pin gearing, 416
 - Single-thread hobbing (STH), 316
 - Spiroid gearing, 46
 - Standard-based formats, 191
 - Standard milling cutters, 314, 322
 - Steam engine, 411, 417–419, 431
 - Sun dials, 412
 - Surface-to-surface contact, 95
 - Synthesis development format, 191, 192
- T**
- Task-based analyses, mechanical objects, 185
 - Task-based conceptual design, 184, 185
 - and optimization, 186
 - Temperature measurements, 60
 - Thermal properties
 - energy loss, 57
 - external tooth root, 56
 - flank and tooth shape, 54
 - heat, 57
 - kinematic pole, 54
 - length difference, 58
 - path of contact characteristics, 57
 - power of friction, 59
 - power transmission, 57
 - rack profiles, 54
 - scaling factor, 54
 - S-gears, 53
 - transformations, 54
 - trigonometrical procedure, 54
 - Thermoplastic materials, 146
 - 3D printing, 294
 - manufacturing processes, 294
 - Threesome gear train, 422

Tooth rolling, 294
Torque method, 347, 348
Transformation, 233
Translation vector, 23
Transmission, 233
True-point-contact, 104, 106, 108, 109, 111

U

Überlingen clock mechanism, 413

V

VBB (Vickers–Bostock–Bramley) gearing,
426, 427
Visualization, 189, 190

W

Water clocks, 412
Watt, J., 418, 419
Watt steam engine, 419
Whim-based lifting machine, 412
Worm cutting gearing, 310
Worm gear cutting tools, 295
Worm gears, 407
Worm-type grinding wheel, 294, 300, 301,
305, 326, 327
Worm-type shavers, 302, 305, 308, 309,
324, 325

Z

Zero degrees of complexity, 196